Transient Chaos

Complex Dynamics on Finite-Time Scales

Springer

Applied Mathematical Sciences
Volume 173

Ying-Cheng Lai · Tamás Tél

Transient Chaos

Complex Dynamics on Finite-Time Scales

Springer

Ying-Cheng Lai
Department of Electrical Engineering
Arizona State University
Tempe Arizona
USA
Ying-Cheng.Lai@asu.edu

Tamás Tél
Department of Theoretical Physics
Institute of Physics
Eötvös University
1117 Budapest
Hungary
tel@general.elte.hu

Printed on acid-free paper

Preface

In a dynamical system, transients are temporal evolutions preceding the asymptotic dynamics. Transient dynamics can be more relevant than the asymptotic states of the system in terms of the observation, modeling, prediction, and control of the system. As a result, transients are important to dynamical systems arising from a wide range of disciplines such as physics, chemistry, biology, engineering, economics, and even social sciences. Research on nonlinear dynamical systems has revealed that sustained chaos, as characterized by a random-like yet structured dynamics with sensitive dependence on initial conditions, is ubiquitous in nature. A question is, then, can chaos be transient?

A common perception, as conveyed in many existing books on nonlinear dynamics, is that chaos is an asymptotic property that manifests itself only after a long observation. Indeed, standard characteristics of chaos, such as the Lyapunov exponents that measure the exponential separation rates of nearby trajectories and hence quantify the degree of the sensitivity to initial conditions, are defined in the infinite time limit. These features seem to be incompatible with the possibility of chaotic transients.

Research on nonlinear dynamics has shown, however, that the essential feature of chaos is the existence of so-called *chaotic sets* in the phase space, and quantitative characterization of chaos is meaningful with respect to the dynamics on such sets only. Since this does not imply that trajectories from random initial conditions would necessarily approach these sets asymptotically, transient chaos can arise. Transient chaos is associated with the existence of *nonattracting* chaotic sets. Research has also revealed that transient chaos is in fact more common and possibly richer than sustained or permanent chaos, since the latter can be regarded merely as a limit of transient chaos when the average lifetime of the underlying chaotic set becomes infinite. Transient chaos thus plays a similar role in the realm of complex dynamics to that of a weakly unstable equilibrium state in regular dynamics. In fact, transient chaos can be regarded as a kind of metastable state. The concept of transient chaos is ideally suited to the description of nonequilibrium processes.

The aim of this book is to give an overview, based on the results of nearly three decades of intensive research, of transient chaos. One belief that motivates us to write this book is that transient chaos may not have been appreciated even within the nonlinear-science community, let alone other scientific disciplines. During the

course of research and interactions with various scientific communities, we have become increasingly convinced that knowledge of transient chaos can be particularly important and useful as we witness a proliferation of applications in various branches of science and engineering based on or motivated by nonlinear dynamics.

We shall show in this book that the basic concepts required to understand transient chaos are actually fairly easily generalized from concepts of standard nonlinear dynamics. One special emphasis will be on the fact that certain interesting dynamical phenomena can be understood only in the framework of transient chaos.

That transient chaos can arise in a broad array of fields can be illustrated by the following examples:

- Chemical reactions in closed containers can lead to thermal equilibrium only. However, the transients can be chaotic if one begins sufficiently far from equilibrium states.
- Certain epidemiological data, e.g., on the spread of chickenpox, can be consistently and meaningfully interpreted only in terms of transient chaos.
- The so-called shimmy (an irregular dancing motion) of the front wheels of motorcycles and airplanes, which can lead to disastrous incidents, turns out to be a manifestation of transient chaos.
- Satellite encounters and the escapes from major planets are chaotic transients.
- The trapping of advected material or pollutant around obstacles, often seen in the wake of pillars or piers, is a consequence of transient chaos.
- In nanostructures, today a cutting-edge field of science and engineering, the classical dynamics of electrons bear the signature of transient chaos.

This book should be regarded as a research monograph and is intended for graduate students and researchers in science and engineering who are interested in understanding and applying this extended concept of chaotic dynamics to their respective areas of research. Preliminary knowledge of sustained chaos, e.g., chaotic attractors, Lyapunov exponents, fractals, periodic orbits, stable and unstable manifolds, is assumed. These concepts can be found in almost any existing textbook on chaotic dynamics.[1]

Our Book not only gives an introduction to the novel concepts needed for understanding and for properly treating transient chaos, but also provides an overview of various transient-chaos-related phenomena. The book is organized as follows.

Part I: Basics of Transient Chaos. The first part covers the basic concepts, notions, ideas, theories, and algorithms required for understanding transient chaos.

- *Chapter 1: Introduction to Transient Chaos.* This chapter is devoted to a preliminary acquaintance with transient chaos, where basic properties of nonattracting chaotic sets are presented. To underline the relevance of transient chaos, a brief presentation of a number of experiments is given, which also illustrate different aspects of the applicability.

---

[1] The textbooks [564, 773] also provide an elementary treatment of transient chaos.

- *Chapter 2: Transient Chaos in Low-Dimensional Systems.* Dynamics from a one-dimensional map mimic those along the unstable manifold of, for example, a two-dimensional invertible map associated with a three-dimensional flow. Many fundamental insights into transient chaos can be gained by investigating one- and two-dimensional dynamical systems.
- *Chapter 3: Crises.* Transient chaos often precedes the birth of permanent chaos. Attractor destructions, explosions, and merging are often accompanied by transient chaos. Dynamical properties of transient chaos are partially inherited by the enlarged attractor. Transient chaos thus provides the *backbone* of the motion on composed attractors. Periodic windows, in spite of their name, are in fact parameter regions in which transient chaos is typically present.
- *Chapter 4: Noise and Transient Chaos.* In systems subject to external random forces, the attractor and the associated dynamics depend on the noise intensity. The phenomenon that a dynamical system with simple periodic attractors becomes chaotic in the presence of noise is noise-induced chaos. It is due to the transient chaotic dynamics coexisting with the periodic attractors in the noise-free system, which become stabilized by noise. This chapter presents an extensive treatment of the effects of noise on dynamical systems exhibiting transient chaos, which is physically important because noise is inevitable in any realistic dynamical systems.

Part II: Physical Manifestations of Transient Chaos. This part presents physical manifestations of transient chaos in various natural systems. A striking aspect of transient chaos is that it can lead to fundamental difficulties in predictability. Chaotic scattering, the manifestation of transient chaos in open Hamiltonian systems, will also be described both in classical and in quantum mechanics.

- *Chapter 5: Fractal Basin Boundaries.* If two or more periodic or chaotic attractors coexist, a trajectory may wander for a long time before approaching one of the attractors asymptotically. When there is transient chaos on the boundaries separating the basins of attraction, prediction of the final (asymptotic) state of the system may not be possible. There can also be situations in which the boundaries are severely interwoven (riddled basins), so that the motions on the boundaries dominate the dynamics. Fractal basin boundaries or riddled basins cause a fundamental difficulty in predicting the asymptotic state of the system.
- *Chapter 6: Chaotic Scattering.* For scattering processes in open conservative systems the only way chaos can appear is in the form of transients, as a consequence of the asymptotic freedom of the incoming and outgoing motions. Physical trajectories are usually trapped in a scattering region of the configuration space for a finite amount of time before leaving the system. Applications range from chemical reactions to celestial mechanics.
- *Chapter 7: Quantum Chaotic Scattering and Conductance Fluctuations in Nanostructures.* This chapter deals with signatures of chaotic scattering when the same system is treated quantum-mechanically in the semiclassical regime. Scattering-matrix elements exhibit random fluctuations as some physical parameters of the system change. Depending on whether the classical scattering

is hyperbolic or nonhyperbolic, statistical properties of the fluctuations can be quite distinct. One area in which quantum chaotic scattering finds significant applications is electronic transport in semiconductor nanostructures.

Part III: High-Dimensional Transient Chaos. Although low-dimensional transient chaos for which the underlying nonattracting chaotic sets have only one positive Lyapunov exponent is relatively well understood, high-dimensional transient chaos generated by chaotic sets with multiple positive Lyapunov exponents remains a forefront area of research in nonlinear dynamics. This part summarizes what is known so far about high-dimensional transient chaos.

- *Chapter 8: Transient Chaos in Higher Dimensions.* The increase in the unstable dimension from dimension one represents a highly nontrivial extension in terms of what has been known about transient chaos. Topics treated include the dimension formulas, algorithms for computing high-dimensional chaotic saddles, and chaotic scattering in physical systems with three degrees of freedom. In high-dimensional dynamical systems, transients can differ from those in low-dimensional systems in that the average lifetime is often extremely long before the system settles into a final attractor, which is usually nonchaotic. The presence of such transients implies that observation of the actual attractors of the system is practically impossible. The basic scaling law characterizing the so-called superpersistent chaotic transients and the effect of noise are treated.
- *Chapter 9: Transient Chaos in Spatially Extended Systems.* In a spatially extended system, transient lifetime often grows with the system size, and this growth can be as fast as exponential, or even faster. The presence of such superlong transients implies that the observed spatiotemporal behavior is not related to chaotic attractors. Certain phenomena such as pipe turbulence may thus turn out to exist on finite time scales only. An overview of transient chaos in spatially extended dynamical systems and open issues is presented in this chapter.

Part IV: Applications of Transient Chaos. This part focuses on different aspects of applications of transient chaos in physical, chemical, biological, and engineering systems. A physical context in which transient chaos is ubiquitous is fluid systems. Another broad area of application is control and maintenance of transient chaos for desirable system performance. The collection and analysis of transient chaotic time series for probing the underlying system are also applicable in many areas of science and engineering.

- *Chapter 10: Chaotic Advection in Fluid Flows.* The passive advection of tracer particles (e.g., small dye droplets) in open hydrodynamical flows with uniform inflow and outflow velocities turns out to be an appealing application of chaotic scattering. The unstable manifold of the nonattracting chaotic set becomes a direct physical observable in such cases as this manifold is traced out by particles or pollutants while being advected downstream. These manifolds form the backbone of possible chemical and biological reactions taking place in the flow. The transient-chaos-based approach to advection in fluid flows can have significant applications in engineering and environmental sciences.

- *Chapter 11: Controlling Transient Chaos and Applications.* We demonstrate in this chapter that transient chaos can be controlled by small perturbations. As in the control of permanent chaos, an unstable orbit on the chaotic set can be stabilized. A different form of control is to convert transient chaos into permanent chaos. Applications presented include voltage collapse in electrical-power systems and prevention, population control in ecology, and digital-information encoding.
- *Chapter 12: Transient Chaotic Time Series Analysis.* For transient chaos, only short time series are available, which makes the application of the methods developed in data analysis nontrivial. This chapter is devoted to basic issues in transient chaotic time series analysis, which include delay-coordinate embedding, and estimation of fractal dimension and Lyapunov exponents.

The main text is closed by a few final remarks. In the appendices, we treat a number of technical issues such as multifractal spectra, open random baker maps, semiclassical theory of chaotic scattering, and scattering cross sections.

To preview the applicability of the subject, we give in Table 1 a list of applications of transient chaos in various disciplines, all of which will be treated (although not in the same depth) in different chapters, including those outside of Part IV of this book.

We try to give as broad as possible an overview. The field is, however, actively developing, and full coverage of the literature is hardly possible by now. The selection of the material is therefore unavoidably biased, influenced by the authors' own experience.

Phoenix and Budapest, 2009   *Ying-Cheng Lai*
                                                                                                                  Tamás Tél

Table 1 Applications of transient chaos in different disciplines

Discipline	Subject	Chapters
Mathematics	Continued fraction	2
	Transfer operators	2
	Almost invariant sets	2,10
	Snapshot attractors and saddles, random maps	4,10
	Leaked dynamics	2,10
Astronomy	Escape of celestial bodies	6
Statistical physics	Poincaré recurrences	2,6,7
	Random systems and noise	2,4,11
	Lobe dynamics	6,10
	Transport processes	6,7,10
Optics	Dielectric cavities	6,7
	Lasers	6,12
Quantum mechanics	Open quantum systems	7
	Quantum echoes	7
	Fractal Weyl law	7
Nanoscience	Quantum dots	7
	Graphene	7
	Microfluidics	10
Fluid dynamics	Stirring and mixing	10
	Vortex dynamics	10
	von Kármán vortex street	8,10
	Turbulence	9
Engineering	Shimmying wheels	2
	Voltage collapse	11
	Encoding digital information	11
Chemistry	Classical molecular reactions	6,8
	Reactions in open flows	10
	Reaction–diffusion systems	9
Biology	Population and plankton dynamics	6,10,11
	Epidemiology and ecology	4
	Food chains	11
	Species extinction	11
Environmental sciences	Spreading of pollutants	10
	Lagrangian coherent structures	10
	Convection in the Earth's mantle	10
	Advection of finite-size particles	10

Contents

Part II Physical Manifestations of Transient Chaos

Part III High-Dimensional Transient Chaos

Part I
Basics of Transient Chaos

Chapter 1
Introduction to Transient Chaos

In numerical or experimental investigations one never has infinitely long time intervals at one's disposal. In fact, what is needed for the observation of chaos is a well-defined *separation of time scales*. Let t_0 denote the internal characteristic time of the system. In continuous-time problems, t_0 can be the average turnover time of trajectories on a Poincaré map in the phase space. In a driven system, it is the driving period. In discrete-time dynamics, t_0 can be the time step itself.

Suppose one observes signals that appear random for an *average lifetime τ*. Since chaos is characterized by a sensitive dependence on initial conditions, which is meaningful only on sufficiently long time scales, the appearance of chaotic signals requires that τ be much greater than the internal characteristic time:

$$\tau \gg t_0 . \tag{1.1}$$

The difference between sustained and transient chaos lies in the actual value of τ: for the former, τ is infinite, but it is finite for the latter. As a matter of practicality, one cannot exclude the possibility that a system apparently exhibiting a chaotic attractor may turn out to be transiently chaotic if a much longer period of observation is allowed. It is therefore useful to consider an additional time scale: the observation time T_O. The sustained or transient nature of chaos then depends on how τ is compared with T_O. We can speak of transient chaos if

$$\tau < T_O . \tag{1.2}$$

In the numerical investigation of attractors, a general habit is to discard a long sequence of the trajectory in order to concentrate on the asymptotic properties. A much richer dynamics may be observed, however, if one follows the trajectories from the beginning, i.e., if transients are not thrown out. One often finds then complex dynamics over some time, different from the dynamics governed by the attractor. The lifetime of a chaotic transient depends on the initial condition. An example can be seen in Fig. 1.1, where transiently chaotic trajectories are shown from the Hénon map [325, 564] at a parameter set where the attractor is a limit cycle. Such signals can also be observed in experiments. An example is shown in Fig. 1.2, where the measured quantity is the temperature difference between two
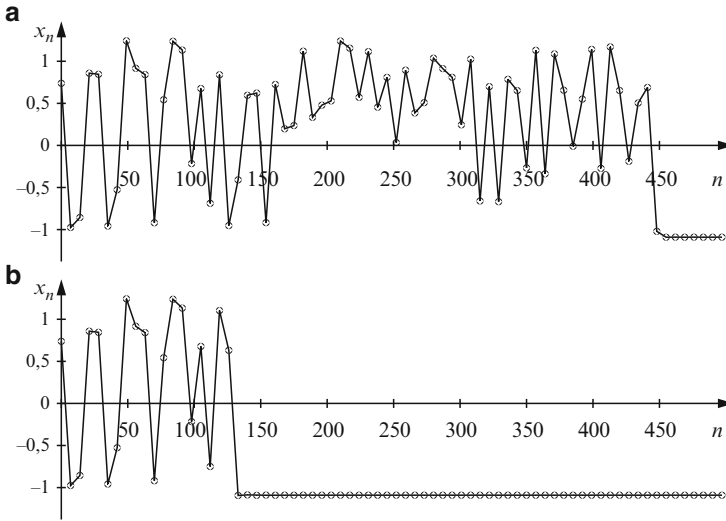
Fig. 1.1 Transient chaotic signals from the Hénon map $x_{n+1} = 1 - ax_n^2 + by_n$, $y_{n+1} = x_n$ for parameters $a = 1.25$ and $b = 0.3$, with a period-7 attractor. For clear visualization, only every seventh iterate is shown. (**a**) Trajectory initiated at $x_0 = 0.738816$, $y_0 = 0.893088$ exhibits chaotic behavior over 441 iterates. (**b**) The initial condition is shifted by $2 \cdot 10^{-19}$ in the x direction and the length of the chaotic transient is only 126
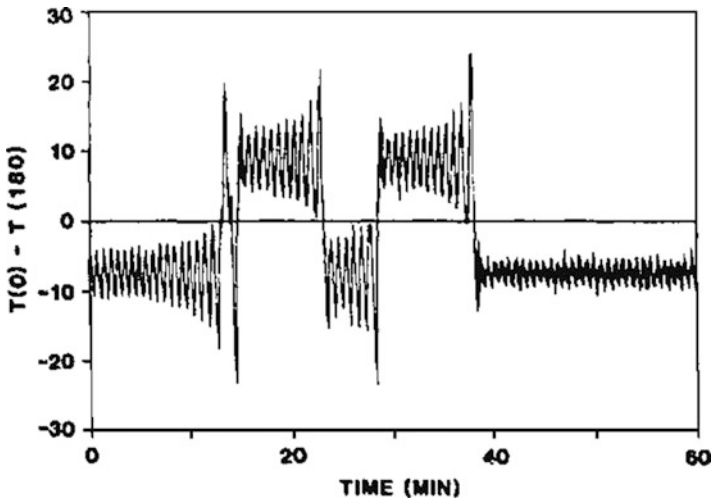
Fig. 1.2 Transient chaotic signal of the temperature difference observed between two points of an experimental loop of fluid heated from below with a constant heat flux (see Sect. 1.3 for more details). In this run, chaotic oscillations last up to nearly 40 min [823] (with kind permission from Elsevier Science)

points in a fluid loop. Over some time chaotic temperature oscillations are observed, which are accompanied by chaotic velocity oscillations of the laminar flow in the loop, and then, rather suddenly, a crossover takes place towards a nearly constant temperature difference corresponding to a uniform rotation of the fluid motion. (For a list of other representative experiments, see Sect. 1.3.)

Based on these and many other examples, one concludes that transiently chaotic signals (whose precise characterization will be discussed in Sect. 1.2) have the following characteristic properties:

1. For a fixed initial condition the signal appears chaotic up to certain time and then switches over, often quite abruptly, into a different, often nonchaotic, behavior that governs all the rest of the signal. The average lifetime, τ, can be obtained from an ensemble of such observations, although for individual observations, the actual lengths of transients depend sensitively on initial conditions: nearby trajectories typically have drastically different lifetimes.
2. The probability *distribution*, $P(t)$, of finding lifetimes longer than t is a smooth function, which satisfies $P(t) \to 0$ for $t \to \infty$.
3. There exist infinitely long transients. Mathematically, however, the set of initial conditions leading to infinite transients has zero volume in the phase space (has Lebesgue measure zero). Physically, this means that such infinite transients cannot be realized by initial conditions chosen randomly. In fact, for a typical (i.e., randomly chosen) initial condition, the transient lifetime is finite. Nonetheless, it is the presence of the measure-zero set of the initial conditions with infinite transients which causes the random distribution of the transient lifetimes for typical initial conditions.
4. It is known [564] that in a parameter region where chaotic attractors arise, periodic windows are dense. That is, for a specific parameter value that leads to a chaotic attractor, an arbitrarily small perturbation in the parameter can lead to a periodic attractor. In this sense, chaotic attractors are not structurally stable. Transient chaos is, however, robust against small parameter perturbations.

Similar to the fact that sustained chaotic signals are due to chaotic attractors in the phase space, there exist chaotic invariant sets that are responsible for transiently chaotic signals. Globally, such a chaotic set does not attract trajectories from its neighborhood, and hence it is *nonattracting*. Nonattracting chaotic sets (chaotic saddles or repellers; see Sect. 1.1.2) are therefore the *phase-space objects* that underly transient chaos. We thus accept the following definition: *transient chaos is the form of chaos due to nonattracting chaotic sets in the phase space*.

This chapter serves as a "first acquaintance" with transient chaos. The basic properties of nonattracting chaotic sets will be described. The average lifetime and the *escape rate* from these sets will then be introduced. Different methods for numerically constructing nonattracting chaotic sets will be given. The construction of the *natural* probability distribution on these sets will also be discussed, and an important related distribution, the *conditionally invariant measure* (c-Measure), will be introduced, from which characterizing quantities such as the Lyapunov exponents of the transients and dimensions of the nonattracting chaotic sets can be defined

and calculated. To underline the scientific relevance of transient chaos, a list of experiments taken from different disciplines will be presented, which also illustrate different aspects of transient chaos. Finally, a brief history of transient chaos will be given.

1.1 Basic Notions of Transient Chaos

1.1.1 Dynamical Systems

Dynamical systems are usually described by a set of ordinary differential equations:

$$\frac{d\mathbf{x}}{dt} = \mathbf{F}(\mathbf{x}, p), \tag{1.3}$$

where $\mathbf{x}(t)$ is the vector characterizing the state of the system at time t and p represents a set of parameters. Alternatively, discrete-time dynamical systems, or maps, of the form

$$\mathbf{x}_{n+1} = \mathbf{f}(\mathbf{x}_n, p) \tag{1.4}$$

can be investigated, where $\mathbf{x}_n$ is the state vector at discrete time n. Unless otherwise stated, the map is assumed to be autonomous, i.e., $\mathbf{f}$ does not depend explicitly on n. Maps can always be deduced from flows (1.3) by taking an appropriately defined Poincaré surface of section or stroboscopic map [564], the latter corresponding to repeatedly taking snapshots of the system at the multiples of some characteristic time t_0. Using such maps, the phase-space dimension is reduced effectively by one, facilitating visualization and analysis. In fact, Poincaré or stroboscopic maps have been used commonly in numerical and laboratory experiments on transient chaos (see Sect. 1.3). In order to have a consistent terminology, maps will be used for the rest of the chapter to illustrate the basic dynamical properties of transient chaos, but the main results apply also to flows (see also [398]).

1.1.2 Saddles and Repellers

The actual form of a nonattracting chaotic set depends on whether the dynamics is invertible. A dynamical system is invertible if its motion can be uniquely followed when time is reversed. This does not imply, however, that the time-reversed dynamics can actually occur in reality (although this is true for Hamiltonian systems, which are invariant under time reversal if no external magnetic field or Coriolis effect is present). Dynamical systems described by differential equations are typically invertible due to the uniqueness of solutions. Invertible dynamical systems are thus physically relevant. Noninvertible systems such as those described by one-dimensional maps can, however, be quite useful models for understanding specific features of transient chaos, and we shall consider them as well.

In an invertible dynamical system, a typical nonattracting chaotic set repels trajectories only along some special hypersurface in the phase space, which is called the *unstable manifold*. Along a different invariant hypersurface, or the *stable manifold*, the set can actually attract nearby trajectories. Usually, the local phase space at a point in the chaotic set can be decomposed into the stable and the unstable subspaces. For this reason, nonattracting chaotic sets in invertible dynamical systems are called *chaotic saddles*. Because differential equations are, in general, invertible, and many real-life phenomena are described by differential equations, *transient chaos in experiments is typically related to chaotic saddles*.

In contrast, for noninvertible dynamical systems in which the inverse is not unique, nonattracting chaotic sets are often *chaotic repellers*, objects that are repellent in all possible directions of the phase space. Chaotic repellers possess only unstable manifolds. These considerations are summarized in Table 1.1. The geometrical appearances of chaotic saddles and chaotic repellers can be quite different, as Fig. 1.3 illustrates.

The dynamical difference between chaotic repellers and saddles is that long-lived trajectories can start only from a neighborhood of the repeller, but for saddles

Table 1.1 Types of typical nonattracting chaotic sets in nonlinear dynamical systems

Dynamics	Nonattracting chaotic set
Invertible	Chaotic saddle
Noninvertible	Chaotic repeller
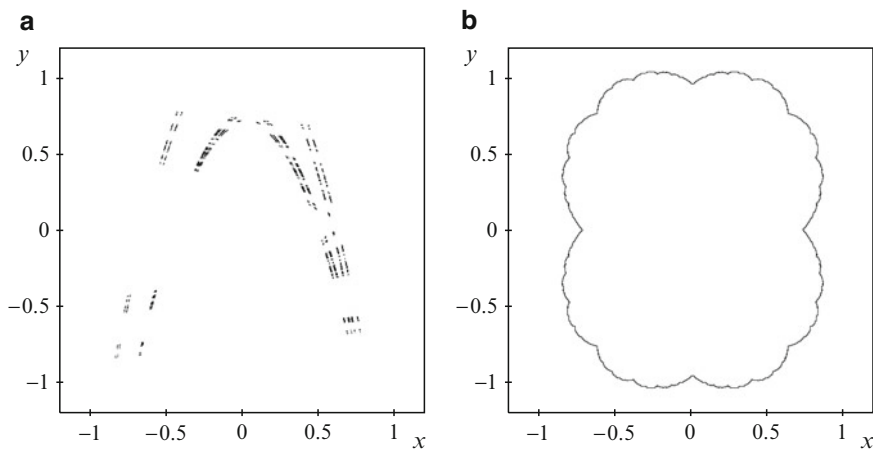
Fig. 1.3 Comparison of a chaotic saddle and a chaotic repeller. (**a**) A chaotic saddle from a periodically kicked harmonic oscillator. On a stroboscopic plane the position x_n and the velocity y_n of the oscillator evolve according to the map [773] $x_{n+1} = y_n$, $y_{n+1} = 1 - 3.2y_n^2 - 0.49x_n$. (**b**) A chaotic repeller of the quadratic map $z_{n+1} = z_n^2 + 0.2$ in the complex plane $z = x + iy$, which is in fact a Julia set [824]. The saddle in (**a**) appears as a fractal set of points, which is in fact the direct product of two Cantor-like sets, while the repeller in (**b**) is a complicated but nonetheless continuous curve in the plane

they can also start from a neighborhood of the stable manifold, a typically much larger set. If a chaotic repeller and saddle coexist,[1] transient chaos is primarily governed by the chaotic saddle.

Because a nonattracting chaotic set is invariant, trajectories starting from points on the set *never* leave the set and in fact exhibit chaotic motion for infinitely long time. However, because the Lebesgue measure of the set is zero, the probability that a randomly chosen point of the phase space is in the set is zero. What is *observable* is not the nonattracting set but a *small neighborhood* of it. In particular, trajectories can originate from points in the vicinity of the set and can then stay in the neighborhood of the set for a long but finite amount of time, and they eventually leave the nonattracting chaotic set. These are the trajectories that generate transiently chaotic signals. The phenomenon of transient chaos thus illustrates that the existence of a set of Lebesgue measure zero can be observed via *finite-time properties*. As a consequence, we shall also see that the fractal features of a nonattracting chaotic set are different from those of a chaotic attractor.

A related point is that the natural measure, a special invariant distribution characterizing the dynamics on a nonattracting chaotic set, not only exists but can be obtained approximately in numerical or actual experiments. In particular, the distribution can be approximately specified on a small neighborhood of the set. The approximate natural measure can then be used to perform *ensemble averages* of physical quantities of interest, similar to the situation with chaotic attractors. Since the distribution is only approximate, any ensemble average will contain errors, but they can be controlled.

Transient chaotic dynamics can also be classified according to whether the process is dissipative or conservative. In a strictly dissipative system where the local phase-space volume contracts everywhere, the asymptotic states of the system are attractors that may be regular, but transient chaos provides a "platform" for approaching the attractors. In such a case the transient dynamics before the final state of the system is reached is chaotic. In *dissipative* systems, transient chaos appears in the form of *chaotic transients*. In conservative or Hamiltonian systems, the phase-space volume is constant under time evolution. As a result, there are no attractors, but some simple asymptotic states of the system can still be defined. Consider, for example, a particle-scattering experiment in which the underlying dynamics is Hamiltonian. Particles coming from far away approach the scattering region, and after a finite amount of time, they leave the region and escape to "infinity." There can, however, be qualitatively different exit routes to infinity. In this case, the different exit routes can be regarded as asymptotic states (but not attractors) of the system. The dynamics in the scattering region can, however, be regular or chaotic, where the latter, i.e., transient chaos in *Hamiltonian systems*, defines the phenomenon of *chaotic scattering*. Hamiltonian systems are invertible, so the nonattracting set underlying chaotic scattering is typically a saddle.

---

[1] For instance, in the time-reversed dynamics of an invertible system possessing a chaotic attractor and a coexisting chaotic saddle.

It should be noted that *nonchaotic transients* may also exist in dynamical systems. An example is provided by trajectories that approach an attractor but are far away from any nonattracting chaotic set. These transients are typically short and do not exhibit chaotic features, although the actual asymptotic state may be chaotic. Thus, *transients to chaos* can be quite different from chaotic transients, since the latter, but not the former, are due to an underlying nonattracting chaotic set.

1.1.3 Types of Transient Chaos

According to the type of attractor(s) with which a nonattracting chaotic set coexists, we can distinguish two main types of transient chaos. The first type is for the case in which the coexisting attractor is simple, e.g., a periodic attractor. While the asymptotic behavior of the system is relatively simple, the transients are chaotic. Transient chaos arising in situations in which there is an attractor at infinity, and in open Hamiltonian systems in which attractors are replaced by different exit routes also exhibit this type of transient chaos.

The second type occurs when a nonattracting chaotic set coexists with a chaotic attractor. In this case, there are two distinct forms of chaotic behavior. A signal from the system typically exhibits one form of chaotic behavior, the one due to the nonattracting set, on time scale τ, and then switches over to another form of chaos asymptotically. A common situation is that the motion determined by the nonattracting set is more chaotic than that due to the chaotic attractor (for more detail see Fig. 1.16 and Chap. 3). Thus, focusing on the asymptotic properties will "miss" the dominant chaotic part of the full complex dynamics that contains important information about the underlying dynamical system.

1.2 Characterizing Transient Chaos

Having introduced the basic concepts of transient chaos in a qualitative manner, we now discuss its quantitative characterization. A natural question is whether there is actually chaos in the seemingly chaotic signals observed over finite time scales. There are different levels of characterization of increasing complexity, as follows:

1. Measurement of the lifetime distribution, the escape rate, and the average lifetime.
2. Construction of nonattracting chaotic sets in the phase space.
3. Construction of invariant measures on the chaotic set.
4. Determination of dynamical invariants such as the Lyapunov exponents and the fractal dimensions of the nonattracting chaotic set and its natural measure.

Following this hierarchy, one can find criteria to address the question of whether the system is indeed chaotic and if so, to calculate some measure of the strength of chaoticity. In the following we discuss these levels of characterization.

1.2.1 Escape Rate

In transient chaos, typical trajectories, i.e., trajectories initiated from random initial conditions, escape any neighborhood of the nonattracting chaotic set. A quantity measuring how quickly this occurs is the *escape rate* [824]. To define the escape rate, imagine distributing a large number N_0 of initial points according to some initial density ρ_0 in a phase-space region R that does not contain any attractor or asymptotic state of the system. The density ρ_0 is often chosen to be uniform, and the geometry of R can be chosen to be simple, e.g., a rectangle in a two-dimensional phase space. Many trajectories from the initial points may come close to the nonattracting chaotic set at some later time. We define a *restraining region Γ* as a bounded, compact region containing the nonattracting set. Once a point leaves the restraining region, it cannot return to it. After visiting a neighborhood of the set, almost all trajectories eventually leave Γ. Let $N(n)$ denote the number of trajectories remaining inside Γ after n steps, and choose N_0 to be sufficiently large that $N(n) \gg 1$. As n is increased, one observes in general an exponential decay in the number of trajectory points that are still in Γ (surviving points) [373, 596, 843]:

$$N(n) \sim e^{-\kappa n} \quad \text{for} \quad n \gg 1, \tag{1.5}$$

where κ is called the escape rate.[2] A small value of κ implies weak "repulsion" of typical trajectories by the nonattracting chaotic set. The escape rate turns out to be *independent* of the distribution ρ_0 of the initial conditions, of its support R, and of the choice of the restraining region Γ. The escape rate κ is thus a property *solely* of the nonattracting chaotic set. However, the prefactor of the exponential form in (1.5), and the behavior of the system preceding the exponential decay do depend on details such as the choices of ρ_0, R, and Γ.

A practical issue concerns about the choice of the support R of the initial density. In a noninvertible system, R should overlap with the chaotic repeller, while in an invertible system it is sufficient to choose R so that it overlaps with the stable manifold of the chaotic saddle. In any case, if an exponential decay is found, its rate should be given by the escape rate κ. In practice, the initial density is often distributed on the restraining region, implying $R = \Gamma$.

In a realistic physical system, the exponential decay can be observed with high accuracy after a finite, often short, time n^*, i.e.,

$$N(n) = Ne^{-\kappa n} \quad \text{for} \quad n \geq n^*, \tag{1.6}$$

---

[2] There are situations in which the decay follows a power law for certain types of nonhyperbolic chaotic sets, which will be treated in Sect. 2.4 and Chap. 6. Such decays cannot be characterized by escape rates.
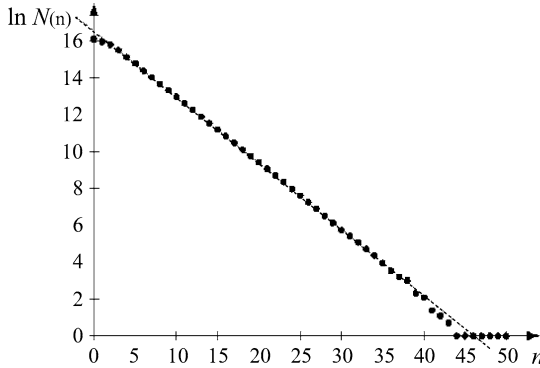
Fig. 1.4 Survival in the Hénon map $x_{n+1} = 1 - ax_n^2 + by_n$, $y_{n+1} = x_n$ for parameters $a = 2.0$ and $b = 0.3$. Number $N(n)$ of surviving trajectory points in the square defined by $\Gamma : |x_n|, |y_n| \leq 1.0$, obtained from $N_0 = 10^6$ initial points distributed uniformly in the same square ($R = \Gamma$). The fitted *dashed line* has slope approximately -0.36, giving $\kappa \approx 0.36$. The value of n^* is approximately 4. The survival probability $P(n)$ is approximately $N(n)/N_0$

where the value of n^* and the prefactor N may also depend on ρ_0, R, and Γ.[3] An example is shown in Fig. 1.4, where we see that the value of n^* is relatively small.

The definition of the escape rate indicates that the number of surviving points is decreased by a factor of $1/e$ after about $1/\kappa$ time steps. This implies that most trajectories do not live longer than $1/\kappa$ in the restraining region. It is thus reasonable to *estimate* the average lifetime τ of the chaotic transient as

$$\tau \approx \frac{1}{\kappa}. \tag{1.7}$$

Since the escape rate can be obtained by following the decay law over a finite time interval, cf. (1.5), transient chaos of short average lifetime may be difficult to identify. A condition for the practical observability of transient chaos is thus that κ be small.

In a more general context, for any initial distribution on R and choice of Γ, we can define the *probability $P(n)$* of finding survival times larger than $n \geq 1$. The *survival probability $P(n)$* is thus the probability of finding initial points that have not escaped Γ up to time n, which can be approximated by $N(n)/N_0$ for large N_0. In view of (1.6), the decay of $P(n)$ is exponential:

$$P(n) = ge^{-\kappa n} \quad \text{for} \quad n \geq n^*. \tag{1.8}$$

---

[3] The prefactor N yields what the number of initial points would be if the decay were exponential from the very beginning. Therefore N is different from N_0.

A related probability is the *escape-time distribution*, $p(n)$, the probability that a particle escapes region Γ exactly in the nth iterate. This quantity can be estimated as $[N(n-1) - N(n)]/N_0$ and is therefore the "density" of the cumulative distribution $P(n)$. We have

$$P(n) = \sum_{n'=n+1}^{\infty} p(n'). \tag{1.9}$$

Being the "derivative" of an exponential function, the long-time behavior of $p(n)$ is also exponential and can be written in the form of (1.8) (with a different n^*, but the *same* escape rate).[4]

The average lifetime τ is *defined* as the average escape time, i.e.,

$$\tau \equiv \bar{n} = \sum_{n=1}^{\infty} np(n). \tag{1.10}$$

Since the distribution is not exponential for $n < n^*$, the exact average lifetime τ *does* depend on the choices of ρ_0, R, and Γ. Note that the estimate (1.7) does not reflect this property.[5] Since the average lifetime depends on many details, the escape rate κ is a *more appropriate characteristic* of the decay process than τ. The escape rate is a unique property of the underlying nonattracting chaotic set, in contrast to the average lifetime, which also contains information about, e.g., the initial distribution of particles. While the values of τ and $1/\kappa$ are typically different even for slow decays, their *scaling properties* in terms of, for example, parameter changes are usually the same.

There can be situations in which two (or more) nonattracting chaotic sets coexist with different escape rates κ_1 and κ_2. In such a case, the number of surviving trajectory points in a given restraining region Γ is the sum of two exponentials for large n:

$$N(n) \sim N_1 e^{-\kappa_1 n} + N_2 e^{-\kappa_2 n}, \tag{1.11}$$

and the prefactors N_i depend on the choices of ρ_0, R, and Γ.

It should be emphasized that the existence of a positive escape rate κ for transients does not at all imply their chaoticity. One should also measure, for example, the Lyapunov exponents on time scale $1/\kappa$ [714] and check whether at least one of the exponents is positive. A complication is that even simple nonattracting sets, for instance a *single, regular saddle point* (also called a hyperbolic point) are at least partially repelling. Trajectories deviate from them exponentially. Regular

---

[4] For continuous-time systems, (1.5)–(1.8) remain valid under the transform $n \to t$. The escape-time distribution becomes then a probability density, and the sum in (1.9) is replaced by an integral. The escape rate in the corresponding continuous-time system is κ/t_0, where t_0 denotes the internal characteristic time mentioned in the introduction to this chapter. Analogously, the average lifetime can be estimated as t_0/κ.

[5] Equation (1.7) is a rough estimate, since even in the ideal case of $n^* = 1$, when $p(n) = (\exp(\kappa) - 1)\exp(-\kappa n)$, we obtain $\tau = (1 - \exp(-\kappa))^{-1}$ from (1.10) [147], which is consistent with (1.7) for $\kappa \ll 1$ only.

Fig. 1.5 Lifetime function: dependence of the lifetime n on the initial position x along the interval defined by $y = -1.5$ and $|x| \leq 1$ in the Hénon map at the parameters of Fig. 1.4. (For the corresponding phase-space patterns, see Figs. 1.7 and 1.9.) The fractal irregularity of this lifetime function is a sign of transient chaos
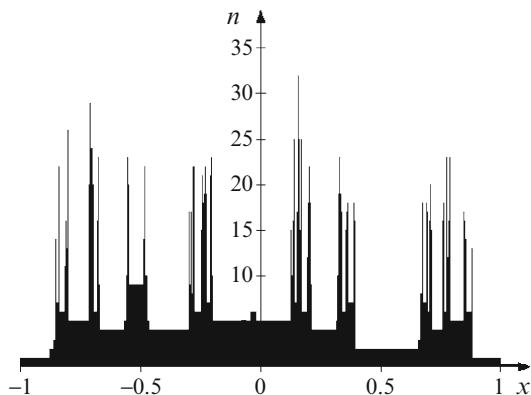
nonattracting sets are therefore characterized by a positive Lyapunov exponent, although the dynamics about them are not chaotic. The positivity of at least one Lyapunov exponent is thus not sufficient for the chaotic behavior of transients. This is why we accept the definition, used throughout the book, that transient chaos is the dynamics associated with nonattracting chaotic sets.

To determine whether the transients are truly chaotic, one therefore needs more information than the mere positivity of the Lyapunov exponent. Qualitatively, the visual appearance of the signal can be helpful: about chaotic nonattracting sets trajectories should be complicated. This is, nonetheless, only a hint. A property uniquely indicating the chaotic nature of the transients is the *irregular* dependence of lifetimes on initial conditions, as illustrated by Fig. 1.5. Suppose one starts trajectories along a smooth curve in the phase space that intersects a chaotic repeller or the stable manifold of a chaotic saddle. One then finds that for some points the lifetimes are large. In principle, points of infinitely large lifetimes belong to a *fractal* subset of initial conditions, since these must be points of the chaotic repeller or of the saddle's stable manifold. A fingerprint in a finite-accuracy numerical simulation is large lifetimes separated by small values in between.

1.2.2 Constructing Nonattracting Chaotic Sets

Repellers are straightforward to construct, since they are the attractors of the inverted dynamical systems. Noninvertibility is generally due to the existence of more than one inverted branch. When following the time-reversed dynamics, all possible inverses should be taken into account.

For an invertible dynamical system, the calculation of chaotic saddles is more delicate. While such a system can be inverted, the inverted dynamics still results in a chaotic saddle. This feature can in fact be viewed as an illustration of the robustness of the *hyperbolic structure* that is often seen for chaotic saddles. Roughly, a chaotic saddle is the set of intersections between the stable and the unstable manifolds, and

in hyperbolic cases, the angles at the intersecting points are bounded away from zero. In what follows, we will describe an intuitive numerical procedure for calculating chaotic saddles, which serves to further illustrate their dynamical structures. More practical numerical methods will then be introduced.

1.2.2.1 Horseshoe Construction

The intuitive method is based on the observation that a chaotic saddle has typically embedded within itself a dense set of unstable periodic orbits, a property of any chaotic set. Imagine that we choose an unstable periodic orbit in an invertible two-dimensional map and plot its stable and unstable manifolds, which are the curves along which the orbit is attracting in the direct and in the inverted dynamics, respectively. If these curves cross each other once at a point (a homoclinic point), they must do so infinitely many times, since the images and the preimages of such an intersection are of the same type. All the homoclinic points form a *homoclinic orbit*. Since it belongs simultaneously to the stable and the unstable manifolds of the original periodic orbit, a homoclinic orbit approaches asymptotically, but can never reach, the periodic orbit. As a result, the stable and unstable manifolds exhibit a complex, intertwined structure, as shown schematically in Fig. 1.6. The *horseshoe* structure of the manifolds and the existence of homoclinic orbits have been known since the works of Smale [300, 721]. Thus, mathematically, chaotic saddles are closed, bounded, and invariant sets with dense orbits. They are the "soul" of chaotic dynamics [721]. Similar to the formation of homoclinic orbits, the stable (unstable) manifold of a periodic orbit can intersect with the unstable (stable) manifold of a *different* orbit, forming a *heteroclinic orbit*. The stable and the unstable manifolds of different periodic orbits of a chaotic saddle are usually close to each other in the phase space, and all the resulting homoclinic and heteroclinic orbits belong to the chaotic saddle.
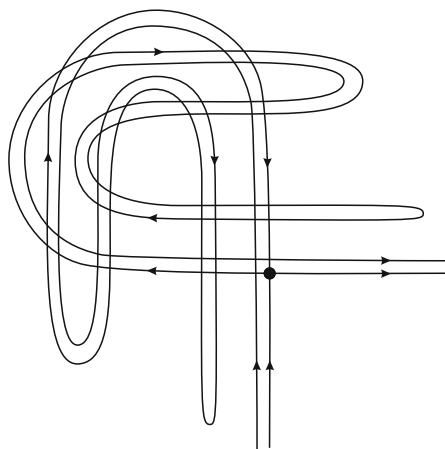
Fig. 1.6 Horseshoe structure: schematic illustration of horseshoes formed by the stable and the unstable manifolds of a fixed point (period-1 orbit) denoted by the *dot*. The set of intersection points (homoclinic points) between the manifolds belongs to the chaotic saddle

Fig. 1.7 A horseshoe construction: a few branches of the stable and the unstable manifolds of the fixed point H_+ of the Hénon map $x_{n+1} = 1 - 2.0x_n^2 + 0.3y_n$, $y_{n+1} = x_n$
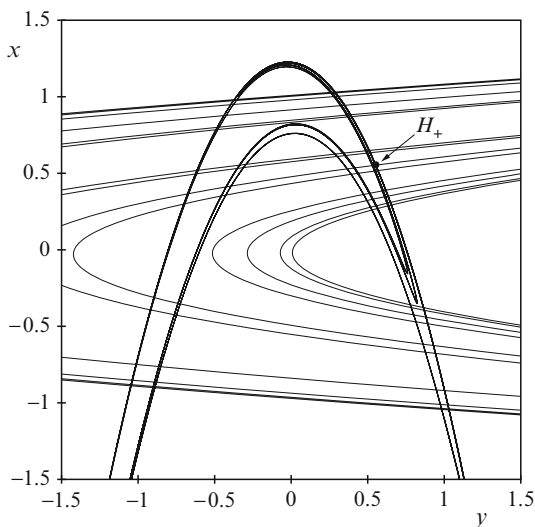
The above discussion suggests the following procedure for numerically calculating a chaotic saddle. One first finds a simple hyperbolic orbit, such as a fixed point or a periodic orbit of low period, and then calculates its stable and unstable manifolds. In particular, the unstable (stable) manifold can be obtained by distributing a large number of initial points in a small neighborhood of the hyperbolic orbit and iterating them under the forward (inverted) dynamics. The set of intersecting points between the manifolds is part of the chaotic saddle. Since in practice, only a finite number of branches of the manifolds can be constructed, the intersections provide an approximate representation of the saddle. If the number of initial points used in the calculation is reasonably large, the fractal nature of the saddle and its stable and unstable manifolds can be revealed. An example is shown in Fig. 1.7. In general, the appearance of a fractal geometry along both the stable and the unstable manifolds and the existence of a horseshoe type of structure are indications that a chaotic saddle exists in the phase space of interest. Note that if the manifolds of the hyperbolic orbit chosen do not intersect each other, the orbit does not belong to a chaotic saddle. In this case, it is necessary to choose a different periodic orbit to start with.

1.2.2.2 Ensemble Method

The idea of this method, introduced by Kantz and Grassberger [380], is to follow an ensemble of trajectories and select the pieces that remain in the vicinity of the saddle. In particular, one first chooses a region R close to the suspected chaotic saddle but not containing any attractor, distributes uniformly a large number N_0 of points in R, and iterates these initial conditions under the forward dynamics. A criterion is needed for deciding when a trajectory is away from the saddle, which can simply be that the trajectory moves out of a restraining region Γ surrounding the

saddle (regions R and Γ can be the same as the respective ones used for computing the escape rate). Another criterion can be [380] to calculate the effective Lyapunov exponents over a finite number of time steps and examine whether they are close to the corresponding exponents characterizing an attractor. In the case of a point attractor, it is simply the negativity of all local Lyapunov exponents that can be used as an indicator of the trajectory's having left the saddle. All trajectories leaving the saddle earlier than n_0 steps are discarded, and trajectories of lifetime longer than or equal to n_0 are kept. The choice of the value of n_0 can be somewhat arbitrary, but some large value should be chosen if the lifetime τ of the chaotic saddle is large. (Experience indicates that choosing n_0 a few multiples of $1/\kappa$ is proper.) One can then select *long-lived* trajectories in the neighborhood of the saddle to approximate it. For example, if the desirable number of trajectories whose lengths are not less than n_0 is M_0, the number N_0 of initial points should be of the order of $n_0 M_0 \exp(\kappa n_0)$, which can be a few orders of magnitude larger than M_0. To ensure that trajectories close to the saddle are selected, the long-lived trajectories need to be *truncated* at both the beginning and the end. For example, for a trajectory of length larger than n_0, one can discard the first n_1 and the last n_2 points so that the resulting trajectory is close to the saddle but not close to its stable and unstable manifolds, respectively, where n_1 and n_2 are each a fraction of n_0. A representative example is shown in Fig. 1.8.
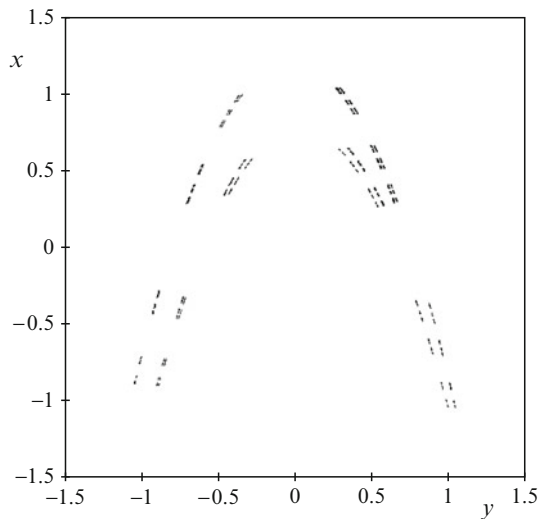
Fig. 1.8 Chaotic saddle in the Hénon map ($a = 2.0$, $b = 0.3$) obtained by the ensemble method, where $N_0 = 10^6$ initial points are distributed uniformly in the interval $R = (|\, y_0 \,| < 0.5,\ x_0 = 0)$. The restraining region is $\Gamma = |\, x_n \,| \leq 1.2$. The first 10 and the last 20 steps of long-lived trajectories are discarded ($n_0 = 30$). Observe that the pattern is practically the same as the one formed by the set of homoclinic points in Fig. 1.7. The direct product structure of two Cantor-like sets is a generic characteristic of chaotic saddles of two-dimensional maps

1.2.2.3   Sprinkler Method

A variant of the ensemble method, the *sprinkler method* [341], can be used to calculate not only a chaotic saddle but also its stable and unstable manifolds [453]. Again, one starts from $N_0 \gg 1$ trajectories distributed uniformly over a region R enclosing at least a part of the saddle. One then chooses an iteration number n_0 that is several times larger than the estimated lifetime (1.7) of the saddle, and follows the time evolution of each initial point up to exactly time n_0. Only trajectories that do not escape R in n_0 steps are kept, whose number is approximately $N_0 e^{-n_0 \kappa}$. If $n_0 \kappa$ is sufficiently large (but not so large that only a few points remain inside R), trajectories with this long lifetime come close to the saddle in the course of dynamical evolution, implying that their initial points will be in the immediate vicinity of the stable manifold of the saddle, or of the saddle itself, and that their end points will be close to the unstable manifold of the saddle. The latter is so because most points still inside after n_0 steps might already be in the stage of leaving the region. The points from the middle of these trajectories (with $n \approx n_0/2$) are then in the vicinity of the saddle. In general, the initial, middle, and end points of trajectories of lifetimes of at least n_0 approximate the stable manifold, the saddle, and the unstable manifold, respectively, within the region R, as exemplified by Fig. 1.9. In order to obtain the full saddle, R should be chosen to fully contain the saddle (which corresponds to the choice $R = \Gamma$ in the ensemble method). An advantage of the sprinkler method is that it is computationally fast and is easy to apply to high-dimensional cases.

1.2.2.4   Single-Trajectory (PIM-Triple) Method

The PIM-triple method, proposed by Nusse and Yorke [557], sets out to find a single and arbitrarily long trajectory very much near the chaotic saddle. The procedure is
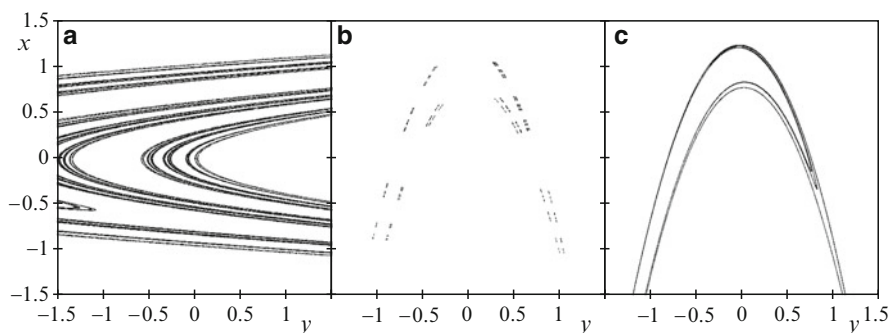
Fig. 1.9 Sprinkler method: an example of finding the chaotic saddle and its manifolds for the Hénon map in Figs. 1.7 and 1.8 by the sprinkler method. Region $R = \Gamma$ is a square of size 2×2 centered at the origin, $N_0 = 10^7$, $\kappa = 0.36$. Parts (**a**), (**b**), and (**c**) show points of trajectories with a minimum lifetime $n_0 = 16$ at iteration numbers $n = 0$, $n = 8$, and $n = 16$, well approximating the stable manifold, the saddle, and the unstable manifold, respectively. Note that the stable manifold here shows a more detailed structure than in Fig. 1.7

based on the observation that trajectories starting close to the *stable* manifold of the saddle stay for a long time in the vicinity of the saddle. The closer they start out to the stable manifold, the longer their lifetime is. One begins by taking an interval $\overline{AB}$ somewhere in a restraining region Γ so that it intersects the stable manifold of the chaotic saddle. One next chooses initial points uniformly distributed on $\overline{AB}$ and measures their lifetimes in Γ. A triplet of points, i.e., three points on $\overline{AB}$ such that the midpoint has a lifetime longer than those of the two neighboring points, can then be identified. Such a triplet is called a PIM-triple, where "PIM" stands for *proper interior maximum*. For the PIM-triple whose middle point has the maximum lifetime, the two external points are expected to lie on two different sides of a branch of the stable manifold. These two points then define a new interval $\overline{A'B'}$ that intersects the stable manifold. One can then repeat this *refining* procedure to find a PIM-triple whose size is smaller than a prescribed value $\delta \ll 1$. The triple can then be iterated forward under the dynamics. Points on the triple approach the saddle along the stable manifold but simultaneously move apart along the unstable manifold. When the size of the evolving triplet becomes larger than δ, the refining procedure is activated to reduce the size of the triple to within δ, and the new triple is iterated forward again, and so on. One thus finds a set of PIM-triples of size less than δ, and the set of middle points can be taken as an approximation of a typical trajectory on the chaotic saddle. While the PIM-triple procedure is computationally expensive (as compared with the previous methods), it is applicable to chaotic saddles even with relatively short lifetimes. The desirable feature of the PIM-triple method is that it enables a *long* trajectory near the saddle to be found, facilitating characterizations of the saddle by dynamical invariants such as the Lyapunov exponents and the fractal dimensions.

On a given interval, several PIM-triples can usually be found. If one selects from those the PIM-triple for which the lifetime at the middle is the largest, not only can the geometry of the saddle be revealed, but such a long trajectory also generates a good approximation to the natural measure on the saddle [353].

1.2.3 The Invariant Measures of Transient Chaos

1.2.3.1 Natural Measure

The natural measure (or natural invariant distribution) μ characterizes how often different pieces of a nonattracting chaotic set are visited by a dense trajectory on the set [380]. This distribution can be obtained from a *smooth* distribution about the set by selecting long-lived trajectories on the set. In practice, however, infinitely long trajectories cannot be found, nor can such trajectories be calculated with arbitrarily high precision. It is thus necessary to approximate the natural measure. For example, one can choose a fine but finite *coverage* of the chaotic set by boxes is the phase space of dimensionless linear size $\varepsilon \ll 1$, and consider trajectory points that stay for a long time close to the set.

Fig. 1.10 Distribution of the natural measure μ of the Hénon chaotic saddle in Fig. 1.8 in a two-dimensional region in the phase space, specified on a grid of size $\varepsilon = 1/400$ (Picture by M. Gruiz and Sz. Hadobás)
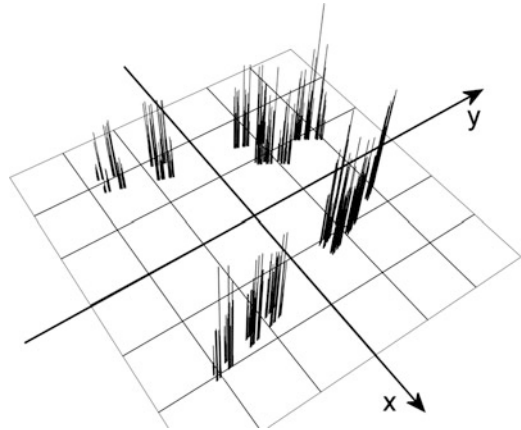
Let N be the number of such points. All nonempty boxes define a *coarse-grained* version of the chaotic set at the resolution ε. The approximate natural measure on this coarse-grained set is given by the frequencies of visits to different boxes by long trajectories in the vicinity of the chaotic set. More precisely, the natural measure $P_i(\varepsilon)$ of nonempty box i is

$$P_i(\varepsilon) = \frac{N_i}{N}, \tag{1.12}$$

where N_i is the total number of trajectory points falling into box i. It is desirable to take N large enough that the condition $N_i \gg 1$ is satisfied in all nonempty boxes. The quantity $P_i(\varepsilon)$ is also called the *box probability* and represents the natural measure μ inside box i with an accuracy of order ε:

$$P_i(\varepsilon) = \int_{x \in \text{box } i} d\mu(x). \tag{1.13}$$

Points of long-lived trajectories can be generated either by the ensemble, the sprinkler, or the PIM-triple method. An example of the natural measure of a chaotic saddle specified with finite resolution is shown in Fig. 1.10.

1.2.3.2 Conditionally Invariant Measure

A concept that is closely related to the natural measure is the c-measure introduced by Pianigiani and Yorke [595, 596]. For a nonattracting chaotic set, this measure is defined with respect to its unstable manifold. While there can be different c-measures for a given system [400], the "natural" c-measure is particularly relevant; it can be obtained as the *limiting distribution* of iterating trajectories starting from a *smooth* distribution of initial conditions about the chaotic set. In this sense, the c-measure is the analogue of the SRB measure [564] for attractors. For

transient chaos, the c-measure also describes how points *deviate* from the chaotic set, and can be regarded as being maintained by *supplying* new points into the region of interest according to the rate at which trajectories escape from the region asymptotically. Formally, this can be achieved by multiplying the number of points everywhere by the constant e^κ at each time step. Because of the contraction along the stable direction (if it exists), the limiting distribution will be nonzero *along the unstable manifold* only. This distribution, the c-measure, thus characterizes how points leave the neighborhood of the underlying nonattracting chaotic set asymptotically, and how often certain regions are visited by trajectories in the process of escaping. The natural measure μ can also be considered as the c-measure μ_c *restricted to* a small neighborhood of the nonattracting chaotic set itself.

Under the map **f**, the region not escaping the restraining region Γ within one iterate is the preimage $\mathbf{f}^{-1}(\Gamma)$ of Γ. Since the c-measure characterizes how points are distributed along the unstable manifold before escaping, from a probabilistic point of view, it is the c-measure of $\mathbf{f}^{-1}(\Gamma)$ which is proportional to the number of trajectory points not escaping in one time step. By normalizing the c-measure of the restraining region to be unity, $\mu_c(\Gamma) = 1$, one finds, as pointed out by Pianigiai and Yorke [596], that the compensation factor is the reciprocal of $\mu_c[\mathbf{f}^{-1}(\Gamma)]$, i.e.,

$$e^{-\kappa} = \mu_c[\mathbf{f}^{-1}(\Gamma)]. \tag{1.14}$$

The escape rate is thus uniquely expressed by the c-measure of the nonescaping points within one iterate. Since the c-measure describes the asymptotic escape process, which is purely exponential, in choosing the density ρ_c of the c-measure as an initial density ρ_0 on Γ, the exponential form of the survival probability (1.8) is valid by the first time step. We see that ρ_c is thus the special initial distribution for which $n^* = 1$.

The c-measures of one-dimensional maps will be studied in detail in the next chapter. Here we briefly describe the construction of the c-measure for invertible two-dimensional maps. For such a system, the c-measure can be defined as follows [341]. Since trajectories escape the chaotic saddle along the unstable manifold, after $n \gg 1$ iterations, the surviving trajectory points of number N_n in Γ will be in the vicinity of the unstable manifold. Let B be a small box within Γ that contains part of the unstable manifold. The c-measure along the unstable manifold in B is thus

$$\mu_c(B) = \frac{N_{u,n}(B)}{N_n}, \quad \text{for} \quad n \gg 1, \tag{1.15}$$

where $N_{u,n}(B)$ is the number of the N_n points that fall in B at time n. An example of the c-measure is shown in Fig. 1.11. A comparison with the natural distribution in Fig. 1.10 indicates that the singular spikes of the c-measure fall outside the saddle, and that the natural distribution is nothing but the c-measure restricted to the saddle (with a proper normalization).

The natural measure μ of the chaotic saddle can also be defined based on $N_n^{(r)}(B)$, the number of trajectory points in B at a time rn between zero and n:

Fig. 1.11 Conditionally
invariant measure μ_c of the
Hénon saddle ($a = 2$, $b = 0.3$)
on the restraining region
$\Gamma : |x|, |y| \leq 1.5$, identified
on a grid of size $\varepsilon = 1/400$.
The support of the c-measure
is the unstable manifold of
the saddle (cf. Fig. 1.7)
(Picture by M. Gruiz and
Sz. Hadobás)
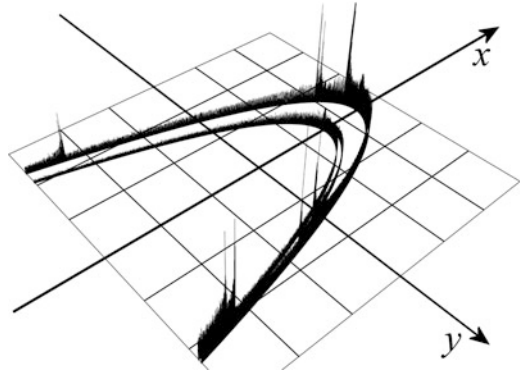
$$\mu(B) = \frac{N_n^{(r)}(B)}{N_n}, \quad \text{where } 0 < r < 1, \, n \gg 1. \tag{1.16}$$

We have $N_n^{(1)}(B) = N_{u,n}(B)$. For large N_0 and n, trajectories remaining in Γ will stay near the chaotic saddle for most of the time between zero and n, except at the beginning, when they are attracted toward the saddle along the stable manifold, and at the end, when they exit along the unstable manifold. Thus, the measure defined in (1.16) is independent of r, insofar as r deviates considerably from both 0 and 1.

A measure along the stable manifold can be defined as

$$\mu_s(B) = \frac{N_{s,n}(B)}{N_n}, \quad \text{for } n \gg 1, \tag{1.17}$$

where $N_{s,n}(B)$ is the number of *initial conditions* in B whose trajectories do not leave Γ before time n (Fig. 1.12). Formally, this corresponds to evaluating (1.16) at $r = 0$. Measure μ_s can in fact be regarded as the c-measure of the time-reversed dynamics,[6] and a restriction of this measure to the saddle provides the natural measure of the saddle in the time-reversed dynamics. When plotting the measure of the two manifolds together, as in Fig. 1.13, one notes the following two features: (1) the singularities of the c-measure fall outside the saddle, an indication of the hyperbolic nature of the saddle, and (2) the restriction of the stable manifold measure to the saddle is different from the natural measure (Fig. 1.10, and red columns in Fig. 1.13). Both restricted measures are defined on the chaotic saddle, but they agree only if the dynamics is invariant under time reversal (e.g., as in Hamiltonian problems).

Note that the sprinkler method (Sect. 1.2.2.3) for the construction of the saddle and its manifolds is based on the concept of numbers $N_n^{(r)}$, and corresponds to the particular choice $r \approx 1/2$ for plotting points of the saddle.

---

[6] Because of the analogy between μ_c and μ_s, we can also call the conditionally invariant measure the measure of the unstable manifold.

Fig. 1.12 Measure along the
stable manifold (cf. Fig. 1.7)
of the Hénon saddle for $a = 2$,
$b = 0.3$, identified on a grid
of size $\varepsilon = 1/400$. The region
Γ is $|x|, |y| \leq 1.5$ (Picture by
M. Gruiz and Sz. Hadobás)
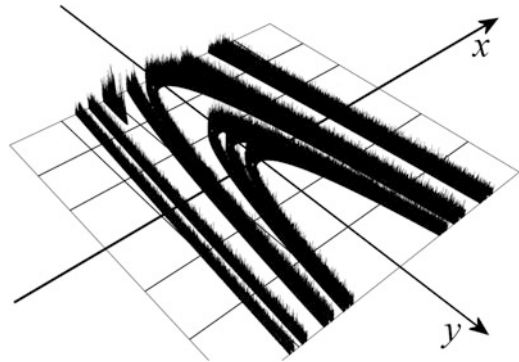
Fig. 1.13 Measure of the
stable and the unstable
manifolds. The natural
measure of the Hénon saddle
is shown in *red*. The
distribution in *red* is the same
as that of Fig. 1.10 but the
spatial view is different. The
restriction of the stable
manifold's measure to the
saddle differs from the natural
measure. (Picture by
M. Gruiz and Sz. Hadobás)
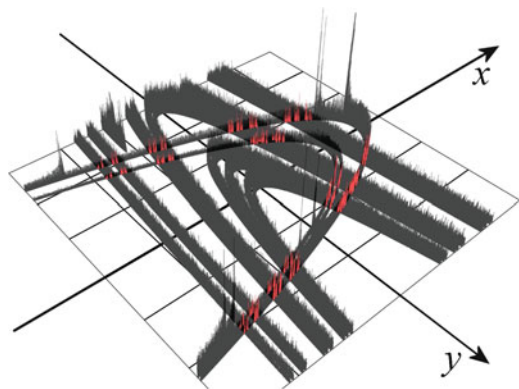
1.2.3.3 Characterization of the Natural Measure

Both the nonattracting set and its natural measure can possess complicated structures. To characterize the natural measure by certain numbers or simple functions is therefore of interest. In fact, such convenient characteristics are used widely in the study of chaotic attractors. While the characteristics can be worked out for *any type of invariant distributions* on the nonattracting set, we discuss here characterization of the natural measure, since it is physically most relevant. The typical characteristics are the Lyapunov exponents, the box-counting and information dimensions, the metric and the topological entropies, which are the dynamical invariants that we shall focus on in this book. For a more detailed analysis, full spectra of Lyapunov exponents, dimensions, and entropies can be introduced (see Appendix A). For simplicity we assume that there is only *one* expanding direction in the system. More-complicated cases will be treated in Chap. 8.

Consider first the *Lyapunov exponent*. Take a small interval of length Δ_0 along the unstable direction in a nonempty box i. It will be mapped after n steps onto a larger interval of some length Δ_n. The *stretching factor* Δ_n/Δ_0 can be written as $\exp[\Lambda_{1i}(n)]$, where the positive quantity $\Lambda_{1i}(n)$ is the *stretching exponent* belonging to box i. Here $\Lambda_{1i}(n)/n$ plays the role of a *local* Lyapunov exponent. The average

Lyapunov exponent λ_1 is simply the average of the stretching exponent with respect to the natural measure divided by n, i.e.,

$$\lambda_1 = \frac{1}{n} \sum_i \Lambda_{1i}(n) P_i(\varepsilon) \quad \text{for} \quad n \gg 1. \tag{1.18}$$

It should be noted again that the positivity of the Lyapunov exponent is not a defining characteristic for transient chaos, since any kind of nonattracting sets, e.g., unstable fixed points, can have a positive Lyapunov exponent. For an isolated saddle (hyperbolic) point one has, e.g., $\lambda_1 = \kappa > 0$.

The *fractal* properties of the nonattracting chaotic set and its natural measure describe how quantities scale with the box size ε. The box-counting dimension D_0 reflects how rapidly the number $N(\varepsilon)$ of nonempty boxes of dimensionless size ε covering the set increases with refining resolution:

$$N(\varepsilon) \sim \varepsilon^{-D_0} \quad \text{for} \quad \varepsilon \ll 1. \tag{1.19}$$

If the set is covered by boxes of different sizes ε_i, $i = 1, \ldots, N(\varepsilon)$, which are all bounded from above by an $\varepsilon \ll 1$, then (1.19) can be generalized to yield [45] the following implicit equation for D_0:

$$\sum_{i=1}^{N(\varepsilon)} \varepsilon_i^{D_0} = 1 \quad \text{for} \quad \varepsilon \ll 1. \tag{1.20}$$

This dimension characterizes only the geometry of the nonattracting set.

The *information dimension* is a measure of the inhomogeneity of the natural distribution. It measures how the information content of the box probabilities $P_i(\varepsilon)$ changes with the resolution:

$$-\sum_{i=1}^{N(\varepsilon)} P_i(\varepsilon) \ln P_i(\varepsilon) = D_1 \ln(1/\varepsilon) \quad \text{for} \quad \varepsilon \ll 1. \tag{1.21}$$

When the coverage consists of unequal small boxes of *different* sizes ε_i, but all bounded from above by some $\varepsilon \ll 1$, the information dimension D_1 can be expressed [45] by P_i, the probability that box i of size ε_i is visited, as

$$D_1 = \frac{\sum_i P_i \ln P_i}{\sum_i P_i \ln \varepsilon_i} \quad \text{for} \quad \varepsilon \ll 1. \tag{1.22}$$

The information dimension in fact belongs to a subset of the nonattracting set, the one that contributes dominantly to the information $-\sum_i P_i \ln P_i$. It therefore cannot be greater than the box-counting dimension:

$$D_1 \leq D_0. \tag{1.23}$$

The equality holds only when the distribution is uniform: $P_i(\varepsilon) = \text{constant}$ on the nonattracting set.

Typically, one can associate a few symbols to different regions containing the nonattracting set, and assign a symbol when the trajectory visits a given region. This defines a *symbolic representation* of trajectories on the set [45,220,564]. By following trajectories of length m about the nonattracting set, one can specify how often a given symbolic sequence $\{S_j\}_1^m$ occurs. These *path probabilities* $P(\{S_j\})$ provide a complementary characterization of the chaotic set: entropies.

In particular, the *metric entropy* K_1 is defined as the growth rate of the information content of the path probabilities with length m of symbolic sequences [45,220,564]:

$$-\sum_{\{S_j\}} P(\{S_j\}) \ln P(\{S_j\}) = K_1 m \quad \text{for} \quad m \gg 1, \qquad (1.24)$$

where the summation is taken over all symbolic sequences. Since the path probabilities depend on the natural measure, the metric entropy is also a characteristic of this measure. In terms of an information-theoretic interpretation [283], the metric entropy is the rate at which information stored in the insignificant digits of the initial condition flows toward the significant ones with time. The Lyapunov exponent λ_1 is in fact the mean velocity of this flow.

The *topological entropy* [2] K_0 reflects how complicated the organization of the symbolic encoding is: it is the growth rate of the number Ω_m of all allowed symbolic sequences of length m:

$$\Omega_m \sim e^{K_0 m} \quad \text{for} \quad m \gg 1. \qquad (1.25)$$

Here the different symbolic sequences are not weighted in terms of the path probabilities, whence the term "topological." The topological entropy can be also defined as the growth rate of the number N_m of all points of unstable periodic orbits of length m:

$$N_m \sim e^{K_0 m} \quad \text{for} \quad m \gg 1. \qquad (1.26)$$

A straightforward method for numerically calculating the topological entropy is due to Newhouse and Pignataro [548], which is based on the stretching of line segments in two-dimensional maps. Let L_n denote the length of the nth image of a line segment of initial length L_0 falling *within* some restraining region Γ enclosing the nonattracting set. One has

$$\frac{L_n}{L_0} \sim e^{K_0 n} \quad \text{for} \quad n \gg 1. \qquad (1.27)$$

Similar to the relation between the fractal and the information dimensions (1.23), we have the following inequality between the topological and the metric entropies [45]:

$$K_1 \le K_0, \qquad (1.28)$$

where the equality holds only for the special case in which all the symbolic sequences are equally probable.

An important feature of transient chaos is that there are exact and simple relations among the escape rate of the underlying nonattracting chaotic set, the information dimension, the Lyapunov exponents, and the metric entropy. In particular, one has

$$\kappa = g(\lambda_1, K_1) \tag{1.29}$$

and

$$D_1 = g_D(\lambda_1, K_1). \tag{1.30}$$

The particular forms of the right-hand sides of (1.29) and (1.30) depend on the dimensionality of the system. For maps of arbitrary phase-space dimensions, explicit expressions for g and g_D can be obtained, which we shall derive in later chapters.

Summarizing briefly, so far we have given, in terms of the quantities introduced, the criteria based on which the existence of a nonattracting chaotic set and consequently transient chaos can be established: (1) positivity of the topological entropy ($K_0 > 0$), and (2) fractality of the nonattracting set (noninteger values for the box-counting dimension D_0 or the information dimension D_1).[7]

That period three implies chaos [483], or equivalently, the existence of unstable cycles of infinite length, in fact implies the positivity of the topological entropy. It is then true that *period*-3 *implies transient chaos*.

1.3 Experimental Evidence of Transient Chaos

There has been ample experimental evidence of transient chaos. Here we shall present results from a few such experiments. In terms of quantification, earlier experiments mainly focused on determining the average transient lifetime, while more recent works have extended to characterizing the nonattracting chaotic set and its natural measure.

1.3.1 Convection Loop Experiment

The apparatus consists of a loop-shaped reservoir filled with water, which is heated from below along the lower semicircle and cooled from above, as shown in Fig. 1.14. The system was investigated from the point of view of chaotic dynamics by Widmann, Gorman, and Robbins [273, 274, 823], and by Bau and coworkers [822]. The system is the one-dimensional analogue of the Rayleigh–Bénard convection problem, and its dynamics can be described in certain parameter regimes

---

[7] The positivity of the largest Lyapunov exponent cannot be taken as a criterion because of the example of an isolated saddle point.
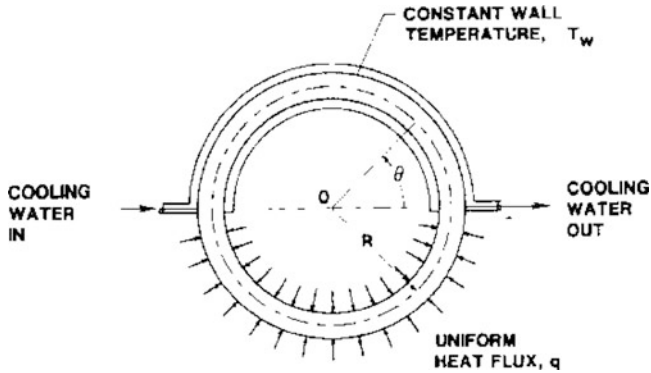
Fig. 1.14 Schematic diagram of the convection loop experiment. Representative results from the experiment are shown in Fig. 1.2 [823] (with kind permission from Elsevier Science)

by the Lorenz model [488]. After convection sets in at sufficiently high heat flux, the velocity of the fluid along the loop changes its sign and magnitude *in a chaotic manner*. There is a broad range of system parameters for which the chaotic oscillations last for a finite amount of time before settling into a state in which the system ceases to oscillate, as exemplified by Fig. 1.2. The duration of the transient chaotic oscillations depends sensitively on the initial state of the system.

1.3.2 Chemical Reactions Preceding Thermal Equilibrium

Stirred chemical reactions in closed containers cannot be chaotic in a sustained manner, since the system typically approaches thermal equilibrium after a transient period of time, corresponding to a fixed-point attractor in the space of the concentrations. Scott, Showalter and coworkers conjectured, however, that the *approach toward equilibrium*, i.e., the reaction dynamics before settling into the final fixed-point attractor, can be chaotic [700]. The conjecture was experimentally verified by Wang, Sorensen, and Hynne [820, 821] using the Belousov–Zhabotinsky reaction. Chaotic oscillations as the light transmission have been observed (Fig. 1.15) over several hours before a stage close to thermal equilibrium is reached.

1.3.3 Nuclear Magnetic Resonance Laser Experiment

The high quality of the data from an nuclear magnetic resonance (NMR) laser makes it appropriate for experimental investigations of a variety of chaotic phenomena. The laser output is a time-dependent voltage signal, and the control parameter is usually the modulation amplitude. At a bifurcation called a *crisis* (see Chap. 3), a chaotic
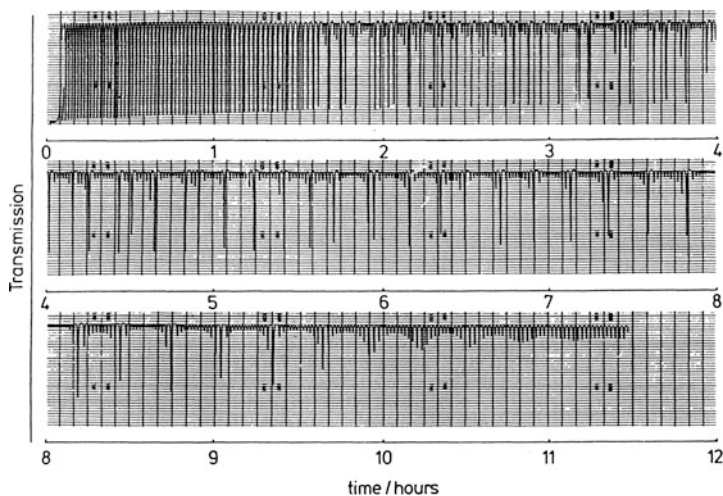
Fig. 1.15 Transiently chaotic oscillations (which start after about 1.5 h and continue for about 7 h) in a closed Belousov–Zhabotinsky reaction ending with small-scale oscillations that ultimately diminish as the system approaches thermal equilibrium [820] (Copyright 1994 by the American Chemical Society)

attractor undergoes a sudden explosion in its size. In particular, slightly before the crisis only a small-size attractor exists. In this regime, before settling into the small attractor, trajectories started from random initial conditions exhibit chaotic motion in the region where the postcrisis attractor lives, signifying transient chaos coexisting with permanent chaos. Time-series analysis of transient chaos [356] led to a successful reconstruction of the chaotic saddle responsible for the observed transient behavior, which was accomplished by considering only the parts of the signals that do not belong to the small attractor. By combining a number of such truncated signals, a long time series can be generated that is amenable to chaotic time-series analysis [382]. In this way, not only can the chaotic saddle be reconstructed, but also its dynamical characteristics, such as the average Lyapunov exponent, can be determined (Fig. 1.16).

1.3.4 Driven Pendulum

The parametrically driven damped pendulum is another example in which high-precision experiments [479, 480] on transient chaos can be carried out. In such an experiment, the angle and the angular velocity of the pendulum are measured, with the damping constant as a bifurcation parameter. The chaotic saddle can be reconstructed using a stroboscopic map. The experiment demonstrates, explicitly, fractality along both the stable and the unstable manifolds (Fig. 1.17). The box-counting dimension of the saddle was determined to be about $D_0 = 1.7$. For a more recent pendulum experiment, see [170]
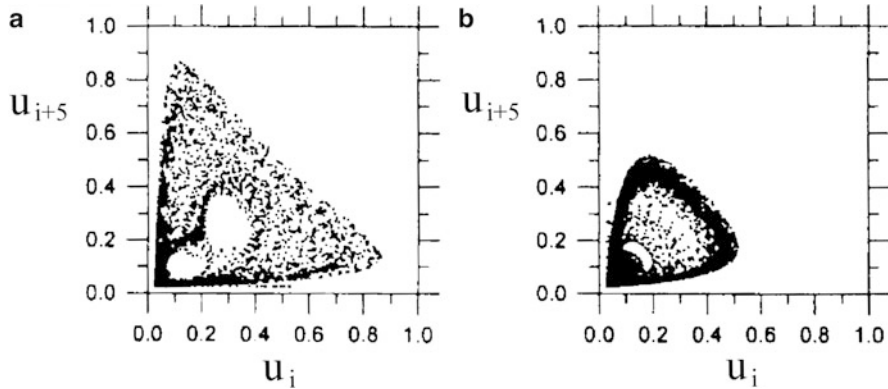
Fig. 1.16 Reconstruction of the chaotic sets from a nuclear magnetic resonance (NMR) laser experiment via time series analysis. (**a**) Chaotic saddle, (**b**) coexisting chaotic attractor. Note that the saddle not only appears larger, it is also more chaotic: its average Lyapunov exponent is about twice as large as that of the attractor [356] (Copyright 1994 by the American Physical Society)
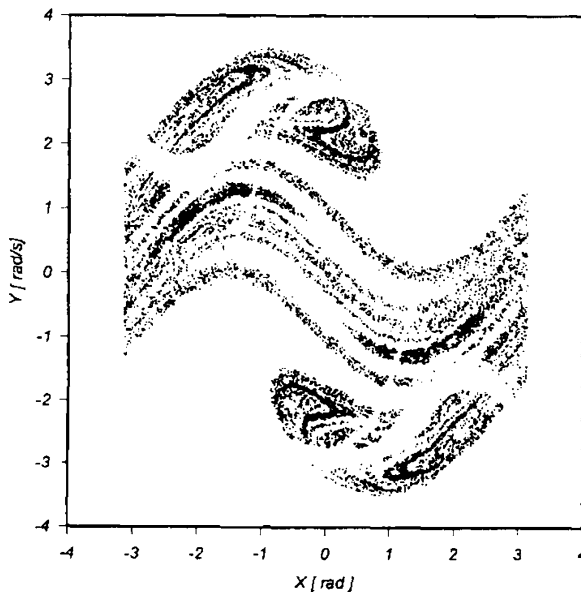
Fig. 1.17 A chaotic saddle reconstructed from the driven-pendulum experimental data. The double Cantor set character can be seen through the blank saps amid the points [480] (with kind permission from Elsevier Science)

1.3.5 Fractal Basin Boundaries

The boundaries between basins of attractions can often be fractal in nonlinear dynamical systems, and transient chaos can arise in a phase-space region containing such boundaries. Experimental observation of fractal basin boundaries can be quite

Fig. 1.18 For an electric circuit system of four coupled chaotic oscillators: basin of the synchronous chaotic attractor in *black*, and basin of one of the periodic attractors in *white*. The horizontal and vertical coordinates are proportional to the initial deviations of two coordinates of the oscillators from a point on their common chaotic attractor. Points of the white basin are dense in the black basin: the black basin is riddled [322] (copyright 1994, the American Physical Society)
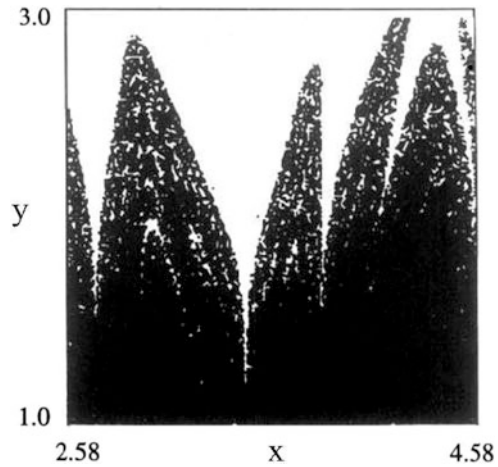
challenging because of the necessity to choose initial conditions on a fine scale and to monitor each trajectory until it approaches one attractor. An experimental investigation of an extreme type of fractal boundaries is due to Heagy et al. [322], who studied a system of a set of four weakly coupled, nearly identical oscillators. Each isolated oscillator exhibits a chaotic attractor, and the attractor associated with the whole coupled system corresponds to a synchronous motion of the chaotic oscillators. The coupled system also possesses periodic attractors. Figure 1.18 shows the basins of the synchronized state (set of black points) and of one of the periodic attractors (white regions). The black basin exhibits a rather special property: it is the *riddled* basin where every point in the black basin has points of the white basin arbitrarily nearby.

1.3.6 Advection in the Wake of a Cylinder

In two-dimensional laminar flows around some obstacles, von Kármán vortex streets are typically formed. Due to the periodic detachment of vortices in the wake, the flow is periodic in time. The advection of particles is generally chaotic in time-periodic flows. In particular, since strong time-dependence is restricted to the wake only, advective chaos is transient, as illustrated in an experiment with a towed cylinder by Sommerer, Ku, and Gilreath [725]. The physical space of the fluid motion happens to coincide with the phase space, rendering directly observable fractal patterns that usually exist in the phase space. Of particular interest is the unstable manifold of the chaotic saddle in the wake, since dye particles flow away along this manifold. The experiment not only illustrated that dye (or pollution) often spreads out along fractal patterns, but also provided an example in which a fractal unstable manifold can be seen even by the naked eye, as shown in Fig. 1.19.

Fig. 1.19 For the experiment
of advection in the wake of a
cylinder (*black disk*), fractal
pattern traced out by
spreading a dye droplet the
unstable manifold of a chaotic
saddle existing in the wake.
The flow is from left to right,
and the droplet is injected into
the upstream of the flow. The
lower panel shows the results
of a numerical simulation of
the same problem [725]
(copyright 1996, the
American Physical Society)
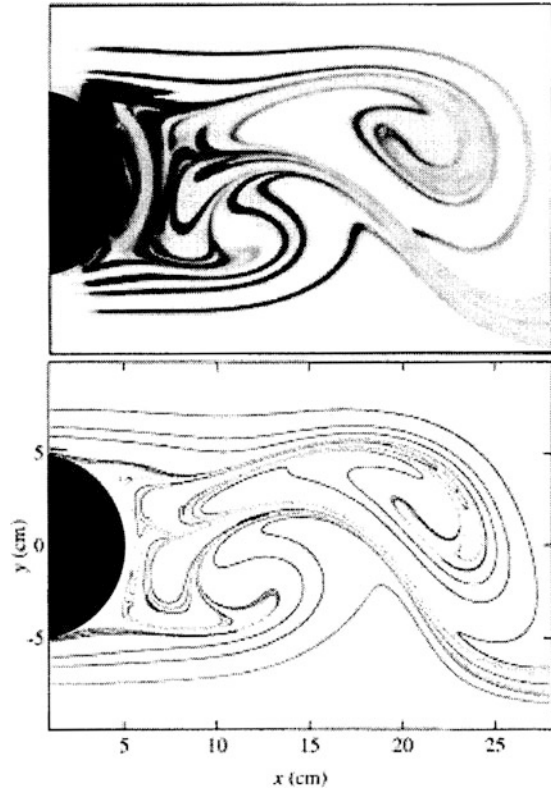
1.3.7 Semiclassical Fluctuations in Chaotic Scattering

Interference effects of the scattering process become important in the semiclassical
regime where wave properties are observable. Chaotic wave scattering, the scatter-
ing of waves from systems for which the underlying classical dynamics is chaotic, is
observable not only in nanoscale electronic devices, but also in microwave scattering
from macroscopic objects. Doron, Smilansky, and Frenkel [204] investigated the re-
flection of microwaves from an elbow-shaped cavity, where the underlying classical
ray dynamics is chaotic with an exponential decay of rate κ in the survival probabil-
ity of particles in the cavity. The basic quantity characterizing the wave-scattering
process is the scattering matrix $S(\omega)$ as a function of the frequency. According to
the semiclassical theory, the squared modulus of its Fourier transform $S(t)$ tends to
decay with the *classical* escape rate κ. This is consistent with the experimental find-
ings, as shown in Fig. 1.20. It can also be seen that the absolute value of the squared
frequency-dependent autocorrelation function is a Lorentzian of half-width κ.
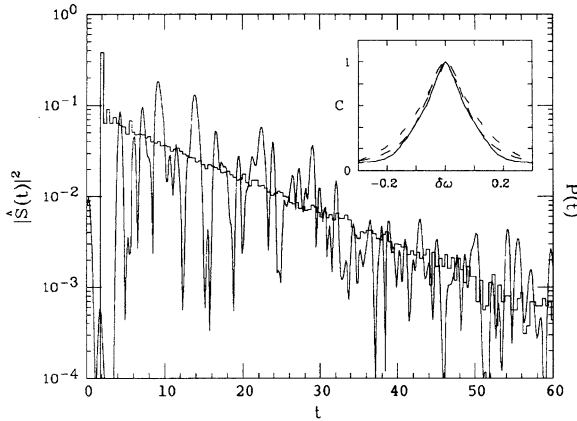
Fig. 1.20 For microwave scattering from an an elbow-shaped cavity, squared modulus of the time-dependent S-matrix, $|S(t)|^2$ (oscillating curve), exhibiting an overall decay that agrees with that of the classical escape-time distribution (curve in background). *Inset*: squared modulus of the frequency- (energy-) dependent autocorrelation function from the measured data (*continuous line*) and from the semiclassical theory (*dashed line*). The dimensionless half-width is $\kappa = 0.1$ [204] (copyright 1990, the American Physical Society)

1.3.8 Emission of Light from Dielectric Cavities

Dielectric cavities of cylindrical or spherical geometry are of technological importance because they can keep light trapped for a long time. When light circulates almost tangent to the surface of such a cavity via total internal reflection, it suffers minimal loss. Slightly deformed cavities emit light of nonnegligible intensity, and it was observed with surprise that these emissions are peaked in certain directions. A measurement by Schwefel and coworkers [699] records the light intensity for billiard-shaped cavities as a function of two angles: the angle Φ along the sidewall of the billiard, and an angle θ by which the camera is rotated in the far field from the major axis. Figure 1.21 shows the result for three different shapes with a deformation corresponding to approximately the same major-to-minor-axis ratio. Light intensity is localized to certain regions of the (Φ, θ) plane, meaning that light is emitted at specific points of the sidewall only, and in an approximately predetermined direction. Although the billiard shapes (shown as insets) appear similar in the last two cases, the emission patterns are rather different: the intensity integrated over the sidewall angle is peaked, e.g., about $90°$ and $30°$. In the geometrical optics approximation, the patterns can be explained by the existence of a chaotic saddle of exceptional light rays that are never transmitted, i.e., they are subject to permanent total internal reflection both forward and backward in time. The form of these saddles depends sensitively on the shape of the billiard. In addition, the directionality of the light has been shown to be intimately related to the unstable manifold of
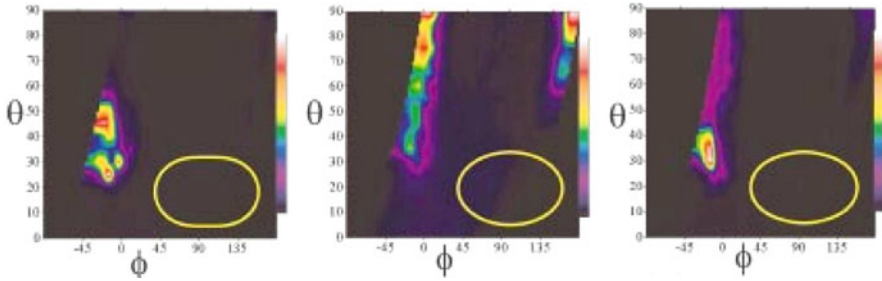
Fig. 1.21 Light emission intensity in false color (*color bar* at the sides) as a function of the side-wall angle Φ and of the camera angle θ for three microcavities, whose shapes are drawn as insets [699] (copyright 2004, the Optical Society of America)

certain unstable fixed points [699], and more rigorously, of the entire chaotic saddle [15]. This is thus a further example in which the unstable manifold of chaotic saddle become related to physical observables.

1.3.9 Maintaining Chaos in a Magnetoelastic Ribbon

Since there are systems that require chaos in order to function properly, it is important that transient chaos be convertible into permanent chaos. The aim of this procedure, which is called *maintenance of chaos*, is to intervene in the dynamics in such a way as to keep chaotic behavior alive in situations in which it would naturally be absent. A possible realization is to apply properly chosen perturbations to the signal in order to keep it always on that side of the stable manifold of a hyperbolic point from which a return to a nonattracting chaotic set is allowed. The method can be improved by finding a target point on this side from which a transiently chaotic trajectory of long lifetime is initiated, and trying to direct the signal to the target point [697]. In an experiment by In et al. [351], chaos in a magnetoelastic ribbon was successfully maintained at a parameter set where a fixed-point attractor exists; see Fig. 1.22. The quantity X_n plotted is proportional to the position of a point on the ribbon measured once every driving period of an applied external magnetic field.

1.3.10 Turbulence in Pipe Flows

In a pipe flow, a steady laminar solution is linearly stable for *all* Reynolds numbers $Re \equiv UD/\nu$, where U is the average velocity in a pipe of diameter D, and ν is the kinematic viscosity. The turbulent state can be considered as a high-dimensional chaotic state associated with a chaotic saddle. In an experiment, Peixinho and Mullin followed turbulent puffs downstream and measured their positions along the pipe
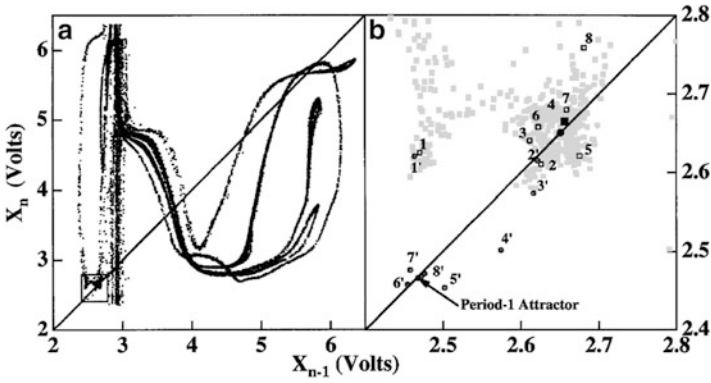
Fig. 1.22 Maintaining chaos in an experiment by In et al. [351]. (**a**) Projection of the stabilized chaotic attractor. (**b**) Blowup of the square shown in (**a**). The *filled circle* on the diagonal marks the hyperbolic point and the *filled square* marks the target. *Small circles* $1'$–$8'$ show an unperturbed sequence and *small squares* 1–8 illustrate the perturbed sequence (Copyright 1998, the American Physical Society)

Fig. 1.23 For an experiment of turbulence in a pipe flow, probability of observing a turbulent puff as a function of the dimensionless downstream distance from the point where the puff is generated. The numbers associated with different experimental curves denote the Reynolds number *Re*. It can be seen that the escape rate decreases with *Re* [589] (Copyright 2006, the American Physical Society)
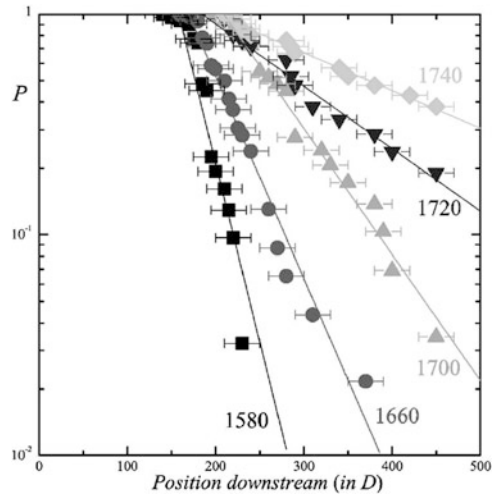
where the puffs are relaminarized [589]. The distributions exhibit exponential decay, as shown in Fig. 1.23. Normalized by length D and time D/U, the dimensionless distance and the dimensionless time to reach this distance are proportional to each other, i.e., the dimensionless velocity is of the order of unity. Turbulence in pipe flows is thus a high-dimensional chaotic transient with finite lifetime. Recent investigations indicated that the average lifetime tends to grow extremely rapidly with the Reynolds number [334, 336].

1.4   A Brief History of Transient Chaos

The first observation of chaotic transients was part of the prehistory of chaos science. In the late 1940s, in their early studies of the forced Van der Pol oscillator, Cartwright and Littlewood [114] and Levinson [482] found signatures of chaotic transients as the system settles into one of the coexisting attractors (there are in fact fractal basin boundaries between the basins of attraction). Later, in 1973, Chirikov and Izraelev identified certain transient features in weakly dissipative systems [134, 135].

A systematic investigation of transient chaos began in the late 1970s with the works of Shimizu and Morioka [714], Kaplan and Yorke [386], and Yorke and Yorke [843] on the dynamics of the Lorenz system in parameter regimes that differ from the standard one with a chaotic attractor, where the attractors are either limit cycles or fixed points. An important step toward a firm mathematical foundation of the phenomenon was the introduction of the concept of the conditionally invariant measure by Pianigiani and Yorke [595, 596]. Subsequently, several theoretical papers reported this phenomenon in all kinds of nonlinear systems: low-dimensional maps [141, 184, 500], nonlinear oscillators [337, 338, 512], systems modeled by time-delayed equations [380], partial differential equations [348, 715], and coupled oscillators [795].

A comprehensive investigation of transient chaos originated from the discovery that chaotic transients arise typically in systems passing through a type of global bifurcation called crisis (Grebogi, Ott, and Yorke in 1983 [293]). The Maryland Chaos Group has played since then an important role in the understanding of further transient-chaos-related phenomena, which include fractal basin boundaries, Wada boundaries [406, 780], and riddled basins [11]. The importance of the natural measure on nonattracting chaotic sets and of quantities related to it was pointed out by Kantz and Grassberger in 1985 [380] and later by Hsu, Ott, and Grebogi [73, 341], generating further interest in the topic (see reviews in [766] and [770]).

Interest in the chaotic aspects of scattering processes dates back to early studies of classical chemical reactions [56, 275, 555, 622] and point–vortex interactions [25]. A systematic study of the subject began in the late 1980s with the work of Jung [360], Eckhardt [210, 211], Hénon [326], and Bleher, Ott, and Grebogi [73, 74]. The concept of chaotic advection, coined by Aref [26] and generalized to open hydrodynamical flows, corresponds to a transiently chaotic spreading of particles [371]. This is in fact a chaotic scattering process, which has important applications in pollutant transport. The quantum-mechanical aspects of chaotic scattering were addressed by Blümel and Smilansky [76], Jung [368], Gaspard and Rice [259], and Cvitanović and Eckhardt [152].

The work by Crutchfield and Kaneko [146] on transient chaos in spatiotemporal systems generated a new perspective of research aiming at understanding whether spatiotemporal complexity, or turbulence, is related in general to attractors or rather to nonattracting chaotic sets generating long-lived transients.

The first experimental indications of irregular transient behavior were found in hydrodynamical systems, where transients were followed over days before

settling down on a periodic attractor [9]. Although in current terminology these were spatiotemporal chaotic transients, a number of papers appeared afterward reporting low-dimensional transiently chaotic behavior in systems exemplified by a compass forced by a magnetic field [145], lasers [23,154,577], electronic oscillators [22,333,646], and a parametrically forced pendulum [479]. Besides the convection-loop [273,274] and the pendulum [479,480] experiments (cf. Sect. 1.3), a spin-wave experiment [110, 111, 113] seemed to have provided high-quality measurements of chaotic transients. Other investigations included the dynamics of a bouncing ball [422] and a driven magnetoelastic ribbon [196]. Many experimental systems in which transient chaos has been observed are in fact systems with fractal basin boundaries (e.g., [22, 422, 577]). In spite of these experimental works and the several experiments carried out in the last 20 years, it is possible that due to the limited awareness of the phenomena of transient chaos even among researchers in the nonlinear-dynamics community, transiently chaotic signals were considered to be uninterpretable and were discarded.

Chapter 2
Transient Chaos in Low-Dimensional Systems

We study low-dimensional dynamical systems, i.e., systems described by one-dimensional noninvertible or two-dimensional invertible maps. For such systems it is often possible to obtain analytic understanding of generic properties of transient chaos that are shared by more realistic physical systems. For example, for a higher-dimensional system, one-dimensional maps can be used to model the dynamics along the unstable manifold [220, 564].

For one-dimensional maps, we shall analyze in detail the relation between the natural and the conditionally invariant measures of repellers, and introduce analytic tools based on the Frobenius–Perron type of *eigenvalue equations*. These considerations allow us to derive explicit dimension and entropy formulas. We will also elaborate the relevance of transient chaos to problems in mathematics, physics, and engineering, and address the issue of nonhyperbolicity. In particular, we will show that nonhyperbolic dynamics can lead to a power-law decay, and to the concentration of the natural measure on a single point, despite the fractal character of the repeller.

Two-dimensional invertible maps are equivalent to three-dimensional flows and can be obtained by the standard technique of stroboscopic or Poincaré surface of section [564]. We shall discuss again the relation between the natural and the c-measures, derive the corresponding entropy and dimension formulas, and provide an information-theoretic motivation. A fundamental feature of any chaotic set is the existence of an infinite number of unstable periodic orbits. We will discuss how transient chaos is organized about the periodic orbits. While chaotic saddles are often hyperbolic, meaning that the stable and the unstable manifolds do not become tangent to each other (i.e., there are no homoclinic or heteroclinic tangencies), nonhyperbolic chaotic saddles can also arise [454].

For completeness, the multifractal formalism, a more systematic characterization of the natural measure, will be discussed briefly in Appendix A.

2.1 One-Dimensional Maps, Natural Measures, and c-Measures

2.1.1 Basic Properties of One-Dimensional Maps Generating Transient Chaos

Strong dissipation leads to significant contraction in the phase space and consequently to an approximately one-dimensional discrete map on a stroboscopic or Poincaré plane. One-dimensional maps are typically noninvertible. They are the simplest class of dynamical systems in which transient chaos can occur, and insights obtained from studying them can often be useful for exploring transient chaos in higher-dimensional systems.

Let $f(x)$ be a one-dimensional noninvertible map. Transient chaos occurs if an interval I is mapped partially *outside* itself. We shall consider here single-humped map functions, as illustrated by Fig. 2.1. There is a primary escape interval I_0 that is mapped outside I in a single iterate. The dynamics of the map outside I is irrelevant. For example, there can be one or more attractors far away, but if there is no feedback from these regions onto I, the transient chaotic behavior is completely specified by the function f defined *on* I.

As an illustrative example, we consider the classical logistic map $x_{n+1} = f(x_n, r) = rx_n(1 - x_n)$, which generates transient chaos for $r > 4$. There is a chaotic repeller in the unit interval $I = (0, 1)$, and this interval can be chosen as the restraining region Γ. Figure 2.2 shows the approximate invariant measure on the repeller for $r = 4.03$ covered by uniform boxes of size $\varepsilon = 2 \cdot 10^{-3}$, where the box probabilities $P_i(\varepsilon)$ are displayed. Figure 2.2 also contains information about the repeller's structure. For example, it can be noticed that the crudest approximation to the

Fig. 2.1 A typical one-dimensional map generating transient chaos on some interval I. Note that points lying outside the two subintervals $I_1^{(1)}$ and $I_2^{(1)}$ escape I after one time unit. Points that do not exit in n steps are contained in the $(n-1)$th preimages of the two subintervals (i.e., in the nth preimages of I), and exhibit chaotic behavior on time scale n due to the global expansivity of the map
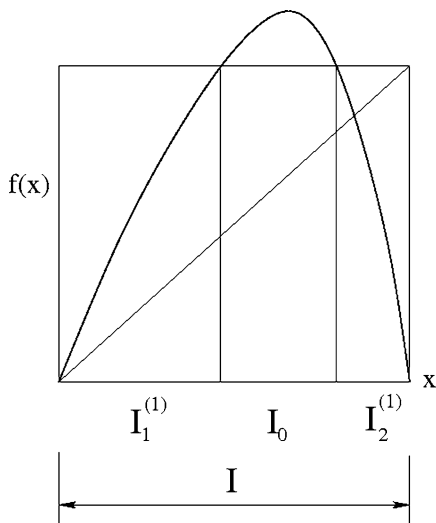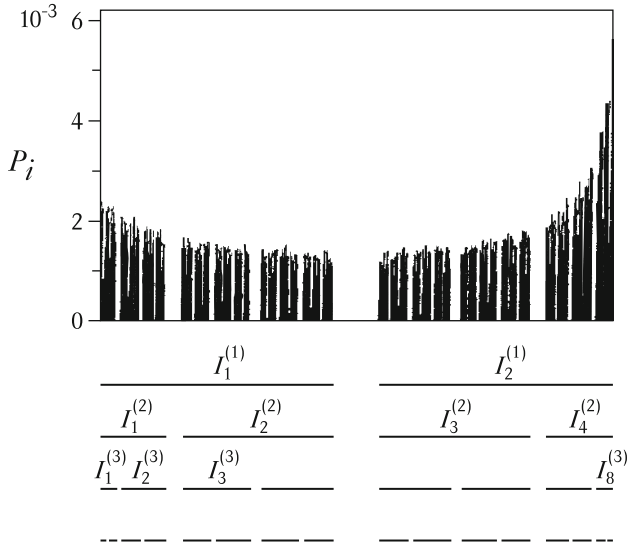
Fig. 2.2 Natural distribution for the logistic map $x_{n+1} = rx_n(1 - x_n)$ for $r = 4.03$ obtained by the ensemble method (cf. Sect. 1.2.2.2) on a grid of size $\varepsilon = 0.002$. The number of initial points distributed uniformly in $I = R = \Gamma$ is $N_0 = 10^7$, and the first 10 and the last 30 steps of trajectories are discarded. The truncated trajectories contain about 10^6 points, so that reasonable statistics can be obtained. The escape rate can be estimated by comparing the number of trajectories of length 10 and 30 in I, which yields, via (1.6), $\kappa \approx 0.07$. The lower part of the figure illustrates the organization of the repeller, where $I_i^{(n)}$ denotes the cylinders at level n, i.e., the nth preimages of $I = (0, 1)$ (cf. Fig. 2.3), and resembles the construction of a Cantor set

repeller cover consists of two intervals, the two preimages $I_1^{(1)}$ and $I_2^{(1)}$ of I. At the next stage, each of them splits into two smaller intervals. Subsequent successive refinements will then yield a complete *hierarchy*, the nth level of which contains all the nth preimages of I. The preimage intervals are called *cylinders* and are denoted by $I_i^{(n)}$, where the subscript i enumerating them runs, at the nth level, up to 2^n. Note that here, the base 2 is due to the two branches that the inverse map f^{-1} exhibits. Also note that the cylinders provide coverage of the repeller with *nonuniform* boxes that fit the repeller's structure in a natural manner. An equivalent way of defining the cylinders is to consider the n-fold iterated map f^n, whose graph contains 2^n branches (Fig. 2.3). The intervals mapped exactly onto I by the nth iterated map are nothing but the cylinders of level n, indicating that points in any subinterval $I_i^{(n)}$ do not leave the restraining region I sooner than $n + 1$ steps. Since the folds with derivatives smaller than unity are, for sufficiently large n, outside I, the dynamics are *expansive*, or in this one-dimensional case, are *hyperbolic* on the repeller.

Fig. 2.3 The threefold
iterated logistic map for
$r = 4.03$, and cylinders
$I_i^{(3)}, i = 1, \ldots, 8$. The *dots*
denote points of 3-cycles

$$f^3(x)$$

$$I_1^{(3)} \quad I_2^{(3)}$$
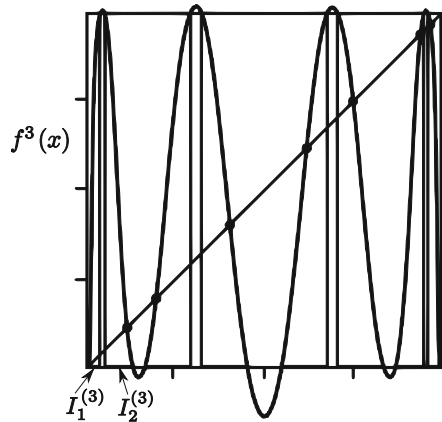
2.1.2 Conditionally Invariant Measure

We now consider the *conditionally invariant* (c-)measure [596] for one-dimensional
maps. This measure is defined on any region Γ containing the repeller, and de-
scribes how trajectories escape this region. For simplicity we take $\Gamma = I$. Consider
the conditional probability that a given region is visited by trajectories originated
from random initial conditions in I that do not escape I in m steps. A fraction of
these trajectories will escape at the next time step, and hence their last points in I
are in the gaps among the cylinders. The conditional probability is thus defined on
the *entire* interval I. The limit to which this conditional probability converges for
$m \to \infty$ is the conditionally invariant measure. As mentioned in Sect. 1.2.3.2, the
c-measure is effectively the time-independent distribution maintained by supplying
new points into the system exactly according to the escape rate.

The density of the c-measure can be constructed from trajectories of minimal
length m in the basic interval. For example, one can select trajectories whose first m
points are disregarded and all the remaining points are kept before escaping I. This
procedure usually converges exponentially fast for rather arbitrary choice of m (e.g.,
$m = 10$), as exemplified by Fig. 2.4. It can be seen that the measure has a *smooth
density* everywhere on the interval I, due to the fact that it is in general smooth along
the unstable manifold (cf., e.g., Fig. 1.11).

To connect the conditionally invariant measure with the natural measure, we
restrict the density of the c-measure to cylinders of level n. This requires a renor-
malization so that the total measure on the cylinders is unity. The c-measure $\mu_{ci}^{(n)}$
of intervals $I_i^{(n)}$ characterizes then the motion of trajectories visiting the cylinders
of level n. For sufficiently large n, these are the trajectories exhibiting long-lived
chaotic transients. Therefore, the limit of the cylinder measures $\mu_{ci}^{(n)}$ for $n \to \infty$ can
be considered as the *exact* natural measure μ on the repeller:

$$\mu_{ci}^{(n)} \to \mu_i^{(n)}. \tag{2.1}$$
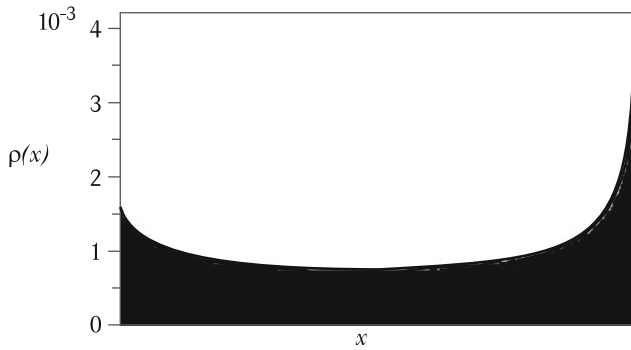
Fig. 2.4 Density $\rho(x)$ of the conditionally invariant measure for the logistic map on $I = (0, 1)$, obtained by discarding the first 10 steps of trajectories and keeping all points that stay inside the restraining region I. Parameter, initial conditions, and the box size ε are the same as in Fig. 2.2
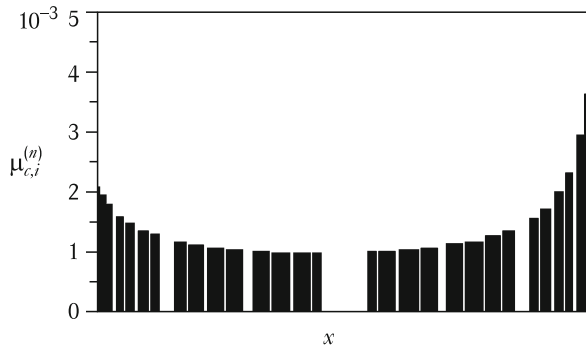
Fig. 2.5 Measure obtained by restricting the conditionally invariant measure of Fig. 2.4 to cylinders of level $n = 5$ specified by the accuracy $\varepsilon = 0.002$. The cylinder measures in this approximation are $\mu_i^{(5)}$, for $i = 1, \ldots, 32$. Note that the two outermost cylinders are not resolved by the grid

For large n we can omit the subscript c and denote the cylinder measure by $\mu_i^{(n)}$. We thus have two different approximations to the natural measure: the box probabilities $P_i(\varepsilon)$ and $\mu_i^{(n)}$. The equivalence of the two quantities is illustrated in Fig. 2.5, which displays the c-measure restricted to cylinders of level 5. Alternatively, one can smooth out the approximate natural measure shown in Fig. 2.2 on the same set of cylinders. The resulting distribution is essentially the same as that of $\mu_i^{(n)}$ even for the relatively low value of $n = 5$.

2.1.3 The Frobenius–Perron Equation

The Frobenius–Perron equation provides a framework from which analytic insights into the density $\rho(x)$ of the c-measure can be obtained. In general, the equation

governs the time evolution of a density $\rho_n(x)$ via an iterative scheme. For a one-dimensional map exhibiting transient chaos, the equation is

$$\rho_{n+1}(x') = R \sum_{x \in f^{-1}(x')} \frac{\rho_n(x)}{|f'(x)|}, \tag{2.2}$$

where R is a prefactor and the summation is taken over the preimages of x'. For $R = 1$, the equation is the Frobenius–Perron equation for attractors [220, 564], corresponding to a situation without escape. For transient chaos, escapes can be taken into account by choosing properly the prefactor R. In particular, by iterating any smooth, positive initial function $\rho_0(x)$ on I, the series $\rho_n(x)$ either diverges or tends to zero unless we choose [596, 764]

$$R = e^\kappa, \tag{2.3}$$

which is the compensation factor described in Sect. 1.2.3.2 with κ being the escape rate. With this choice of R, the series $\rho_n(x)$ converges to a finite $\rho(x)$:

$$\rho_n(x) \rightarrow \rho(x) \tag{2.4}$$

independently of the choice of the initial function. The limit $\rho(x)$ is the *density* of the c-measure and satisfies the following self-consistent equation:

$$\rho(x') = e^\kappa \sum_{x \in f^{-1}(x')} \frac{\rho(x)}{|f'(x)|}. \tag{2.5}$$

This equation can be considered as an eigenvalue problem of the Frobenius–Perron, or transfer, operator $\sum_{x \in f^{-1}(x')} |f'(x)|^{-1}$. The fact that its largest eigenvalue $\exp(-\kappa)$ less than unity is the mathematical reason for the long-term exponential decay of the survival probability (1.8).

In numerical experiments where the escape rate κ is not known a priori, different values for R can be chosen and tested until convergence in $\rho(x)$ is achieved. For transient chaos in typical one-dimensional maps, the convergence is usually quite fast and the limiting $\rho(x)$ of reasonable accuracy can be achieved after a few iterations [764], as shown by one example in Fig. 2.6. In this case, both the escape rate and the density can be found by numerically solving the eigenvalue problem.

In general, the escape rate can be obtained as an integral of density ρ over the intervals $I_1^{(1)}$, $I_2^{(1)}$ (see Fig. 2.1 and (1.14)) not escaping within a single step:

$$e^{-\kappa} = \mu_c(f^{-1}(I)) \equiv \int_{I_1^{(1)}} \rho(x)dx + \int_{I_2^{(1)}} \rho(x)\,dx, \tag{2.6}$$

provided that the c-measure is normalized to unity on I: $\int_I \rho(x)\,dx = 1$. As a consequence, the escape rate can also be expressed by the c-measure of the primary escape interval I_0,
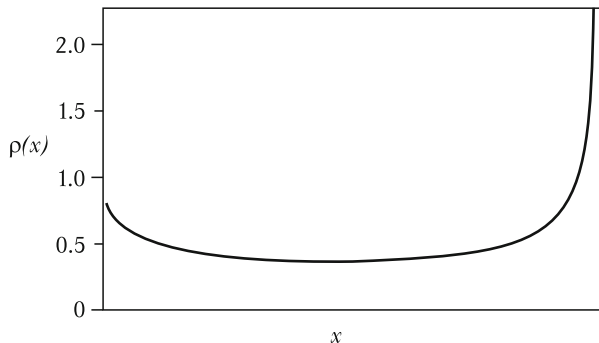
Fig. 2.6 Density $\rho(x)$ of the logistic map on I for $r = 4.03$, obtained from (2.2) as the eighth iterate of a constant initial function. The relative error is about 10^{-3}

$$1 - e^{-\kappa} = \int_{I_0} \rho(x)\,dx. \tag{2.7}$$

When the escape rate is small so that the approximation $\exp(-\kappa) \approx 1 - \kappa$ holds, we have

$$\kappa = \int_{I_0} \rho(x)\,dx \approx \rho(x_c)L, \tag{2.8}$$

where L is the size of I_0. The approximate equality expresses that for small κ the primary escape interval is short, and the integral over I_0 can then be approximated as the density about a typical point x_c in I_0 multiplied by the length L of the escape interval.

By iterating (2.2), one can see the presence of a singularity at the maximum of $f(x)$, but it falls *outside I*. This supports again the view that the density of the c-measure is a smooth function on close neighborhoods of hyperbolic repellers. Using the definition of the density, the cylinder measure $\mu_i^{(n)}$ can be expressed as

$$\mu_i^{(n)} = \frac{\int_{x \in I_i^{(n)}} \rho(x)\,dx}{\sum_j \int_{x \in I_j^{(n)}} \rho(x)\,dx}. \tag{2.9}$$

The smoothness of ρ enables us to obtain the actual value of the density from the integrals, for sufficiently small cylinders. Since the density does not change with the refinement, the asymptotic scaling with n is governed by the length scales only. Thus, for large n, *the measure of a cylinder is proportional to its length*. More precisely, we have

$$\mu_i^{(n)} \sim \frac{\varepsilon_i^{(n)}}{\sum_j \varepsilon_j^{(n)}} \quad \text{for } n \gg 1, \tag{2.10}$$

where $\varepsilon_i^{(n)}$ stands for the length of the cylinder $I_i^{(n)}$. The n-independent proportionality factor not written out here depends on the actual form of ρ. Equation (2.10)

is essential for our subsequent discussions. Note that the total length of cylinders at level n is proportional to the number of points not yet having escaped I after n steps. The cylinder measure can therefore be expressed as

$$\mu_i^{(n)} \approx e^{\kappa n} \varepsilon_i^{(n)}. \tag{2.11}$$

2.2 General Relations

There exist general relations in simple form among the metric entropy, the Lyapunov exponent, the information dimension, and the escape rate. The box-counting dimension and the topological entropy, however, can be related to the escape rate in a more complicated manner only. We shall derive these relations in this section.

2.2.1 Lyapunov Exponent, Information Dimension, and Metric Entropy

With each cylinder $I_i^{(n)}$, one can associate a unique symbol sequence $\{S_j\}$ ($j = 1, 2, \ldots, n$) of length n. In a single-humped map, the symbols are binary: S_j takes on the value 0 (1) if a trajectory started in the cylinder is at time step $j - 1$ in the subinterval $I_1^{(1)}$ ($I_2^{(1)}$) (see Fig. 2.1). The leftmost and the rightmost cylinders have the code $\{0, 0, \ldots, 0\}$ and $\{1, 0, \ldots, 0\}$, respectively. The cylinders can then be labeled by the corresponding symbol sequences. Moreover, the cylinder measures are exactly the path probabilities $P(\{S_j\})$ (1.24) for finding a symbolic trajectory $\{S_j\}$ of length n:

$$\mu_i^{(n)} = P(\{S_j\}). \tag{2.12}$$

To obtain the Lyapunov exponent, one observes that the logarithm of the slope of the n-fold iterated map f^n at x is just the stretching factor (see Sect. 1.2.3.3) at this point. The slope is, however, approximately constant in a cylinder, as illustrated by Fig. 2.3. Since the length of I can, in general, be chosen to be unity, the stretching factor in cylinder $I_i^{(n)}$ of size $\varepsilon_i^{(n)}$ is approximately $1/\varepsilon_i^{(n)}$. The stretching exponent is then $\Lambda_{1i}(n) = -\ln \varepsilon_i^{(n)}$. The average Lyapunov exponent (1.18) is given by

$$\lambda_1 = \frac{1}{n} \sum_i \Lambda_{1i}^{(n)} \mu_i^{(n)} = -\frac{1}{n} \sum_i \varepsilon_i^{(n)} e^{\kappa n} \ln \varepsilon_i^{(n)} \tag{2.13}$$

for $n \gg 1$. The metric entropy from (1.24), according to (2.11), and (2.12), is

$$K_1 = -\frac{1}{n} \sum_i \varepsilon_i^{(n)} e^{\kappa n} \left(\kappa n + \ln \varepsilon_i^{(n)} \right). \tag{2.14}$$

Comparing (2.13) and (2.14), we obtain

$$K_1 = \lambda_1 - \kappa. \tag{2.15}$$

This indicates that for a chaotic repeller of a one-dimensional map, the metric entropy K_1 is *not* equal to the Lyapunov exponent (in contrast to the situation of a chaotic attractor, where the two are equal [220, 564]), with the difference being the escape rate.

The information dimension of the repeller can be calculated using the probabilities $P_i = \mu_i^{(n)}$ in (1.22). A straightforward substitution of P_i in (1.22) yields

$$D_1 = 1 - \frac{\kappa}{\lambda_1}. \tag{2.16}$$

We see that the information dimension of the natural distribution on a chaotic repeller is always less than unity. The difference is given by the ratio of two rates: the escape rate and the Lyapunov exponent. In addition, since D_1 is nonnegative, we have

$$\kappa \leq \lambda_1, \tag{2.17}$$

where the equality holds only for point repellers whose natural distribution is concentrated in a point ($D_1 = 0$). A chaotic repeller is thus globally *less* repelling than typical points in it, since the escape rate is smaller than the average Lyapunov exponent. It may be said that the fractal structure tends to "stabilize" the repeller because a larger dimension implies generally slower escape.

Finally, from (2.15) and (2.16), we obtain

$$K_1 = \lambda_1 D_1. \tag{2.18}$$

The metric entropy is thus the product of the Lyapunov exponent and the information dimension. Equations (2.15), (2.16), and (2.18) are particular instances of the general relations expressed by (1.29) and (1.30).

2.2.2   Box-Counting Dimension and Topological Entropy

The idea behind the Frobenius–Perron equation (2.5) can be exploited for calculating the box-counting dimension. In particular, note that in fitting a smooth curve to the natural distribution on a grid of size $\varepsilon \ll 1$ such as the one in Fig. 2.2, one finds that its form $\tilde{\rho}(x)$ differs from the density $\rho(x)$ of the c-measure. The reason is that the cylinders of level $n \gg 1$ are by far not of equal size. It is possible to find an equation of the type of the Frobenius–Perron equation (2.5) whose solution is $\tilde{\rho}(x)$.

Consider the coarse-grained chaotic repeller specified on a grid of fine resolution ε. Take an interval of length $\Delta x \ll 1$ within I that is much larger than ε. The probability of finding a point on the repeller within the interval of length Δx is

$N(\varepsilon)\varepsilon/\Delta x$, where $N(\varepsilon)$ is the number of bins of size ε covering the repeller inside Δx, and $N(\varepsilon)\varepsilon$ is the total length of such bins. By the definition of the box-counting dimension (1.19), this quantity scales with ε as ε^{1-D_0}. The probability that a point of the image interval $\Delta x' = f'(x)\Delta x$ belongs to the repeller is $N(\varepsilon\Delta x/\mid\Delta x'\mid)\varepsilon/\mid\Delta x'\mid$, since the map is locally linear over the interval of length Δx, and a longer interval $\Delta x'$ corresponds to using a finer resolution $\varepsilon\Delta x/\Delta x'$ in N. After one iterate, the probability of being on the repeller has changed by a factor of $\mid\Delta x/\Delta x'\mid^{1-D_0}$, which is typically less than unity. A *local* escape rate $\kappa(x)$ can thus be defined as

$$e^{\kappa(x)} = \mid f'(x)\mid^{1-D_0} . \tag{2.19}$$

The decrease of the probability from a coarse-grained repeller accompanying the escape process can be compensated by multiplying the probability of being on the repeller by $\exp[\kappa(x)]$ for every point x. In an equation analogous to (2.2), there is then no overall correctional factor R, but the exponent of the derivative changes from unity to D_0. These considerations lead to [753]

$$\tilde{\rho}_{n+1}(x') = \sum_{x \in f^{-1}(x')} \frac{\tilde{\rho}_n(x)}{\mid f'(x)\mid^{D_0}}, \tag{2.20}$$

which we call the *dimension equation*. By iterating any smooth, positive initial function $\tilde{\rho}_0(x)$ on I, one can find convergence to a finite density if the exponent is chosen to be the repeller's box-counting dimension. Equation (2.20) is a kind of eigenvalue equation for the dimensions, and it provides a fast numerical algorithm for determining D_0. For our example in Fig. 2.2, the calculation yields $D_0 = 0.905344$. The series of $\tilde{\rho}_n(x)$ converges to the density $\tilde{\rho}(x)$, a smooth covering curve for the *natural* distribution on the repeller *coarse-grained* on a uniform grid [753].

Similar types of equations exist for the information dimension and other quantities, as shown in Appendix A (A.12). Using a cumulant expansion of the local Lyapunov exponents applied to these equations, one finds a relation between the box-counting dimension and these cumulants in the form of

$$\kappa = (1 - D_0)\lambda_1 + \frac{1}{2}(1 - D_0)^2 Q_2 + \cdots, \tag{2.21}$$

where Q_2 is the second cumulant. An analogous relation for the topological entropy [380] can be obtained, which is

$$K_0 = \lambda_1 - \kappa + \frac{1}{2}Q_2 + \cdots, \tag{2.22}$$

as also derived in Appendix A. Equations (2.21) and (2.22) show that, in contrast to D_1 and K_1, the box-counting dimension and the topological entropy can be related to the escape rate only if an infinite series containing the cumulants of the local Lyapunov exponents is also taken into account.

Since all possible binary sequences are allowed to occur in the class of maps in Fig. 2.1 (there are $\Omega_m = 2^m$ sequences of length m), the topological entropy from (1.25) is

$$K_0 = \ln 2, \tag{2.23}$$

regardless of the particular form of $f(x)$.

2.2.3 An Analytically Tractable Example: The Tent Map

As an analytic example, we consider the tent map defined on the unit interval $I = (0,1)$:

$$f(x) = \begin{cases} ax & \text{for } x < b/(a+b), \\ b(1-x) & \text{for } x > b/(a+b), \end{cases} \tag{2.24}$$

where $a > 1$ and $b > a/(a-1)$. The lengths of the two subintervals $I_1^{(n)}$ and $I_2^{(n)}$ (cf. Fig. 2.1) are $1/a$ and $1/b$, respectively. For the tent map, the convergence of an initial distribution $\rho_0(x)$ to the density of the c-measure can be followed explicitly under the Frobenius–Perron equation (2.2):

$$\rho_{n+1}(x') = R\left(\frac{\rho_n(x'/a)}{a} + \frac{\rho_n(1-x'/b)}{b} \right). \tag{2.25}$$

To find a solution to (2.25), we assume that the distribution is linear at any iteration:

$$\rho_n = \alpha_n x + \beta_n. \tag{2.26}$$

A direct substitution yields the following mapping for the coefficients:

$$\alpha_{n+1} = R\left(\frac{1}{a^2} - \frac{1}{b^2} \right)\alpha_n, \quad \beta_{n+1} = R\left(\frac{1}{a} + \frac{1}{b} \right)\beta_n + \frac{R}{b}\alpha_n. \tag{2.27}$$

A finite nonzero limiting value of β exists only if the factor in front of β_n is unity, which gives $R(1/a + 1/b) = 1$. The escape rate is thus given by

$$\kappa = \ln R = -\ln(1/a + 1/b) = \ln a + \ln b - \ln(a+b). \tag{2.28}$$

With this value of R, the factor in front of α_n is less then unity in modulus, and hence the series of α_n converges to zero, so that the asymptotic distribution is a constant. Taking into account normalization, we obtain $\rho(x) \equiv 1$.

Applying (2.20) also yields a constant asymptotic density $\tilde{\rho}$, provided that the box-counting dimension satisfies[1]

$$a^{-D_0} + b^{-D_0} = 1. \tag{2.29}$$

Due to the strict self-similarity of the cylinder construction, other dynamical invariants can be found from the first level. In particular, since $\rho = 1$, the first-level cylinder measures are $\mu_1^{(1)} = b/(a+b)$ and $\mu_2^{(1)} = a/(a+b)$ with local slopes a and b on these cylinders, respectively. From (2.13) we obtain

$$\lambda_1 = \frac{a\ln b + b\ln a}{a+b}. \tag{2.30}$$

For the metric entropy (2.14), we have

$$K_1 = -\frac{a\ln a + b\ln b}{a+b} + \ln(a+b). \tag{2.31}$$

From (1.22), the information dimension of the natural measure of the repeller is

$$D_1 = \frac{-a\ln a - b\ln b + (a+b)\ln(a+b)}{a\ln b + b\ln a}. \tag{2.32}$$

One can see that indeed, the general relations (2.15), (2.16), and (2.18) are nontrivially satisfied for the tent map. It is only for the symmetric case $a = b$ that the dimensions are equal to each other, and so are the entropies. In particular, in this case we have $D_0 = D_1 (= \ln 2/\ln a)$ and $K_0 = K_1 (= \ln 2)$.

2.3 Examples of Transient Chaos in One Dimension

The following examples, taken from different disciplines including number theory, engineering, and statistical mechanics, illustrate the ubiquity of transient chaos.

2.3.1 Numbers with Incomplete Continued Fractions

It is known that every positive number x can be expanded in a unique continued fraction [331, 408], i.e., the number can be written as

---

[1] The same result follows for arbitrary choices of the initial densities, and the constant-valued distribution is indeed an attractor of the functional recurrences (2.2) and (2.20).

$$x = \cfrac{1}{i_1 + \cfrac{1}{i_2 + \cfrac{1}{i_3 + \cdots}}}, \tag{2.33}$$

where the i_k are natural numbers. The expansion is obtained by subtracting from the reciprocal of the number the integer part (i_1) of the reciprocal, then taking the resulting reciprocal and subtracting from it its integer part (i_2), and so on.

The one-dimensional Gauss map[2] defined on $I = (0, 1]$ as the difference between the reciprocal and its integer part is

$$x_{n+1} = f(x_n) \equiv \frac{1}{x_n} - \left[\frac{1}{x_n}\right]. \tag{2.34}$$

The map is related to continued fractions. In particular, it contains infinitely many branches; see Fig. 2.7a. Starting the counting from the rightmost branch as branch f_1, branch i is of the form $f_i(x) = 1/x - i$ and is defined over the interval $(1/(i+1), 1/i)$. Taking an initial point x_0 in this interval, we obtain $x_1 = 1/x_0 - i$ and hence $x_0 = 1/(i + x_1)$. The number x_1 can thus be considered as the remnant after a single step of the continued fraction expansion. The expansion can be continued. For example, taking an initial point x_0 mapped by f_{i_1} first and then by f_{i_2}, we get

$$x_0 = \cfrac{1}{i_1 + \cfrac{1}{i_2 + x_2}}. \tag{2.35}$$

A comparison with (2.33) shows that the sequence $i_1, i_2, i_3, \dots$ of branch indices encountered while iterating map (2.34) with any irrational initial condition x_0 corresponds precisely to the infinite continued fraction expansion of x_0. Accordingly,
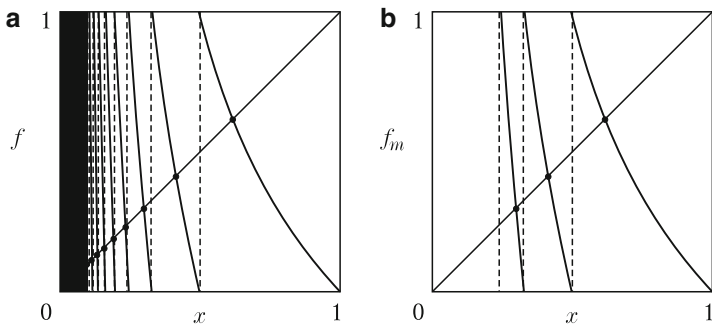
Fig. 2.7 (**a**) Gauss map f and (**b**) truncated Gauss map f_m that contains only branches with $i \le m$. Here $m = 3$

[2] Gauss was aware of the fact that this map has an invariant density proportional to $1/(1+x)$. The map is in fact chaotic in modern terminology [328].

the fixed point x_i^* belonging to branch i is a number that contains only i in its continued fraction, where x_1^* is in fact the golden mean. Since any number in $(0, 1]$ can be expanded if all positive integers can appear in the expansion, the full interval $I = (0, 1]$ remains invariant under the map (2.34).

One can, however, ask what the numbers whose continued fractions contain *certain* integers only are. They form fractal subsets of the unit interval. In particular, we shall be interested only in numbers with continued fractions containing integers less than or equal to a certain threshold m. These numbers must be *invariant* under the truncated Gauss map $f_m(x_n)$ that is of the same form as (2.34) but does not contain the branches $i = m + 1, m + 2, \dots$, as shown in Fig. 2.7b. The truncated map f_m is thus of the form of (2.34) but is defined on the interval $[1/(m+1), 1]$ only.

Points from the interval $I_0 = (0, 1/(m+1))$ have integers larger than m in their expansion. As a result, whenever a point under iteration enters this region, it should be discarded. Map f_m is therefore a map from which escape takes place, generating transient chaos. The numbers with continued fractions containing integers less than or equal to m form the *chaotic repeller* of the map f_m. The repellers can be constructed numerically. Several representative repellers are shown in Fig. 2.8.

The box-counting dimension D_{0m} of the repeller of the map f_m follows from the dimension equation (2.20), which now reads

$$\tilde{\rho}_{n+1}(x') = \sum_{i=1}^{m} (x' + i)^{-2D_{0m}} \tilde{\rho}_n\left(\frac{1}{x' + i}\right). \tag{2.36}$$

The values of D_{0m} can be determined from (2.36) numerically, and the results [328] are summarized in Table 2.1. By now, efficient algorithms exist [330, 358] for determining these dimensions up to many more digits than shown here. It is interesting to mention that by means of spectral methods, D. Hensley derived [329] an analytic expression for D_{0m}, valid for large m:

$$D_{0m} = 1 - \frac{6}{\pi^2 m} - \frac{72 \ln m}{\pi^4 m^2}. \tag{2.37}$$
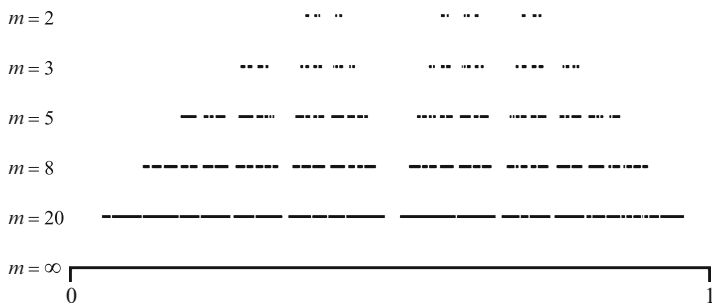
Fig. 2.8 Numbers of the unit interval with continued fraction expansions containing integers less than or equal to m for $m = 2, 3, 5, 8, 20$, obtained as invariant chaotic repellers under the map f_m. Each set is similar to a Cantor set

Table 2.1 Box-counting dimension D_{0m} of irrational numbers with continued fraction expansions containing integers less than or equal to m

m	2	3	4	5	6	7	8
D_{0m}	0.5313	0.7057	0.7889	0.8368	0.8676	0.8890	0.9046

For $m > 8$, this expression is quite accurate: its predicted values agree with the numerically obtained dimension values within less than half of 1%.

2.3.2 Shimmying Wheels

The lateral vibrations of towed wheels, the shimmies (called after a dance that was popular back in the early 1920s), are self-excited nonlinear oscillations of great engineering relevance. These vibrations can be observed during the motion of the towed wheels of shopping carts, wheelchairs, trailers, or on the front wheels of airplanes, bicycles, or motorcycles. In the simplest setting, the vehicle can be modeled as a rigid body moving along a straight line at a constant speed v. For practical purposes, a stationary rolling of the wheel is desirable so that the wheel's center of mass moves parallel to the towing velocity. Shimmy may occur if some part of the wheel system, either the wheel itself or the point at which it is affixed, is elastic [738].

To gain insight here we consider an idealized model that exhibits shimmying motion [272]. The wheel is assumed to be rigid, but the connecting assembly can move laterally, as shown schematically in Fig. 2.9. The vehicle moves at a constant velocity v along the x-axis. The vertical center of rotation of the wheel, the kingpin, is attached to the vehicle via a spring that allows the kingpin to oscillate in the y direction. An important parameter of the system is the caster length l, i.e., the offset of the wheel's axis with respect to the kingpin. The deflection angle of the wheel assembly with respect to the x-axis is ψ; the rotational angle of the wheel is ϕ. In a reference frame co-moving with the vehicle, the degrees of freedom are the angles ψ and ϕ, and the instantaneous position y of the kingpin. If the wheel rolls, i.e.,
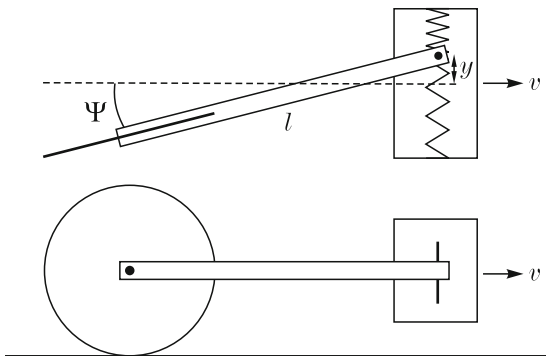
Fig. 2.9 Schematic diagram of an idealized wheel model that exhibits chaotic shimmying

its contact point has zero velocity relative to the ground, the rotational angle is no longer an independent variable. The system thus has two degrees of freedom, and the phase space is four-dimensional. Note, however, that due to the prescribed towing velocity, the total energy is not conserved; either the system can be dissipative, or it can absorb energy via the constraining force of the vehicle's engine that provides the constant speed.

The state of straight rolling ($\psi = 0$, $y = 0$) is unstable for short caster length for $l < l_c$, where the critical length l_c is determined by other parameters such as the wheel's radius, the masses, and the towing velocity [738]. Even when the caster length is sufficiently long that the system is in the regime of stable straight rolling, the dynamics is nontrivial, since there exists an unstable limit cycle outside the fixed-point attractor at the origin. For vibrations of amplitude larger than that of the limit cycle, the corresponding ψ values increase in time. In this process, the angle of deflection reaches a critical value for which the static friction is no longer able to provide the necessary constraining force for rolling. That is, the wheel *slides*. It is insightful to focus on the dynamics of a sliding wheel for which ϕ is a relevant variable, and the phase space becomes six-dimensional. Due to the sliding friction, the dynamics is strongly dissipative, and the velocity of the contact point starts decreasing after some time and sooner or later it approaches zero asymptotically, recovering the rolling state. An essential feature of the full dynamics is thus the temporary change between a four- and a six-dimensional phase space. When a trajectory enters the former, its destination depends on whether it is inside or outside the unstable limit cycle. If it is outside, the amplitude of the ψ-oscillations starts growing, the condition of rolling cannot be satisfied, and the trajectory will be in the larger phase space again. Due to such events, the wheel exhibits chaotic "dance" (motion). If, however, a return occurs to some region inside the limit cycle and into the basin of attraction of the fixed-point attractor, the straight rolling of the wheel is approached asymptotically. This actually occurs with a finite probability.

The transiently chaotic shimmying of wheels, occurring for a broad range of parameters, can be represented by an approximately one-dimensional map due to the strong dissipation in the underlying dynamics [739]. On the Poincaré section taken at $y = 0$, the map $\psi_{n+1} = f(\psi_n)$ consists of two branches, as shown in Fig. 2.10. Rolling is represented by the left branch with an unstable fixed point at ψ^* that represents the unstable limit cycle. The critical value at which sliding starts is denoted by ψ_{sl}. There is a jump in the dynamics because the right branch corresponding to sliding decreases and stretches somewhat *below* the level of ψ^*. The narrow interval I_0 is thus the escape interval, and it provides a mechanism for trajectories to return to the attractor at the origin. Insofar as the trajectory is inside the box above ψ^*, the dynamics is chaotic. Thus, we conclude that the shimmying motion of wheels can be transiently chaotic for typical parameters, which can indeed be observed, for example, when trolleys at supermarkets or airports are towed. Control of such transient chaotic motions in motorcycles and in airplanes is a basic task in vehicle engineering [738, 754, 755].

A numerical investigation of the transient chaotic dynamics within the interval $(\psi^*, \psi_{max}) = (6, 9)$ degrees in a realistic case leads to the conclusion that the

Fig. 2.10 Schematic diagram
of the one-dimensional return
map of the deflection angle ψ
of a shimmying wheel. The
square indicates the box
within which chaotic
dynamics occur. Due to the
small gap I_0 at its lower right
corner, the map is open, and
shimmying is transiently
chaotic
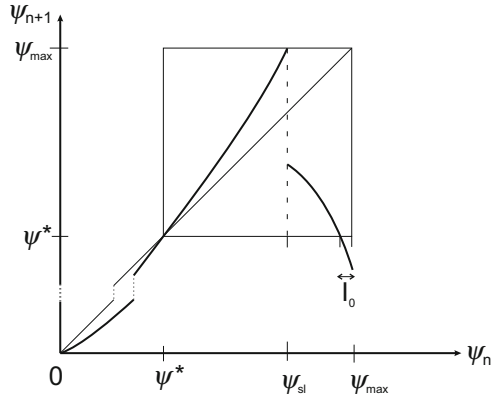
Fig. 2.11 Chaotic repeller associated with shimmying motion on the angle interval (ψ^*, ψ_{max}) $= (6,9)$ degrees

underlying chaotic repeller is rather dense, with box-counting dimension $D_0 \approx 0.95$, as shown in Fig. 2.11. The escape rate is $\kappa \approx 0.006$. Taking into account the characteristic time of oscillations $t_0 = 0.63$ s [739], one can estimate that the average lifetime is $\tau \approx t_0/\kappa = 100$ s (using (1.7)), which is the typical duration of shimmying observed, say, when trolleys are towed.

2.3.3 Random-Field Ising Chain

Take a semi-infinite chain of Ising spins $\{s_1, s_2, \ldots, s_n, \ldots\}$ in an inhomogeneous external field $\{h_1, h_2, \ldots, h_n, \ldots\}$ with the interaction Hamiltonian

$$H = \sum_{j=1}^{\infty} (K s_j s_{j+1} + h_j s_j), \tag{2.38}$$

where K is a coupling constant. For simplicity we use units in which $k_B T = 1$. The set of local fields $\{h_j\}$ is considered a particular realization of a random field distribution assuming at each site the values $+h$ and $-h$ with probabilities p and $1 - p$, respectively. The thermodynamic properties are determined by the following partition function:

$$Z = e^{-F} = \sum_{\{s_1, s_2, \ldots\}} \exp\left[-K s_1 s_2 - h_1 s_1 - \sum_{j=2}^{\infty} (K s_j s_{j+1} + h_j s_j) \right] \tag{2.39}$$

for a fixed realization of the fields $\{h_j\}$ and then by averaging the free energy over different realizations. The summation over spins can be obtained recursively [658]. Since the first spin appears in two terms of H only, the partition function can be evaluated, yielding

$$Z = \sum_{\{s_2,s_3,...\}} 2\cosh\left(Ks_2 + h_1\right) \exp\left[-\sum_{j=2}^{\infty} (Ks_j s_{j+1} + h_j s_j)\right]. \tag{2.40}$$

Since s_2 can take on the values ± 1 only, an exponential representation of the hyperbolic cosine function gives

$$\cosh\left(Ks_2 + h_1\right) = \exp\left[A(K,h_1) + g(K,h_1)s_2\right], \tag{2.41}$$

where

$$A(K,x) = \frac{1}{2}\ln\left[\cosh\left(K+x\right)\cosh\left(K-x\right)\right],$$

$$g(K,x) = \frac{1}{2}\ln\left[\cosh\left(K+x\right)/\cosh\left(K-x\right)\right].$$

This form shows that spin 1 contributes an amount $-A(K,h_1)$ to the free energy F, and generates simultaneously also an extra field $g(K,h_1)$ for spin 2. The partition sum can thus be rewritten as

$$Z = \sum_{\{s_2,s_3,...\}} \exp\left(A(K,h_1)\right)\exp\left[-Ks_2 s_3 - x_2 s_2 - \sum_{j=3}^{\infty} (Ks_j s_{j+1} + h_j s_j)\right], \tag{2.42}$$

where x_2 is an effective field acting on spin 2 and is given by

$$x_2 = h_2 + g(K,h_1). \tag{2.43}$$

Note that the partition sum has a form similar to the original one (with x_2 replacing h_2). The summation over subsequent spins can then be carried out in an analogous way. After n steps we find the field acting on spin $(n+1)$ as

$$x_{n+1} = h_{n+1} + g(K,x_n), \tag{2.44}$$

and the actual contribution to the free energy becomes $-A(K,x_n)$. As a result, a recurrence can be found that is actually *random*, since the fields $\{h_j\}$ are random variables [302]. According to rule (2.44), the effective field x_{n+1} takes on the values $h + g(K,x_n)$ and $-h + g(K,x_n)$ with probabilities p and $1-p$, respectively. Consequently, the recurrence can be written as a *two-valued* map in which trajectories stay on the upper and lower branches with probabilities p and $1-p$, respectively, as shown in Fig. 2.12. The actual form of the map depends on the coupling constant K and the field magnitude h. Although the branches alone are not
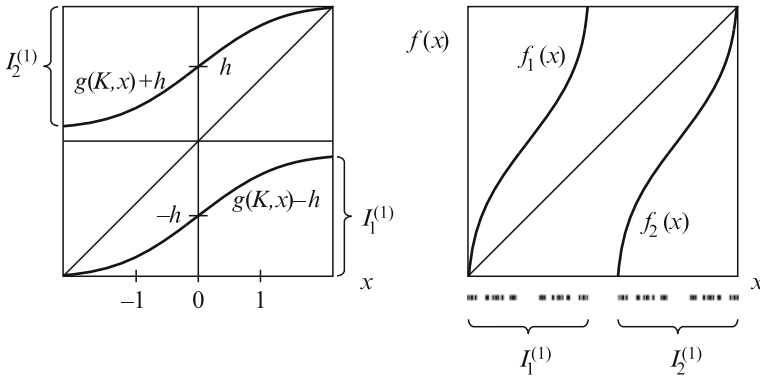
Fig. 2.12 For a random Ising chain, random map generating the local field x (*left*) and the inverse of the map (*right*). The repeller of this map ($K = 1$, $h = 1.1$) shown at the *bottom* is the attractor of the random iteration (2.44) for any choice of the probability p

expanding, the random map exhibits chaotic motion on an *attractor*. The natural invariant measure on this attractor is physically important, since the averaged thermal free energy per spin is just the mean value of $-A(K,x)$ taken with respect to the natural measure of variable x on the attractor. The averaged magnetization per spin and other thermodynamic properties can also be expressed by the natural measure of the attractor [302].

When there is a gap between the branches, as shown in Fig. 2.12, the attractor is a *fractal*. This can be seen by noting that the whole interval I on which the dynamics is defined is mapped into two smaller subintervals $I_1^{(1)}$ and $I_2^{(1)}$ with a gap in between. The images of the small subintervals also have gaps at every level. In fact, these subintervals are exactly the *cylinders* in the *inverted* map $f(x)$ shown in the right panel of Fig. 2.12. It can thus be concluded that the attractor of the random map is nothing but the *repeller* of the inverted map, which holds for all values of p. The natural measure on the attractor, however, depends on the choice of p and is not related to the natural measure of the repeller [54]. The former can be obtained by iterating the map f backward with branching probabilities p and $1 - p$ and is independent of the choice of the initial point. The attractor geometry (the fractal pattern in Fig. 2.12) and its box-counting dimension ($D_0 = 0.8$), however, follow from the dynamics of the inverted map.

2.4 Nonhyperbolic Transient Chaos in One Dimension and Intermittency

Nonhyperbolicity in a one-dimensional map arises when the local slope of the map is unity or infinite, which can lead to escaping dynamics differing from those in hyperbolic systems.
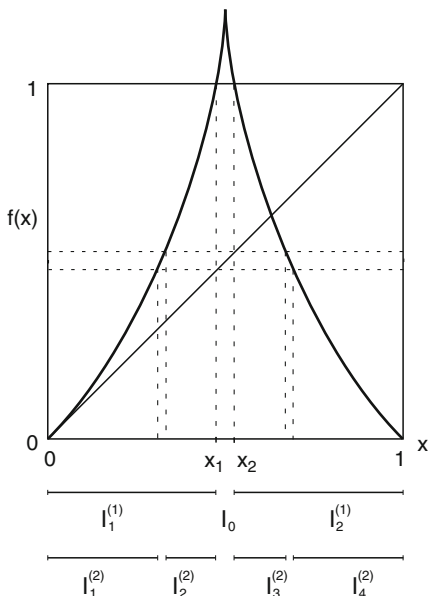
In particular, the presence of a single marginally stable orbit implies a slow, nonexponential decay process and an intermittent type of behavior before escaping. To illustrate these features, we consider the class of maps shown in Fig. 2.13. About the origin, for $x \ll 1$ the maps are assumed to have the form

$$f(x) = x + Ax^{k-1}, \quad k \geq 3, \tag{2.45}$$

and they are expanding otherwise: $|f'(x)| > 1$. The origin is thus marginally stable, leading to weak repulsion of trajectories that come close to the origin and relatively long dwelling times there. This region can thus be said to be *sticky*. Because of the long dwelling time, iterations of the map can be approximated by a continuous-time differential equation:

$$\frac{dx}{dt} = Ax^{k-1}, \tag{2.46}$$

solutions to which indicate that the time t needed to reach a finite distance l from any initial point x_0 close to the origin scales as $t \sim x_0^{-(k-2)}$. This implies that for a smooth initial distribution, the number $N(n)$ of trajectories staying inside a small interval about the origin changes, after a large number n of iterations, as

$$N(n) \sim n^{-1/(k-2)}. \tag{2.47}$$

As a consequence, the survival probability (see Sect. 1.2.1) also scales as

$$P(n) \sim n^{-1/(k-2)}. \tag{2.48}$$

Its decay follows a power law $n^{-\sigma}$ with an algebraic-decay exponent $\sigma = 1/(k-2)$ for $n \gg 1$, and hence the escape rate is zero: $\kappa = 0$. The cylinder construction shows, however, that the repeller, in fact a nonhyperbolic repeller, is a fractal set of dimension $D_0 > 0$ [161].

We now consider the c-measure. Observe first that for maps having a local form $f(x) \sim 1 - a|x - x_i|^z$ $(i = 1, 2)$ in the vicinities of the internal endpoints x_i of intervals $I_1^{(1)}$, $I_2^{(1)}$, the relation between point $x' \approx 1$ and its preimages x is $x - x_i = (-1)^i[(1-x')/a]^{1/z}$. From the Frobenius–Perron equation (2.5) with $\kappa = 0$, we obtain

$$\rho(x') \sim (1 - x')^{1/z - 1} \quad \text{for } x' \to 1. \tag{2.49}$$

Note that for maps of the type in Fig. 2.13, $z = 1$ and $\rho(x')$ tends to a constant for $x' \to 1$. The Frobenius–Perron equation (2.5) for $x' \to 0$ becomes

$$\rho(x') = \frac{\rho(x)}{1 + (k-1)Ax^{k-2}} + \frac{\rho(1)}{|f'(1)|}. \tag{2.50}$$

Since in this regime $x' \approx x$, the equation can be satisfied only if $\rho(x')x'^{k-2} = \text{const}$, i.e.,

$$\rho(x') \sim x'^{-(k-2)} \quad \text{for } x' \to 0. \tag{2.51}$$

The density of the c-measure is *singular* at the origin, implying that the c-measure $\mu_1^{(n)}$ of the leftmost cylinder is much larger than any other $\mu_i^{(n)}$ at level n. Since the length $\varepsilon_1^{(n)}$ shrinks with n much more slowly than that of the others, in the asymptotic limit the full measure is concentrated at the origin: $\mu_1^{(\infty)} = 1$. The natural measure of this nonhyperbolic repeller can thus be represented by a Dirac delta function situated at the origin. As a consequence, the information dimension is $D_1 = 0$, and the average Lyapunov exponent is that of the origin, i.e., $\lambda_1 = 0$. The repeller is therefore nonchaotic in the sense of zero Lyapunov exponent, but strange since it is fractal. It has therefore been called a *strange nonchaotic repeller* [161] (in analogy with strange nonchaotic attractors [241]). Trajectories spend long times near the origin, but burst into other regions of the repeller from time to time, return to the origin again, and so on. The dynamics is thus *intermittent* [612] before escape takes place.

In the case of nonhyperbolicity due to infinite derivatives, $z < 1$ at the endpoints x_1, x_2 of the primary escape interval, so the density vanishes at $x' = 1$, as indicated by (2.49). The Frobenius–Perron equation about the origin reads

$$\rho(x') = R\frac{\rho(x)}{|f'(x)|}. \tag{2.52}$$

The density can remain constant at the origin, provided that the slope $|f'(0)|$ and $R = e^\kappa$ are equal.

Maps for which the logarithm of the slope at the origin is equal to the escape rate are infinitely steep at the endpoints of the escape interval. Such systems are therefore said to be in the *border state of transient chaos* [400, 541]. Since the density is finite at the origin, the c-measure of the leftmost cylinder at level n is proportional to its length, which in turn is proportional to $| f'(0) |^{-n}$. Taking into account the compensation factor R, we have

$$\mu_1^{(n)} \sim R^n | f'(0) |^{-n}. \tag{2.53}$$

Since the slope is exactly R, $\mu_1^{(n)}$ tends to a constant in the large-n limit. In this case, the natural measure is again concentrated at the origin, and we have $D_1 = 0$. The slope is, however, larger than unity here, and therefore the average Lyapunov exponent is finite: $\lambda_1 = \kappa = \ln R$. The underlying dynamics is intermittent-like, and in spite of the high concentration of trajectories near the origin and the rare bursts, the system is sensitive to initial conditions. The escape process is in fact exponential. This case is called the border state because for the slope $| f'(0) |$ larger (smaller) than e^κ, transient chaos is hyperbolic (nonhyperbolic). An additional feature of the border state is that, besides the c-measure whose density is finite at the origin and tends to zero at the right end, there exist one or more smooth c-measures that vanish at both ends and have escape rates different from $\ln R$. The asymptotic character of the escape process depends then on the exponent of the initial density ρ_0 at the origin [400, 497].

2.5   Analytic Example of Transient Chaos in Two Dimensions

A chaotic saddle arising in an invertible two-dimensional map has the appearance of the direct product of two Cantor sets, as shown in Fig. 1.8. A pedagogical dynamical system capable of exhibiting many typical features of a chaotic saddle is the open baker map [753]. The action of the mapping can be described as follows. Take the unit square and cut it by a horizontal line into two pieces of surface area c_0 and $1 - c_0$, respectively. The lower rectangle of width c_0 is then stretched in the vertical direction by a factor of $a > 1$ and simultaneously compressed in the horizontal direction by a factor $c < 1/2$, while keeping the lower left corner fixed. The upper rectangle is transformed by stretching and compression factors $b > 1$ and $d < 1/2$, respectively, during which its upper right corner is fixed. If stretching is sufficiently strong, i.e., $ac_0 > 1$, $b(1 - c_0) > 1$, the map generates transient chaos. Mathematically, the map can be written as

$$x_{n+1} = cx_n, \quad y_{n+1} = ay_n, \tag{2.54}$$

for $y_n < c_0$, and
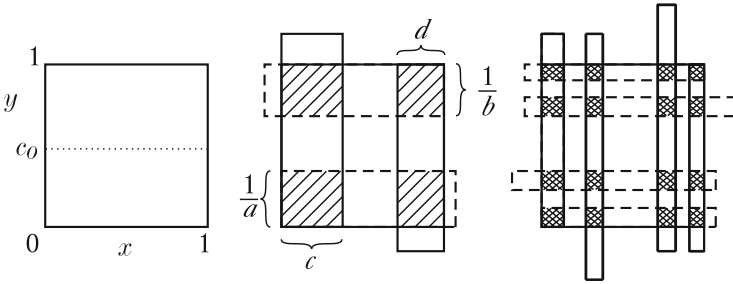
Fig. 2.14 Open baker map defined on the unit square (the restraining region Γ). The image (*continuous line*) and preimage (*dashed line*) of the unit square after one and two iterations are shown. Points in the *shaded* and *cross-shaded* regions do not escape the unit square after one and two iterations (forward or backward), respectively

$$x_{n+1} = 1 - d(1 - x_n), \quad y_{n+1} = 1 - b(1 - y_n), \tag{2.55}$$

otherwise. The one and two-step forward and backward images of the unit square are shown in Fig. 2.14. Note that the inverted map is obtained by interchanging the roles of x and y and by replacing a, b by $1/c$, $1/d$, and c, d by $1/a$, $1/b$, respectively.

Say we distribute N_0 initial points on the unit square uniformly. A portion c_0 of them falls on the strip elongated by a factor a after the first step. Since only a ratio $1/ac_0$ of the total length overlaps with the unit square, the number of trajectories staying inside the unit square is N_0/a. Analogously, from the other strip there are N_0/b surviving trajectories. Altogether, a portion of $(1/a + 1/b)$ of the initial points does not escape the unit square in one time step. The same consideration applies to future iterations as well. As a result, the escape rate is

$$\kappa = -\ln(1/a + 1/b), \tag{2.56}$$

which is the same as that for the tent map (2.28). The positive Lyapunov exponent is also the same as that of the tent map (2.30).

The chaotic saddle of the baker map can be viewed as the direct product of two Cantor sets, and the concept of *partial dimensions* [380, 564] can then be used to characterize the saddle. Specifically, along the y-axis the contraction rates defining the Cantor set are $1/a$ and $1/b$, and hence the box-counting dimension along this direction is the solution to the following equation; cf. (1.20):

$$a^{-D_0^{(1)}} + b^{-D_0^{(1)}} = 1, \tag{2.57}$$

where $D_0^{(1)}$ is the *partial box-counting dimension along the unstable direction*. Along the other axis, the contraction rates are c and d, and the corresponding dimension is the solution of

$$c^{D_0^{(2)}} + d^{D_0^{(2)}} = 1, \tag{2.58}$$

where $D_0^{(2)}$ is the *partial box-counting dimension along the stable direction*. The box-counting dimension of the chaotic saddle is the sum of the partial dimensions along the stable and the unstable directions:

$$D_0 = D_0^{(1)} + D_0^{(2)}. \tag{2.59}$$

As the concept of c-measure implies (Sect. 1.2.3.2), escape can be compensated by multiplying the number of trajectory points staying *on* the unit square by $\exp(\kappa)$ at each time step. Starting from a uniform distribution on the unit square $\rho_0 \equiv \text{const}$, the probabilities for the two strips in the first step of the open baker map are $\exp(\kappa)/a$ and $\exp(\kappa)/b$. At the nth step there are 2^n vertical strips of different widths given by $c^m d^{n-m}$, $m = 0, 1, 2, \ldots, n$. The probability of finding trajectory points in strip j of width $c^m d^{n-m}$ is then $\exp(\kappa n) a^{-m} b^{m-n}$. Since the factor appearing after $\exp(\kappa n)$ is just the reciprocal value of the stretching factor (see Sect. 1.2.3.3) $\exp[\Lambda_{1j}(n)]$ for all points in a horizontal strip, we can express the c-measure of strip j at level n by the escape rate and the stretching exponent as

$$\mu_{cj}^{(n)} = e^{\kappa n} e^{-\Lambda_{1j}(n)}. \tag{2.60}$$

Qualitatively, this implies that unstable regions with relatively large stretching exponents are less frequently visited. It can also be seen that the limiting c-measure is concentrated on the unstable manifold, whose branches are parallel to the y-axis, with constant density.

The natural measure can be obtained in a similar manner. In particular, the common region between the first preimage and image of the square contains points that have not escaped after one forward or one backward iteration. Similarly, the union of the nth image and preimage defines trajectories staying inside the square for at least n steps under both the direct and the inverted map, as shown in Fig. 2.14. Points that do not escape thus belong to a double fractal set, the chaotic saddle. Boxes generated by the overlaps of the nth images and preimages provide a natural partition of the saddle (the so-called generating partition [220]). To be explicit, we note that the width $\varepsilon_{1i}^{(n)}$ of horizontal strip i is of the type $a^{-m} b^{m-n}$, for $m = 0, 1, \ldots, n$. We can then write

$$\varepsilon_{1i}^{(n)} = e^{-\Lambda_{1i}(n)}, \tag{2.61}$$

and the width of the vertical strips is

$$\varepsilon_{2j}^{(n)} = e^{\Lambda_{2j}(n)}, \tag{2.62}$$

where Λ_{2j} is the contraction exponent, i.e., the stretching exponent of the inverted map multiplied by (-1). To obtain the natural measure, we note that the smooth density of the c-measure is restricted to boxes of the partition at level n, and should be renormalized. Since the weight of a strip has been determined, the renormalization can be done by *keeping the measure of the strip constant*. This means that
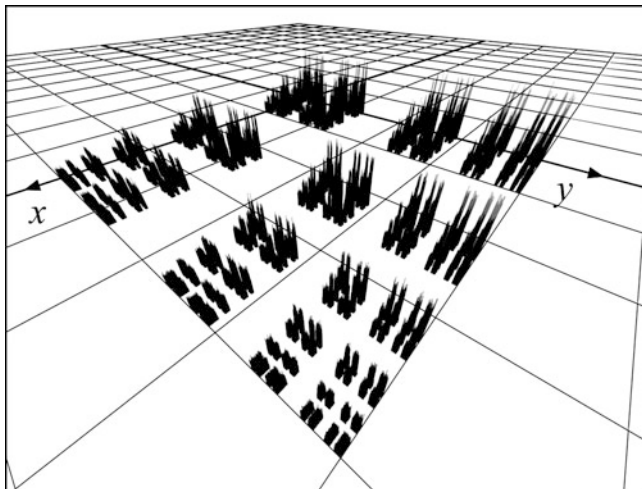
Fig. 2.15 Natural measure of a chaotic saddle from the baker map. The parameters are a=3, b=2.6, $c = 0.25$, and $d = 0.45$. (Picture by M. Gruiz and Sz. Hadobás.)

(2.60) is valid for the natural measure $\mu_j^{(n)}$ of a full vertical strip as well. For a box of vertical size $\varepsilon_{1i}^{(n)}$ inside a given vertical strip j, the natural measure is given by

$$\mu_{ij}^{(n)} = \mu_{cj}^{(n)} e^{\kappa n} \varepsilon_{1i}^{(n)}. \tag{2.63}$$

The exact natural measure can be obtained by taking the $n \to \infty$ limit, as shown by an example in Fig. 2.15. It can be seen that the projections of the natural measure on the y- and x-axes can be regarded as the measures of the stable and the unstable manifolds, respectively, for $n \gg 1$. There are thus two different fractal distributions embedded in the unit square, characterized by the *partial information dimensions* $D_1^{(1)}$ and $D_1^{(2)}$ along the unstable and the stable directions, respectively. The dimensions are given by

$$D_1^{(1)} = \frac{-a\ln a - b\ln b + (a+b)\ln(a+b)}{a\ln b + b\ln a}, \tag{2.64}$$

$$D_1^{(2)} = \frac{a\ln a + b\ln b - (a+b)\ln(a+b)}{a\ln d + b\ln c}. \tag{2.65}$$

A few remarks are in order.

1. Since the natural measure of a stable strip of order n is also the probability $P(\{S_j\})$ for a binary symbols sequence $\{S_j\}$ of length n to occur ($S_j = 0(1)$ if $y < c_0(> c_0)$), the metric entropy is the same as in (2.31). The topological entropy is $K_0 = \ln 2$, since all possible binary sequences can occur.

2. The local Jacobian determinant associated with the first iteration of the map is ac_0c/c_0 for the lower band and $b(1 - c_0)d/(1 - c_0)$ for the upper band. The average of the logarithms of these elements is

$$\overline{\ln J} = \frac{b}{a+b} \ln ac + \frac{a}{a+b} \ln bd = \lambda_1 + \lambda_2, \qquad (2.66)$$

where $\lambda_2 < 0$ is the negative Lyapunov exponent of the saddle. The dynamics is dissipative if it is phase-space contracting on average, i.e., if $\overline{\ln J} < 0$. The area-preserving case can be obtained if all the local Jacobians are unity, which is the case for $ac = 1 = bd$. This corresponds to an open Hamiltonian system, to be treated in the chapter on chaotic scattering.

3. Note that the dynamical invariants are all independent of the parameter c_0. It becomes, however, important in the limit of vanishing escape rates when $c_0 = 1/a$ and $c_0 = 1 - 1/b$ hold, i.e., when both stretching rates are determined by the parameter c_0.

4. General hyperbolic chaotic saddles turn out to be smoothly deformed versions of the baker saddle.

2.6 General Properties of Chaotic Saddles in Two-Dimensional Maps

2.6.1 Natural Measure and c-Measure

To gain insight into the properties of hyperbolic chaotic saddles arising in two-dimensional maps, we take a restraining region Γ of size of the order of unity containing the chaotic saddle, distribute a large number of initial conditions in Γ, and follow the resulting trajectories in the phase space. The map stretches (contracts) Γ along the unstable (stable) direction and bends it so that a part of the image will lie outside Γ. After $n \gg 1$ iterations the overlap of the image with the original region consists of narrow strips that follow the local unstable directions of the chaotic saddle, which are *unstable strips*, as illustrated in Fig. 2.16. For a hyperbolic chaotic saddle, folds of the unstable manifolds fall outside Γ, and the corresponding unstable strips will be only slightly bent. The average width $\varepsilon_2^{(n)}$ of an unstable strip is, by definition, proportional to the local contraction factors $\exp[\Lambda_2(n)]$ of points falling, after n steps, in the strip. Due to escape, the majority of the points will be outside Γ. If after each step the density of points inside is compensated by the factor $\exp(\kappa)$, then a finite limit is found, the density of the conditionally invariant measure.

The equation describing this density can be obtained as follows. The probability of finding points in a small region about $\mathbf{x}$ defines a distribution $\rho_n(\mathbf{x})$ after n steps. Its dynamics is governed by the requirement that the total probability in a

Fig. 2.16 Schematic diagram of the phase-space partition for a chaotic saddle obtained by taking the nth image and preimage of region Γ of size unity that covers the saddle. Shown are stable strips (*dashed lines*), unstable strips (*solid lines*), invariant manifolds, and the directions along which the partial dimensions are defined
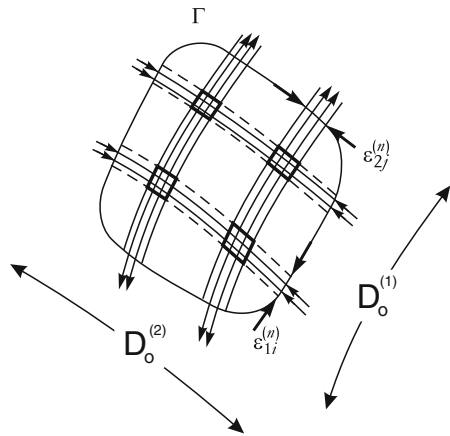
small region at step n be the same as in the image of that region under the map $\mathbf{f}$, after taking into account the compensation factor [764]:

$$\rho_{n+1}(\mathbf{x}') = e^\kappa \frac{\rho_n(\mathbf{x})}{|J(\mathbf{x})|}\Big|_{\mathbf{x} \in \mathbf{f}^{-1}(\mathbf{x}')}, \tag{2.67}$$

where $J(\mathbf{x})$ is the Jacobian determinant at the point $\mathbf{x}$. This is the Frobenius–Perron equation for open invertible two-dimensional maps. Similar to the one-dimensional case (cf. (2.2)), for any smooth initial density $\rho_0(\mathbf{x})$ the density $\rho_n(\mathbf{x})$ converges for $n \to \infty$ to a limit density $\rho(\mathbf{x})$, the density of the c-measure. The resulting c-measure has a smooth, but *not necessarily constant*, density along the unstable manifold. The fact that the largest eigenvalue $\exp(-\kappa)$ of the Frobenius–Perron operator is less than unity ensures again the exponential decay.

It is worth pointing out an analogy with the concept of *almost invariant sets* introduced by Dellnitz, Froyland, and coworkers [174,250]. Such sets are regions in the phase space from which a point escapes with a small probability in a period of time. Chaotic saddles and their manifolds are invariant sets. A neighborhood of the unstable manifold, e.g., can, however, be considered to be almost invariant, provided that the escape rate is low. The regions of slow escape determine, in general, a pattern related to the Frobenius–Perron (or transfer) operator defined by (2.67). The eigenfunction belonging to the largest eigenvalue below unity provides the backbone of this pattern. This largest eigenvalue is $\exp(-\kappa)$ in our case, and the eigenfunction $\rho(\mathbf{x})$ concentrates on the pattern of the unstable manifold, as Fig. 1.11 illustrates.

We turn now to the determination of the natural measure. Without compensating for the escaping, the measure of an unstable strip is proportional to the area of its nth preimage. The nth preimage of Γ consists of strips that are parallel to the local stable directions of the chaotic saddle. The average width $\varepsilon_{1,j}^{(n)}$ of a stable strip, as shown in Fig. 2.16, is proportional to the contraction factor of the inverted map, i.e., to the reciprocal of the stretching factor of the forward map: $\varepsilon_{1,j}^{(n)} \sim \exp[-\Lambda_{1,j}(n)]$, where $\Lambda_{1,j}(n)/n$ is the positive Lyapunov exponent of points inside the strip.

The nth image of such a strip will then have side lengths of order unity and of order $\exp[\Lambda_{2,i}(n)]$ along the unstable and the stable directions, respectively. As a result, a stable strip is nothing but the nth preimage of an unstable one. The measure of an unstable strip j without compensating for the escape is thus proportional to $\varepsilon_{1,j}^{(n)}$, the width of the nth preimage of the unstable strip. Taking into account the compensation, we find that the c-measure contained in the unstable strip j is given by

$$\mu_{cj}^{(n)} \approx e^{\kappa n}\varepsilon_{1j}^{(n)} \sim e^{\kappa n}e^{-\Lambda_{1j}(n)}. \qquad (2.68)$$

The natural measure is obtained by taking the overlap between the nth image and preimage of the region Γ, which provides, for large n, a partition of the phase space and an accurate coverage of the chaotic saddle [45, 220]. The natural measure of a box in the partition can be obtained by redistributing the c-measures of unstable strips according to the length scales $\varepsilon_1^{(n)}$. In particular, in unstable strip j, the natural measure of box i of length ε_{1i} can be expressed as

$$\mu_{ij}^{(n)} \approx \mu_{cj}^{(n)}e^{\kappa n}\varepsilon_{1i}^{(n)}. \qquad (2.69)$$

It should be emphasized that $\mu_{cj}^{(n)}$ as given by (2.68) is in fact the natural measure μ of strip j: $\mu_j^{(n)} = \mu_{cj}^{(n)}$. Formally, this follows from $\sum \varepsilon_{1i}^{(n)} \approx \exp(-\kappa n)$, which holds because escape takes place along the unstable direction only.

The natural measure of stable strips can be obtained in a similar manner. By summing (2.69) over j and utilizing $\sum_j \mu_{cj}^{(n)} = 1$, one finds the natural measure of stable strip i to be

$$\mu_i^{(n)} \approx e^{\kappa n}\varepsilon_{1i}^{(n)}, \qquad (2.70)$$

which is the same as for its nth image, an unstable strip. This reflects the fact that the natural measure is preserved under the map.

Qualitatively speaking, maps generating hyperbolic chaotic saddles can be locally decomposed into baker's transformations. The actual form of the local map can change with the position only smoothly. This is the reason that the general expressions for the natural measures are similar to those obtained for the chaotic saddle of the baker's map.

2.6.2 Entropy and Dimension Formulas

The stretching factor for points in the stable strip i is given by $\exp[\Lambda_{1i}(n)] \sim 1/\varepsilon_{1i}^{(n)}$. The natural measure of this strip is given by (2.70). Replacing $P_i(\varepsilon)$ in (1.18) by $\mu_i^{(n)}$, we obtain the average Lyapunov exponent $\lambda_1 > 0$ as

$$\lambda_1 = -\frac{1}{n}\sum_i \varepsilon_{1i}^{(n)}e^{\kappa n}\ln\varepsilon_{1i}^{(n)}, \qquad (2.71)$$

where the summation is over all stable strips. In an analogous way, the contracting average Lyapunov exponent $\lambda_2 < 0$ is obtained as

$$\lambda_2 = \frac{1}{n} \sum_j \varepsilon_{1j}^{(n)} e^{\kappa n} \ln \varepsilon_{2j}^{(n)}. \tag{2.72}$$

The negative Lyapunov exponent ensures that trajectories from random initial conditions approach the chaotic saddle. In fact, the time needed for the survival probability to begin to decay exponentially (the value of n^* in (1.8)) is approximately $1/|\lambda_2|$.

The metric entropy follows from (1.24) by observing that the measure $\mu_i^{(n)}$ of a stable strip is simultaneously a path probability for all points within that strip, and can be written as

$$K_1 = -\frac{1}{n} \sum_i \varepsilon_{1i}^{(n)} e^{\kappa n} \left(\kappa n + \ln \varepsilon_{1i}^{(n)} \right). \tag{2.73}$$

Comparing (2.71) and (2.73), we obtain again the relation

$$K_1 = \lambda_1 - \kappa, \tag{2.74}$$

which implies that the dynamics along the unstable manifold of an invertible two-dimensional map is indeed similar to that in a one-dimensional map. This can also be seen by examining the partial information dimension along the unstable manifold (cf. Fig. 2.16). In particular, from (1.22), we have

$$D_1^{(1)} = \frac{\sum_i \mu_i^{(n)} \ln \mu_i^{(n)}}{\sum_i \mu_i^{(n)} \ln \varepsilon_{1i}^{(n)}}, \tag{2.75}$$

which leads to

$$D_1^{(1)} = 1 - \frac{\kappa}{\lambda_1}. \tag{2.76}$$

The partial information dimension along the stable manifold is given by

$$D_1^{(2)} = \frac{\sum_j \mu_j^{(n)} \ln \mu_j^{(n)}}{\sum_j \mu_j^{(n)} \ln \varepsilon_{2j}^{(n)}}. \tag{2.77}$$

Since the denominator is n times the negative Lyapunov exponent λ_2, we obtain

$$D_1^{(2)} = \frac{\lambda_1 - \kappa}{|\lambda_2|} = \frac{\lambda_1}{|\lambda_2|} D_1^{(1)}. \tag{2.78}$$

Relations (2.76) and (2.78) are the dimension formulas, also called the Kantz–Grassberger relations [380], for chaotic saddles arising from two-dimensional maps.

The total information dimension is the sum of the partial dimensions:

$$D_1 = K_1 \left(\frac{1}{\lambda_1} + \frac{1}{|\lambda_2|} \right). \tag{2.79}$$

In the limit of chaotic attractors where $\kappa = 0$, $K_1 = \lambda_1$, (2.79) reduces to the Kaplan–Yorke formula [386] for two-dimensional maps.

One can see that the metric entropy is the product of the magnitude of the Lyapunov exponent and the partial information dimension along either the stable or the unstable direction [564, 773]:

$$K_1 = \lambda_1 D_1^{(1)} = |\lambda_2| D_1^{(2)}. \tag{2.80}$$

For a two-dimensional map, there is only one positive Lyapunov exponent. The topological entropy K_0 is then determined by the exponent and its cumulants, as for a one-dimensional map. Formula (2.22) thus remains valid. Similarly, the formula for the escape rate can be generalized by replacing D_0 in (2.21) by the partial box-counting dimension along the unstable direction. We have

$$\kappa = \left(1 - D_0^{(1)}\right) \lambda_1 + \frac{1}{2} \left(1 - D_0^{(1)}\right)^2 Q_2 + \cdots. \tag{2.81}$$

The box-counting and information dimensions $D_{s,i}$ and $D_{u,i}$ ($i = 0, 1$) of the stable and unstable manifolds are related to the partial dimensions as

$$D_{s,i} = 1 + D_i^{(1)} \quad \text{and} \quad D_{u,i} = 1 + D_i^{(2)}, \tag{2.82}$$

since the manifolds are locally smooth (one-dimensional) curves. The dimension of the full chaotic saddle can also be expressed through the manifold dimensions as

$$D_i = D_{s,i} + D_{u,i} - 2. \tag{2.83}$$

Note that in the dimension and entropy formalism discussed, the roles of the sets $\{\varepsilon_1^{(n)}\}$ and $\{\varepsilon_2^{(n)}\}$ are not equal, since the natural measure is connected with one of them only; cf. (2.69). Interchanging $\{\varepsilon_1^{(n)}\}$ and $\{\varepsilon_2^{(n)}\}$ in fact yields dimension and entropy formulas associated with the natural distribution of the inverted map.

2.6.3 Information-Theoretic Arguments

The dimension and entropy formulas treated in Sect. 2.6.2 play a central role in the study of transient chaos, which can in fact be derived using an information-theoretic approach. In particular, the evolution of a chaotic system is unpredictable in long terms. In communication, it was realized by Shannon in 1948 that a sequence of

events conveys information if the events are not fully predictable [71, 283, 708]. The fundamental unpredictability of chaos thus implies that chaotic systems can be regarded as sources of information. We have seen that the metric entropy K_1 is the rate at which information flows toward the significant digits, with the mean flow velocity given by the average Lyapunov exponent λ_1 (Sect. 1.2.3.3). This observation led Kantz and Grassberger to argue [380] that the partial information dimension $D_1^{(1)}$ is nothing but the density of information per digit on average. As a result, (2.80) expresses that the flow rate equals the product of velocity and density. The same amount of information flow is expected along the stable direction.

Escape can take place only along the unstable manifold. If its partial information dimension were unity, no exponential decay would occur along this direction. The difference $(1 - D_1^{(1)})$ is thus proportional to the escape rate. Since the velocity of the information flow is λ_1, we have $\kappa = \lambda_1(1 - D_1^{(1)})$, which is equivalent to (2.76).

Similarly, the relation $\lambda_1 = K_1 + \kappa$ (see (2.74)) can be viewed as a consequence of the fact that only a portion of the mean velocity of the information flow contributes to information generation, since only the fraction K_1/λ_1 of the mean velocity contributes to the unpredictability associated with the dynamics on the nonattracting set. The remaining fraction κ/λ_1 is in fact associated with the process of escape.

Although the information-theoretic arguments are heuristic, assumptions such as hyperbolicity and invertibility of the dynamics are not necessary. Thus the basic formulas as given by (2.74), (2.76), (2.78), and (2.80) are expected to be valid for *nonhyperbolic* dynamical systems in general.

2.6.4 Organization About Unstable Periodic Orbits

Unstable periodic orbits are the fundamental building blocks of any chaotic set, attracting or nonattracting. A chaotic set is densely covered by an infinite number of unstable periodic orbits, and hence they determine the natural distribution on the set. Chaotic motion can be interpreted as a *random walk among periodic orbits*, or cycles. In particular, when a chaotic trajectory approaches a specific periodic orbit, in a short time interval the behavior of the trajectory is approximately periodic. Since the orbit is unstable, the trajectory will leave the orbit but then approach a different periodic orbit, and so on. This suggests that the invariant characteristics of the chaotic set can be expressed in terms of the properties of the various unstable periodic orbits. Indeed, natural measures associated with chaotic attractors can be characterized by unstable periodic orbits [63, 297, 435, 459], and the same can be done for chaotic saddles [151, 187, 765]. Chaotic saddles are the *closures* of all the embedded unstable periodic orbits.

The stability of an unstable periodic orbit of period n is determined by its cycle eigenvalues, which for a map system are the eigenvalues of the linearized nth iterated map evaluated at the orbit. Chaos can thus be characterized by means of the cycle eigenvalues, provided that sufficiently many periodic orbits can be determined and analyzed.

For a one-dimensional map of the type in Fig. 2.1, the various cylinder lengths can be expressed by the cycle eigenvalues. The fixed points of the nth iterated map, all period-n points, are the intersecting points of the diagonal line with the graph of f^n. It can be seen from Fig. 2.3 that each cylinder of level n contains one n-cycle point. The slope of f^n at a cycle point is approximately the same for any point of the cylinder containing this periodic orbit. As a result, we have $\varepsilon_i^{(n)} \sim 1/\mid f^{n\prime}(x_i^*)\mid$, where x_i^* is the n-cycle point belonging to cylinder i. We see that the length scales of the generating partition for the natural distribution are determined by the stabilities of various periodic orbits embedded in the underlying chaotic set.

Now consider a two-dimensional map. To be concrete, we can take unstable strip j and determine its nth preimage. The overlap between them defines points that return approximately to their initial positions after n steps, and the overlap thus contains a hyperbolic n-cycle point. The magnitudes of the cycle eigenvalues can be written as $\exp(\lambda_{lj}^* n)$ ($l = 1, 2$), where $\lambda_{1j}^* > 0$ and $\lambda_{2j}^* < 0$ are the local Lyapunov exponents of the periodic orbit. The contracting eigenvalue λ_{2j}^* of the period-n point in unstable strip j defines the width of this strip:

$$\varepsilon_{2j}^{(n)} \approx e^{\lambda_{2j}^* n}. \tag{2.84}$$

Similarly, the width of the nth preimage strip is the reciprocal value of $\exp(\lambda_{1j}^* n)$:

$$\varepsilon_{1j}^{(n)} \approx e^{-\lambda_{1j}^* n}. \tag{2.85}$$

With this expression, the measure (2.68) of the unstable strip can be expressed by the eigenvalue of the period-n orbit in this strip as

$$\mu_j^{(n)} \approx \frac{e^{\kappa n}}{e^{\lambda_{1j}^* n}}. \tag{2.86}$$

This relation has been shown to hold for nonhyperbolic chaotic saddles in dissipative dynamical systems as well [186].

We see that strips with more unstable orbits are less probable. Taking into account the normalization condition $\sum_j \mu_j^{(n)} = 1$, where the summation is taken over all the strips at level n, i.e., all the periodic orbits of length n, we see that the sum of the reciprocals of the expanding eigenvalues is not of order unity (as it would be for attractors), but tends toward zero for large n. The escape rate can be expressed in terms of the eigenvalues of all period-n orbits as

$$e^{-\kappa n} = \sum_j \frac{1}{e^{\lambda_{1j}^* n}} \quad \text{for } n \gg 1, \tag{2.87}$$

where the summation is taken over all period-n points on the chaotic saddle. The average Lyapunov exponent can be expressed as a similar sum, from (2.71),

$$\lambda_1 = \sum_j \lambda_{1j}^* \frac{e^{\kappa n}}{e^{\lambda_{1j}^* n}} \quad \text{for } n \gg 1. \tag{2.88}$$

The metric entropy (2.73) then appears as the average of $\lambda_{1j}^* - \kappa$, from which (2.74) follows.

The fractal properties of the natural measure can also be related to the cycle eigenvalues. To see this, consider a small box of dimensions l_1 and l_2 along the unstable and stable directions, respectively, about a point of the ith cycle of length n. Since the c-measure is smooth along the unstable direction, the c-measure of the box scales with l_1 and l_2 as

$$\mu_c(l_1, l_2) \sim l_1 l_2^{\alpha_{2i}}, \tag{2.89}$$

where $\alpha_{2i} < 1$ is a nontrivial exponent, the local *crowding index* characterizing the local fractal structure along the stable direction. After n iterations, the box is stretched (compressed) by factors of $\exp(\lambda_{1i}^* n)$ and $\exp(\lambda_{2i}^* n)$ along the unstable and stable manifolds, respectively, where λ_{1i}^* and λ_{2i}^* are the local Lyapunov exponents of the whole cycle. The side lengths of the n-fold image of the box are thus $l_1 \exp(\lambda_{1i}^* n)$ and $l_2 \exp(\lambda_{2i}^* n)$. Due to escape, the c-measures of the original box and of its images are different. A stationary distribution can be obtained when the escape is compensated for by the factor $\exp(\kappa n)$:

$$e^{\kappa n} \mu_c(l_1, l_2) = \mu_c(l_1 e^{\lambda_{1i}^* n}, l_2 e^{\lambda_{2i}^* n}). \tag{2.90}$$

Using the scaling from (2.89), we obtain

$$\lambda_{1i}^* - \kappa + \lambda_{2i}^* \alpha_{2i} = 0. \tag{2.91}$$

The natural measure μ of the same box scales with l_1 and l_2 as

$$\mu(l_1, l_2) \sim l_1^{\alpha_{1i}} l_2^{\alpha_{2i}}, \tag{2.92}$$

where $\alpha_{1i} < 1$ is the crowding index along the unstable direction, and α_2 is the same for both the natural and the c-measures. Preservation of the natural measure requires

$$\lambda_{1i}^* \alpha_{1i} + \lambda_{2i}^* \alpha_{2i} = 0. \tag{2.93}$$

Equations (2.91) and (2.93) indicate that the set of local crowding indices are uniquely determined by the cycle eigenvalues, from which α_1 can be obtained as

$$\alpha_{1i} = 1 - \frac{\kappa}{\lambda_{1i}^*}. \tag{2.94}$$

Since the crowding indices are a kind of local partial information dimensions, (2.94) and (2.93) are the local analogues of the dimension formulas (2.76) and (2.78), respectively.

2.7 Leaked Dynamical Systems and Poincaré Recurrences

2.7.1 Chaotic Saddles Associated with Leaked Systems

When a closed chaotic system is probed experimentally, the window through which observations are made can induce "leaking" of trajectories. Escape can thus occur, leading to transient chaos. The invariant sets of a leaked dynamical system are *subsets* of those in the corresponding closed system. Cutting a hole in a closed system to generate transient chaos was first suggested by Pianigiani and Yorke [596], and has since been studied in several contexts (see, e.g., [354, 572, 573], and [19] for a recent review). Since leaked chaotic systems provide a tool for a better understanding of the closed dynamics, leaking can be regarded as a type of chaotic spectroscopy [202, 203], or a way of "peeping at chaos" [105, 179].

To define leaking, we take a closed system described by a map $\mathbf{f}_{\text{closed}}(\mathbf{x})$ and choose a subset I of the phase space Ω, which is the leaking region, or the leak for short. A trajectory is regarded as having escaped the system after entering the region I. The leaked dynamics can thus be described by the following map:

$$\mathbf{x}_{n+1} = \mathbf{f}(\mathbf{x}_n) = \begin{cases} \mathbf{f}_{\text{closed}}(\mathbf{x}_n) & \text{if } \mathbf{x}_n \notin I, \\ \text{escape} & \text{if } \mathbf{x}_n \in I. \end{cases} \tag{2.95}$$

Since escape is considered to occur one step *after* entering I, the map $\mathbf{f}$ is defined in I. There is a chaotic saddle in the leaked system, which is the set of points that do not escape the *complement* of the leaking region I for both forward and backward iterations and is responsible for the exponential decay of the survival probability of trajectories in the system with some escape rate κ. The saddle is a subset of the original chaotic set in the corresponding closed system. An example from the Hénon map [325] is shown in Figs. 2.17a, b, where (a) shows a chaotic attractor and (b) displays the resulting chaotic saddle when the leaking region is a disk in the phase space. The chaotic saddle resembles mostly that of the Hénon map in the transiently chaotic regime (Fig. 1.8) except that the unstable manifold of this saddle is no longer a continuous curve as in Fig. 1.7. In general, the unstable manifold of a leaked dynamical system consists of disjoint pieces separated by the leaking region and its images.

As another example, consider the single-scale, area-preserving baker map. The phase space Ω is the unit square. Without any leak, a typical trajectory originated from a random initial condition visits the entire square with uniform probability. The natural measure μ is thus the Lebesgue measure. Suppose there is a leak in the system defined as a band extending over the full phase, where the center of the leaking region I is chosen to be the center of the unit square. The area $\mu(I)$ of the leak and the angle θ of the band relative to the y-axis are the two parameters that can be changed systematically. Invariant sets of the leaked baker map for leaks of the same area but with opposite tilt angles are shown in Fig. 2.18. The escape rates for these sets are different: $\kappa(25°) = 0.11$ and $\kappa(-25°) = 0.09$. For better visibility,
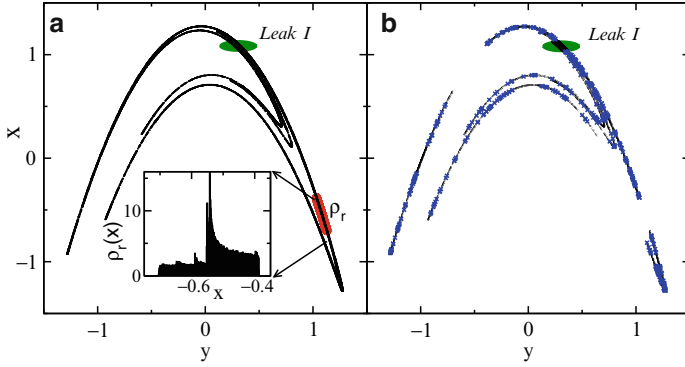
Fig. 2.17 For the Hénon map $x_{n+1} = 1 - 1.4x_n^2 + y_n$ and $y_{n+1} = 0.3x_n$, (**a**) chaotic attractor (*thin line*), the leaking region I and its first image $\mathbf{f}(I)$ (*gray regions*). The inset shows the projection $\rho_r(x)$ of the first image of the natural measure of the attractor in the leaking region on the x-axis. (**b**) Chaotic saddle (*crosses*) and its unstable manifold (*thin line*) of the corresponding leaked system. These invariant sets are generated using the sprinkler method (Sect. 1.2.2.3) with $n_0 = 40$
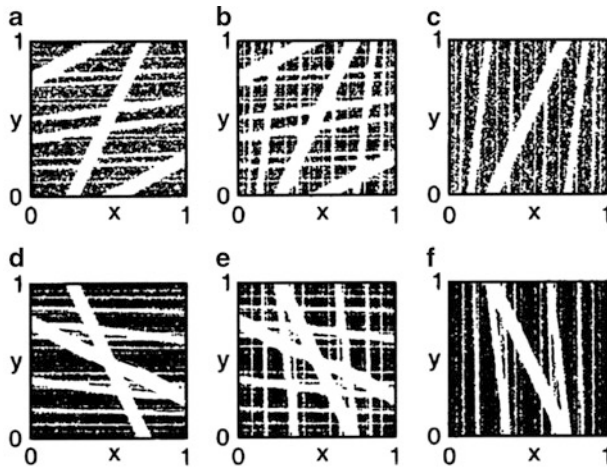
Fig. 2.18 For the baker map given by $(x_{n+1}, y_{n+1}) = (x_n/2, 2y_n)$ for $y_n \leq 1/2$ and $(x_{n+1}, y_{n+1}) = (1 + 1/2(x_n - 1), 1 + 2(y_n - 1))$ for $y_n > 1/2$ with a tilted leak of area $\mu(I) = 0.1$ at the angle $\theta = 25°$ and $\theta = -25°$, respectively, the stable manifold (**a**), (**d**), the chaotic saddle (**b**), (**e**), and the unstable manifold (**c**), (**f**). The difference in the contrast of the pictures is due to the difference in the escape rates [688] (Copyright 2002, the American Physical Society)

points of the invariant manifolds are not displayed within the leak. The leak is thus visible in Fig. 2.18 as a white band crossing the center of the square. There are in fact many more white bands. In particular, in the plot of the stable (unstable) manifold, these are the preimages (images) of the leak, and in the plot of the chaotic saddle

both the preimages and the images are present. In spite of the uniform density, the action of the baker map is asymmetric. The preimages of the left- and right-tilted bands are quite different. As a result, the first preimage of the 25° leak does not overlap with the leak, but there is an overlap in the other case. Thus, the total area of the leak and its first preimage is larger for the positive-angle case than that for the negative-angle case. The asymmetry persists in subsequent iterations, leading to different escape rates.

Figure 2.19 provides an overview of the chaotic saddles for the same leak area $\mu(I)$ but at a different set of angles θ. The textures at angles of opposite signs are quite different. The dependence of the escape rate on both parameters is summarized in Fig. 2.20. The escape rates associated with narrow leaks are nearly orientation-independent. In addition, the values of κ are close to the total area of the leak. Orientation dependence becomes significant for $\mu(I) > 0.05$, and the amount of fluctuations about the mean increases as the area is increased. In all cases, the intuitive estimate obtained from the assumption that $\exp(-\kappa)$ equals $1 - \mu(I)$,

$$\kappa(I) \approx -\ln[1 - \mu(I)], \tag{2.96}$$

is below the average escape rate over all the angles, but as Fig. 2.20 indicates, it provides a good approximation for small areas.

Since all periodic orbits in the used baker map have the same Lyapunov exponent, the average positive Lyapunov exponent of the chaotic saddle is $\lambda_1 = \ln 2$. The topological entropy is equal to the metric entropy. From (2.74), we obtain

$$K_0 = \lambda_1 - \kappa = \ln 2 - \kappa. \tag{2.97}$$
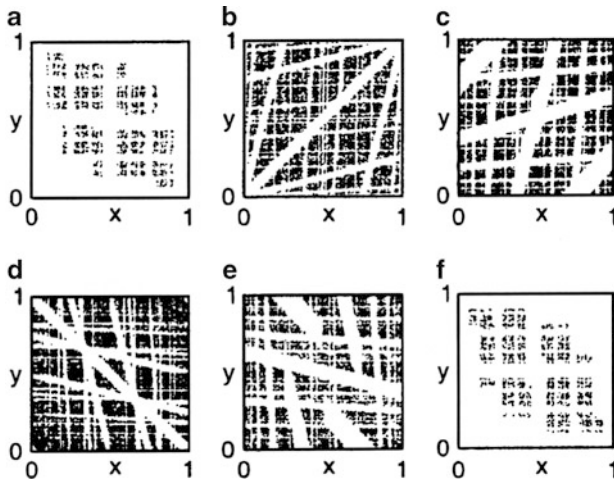
Fig. 2.19 Chaotic saddles of the leaked baker map ($\mu(I) = 0.1$) at leak angles $\theta = 0°$ (**a**), 45° (**b**), and 75° (**c**), and $\theta = -45°$ (**d**), $\theta = -75°$ (**e**), and $\theta = \pm 90°$ (**f**) [688] (Copyright 2002, the American Physical Society)
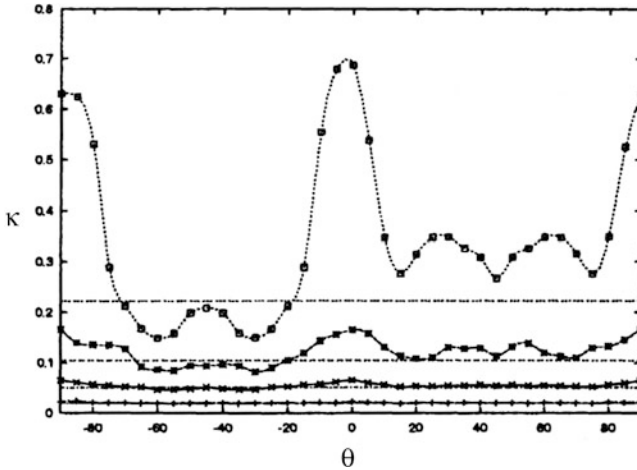
Fig. 2.20 Dependence of the escape rate on the tilt angle for different leak areas $\mu(I) = 0.02$ (*plus*), 0.05 (*crosses*), 0.1(*asterisk*), and 0.2 (*squares*). *Horizontal lines* correspond to the values $-\ln(1 - \mu(I))$ [688] (Copyright 2002, the American Physical Society)

The deviation of K_0 from $\ln 2$ indicates that not all possible sequences in the symbolic encoding are allowed to exist. The relatively large difference in the escape rates for different leaks thus reflects the difference in the topological entropies and in the rules underlying the symbolic dynamics.

From (1.14), it can be seen that the escape rate can be expressed in terms of the c-measure of the set of points that do not escape within one iteration. This set is $\Omega \setminus I$, where Ω is the phase space of the closed system. Since $\mu_c(\Omega \setminus I) = \mu_c(\Omega) - \mu_c(I)$ and the c-measure of the full phase space is normalized to be unity, we have $\mu_c(\Omega \setminus I) = 1 - \mu_c(I)$. This leads to an exact relation for the escape rate of the leaked system:

$$\kappa(I) = -\ln[1 - \mu_c(I)]. \tag{2.98}$$

That is, the escape rate is determined by the c-measure of the leak. The strong dependence of the escape rate on the orientation in Fig. 2.20 reflects that the c-measure can be drastically different even if the natural measure of the leak is kept constant [102]. The strong dependence of the c-measure on the orientation is also a consequence of the different kinds of grammatical rules in the symbolic dynamics due to the different overlaps of the preimages.

In the limit where the leak area becomes infinitesimally small, the escape rate approaches zero and the c-measure tends thus to the Lebesgue measure [5, 167]. It is only in the limit of $\mu_c(I) \to \mu(I) \to 0$ that the estimate (2.96) coincides with the exact result in (2.98). In this case, we have $\kappa = \mu(I)$, so that both the survival probability and the escape time distribution decay with time as

$$P(n) \sim p(n) \sim e^{-\mu(I)n}. \tag{2.99}$$

The average lifetime is then

$$\tau = \frac{1}{\mu(I)} \quad \text{for } \mu_{\mathrm{c}}(I),\, \mu(I) \to 0. \tag{2.100}$$

For larger leaks, the escape rate is given by (2.98), and no general formula can be obtained for the average lifetime, since this quantity depends also on the initial conditions.

Relation (2.99) has been used in several problems in dynamical systems ranging from fractal exit boundaries [72,538,623,668] and the control of chaos [101,571] to leaked billiards [43,179–181,475,476,539] and intermittency [836]. An interesting application is the reinterpretation of Sabine's law, a central object of architectural acoustics. The law says that the residual sound intensity in a room decays exponentially with time, and the decay rate is independent of the location of the source and the details of the room, provided that the room's shape is sufficiently irregular [532]. The duration to decay below the audible intensity is called the reverberation time. What is escaping here is not trajectories, but the energy of the sound waves, and the leak is the union of all energy-absorbing surfaces. In the language of the theory of dynamical systems, the reverberation time is the reciprocal of the escape rate, which is proportional to the natural measure of the leak, provided that the escape rate is small. Sabine's law, dating back to 1898, appears thus to be the first application of transient chaos in the history of science.

Finally, we mention the general case of more than one separated leak. For instance, with two leaks I_1 and I_2, the escape rate is in general different from the sum of the single leaked cases:

$$\kappa(I_1 + I_2) \neq \kappa(I_1) + \kappa(I_2). \tag{2.101}$$

The difference is due to the overlap of the preimages of the two leaks [101, 574], which has been established rigorously by Bunimovich and Dettmann [105]. In the limit of small leaks, the difference can be expressed in terms of the correlation function of the temporal dynamics.

2.7.2 Poincaré Recurrences

Poincaré recurrence, the return of trajectories to a specific region in the phase space, have played an important role in the study of closed dynamical systems because they constitute the foundation of the kinetic description of nonequilibrium processes [201, 851, 852]. In a macroscopic system the average recurrence time is typically large, but it tends to be smaller in low-dimensional systems. Poincaré recurrences have also been shown to provide useful insights into the dynamics of chaotic systems [16, 38, 136, 853]. An important quantity is the distribution $p_{\mathrm{r}}(k)$ of the first Poincaré recurrence times k to a preselected region I in the phase space.

As originally proposed by Chirikov and Shepelyansky [136], the *recurrence time distribution* $p_r(k)$ is a useful quantity in the analysis of dynamics in the full phase space. The Poincaré recurrence theorem ensures that for almost all initial conditions $\mathbf{x}_0$ in I, there are infinitely many time instants $n = n_1, n_2, \ldots$ such that $\mathbf{f}^n(\mathbf{x}_0) \in I$. The first recurrence times are defined as $k = n_i - n_{i-1}$ for $i = 0, 1, \ldots$, and $k = 1$ if the point remains in I. The recurrence time distribution $p_r(k)$, $k \geq 1$, is the probability of finding recurrence time k from an infinitely long trajectory. Due to the ergodicity of the natural measure of the closed system, the specific choice of the initial point $\mathbf{x}_0 \in I$ is irrelevant for $p_r(k)$. In the original setting, the recurrence region I is taken to be arbitrarily small, but in practical applications the size of I is finite, which we will assume in what follows.

For a generic chaotic system, the distribution $p_r(k)$ of recurrence times is found for any leak size to have the form [16]

$$p_r(k) \approx \begin{cases} \text{fluctuations} & \text{for } 1 < k < k_r^*, \\ g_r e^{-\gamma k} & \text{for } k \geq k_r^*. \end{cases} \tag{2.102}$$

The asymptotic behavior is an exponential decay with a decay rate γ. The short-time nonexponential behavior occurring before the exponential decay depends on the choice of the recurrence region I. A consequence of ergodicity of the natural measure is Kac's lemma [372], which states that the mean recurrence time $\tau_r \equiv \sum_k k p_r(k)$ is the reciprocal of the *natural measure* of the recurrence region:

$$\tau_r = \frac{1}{\mu(I)}. \tag{2.103}$$

Equation (2.103) is valid for any size of the recurrence region I. The decay rate γ, however, cannot be given in terms of the natural measure.

The recurrence problem can be better understood in the context of leaked dynamical systems. In particular, one can choose the *recurrence region to be the leak* and examine the interplay between the recurrence and escape times [18]. In this setting, trajectories contributing to the asymptotic decay of Poincaré recurrences must, after exiting the recurrence region I, fall into the neighborhood of the stable manifold of the chaotic saddle of the leaked system. The long-time dynamics preceding the first arrival back to the recurrence region is governed by the same saddle underlying the escape process in the leaked system. As a result, the relaxation rate of the recurrence statistics coincides with the decay rate of the escape statistics:

$$\gamma = \kappa. \tag{2.104}$$

The slopes of the recurrence time distribution $\ln p_r(n)$ and of the escape time distribution $\ln p(n)$ are thus identical, as illustrated in Fig. 2.21 for the standard Hénon attractor with the recurrence/leak region I chosen as in Fig. 2.17. Equation (2.104) implies that for any Poincaré recurrence problem, there exists a chaotic saddle in the corresponding leaked system and the relaxation rate γ is given by the escape rate from the saddle. It is remarkable that in view of (2.98), the relaxation
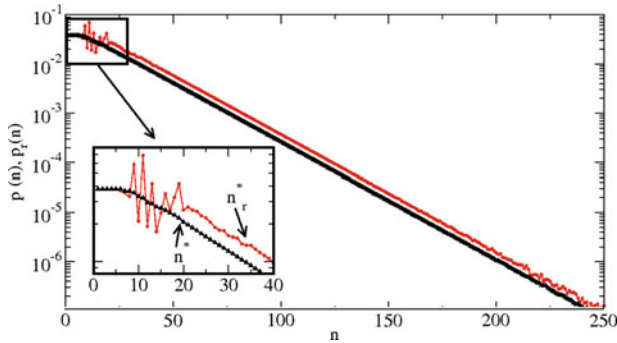
Fig. 2.21 For the Hénon map with leaking region I chosen as in Fig. 2.17, (**a**) distributions of recurrence time $p_r(n)$ and of escape time $p(n)$. To generate $p_r(n)$, a trajectory of length 10^{11} originated from the center point of the recurrence region is used. The initial conditions for the escape-time distribution $p(n)$ of the leaked system are chosen according to the natural distribution of the Hénon attractor. Short-time behaviors of the distributions are shown in the *inset*; $\gamma = \kappa = 0.055$. The value n^* (respectively n_r^*) indicates the time after which the decay of $p(n)$ (respectively $p_r(n)$) is exponential with good accuracy [18] (Copyright 2008, the American Physical Society)

rate of the Poincaré recurrences of a closed system is given by the c-measure (rather than by the natural measure) of the recurrence region when viewed as a leaked system.

Despite exhibiting the same exponential decay, the distributions $p_r(n)$ and $p(n)$ are different for typical initial distributions ρ_0. There is, however, a special initial condition $\rho_0 = \rho_r$ for the leaked problem for which the escape statistics are fully equivalent to the recurrence statistics. Consider the distribution obtained as the first iterate of the points $\mathbf{x} \in I$ distributed according to the natural density ρ_μ of the closed system within the leak. For invertible maps $\mathbf{f}$ with constant Jacobian, this can be written as

$$\rho_r(\mathbf{x}) = \begin{cases} \rho_\mu[\mathbf{f}^{-1}(\mathbf{x})]/\mu(I) & \text{if } \mathbf{x} \in \mathbf{f}(I), \\ 0 & \text{otherwise,} \end{cases} \qquad (2.105)$$

where a proper normalization factor has been included in the denominator. The inset of Fig. 2.17a shows an example: the projection of the distribution on one of the dynamical variables of the Hénon map. Due to ergodicity, points of a long trajectory generating the recurrence-time distribution, one iteration after returning to I, are distributed precisely according to ρ_r. As illustrated in Fig. 2.22, due to the definition (2.95), according to which escape takes place one step after entering the leak, all escape times n correspond to the recurrence time $k = n$. Accordingly, we have

$$p_r(n) = p(n) \quad \text{with } \rho_0 = \rho_r. \qquad (2.106)$$

We see that the two distributions are identical, including the short-time fluctuations appearing for $n < n_r^* = n^*$. The key observation is then that any *recurrence problem*

Fig. 2.22 Illustration of the equivalence between recurrence and escape times
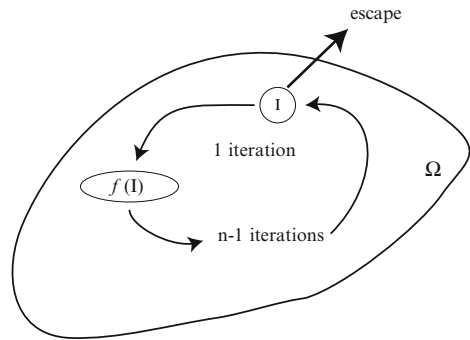
can be considered as a leaked problem with the special initial condition $\rho_0 = \rho_r$ (2.105).

The average lifetime is then given by Kac's formula (2.103) $\tau = 1/\mu(I)$. For finite I it deviates *considerably* from the mean lifetime estimated according to (1.7) as $1/\kappa = -1/\ln[1 - \mu_c(I)]$, which contains the c-measure of the leak. The reason for the large deviation is that ρ_r in (2.105) is *atypical* from the point of view of the c-measure that concentrates along the unstable manifold of the chaotic saddle, i.e., it contains points that never escape under the backward dynamics, while all points associated with ρ_r come from the leak.

It has been observed that different recurrence/leak regions of the same natural measure can lead to quite different exponential decays, particularly if an unstable periodic orbit of low period falls into I [3, 16, 103, 571]. According to (2.104), there is a common phenomenon behind these results. Say there is a periodic orbit of period n_p in I. We then expect a high recurrence probability $p_r(k = n_p)$. Since the average recurrence time is fixed and given by (2.103), the probabilities of other recurrence times $k \neq n_p$ are lower, leading to a reduced decay rate. In the context of leaked systems, the anomalously low escape rate is due to the significant overlaps between the leak and its preimages.

Chapter 3
Crises

As a system parameter is varied, sudden and qualitative changes in the chaotic attractor can occur, the so-called *crises* [292, 293]. These qualitative changes can be seen in bifurcation diagrams where one coordinate, say x^*, of the attractor is plotted versus a system parameter, as shown in Fig. 3.1. Sudden shrinkage or enlargements of the set of x^* values are visible at several parameter values, indicating the complexity of crisis events in a typical dynamical system.

In generic dynamical systems, there are two major types of crises: *boundary* crises and *interior* crises. A boundary crisis occurs when a chaotic attractor collides with an unstable periodic orbit (or its stable manifold) on the basin boundary, converting the attractor into a nonattracting chaotic set and generating transient chaos. At an interior crisis, a chaotic attractor, typically of small size, collides with a coexisting nonattracting chaotic set (or its stable manifold), resulting in a larger chaotic attractor. While boundary crisis is a mechanism for chaotic transients, interior crisis provides a mechanism for sudden enlargement of a chaotic attractor in the phase space, and intermittency. Crises are quite common in nonlinear dynamical systems. For example, in a parameter regime where chaotic attractors arise, there can be various saddle-node bifurcations, generating stable periodic attractors and consequently *periodic windows* [564]. In a periodic window, there is transient chaos caused by a nonattracting chaotic set, the remnant of the chaotic attractor before the saddle-node bifurcation. The end of the periodic window is marked by a sudden enlargement of a small attractor, which is caused by an interior crisis. As will be discussed in this chapter, such an interior crisis leads to physically observable phenomena such as *crisis-induced intermittency*. From a different standpoint, a chaotic attractor can be regarded as consisting of a number of nonattracting chaotic sets with distinct dynamical properties, which form the *backbone* of the chaotic attractor.

The goal of this chapter is to present a comprehensive treatment of the fundamental phenomenon of crisis and the associated universal scaling laws.
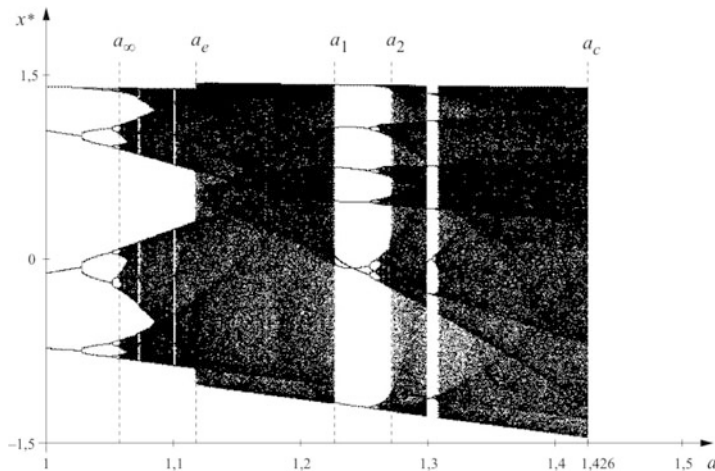
Fig. 3.1 Bifurcation diagram of the Hénon map $x_{n+1} = 1 - ax_n^2 + 0.3y_n$, $y_{n+1} = x_n$ in the parameter range $1 < a < 1.5$. The parameter values of a few crisis events are indicated: an attractor enlargement point a_e, the endpoints of the main period-7 window a_1, a_2, and the endpoint a_c of permanent chaos (the accumulation point of the period-doubling cascade is marked as a_∞)

3.1 Boundary Crises

A boundary crisis [292, 293] occurs when a chaotic attractor "touches" its own basin boundary at a critical parameter value p_c. When this happens, certain points of the attractor belong to the boundary as well, as shown in Fig. 3.2. As the system parameter is increased beyond the crisis point, say for $p > p_c$, the boundary "penetrates" into a region that contains part of the original chaotic attractor for $p < p_c$, as shown in Fig. 3.3. Since the attractor is enclosed in the unstable manifold of an embedded
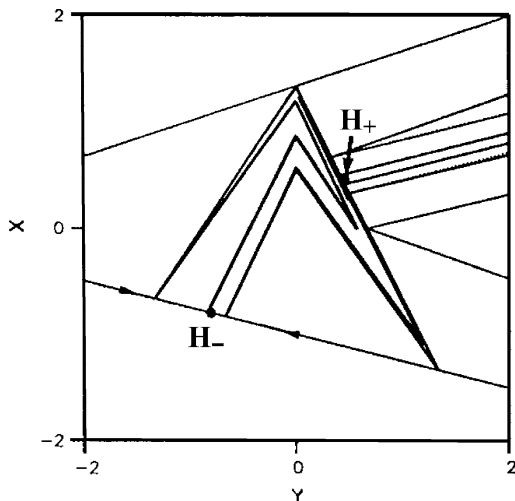
Fig. 3.2 Invariant manifolds for the Lozi map: $x_{n+1} = 1 - a \mid x_n \mid + by_n$, $y_{n+1} = x_n$. Shown are the unstable manifold of the upper fixed point H$_+$ and the stable manifold of the lower fixed point H$_-$ for precisely the crisis parameter value $a = a_c = 2 - b/2 = 1.75$, where $b = 0.5$. Note that the stable manifold is in fact the basin boundary

Fig. 3.3 Stable and unstable
manifolds for the Lozi map in
Fig. 3.2 but slightly beyond
the crisis value: $a = 1.8 > a_c$.
Almost all points in the
region now escape to the
attractor at infinity
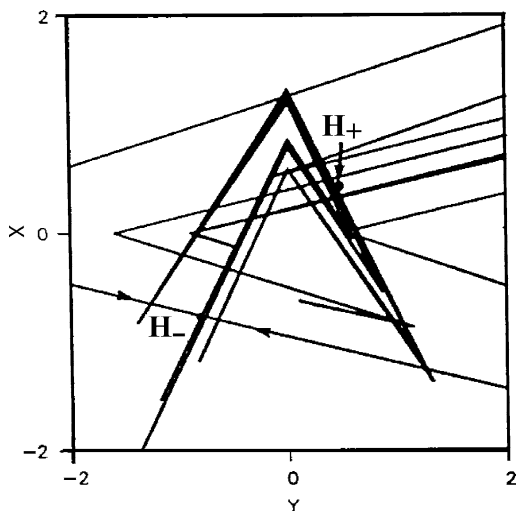
periodic orbit, for $p > p_c$ the boundary effectively converts "pieces" of the unstable
manifold into "pieces" of the basin of a different attractor. If one piece is removed,
so are all its preimages, and hence almost all points of the unstable manifold now
belong to the basin of the different attractor. As a result, the basin of the original
chaotic attractor is destroyed and the attractor is converted into a chaotic saddle.
All these features can be visualized using the Lozi map, a piecewise linear map for
which the exact crisis parameter value can be obtained. In fact, the stable and the
unstable manifolds can be constructed analytically [762]. The manifolds at and be-
yond the crisis are shown in Figs. 3.2 and 3.3, respectively. A numerically obtained
chaotic saddle is shown in Fig. 3.4, which is to be compared with the intersection
point in Fig. 3.3.

While boundary crisis provides a mechanism for transient chaos to arise, it can
also be viewed as a mechanism for generating a chaotic attractor. Specifically, when
the crisis is approached from the side of transient chaos, the opposite situation oc-
curs: the underlying nonattracting chaotic set becomes denser and less repelling in
the phase space. At the crisis all pieces of the set are connected by the unstable
manifold, generating a chaotic attractor. From this point of view, crisis represents a
route to chaotic attractors [292, 293].

For a one-dimensional map, a boundary crisis occurs when the trajectories fill
entirely the interval available for chaos, as can be seen from Fig. 3.5a–c for a
single-humped map $f(x)$, corresponding to the precrisis, the crisis, and the postcri-
sis situations. To make an analogy with the two-dimensional case, we can expand
$f(x)$ into the plane as

$$x_{n+1} = f(x_n, p), \quad y_{n+1} = x_n. \tag{3.1}$$

Chaotic sets then appear on the curve $x = f(y, p)$ is the (y, x)-plane. If $f(x)$ is defined
on the unit interval, the fixed point at the origin can be reached along the horizontal

Fig. 3.4 Chaotic saddle of the Lozi map for parameters $a = 1.8$ and $b = 0.5$. A topologically similar chaotic saddle can be obtained with the Hénon map for $a = 1.5$ and $b = 0.3$, which is slightly beyond a crisis at $a_c \approx 1.4269$
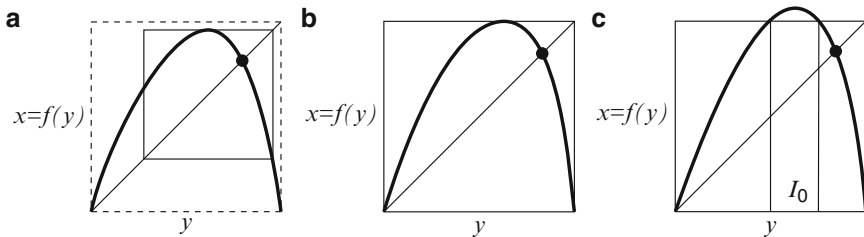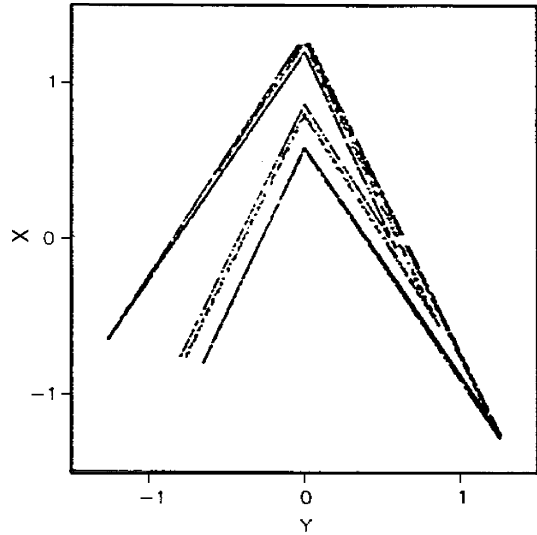
Fig. 3.5 Precrisis (**a**), crisis (**b**) and postcrisis (**c**) configurations of a single-humped one-dimensional map defined on the unit interval. In (**a**), chaotic motion is confined to the solid square

lines $x = 0$ and $x = 1$ of the plane. In this special case, the stable manifold of the fixed point consists of these two lines in the (y, x)-plane. Insofar as $f(x_c) < 1$, where x_c is the point at which $f(x)$ reaches a maximum, the chaotic attractor extends over an interval (both in x and y) that does not contain either 0 or 1; cf. Fig. 3.5a. At the crisis, the attractor covers the entire unit interval (both in x and y) and thus touches the stable manifold of the fixed point, similar to Fig. 3.2.

A typical situation leading to boundary crises in chaotic dynamical systems is shown schematically in Fig. 3.6. First, a saddle-node bifurcation generates two fixed points: one stable and another unstable. The former undergoes a period-doubling cascade to a chaotic attractor, while the latter remains unstable. In a large portion of the parameter space where there is sustained chaos, the chaotic attractor often consists of a number of pieces, and the phase-space regions where sustained chaotic motions occur are called *bands*, and the regions in between are *gaps*. A boundary crisis occurs when the stable manifold of the unstable periodic orbit created at
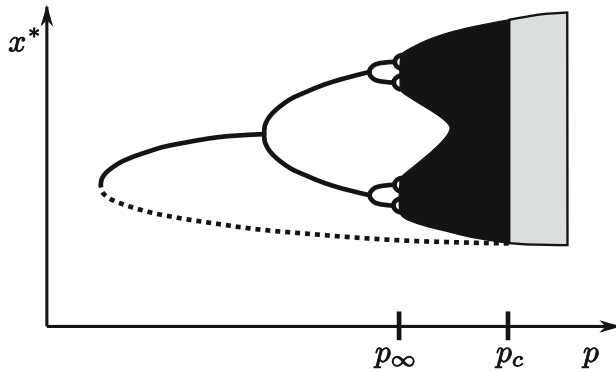
Fig. 3.6 A schematic bifurcation diagram leading to transient chaos via a boundary crisis at p_c: *black dots* mark the region of permanent chaos. In the *gray region* the chaotic set is nonattracting. The accumulation point of the period-doubling cascade is marked as p_∞

Fig. 3.7 Extended bifurcation diagram of the Hénon map as a function of parameter a ($b = 0.3$). A boundary crisis occurs at $a_c \approx 1.4269$, as indicated by the *vertical line*. *Black dots* for $a > a_c$ represent points of the chaotic saddle projected on the x-axis [447] (Copyright 1994, the American Physical Society)
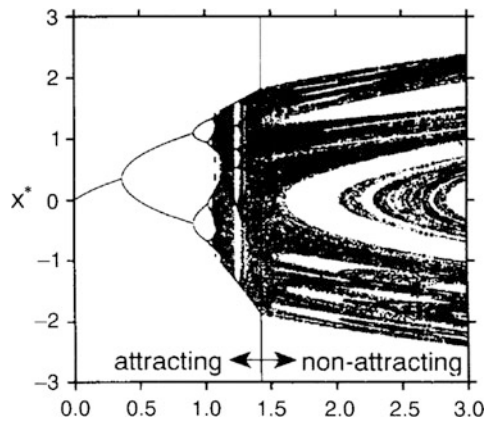
the saddle-node bifurcation collides with the chaotic attractor. After the crisis only transient chaos is present. An example illustrating the existence of a chaotic saddle in the postcrisis region is shown in Fig. 3.7.

3.1.1 Nonhyperbolicity of Chaotic Saddles

The chaotic saddles treated in the previous two chapters have the property that for every point on the saddle, the local stable and unstable manifolds are distinct. Roughly, this occurs when all the local turning points of the unstable manifold lie outside the saddle. These are hyperbolic chaotic saddles. However, situations can arise in which there are points in a chaotic saddle at which the stable and the unstable manifolds are tangent. Such a saddle is nonhyperbolic, which can often
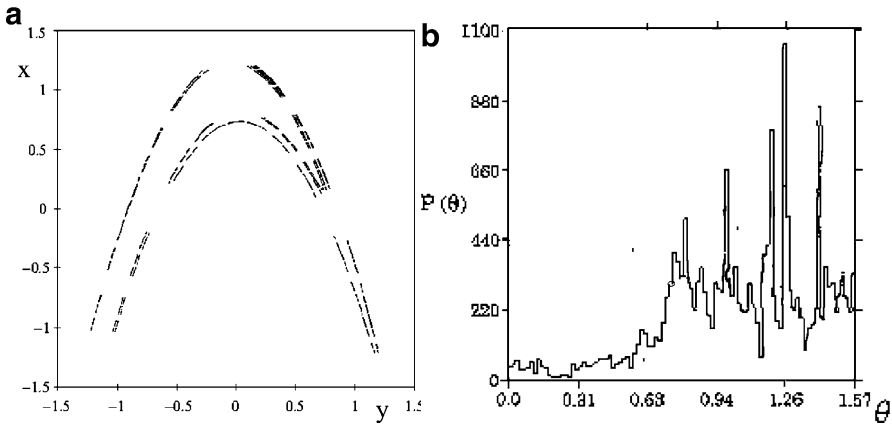
Fig. 3.8 (**a**) A nonhyperbolic saddle from the Hénon map for $a = 1.6$ and $b = 0.3$, and (**b**) histogram of angles between local stable and unstable manifolds. The angles can be arbitrarily close to zero [454] (with kind permission from the Institute of Physics)

occur in the parameter regime slightly beyond a boundary crisis.[1] An example of a nonhyperbolic chaotic saddle is shown in Fig. 3.8a. The main difference between this saddle and that in, e.g., Fig. 1.8 is that here a seemingly continuous arch of points along a filament of the unstable manifold (such as, e.g., about $x = 0.7, y = 0$) belongs to the saddle and can have tangencies with the stable foliation. Figure 3.8b presents a distribution of the angles between the local stable and unstable manifolds. It can be seen that the angle can be arbitrarily close to zero, which should be contrasted to hyperbolic chaotic saddles, such as the one shown in Fig. 1.8, where the angles between the manifolds (see, e.g., Fig. 1.7) are bounded away from zero. Since for an invertible map, the images and preimages of a tangency point are also tangency points, they are dense on a nonhyperbolic chaotic saddle. That is, for any point on the chaotic saddle, there are tangency points arbitrarily nearby. Furthermore, if there is one parameter value p at which the saddle is nonhyperbolic, around this value there exists a parameter interval of *finite* length for which the saddles are nonhyperbolic. Such intervals are called Newhouse intervals [546, 547].

Chaotic saddles arising in naturally open systems, such as systems after a boundary crisis, often have the feature that, beyond a certain parameter value, say $p_h > p_c$, where p_c is the crisis value, they are all hyperbolic.[2] Newhouse intervals can thus exist only in the parameter interval (p_c, p_h). The results in [454] suggest, however, that within this interval, nonhyperbolic chaotic saddles are quite typical, and the

---

[1] It should be noted that chaotic attractors in physical systems are generally nonhyperbolic, due to the existence of a set of points in the attractor at which the angles between the stable and the unstable directions are zero.

[2] In contrast, chaotic saddles in leaked dynamical systems are generally nonhyperbolic; see Sect. 2.7.

Fig. 3.9 Parameter values of the plane a, b that belong to nonhyperbolic Hénon saddles are marked by *gray dots*. The *gray region* is bounded from the left by the curve a_c of crisis and from the right by the curve of hyperbolicity a_h. For $b = 0.3$, $a_h(b) = 2.89$. All saddles for $a > a_h(b)$ are hyperbolic [454] (with kind permission from the Institute of Physics)
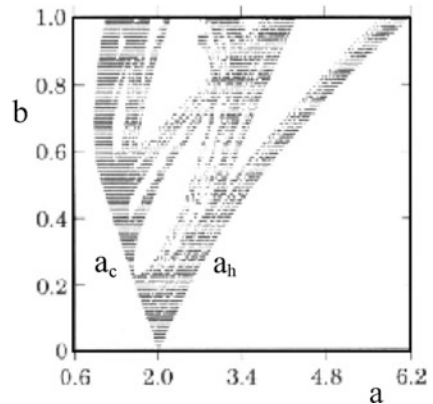
length of the largest Newhouse interval can be several hundredths of the value of $(p_h - p_c)$. The close vicinity of the boundary-crisis point is always covered by Newhouse intervals. Crisis itself is a phenomenon strongly related to nonhyperbolicity, since it is accompanied, by definition, by the formation of tangencies between manifolds.

Results about the Newhouse intervals obtained for the particular case of the Hénon map are illustrated in Fig. 3.9 in the parameter space where parameter b is between zero and unity. The fraction of parameter values for nonhyperbolic chaotic saddles is for many b values more than 20%. The maximum length of the Newhouse intervals are of order 0.1 [454].

An important property of hyperbolic dynamical systems is their structural stabilities, where small changes in the parameters cause small changes in the angle distribution and to the system dynamics [300]. Dynamical invariants characterizing the underlying chaotic sets thus change smoothly with the parameters. In particular, one such quantity, the topological entropy, does not change outside the Newhouse intervals. It is the tangency between the stable and the unstable manifolds that generates new periodic orbits, leading to an increase in the topological entropy. When there are no tangencies, the topological entropy remains constant. In this sense, it can be said that crisis is generally an event that increases the "complexity" of the system. The subsequent homoclinic and heteroclinic crossings of the stable and the unstable manifolds beyond p_c create an infinite number of new unstable periodic orbits and consequently an increase in the topological entropy of the resulting chaotic set. An example of the topological entropy of the chaotic saddles from the Hénon map versus a system parameter is shown in Fig. 3.10. Note that there are plateau regions where the saddle is hyperbolic (complements of the Newhouse intervals). The function $K_0(p)$ exhibits a devil-staircase character [125, 466]. At $a_h(b)$, K_0 reaches its maximum value: all symbolic sequences can occur (the symbolic dynamics is complete). Beyond $a_h(b)$, the topological entropy remains constant.

In spite of nonhyperbolicity, the survival time probability exhibits exponential decay, and the escape rate is well defined for any $p > p_c$ and typically grows with p. This indicates (as also Fig. 3.8b suggests) the overall dominant role of hyperbolic

Fig. 3.10 Dependence of the topological entropy K_0 in the Hénon map as a function of parameter a ($b = 0.3$). The plateau regions correspond to the white intervals of Fig. 3.9 within the *gray region* [125] (with kind permission from Elsevier Science)
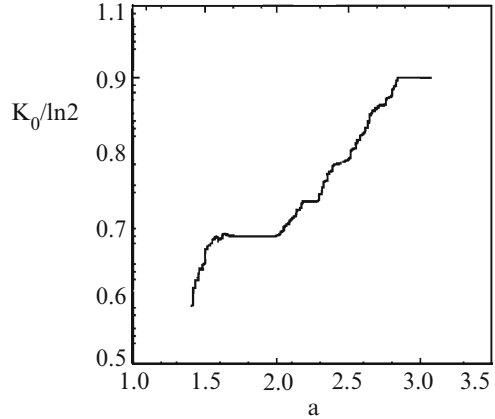
points on the chaotic saddle in dynamics. In cases in which nonhyperbolic points dominate, the long-term decay is no longer exponential, but a power law, as illustrated by the one-dimensional example in Fig. 2.13. Similar long-time decays will be discussed in the context of nonhyperbolic chaotic scattering (Sect. 6.4).

3.1.2 Critical Exponent of Chaotic Transients

The escape rates for parameters slightly beyond the crisis value are usually small, so that the corresponding chaotic transients have long lifetimes. This parameter regime is thus particularly suitable for experimental investigation of transient chaos (see, e.g., [112, 196, 479, 577, 646]). In general, the escape rate scales with the parameter difference $(p - p_c)$ as a power law [290, 291], for p slightly above p_c:

$$\kappa(p) \sim (p - p_c)^\gamma, \quad p \gtrsim p_c, \tag{3.2}$$

where γ is the *critical exponent* of the chaotic transients. A remarkable feature of transient chaos is that the exponent γ is determined by the stability of an unstable periodic orbit, the *mediating* periodic orbit. In systems with constant phase-space contraction (constant Jacobian), two different situations can arise, depending on whether the crisis is triggered by a homoclinic or a heteroclinic tangency, as shown in Fig. 3.11, and correspondingly, there are two different expressions for γ. (Scaling rule (3.2) remains valid even if the nonattracting chaotic set is a fat fractal [321, 359]).

3.1.2.1 Heteroclinic Tangency

A heteroclinic-tangency-induced crisis occurs when the stable manifold of an unstable periodic orbit (say H_-) becomes tangent to the unstable manifold of another
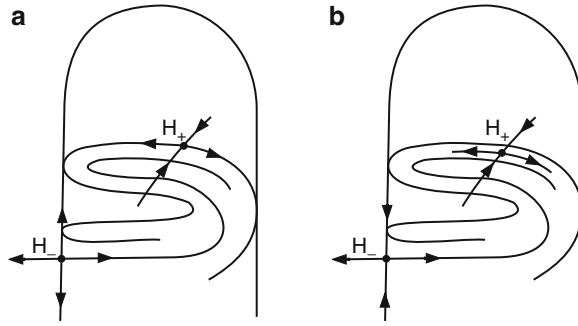
Fig. 3.11 Schematic illustration of a crisis induced by (**a**) heteroclinic tangencies and (**b**) homoclinic tangencies. The chaotic attractor is in the closure of the unstable manifold of the fixed point H_+. In case (**b**) the attractor is enclosed by the unstable manifold of H_-

Fig. 3.12 Configuration of stable and unstable manifolds slightly beyond a heteroclinic crisis, and the characteristic lengths of the shaded regions from which escape takes place, where $A'B'$ is the nth preimage of AB
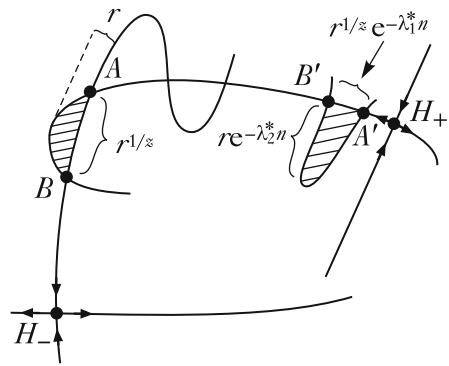
hyperbolic periodic orbit (H_+), where H_+ is embedded in the attractor in the pre-crisis regime. As p is increased slightly beyond p_c, the unstable manifold of H_+ crosses the stable manifold of H_- at infinitely many locations, and the heights of the "overshoots" through both manifolds are proportional to $r \equiv p - p_c$, as shown in Fig. 3.12. The local form of the unstable manifold in the overshoot region is a parabola of order z, where for generic cases the order is $z = 2$ (in nonsmooth dynamical systems z can assume different values, e.g., $z = 1$ for the Lozi map). The width of the parabolic piece (shaded region AB in Fig. 3.12) along the stable manifold is of order $r^{1/z}$. Trajectories landing in this parabolic piece leave the chaotic saddle rapidly.

Consider the nth preimage of region AB, denoted by $A'B'$. For large n, the deformation of the region is governed by the linearized map about H_+. The side lengths of $A'B'$ are of order $r \exp(-\lambda_2^* n)$ and $r^{1/z} \exp(-\lambda_1^* n)$, where λ_1^* and λ_2^* are the local Lyapunov exponents of the mediating periodic orbit H_+ (a fixed point in our case), so that $\exp(\lambda_1^*)$ and $\exp(\lambda_2^*)$ are the moduli of the expanding and contracting eigenvalues at H_+, respectively. Now focus on trajectories that stay near the chaotic saddle for a finite amount of time before escape. For such a trajectory, when

it enters $A'B'$, it will subsequently fall in AB. The escape rate is thus approximately the probability for the trajectory to land in the region $A'B'$, which is in fact the c-measure associated with the region. For small r, we can write

$$\kappa(r) \sim \mu_c(A'B') \sim r^\gamma. \tag{3.3}$$

We have seen in (2.89) how the c-measure in a box about a periodic orbit scales with the lengths of the edges parallel to the unstable and the stable directions. With the side lengths of region $A'B'$ shown in Fig. 3.12, we have

$$\kappa(r) \sim \mu_c(r^{1/z}e^{-\lambda_1^* n}, re^{-\lambda_2^* n}) \sim r^{1/z}e^{-\lambda_1^* n}\left(re^{-\lambda_2^* n}\right)^{\alpha_2} \sim r^{1/z+\alpha_2}, \tag{3.4}$$

where the local crowding index α_2 follows from relation (2.91) applied to the fixed point H_+ as

$$\alpha_2 = -\frac{\lambda_1^* - \kappa}{\lambda_2^*}. \tag{3.5}$$

Slightly above the crisis, κ is small. We thus have $\alpha_2 \approx -\lambda_{1c}^*/\lambda_{2c}^*$, where the eigenvalues are those evaluated *at* the crisis. These considerations yield

$$\gamma = \frac{1}{z} + \frac{\lambda_{1c}^*}{|\lambda_{2c}^*|}. \tag{3.6}$$

This formula reveals that the critical exponent is determined by the stability of H_+ at the crisis and the singularity properties of the map as characterized by the degree z of the tangency.

3.1.2.2 Homoclinic Tangency

For a homoclinic-tangency-induced crisis, the stable and the unstable manifolds of the mediating unstable periodic orbit H_- become tangent to each other. This is the case for Hénon-type maps with positive Jacobian. Since Poincaré or stroboscopic maps derived from flows can have only positive Jacobians [773], this case is generic for flows and actual experimental systems.

To obtain the critical exponent, it is useful to first examine the situation at crisis. Choose the height of the parabolic region (again of order z) of the base AB around the first homoclinic tangency point to be $r \ll 1$, as in Fig. 3.13. This value is chosen so that the unstable manifold of the fixed point pokes over to the other side of the stable manifold by the same amount r for $p > p_c$. We thus write $r \sim p - p_c$, and the natural measure $\mu(r)$ of the parabolic region of base AB of the attractor is proportional to the escape rate $\kappa(r)$. Let $A'B'$ denote the baseline segment of the parabolic region, which is a preimage of the tangency region lying close to H_-. The height of this region is also proportional to r.

Consider next a small box around the fixed point of side lengths l_1 and l_2 along the unstable and stable directions, respectively. The natural measure of the box scales with l_1 and l_2 as, (2.92),
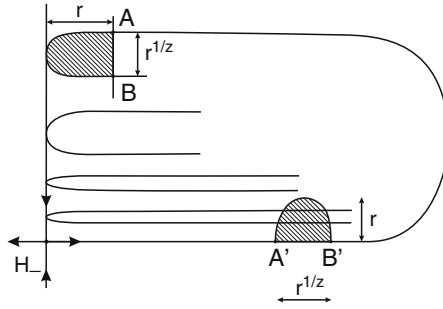
Fig. 3.13 Schematic illustration of the configuration of the stable and unstable manifolds of the fixed point H_ at a homoclinic crisis. The characteristic lengths and the shaded region whose measure determines the escape rate are indicated. Close to the fixed point, the attractor contains several branches that appear parallel to the unstable manifold

$$\mu(l_1, l_2) \sim l_1^{\alpha_1} l_2^{\alpha_2}. \tag{3.7}$$

In this special situation the measure is not proportional to the box length l_1 along the unstable direction, so we can assume $\alpha_1 \neq 1$. After n iterations the box is stretched and compressed by factors of $\exp(\lambda_{1c}^* n)$ and $\exp(\lambda_{2c}^* n)$ along the unstable and the stable manifolds, respectively, where λ_{ic}^* $(i = 1, 2)$ are the local Lyapunov exponents of the mediating periodic orbit, H_, at the crisis. The side lengths of the n-fold image of the box can thus be written as $l_1 \exp(\lambda_{1c}^* n)$ and $l_2 \exp(\lambda_{2c}^* n)$, and the preservation of the natural measure $\mu(l_1, l_2) = \mu(l_1 e^{\lambda_{1c}^* n}, l_2 e^{\lambda_{2c}^* n})$ implies

$$\lambda_{1c}^* \alpha_1 + \lambda_{2c}^* \alpha_2 = 0, \tag{3.8}$$

which is similar to that found for arbitrary points on a chaotic saddle, (2.93).

Since the images of the tangency point and of the parabolic region AB will, for small enough r, fall into the box about H_, we expect [291] that the scaling with the distance along the unstable direction goes with α_1:

$$\mu(r) \sim r^{\alpha_1}.$$

Similarly, for measure μ' of the parabolic region of base $A'B'$ the scaling with vertical size l_2 remains unchanged. As Fig. 3.13 indicates, the measure is differentiable along the unstable direction. The measure of the parabolic region is therefore also proportional to the size $r^{1/z}$ of the base. We have

$$\mu'(r) \sim r^{\alpha_2 + 1/z}.$$

Since the parabolic region of base AB is the image of that of base $A'B'$, the measures are equal. We obtain

$$\alpha_1 = \alpha_2 + 1/z$$

relating the two crowding indices. Using (3.8), we obtain α_1. The scaling $\mu \sim r^\gamma$ implies $\gamma = \alpha_1$, and thus

$$\gamma = \frac{1}{z} \frac{|\lambda_{2c}^*|}{|\lambda_{2c}^*| - \lambda_{1c}^*}. \tag{3.9}$$

This result indicates indeed that $\alpha_1 = \gamma \neq 1$, i.e., the natural measure does not grow linearly along the unstable manifold. The critical exponent is now determined by the stability properties of the mediating periodic point, H_-, on the boundary and the degree z of tangency.

3.1.2.3 One-Dimensional Maps

For one-dimensional maps, close to crisis, the escape rate is proportional to the size of the primary escaping interval I_0, i.e., the length of the primary escape interval for $f(x) > 1$, as shown in Fig. 3.5c. For maps defined on the unit interval with local maxima at x_c of order z, where

$$f(x) \approx f(x_c) - b|x - x_c|^z, \tag{3.10}$$

the size is

$$L = 2 \left(\frac{f(x_c) - 1}{b} \right)^{1/z}. \tag{3.11}$$

Since the overshoot $f(x_c) - 1$ is proportional to $p - p_c$, we have $L \sim |p - p_c|^{1/z}$. The critical scaling exponent for one-dimensional maps is thus given by

$$\gamma = \frac{1}{z}. \tag{3.12}$$

This result can also be obtained from the two-dimensional results for the strong dissipation case, i.e., when the magnitude of the negative Lyapunov exponent tends to infinity. We see that the exponent γ is larger for two-dimensional maps, suggesting that chaotic transients are *more persistent* in higher-dimensional systems [290].

In higher-dimensional systems the escape rate may be much smaller than that determined by a power of the parameter difference from the crisis value. In this case, chaotic transients can be *superpersistent*, which will be treated in Chap. 8.

3.2 Interior Crises

In the case of an interior crisis, there is a sudden increase in the size of a chaotic attractor as a parameter p passes through a critical value p_c. Because unstable periodic orbits are dense on chaotic attractors, at interior crisis there is a sudden increase in the number of unstable periodic orbits, which are mostly from the coexisting nonattracting set in the precrisis regime.

3.2.1   An Example of Interior Crisis

An enlightening example of interior crisis is provided by the so-called Ikeda map, an invertible two-dimensional map that is an idealized model of a laser cavity. The system is expressed in terms of a complex variable $z = x + iy$ as

$$z_{n+1} = A + Bz_n \exp\left(ik - \frac{ip}{1 + |z_n|^2} \right), \tag{3.13}$$

where the modulus and the phase of z represent the amplitude and the phase of the electromagnetic field of the laser pulse, respectively, and A, B, k, and p are parameters. A dramatic example of interior crisis, when A, B, and k are fixed and p is varied, is shown in Fig. 3.14a,b, where a small four-piece chaotic attractor (a) becomes a single-piece but much larger chaotic attractor (b). The parameter difference between the two cases is of order 10^{-4}, but the chaotic attractor emerging after the crisis is large and appears characteristically different from the small attractor before the crisis. This can be understood by noting that for $p < p_c$, there is a large chaotic saddle coexisting with the small chaotic attractor, as shown in Fig. 3.15, for the same parameter values as for Fig. 3.14a. Figure 3.15 indicates the fractal character associated with typical chaotic saddles in two-dimensional maps: there are gaps of different sizes along both the stable and the unstable directions. The similarity of the overall structure of the saddle to that of the chaotic attractor after the crisis is remarkable (Fig. 3.14b versus Fig. 3.15). At the interior crisis the chaotic saddle collides with the small attractor, and together they make up the large attractor. The unstable periodic orbits of the saddle are then added to the original attractor, and new periodic orbits are created due to heteroclinic connections.

The rising of the chaotic saddle is in general due to a long sequence of bifurcations, in the course of which small-size chaotic attractors are created, typically via saddle-node bifurcations and period-doubling cascades, and are destroyed by boundary crises. The large chaotic saddle is thus partly a result of a series of boundary crises prior to the interior crisis. The scenario is schematically illustrated in Fig. 3.16, a typical bifurcation diagram of a dynamical system exhibiting an interior crisis. Notice that accumulation of the period-doubling bifurcations occurs before the crisis, so there is a small multipiece chaotic attractor present right before p_c. The scales indicate how dramatic the increase in the extent of chaos is at the interior crisis point p_c.

A somewhat related phenomenon is *attractor-merging crisis*. In this case, in the precrisis regime $p < p_c$, two chaotic attractors coexist, each having its own basin of attraction. As p is increased, the two attractors enlarge, and at p_c they collide with the basin boundary separating their basins. Merging crisis can happen in systems possessing some symmetry whereby the precrisis attractors, as well as their basins, are symmetric images of each other in the phase space.

Another situation in which interior crisis occurs is *band-merging crisis* [649], the pairwise merging of chaotic bands (the inverse of the period-doubling cascade taking place in the chaotic regime when approaching the accumulation point

Fig. 3.14 For the Ikeda map
(3.13) for $A = 0.85$, $B = 0.9$,
and $k = 0.4$, an interior crisis
occurs at $p_c \approx 5.169789$.
(**a**) For $p = 5.1697 < p_c$,
a small four-piece chaotic
attractor and (**b**) a much
larger and characteristically
different chaotic attractor for
$p = 5.17 > p_c$

a $p = 5.1697$

b $p = 5.1700$
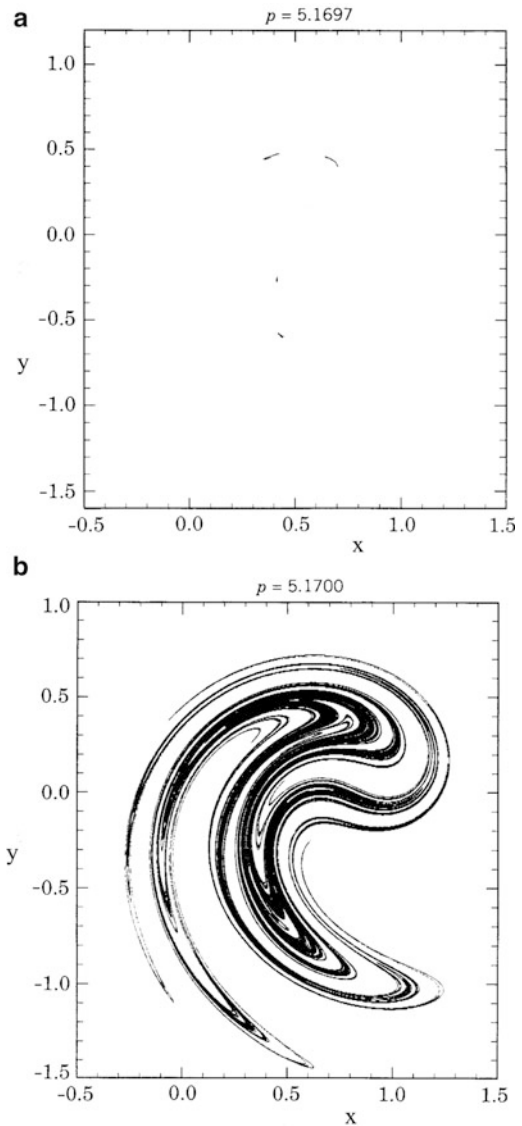
from above). In particular, if the attractor has 2^m pieces, these chaotic bands appear
as separate attractors of the 2^m-fold iterated map that merge pairwise at the crisis
point. Note that the coexistence of a nonattracting set in this case is not necessary
for the crisis, since at least two chaotic components already exist before the crisis
(although in the form of attractors).

Nonattracting chaotic sets can also undergo crises [384, 641, 642]. If two
chaotic saddles merge [423, 451], the new saddle is not only more extended but
also more dense, as characterized by an increased box-counting dimension.

Fig. 3.15 For the same parameter setting as in Fig. 3.14a, the chaotic saddle coexisting with the small four-piece chaotic attractor
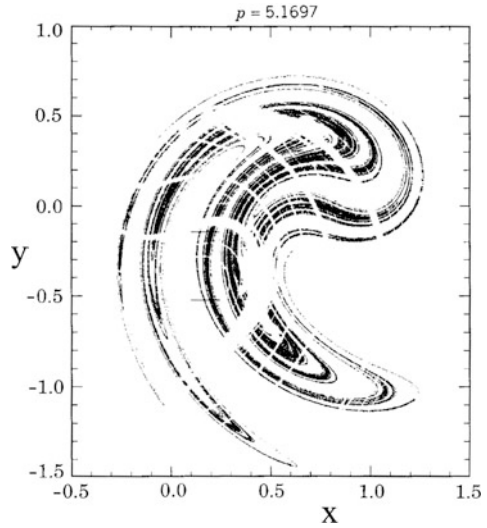
Fig. 3.16 A schematic bifurcation diagram of a nonlinear system with an interior crisis, beyond which the extent of chaos is characteristically increased (*black dots* denote attractor points). The increase can be attributed to transient chaos that exists before the crisis
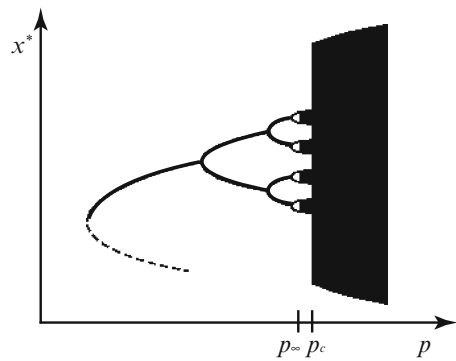
When more than one parameter of the system is changed simultaneously, it is possible to move along a crisis line determined by boundary crises. The chaotic attractor keeps touching its basin boundary along this line, which turns out to be interrupted by many tiny intervals where the attractor is periodic [563]. It may happen, however, that the attractor undergoes an interior crisis so that its size is increased. It can also happen that its basin suddenly increases in extent. In this case, nondifferentiable *breakpoints* occur along the crisis line [255]. Such a point represents a *double crisis* characterized by simultaneous sudden changes in the structure of both the chaotic attractor and its basin boundary.

3.2.2 Periodic Windows

The parameter regions where chaotic attractors exist are generically interspersed with regions of *periodic windows*. The beginning of a periodic window is marked by

a saddle-node bifurcation that generates a pair of stable and unstable periodic orbits. Immediately after the bifurcation point, the stable periodic orbit replaces the original chaotic attractor, which becomes a nonattracting chaotic set and embeds in it, among others, the unstable periodic orbit born at the saddle-node bifurcation. The periodic attractor can go through a cascade of period-doubling bifurcations, resulting in a chaotic attractor typically of small size in the phase space (as compared with the original chaotic attractor). The end of the periodic window is caused by the collision of the small chaotic attractor with the nonattracting chaotic set, mediated by the unstable periodic orbit created at the original saddle-node bifurcation. A periodic window has period m if the stable and the unstable periodic orbits generated by the saddle-node bifurcation have the period m. As examples, a period-3 window from the logistic map is shown in Fig. 3.17a, and a period-7 window from the Hénon map is shown in Fig. 3.17b. For any periodic window, a generic feature is that a nonattracting chaotic set exists *throughout the window*. For example, for the period-3 window in Fig. 3.17a, there is a chaotic repeller, whose natural distribution is shown in Fig. 3.18. Figure 3.19 displays the natural measure of the chaotic saddle in the period-7 window of the Hénon map displayed in Fig. 3.17b.
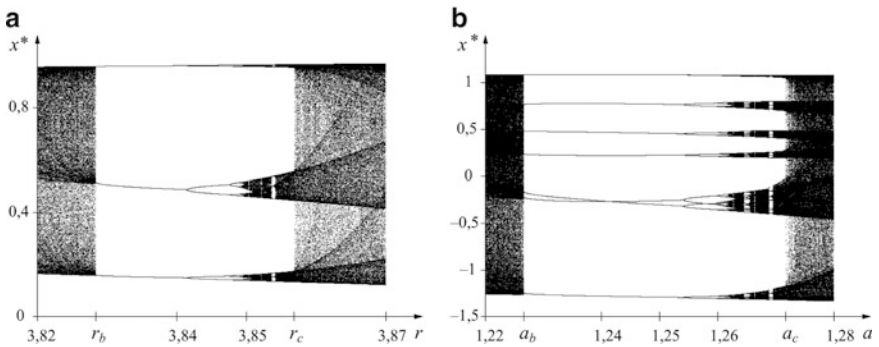
Fig. 3.17 (**a**) Main period-3 window of the logistic map $x_{n+1} = rx_n(1 - x_n)$ in the parameter range $3.828 < r < 3.857$. (**b**) A period-7 window from the Hénon map $x_{n+1} = 1 - ax_n^2 + 0.3y_n$, $y_{n+1} = x_n$ for $1.227 < a < 1.2727$

Fig. 3.18 Chaotic repeller and its natural distribution in the period-3 window of the logistic map coexisting with the period-3 attractor (denoted by *large dots*) for $r = 3.832$
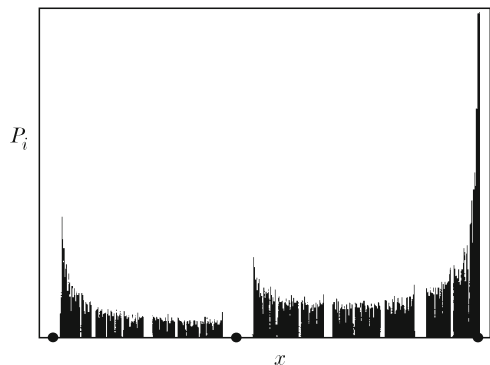
Fig. 3.19 Chaotic saddle and
its natural distribution in the
period-7 window of the
Hénon map in Fig. 3.17b,
which coexists with a
period-7 attractor (indicated
by *large dots*). The
parameters are $b = 0.3$ and
$a = 1.25$ (Picture by M. Gruiz
and Sz. Hadobás)
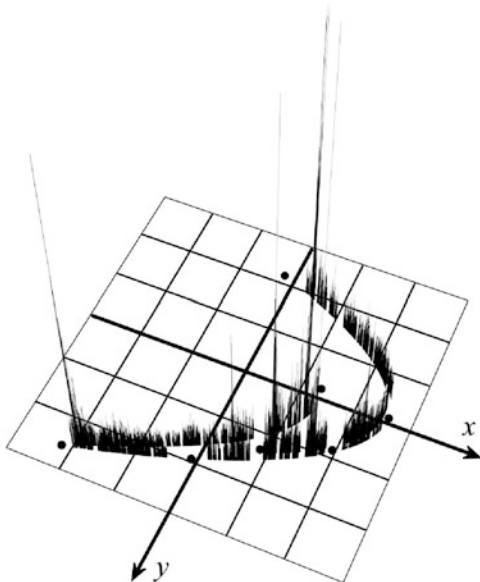
It can then be said that periodic windows are parameter regions where transient
chaos occurs. The presence of nonattracting sets in the windows can be understood
by observing that the infinite number of unstable periodic orbits born earlier, for ex-
ample via various period-doubling cascades, cannot simply disappear. Most of these
orbits are embedded in the nonattracting chaotic set [106]. In fact, if a nonattracting
set exists for some parameter value in the window, it must be present for all other
parameter values, since the set is generally hyperbolic and hence robust against pa-
rameter changes. As a result, the topological entropy K_0 of the system within an
entire periodic window is approximately constant. Although the small chaotic at-
tractor has embedded within itself infinitely many periodic orbits, they represent
only a negligible fraction of all periodic orbits present in the window. As a result,
the topological entropy of the small chaotic attractor is usually much smaller than
that of the coexisting nonattracting chaotic set. For the period-3 window of the lo-
gistic map, for example, the topological entropy of the attractor is $K_0 \leq \ln(2)/3$,
while that of the repeller is $K_0 = \ln\left[\left(1 + \sqrt{5}\right)/2\right]$.

For further analysis of transient chaos in periodic windows, we summarize in
Fig. 3.20 the genesis of a period-m window. The saddle-node bifurcation occurs at
parameter value p_b. The basin of the periodic attractor is bounded by the stable
manifold of the accompanying unstable period-m orbit. (In one-dimensional maps,
the unstable orbit and its first preimage bound the basin of attraction.) The unstable
period-m orbit is in fact the *mediating* orbit (denoted by M) of the interior crisis that
destroys the window at the end (at $p = p_c$). As the parameter changes, the period-m
attractor undergoes period-doubling bifurcations and evolves into a small chaotic
attractor that contains $m \cdot 2^n$ pieces. The chaotic attractor gradually grows within
its basin, characterized by a gradual decrease in n toward unity. The small chaotic
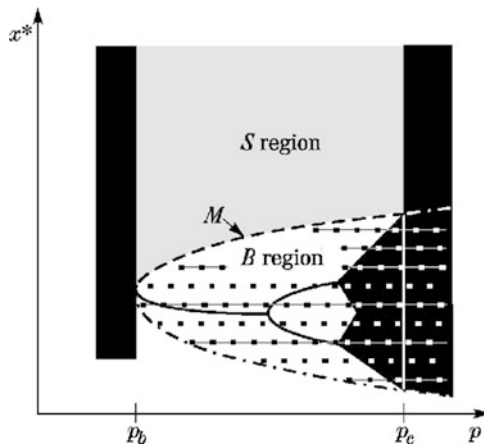
Fig. 3.20 Genesis of a period-m window, where the bifurcation diagram of one component of the period-m attractor is shown. The *dotted region* represents the band region B bounded by the basin boundary of the m-piece attractor. The unstable period-m orbit, the mediating orbit M, is on the basin boundary. For $p = p_b$, a large chaotic attractor loses its stability due to a saddle-node bifurcation, and is converted into a nonattracting chaotic set that exists for $p_b < p < p_b$ in the surrounding region S

attractor thus consists of m pieces, and collides with the chaotic saddle at the interior crisis value p_c. Since the basin of attraction of this attractor consists of m pieces in the phase space (or m bands in the bifurcation diagram), it is convenient to refer to the basin of attraction as the *band region* (B). The complement of it can be called the *surrounding region* (S). As p passes through the critical value p_c, a larger attractor emerges: the small chaotic attractor in region B collides with the extended chaotic saddle in S, as mediated by the orbit M on the boundary between the B and S regions. An example from the Hénon map illustrating the two types of invariant sets in the phase space immediately before and after p_c is shown in Fig. 3.21.

Since transient chaos exists in all periodic windows, it can be said that chaos *exists on continuous parameter intervals*, although chaotic attractors occur on a set of parameters that can be characterized as a fat fractal [234, 564, 773]. In particular, the Lyapunov exponent of the chaotic set, being nonattracting or attracting, is a monotonically increasing function of the parameter beyond the accumulation point of the period-doubling cascade, in contrast to the wild alternation between regions of positive and negative values when it is evaluated, as usual, with respect to the actual attractor. That is, transient chaos is *robust*.

When examining the parameter space of a chaotic system, e.g., the (a, b)-plane of the Hénon map, periodic windows appear to be organized in the following way, as described by Gallas and coworkers: they typically have a shrimp-like structure with sharp boundaries [92, 93, 247, 253, 254, 490]. Every shrimp contains a region of periodicity k, an infinite succession of adjacent layers of periodicity $k \times 2^n$, for $n = 1, 2, 3, \ldots$, of the period-doubling route toward chaos, and the layers containing the small-size chaotic attractors resulting from the period-doubling bifurcations. Most shrimps consist of four main thin and long legs, as can be seen in Fig. 3.22,
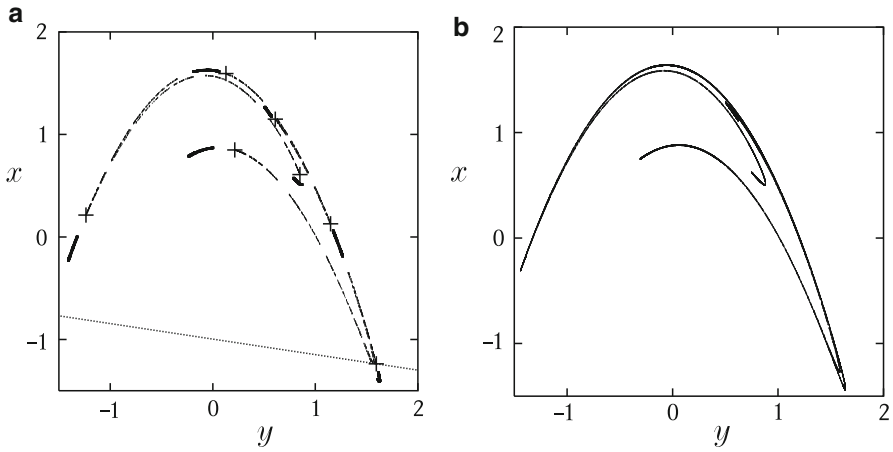
Fig. 3.21 For the Hénon map, at the end of the period-7 window in Fig. 3.17b, (**a**) chaotic saddle (*light dots*) and the coexisting 7-piece chaotic attractor (*heavy dots*) for $a = 1.266 < a_c$. The *dotted line* represents the tangent to the stable manifold of the rightmost point of the mediating period-7 orbit. (**b**) A single-piece, larger chaotic attractor for $a = 1.276 > a_c$ [752] (with kind permission from Elsevier Science)

Fig. 3.22 Parameter plane of the Hénon map for $1.1 < a < 2.4$, $\mid b \mid < 0.4$. The region of bounded/transient chaos appears in *light blue/black*. Within the chaotic region, periodic windows are present in the form of shrimps. The largest one is of period $k = 5$. The boundary between *light blue* and *black* defines the line of boundary crisis, along which breakpoints, mentioned in Sect. 3.2, can be seen. Broad color bands represent regions of the main period-doubling cascade starting from a fixed point (*dark blue*) [253] (Copyright 1993, the American Physical Society)

which leads to a remarkable property: shrimps of all periodicities define a complex connected network of finite volume within the chaotic region of the parameter space in which the attractor is periodic. In fact, there exists a nonattracting chaotic set at any point of this network, further illustrating the ubiquity of transient chaos.

3.3 Crisis-Induced Intermittency

For parameter values slightly beyond the interior-crisis point, a trajectory originated in the band region B about the precrisis attractor (cf. Fig. 3.20) spends a long stretch of time there. It can enter the surrounding region S only when it comes close to the boundary between B and S. Because of the relatively dense structure of the stable manifold of the nonattracting chaotic set in B, the remainder of the precrisis attractor, the trajectory tends to spend relatively short time in S before crossing the boundary back to B, and so on. The dynamical behavior of the trajectory is thus characteristic of intermittency, and this phenomenon is known as *crisis-induced intermittency* [290], where a sequence of trajectory points falling in the surrounding region S is called a *burst*. The dynamical behavior of the bursts is characteristically different from that of motions in the band region B, as shown in Figs. 3.23 and 3.24.

The intermittent switches of trajectories between the band and the surrounding regions can be described more accurately in terms of the mediating orbit. In particular, when a trajectory comes close to the boundary between the two regions, it in fact does so by approaching the mediating orbit M along its stable manifold and leaves
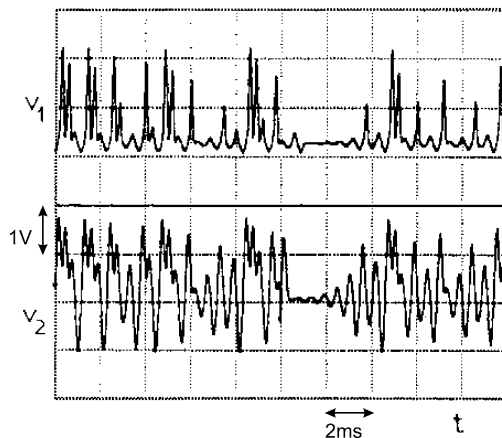
Fig. 3.23 Crisis-induced intermittency in an electronic-circuit experiment by Kyprianidis et al. [432]. The bifurcation parameter is a capacitance in the circuit, denoted by C. For this particular experimental setting, a crisis occurs as C is decreased through the critical value of $C_c = 60$ nF. That is, the precrisis and postcrisis regimes correspond to $C > C_c$ and $C < C_c$, respectively. Shown are two voltage signals in the precrisis region for $C = 60.1$ nF (Copyright 1995, the American Physical Society)

Fig. 3.24 For the same circuit system as in Fig. 3.23, the respective voltage signals in the postcrisis regime for $C = 58$ nF. The signals appear intermittent with bursts, which is characteristic of crisis-induced intermittency [432] (Copyright 1995, the American Physical Society)
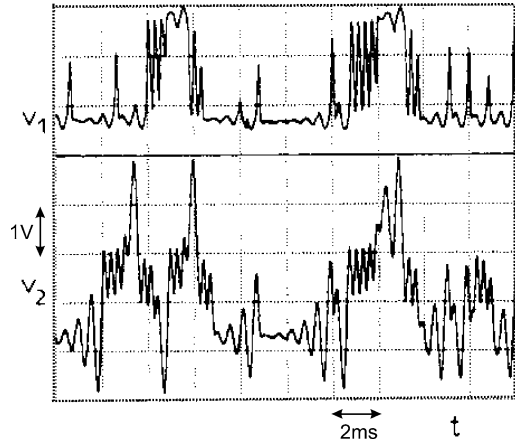
along its unstable manifold. The trajectory's motion in the vicinity of M follows approximately its dynamics. For example, if M is of period m, then the trajectory tends to exhibit a periodic motion of the same period at least temporarily when it is near the boundary. The evolution of a typical trajectory in the postcritical regime thus follows the following scenario:

$$(\text{chaos})_1 \rightarrow \begin{pmatrix} \text{approximately} \\ \text{periodic} \end{pmatrix} \rightarrow (\text{chaos})_2 \rightarrow (\text{chaos})_1 \rightarrow$$

$$\rightarrow \begin{pmatrix} \text{approximately} \\ \text{periodic} \end{pmatrix} \rightarrow (\text{chaos})_2 \rightarrow (\text{chaos})_1 \rightarrow \cdots \quad (3.14)$$

Note that for conventional intermittency in nonlinear dynamical systems [612], there is only one chaotic phase and a trajectory tends to spend long stretches of time in some regular phase. For crisis-induced intermittency, however, both phases are chaotic with typically different positive Lyapunov exponents.

A basic experimentally accessible quantity characterizing crisis-induced intermittency is the average time τ between successive bursts. At the crisis value, there is no burst, so τ is infinite. Beyond crisis, bursts become more frequent so that τ decreases. Of particular interest is then how τ scales with the parameter difference $p - p_c$. For $p > p_c$, the precrisis attractor is no longer an invariant set, but in the band region, where it is originally situated, there is a nonattracting set. Associated with this nonattracting set is an escaping problem similar to that with, for example, a boundary crisis. We thus expect the escape-rate scaling (3.2) to hold. Since τ is proportional to the reciprocal of the escape rate, we have [290]

$$\tau(p) \sim (p - p_c)^{-\gamma}, \quad p \gtrsim p_c, \quad (3.15)$$

where γ is the critical exponent that is determined by the local Lyapunov exponents of the periodic orbit mediating the crisis (see Sect. 3.1.2). The scaling law (3.15)

is quite general: it applies not only to interior crises, but also to band-merging crises where the chaotic attractors before the crisis are replaced by nonattracting chaotic sets in their respective band regions after the crisis. The validity of (3.15) has been established extensively both numerically [713] and experimentally [154, 196, 646, 675].

To better understand the basic dynamical components associated with crisis-induced intermittency, we reexamine a periodic window, say of period m. Before the crisis (in the window), there is an attractor in the m-piece band region B and a nonattracting chaotic set located in the surrounding region S, as exemplified by Fig. 3.20, which are dynamically separated. That is, every periodic orbit is restricted exclusively either to the B or to the S region. After the crisis ($p > p_c$), there is a single chaotic attractor containing nonattracting sets in both regions. It is thus intuitively reasonable to regard the chaotic attractor as consisting of two *basic components*, the nonattracting chaotic sets in the B and in the S regions, respectively, which are separated by the stable manifold of the mediating orbit M. The dynamical behaviors of trajectories associated with them are distinct in terms of the escape rates, the Lyapunov exponents, and the fractal dimensions. In fact, slightly beyond the crisis, the dynamical invariant properties of the basic components are similar to those of their respective sets before the crisis. The basic components provide a backbone for the postcrisis attractor, both geometrically and dynamically. In this picture, the average time τ between bursts in (3.15) is nothing but the average lifetime of chaotic transients on the basic component in the B region.

Beyond the crisis, there is a single chaotic attractor, so the basic components are dynamically coupled. This is accomplished via heteroclinic connections, which contribute a third, *coupling component* to the dynamics. This component contains an infinite number of new unstable periodic orbits that do not exist before the crisis, which are originated from a single periodic orbit at the crisis: the mediating orbit. The dynamics associated with the coupling component can be seen through long-time observations when a typical trajectory has visited both components for certain numbers of times. As we will see below from examples of both one-dimensional and two-dimensional maps, it is orbits in this component which *fill in* the gaps along the unstable foliation of the nonattracting set before the crisis.

3.3.1 Example of Basic Components: One-Dimensional Map

Consider the main period-3 window of the logistic map close to its end. As shown in Fig. 3.25, the dynamics restricted to the three bands $B_1 \equiv (x_A, x_a)$, $B_2 \equiv (x_b, x_B)$, and $B_3 \equiv (x_C, x_c)$ have the following properties: B_2 is mapped onto B_3, B_3 onto B_1, and B_1 *into* B_2. The last property follows because the image of the maximum point of the parabola, $f(1/2) = r/4$, is less than x_B. The three intervals thus constitute the basins of attraction, each containing a piece of the chaotic attractor. The boundary consists of points of the unstable period-3 orbit x_a, x_b, and x_c, and their respective preimages, denoted by x_A, x_C, and x_B, as shown in Fig. 3.25.

Fig. 3.25 Dynamical
structure of the main period-3
window of the logistic map.
The mediating period-3 orbit
(x_a, x_b, x_c) and the points x_A,
x_C, and x_B determine the
endpoints of the B and S
regions. The *arrows* indicate
how they map into each other.
The *broken line* shows the
mapping of the maximum
point under forward
dynamics: either into B_2
($r < r_c$), exactly on x_B
($r = r_c$), or outside B_2 ($r > r_c$)
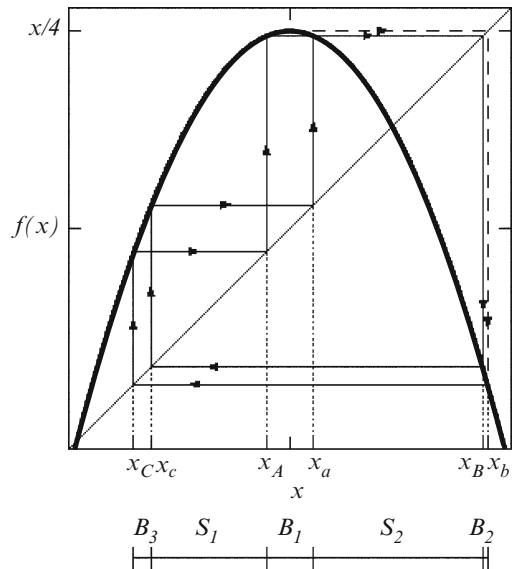
Focus now on the mapping on the surrounding region S, the two intervals between the three bands of the B region. Interval $S_1 \equiv [x_c, x_A]$ is mapped into interval $S_2 \equiv [x_a, x_b]$, but S_2 is mapped onto $[x_c, x_b] = S_1 \cup B_1 \cup S_2$. The map restricted to $S \equiv S_1 \cup S_2$ is thus *not closed* dynamically: a typical trajectory started from S leaves this region when it is mapped into B_1. There is, however, a chaotic repeller in S, as shown in Fig. 3.18. The period-3 points x_a, x_b, and x_c and the boundary points of B belong also to the repeller. For $r < r_c$ there are then two chaotic sets in the phase space that are dynamically disconnected: the three-piece attractor in B and the repeller in S. For the crisis value $r = r_c$, the maximum point is mapped to x_B. As a result, the three-piece chaotic attractor covers the whole basin of attraction (B_1, B_2, and B_3). The attractor in fact touches the repeller in S at the boundary points, making the mediating unstable period-3 orbit M shared by both the three-piece attractor and the repeller. The existence of M as a periodic orbit common to both the chaotic attractor and the chaotic repeller is a key ingredient of interior crises.

For parameter values beyond crisis, i.e., for $r/4 > x_B$, the maximum point is mapped *outside* B_2, as shown in Fig. 3.25. In this case, the map restricted to region B is no longer closed. The enlarged chaotic attractor now extends to the whole interval $I \equiv [f(r/4), r/4]$. However, the regions B and S remain well defined due to the existence of the period-3 orbits. There are orbits that never leave the region S and form a chaotic repeller. Analogously, it is also possible to construct the set consisting of orbits that never escape from the B region. There is in fact an independent chaotic repeller in B. The repeller in S resembles geometrically that before the crisis: it has wide gaps and a relatively small fractal dimension. However, the gaps of the repeller in B gradually appear: their width is proportional to $(r - r_c)^{1/2}$, so the fractal dimension of this set is close to unity for r slightly larger than r_c. In a small

parameter interval beyond the crisis, the mediating period-3 orbit $\{x_a, x_b, x_c\}$, originally on the boundary between B and S, still belongs to both basic components. In this range the topological entropies of the basic components are $K_0^{[B]} = \ln(2)/3$ and $K_0^{[S]} = \ln[(1 + \sqrt{5})/2]$. The constant entropy values are indications of the structural stability of the chaotic repellers.

3.3.2 Example of Basic Components: Two-Dimensional Map

Consider a period-7 window of the Hénon map, where the basin of attraction of the seven-piece attractor is bounded by the seven branches of the stable manifold of a mediating period-7 orbit located at the edge of the chaotic saddle, as shown in Fig. 3.21a. The distances between the attractor and the mediating-orbit points decrease gradually as the bifurcation parameter (say a) is increased toward the crisis value a_c, and they vanish for $a = a_c$. Beyond the crisis, the stable manifold of the mediating period-7 orbit can be used to define the continuations of the band and surrounding regions (see Fig. 3.20). The remnant of the seven-piece attractor and the continuation of the precritical saddle become the two basic components after the crisis, as shown in Fig. 3.26. For $a > a_c$, the chaotic attractor is structurally made up of two chaotic saddles, one within the continuation of the band region B, the *band chaotic saddle* (BCS), and another within the continuation of the surrounding region S, the *surrounding chaotic saddle* (SCS). Note that the shape of the SCS is similar to that of the chaotic saddle in the precrisis region (Fig. 3.21).

Typically, the precrisis attractor is smaller in size and less chaotic than the coexisting nonattracting set as measured by the Lyapunov exponents. Since their continuations beyond crisis constitute the basic components of the postcrisis chaotic attractor, we expect the same features to hold. In particular, the positive Lyapunov

Fig. 3.26 Basic components of the Hénon map at the same parameter values as in Fig. 3.21b. The band chaotic saddle (BCS) (*heavy dots*) is formed by points that never escape the seven bands of the B region under either the forward or the backward dynamics. The surrounding chaotic saddle (SCS) in the S region (*light dots*) is the invariant subset restricted to the surrounding region S. The *dotted line* is the tangent to the stable manifold of the rightmost period-7 point
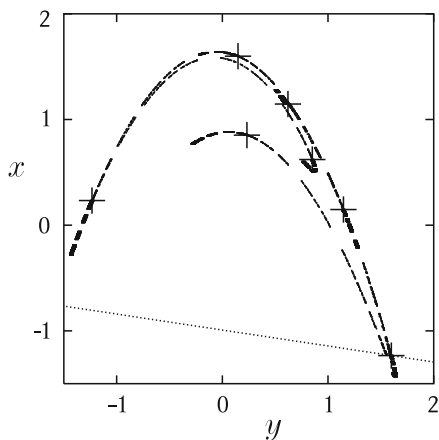
exponent and the topological entropy of the S-component tend to dominate those of the postcrisis attractor, respectively. (For an experimental example, see Fig. 1.16.) This can also be seen from the distribution of the local Lyapunov exponents.[3] In particular, each basic component possesses its own distribution of local Lyapunov exponents, but the distribution associated with the S-component has a larger maximum and its center is farther away from zero. Slightly beyond crisis, for short time scales the distribution of the local Lyapunov exponent of the attractor is approximately the sum of the distributions from the two basic components. With respect to the chaotic attractor, its Lyapunov distribution thus suddenly widens at crisis [751, 752].

The methodology based on the basic components has proven to be quite useful in the analysis of crisis-related phenomena in a number of different fields [94, 127–130, 526, 636, 637], and is applicable to spatially extended systems, as will be discussed in Sect. 9.4.

3.4   Gap-Filling and Growth of Topological Entropy

Before an interior crisis, there are a chaotic attractor (typically small) and a nonattracting chaotic set. Associated with the latter are gaps of hierarchical sizes in the phase space. After the crisis, a larger chaotic attractor arises, which encloses the continuations of both the attractor and the nonattracting set. As a result, the gaps are "filled." Dynamically, gap-filling is accomplished by the creation of a large number of *new unstable periodic orbits* that are not present before the crisis. These coupling periodic orbits provide the support for the dense filling of the gaps after the crisis. The creation of the coupling orbits thus provides a mechanism for the structural development of chaotic attractors. Quantitatively, this process can be characterized by an increase in the topological entropy K_0 of the chaotic attractor after crisis. A scaling theory based on diagrammatic expansions has been developed to calculate the increase in the topological entropy [749, 750].

To gain insight, we estimate the time $l(p)$ that a trajectory spends in the vicinity of the mediating orbit, M, before spreading over the surrounding region. This can be estimated as the time spent around any hyperbolic point. Assume that a trajectory falls initially to a distance proportional to the parameter difference $\sim (p - p_c)$ (for $p > p_c$) from the stable manifold of M. The distance grows to order unity in $l(p)$ steps: $(p - p_c)e^{\lambda_{1c}^* l} \sim 1$, where λ_{1c}^* is the positive local Lyapunov exponent of the mediating orbit at crisis. We have

$$l(p) \approx -[\ln(p - p_c)]/\lambda_{1c}^*. \tag{3.16}$$

For $p \to p_c$, $l(p)$ diverges, indicating that close to the crisis, trajectories escaping from the band region spend a long time in the vicinity of M, in the course of which the motion is practically indistinguishable from the behavior of the mediating orbit.

---

[3] This distribution can be given in terms of the entropy function $S(E)$ defined in Appendix A.

Thus, *every burst starts with an approximately periodic motion* whose duration l is much longer than the period m of M. Consequently, since every coupling orbit must contain at least one burst, (3.16) also represents an asymptotic scaling relation for the minimum lengths of coupling periodic orbits. As the parameter increases beyond the crisis value, $l(p)$ decreases, indicating the appearance of new, shorter and shorter coupling orbits. The creation of the new coupling orbits leads to an increase in the topological entropy K_0 of the enlarged attractor, determined by the growth rate of the number N_m of points in cycles of length m (see (1.26)).

A difficulty in determining the entropy gain beyond crisis is due to the fact that the new orbits are rather long. A diagrammatic technique has proven to be efficient for this task [749, 750]. In particular, let the diagram

$$\text{(diagram)} \sim e^{K_0 n} =: t^n \tag{3.17}$$

represent the number of unstable periodic orbits of length n in the attractor after the crisis, i.e., N_n itself. Let

$$\text{(diagram)} \sim e^{K_0^{[B]} n} =: b^n \tag{3.18}$$

and

$$\text{(diagram)} \sim e^{K_0^{[S]} n} =: s^n \tag{3.19}$$

denote the number of periodic orbits of length n located *entirely* within the band and the surrounding regions, respectively. These two sets of periodic orbits belong to two nonattracting chaotic sets, both embedded in the enlarged attractor. The respective partial topological entropies $K_0^{[B]}$ and $K_0^{[S]}$ of these chaotic saddles determine the growth rates of the two latter diagrams. The bases b and s in the representations (3.18) and (3.19), respectively, can be regarded as the *propagators* for the corresponding diagrams, in the terminology of diagram calculus [505]. These propagators take into account the contributions to N_n from the periodic orbits in the band and in the surrounding regions. Similarly, t in (3.17) acts as the propagator representing the total number of allowed periodic orbits.

To determine t, we also have to take into account the contribution of the coupling orbits to N_n. In fact, the essence of the gap-filling phenomenon is *the growth in the number of coupling orbits*, comprising of various combinations of the orbits already existing before the crisis. The counting of the total number of orbits of length n, with $0, 1, 2, \ldots$ bursts during their period, can be expressed by the following diagrammatic equation:

$$\text{(diagrammatic equation)} \tag{3.20}$$

The first two terms correspond to the periodic orbits that never escape from the B and S regions, as represented by the diagrams (3.18) and (3.19), while the additional terms correspond to the coupling orbits. The approximately periodic components of the coupling orbits invoking the bursts give only a constant contribution, because they closely follow the same mediating orbit, giving rise to a zero topological entropy. This feature can be incorporated in (3.20) by inserting the dotted "interaction" diagram with the corresponding propagator $k \equiv 1$ at the beginning of each burst. Thus the number of dotted insertions is equal to the number of escapes from a close vicinity of the mediating orbit M during n time steps. Note that before each burst, the trajectory must spend at least one step in the band region, and due to (3.16), at least l steps to go over the mediating orbit. This implies that the lengths n_b and n_l of the double-line and the dotted propagators are at least 1 and l, respectively. The full length of each diagram term is n.
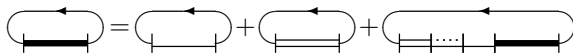
The number of the simplest coupling orbits with exactly one burst, i.e., the third diagram on the right-hand side of (3.20), is given by

$$N_n^{(1)} \approx \sum_{n_b=1}^{n-l} \sum_{n_l=l}^{n-n_b} b^{n_b} \cdot k^{n_l} \cdot s^{n-n_b-n_l} = C \cdot k^l \left[s^{n-l} + Bb^{n-l} + Ak^{n-l} \right] \qquad (3.21)$$

for $n > l \gg 1$. Here the asymptotic coefficients A, B, and C depend on the values of the propagators and reflect the effect of short-range correlations between subsequent orbit segments. Equation (3.21) describes the simplest interaction, or coupling, between the two chaotic saddles in the band and surrounding regions. The number of possible orbit combinations characterizes the strength of the coupling. Equation (3.20) can be viewed as a perturbation series, with (3.21) being its first "loop order" term and the subsequent diagrams accounting for the higher "loop order" terms.

We have seen that before the crisis, the topological entropy of the chaotic set (the small attractor) in the band region is smaller than that of the coexisting nonattracting chaotic set in the surrounding region. This behavior persists after the crisis. Thus, we have for the propagators $t > s > b > k = 1$, which for large n implies $t^n > s^n \gg b^n \gg 1$. In the limit $n \gg l$ the simplest coupling term in (3.21) gives $N_n^{(1)} \approx Cs^{n-l}$. Since this is $C/s^l \ll 1$ times the unperturbed result, s^n, the coupling is weak. This fact guarantees the convergence of the perturbation series (3.20).

Since the union of all long diagrams contains, after the single line propagator, all possible propagator combinations, the entire bold-line propagator (3.20) can be rewritten in the following self-consistent form:

$$\text{(diagram)} = \text{(diagram)} + \text{(diagram)} + \text{(diagram)} \qquad (3.22)$$

By substituting the propagators, we obtain

$$N_n \approx t^n = s^n + b^n + \sum_{n_1=l}^{n} N_{n_1}^{(1)} N_{n-n_1}.$$

With the expression for the first loop order term, (3.21), the solution to the implicit equation for t is, in the scaling region $1 \ll l \ll n \to \infty$ [749],

$$t \approx s \cdot (1 + C t^{-l}). \tag{3.23}$$

By taking the logarithm, close to the crisis, the topological entropy is obtained as

$$K_0 \approx K_0^{[S]} + C \cdot e^{-K_0^{[S]} l}. \tag{3.24}$$

Using the property that at p_c the topological entropy of the enlarged attractor coincides with that of the nonattracting chaotic set in the surrounding region, $K_0^{[S]} = K_0(p_c)$, and combining (3.24) and (3.16), we obtain

$$K_0(p) - K_0(p_c) \sim (p - p_c)^{\chi}, \quad \text{with } \chi = K_0(p_c)/\lambda_{1c}^*. \tag{3.25}$$

This formula gives the parameter-dependence of the increase in the topological entropy after the crisis. The exponent χ is the *gap-filling exponent*, which is simply the ratio of the topological entropy at the crisis to the Lyapunov exponent of the mediating orbit.

Numerical verification for the scaling law (3.25) has been obtained [749, 750] using the example of the period-7 window of the Hénon map. The method of monitoring the growth of the length of an infinitesimal curve, (1.27), is efficient for numerically calculating the topological entropy $K_0(a)$ of the attractor. The data $K_0(a) - K_0(a_c)$ versus $(a - a_c)$ on a logarithmic scale can be fitted roughly by a straight line with slope 1.13. The theoretical value of the exponent χ can be estimated as follows. The positive eigenvalue of the period-7 mediating orbit is $10.87^{1/7}$, corresponding to the Lyapunov exponent $\lambda_{1c}^* = 0.34$. The topological entropy at the crisis can be estimated to be $K_0(a_c) = 0.38$. The scaling exponent from the theory is then expected to be $\chi \approx 0.38/0.34 \approx 1.12$. We see that the numerical and theoretical values of the exponent agree.

Chapter 4
Noise and Transient Chaos

In this chapter, we treat transiently chaotic dynamical systems under the influence of noise, focusing on a number of physical phenomena. Firstly, we will demonstrate that noise can *increase* the lifetime of transient chaos and induce dynamical interactions among different invariant sets of the system. As a result, the stationary distributions of dynamical variables in a noisy system can be much more extended in the phase space than those in the corresponding deterministic system. Secondly, if the system has a nonchaotic (e.g., periodic) attractor but there is transient chaos due to a coexisting nonattracting chaotic set, noise can cause a trajectory to visit both the original attractor and the chaotic saddle, leading to an extended chaotic attractor. This is the phenomenon of *noise-induced chaos*, which can arise, for instance, when the dynamical system is in a periodic window. Of particular interest is how the Lyapunov exponent and other ergodic averages scale with the noise strength. Thirdly, if the system has a chaotic attractor, noise can cause trajectories on the attractor to move out of its basin of attraction so that either the attractor is enlarged or the originally attracting motion becomes transient. This is the phenomenon of *noise-induced crisis*, dynamically due to noise-induced heteroclinic or homoclinic tangencies that cause the attractor to collide with its own basin boundary. An issue of both theoretical and experimental interest is how the average transient lifetime depends on the noise strength.

We will also discuss physical situations in which some parameters of a dynamical system fluctuate randomly with time. Mathematically, such systems can be modeled by *random maps* which, in spite of the random fluctuations, can generate both persistent and transient chaos with underlying chaotic sets of well-defined fractal properties. However, due to the randomness, a single trajectory cannot reveal the fractal patterns. Instead, an ensemble of trajectories is needed. In particular, if the noisy perturbation to each trajectory is identical at any fixed time, the snapshot pattern of all trajectories in the ensemble is typically fractal if the largest Lyapunov exponent of the random system is positive. The details of the fractal pattern change from time to time, but the dimensions remain well defined and time-independent. When a small amount of phase-space inhomogeneity in the noisy perturbation is present, the fractal properties of the snapshot pattern can be observed only for a finite amount of time.

4.1 Effects of Noise on Lifetime of Transient Chaos

4.1.1 General Setting

In experimental situations, an observed trajectory is always subject to some external perturbations, e.g., of thermal or of technical origin. In the lack of any specific information about their own dynamics, other than their time scale being much shorter than that of the original signal, we can assume that the external perturbations are *random*. Their inclusion into the dynamics can be modeled via an additive noise term, which converts the purely deterministic equation of motion into a *stochastic* equation. We are thus interested in the noisy version of the continuous- and discrete-time dynamics, which in dimensionless forms are described by

$$\frac{d\mathbf{x}}{dt} = \mathbf{F}(\mathbf{x}, p) + \sigma \boldsymbol{\xi}(t) \qquad (4.1)$$

and

$$\mathbf{x}_{n+1} = \mathbf{f}(\mathbf{x}_n, p) + \sigma \boldsymbol{\xi}_n, \qquad (4.2)$$

respectively, where the parameter $\sigma > 0$ represents the noise amplitude, and the $\boldsymbol{\xi}$-terms are independent, identically distributed random variables of zero mean and unit variance. The distribution $P(\boldsymbol{\xi})$ is assumed to be known and to be *independent of time*, so that the stochastic process generating the noise is stationary. An example of $P(\boldsymbol{\xi})$ is Gaussian distribution,

$$P(\boldsymbol{\xi}) \sim \exp(-\boldsymbol{\xi}^2/2). \qquad (4.3)$$

This form implies that even for small noise strength σ, the random perturbation can be arbitrarily large, but the probabilities for large perturbations are exponentially small. It is useful to broaden the class of noise by considering distributions of the type

$$P(\boldsymbol{\xi}) \sim \exp(-\boldsymbol{\xi}^r/r), \qquad (4.4)$$

where r is an even integer. The limit $r \to \infty$ is of special importance, since it corresponds to a uniform distribution of $\boldsymbol{\xi}$ in the interval $(-1, 1)$, which is often used in numerical experiments. Unless otherwise stated, we shall assume Gaussian noise ($r = 2$).

Strong noise can suppress most deterministic features of the underlying system. The chaotic characteristics of a deterministic dynamical system can be preserved in the presence of *weak* noise, which is often the case in experimental situations. We shall therefore be interested in the effect of weak random perturbations, i.e., $\sigma \ll 1$. It is a general observation due to Ben-Mizrachi, Procaccia, and Grassberger [49] that a weak noise usually does *not* modify the fractal characteristics of the chaotic dynamics. What noise does is to make the dynamics fuzzy below a certain threshold scale ε_c in the phase space, which increases with the noise strength.

Fig. 4.1 Schematic
illustration of the effective
scaling region, in the presence
of noisy perturbations of two
different strengths σ, of the
number $N(\varepsilon)$ of boxes needed
to cover a fractal invariant set
of dimension D_o with boxes
of size ε in the phase space of
dimension d
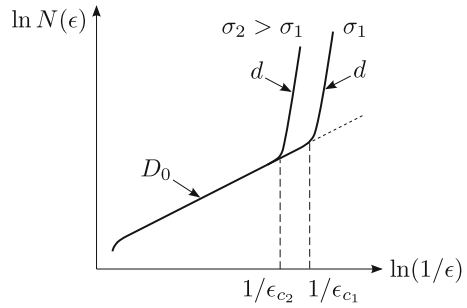
In an ε_c-neighborhood of the deterministic fractal set, trajectories fill the phase
space. The fractal nature of the set can be revealed on distance scales larger than
ε_c in the phase space. The breakdown of the fractal scaling depends on the noise
strength, as shown schematically in Fig. 4.1. The effect of weak noise is thus a re-
duction of the scaling region where a nontrivial fractal dimension can be extracted,
but this in general does not affect the value of the fractal dimension.

In the case of transient chaos, we expect weak noise to affect the escape rate
(Sect. 4.1.2). More generally, noise can have an effect on the probability distribution
on or about the deterministic invariant set (Sect. 4.2). The effect of noise can be
significant for dynamical systems near bifurcations or crises. These issues will be
addressed in the sequel.

4.1.2 Enhancement of Transient Lifetime by Noise

The surprising phenomenon that transient chaos can be stabilized by weak noise in
the sense that the escape rate *decreases* (or the lifetime increases) was first observed
by Franaszek [243] in two-dimensional maps. Here we give a heuristic explanation,
following the argument of Reimann [625–627] based on one-dimensional maps.

Consider first a weak dichotomous noise, i.e., a random signal that can take on
two values, $\pm\sigma_0$, with probability $1/2$ for each. At any time step the dynamics is
governed with probability $1/2$ by either the map $f(x) + \sigma_0$ or the map $f(x) - \sigma_0$.
We assume that σ_0 is small enough that there is escape from both maps, which are
of the type of Fig. 2.1. According to (2.8), we can approximate the escape rate as
the product of the density of the c-measure with the length of the primary escape
interval. Denoting their lengths by L_1 and L_2 for the two maps, we find the overall
escape rate as

$$\kappa = \rho(x_c)\frac{L_1 + L_2}{2}, \tag{4.5}$$

where we have used the fact that the density of the c-measure is smooth, and, being
normalized to unity, does not change significantly due to noise. The quantity $\rho(x_c)$
represents thus the conditionally invariant density of the deterministic map f at its

maximum point x_c. Considering maps of local maxima of order z as in (3.10) and using (3.11), we obtain

$$\kappa(\sigma_0) = \frac{\rho(x_c)}{b^{1/z}} \left[(f(x_c) - 1 + \sigma_0)^{1/z} + (f(x_c) - 1 - \sigma_0)^{1/z} \right]. \qquad (4.6)$$

In the presence of noise, L_1 is larger than and L_2 is smaller than the size of the escape window in the deterministic case. Their average is different from the deterministic size unless the mapping function f is piecewise linear. For $z \neq 1$, the decrease in L_2 exceeds the increase in L_1 for $z > 1$. The escape rate is then smaller than that for the deterministic case. This is the basic mechanism leading to an enhancement of the average lifetime of transient chaos by noise.

For a general noisy perturbation characterized by probability density $P(\xi)$, the map is shifted by $\sigma\xi$ for any noise realization ξ. Using the same approximation, we obtain

$$\kappa(\sigma) = 2\rho(x_c) \left(\frac{f(x_c) - 1}{b} \right)^{1/z} \int_{-\infty}^{\infty} \left(1 + \frac{\sigma\xi}{f(x_c) - 1} \right)^{1/z} P(\xi)\mathrm{d}\xi, \qquad (4.7)$$

where we have assumed that the probability for having $f(x_c) + \sigma\xi - 1 < 0$, which does not generate escape, is negligible. For weak noise, a Taylor expansion up to second order in ξ yields

$$\kappa(\sigma) = \kappa(0) \left(1 + \frac{1}{2z} \left(\frac{1}{z} - 1 \right) \frac{\sigma^2}{(f(x_c) - 1)^2} \right), \qquad (4.8)$$

where we have used the fact that the second moment of ξ is unity and $\kappa(0)$ denotes the deterministic result (2.8). Equation (4.8) shows that the correction is negative for $z > 1$. Thus, for maps with local maxima of order larger than unity, an increase in the transient's lifetime is expected due to weak noise, but the opposite is true for maps with a cusp, where $z < 1$.

These heuristic arguments are based on the behavior observed about the map's maximum. Noise can drive trajectories out of the unit interval through its edges, or can push back trajectories that have already left the interval. By taking into account all these effects, Reimann [627] showed that the phenomenon as suggested by the qualitative arguments holds for one-dimensional maps. For two- or higher-dimensional maps, a rigorous argument is not available. However, for the generic situation of $z = 2$, the turns of the unstable manifold are locally quadratic. In this case, stabilization of transient chaos by weak noise is expected to be typical [20].[1] These considerations imply only that the lifetime can increase with the noise strength. In fact, for stronger noise, a decrease in the lifetime can take place [20, 243, 244, 625]. There can then be an optimal noise strength for which the escape rate is minimized (or the average transient lifetime is maximized), as shown

---

[1] Although in some experiments [70] and in time-delayed systems [850] no apparent effect of noise on transient chaos has been found.

Fig. 4.2 General dependence of escape rate on noise strength
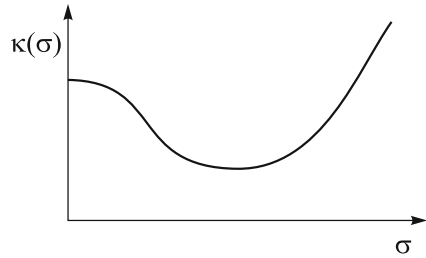
schematically in Fig. 4.2. For the determination of $\kappa(\sigma)$, perturbative methods are also available [150, 182, 230].

4.2 Quasipotentials

The concept of quasipotentials provides a theoretical paradigm to address the effect of noise on nonlinear dynamical systems. We shall introduce the concept and focus on its applications to transient chaos.

4.2.1 Basic Notions

For a nonlinear dynamical system under noise, it is often desirable to know the probability distribution over the entire phase space. A normalizable distribution can exist only if there are attractors in the system. Based on a well-established theory in the weak-noise limit [246, 279, 282], we summarize the results for maps of the type of (4.2). The steady-state probability distribution $W(\mathbf{x})$ can be written for Gaussian noise with $\sigma \ll 1$ as[2]

$$W(\mathbf{x}) \sim Z(\mathbf{x})e^{-\Phi(\mathbf{x})/\sigma^2}. \tag{4.9}$$

The proportionality factor not written out is a normalization constant depending only on σ. The exponential factor is of special importance, since it is similar to the form describing fluctuations in thermal equilibrium. The function Φ plays a central role in the theory: it is the analogy of the free energy. The noise intensity σ^2 plays the role of temperature $k_{\mathrm{B}}T$. A difference from equilibrium thermodynamics is that here, an explicit form of Φ cannot be obtained from the first principles; Φ is therefore called the *quasipotential* (or nonequilibrium potential) of the map. An example of the quasipotential is shown in Fig. 4.3. Note that neither Φ nor the prefactor Z depends on the noise strength; each depends solely on the underlying deterministic dynamics.

---

[2] For noise of order r, $W(\mathbf{x}) \sim Z(\mathbf{x})e^{-\Phi(\mathbf{x})/\sigma^r}$.

Fig. 4.3 Schematic diagram
of the quasipotential for a
one-dimensional map that has
two coexisting fixed-point
attractors and a chaotic
repeller. The activation
energy $\Delta\Phi$ in the valley of
the left fixed point is marked
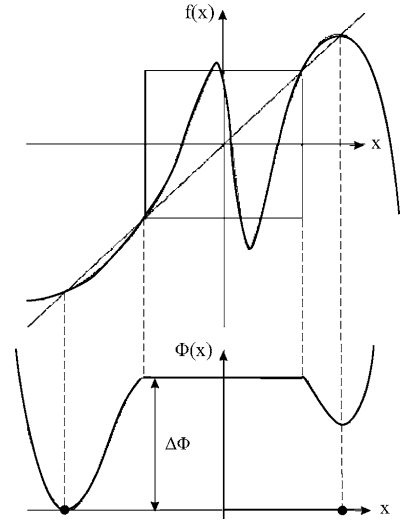
The quasipotential satisfies an extremum principle and can be constructed based
on methods from Hamiltonian mechanics [281, 285, 311, 629]. The basic observation
is that the system can come to a phase-space point $\mathbf{x}$ via a large number of noise
realizations. Since, however, noise is weak, there are realizations that are sharply
peaked about a single optimal realization, namely, the most probable path that leads
to $\mathbf{x}$. In N iterations, the optimal path for noise should *maximize* the probability

$$P(\boldsymbol{\xi}_0)P(\boldsymbol{\xi}_1)\cdots P(\boldsymbol{\xi}_N) \sim \exp\left(-\sum_{n=0}^{N}\frac{\boldsymbol{\xi}_n^2}{2}\right) \sim \exp\left(-\sum_{n=0}^{N}\frac{(\sigma\boldsymbol{\xi}_n)^2}{2\sigma^2}\right). \qquad (4.10)$$

Equivalently, the path corresponds to the *minimum* of the "noise energy"
$\sum_{n=0}^{N}(\sigma\boldsymbol{\xi}_n)^2/2$. The iteration process (4.2) plays the role of a constraint that can be
taken into account by means of Lagrangian multipliers $\boldsymbol{\eta}_n$ that are effectively con-
trol variables. The task of finding the optimal path thus boils down to minimizing
the following "Lagrangian":

$$L(\boldsymbol{\xi}, \mathbf{x}) = \sum_{n=0}^{N}\left(\frac{1}{2}(\sigma\boldsymbol{\xi}_n)^2 + \boldsymbol{\eta}_{n+1}[\mathbf{x}_{n+1} - \mathbf{f}(\mathbf{x}_n, p) - \sigma\boldsymbol{\xi}_n]\right). \qquad (4.11)$$

In the presence of the multipliers, the variables $\boldsymbol{\xi}_n$ and $\mathbf{x}_n$ can be regarded as inde-
pendent. Setting the partial derivatives of L equal to zero yields, in view of (4.2), the
following coupled map between $\boldsymbol{\eta}_n$ and $\mathbf{x}_n$ for the optimal path[3]

---

[3] For noise of order r, the first equation should be replaced by $\mathbf{x}_{n+1} = \mathbf{f}(\mathbf{x}_n, p) + \boldsymbol{\eta}_{n+1}^{1/(r-1)}$, for r
even.

$$\mathbf{x}_{n+1} = \mathbf{f}(\mathbf{x}_n, p) + \boldsymbol{\eta}_n, \quad \boldsymbol{\eta}_{n+1} = \mathbf{J}(\mathbf{x}_{n+1}, p)^{-1}\boldsymbol{\eta}_n, \tag{4.12}$$

where $\mathbf{J}$ denotes the transpose of the derivative matrix of map $\mathbf{f}$. A comparison with (4.2) shows that $\boldsymbol{\eta}_{n+1}/\sigma$ is nothing but the optimizing noise process. Another feature is that the map (4.12) is area-preserving, even if $\mathbf{f}$ is dissipative. It can therefore be regarded as a kind of Hamiltonian extension of the deterministic dynamics $\mathbf{x}_{n+1} = \mathbf{f}(\mathbf{x}_n, p)$ through the control variable $\boldsymbol{\eta}_n$.

From (4.10), the probability for a trajectory to be at point $\mathbf{x} = \mathbf{x}_{N+1}$ after the Nth iteration is

$$P(\boldsymbol{\xi}_0)P(\boldsymbol{\xi}_1)\cdots P(\boldsymbol{\xi}_N) \sim \exp\left(-\frac{1}{\sigma^2}\sum_{n=0}^{N}\frac{1}{2}[\mathbf{x}_{n+1} - \mathbf{f}(\mathbf{x}_n, p)]^2\right). \tag{4.13}$$

In order to find a time-independent distribution of $\mathbf{x}$, we take the limit $N \to \infty$. The quasipotential defined by (4.9) becomes

$$\Phi(\mathbf{x}) = \min\sum_{n=0}^{\infty}\frac{1}{2}[\mathbf{x}_{n+1} - \mathbf{f}(\mathbf{x}_n, p)]^2|_{|\mathbf{x}_\infty \equiv \mathbf{x}} + \text{constant}, \tag{4.14}$$

where the minimum is taken with respect to the value of the control variable at the initial and end points.[4] The quasipotential must be independent of the initial conditions $\mathbf{x}_0, \boldsymbol{\eta}_0$ within the basin of attraction of an attractor A. This can be realized by letting (4.12) evolve according to the deterministic dynamics ($\boldsymbol{\eta}_n = 0, n = 0, 1, \cdots$) until the attractor is reached. This initial evolution does not contribute to Φ, and hence for all practical purposes, the initial conditions can be taken to be $\mathbf{x}_0 \in A$, and $\boldsymbol{\eta}_n \to 0$ for $n \to 0$. The minimization process taken with respect to $\boldsymbol{\eta}_\infty$ remains to be carried out.

Since the probabilities of visiting different regions of an attractor cannot differ exponentially, the quasipotential is *constant* on the attractor. For a chaotic attractor, the quasipotential is constant on the entire fractal set. The differences in the probabilities of visiting different regions of the attractor are characterized by the prefactor $Z(\mathbf{x})$ of (4.9). Since it is σ-independent, the prefactor evaluated on the attractor must coincide with the density ρ associated with the natural measure. The role of noise becomes thus important outside the attractor where the essential contribution to the dynamics is characterized by $\exp(-\Phi/\sigma^2)$. In particular, the quasipotential increases with the distance from the attractor, and the "Boltzmann factor" $\exp(-\Phi(\mathbf{x})/\sigma^2)$ yields the probability that noise pushes a trajectory point to $\mathbf{x}$, away from the attractor. In the case of a fractal chaotic attractor, the Boltzmann factor yields the probability for a trajectory to fall between two branches of the chaotic attractor (which is the closure of unstable manifolds) as a result of noise.

It should be emphasized that both the map in (4.12) and the quasipotential given by (4.14) are independent of σ. They characterize the *deterministic* dynamics.

---

[4] For noise of order r, $\Phi(\mathbf{x}) = \min\sum_{n=0}^{\infty}\frac{1}{r}(\mathbf{x}_{n+1} - \mathbf{f}(\mathbf{x}_n, p))^r|_{|\mathbf{x}_\infty \equiv \mathbf{x}} + \text{constant}$.

4.2.2 Quasipotential Plateaus Associated with Nonattracting Chaotic Sets

Analogous to the situation of attractors, quasipotentials *are constant* on chaotic repellers. For example, in a one-dimensional map, the potential is constant on the shortest intervals containing the repeller, as shown in Figs. 4.3 and 4.4. In addition, the prefactor $Z(x)$ is proportional to the density $\rho(x)$ of the c-measure.

For a two-dimensional noninvertible map, the quasipotential is constant over a two-dimensional region surrounding the repeller. The existence of such quasipotential plateaus is especially apparent in the case of Julia-type sets of the iterations of the complex plane, as shown in Fig. 4.5, where the repeller is generated in the process of finding the roots of the cubic equation $z^3 - 1 = 0$ by Newton's method. In particular, the attractors are the three roots $z_i = \exp{(i2\pi/3)}$ $(i = 0, 1, 2)$. Their common basin boundaries form a Julia-set type repeller. The potential plateau extends up to those points of the chaotic repeller that fall closest to the roots z_i.

The situation is somewhat different for chaotic saddles arising from invertible two-dimensional maps. For such a case, noise is more likely to push trajectories along than across the unstable manifold. In this case, a quasipotential plateau extends *along the unstable manifold* of the saddle only, and the prefactor Z coincides with the density ρ of the c-measure on the unstable manifold. In between branches of the unstable manifold, the potential assumes larger values. As a result, Φ changes in the stable direction outside the saddle but remains constant along the unstable direction. An example is shown in Fig. 4.6 for a map whose deterministic version will be treated in the context of basin boundaries in Chap. 5.
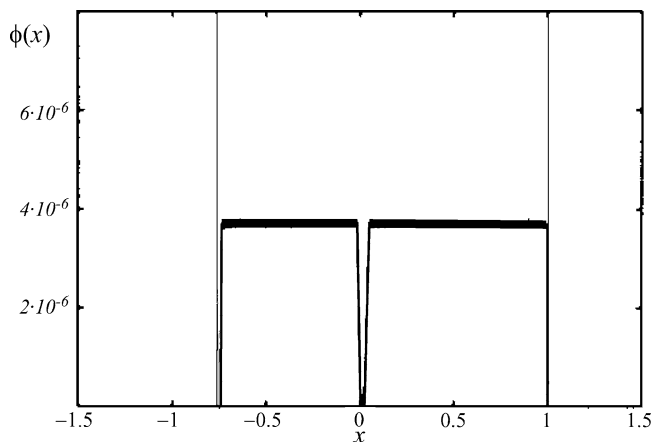
Fig. 4.4 Numerically computed quasipotential $\Phi(x)$ for the logistic map in the main period-3 window: $f(x) = 1 - ax^2$, $a = 1.752$. A chaotic repeller coexists with a period-three attractor (cf. Fig. 3.17, where $r = \sqrt{1 + 4a} + 1 = 3.83$). The potential is chosen to be zero on the period-three attractor. A plateau in the potential occurs on the intervals containing the chaotic repeller [312] (with kind permission from Elsevier Science)
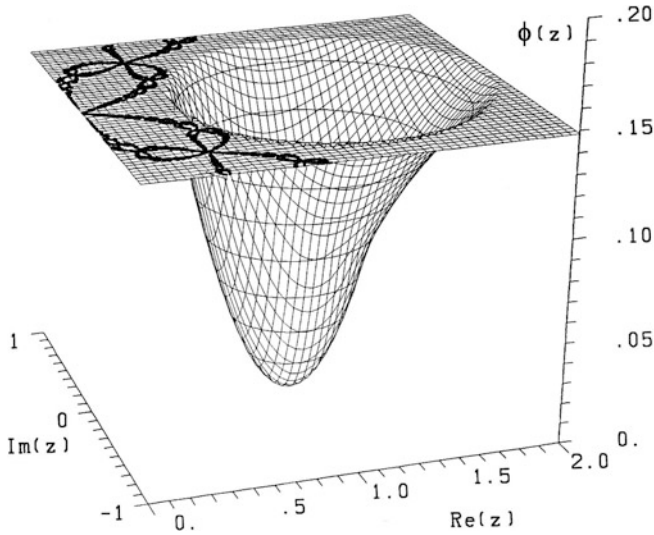
Fig. 4.5 Numerically computed quasipotential $\Phi(z)$ arising from the complex iteration $z_{n+1} = z_n - (z_n^3 - 1)/(3z_n^2)$. The attractors are $z_1 = 1$ and $z_i = \exp(i2\pi/3)$ $(i = 1, 2)$. In the common fractal boundaries among the basins of the attractors lies the chaotic repeller, the Julia set, on which the quasipotential is constant. Only the potential about the valley of root $z = 1$ is shown [280] (with kind permission from World Scientific Publishing Co.)
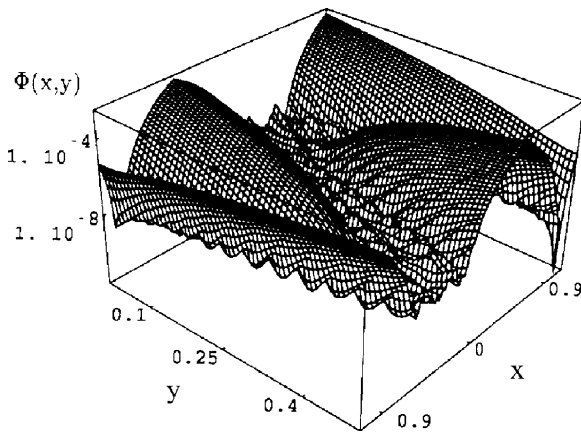
Fig. 4.6 Quasipotential for the map $\theta_{n+1} = \theta_n + 1.32\sin 2\theta_n - 0.9\sin 4\theta_n - x_n\sin\theta_n + \sigma\xi_n^{(1)}$, $x_{n+1} = -0.9\cos\theta_n + \sigma\xi_n^{(2)}$, where $y \equiv \theta/(2\pi)$ and $\xi_n^{(i)}$ are random Gaussian variables. The system has two coexisting attracting fixed points at $(x, y) = (-0.9, 0)$ and $(0.9, 0.5)$, respectively, which are separated by a chaotic saddle whose unstable manifold consists of S-shaped curves, foliations of which are approximately orthogonal to those of the basin boundary, shown in Fig. 4.10a. Observe the quasipotential plateau along the unstable manifold [312]. The plateau's length follows from the minimum requirement of (4.14) (with kind permission from Elsevier Science)

4.2.3   Exit Rates from Attractor and Most Probable Exit Paths

The quasipotential, besides being the leading contribution to the stationary distribution, governs the transient dynamics from the basin of an attractor [44, 285, 401, 402, 423–426, 628, 630, 645] when an exit exists that allows for trajectories to leave the basin. Under noise, the probability $P(n)$ that a trajectory of the system stays within the basin of attraction of an attractor for n steps decays exponentially with n:

$$P(n) \sim \exp(-kn), \tag{4.15}$$

where k is the *exit rate from the attractor* (not to be confused with the escape rate κ for nonattracting chaotic sets). This rate k can be expressed as the integral of the probability current through the basin boundary. Since this current is proportional to the probability W itself, the exit rate is given, in leading order, by the integral of $\exp[-\Phi(\mathbf{r})/(\sigma^2)]$ over the boundary. For $\sigma \to 0$, the main contribution to the integral comes from the point $\mathbf{x}_e$ for which the quasipotential is minimal on the boundary. This exit point is a repeller or a saddle (hyperbolic) point for smooth boundaries.[5] We thus have[6]

$$k \sim e^{-\Delta\Phi/\sigma^2}, \tag{4.16}$$

where

$$\Delta\Phi \equiv \Phi(\mathbf{x}_e) - \Phi(A) \tag{4.17}$$

is the difference between the minimum of the potential along the boundary and its value on the attractor.[7] The mean first exit time, t_e, is then proportional to the reciprocal of the exit rate

$$t_e = \tau_0 e^{\Delta\Phi/\sigma^2}, \tag{4.18}$$

which resembles the Arrhenius factor, or Kramers's relation [314] that characterizes the escape from a potential well in the presence of thermal noise. This indicates that $\Delta\Phi$ can be regarded as a kind of activation energy, and is a basic global measure of the stability of the attractor.

Relations (4.16) and (4.17) imply that the escape process is dominated in the weak noise limit by a *single* noisy trajectory, the *most probable exit path*. This is a solution of the optimal path map (4.12) with initial and final conditions

$$\mathbf{x}_0 \in A, \quad \mathbf{x}_\infty = \mathbf{x}_e, \quad \boldsymbol{\eta}_{0,\infty} \to 0, \tag{4.19}$$

where the constraint that the control variable vanishes in the long-time limit comes from the minimum condition given by (4.14). The optimal escape path from an

---

[5] In the case of fractal basin boundaries, the exit point is a point of the nonattracting chaotic set belonging to the fractal boundary.

[6] For noise of order r, $k \sim e^{-\Delta\Phi/\sigma^r}$.

[7] For fractal boundaries the exit point $\mathbf{x}_e$ is on the quasipotential plateau, and hence $\Delta\Phi$ is the difference between its values on the plateau and on the attractor.
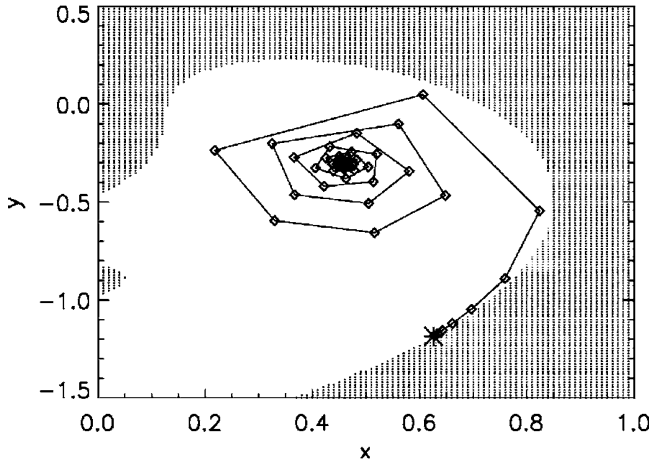
Fig. 4.7 Most probable exit path for the Ikeda map (3.13) for parameters $A = 0.85$, $B = 0.9$, $k = 0.4$, and $p = 3$. The basin of one of the fixed-point attractors is denoted by the blank region, while that of another fixed-point attractor (lying outside the frame) is shown in *gray*. Exit takes place over the hyperbolic point $\mathbf{x}_e$, denoted by an *asterisk*, on a smooth boundary (the stable manifold of $\mathbf{x}_e$). Points on the exit path are connected with *lines* to guide the eye. This path spirals out of the attractor and approaches asymptotically the hyperbolic point. The activation energy is $\Delta \Phi \approx 1.4 \cdot 10^{-2}$ [426] (with kind permission from Elsevier Science)

attractor has been numerically determined in a number of cases [57, 424, 426, 717, 718]. Here we show an example for the Ikeda map (Fig. 4.7).

The equation governing the dynamics of the control variable in (4.12) contains the inverse of the deterministic derivative matrix. In the vicinity of a fixed point of the original map, the dynamics governing $\boldsymbol{\eta}$ is approximately linear and is the inverse dynamics governing the evolution of $\mathbf{x}$. This enables us to estimate the rate at which the control variable $\boldsymbol{\eta}$ vanishes at both ends of the most probable exit path as

$$| \boldsymbol{\eta}_n | \sim \exp(| \lambda' | n), \ \ n = 1, 2, \ldots, \quad \text{and} \quad | \boldsymbol{\eta}_n | \sim \exp(-\lambda_1 n), \ \ n \to \infty. \quad (4.20)$$

The control variable initially grows according to the modulus of the contracting Lyapunov exponent $\lambda' < 0$ of the attractor, and approaches, after long times, zero with $\lambda_1 > 0$, the largest positive Lyapunov exponent of the nonattracting (chaotic or nonchaotic) set on the boundary.

4.2.4 Enhancement of Exit Rates by Transient Chaos

When a nonattracting chaotic set is present *in* the basin of attraction of an attractor, it is possible to reduce the activation energy $\Delta \Phi$ and consequently to increase the exit rate as described by Kraut and Feudel [423, 425, 426]. To understand

this, consider an invertible system with smooth basin boundaries, where the optimal (most probable) exit path passes through an unstable periodic point $\mathbf{x}_e$ on the boundary. However, before reaching the boundary, the path also extends through the chaotic saddle, since from the point of view of energy, motion along the unstable manifold of the saddle (or more generally, along any deterministic orbit) does not contribute to the activation energy. From the quasipotential plateau of the chaotic saddle, a trajectory can reach $\mathbf{x}_e$ on the boundary with a relatively low increase in the quasipotential, as exemplified by Fig. 4.8. Numerical simulations reveal [423, 425, 426] that although the activation energy is smaller than that in the absence of the saddle by about fifty percent only, the exit rate can be enhanced by several orders of magnitude, since the reduction in the quasipotential appears in the exponent of (4.16) divided by the small noise intensity. The origin of the reduction in the activation energy can be understood by noting that the exit process actually consists of three stages: reaching the quasipotential plateau of the saddle, moving on the plateau, and leaving the plateau to reach the boundary. The chaotic saddle thus acts as a "shortcut" for minimizing the quasipotential in the exit process.[8]
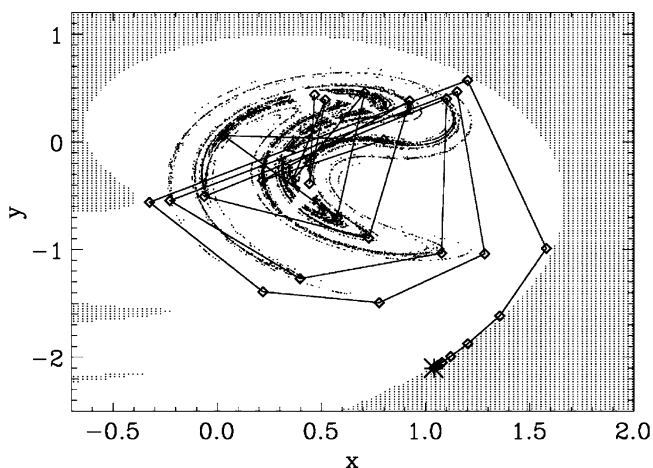
Fig. 4.8 A most probable exit path in the phase space of the Ikeda map (3.13) for parameters $A = 0.85$, $B = 0.9$, $k = 0.4$, and $p = 5$. For this parameter setting, there are a fixed-point attractor and a coexisting chaotic saddle (*black dots*) in the basin of the attractor. Exit from the basin is through a hyperbolic periodic point $\mathbf{x}_e$ (denoted by the *asterisk* on the smooth boundary). The exit path in fact wanders through the chaotic saddle before approaching $\mathbf{x}_e$. The activation energy is $\Delta\Phi \approx 7 \cdot 10^{-3}$ [426] (with kind permission from Elsevier Science)

---

[8] The role of a chaotic saddle in enhancing the exit rate suggests that when a dynamical system undergoes a basin boundary metamorphosis (see Sect. 5.4.1) by which a smooth boundary becomes fractal so that a nonattracting chaotic set arises on the boundary, the rate of exiting the basin due to noise can be enhanced significantly. This has indeed been observed [729].

4.3 Noise-Induced Chaos

In a dynamical system with a regular periodic attractor, the addition of weak
noise can lead to a chaotic attractor. This phenomenon of *noise-induced chaos*
[104, 332, 349] occurs when there is a coexisting *nonattracting* chaotic set in the
phase space of the noise-free system. A typical setting in which noise-induced chaos
can occur is periodic windows. Specifically, let the system parameter p be chosen
so that the system is in a periodic window where a periodic attractor and a nonat-
tracting chaotic set coexist. Imagine placing the system under noise. As the noise
strength is increased through a critical value, the asymptotic attractor of the system
becomes chaotic, as characterized by the appearance of a positive Lyapunov expo-
nent. Here the notions of attractor and its basin of attraction are still meaningful,
since noise is weak.

Figure 4.9 presents an example of the phenomenon from the one-dimensional
logistic map in a period-8 window, where the noise-induced chaotic attractor in the
(x_{n-1}, x_n)-plane is shown in Fig. 4.9a and a representative noisy chaotic time series
is shown in Fig. 4.9b. An intermittent behavior can be seen, where the noisy trajec-
tory visits the period-8 attractor and a coexisting chaotic repeller in different times.
A two-dimensional example is shown in Fig. 4.10. The deterministic system pos-
sesses two fixed-point attractors and a fractal basin boundary separating the basins
of attraction, as shown in Fig. 4.10a. In the presence of weak noise of strength ex-
ceeding a certain threshold value σ_c, the attractors merge with the unstable manifold
of the chaotic saddle to form a noisy chaotic attractor, as shown in Fig. 4.10b.
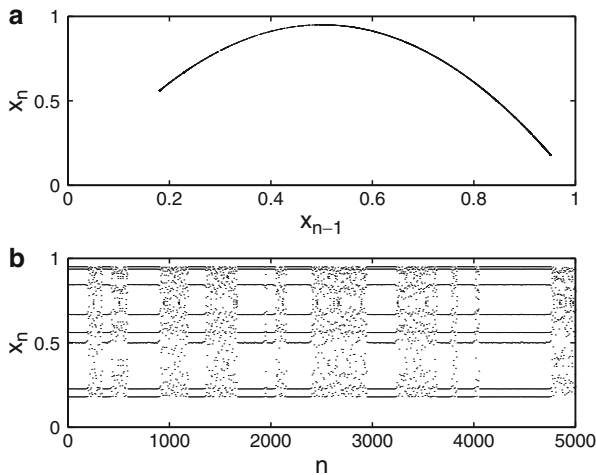
Fig. 4.9 Nose-induced chaos for the logistic map $x_{n+1} = rx_n(1 - x_n) + \sigma \xi_n$ for $r = 3.8008$ (in a
period-8 window of the deterministic map) and noise strength $\sigma = 10^{-4.8} \approx 1.6 \times 10^{-5}$: (**a**) noisy
chaotic attractor and (**b**) intermittent time series $\{x_n\}$ [458] (Copyright 2003, the American Physi-
cal Society)
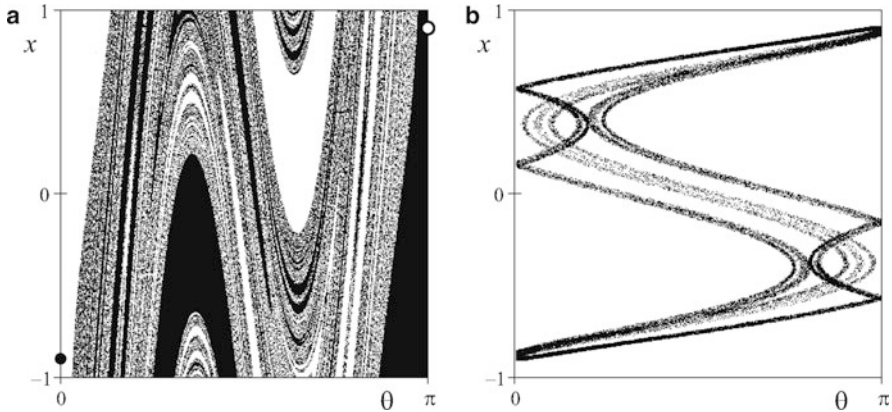
Fig. 4.10 Noise-induced chaos in the map system defined in Fig. 4.6. (**a**) Deterministic case, two fixed-point attractors (denoted by *large black* and *blank dots*) and their basins of attraction. (**b**) Noise-induced chaotic attractor with uniform noise for $\sigma = 0.01$. A comparison with Fig. 4.6 indicates that the attractor extends through the plateau of the quasipotential, containing the unstable manifold of the chaotic saddle. The critical noise strength is $\sigma_c = 0.009$ [717] (Copyright 2010, the American Physical Society)

While the coexistence of a chaotic saddle and a periodic attractor can result in a chaotic attractor under noise [66, 171], a situation can arise in dynamical systems whereby there are some unstable periodic orbits and a periodic attractor in the phase space. In this case, if homoclinic tangencies between the stable and the unstable manifolds of the unstable periodic orbit are imminent, the addition of noise can induce homoclinic intersections and consequently a chaotic saddle, generating the conditions for a noise-induced chaotic attractor. Such chaotic saddles are called *stochastic chaotic saddles* and have been demonstrated in a class of biological systems [65, 696].

4.3.1 Critical Noise Strength for Noise-Induced Chaos

The concept of quasipotential provides a convenient way for estimating the critical noise strength required for noise-induced chaos. The first observation is that the periodic attractor appears to be fuzzy in the presence of noise. We can define a noisy attractor as the region in which the probability distribution takes on large values. Note that any practical observation of the stationary distribution relies on the existence of a finite threshold resolution, χ (say 10^{-3} of the maximum of the probability density W). To leading order, we can define, depending on the threshold, a noisy attractor as the set of phase-space points $\mathbf{x}$ that satisfy $Z \exp[-(\Phi(\mathbf{x}) - \Phi(P))/\sigma^2] \geq \chi$, where $P = A$ denotes the periodic attractor and Z is a constant. For small σ, the distribution is strongly localized and the extension of the noisy attractor beyond the deterministic attractor is small but increases with the noise strength. A noise-induced chaotic attractor appears at a critical noise strength σ_c where the noisy attractor touches the edge of the *quasipotential plateau*.

Denoting the quasipotential difference between the plateau and the attractor by $\Delta\Phi$, which is the activation energy (4.17) from the attractor, the condition for the critical noise strength is $Z\exp(-\Delta\Phi/\sigma_c^2) = \chi$. We thus obtain[9]

$$\sigma_c = \sqrt{\Delta\Phi/\ln(Z/\chi)} \sim \Delta\Phi^{1/2}. \tag{4.21}$$

A sudden spreading of the support of distribution W has indeed been observed, as shown in Fig. 4.11 for the system of Fig. 4.6 at a critical value compatible with the above estimate.
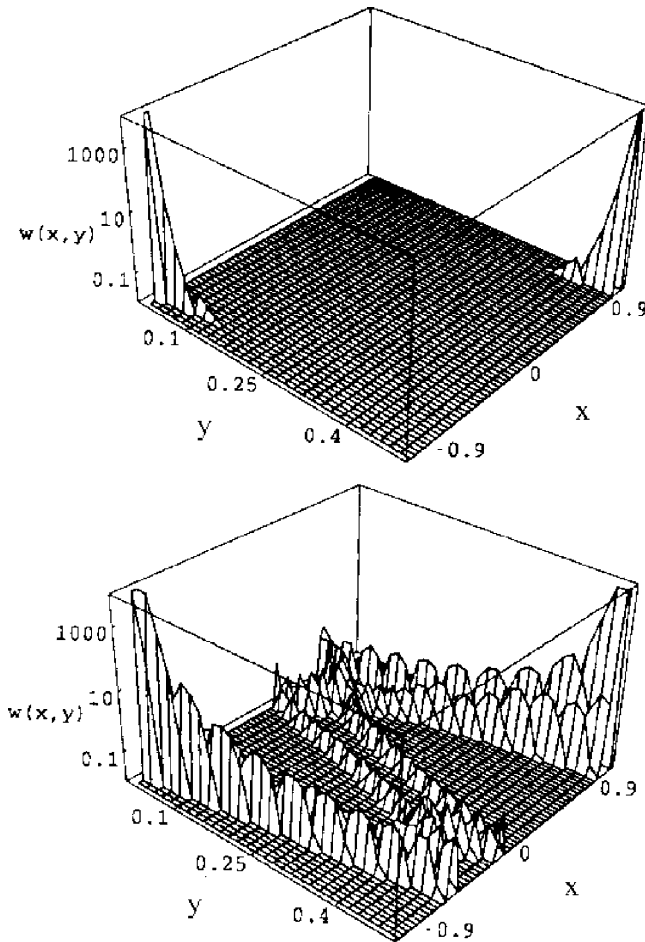
Fig. 4.11 Stationary probability $W(x,y)$ of the map in Fig. 4.6 plotted with resolution $\chi = 0.01$ for noise strength $\sigma = \sqrt{2}\cdot 10^{-3}$ in the *upper panel* and $\sigma = \sqrt{20}\cdot 10^{-2}$ in the *lower panel*, where noise-induced chaos is present [312] (with kind permission from Elsevier Science)

---

[9] For noise of order r, we have $\sigma_c = [\Delta\Phi/\ln(Z/\chi)]^{1/r}$.

For noise strength slightly above σ_c, the probability distribution observed with resolution χ extends over the whole chaotic attractor, but the probability about the original periodic attractor is much larger than that of being farther away, as shown in Fig. 4.11. The mean first-exit time, t_e, from the corresponding potential well is given by (4.18), which is equal to the average lifetime in the noisy system about the periodic attractor.

4.3.2   Scaling Laws for Critical Noise Strength and for Lifetime at a Saddle-Node Bifurcation

Close to certain bifurcations, a scaling law of the critical noise strength can be obtained from (4.21). For example, close to the saddle-node bifurcation that initiates a period-m window, the deterministic dynamical system can effectively be reduced to a normal form that is one-dimensional [300]. The quasipotential about the fixed-point attractor, the node, increases quadratically with the distance from the attractor with a coefficient proportional to $(p - p_b)^{1/2}$ [44, 311]:

$$\Delta\Phi(\Delta x) \sim (p - p_b)^{1/2}\Delta x^2,$$

where p_b denotes the bifurcation point. For a smooth one-dimensional map, the phase-space distance between the saddle and the node about the bifurcation point is proportional to $(p - p_b)^{1/2}$. Since the saddle is part of the nonattracting chaotic set, the activation energy is

$$\Delta\Phi = c(p - p_b)^{3/2}, \tag{4.22}$$

where c is a constant. From (4.21), at a fixed resolution, the critical noise strength scales with $(p - p_b)$ as

$$\sigma_c \sim (p - p_b)^{3/4}, \tag{4.23}$$

which has been verified numerically [44, 401, 402].

The average lifetime t_e about the node can be calculated using (4.18), which for a saddle-node bifurcation is

$$t_e(p) \sim e^{c(p-p_b)^{3/2}/\sigma^2} \tag{4.24}$$

for sufficiently weak noise [207, 312]. The scaling of the prefactor with the parameter, not written out in (4.24), can be obtained by combining this form with the deterministic result. As pointed out by Pomeau and Manneville [612], the mean duration time of the laminar phase in intermittency is proportional to the power $-1/2$ of the parameter difference. This leads to the scaling law [218]

$$t_e(p) \sim (p - p_b)^{-1/2} g[(p - p_b)^{3/4}/\sigma], \tag{4.25}$$

where g is an arbitrary function. A comparison of (4.24) with (4.25) fixes the scaling function g to be

$$g(z) \sim e^{cz^2}, \tag{4.26}$$

which is valid for Gaussian noise.[10] This rule implies that the quantity $t_e(p)$ $(p-p_b)^{1/2}$ versus $(p-p_b)^{3/2}/\sigma^2$ falls on a straight line on a semilogarithmic plot, a scaling form that can be verified numerically [312].

It should be emphasized that the quasipotential approach is applicable if the deterministic influence dominates the stochastic influence. This implies that given a fixed finite value of σ, the results presented here are valid only if $p-p_b$ exceeds some minimal value, because noise is dominant for parameter values quite close to the bifurcation point.

4.3.3 Appearance of a Positive Lyapunov Exponent

An alternative way of defining an attractor under noise to be chaotic is the sensitive dependence on initial conditions, as characterized by the existence of at least one positive Lyapunov exponent.[11] In particular, in the absence of noise, since the attractor is not chaotic, the largest Lyapunov exponent of the asymptotic attractor is a negative number for maps (zero for flows). As noise is turned on and its strength becomes sufficiently large, there is a nonzero probability that a trajectory originally on the attracting set escapes it and wanders near the coexisting chaotic saddle. In this case, the largest Lyapunov exponent λ_1 becomes positive, indicating that the asymptotic attractor of the system has become chaotic for trajectories starting from random initial conditions.

The spectra of the Lyapunov exponents is changed due to the noise. This can be seen, heuristically, as follows. For maps, let $\lambda_1^P < 0$ and $\lambda_1^C > 0$ be the largest Lyapunov exponent of the periodic attractor and that of the chaotic saddle (or a chaotic repeller), respectively, in the absence of noise. The largest Lyapunov exponent of the noisy system is denoted by λ_1. For $\sigma < \sigma_c$, the noisy attractor is only a fattened version of the original periodic attractor. Thus, we have $\lambda_1 = \lambda_1^P$. For $\sigma > \sigma_c$, there is an intermittent hopping of the trajectory between regions that contain the original periodic attractor and the nonattracting chaotic set. Let $f_P(\sigma)$ and $f_C(\sigma)$ be the fractions of time that the trajectory spends asymptotically in the corresponding regions. We have

$$\lambda_1(\sigma) \approx f_P(\sigma)\lambda_1^P + f_C(\sigma)\lambda_1^C, \tag{4.27}$$

---

[10] For noise of order r, $\Delta\Phi = c(p-p_b)^{r-1/2}$, and $t_e(p) \sim (p-p_b)^{-1/2}g[(p-p_b)^{1-1/(2r)}/\sigma]$ with $g(z) \sim \exp(cz^r)$.

[11] The Lyapunov exponents are the time-averaged stretching or contracting rates of infinitesimal vectors along a typical trajectory in the phase space, which can be defined for both deterministic and stochastic dynamical systems.

where the Lyapunov exponent changes sign for $\sigma = \sigma_c$. We thus have $f_C(\sigma_c)\lambda_1^C = f_P(\sigma_c) \mid \lambda_1^P \mid$. For σ about σ_c, the fraction of time spent near the periodic attractor is relatively large, i.e., $f_P(\sigma) \approx 1$, and we have

$$\lambda_1(\sigma) \approx f_C(\sigma)\lambda_1^C + \lambda_1^P. \tag{4.28}$$

We see that immediately after the noise strength exceeds the critical value σ_c, the noisy attractor is chaotic in the sense that its largest Lyapunov exponent becomes positive. For $\sigma > \sigma_c$, the periodic attractor and the chaotic saddle are dynamically connected, but for σ slightly above σ_c, a trajectory visits the chaotic saddle only occasionally. Under this circumstance the sets can be regarded as distinct but only in an approximate sense. That is, (4.27) is valid only for σ slightly above σ_c.

The above discussion can be extended to continuous-time dynamical systems. Consider, for example, a three-dimensional flow. Let $\lambda_3^P \leq \lambda_2^P < \lambda_1^P = 0$ and $\lambda_3^C < \lambda_2^C = 0 < \lambda_1^C$ be the Lyapunov spectra of the periodic attractor and of the chaotic saddle, respectively, in the absence of noise. Let $\lambda_3 < \lambda_2 < \lambda_1$ be the Lyapunov spectrum of the noisy system. For $\sigma < \sigma_c$, we have $\lambda_i = \lambda_i^P$ $(i = 1, 2, 3)$. In particular, there is still a null Lyapunov exponent $\lambda_1 = 0$, despite the presence of noise, indicating that the topology of the flow is preserved. The critical noise strength, σ_c, is set by the condition that an intermittent hopping of the trajectory between regions that contain the original periodic attractor and the chaotic saddle becomes observable. In terms of the fraction f_C of time that the trajectory spends asymptotically about the saddle, this implies $f_C(\sigma) > 0$ for $\sigma > \sigma_c$. The Lyapunov spectrum can then be written as

$$\begin{aligned}
\lambda_1(\sigma) &\approx f_P(\sigma)\lambda_1^P + f_C(\sigma)\lambda_1^C = f_C(\sigma)\lambda_1^C, \\
\lambda_2(\sigma) &\approx f_P(\sigma)\lambda_2^P + f_C(\sigma)\lambda_2^C = f_P(\sigma)\lambda_2^P < 0, \\
\lambda_3(\sigma) &\approx f_P(\sigma)\lambda_3^P + f_C(\sigma)\lambda_3^C < 0. \tag{4.29}
\end{aligned}$$

What is the way by which $\lambda_1(\sigma)$ varies through the transition? As we will see, the transition is smooth in the sense that the largest Lyapunov exponent becomes positive continuously from zero as the noise strength is increased through the critical value σ_c.

4.3.4 Scaling Law for the Largest Lyapunov Exponent

Because of the averaging effect of noise, we expect the dependence on noise of the largest Lyapunov exponent λ_1^C of the original chaotic set to be weak. For flows, the largest Lyapunov exponent from (4.29) is $\lambda_1(\sigma) = f_C(\sigma)\lambda_1^C$, which is positive insofar as the measured value of $f_C(\sigma)$ becomes markedly nonzero. Thus the main dependence of λ_1 on noise comes from $f_C(\sigma)$, the frequency of visit to the originally nonattracting chaotic set. We shall establish that for σ slightly above σ_c, this

probability obeys an algebraic scaling law:

$$f_C(\sigma) \sim (\sigma - \sigma_c)^\alpha, \tag{4.30}$$

where α is a scaling exponent. As a consequence, the largest Lyapunov exponent scales with the noise variation in the same manner, i.e.,

$$\lambda_1(\sigma) \sim (\sigma - \sigma_c)^\alpha. \tag{4.31}$$

To estimate the scaling exponent, we make use of the quasipotential concept again and note that the chaotic saddle lies on a quasipotential plateau. The probability of reaching the plateau is nonzero if the noisy attractor overlaps with the plateau, i.e., if there are points of the noisy attractor for which $\Phi(\mathbf{x}) - \Phi(P) \geq \Delta\Phi$, where $\Delta\Phi$ is the activation energy. The probability of being on the plateau is the integral of $Z \exp[-(\Phi(\mathbf{x}) - \Phi(P))/\sigma^2]$, which is for small σ proportional to the minimum of the integrand. Due to the threshold value χ introduced in Sect. 4.3.1, any measured probability should be larger than χ. Thus, for σ slightly above σ_c, we can express the probability of being on the plateau as

$$f_C(\sigma) = Z e^{-\Delta\Phi/\sigma^2} - \chi. \tag{4.32}$$

Since σ_c is defined as the noise strength for which $Z \exp(-\Delta\Phi/\sigma_c^2) = \chi$ holds (4.21), we can write

$$f_C(\sigma) = \chi \left(e^{-\Delta\Phi(\sigma^{-2} - \sigma_c^{-2})} - 1 \right). \tag{4.33}$$

The exponent is $\Delta\Phi(\sigma^2 - \sigma_c^2)/(\sigma^2 \sigma_c^2) \approx 2\Delta\Phi(\sigma - \sigma_c)\sigma_c^{-3}$. For sufficiently small $\sigma - \sigma_c$, the exponential function can be expanded to yield

$$f_C(\sigma) \sim \Delta\Phi \frac{\sigma - \sigma_c}{\sigma_c^3}. \tag{4.34}$$

Thus, from (4.30), we have

$$\alpha = 1, \tag{4.35}$$

which is independent of any system details such as the phase-space dimension.

A similar argument applies to maps. Since λ_1^P is nonzero, both contributions in (4.27) are nonzero, and the threshold χ can be neglected.[12] Since the problem is basically a two-state problem with a periodic and a chaotic state, the probability of being in state $i = P, C$ can be expressed as a ratio of the average lifetimes:

$$f_i(\sigma) = \frac{\tau_i(\sigma)}{\tau_P(\sigma) + \tau_C(\sigma)}. \tag{4.36}$$

---

[12] The scaling law and the exponent remain unchanged even if the threshold is not neglected [776].

The lifetime $\tau_P \equiv t_e$ about the periodic attractor is given by the Arrhenius factor (4.18). The lifetime about the nonattracting chaotic set depends nonexponentially on the noise strength and can be considered to be constant, i.e., $\tau_C \approx 1/\kappa$, where κ is the escape rate of the chaotic set. Taking this into account in the weak noise limit $\Delta\Phi/\sigma^2 \gg 1$, we have

$$f_P(\sigma) \approx 1, \quad f_C(\sigma) \approx \frac{1}{\kappa\tau_0} e^{-\Delta\Phi/\sigma^2}. \tag{4.37}$$

The critical noise strength at which the largest Lyapunov exponent vanishes in maps thus satisfies, according to (4.28), the following relation:[13]

$$e^{-\Delta\Phi/\sigma_c^2} = \kappa\tau_0 \frac{|\lambda_1^P|}{\lambda_1^C}. \tag{4.38}$$

For σ close to σ_c we obtain

$$\lambda_1(\sigma) = \lambda_1^C f_C(\sigma) + \lambda_1^P = |\lambda_1^P| \left(e^{-\Delta\Phi(\sigma^{-2}-\sigma_c^{-2})} - 1 \right), \tag{4.39}$$

which has the same σ-dependence as in (4.33) and leads again to the exponent $\alpha = 1$.

We note that the argument presented here applies to any physical quantity Q that takes on values Q^P and Q^C on the original periodic attractor and on the nonattracting chaotic set, respectively. The noise dependence of the average value $Q(\sigma)$ of Q is then

$$Q(\sigma) \approx f_P(\sigma)Q^P + f_C(\sigma)Q^C. \tag{4.40}$$

An application of this rule leads to a surprising result in a model of Brownian motion in a symmetric periodic potential in the presence of bias and periodic driving [730, 731]. In particular, the effect of driving pushes the system out of thermal equilibrium even in the presence of temperature fluctuations. For the noiseless system at positive bias, there is a periodic attractor leading to a negative average velocity $v^P < 0$ of particles. At the same parameters, there is a coexisting chaotic saddle to which a positive average velocity $v^C > 0$ belongs. This, however, is not seen with typical initial conditions in long-term observations. The presence of noise connects the two original invariant sets and leads to noise-induced chaos. In the context of transport, the main interest is, however, in the average velocity $v(\sigma)$, which follows from (4.40) with $Q^P = v^P$ and $Q^C = v^C$. It has the property that $v(\sigma)$ changes sign at a critical value σ_c^v, as has also been demonstrated in an experiment with a Josephson Junction [540]. The behavior of the average velocity about the critical point is linear: $v(\sigma) \sim \sigma - \sigma_c^v$, analogous to the average Lyapunov exponent.

The scaling of the Lyapunov exponent with the noise strength has been verified by a number of numerical examples [458], and also experimentally, using a nonlinear electronic circuit [837]. Here we cite one example, the Rössler oscillator with additive noise:

---

[13] The noise strength σ_c corresponds to (4.21) with $\chi/Z = \kappa\tau_0 |\lambda_1^P|/\lambda_1^C$.

$$dx/dt = -y - z + \sigma\xi_x(t),$$
$$dy/dt = x + 0.2y + \sigma\xi_y(t),$$
$$dz/dt = 0.2 + z(x - c) + \sigma\xi_z(t), \qquad (4.41)$$

where c is the bifurcation parameter, σ is the noise strength, and $\xi_{x,y,z}$ are independent Gaussian random variables of zero mean and unit variance. A period-3 window exists about $c = 5.3$. Figure 4.12a shows the projection of the period-3 attractor into the (x, y)-plane for $c = 5.3$. Noise-induced chaos arises for $\sigma > \sigma_c \approx 10^{-2.26} \approx 5.5 \times 10^{-3}$. For σ slightly above σ_c, the asymptotic trajectory of the system deviates from the original period-3 attractor, but the probability density is still large around the 3-cycle, as shown in Fig. 4.12b for $\sigma = 0.01$. For a larger value of σ, the trajectory spends relatively more time in the region where the original chaotic saddle resides, as shown in Fig. 4.12c. Figure 4.13a shows the first two Lyapunov exponents of the asymptotic attractor versus the noise strength σ. We see that for $\sigma < \sigma_c$, the largest Lyapunov exponent is zero, indicating that the noisy flow is not chaotic. The presence of the null Lyapunov exponent means that in spite of noise, there is a neutral direction associated with the flow. For $\sigma > \sigma_c$, the largest Lyapunov exponent becomes positive, so the noisy flow is chaotic. In this case, there is no longer a null Lyapunov exponent, indicating the disappearance of the neutral direction. Figure 4.13b shows the scaling of the largest Lyapunov exponent of the noisy chaotic attractor with $\sigma - \sigma_c$, which is apparently algebraic. A least-squares fit between $\log_{10} \lambda_1$ and $\log_{10}(\sigma - \sigma_c)$ gives the slope 0.94 ± 0.03. There is a reasonable agreement between the theoretical scaling law and numerics.
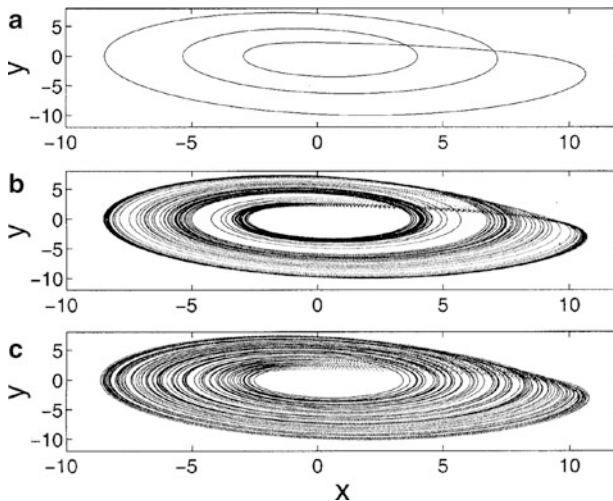
Fig. 4.12 Asymptotic trajectory of the Rössler system for (**a**) $\sigma = 0$, (**b**) $\sigma = 0.01 > \sigma_c$, and (**c**) $\sigma = 0.02$ [458] (Copyright 2003, the American Physical Society)
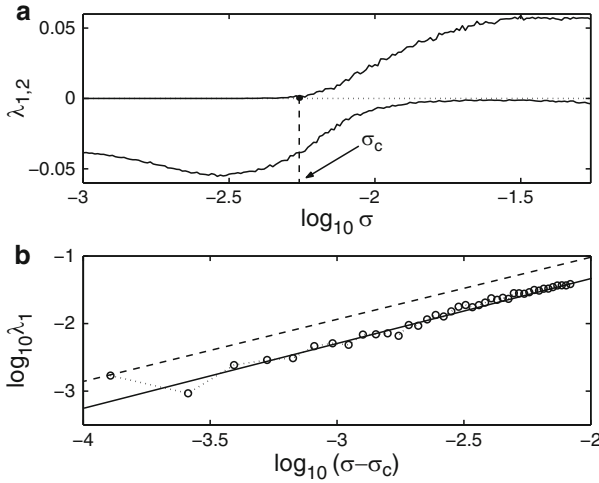
Fig. 4.13 For the Rössler system, (**a**) the first two Lyapunov exponents versus σ about the transition, and (**b**) algebraic scaling of the largest Lyapunov exponent with $\sigma - \sigma_c$. From (**a**), we see that there is no zero Lyapunov exponent for $\sigma > \sigma_c$, indicating the lack of a neutral direction of the flow [458] (Copyright 2003, the American Physical Society)

4.4 General Properties of Noise-Induced Chaos

4.4.1 Fractal Properties

A noise-induced chaotic attractor lies in the union of the periodic attractors and the unstable manifold of the nonattracting set. Since the periodic attractors are zero-dimensional objects on a Poincaré plane, the dimensions D_0 and D_1 of the noise-induced chaotic attractor are the same as those of the unstable manifold of the nonattracting chaotic set in the absence of noise: $D_0 = D_{u,0}$ and $D_1 = D_{u,1}$. For example, for a two-dimensional invertible map, we can use (2.82) and (2.78) to find the information dimension of the noise-induced attractor as

$$D_1 = 1 + \frac{\lambda_1 - \kappa}{|\lambda_2|}. \tag{4.42}$$

Note that the dimension is independent of the noise strength σ, a valid property in the weak-noise limit. In fact, the information dimension of the noise-induced chaotic attractor is determined uniquely by the parameters of the chaotic saddle in the underlying deterministic system.

It is the fractal property of the attractor which can be used as a condition to assess whether noise is weak. As can be seen from Fig. 4.14, which shows the results of the box-counting algorithm carried out for the example of Fig. 4.10, noise makes the dynamics space-filling on small phase-space scales, less than $\varepsilon_c \approx e^{-4} = 0.018$
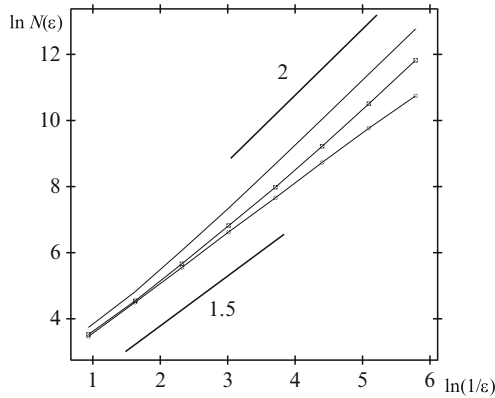
Fig. 4.14 Results of the box-counting algorithm for the unstable manifold of the deterministic map investigated in Fig. 4.10a (*dots*) and for noisy attractors (b) (*filled squares*, $\sigma = 0.01$ (Fig. 4.10b) and *filled diamonds*, $\sigma = 0.03$). The slopes of the *thick solid lines* represent the fractal dimension $D_{u,0} = 1.5$ of the unstable manifold of the chaotic saddle in the deterministic system and of the phase-space dimension $d = 2$. The threshold scale beyond which fractality holds is $\varepsilon_c \approx 0.018$ for $\sigma = 0.01$. For $\sigma = 0.03$, such a threshold value does not exist, indicating that noise dominates the dynamics. A similar plot can be obtained for the scaling of the information dimension of the unstable manifold as determined by (4.42), with $D_{u,1} = 1.4$ [717] (Copyright 2010, the American Physical Society)

for $\sigma = 0.01$. For weak noise, there is always a scaling region, although short, with the slope given by the noise-free fractal dimension, which is $D_{u,0} = 1.5$ in this case. This is consistent with the schematic diagram Fig. 4.1. When this scaling region disappears, it is no longer possible to identify the fractality of the noise-induced chaos, even on larger phase-space scales, as is the case for $\sigma = 0.03$ [777]. In fact, in this case, noise smears out the dynamics into large, finite bands of the phase space, indicating that noise begins to dominate the dynamics. When this happens, the noise can be considered strong.

4.4.2 Noise-Induced Unstable Dimension Variability

For deterministic flows, one of the Lyapunov exponents is zero because the dynamics along the flow is neutral, i.e., it is neither expanding nor contracting. An interesting consequence of noise-induced chaos is that after the transition ($\sigma > \sigma_c$), the topology of the flow is disturbed in a fundamental way: there is no longer a zero Lyapunov exponent, indicating that for noisy chaos, there exists no neutral direction along which infinitesimal distances are conserved.[14] This is caused by a type of nonhyperbolicity, unstable dimension variability, associated with the noise-induced chaotic attractor.

---

[14] This consideration does not apply to nonautonomous systems, for which there is always a neutral direction along the time axis and therefore always a zero Lyapunov exponent.

The phenomenon of *unstable dimension variability* refers to the situation in which a typical trajectory moves in phase-space regions containing unstable periodic orbits with distinct numbers of unstable eigendirections, which was first conceived by Abraham and Smale [1], who constructed a mathematical model of two unstable fixed points with distinct numbers of local unstable eigendirections. It was realized later that the phenomenon is quite common in dynamical systems of high dimensions, and it can have intricate consequences on the shadowability of numerical trajectories in high-dimensional chaotic systems [41, 159, 416, 449, 676]. We have seen in Chap. 3 that an invariant set is nonhyperbolic if there are tangencies between the stable and unstable manifolds. Unstable dimension variability is another source of nonhyperbolicity.

To see how unstable dimension variability arises in the context of noise-induced chaos, we note that for σ above σ_c, both the chaotic saddle and the periodic attractor belong to a single, connected dynamical invariant set. Since periodic orbits embedded in the chaotic saddle are all unstable and the originally attracting periodic orbit is stable, a trajectory moves in regions containing periodic orbits with distinct unstable dimensions. A unique feature of this type of unstable dimension variability is that the subsets with different unstable dimensions are located in distinct regions of the phase space, versus high-dimensional chaotic attractors, such as the kicked double rotor [41, 159, 416, 449, 676], where unstable periodic orbits in these subsets tend to mix with each other in the phase space [158, 452].

We can argue that after the onset of chaos, unstable dimension variability induced by noise will destroy the neutral direction of the flow. For a three-dimensional flow, the original periodic attractor contains no unstable direction, and the chaotic saddle possesses one unstable direction. The role of noise, when it is sufficiently large ($\sigma > \sigma_c$), is to link these two originally dynamical invariant sets with distinct unstable dimensions. Now examine the local eigenplanes that contain the neutral direction of the flow associated with the periodic attractor and with the chaotic saddle, as shown schematically in Fig. 4.15. In the local eigenplane about the periodic attractor, there are a stable direction and a neutral direction (n). Let **v** be the eigenvector in the neutral direction. In the eigenplane of a point in the chaotic saddle, there are an unstable direction and a neutral direction (n). When a trajectory is driven by noise from the periodic attractor to the chaotic saddle, the eigenvector **v** maps to **v'** (see Fig. 4.15), which can point in any direction in the local eigenplane of the corresponding point in the chaotic saddle. After a time, the vector will be aligned in the unstable direction, due to the expanding dynamics associated with the chaotic saddle. Distances along the neutral direction of the original periodic attractor can no longer be preserved. Thus, we see that unstable dimension variability plays a fundamental role in shaping the topology of the flow after the onset of noise-induced chaos. The chaotic attractor is, however, fundamentally different in its flow topology from any deterministic chaotic attractors in that it no longer contains a neutral direction. Readers should keep in mind that this topological disturbance of the flow exists only for $\sigma > \sigma_c$.
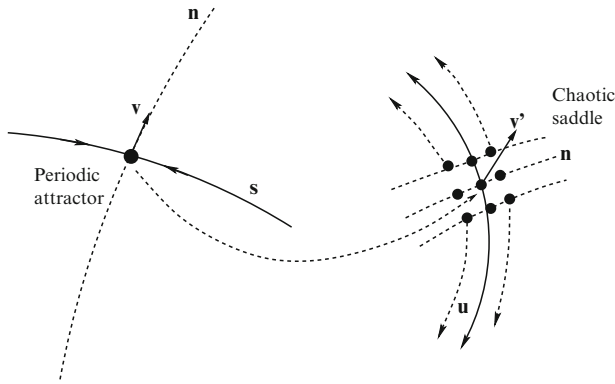
Fig. 4.15 Schematic illustration of the destruction of the neutral direction of the noisy chaotic flow due to unstable dimension variability. The local planes about the periodic attractor and a point in the chaotic saddle do not coincide in general, and these planes are not in a Poincaré surface of section (Copyright 2003, the American Physical Society)

4.4.3 Ubiquitous Applications to Biological Sciences

The concept of noise-induced chaos can play an important role in the dynamical evolution of biological systems, since random environmental influences are always present [177, 221, 683]. Examples for which noise-induced chaotic attractors and hence the results presented here are relevant are the following:

(1) *Epidemiology*. The controversy between the unpredictability observed in records of chickenpox data and the nonchaotic nature of the attractor from the mathematical models for realistic parameter values was first resolved by Rand and Wilson [621], who pointed out that weak intrinsic or external noise can convert a chaotic saddle of the model into a noisy chaotic attractor. Noise-induced chaos has proven to be a ubiquitous source of unpredictability in epidemics since then [64, 65, 222, 696].

(2) *Physiology*. It has been suggested that pathological destruction of chaotic behavior may induce some types of brain seizures [684] and heart failures [266]. In vital physiological systems chaotic dynamics can in fact be considered "normal" [245]. Bifurcations to periodic behavior are viewed as a pathophysiological loss of the range of adaptive possibilities [840]. In these situations the presence of noise can be advantageous, since it can help induce or restore chaos.

(3) *Ecology*. Population-dynamical models sometimes also predict regular behavior although observations find irregular dynamics. Here we present the model in [221] to describe the population dynamics of Fennoscandian voles. The time-continuous equations of motions for the scaled prey (vole) density, n, and predator (weasel) density, p, are
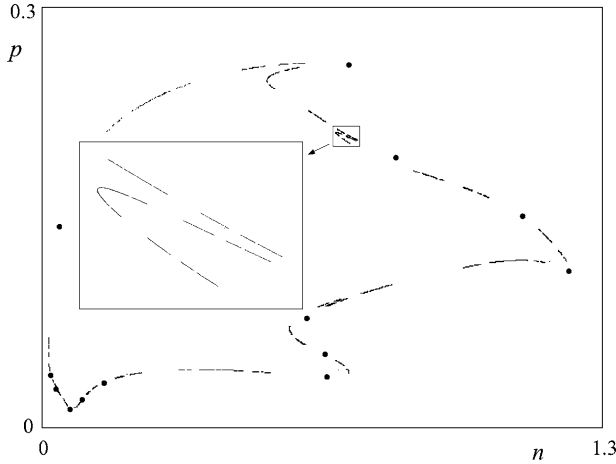
Fig. 4.16 A chaotic saddle from the ecological model described by (4.43) and (4.44) for $g = 0.12$. It is obtained by evolving $N_0 = 5 \times 10^5$ points uniformly distributed on the rectangle Γ: $0.001 < n < 1.3$ and $0 < p < 0.3$. The lifetime of the saddle is $\tau = 56$ years. Trajectories not entering a *circle* of size 0.0005 around any of the attractor points (shown by *black dots*) up to $n_0 = 100$ years are kept, and their points taken at year $n = 25$ provide a good approximation to the saddle. The *inset* shows a magnification of part of the saddle, which exhibits double fractal features [717] (Copyright 2010, the American Physical Society)

$$\frac{dn}{dt} = 4.5n[1 - \sin(2\pi t) - n] - \frac{gn^2}{n^2 + 0.01} - \frac{8np}{n + 0.04}, \tag{4.43}$$

$$\frac{dp}{dt} = 1.25p\left(1 - \sin(2\pi t) - \frac{p}{n}\right), \tag{4.44}$$

where the parameters are taken from [791]. The seasonal variation has period $t = 1$ year. A stroboscopic section is taken with a sampling of once per year (at $t = 1, 2, \ldots$), generating an invertible two-dimensional map. The attractor of the deterministic problem for $g = 0.12$ is a 13-cycle [221]. Figure 4.16 demonstrates a chaotic saddle coexisting with the 13-cycle [777]. It is the chaotic saddle that is responsible for the appearance of noise-induced chaos described earlier [221].

4.5 Noise-Induced Crisis

In the case of a boundary crisis, in the immediate precritical regime, a chaotic attractor is close to the basin boundary (Sect. 3.1). A small amount of noise can drive a trajectory out of the basin of attraction and cause it to go to another attractor, effectively inducing the crisis. For an interior crisis, sudden excursions to a certain region of the phase space can occur when a system parameter passes through a critical value, say $p > p_c$, generating crisis-induced intermittency. The average duration of these excursions is given by (3.15). In the presence of noise, random fluctuations can cause a similar behavior even in the *precrisis* region $p < p_c$ [24,757]. What can happen in this case is that noise can dynamically connect the chaotic attractor with

a coexisting, nonattracting chaotic set before the deterministic-crisis value, causing a sudden increase in the size of the chaotic attractor. *Noise-induced crisis* can therefore be regarded as a type of noise-induced chaos. Because of this analogy, the critical noise strength σ_c above which intermittency can be observed with threshold resolution χ is given by (4.21), where $\Delta\Phi$ is the activation energy in the basin of the small-size attractor. An example of noise-induced crisis is shown in Fig. 4.17, where a two-piece deterministic chaotic attractor expands into a one-piece attractor as a result of noise.

A basic quantity of interest for noise-induced crisis is the characteristic time τ that a trajectory spends on the original deterministic chaotic attractor. This time is the average time interval between bursts into the newly accessible region of the phase space. The issue is how the average time τ depends on both the parameter difference $p_c - p$ and the noise strength σ. Based on the observation that in the *deterministic* case (3.15) holds, Sommerer et al. [723, 728] obtained, for low-dimensional chaotic systems, the following universal scaling law for noise-induced crisis:

$$\tau \sim \sigma^{-\gamma} g\left(\frac{p_c - p}{\sigma}\right), \tag{4.45}$$

where γ is the critical exponent of the corresponding deterministic crisis, and g is a function that depends on the system details and on the distribution of the noise. Note that in contrast to crisis-induced intermittency in the deterministic case, the parameter range needs not be restricted to $p > p_c$ here, as a result of noise.

The particular form of g follows from the exit rate estimates obtained from the properties of the quasipotential. The basic argument in Sect. 4.3.2 can be applied, with some modifications. In particular, away from saddle-node bifurcations, the quasipotential can be assumed to increase quadratically from the attractor, with a parameter-independent coefficient given by $\Delta\Phi(\Delta x) \sim \Delta x^2$. The distance between
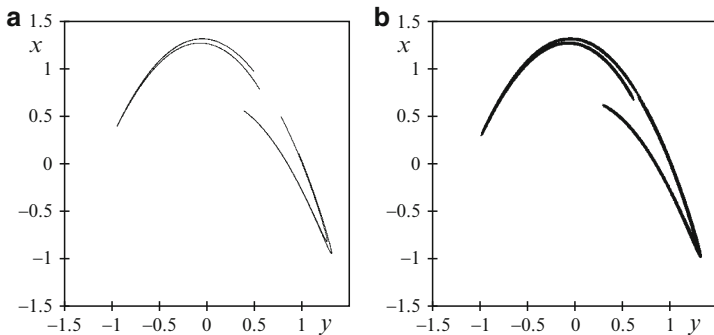
Fig. 4.17 Noise-induced crisis and attractor expansion in the Hénon map: $x_{n+1} = 1 - ax_n^2 + 0.3y_n + \sigma\xi_n^{(x)}$ and $y_{n+1} = x_n + \sigma\xi_n^{(y)}$ for $a = 1.13$ with a uniform noise. (**a**) Deterministic attractor ($\sigma = 0$), and (**b**) attractor in the presence of noise of strength $\sigma = 0.009$. The critical noise strength is $\sigma_c \approx 0.008$. In the absence of noise, a similar attractor would occur for $a = 1.16$

the attractor and the quasipotential plateau then depends linearly on the parameter difference: $\Delta x \sim p_c - p$. We thus obtain $\Delta\Phi \sim (p_c - p)^2$. For typical maps with parabolic tangencies and for Gaussian noise, the average lifetime τ close to the crisis point scales with $(p_c - p)$ as

$$\tau \sim e^{c(p_c - p)^2/\sigma^2}. \tag{4.46}$$

Combining this with the scaling law (4.45), we obtain [723] that[15]

$$\tau \sim \sigma^{-\gamma} \exp\left(\frac{c(p_c - p)^2}{\sigma^2}\right). \tag{4.47}$$

The scaling function is again of the form of (4.26) as for noise-induced chaos, indicating the similarity between these two phenomena. A particular consequence of the scaling form (4.45) is that, at the deterministic crisis value $p = p_c$, the average characteristic time follows a simple algebraic scaling law:

$$\tau \sim \sigma^{-\gamma}. \tag{4.48}$$

That is, the lifetime on the small-size attractor increases with the noise strength with the same exponent γ at p_c as with the parameter difference for $p > p_c$ in the noise-free problem.

Sommerer et al. considered several examples, ranging from map to flow systems [728], to verify the scaling laws (4.45) and (4.48). In addition, experimental evidence was obtained by examining the oscillatory dynamics of a magnetoelastic ribbon in a time-varying magnetic field [723, 724], where the control parameter p is the period of the applied magnetic field of amplitude H_{ac}. Controllable noisy fluctuations are introduced by a random magnetic field of strength σ. Deterministically, an attractor-merging crisis takes place. By plotting $\ln[\tau\sigma^\gamma]$ versus $[(p_c - p)/\sigma]^2$, data from different measurements fall on a single straight line, as shown in Fig. 4.18.

4.6   Random Maps and Transient Phenomena

Without noise, a chaotic attractor typically exhibits a fractal structure caused by the underlying dynamics. Under the influence of small random perturbations, if one examines a long trajectory produced by the dynamics, one usually observes that the fractal structure is smeared up to a distance scale proportional to the strength of the perturbations. In order to observe a clear fractal structure, a remedy is to examine the snapshot pattern formed by an ensemble of trajectories, subject to the *same* random perturbation, as pointed out by Romeiras, Grebogi, and Ott [648]. The

---

[15] For noise of order r, we have $\Delta\Phi(\Delta x) \sim \Delta x^r$ and $\tau \sim \sigma^{-\gamma} \exp\left(\frac{c(p_c - p)^r}{\sigma^r}\right)$.
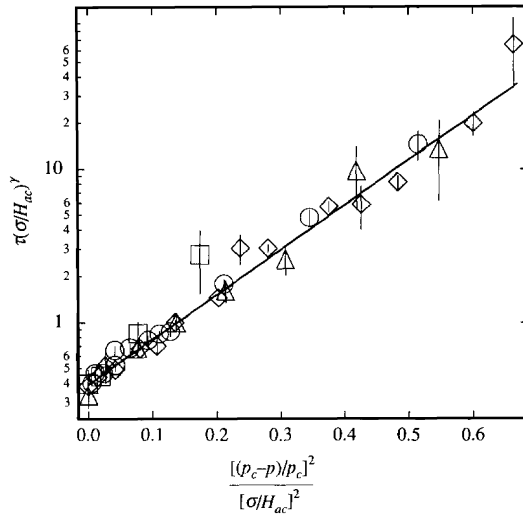
Fig. 4.18 For noise-induced crisis in an experimental magnetoelastic system, scaling of the characteristic time, presented according to the scaling law (4.45), where the value of the critical exponent γ is taken from the deterministic case. Data collapsing onto a *straight line* confirms the exponential form of the general scaling (4.47) [723] (with kind permission from Elsevier Science)

details of the fractal structure differ from time to time, but the fractal dimensions *remain invariant* [471, 648]. The idea of *snapshot attractors* [648] has proven to be useful in the laboratory for visualizing and characterizing fractal patterns arising in physical situations such as passive particles advected on the surface of a fluid [726, 844]. Snapshot attractors have been utilized to study the transition to chaos in quasiperiodically driven dynamical systems as well [446].

A convenient setting for studying the onset of fractal snapshot attractors and visualizing them is random maps. Here, the mapping rule is *not* autonomous. Instead, it depends on the actual instant of time, most often via the time-dependence of a control parameter, denoted by p_n. It is the temporal fluctuations of the parameter which can be considered to be random. A random map is then defined through the mapping rule

$$\mathbf{x}_{n+1} = \mathbf{f}(\mathbf{x}_n, p_n), \tag{4.49}$$

where $\mathbf{f}(\mathbf{x}, p)$ is a known function. The actual value p_n of the parameter can be written as

$$p_n = \bar{p} + \delta p_n, \tag{4.50}$$

where the fluctuating part δp_n is taken randomly on each iterate from a *stationary distribution* $P(\delta p_n)$ of zero mean. Unless otherwise stated, we shall not specify the form of the distribution. Accordingly, $\bar{p}$ is the mean value of the parameters over many realizations. Note that in random map (4.49), there is no additive noise ξ, in contrast to a noisy map (4.2). Another difference in comparison with the map (4.2) is that there, the noise realization can be different for different trajectories even

at the same time. The particular form of (4.49) implies that *all* the points iterated
by the map are subject to the *same noise* at a given time. A single trajectory is as
fuzzy as in a noisy map. An *ensemble* of trajectories, however, behaves in a much
more coherent way, and can exhibit fractal properties. In fact, dynamical properties
averaged over realizations of noise are well defined.

The concepts of *random attractors* and *pullback attractors* [29, 261] that have
appeared in recent publications on climate dynamics [122] are practically the same
as that of snapshot attractors. A slight difference is that in the former cases the
random process is typically white noise, and the deterministic dynamics might be
regular. We use and extend the terminology of snapshot attractors in what follows.

4.6.1 Open Random Maps, Snapshot Chaotic Saddles

In the context of transient chaos, the important feature is that nonattracting chaotic
sets can occur in random maps and they also possess fractal patterns. This is the
case if escape is possible from some finite phase-space region, i.e., if the random
map is open.

Similar to the case of sustained chaos in random systems, there *cannot be* either
periodic orbits or invariant sets in open random maps [352]. The analogues of the
stable and unstable foliations and of the nonattracting chaotic set can nevertheless
be defined. The latter can be called a *snapshot chaotic repeller* or a *snapshot chaotic
saddle*. In the case of invertible deterministic dynamics, for the unstable manifold
in a two-dimensional open random map belonging to the time instant n, we can take
an ensemble of initial points at some earlier time n_i and let them evolve according
to the random map (4.49). The end points (at time n) of trajectories that do not
leave a restraining region Γ up to time n form, for $n - n_i \gg 1$, a fractal set. In the
spirit of the sprinkler method (Sect. 1.2.2.3), the set of end points can be regarded
as an unstable foliation (unstable manifold) lying within region Γ. In general, the
unstable foliations at time n and $n' \neq n$ are different. Similarly, the stable foliation
(stable manifold) at time instant n can be obtained by letting an ensemble of points
move at time n and keeping all starting points of trajectories that do not leave Γ
up to $n_f - n \gg 1$ steps. The snapshot chaotic saddle can be obtained by plotting the
points at time n of all the trajectories started at some n_i that do not escape Γ up to
a final instant n_f, provided $n - n_i$ and $n_f - n \gg 1$. Examples are given in Figs. 4.19
and 4.20. We see that none of these sets is invariant. In fact, their shapes change
with time due to the random parameter change with time. A comparison between
Figs. 4.20 and 4.21 indicates that the change can be considerable even over a single
time step.

A consequence of a fractal stable foliation is that the lifetimes depend sensitively
on the initial conditions, as shown in Fig. 4.22. The lifetimes become infinite for
the intersecting points between the line of initial conditions and the stable foliation.
The number of trajectories in a region covering the chaotic saddle decays exponen-
tially, as just like in the deterministic case. This defines an escape rate κ_r for the
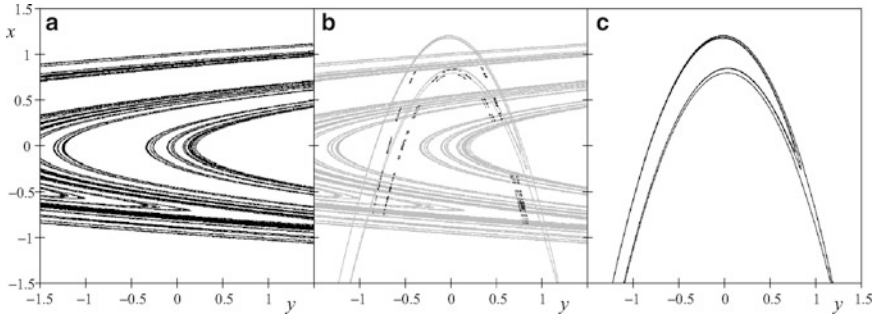
Fig. 4.19 Fractal foliations for the random Hénon map defined by $x_{n+1} = 1 - (2 + \delta a_n)x_n^2 + 0.3y_n$ and $y_{n+1} = x_n$, where δa_n is a random variable chosen from a uniform distribution in $(-1, 1)$ and represents parameter fluctuations. Shown are a stable foliation (**a**), a snapshot chaotic saddle (**b**), and an unstable foliation (**c**). These sets are calculated using an ensemble of $N = 10^7$ initial points uniformly distributed in the square region. Panels (**a**), (**b**) and (**c**) correspond to the initial points, the midpoints ($n = 8$), and the end points ($n = 16$), respectively, of trajectories that stay in the square for at least 16 iterations. The *gray lines* in panel (**b**) are copies of the foliations in (**a**) and (**c**) and indicate that the chaotic set is *not* an intersection of these foliations, since the stable (unstable) foliation belongs to time $n = 0$ ($n = 16$), while the saddle belongs to $n = 8$. The corresponding construction of the invariant sets for the deterministic map can be seen in Fig. 1.9
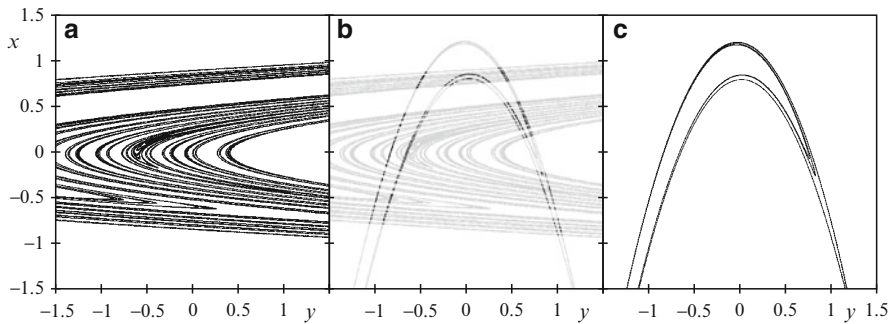
Fig. 4.20 For the same map as in Fig. 4.19, (**a**) initial points of trajectories starting at time $n = 16$ and not escaping the square up to 32 steps, (**b**) midpoints ($n = 16$) of trajectories starting at $n = 8$ and not escaping up to $n = 24$, and (**c**) end points ($n = 16$) of trajectories starting at $n = 0$ and not escaping up to $n = 16$. The *gray lines* in panel (**b**) are copies of the foliations in (**a**) and (**c**) and indicate that the snapshot chaotic saddle at time step $n = 16$ *is* the set of intersections of the foliations belonging to the same time instant

random map. Being an asymptotic property, the escape rate does not depend on the instant that the trajectories are initiated. This is so because over a long period of time, practically all possible parameter values will have been realized. This means that since the parameter distribution is stationary, the escape rate becomes independent of the initial time when the ensemble of trajectories starts to evolve. Similarly, the average Lyapunov exponents $\lambda_{i,r}$ of the random map can be determined, and they are independent of time as well.
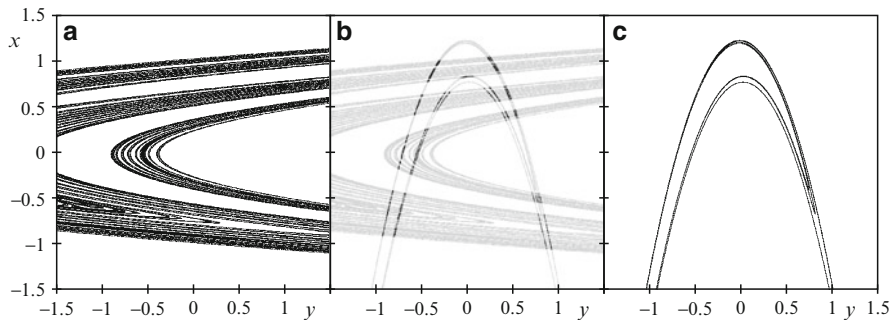
Fig. 4.21 (**a–c**) Similar to Fig. 4.20, (**a–c**), respectively except that all relevant times are shifted by -1
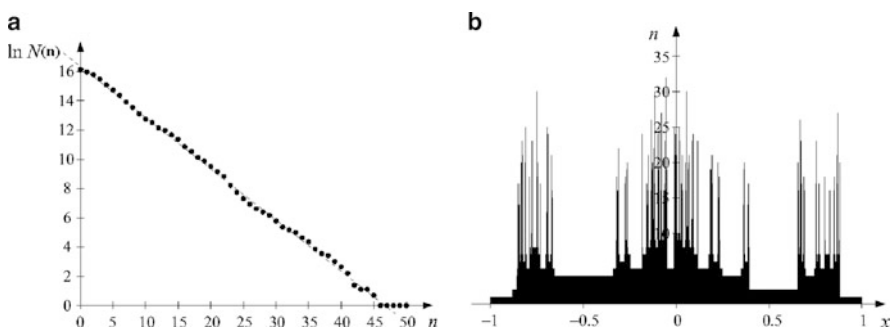
Fig. 4.22 Survival in the random Hénon map. (**a**) Number of survivors in the square $|x_n|, |y_n| \leq 1$. The escape rate is determined to be $\kappa_r \approx 0.35$, which is less than that for the deterministic case ($\kappa \approx 0.36$). (**b**) Dependence of the lifetime n on the initial position x (taken at $n_i = 0$), where the initial conditions are chosen from the interval $|x| \leq 1$ at $y_0 = -1.5$. The fractal nature of this curve is as pronounced as for the deterministic case shown in Figs. 1.4 and 1.5

For snapshot chaotic saddles, the basic relations among the information dimension, the Lyapunov exponents, and the entropies (treated in Sect. 2.6.2) are formally the same as for deterministic maps [471]. For the random baker map, these relations are derived in Appendix B. Here we quote the formula that can be used to determine the partial information dimension along the unstable foliation:

$$D_{1,r}^{(1)} = 1 - \frac{\kappa_r}{\lambda_{1,r}}. \tag{4.51}$$

The fact that this does not depend on the time instant implies that the dimensions of the chaotic set and its manifolds are independent of time, in spite of the change in their shape with time in the phase space. Similar conclusions can be drawn for other formulas. It should be emphasized that the particular values of the escape rate κ_r, the average Lyapunov exponent $\lambda_{1,r}$, and the partial information dimension $D_{1,r}^{(1)}$ are *not* the same as the respective quantities κ, λ_1, and $D_1^{(1)}$ characterizing the

corresponding deterministic map. Nonetheless, the relationships among them are the same. Analogously, the formulas for high-dimensional systems (to be discussed in Chap. 8) are expected to remain valid for open random maps. These formulas remain valid in the limit $\kappa \to 0$ of closed maps, and apply then to attractors of random maps, or snapshot attractors, as well. In the presence of strong noise, noise-induced chaotic attractors (Sect. 4.3) are fuzzy but can successfully be decomposed into fractal snapshot attractors [81].

Open area-preserving random maps generating transient chaos arise naturally in advective fluid dynamics [352, 544]. Whenever the underlying flow is not exactly periodic (e.g., temporally chaotic), the velocity field can be written as an average periodic field plus a fluctuating component. As a result, the particle positions obtained by integrating the equations of motion can also be decomposed in a similar way. Effectively all particles are then subject to the same parameter fluctuations at all times. If the observational time is longer than some typical correlation time of the velocity field, the random-map approach becomes applicable to advection problems, as shall be discussed in Chap. 10 (chaotic advection). There are other physical situations in which random maps are relevant. For example, all scattering processes in force fields that depend on time in a complicated manner can be modeled by random maps. Due to the lack of invariant sets in random maps, KAM tori do not exist, implying that practically no long-lasting transport barriers can be present. (See Chap. 6).

4.6.2 Transient Behavior in Fractal Snapshot Attractors

A necessary condition for snapshot attractors to exhibit fractal structures is that at any instant of time, the influence of the random perturbation on *every* trajectory in the ensemble must be identical. The reason is that a difference in the random perturbation to different trajectories in the ensemble can be regarded as a phase-space diffusion that can smear out the fractal structure even in snapshot attractors. To see this, consider a low-dimensional driven chaotic system described by the following map:

$$\mathbf{x}_{n+1} = \mathbf{f}(\mathbf{x}_n, \mathbf{y}_n), \qquad (4.52)$$

where $\mathbf{x}$ is a state vector and $\mathbf{y}$ represents a random or chaotic driving. Now imagine that we follow the pattern in variable $\mathbf{x}$ with time. In order to observe a pronounced fractal structure, the random perturbations $\mathbf{y}_n$ must *not* depend on the phase-space variable $\mathbf{x}_n$. If they do, the fractal structure of the snapshot attractor will be smeared approximately by an amount proportional to the magnitude of the perturbation. Due to chaos in the driving system, the fractal pattern will be less and less visible because the amount of "fuzziness" in the phase space is magnified exponentially with time.

The extent to which fractal snapshot attractors can be observed in systems driven by random or chaotic perturbations that depend only weakly on the dynamical variables was addressed in [437]. Such weak dependence can be called *phase-space*

inhomogeneity. For the system described by (4.52), it can be assumed conveniently that the chaotic driving signal comes from the following process:

$$\mathbf{y}_{n+1} = \mathbf{g}(\mathbf{y}_n, \varepsilon\mathbf{x}_n), \tag{4.53}$$

where $\mathbf{g}$ is a chaotic map and $\varepsilon > 0$ represents the amount of weak phase-space inhomogeneity. Note that when $\varepsilon = 0$, the $\mathbf{x}$-dynamics does not influence the $\mathbf{y}$-dynamics, and hence (4.52) and (4.53) represent a *unidirectionally coupled* (from $\mathbf{y}$ to $\mathbf{x}$) system. Suppose we choose an ensemble of initial conditions $\mathbf{x}_0$ and evolve them according to (4.52) and (4.53). If $\varepsilon > 0$, the phase-space inhomogeneity will be amplified exponentially due to the chaotic nature of the driving (4.53), and finite-scale fractal structures can be seen in the snapshot attractors *for only a transient period of time*.

The scaling of the average time τ to observe a snapshot attractor with ε can be obtained by examining the sub-Lyapunov exponents [581] defined with respect to (4.52) and (4.53). Let λ_i^x ($i = 1, \ldots, N_x$) and λ_j^y ($j = 1, \ldots, N_y$) be the Lyapunov exponents of the two respective subsystems. They are

$$\lambda_i^x = \frac{1}{N} \sum_{n=1}^{N} \ln \left| \frac{\partial \mathbf{f}}{\partial \mathbf{x}} \right|_{(\mathbf{x}_n, \mathbf{y}_n)} \cdot \mathbf{u}_i \Big|, \quad i = 1, \ldots, N_x, \tag{4.54}$$

$$\lambda_j^y = \frac{1}{N} \sum_{n=1}^{N} \ln \left| \frac{\partial \mathbf{g}}{\partial \mathbf{y}} \right|_{(\mathbf{x}_n, \mathbf{y}_n)} \cdot \mathbf{v}_j \Big|, \quad j = 1, \ldots, N_y,$$

where $N \gg 1$, and $\partial \mathbf{f}/\partial \mathbf{x}|_{(\mathbf{x}_n, \mathbf{y}_n)}$ and $\partial \mathbf{g}/\partial \mathbf{y}|_{(\mathbf{x}_n, \mathbf{y}_n)}$ are the derivative matrices of (4.52) and (4.53) evaluated *along a coupled trajectory*. Vectors $\mathbf{u}_i$ ($i = 1, \ldots, N_x$) and $\mathbf{v}_j$ ($j = 1, \ldots, N_y$) are unit vectors in the ith eigendirection in the tangent space of (4.52) and in the jth eigendirection in the tangent space of (4.53), respectively. The Lyapunov exponents are ordered as $\lambda_1^{x(y)} > \cdots > 0 > \cdots \lambda_{N_x(N_y)}^{x(y)}$.

Suppose we choose a cloud of initial conditions uniformly distributed in a phase-space region covering the attractor of the subsystem $\mathbf{x}$. Let δ be the smallest distance scale to resolve the fractal structure in an observation. The time T_x for the ensemble to converge to a fractal set of resolution δ can be estimated from $\exp(-|\lambda_{N_x}^x|T_x) \sim \delta$ to be $T_x \sim -\ln\delta/|\lambda_{N_x}^x|$. In order to observe the fractal structure, the amount of phase-space inhomogeneity ε must be smaller than δ. The time T_y to reach the distance scale δ in the $\mathbf{x}$ subsystem due to the $\mathbf{y}$-dynamics satisfies $\varepsilon e^{\lambda_1^y T_y} \sim \delta$. We obtain $T_y \sim (\ln\delta - \ln\varepsilon)/\lambda_1^y$. Thus, the time window for a fractal snapshot attractor to be observed is

$$\tau = T_y - T_x \sim \frac{-\ln\varepsilon}{\lambda_1^y} + \ln\delta \left(\frac{1}{\lambda_1^y} + \frac{1}{|\lambda_{N_x}^x|} \right),$$

which gives the following scaling relation:

$$\tau \approx \alpha \ln\frac{1}{\varepsilon} + \beta, \tag{4.55}$$

where α is approximately the inverse of the largest Lyapunov exponent of (4.53), and β is a constant. Demanding $\tau > 0$, we obtain from (4.55) the maximum value of the phase-space inhomogeneity for a fractal snapshot attractor of resolution δ to be observed: $\varepsilon < \delta e^D$, where $D \equiv 1 + \lambda_1^y/|\lambda_{N_x}^x|$. Thus, in order to observe fractal snapshot attractors for a long time, the phase-space inhomogeneity must be small and/or the driving system be only weakly chaotic.

Numerical confirmation of the scaling relation (4.55) has been obtained [437] by considering a random version of the Ikeda map (3.13) given by

$$z_{n+1} = A + Bz_n \exp\left(\mathrm{i}k - \frac{\mathrm{i}p}{1+|z_n|^2} + \mathrm{i}2\pi\theta_n\right), \qquad (4.56)$$

where θ_n represents a chaotic driving, and A, B, k, p are parameters. The effect of phase-space inhomogeneity in the driving can be modeled by assuming that θ comes from the noisy logistic map:

$$\theta_{n+1} = 3.75\theta_n(1 - \theta_n) + \varepsilon x_n. \qquad (4.57)$$

Under the parameter setting $(A, B, k, p) = (0.85, 0.9, 0.4, 5.18)$, the Ikeda map, in the absence of perturbation θ_n, exhibits a chaotic attractor with a fractal structure (cf. Fig. 3.14b).

Figure 4.23a–j show, for $\varepsilon = 10^{-16}$, snapshot attractors at ten different time instants from a grid of 128×128 initial conditions uniformly distributed in the region: $(-2.0 \leq x \leq 4.0, -2.5 \leq y \leq 2.5)$. The attractors are apparently fractal for $20 < n < 80$, beyond which time the fractal structure is smeared out. The apparently nonfractal behavior at very short time, e.g., at $n = 10$, is due to the fact that it takes a finite amount of time for the ensemble of trajectories to settle down to the chaotic attractor. As ε is increased, the time interval for fractal snapshot attractors to be observed decreases. To measure the average transient time interval τ in which snapshot attractors are apparently fractal, the following box-counting procedure can be used. The phase-space region from which the initial conditions are chosen is first divided into a grid of boxes. At each instant of time n, the number of nonempty boxes N_n can be counted. For small time, since the trajectories have not come close to the chaotic attractor, we expect to observe a large number of occupied boxes. As the trajectories begin to settle down in the vicinity of the chaotic attractor, N_n starts to decrease, reaches a small value, and remains approximately at this value when the snapshot attractors are apparently fractal. When the effect of phase-space inhomogeneity in the driving begins to take over so that the fractal structure becomes smeared, we expect the number of nonempty boxes to increase. The time interval in which N_n remains approximately constant is taken to be the average time τ. In the τ versus $\ln \varepsilon$ plot, one observes the scaling relation (4.55) [437].

The phenomenon of transient fractal snapshot attractors has some implications to the study of fractal geometry in high-dimensional chaotic systems, i.e., systems with more than one positive Lyapunov exponent (to be treated in Chap. 8). Consider the following general class of systems,

$$\mathbf{x}_{n+1} = \mathbf{f}(\mathbf{x}_n, \varepsilon_x \mathbf{y}_n), \quad \mathbf{y}_{n+1} = \mathbf{g}(\mathbf{y}_n, \varepsilon_y \mathbf{x}_n), \qquad (4.58)$$
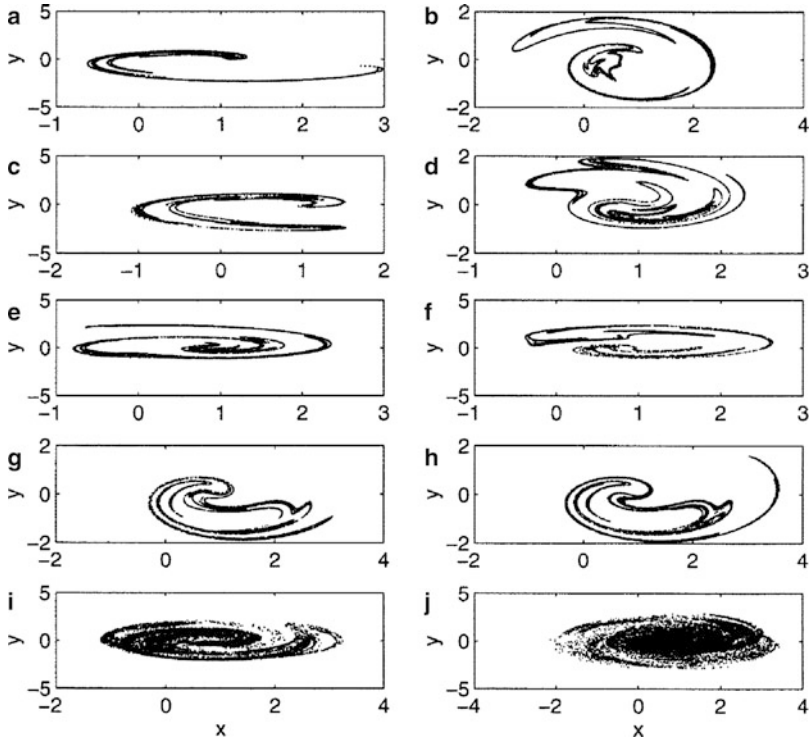
Fig. 4.23 Random Ikeda map. For (4.56) with phase-space inhomogeneity $\varepsilon = 10^{-16}$, snapshot attractors at times $n = 10, 20, \ldots, 100$; (**a**)–(**j**) [437] (Copyright 1999, the American Physical Society)

where both **f** and **g** are chaotic maps, and ε_x and ε_y are respectively two parameters characterizing the coupling from **x** to **y** and vice versa. The system setting of (4.58) arises naturally in the context of coupled chaotic oscillators. The maps **f** and **g** can be *noninvertible*. In order to study the fractal geometry of system (4.58), we assume that when the two maps are uncoupled, i.e., when $\varepsilon_x = \varepsilon_y = 0$, both maps **f**(**x**) and **g**(**y**) exhibit a chaotic attractor with one positive Lyapunov exponent and that the attractors have fractal structures in their own phase spaces **x** and **y**. When couplings are present, the coupling terms $\varepsilon_x\mathbf{y}$ and $\varepsilon_y\mathbf{x}$ can be regarded as two driving terms to the **x** and **y** dynamics, respectively. Since **y** and **x** are chaotic variables, the problem becomes effectively that of studying fractals of randomly driven chaotic systems. Intuitively we expect snapshot attractors in the **x** or **y** space to reveal the fractal structures in the absence of couplings. Nonetheless, due to coupling, the influence of driving is not homogeneous in both the **x** and **y** subspaces. *The phase-space inhomogeneity of the chaotic driving thus becomes a potential obstacle for observing low-dimensional fractal structures in high-dimensional chaotic systems.* The fact that fractal snapshot attractors have been observed in laboratory experiments such as passive particles advected on the surface of fluids [726] indicates that

the experimental condition may be such that the amount of phase-space inhomo-geneity on the fluid surface is near zero (the coupling between the dynamics in the direction orthogonal to the fluid surface and the dynamics of the passive scalar on the surface of the fluid is nearly unidirectional) or the dynamics of the driving is only weakly chaotic with a near-zero positive largest Lyapunov exponent.

Part II
Physical Manifestations of Transient Chaos

Chapter 5
Fractal Basin Boundaries

Dissipative dynamical systems often possess multiple coexisting attractors. The set of initial conditions leading to trajectories landing on an attractor is the basin of attraction of this attractor. Each attractor thus has its own basin, which is invariant under the dynamics, since images of every point in the basin still belong to the same basin. The basins of attraction are separated by boundaries. We shall demonstrate that it is common for nonlinear systems to have *fractal basin boundaries*, the dynamical reason for which is nothing but transient chaos on the boundaries. In fact, fractal basin boundaries contain one or several nonattracting chaotic sets.

We will describe the basic dynamical properties of basin boundaries and introduce the main types of fractal basin boundaries. In general, a basin boundary can be characterized by its box-counting dimension and the predictability of the final state; the latter is quantified by the *uncertainty exponent*. The issue of how fractal basin boundaries can arise as a system parameter changes will be discussed. Topics such as Wada basin boundaries (common fractal basin boundaries among at least three basins of attraction) and sporadically fractal basin boundaries (boundaries consisting of smooth curves or surfaces and nondifferentiable components) will be addressed. Attention will also be paid to riddled basins in symmetrical dynamical systems, an extreme type of basin structure that practically defies predictability of the final state. The consequences of symmetry-breaking perturbations will be discussed.

A primary goal of science is to make predictions based on a set of physical laws. A question of natural concern, due to the inevitable error in the specification of the initial condition, is whether the final state of a trajectory can be predicted from an initial condition chosen in the vicinity of a basin boundary. The various situations to be discussed in this chapter illustrate that the prediction of the final state can be extremely difficult and sometimes practically impossible even for relatively simple deterministic systems.

5.1 Basin Boundaries: Basics

To gain intuition, we consider the following simple physical system in which a particle of unit mass moves under conservative force determined by a one-dimensional potential function $V(x)$. In the two-dimensional phase space $(x, v \equiv dx/dt)$, the equations of motion are

$$\frac{dx}{dt} = v, \quad \frac{dv}{dt} = -\gamma v - \frac{dV}{dx}, \tag{5.1}$$

where we assume that there is a frictional force proportional to the velocity of the particle and $\gamma > 0$ is a dissipation parameter. To create multiple coexisting attractors, consider the class of symmetric double-well potentials, as schematically illustrated in Fig. 5.1a. The two potential wells are located at $x_\pm = \pm a$, and there is a potential barrier at $x_b = 0$. For a particle in the vicinity of a well, if the initial velocity is small such that the initial energy of the particle is not large enough for it to overcome the potential barrier, it will approach asymptotically the bottom of the well, due to the friction. Each well is thus an attractor and there are two attractors in the phase space, located at $(x, v) = (\pm a, 0)$. To understand the structure of the basins of attraction and the basin boundary, we notice that if a still particle sits precisely on the top of the
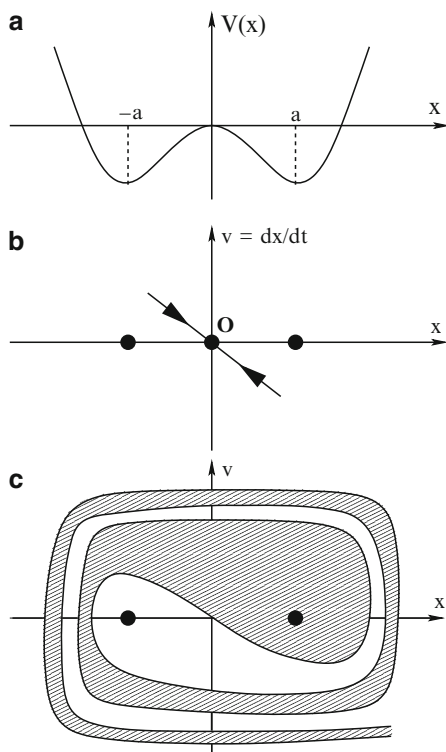

Fig. 5.1 (**a**) Double-well potential $V(x)$, (**b**) Hyperbolic point $\mathbf{O} = (0,0)$ and a linear segment of its stable manifold belonging to the boundary between the basins of attraction of the two attractors located at $(x, v) = (\pm a, 0)$. (**c**) Schematic illustration of the basin boundary and the two basins of attraction

barrier, it will remain there forever, although an arbitrarily small perturbation, either in its position or velocity, or a combination of the two, can move the particle to one of the wells. Thus the point $\mathbf{O} \equiv (0,0)$ is an unstable fixed point on the basin boundary.

Now consider a particle initially located in the right well but near $\mathbf{O}$. If it is given a small initial velocity in the $-x$ direction, it may or may not overcome the potential barrier. There then exists a velocity for which the particle stops precisely at $\mathbf{O}$. Likewise, for a particle initially in the left well but near $\mathbf{O}$, there exists a small initial velocity in the $+x$ direction that lands the particle precisely at $\mathbf{O}$. In the two-dimensional phase space, there then exists a set of initial conditions lying on a one-dimensional curve that is approximately linear[1] near $\mathbf{O}$, which approaches $\mathbf{O}$ asymptotically, as shown schematically in Fig. 5.1b. In the terms of dynamical systems, the one-dimensional curve is the stable manifold of the saddle point $\mathbf{O}$. Since points on the curve do not approach any of the two attractors, it is the basin boundary. The reasoning thus suggests that in situations in which multiple attractors coexist in invertible systems, the basin boundary is the stable manifold of some unstable invariant set on the boundary.

While the basin boundary is approximately linear near the unstable fixed point $\mathbf{O}$, it curves away from $\mathbf{O}$, due to nonlinearity. For the simple example in Fig. 5.1, the boundary crosses the x-axis an infinite number of times. This can be seen by noticing that away from an attractor, say from the one on the right well in the $+x$ direction, the force becomes attractive. There then exists a set of $\bar{x}$ values, where $\bar{x} > a$, for which the amount of force is just right to place an initially still particle right at the top of the potential barrier. The points $(\bar{x}, 0)$ are thus on the basin boundary. This leads to basins consisting of strips near the x-axis for $|x|$ large, as shown schematically in Fig. 5.1c. A basin of attraction typically possesses an infinite phase-space volume.[2]

The simple mechanical example in Fig. 5.1 illustrates that when the invariant set on the basin boundary is simple, e.g., an unstable periodic orbit, the boundary is smooth. One can imagine the situation that there is a nonattracting chaotic set on the basin boundary. Since the stable manifold of the chaotic set is a fractal set, the boundary becomes fractal.

5.2 Types of Fractal Basin Boundaries

In typical dynamical systems, i.e., systems whose behaviors are not due to any special properties such as symmetry, there are at least three known types of fractal basin boundaries, [294] described in the subsequent subsections.

---

[1] Near $\mathbf{O}$, we have $V \approx -s^2 x^2/2$. The solution to (5.1) is $x(t) = c_+ e^{\lambda_+ t} + c_- e^{\lambda_- t}$ with $\lambda_\pm = -\gamma/2 \pm (s^2 + \gamma^2/4)^{1/2}$. Thus, for $c_+ = 0$, we have $v(t) = \lambda_- x(t) \sim e^{\lambda_- t}$ and $x(t) \to 0$, $v(t) \to 0$ as $t \to \infty$, along the line $v = \lambda_- x$

[2] Choose a phase-space region R of nonzero volume that encloses an attractor. That the system is dissipative means that the inverse dynamics is volume-expanding. Since R is completely in the basin of attraction, all its preimages are in the basin as well. In the limit $t \to -\infty$, the volume of the preimage becomes infinite.
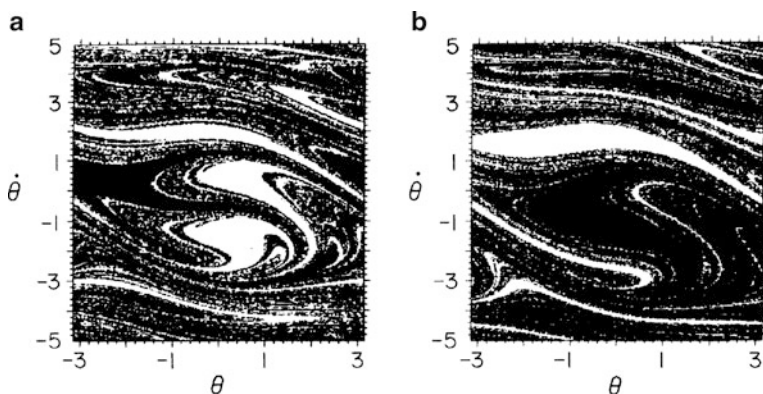
Fig. 5.2 Basins of attraction for the forced damped pendulum (5.2) on the stroboscopic surface of section $(\theta, \dot{\theta})$ defined by $t = 2n\pi$ $(n = 0, 1, \ldots)$. (**a**) For $\gamma = 0.1$, $f_0 = 1.2$, there is a fixed-point attractor at $\theta = -2.2055$ and $\dot{\theta} = 0.3729$. *Black regions* denote initial conditions that go to this attractor. There is another attractor in the *blank region*. (**b**) For $f_0 = 2.0$, the attractor in the *black* basin of attraction is located at $\theta = -0.8058$ and $\dot{\theta} = 0.9375$ [296] (with kind permission from Elsevier Science)

5.2.1 Filamentary Fractal Boundaries

Filamentary fractal boundaries are boundaries locally consisting of a Cantor set of smooth curves or surfaces. This situation typically occurs in invertible dynamical systems, where the asymptotic invariant sets on the boundary contain a chaotic saddle [491, 794]. Examples are shown in Fig. 5.2a, b for the following periodically forced damped pendulum [296]:

$$\frac{\mathrm{d}^2\theta}{\mathrm{d}t^2} + \gamma \frac{\mathrm{d}\theta}{\mathrm{d}t} + \sin\theta = f_0 \cos t, \tag{5.2}$$

where γ is a frictional coefficient and f_0 is the forcing amplitude. Such boundaries may also contain nonfractal parts, e.g., in regions about the attractors. In certain systems, these two types of boundary behaviors are intertwined on arbitrarily fine scales. For any area that contains a fractal part of the boundary, there is a subarea that contains only smooth parts of the boundary. Such fractal boundaries are called *intertwined boundaries*.

5.2.2 Continuous Fractal Boundaries

Continuous fractal boundaries are boundaries that are a continuous but nowhere differentiable curve or surface. An illustrative example is the following class of noninvertible two-dimensional maps: [511, 564]:

Fig. 5.3 For the two-dimensional map (5.3), the basin boundary between the $y = \pm\infty$ attractors. The parameters are $a = 3$ and $\lambda = 1.5$. The boundary is continuous but nowhere differentiable, as represented by a Weierstrass curve [511] (with kind permission from Elsevier Science)
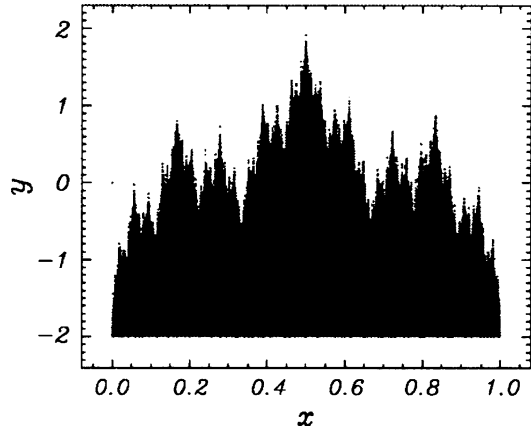
$$x_{n+1} = ax_n \bmod (1), \qquad (5.3)$$
$$y_{n+1} = \lambda y_n + \cos(2\pi x_n),$$

where $a > \lambda > 1$ and a is an integer. Since $\lambda > 1$, almost all initial conditions lead to trajectories that go to $y = \pm\infty$, which can be regarded as two attractors. The term $\cos(2\pi x_n)$ in the y-equation entails that the basin boundary near $y = 0$ can be complicated. Indeed, an explicit expression for the boundary curve can be obtained [511, 564]:

$$y = g(x) = -\sum_{j=1}^{\infty} \lambda^{-j} \cos(2\pi a^{j-1}x). \qquad (5.4)$$

A direct substitution into (5.3) shows that $y = g(x)$ is an invariant curve, i.e., $y_n = g(x_n)$ and $y_{n+1} = g(x_{n+1})$. The curve thus contains an invariant set, a chaotic repeller. The curve $y = g(x)$ is continuous but nowhere differentiable because dy/dx diverges for every value of x. The curve in (5.4) in fact has the box-counting dimension $D_0 = 2 - (\ln\lambda)/(\ln a)$, and is called a *Weierstrass curve*. An example is shown in Fig. 5.3.

5.2.3 Sporadically Fractal Boundaries

In a two-dimensional map, basin boundaries of the sporadically fractal type can be described by a function $g(x)$ that is smooth except for a set of x values of zero measure (i.e., zero length), but nevertheless has a box-counting dimension larger than 1. An illustrative example is [346, 651]

$$x_{n+1} = f(x_n), \qquad (5.5)$$
$$y_{n+1} = \lambda y_n + \sin(2\pi x_n),$$

Fig. 5.4 Example of a
sporadically fractal basin
boundary from the
two-dimensional map (5.5)
[346] (Copyright 1999, the
American Physical Society)
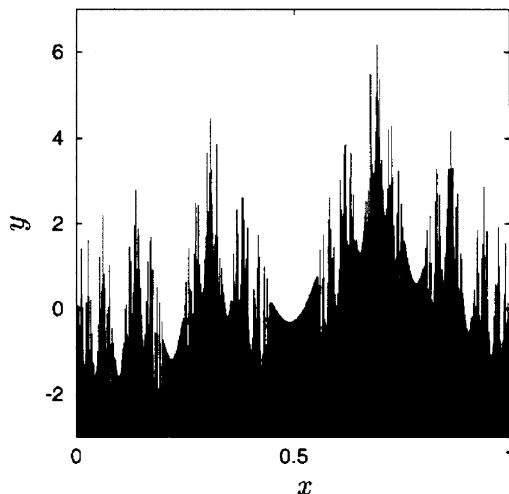
where $\lambda > 1$ and $f(x)$ is a noninvertible one-dimensional map. Part of the basin
boundary is shown in Fig. 5.4. It can be seen that the boundary consists mostly of
smooth parts but with sporadic "spikes" along the curve. Sporadically fractal basin
boundaries can arise in the context of chaotic phase synchronization in continuous-
time dynamical systems.

   If a dynamical system possesses a special property such as simple symmetry, the
topology of the basins of attraction can be quite different from those seen in typical
systems.

5.2.4 Riddled Basins

If the symmetry leads to an invariant subspace in the phase space, where there is a
chaotic attractor, the basin of attraction of this chaotic attractor can be riddled with
holes that belong to the basin of another attractor, provided that such an attractor
exists outside the invariant subspace [11]. A riddled basin thus contains no open
sets (e.g., areas in two dimensions or volumes in three dimensions), in contrast to
fractal basins. Physically, the presence of a riddled basin means that for every initial
condition that goes to the chaotic attractor in the invariant subspace, there are initial
conditions *arbitrarily nearby* that lead to trajectories to the other coexisting attrac-
tor. Prediction of the asymptotic attractor for a given initial condition thus becomes
practically impossible. An example of a riddled basin has been found experimen-
tally, as shown in Fig. 1.18. A numerically obtained riddled basin can be seen in
Fig. 5.5, in which a particle of unit mass moves in a planar potential given by

$$V(\mathbf{x}) = (1 - x^2)^2 + (y^2 - a^2)^2(x - d) + b(y^2 - a^2)^4,$$
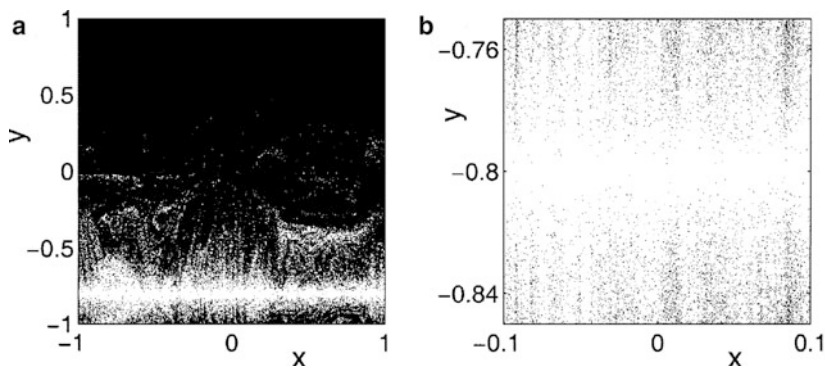
Fig. 5.5 Riddled basins. (**a**) Solution of (5.6) with parameters $f_0 = 2.3$, $\gamma = 0.05$, $\omega = 3.5$, $a = 0.8$, $b = 0.008$, and $d = -0.19$. *Black dots* represent points in the basin of the attractor at $y = a$, $v_y = 0$. (**b**) A magnification of part of (**a**) near the invariant subspace at $y = -a$ and $v_y = 0$. One can see that arbitrarily close to the attractor at $y = -a$ there are points belonging to the attractor at $y = a$ [448] (Copyright 1995, the American Physical Society)

where a, b, and d are parameters. The particle is also subject to friction and periodic forcing. The equation of motion is

$$\frac{d^2\mathbf{x}}{dt^2} = -\gamma \frac{d\mathbf{x}}{dt} - \nabla V(\mathbf{x}) + f_0 \sin(\omega t)\mathbf{e}_x, \tag{5.6}$$

where $\mathbf{x} \equiv (x, y)$, γ is the frictional coefficient, and $\mathbf{e}_x$ is the unit vector in x. There are two invariant subspaces determined by $y = \pm a$ and $v_y = 0$ in which the dynamics are governed by the forced double-well problem (Duffing's equation). For proper choices of the parameters a, b, and d, the basins of the chaotic attractors in the symmetric invariant subspaces are both riddled, as shown in Fig. 5.5. When all basins are riddled by the rest, as is the case here, the basins are said to be *intermingled* [448]. Note, however, that riddled basins rely on the symmetry of the system. A small amount of symmetry-breaking leads to a catastrophic bifurcation whereby a riddled basin immediately becomes fractal with open areas.

A recent review by Aguirre et al. [7] on fractal basin boundaries gives a comprehensive treatment of the topic and presents a large number of applications. Our focus here will be on the interplay between fractal basin boundaries and transient chaos.

5.3 Fractal Basin Boundaries and Predictability

The box-counting dimension D_{b0} can be used to characterize the boundary. Let D be the dimension of the phase space. Since the boundary divides the phase space, we have $D - 1 \leq D_{b0} \leq D$. A question of interest in a practical situation is, what are the

physical meaning and consequences of having fractal basin boundaries of dimension D_{b0}? In particular, suppose we have two D-dimensional dynamical systems with basin boundaries of dimensions $D_{b0}^{(1)}$ and $D_{b0}^{(2)}$, where $D - 1 < D_{b0}^{(1)} < D_{b0}^{(2)} < D$. What are the physical manifestations of the difference in the dimensions?

The answer to the question concerns the predictability of the asymptotic attractor, or the final state, given an initial condition and a set of parameters, specifications of which inevitably contain uncertainties. One is thus interested in how the predictability can possibly be improved when the uncertainties are reduced. For concreteness, consider the situation in which parameters of the system are fixed and the major uncertainty in specifying the system state occurs in the initial condition. Let ε be this uncertainty and let $f(\varepsilon)$ be the probability of making an error in the prediction of the final state, which depends on ε. As ε is reduced, one expects to be able to predict the final state more accurately, so $f(\varepsilon)$ will decrease. Of interest is thus the scaling relation between $f(\varepsilon)$ and ε. In general, we have [289, 511, 528]

$$f(\varepsilon) \sim \varepsilon^{\alpha}, \tag{5.7}$$

where the scaling exponent $\alpha > 0$ is called the *uncertainty exponent* [289, 511]. For fractal boundaries, α satisfies the inequality

$$\alpha < 1, \tag{5.8}$$

and $\alpha = D - D_{b0}$.

For a smooth basin boundary of dimension $D_{b0} = D - 1$ in the D-dimensional phase space, the scaling law (5.7) can be observed straightforwardly, as follows. Since an initial condition is specified with precision ε, we can associate each initial condition with a D-dimensional ball of radius ε, centered at the initial condition. If a ball is located completely in the basin of attraction of an attractor, the fates of all initial conditions in the ball are certain: they all go to this attractor. Only when the ball crosses a boundary is a wrong prediction of the final state possible, because initial conditions contained in the ball can now go to different attractors. The probability of making an error in prediction is thus proportional to the phase-space volume contained within ε of the boundary, which is $S_0 \varepsilon \sim \varepsilon$, where S_0 is the $(D - 1)$-dimensional volume of the basin boundary. We thus have

$$f(\varepsilon) \sim \varepsilon,$$

which gives $\alpha = 1 = D - D_{b0}$.

For a fractal basin boundary Σ of dimension $D - 1 \leq D_{b0} \leq D$, let $V(\varepsilon)$ be the volume of all points within distance ε of Σ. To derive a relation between the uncertainty exponent and the dimension D_{b0}, one can estimate the upper and lower bounds of $V(\varepsilon)$ using different covering schemes [511]. Specifically, imagine that we cover the phase space with a grid of boxes of edge length ε. Each boundary point $\mathbf{x}$ of Σ is in a box that typically has $3^D - 1$ neighboring boxes, points in which can be within ε of $\mathbf{x}$. That is, a point $\mathbf{y}$ within ε of $\mathbf{x}$ can be in one of the 3^D boxes (including the box that contains $\mathbf{x}$ itself), as shown schematically in Fig. 5.6. An upper bound

Fig. 5.6 A grid of boxes of size ε covering basin boundary Σ. In two dimensions, each box containing a boundary point $\mathbf{x}$ has $3^2 - 1 = 8$ neighboring boxes, which contains points that can be within ε of $\mathbf{x}$. Any point $\mathbf{y}$ within $\mathbf{x}$ can be in one of the 3^2 boxes. In a D-dimensional phase space, the number of boxes satisfying this requirement is 3^D
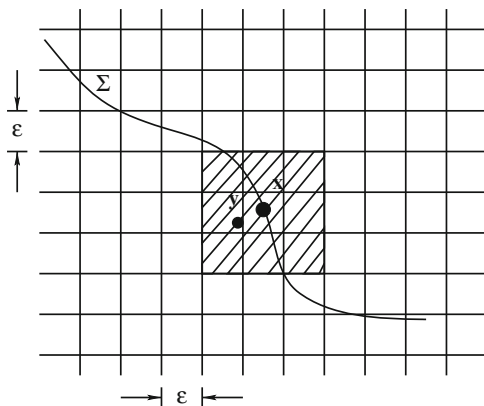
to $V(\varepsilon)$ is a coverage using $3^D N(\varepsilon)$ boxes, where $N(\varepsilon)$ is the number of ε-boxes needed to cover the boundary:

$$V(\varepsilon) \leq 3^D N(\varepsilon)\varepsilon^D. \tag{5.9}$$

Now let us choose a smaller grid covering Σ such that any two points in a box are separated by a distance at most ε, which can be achieved using boxes of edge length $\varepsilon/\sqrt{D}$. The number of such boxes required to cover the entire boundary is $N(\varepsilon/\sqrt{D})$. In this case, every box in the coverage is within distance ε to the boundary Σ. Therefore, we have

$$V(\varepsilon) \geq (\varepsilon/\sqrt{D})^D N(\varepsilon/\sqrt{D}). \tag{5.10}$$

The number $N(\varepsilon)$ of boxes needed to cover Σ scales (see (1.19)) with ε as $N(\varepsilon) \sim \varepsilon^{-D_{b0}}$. We thus have, from (5.9) and (5.10),

$$V(\varepsilon) \sim \varepsilon^{D-D_{b0}}. \tag{5.11}$$

Since $f(\varepsilon) \sim V(\varepsilon)$, we have $f(\varepsilon) \sim \varepsilon^\alpha$ with

$$\alpha = D - D_{b0}. \tag{5.12}$$

The uncertainty exponent is the difference between the dimension of the phase space and that of the boundary.

The physical interpretation of the scaling relation (5.7) is as follows. Suppose one wishes to reduce the probability of error in the prediction of the final state by improving the precision in the specification of the initial conditions. If the basin boundary is smooth so that $\alpha = 1$, a reduction in ε results in an equal amount of reduction in $f(\varepsilon)$. For fractal basin boundaries, where $\alpha < 1$, a more precise specification of the initial conditions results in a much smaller improvement in the probability of predicting the final attractor correctly. In the extreme case in which $\alpha \approx 0$, a vast reduction in the uncertainty of specifying the initial conditions will

result in almost no improvement in one's ability to determine the final state, which can occur, for example, with riddled basins. In this sense, prediction is more difficult for basin boundaries whose dimension values D_{b0} are larger [830].

The uncertainty exponent can be expressed in terms of the properties of the nonattracting chaotic set embedded in the boundary. In invertible systems, fractal basin boundaries typically contain both smooth parts and the stable manifold of a chaotic saddle. Since the dimension of the union of two sets is that of the set with higher dimension, we have $D_{b0} = D_{s0}$, where D_{s0} denotes the box-counting dimension of the stable manifold. For two-dimensional maps $(D = 2)$, we have $D_{s0} = 1 + D_0^{(1)}$, where $D_0^{(1)}$ is the partial box-counting dimension along the unstable direction. These considerations lead to

$$\alpha = 1 - D_0^{(1)} \approx \frac{\kappa}{\lambda_1}. \tag{5.13}$$

The approximate equality follows from (2.76) and the estimate $D_0^{(1)} \approx D_1^{(1)}$, and states that the uncertainty exponent can be approximated by the ratio of the escape rate and the largest Lyapunov exponent of the chaotic saddle embedded in the boundary. For the case of sporadic and riddled basins, see (5.22) and (5.29).

Numerically, the uncertainty exponent α can be calculated as follows. Given a phase-space region containing some basin boundaries, we randomly choose a pair of initial conditions $\mathbf{x}_0$ and $\mathbf{x}_0 + \boldsymbol{\varepsilon}$, where $\boldsymbol{\varepsilon}$ is a small perturbation. We then determine whether these two initial conditions go to the same attractor. If yes, $\mathbf{x}_0$ is called *certain* with respect to the perturbation ε. Otherwise, $\mathbf{x}_0$ is *uncertain*. The probability $f(\varepsilon)$ of making an error in the prediction of the final attractor can be estimated by choosing a large number N_0 of initial conditions in the phase-space region according to some smooth probability distribution. For example, if N_u is the number of uncertain initial conditions with respect to ε, we have $f(\varepsilon) \approx N_u/N_0$. The uncertainty exponent is approximated by the slope of a linear fit in the plot of $f(\varepsilon)$ versus ε on a logarithmic scale.

To illustrate the computation of the uncertainty exponent, we take the two-dimensional map [511]:

$$\theta_{n+1} = \theta_n + 1.32\sin(2\theta_n) - 0.9\sin(4\theta_n) - x_n\sin(\theta_n), \tag{5.14}$$
$$x_{n+1} = -J_0\cos(\theta_n),$$

where x can be regarded as the radial distance from the center of an annulus, θ is an angle variable such that θ and $\theta + 2\pi$ are equivalent, and J_0 is a parameter. (It is this model whose quasipotential is shown in Fig. 4.6 and which has been used for the illustration of noise-induced chaos in Fig. 4.10.) The system is invariant under the symmetry $\theta \to 2\pi - \theta$. The determinant of the Jacobian matrix is $J_0\sin^2(\theta) < 1$ (for $J_0 < 1$). There are two attractors, located at $x = -J_0$, $\theta = 0$ (denoted by A_-) and $x = J_0$, $\theta = \pi$ (denoted by A_+), respectively. The boundaries separating the basins of attraction of the two attractors are fractal, as shown in Fig. 5.7a for $J_0 = 0.3$, where black dots represent the basin of attraction of A_+. To compute the fraction $f(\varepsilon)$ of
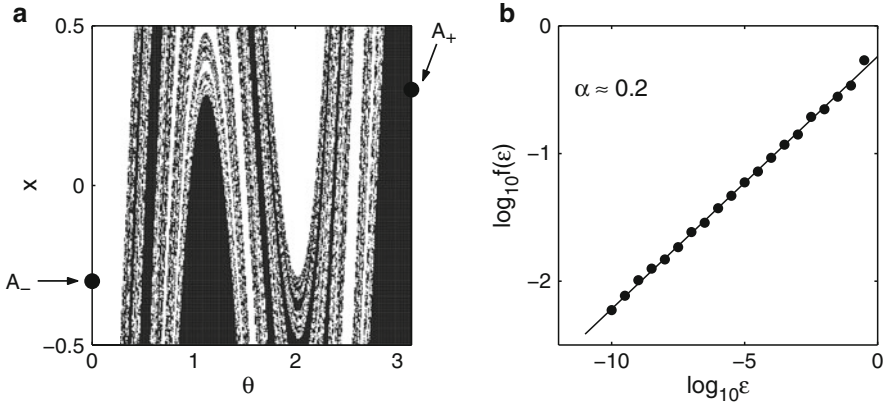
Fig. 5.7 (**a**) Fractal basin boundaries for the map (5.14) with $J_0 = 0.3$. The two point attractors are denoted by A_- and A_+, respectively. (**b**) Plot of $f(\varepsilon)$ versus ε on a logarithmic scale. The uncertainty exponent is estimated to be $\alpha \approx 0.2$ [511] (with kind permission from Elsevier Science)

uncertain initial conditions, we fix a line segment $\theta \in [0, \pi]$ at $x = 0$, choose a pair of initial conditions at ε-distance apart randomly from this line, and numerically determine whether the two initial conditions approach different attractors. For every ε-value the number N_0 of the initial-condition pairs is increased until the number of uncertain initial conditions reaches 1,000, so that $f(\varepsilon) \approx 1,000/N_0$. Figure 5.7b shows the algebraic scaling between $f(\varepsilon)$ and ε. A least-squares fit gives a slope of about 0.2, which is the uncertainty exponent α. The dimension of the basin boundary is thus $D_{b0} = 2 - \alpha \approx 1.8$.

To appreciate the value of the uncertainty exponent, say we make efforts to reduce the uncertainty in the specification of the initial condition by five orders of magnitude. Then $\alpha \approx 0.2$ means that the probability of making an error in predicting the final attractor is reduced only by a factor of $(10^{-5})^{0.2} = 0.1$. Thus the presence of the fractal basin boundaries makes predicting the final state difficult.

In experimental situations or in high-dimensional systems it is often difficult to determine the initial conditions. One can then attempt to evaluate the uncertainty exponent using random variations in the parameter space. A question is whether the value of the uncertainty exponent so obtained is the same as that obtained using random perturbations in initial conditions. The answer is affirmative because a parameter variation can be regarded as being equivalent to a perturbation in the initial conditions. Specifically, consider a D-dimensional map $\mathbf{x}_{n+1} = \mathbf{f}(\mathbf{x}_n, \mathbf{p})$, where $\mathbf{p}$ denotes a set of parameters. Assume that the system under the initial condition $\mathbf{x}_0$ and parameter value $\mathbf{p}_0$ goes to one attractor. The standard approach is to take a slightly different initial condition $\mathbf{x}'_0 = \mathbf{x}_0 + \Delta\mathbf{x}$ at fixed parameter $\mathbf{p}_0$. The image point is then $\mathbf{f}(\mathbf{x}'_0, \mathbf{p}_0)$. Alternatively, one can take a slightly different set of parameter values $\mathbf{p}'_0 = \mathbf{p}_0 + \Delta\mathbf{p}$, at the same initial condition, which leads to $\mathbf{f}(\mathbf{x}_0, \mathbf{p}'_0)$. The image points are identical if $\partial\mathbf{f}/\partial\mathbf{p}|_{\mathbf{x}_0,\mathbf{p}_0} \cdot \Delta\mathbf{p} = \partial\mathbf{f}/\partial\mathbf{x}|_{\mathbf{x}_0,\mathbf{p}_0} \cdot \Delta\mathbf{x}$. We expect then the uncertainty exponents computed with respect to perturbations in the parameter and

in the phase space to be identical. In fact, one of the first determinations of fractal basin boundaries [528] was done using parameter perturbations. This parameter and phase-space equivalence was also used to study basin structures in coupled-map lattice systems [462–464].

## 5.4 Emergence of Fractal Basin Boundaries

5.4.1 Basin Boundary Metamorphoses and Accessible Orbits

The typical dynamical mechanism that creates fractal basin boundaries from a smooth boundary is homoclinic or heteroclinic tangencies, as schematically illustrated in Fig. 5.8, where p is a bifurcation parameter. Throughout the bifurcation there is an unstable periodic orbit (e.g., a saddle fixed point), denoted by S. The stable manifold of S is the basin boundary between an attractor to its right (shown) and another attractor (not shown). As p is changed through the bifurcation point p_c, both the basin boundary and the attractor evolve. For $p < p_c$, the basin boundary is smooth (Fig. 5.8a). Homoclinic tangencies between the stable and the unstable manifolds of S occur at p_c, as shown in Fig. 5.8b. For $p > p_c$, the homoclinic crossings between the stable and the unstable manifolds of S imply a Smale horseshoe-type dynamics (Sect. 1.2.2.1) in the vicinity of S. As a result, a chaotic saddle is created that contains the set of intersecting points between the stable and the unstable manifolds. The stable foliation, and equivalently the basin boundary, becomes fractal. The bifurcation from smooth to fractal basin boundaries is called a *smooth-to-fractal basin boundary metamorphosis* [296].

A basin boundary metamorphosis is typically accompanied by a change in the unstable periodic orbits on the basin boundary that is *accessible* to the attractor [296]. A boundary point **P** is accessible from a region if there is a curve of *finite length* that connects **P** to a point in the interior of the region such that no point on the curve belongs to the boundary except point **P**. From Fig. 5.8, we see that the saddle fixed point S is accessible to the attractor for $p < p_c$. However, for $p > p_c$, the fractal foliations of the stable manifold entail that it is not possible to connect S to a point on the attractor through a curve of finite length. The fixed point S is thus inaccessible to the attractor for $p > p_c$. Instead, a new unstable periodic orbit, one of the infinite number of those embedded in the chaotic saddle, becomes accessible to the attractor.

The change in the accessible unstable periodic orbits can be demonstrated [296] using the Hénon map with a positive Jacobian J. The map has one attractor at infinity. For fixed J, as the bifurcation parameter a is increased through the value $a_1 = -(J+1)^2/4$, a saddle-node bifurcation occurs, creating an attracting fixed point and a saddle point, which separate from each other for $a > a_1$. For a slightly above a_1, the map has two attractors: one at the attracting point and another at infinity. The basin boundary is the stable manifold of the saddle, as shown in Fig. 5.9a for $a = 1.150$. The saddle point is accessible to the period-1 attractor. As a is increased

Fig. 5.8 Dynamical mechanism that creates fractal basin boundaries. (**a**) Smooth basin boundary for $p < p_c$, (**b**) homoclinic tangencies for $p = p_c$, and (**c**) homoclinic crossings for $p > p_c$. The stable foliations and, equivalently, the basin boundaries, become fractal for $p > p_c$
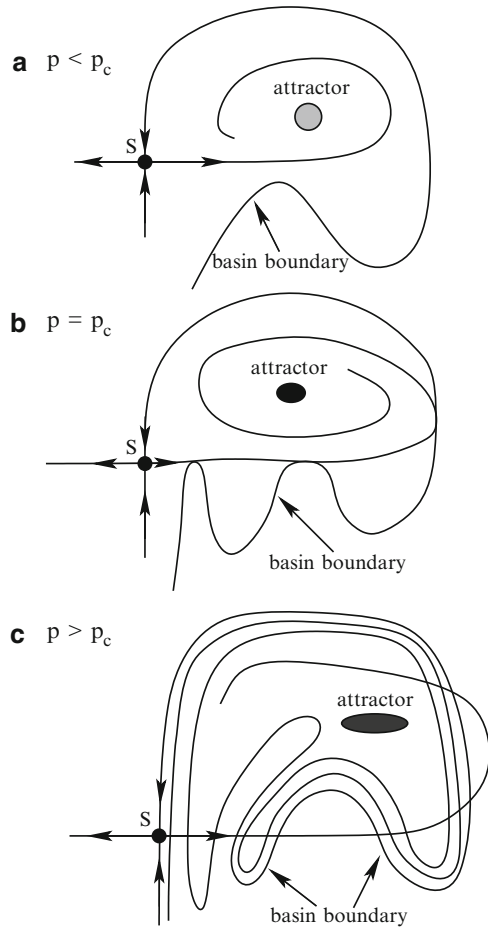
further, a metamorphosis occurs, which converts the smooth boundary into a fractal. An example of the fractal basin boundary is shown in Fig. 5.9b for $a = 1.395$. We see that, because of the fractal foliation of the basin boundary, the original saddle fixed point is no longer accessible to the attractor, which for this parameter value has already evolved into a period-2 attractor through a period-doubling bifurcation. The accessible orbit on the boundary becomes a hyperbolic periodic orbit of period 4.

We can imagine that as the parameter is varied further, this new accessible unstable periodic orbit can also have homoclinic tangencies, after which it becomes inaccessible. The subsequent homoclinic intersections mean that the basin boundary must necessarily undergo another metamorphic change to a fractal one that is distinct from the original boundary. This is a *fractal-to-fractal basin boundary metamorphosis*, after which a different unstable periodic orbit on the boundary becomes accessible, as illustrated in Fig. 5.9c for $a = 1.405$. We see that the fractal boundary appears to be quite distinct from that in Fig. 5.9b, and the originally accessible period-4 orbit in Fig. 5.9b is replaced by a period-3 orbit in Fig. 5.9c.
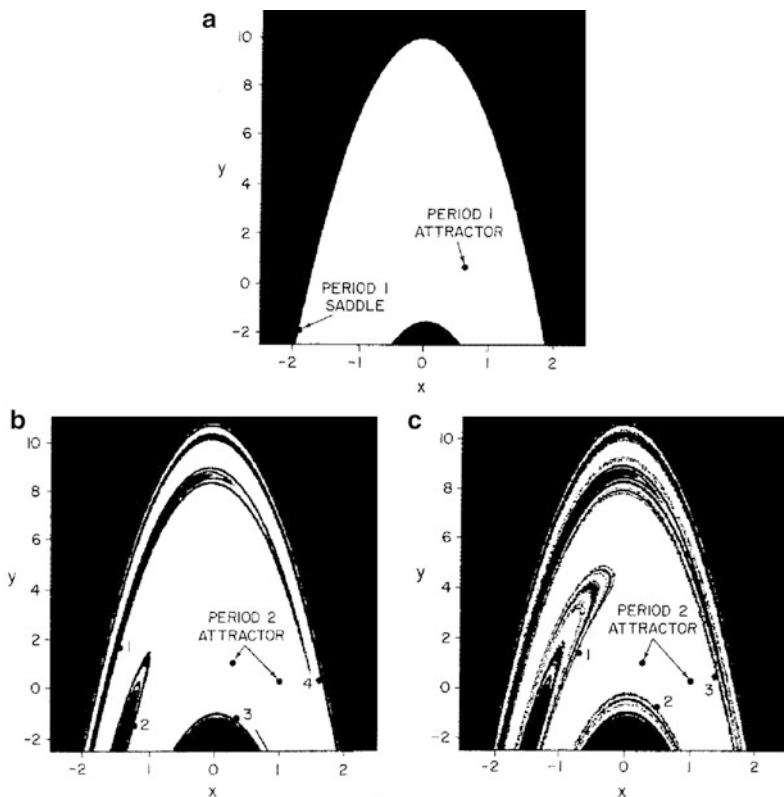
Fig. 5.9 Basin boundary metamorphosis. For the Hénon map $(x_{n+1}, y_{n+1} = (a - x_n^2 - Jy_n, x_n)$ for $J = 0.3$, (**a**) smooth basin boundary for $a = 1.150$, where the accessible orbit on the boundary is the saddle fixed point created at a saddle-node bifurcation. (**b**) Fractal basin boundaries for $a = 1.395$ after a smooth-to-fractal basin boundary metamorphosis. The accessible orbit on the boundary is now a period-4 orbit. (**c**) Qualitatively different fractal basin boundaries after a fractal-to-fractal boundary metamorphosis with a new period-3 accessible orbit for $a = 1.405$. The numerals in (**b**) and (**c**) denote the accessible periodic orbits in the sequences of iterations [296] (with kind permission from Elsevier Science)

5.4.2 Dimension Changes at Basin Boundary Metamorphoses

As the basin boundary changes characteristically, e.g., from smooth to fractal or from fractal to fractal, we expect the dimension of the boundary to change *abruptly*. This can be seen qualitatively from Fig. 5.9a–c. Let a_{sf} and a_{ff} denote the parameter values for the smooth-to-fractal and the fractal-to-fractal boundary metamorphoses that create the fractal basin boundaries in Fig. 5.9b and c, respectively. For $a < a_{sf}$ (Fig. 5.9a), the boundary is a smooth curve in the two-dimensional phase space, so its box-counting dimension is $D_{b0} = 1$. For $a_{sf} < a < a_{ff}$ (Fig. 5.9b), the boundary is locally a Cantor set of smooth curves, so D_{b0} is between one and two. For $a > a_{ff}$ (Fig. 5.9c), the dimension is also a fractional (but distinct) value between one and two.
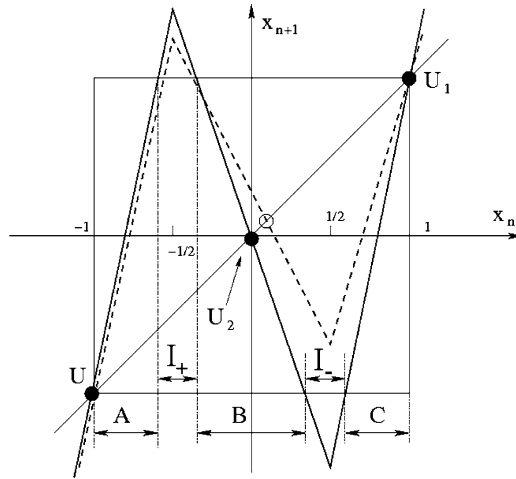
Fig. 5.10 One-dimensional map $x_{n+1} = f(x_n)$ with a positive peak at $x = -1/2$, which is always above 1 ($f(-1/2) > 1$), and a negative peak at $x = 1/2$. As the bifurcation parameter p changes from p_1 to p_2, the negative peak moves from $f(1/2) > -1$ at $p = p_1$ (*dashed lines*) to $f(1/2) < -1$ at $p = p_2$ (*solid lines*). A smooth-to-fractal basin boundary metamorphosis occurs at $p = p_{sf}$ when $f(1/2) = -1$

To understand the abrupt dimension change associated with a basin boundary metamorphosis, an analyzable, piecewise linear, one-dimensional map $f(x)$ was introduced [578], as shown schematically in Fig. 5.10. The map has a positive peak at $x = -1/2$, which remains above one, $f(-1/2) > 1$, and a negative peak at $x = 1/2$ whose height varies as a bifurcation parameter p changes. In particular, say for $p = p_1$ the negative peak is above -1 (dashed line). As p is increased from p_1 to p_2, the negative peak moves to below -1 (solid line). The map has three unstable fixed points: U at $x = -1$, U_1 at $x = 1$, and U_2 in the vicinity of $x = 0$. As p varies in the interval $[p_1, p_2]$, U and U_1 are fixed, but the location of U_2 can shift about $x = 0$. In this parameter interval of interest, the map has two attractors: one at $-\infty$ and another at $x = +\infty$. Since all points in $x < -1$ map to the attractor at $-\infty$ and all points in $x > +1$ go to the attractor at $+\infty$, the basin boundary must lie in the interval $[-1, 1]$.

Let p_{sf} denote the parameter value for which $f(1/2) = -1$, where $p_1 < p_{sf} < p_2$. For $p < p_{sf}$, since the negative peak at $x = 1/2$ stays within the square in Fig. 5.10, the basin of the attractor at $-\infty$ is $x < -1$. The basin of the attractor at $+\infty$ consists of the interval $x > 1$ and almost all points in $(-1, 1)$ except a Cantor set of measure zero. Let I_+ be the primary escape interval in $(-1, 1)$ such that $f(x) > 1$, which maps to $+\infty$. All preimages $\{f^{-n}(I_+)\}$ ($n = 1, \dots$) also map to $+\infty$. What is left in $(-1, 1)$ is a chaotic repeller. Despite the presence of the repeller, for $p < p_{sf}$ the basin boundary between the basins of the $\pm\infty$ attractors is a single point: $x = -1$.

As p increases through p_{sf}, the negative peak of $f(x)$ pokes through $f = -1$. Let I_- be the primary escape interval in $x \in (-1, 1)$ such that $f(x) < -1$, which maps to the attractor at $-\infty$. In addition, all preimages of I_- also map to $-\infty$. The basin of

attraction of the $-\infty$ attractor now consists of $x < -1$ and all preimages of I_-. The preimages of I_+ and I_- intertwine in a complicated way, and the chaotic repeller in $(-1,1)$ that maps neither to $-\infty$ nor to $+\infty$ becomes the new basin boundary, which is a fractal. We see that there is a smooth-to-fractal basin boundary metamorphosis at $p = p_{\text{sf}}$, after which the basin boundary, which was originally the point $x = -1$, jumps far into the interior of the $+\infty$ basin. For p slightly larger than p_{sf}, there are subintervals of the $-\infty$ basin in $(-1,1)$, which for $p < p_{\text{sf}}$ were entirely in the $+\infty$ basin. At the metamorphosis, the dimension of the basin boundary changes abruptly from zero to a fractional value. In particular, as p approaches p_{sf} from above, the box-counting dimension of the basin boundary is the dimension $D_{\text{b0}}^{\text{sf}}$ of the invariant Cantor set in the limit of p's approaching p_{sf} from below. As p increases further, the dimension decreases as the Cantor set becomes "thinner" in the interval $[-1,1]$. The behavior of the dimension of the basin boundary through the metamorphosis is schematically illustrated in Fig. 5.11.

The dimension D_{b0} of the fractal basin boundary for $p \geq p_{\text{sf}}$ can be calculated as follows. Let $N(\varepsilon)$ be the number of intervals of size ε needed to cover the boundary. As specified in Fig. 5.10, let A, B, and C denote the subintervals $[-1, -1/2 - \varepsilon_2/2]$, $[-1/2 + \varepsilon_2/2, 1/2 - \varepsilon_1/2]$, and $[1/2 + \varepsilon_1/2, 1]$, and let $N_A(\varepsilon)$, $N_B(\varepsilon)$, and $N_C(\varepsilon)$ be the number of boxes of size ε needed to cover the subsets of boundary points in these subintervals, respectively. We have

$$N(\varepsilon) = N_A(\varepsilon) + N_B(\varepsilon) + N_C(\varepsilon). \tag{5.15}$$

Self-similarities stipulate

$$N_A(\varepsilon) = N\left[\frac{\varepsilon}{1/4 - \varepsilon_2/4}\right], \tag{5.16}$$

$$N_C(\varepsilon) = N\left[\frac{\varepsilon}{1/4 - \varepsilon_1/4}\right],$$

$$N_B(\varepsilon) = N\left[\frac{\varepsilon}{(1/4 - \varepsilon_2/4) + (1/4 - \varepsilon_1/4)}\right].$$

Fig. 5.11 Schematic dependence of the box-counting dimension D_{b0} of the basin boundary through a smooth-to-fractal boundary metamorphosis
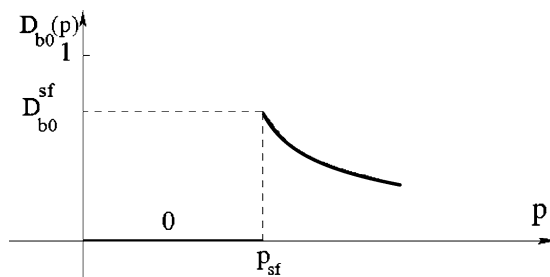
Substituting these into (5.15) and making use of the scaling $N(\varepsilon) \sim \varepsilon^{-D_{b0}}$, we obtain

$$\left(\frac{1}{4} - \frac{\varepsilon_1}{4}\right)^{D_{b0}} + \left(\frac{1}{2} - \frac{\varepsilon_1 + \varepsilon_2}{4}\right)^{D_{b0}} + \left(\frac{1}{4} - \frac{\varepsilon_2}{4}\right)^{D_{b0}} = 1. \qquad (5.17)$$

As $p \to p_{sf}$ from above, $\varepsilon_1 \to 0$, and hence the value of the box-counting dimension $D_{b0}^{sf}(\varepsilon_2)$ for $p = p_{sf} + 0$ follows from (5.17) with $\varepsilon_1 = 0$. For p slightly above p_{sf}, so that $\varepsilon_1 > 0$ is small, we can write $D_{b0} = D_{b0}^{sf} - \eta$, where η is small. Substituting this into (5.17) and expanding for small ε_1 and η yields

$$D_{b0} = D_{b0}^{sf} - K(\varepsilon_2)\varepsilon_1, \qquad (5.18)$$

where $K(\varepsilon_2)$ is a smooth function of ε_2 [578]. Assuming smooth dependencies of ε_1 and ε_2 on the system parameter p for $p > p_{sf}$, we see from (5.18) that D_{b0} varies smoothly with p. For instance, suppose ε_1 has a power-law dependence on p: $\varepsilon_1(p) \sim (p - p_{sf})^\gamma$, where $\gamma > 0$. Then this dependence is reflected in $D_{b0}^{sf} - D_{b0} \sim (p - p_{sf})^\gamma$, for $p > p_{sf}$.

5.4.3 A Two-Dimensional Model

The structure of fractal basin boundaries and basin boundary metamorphoses in two dimensions can be understood by constructing invertible-map models based on the horseshoe dynamics [578], such as the one shown schematically in Fig. 5.12. Consider the rectangle ABFE, outside which there are two attractors, denoted by L and R. All initial conditions to the left of the vertical line AB lead to trajectories approaching the attractor L, and all initial conditions to the right of EF go to the attractor R. In ABFE, there are three unstable periodic orbits, denoted by S_1, S_2, and S_3. The action of the dynamics is that of a double horseshoe, i.e., the rectangle is squeezed vertically, stretched horizontally, and placed back into the original rectangular region, forming a double **S**-shape. As a system parameter p changes from p_1 (Fig. 5.12a) to p_2 (Fig. 5.12b) and to p_3 (Fig. 5.12c), a smooth-to-fractal basin boundary metamorphosis occurs for p_{sf} ($p_1 < p_{sf} < p_2$), and a fractal-to-fractal basin boundary metamorphosis occurs for p_{ff} ($p_2 < p_{ff} < p_3$). Throughout the parameter range, the stable and the unstable manifolds of S_3 cross each other homoclinically. As can be argued below, the smooth-to-fractal boundary metamorphosis at p_{sf} is induced by the homoclinic tangencies between the stable and the unstable manifolds of S_1, while the fractal-to-fractal basin boundary metamorphosis is induced by those between the stable manifold of S_2 and the unstable manifold of S_3.

In Fig. 5.12a, the unstable manifolds of S_2 and S_3 cross the stable manifold of S_3, so there is a vertical bar UR that maps to the region DR located to the right of the vertical line EF. As a result, all initial conditions in the rectangle CDFE, except for a set of measure zero, map asymptotically to the right of EF and approach the attractor R. We also see that the unstable manifolds of S_1 and S_2 cross the stable manifold of S_2, and hence the vertical strip VR maps to the region CR to the right of
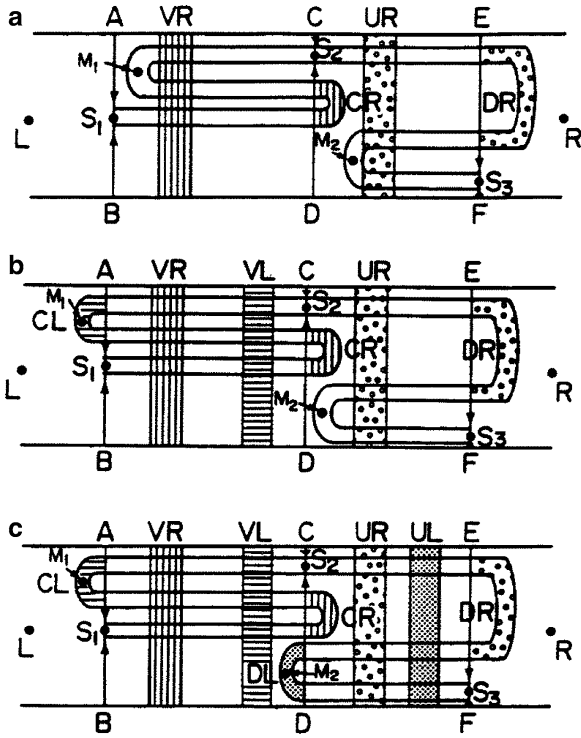
Fig. 5.12 A two-dimensional horseshoe model, where L and R are two attractors, and $S_{1,2,3}$ are saddle points. The double S-shaped band represents the image of rectangle ABFE under the map. (**a**) For $p = p_1 < p_{sf}$, the *vertical line* AB is the smooth basin boundary and S_1 is then accessible to the attractor R. (**b**) For $p_{sf} < p = p_2 < p_{ff}$, the basin boundary consists of a Cantor set of *vertical lines* in the rectangle ABDC and the accessible orbit to R is replaced by S_2. (**c**) For $p = p_3 > p_{ff}$, the basin boundary is a Cantor set of *vertical lines* in the larger rectangle ABFE. In this case, S_2 is no longer accessible to R. The newly accessible orbit on the basin boundary is S_3 [578] (with kind permission from World Scientific Publishing Co.)

the vertical line CD. The consequence is that all initial conditions in ABDC, except for a set of measure zero, map to the right of CD. Combining the dynamics on the rectangles CDFE and ABDC so described, we see that all initial conditions in the larger rectangle ABFE, except for a set of measure zero, result in trajectories that asymptotically go to the attractor R. In this case $p = p_1 < p_{sf}$, and the boundary between the basins of attraction of L and R is AB, the stable manifold of S_1, which is smooth. Furthermore, S_1 is an unstable periodic orbit on the basin boundary that is accessible to the attractor R.

For $p = p_{sf}$ (not shown), homoclinic tangencies between the stable and the unstable manifolds of S_1 occur, resulting in subsequent homoclinic crossings for $p > p_{sf}$, as shown in Fig. 5.12b. In this case, the vertical strip VL maps to the region CL to the left of AB and goes to the attractor L. However, the vertical strip VR still maps

to the right of CD, which eventually goes to the attractor R. In ABDC, all initial conditions (except for a set of measure zero) go either to the attractor R or to the attractor L. The vertical strips that approach asymptotically R and L define two horizontal Cantor sets that intertwine in a fractal manner. The basin boundary is thus fractal with a dimension between 1 and 2. Because of the fractal boundary, S_1 is no longer accessible to R for $p > p_{sf}$. The newly accessible periodic orbit to R is S_2.

As p increases further, we can imagine that for $p_2 < p = p_{ff} < p_3$, the unstable manifold of S_3 becomes heteroclinically tangent to the stable manifold of S_2 (the vertical line CD). As shown in Fig. 5.12c, the subsequent heteroclinic crossings stipulate that the vertical bar UL in CDFE maps to the region DL to the left of CD. As a result, not only a set of vertical strips in ABDC but also such a set in CDFE map to the attractor L. However, there are vertical strips in ABDC and CDFE that map to the attractor R. We see that as p increases through p_{ff}, the fractal basin boundary originally confined to the small rectangle ABDC extends suddenly into the rectangle CDFE, causing a sudden increase in the box-counting dimension of the basin boundary from one fractional value to another between 1 and 2. After the heteroclinic tangencies, S_2 is no longer accessible to the attractor R. For $p > p_{ff}$, the accessible orbit to R on the basin boundary is S_3.

5.5 Wada Basin Boundaries

Our discussion so far has been restricted to situations in which there are two coexisting basins of attraction. When a dynamical system possesses more than two coexisting attractors, a type of fractal basin boundary, namely Wada basin boundaries [406, 558–561, 613], can arise. For such a case, every boundary point of one basin of attraction is simultaneously a boundary point of the other basins.

To imagine a Wada basin boundary, take the map of the continental United States and consider the boundaries between the states. Almost all boundary points are common to two states, but there are a few dozen of points that are common to three states, and there exists a single boundary point that is shared by four states (the Four-State Corner bordering Arizona, Utah, Colorado, and New Mexico). In the realm of nonlinear dynamical systems, more complicated situations can arise: the set of boundary points that are common to more than two basins of attraction can be fractal. The history and the topology of Wada basins are presented in detail in the review of Aguirre et al. [7].

To give an example, we examine the forced Duffing's oscillator for parameters where on the stroboscopic map, there are two fixed-point attractors, and an attractor at infinity. The basins of attraction of these three attractors are shown in Fig. 5.13 in three different colors. The Wada property of the basin boundaries can be seen, since successive magnifications of any region containing the boundary exhibit all three colors. Another example from the forced damped pendulum is shown in Fig. 5.14.
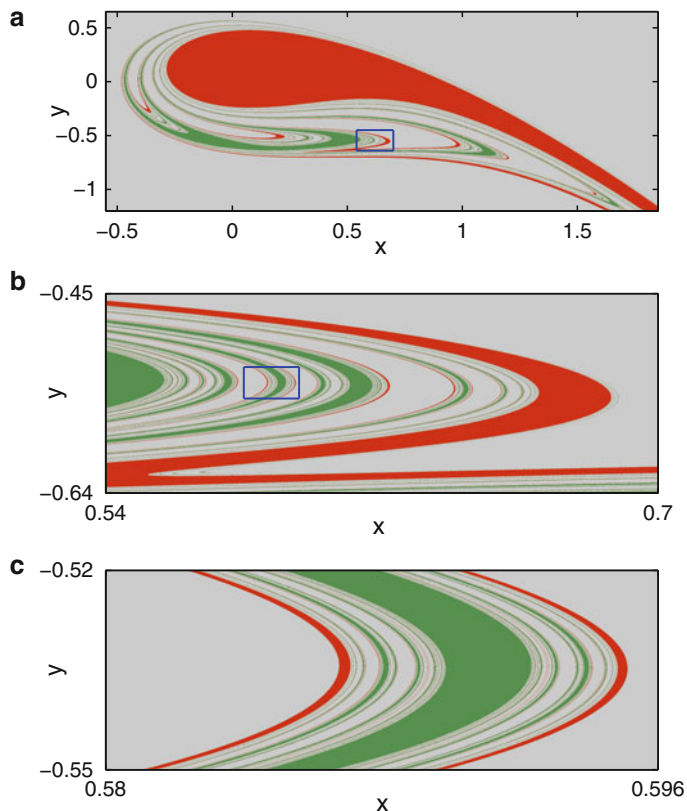
Fig. 5.13 Wada basin boundary for the forced Duffing's oscillator $\ddot{x} + 0.1\dot{x} + x - x^2 = 0.06\sin(0.8t)$ on the stroboscopic section $(x, y \equiv \dot{x})$, where (**b**) is a magnification of the box in (**a**), and (**c**) is the magnification of the box in (**b**) (Figure by Y. Do.)

For two-dimensional invertible maps, or equivalently, three-dimensional flows, the mechanism for Wada basin boundaries is well understood, due to the work of Kennedy, Nusse, and Yorke [406, 558–561]. In particular, Kennedy and Yorke proved a theorem [406] stating that if **p** is a periodic point on the basin boundary, and if the following two conditions are satisfied, (1) its unstable manifold intersects every basin, and (2) its stable manifold is dense in each of the basin boundaries, then the basins have the Wada property. This can be intuitively understood by referring to Fig. 5.15, where there are K coexisting basins, denoted by $B_1, B_2, \ldots, B_K$. Suppose **p** is a periodic point on the boundary of B_1 that is accessible to B_1. Let $W^s(\mathbf{p})$ and $W^u(\mathbf{p})$ be the stable and the unstable manifolds of **p**, where $W^s(\mathbf{p})$ is the basin boundary of B_1. Now arbitrarily choose a point $\mathbf{x} \in W^s(\mathbf{p})$ and imagine a circle $C_\varepsilon(\mathbf{x})$ of radius ε centered at **x**. Since $W^u(\mathbf{p})$ intersects every basin, $C_\varepsilon(\mathbf{x})$ must contain points of every basin, which can be seen by considering a one-dimensional curve segment D_k in the basin B_k that intersects $W^u(\mathbf{p})$, for $k = 1, \ldots, K$. Under inverse iterations of the map, the images of the curves will be arbitrarily close to
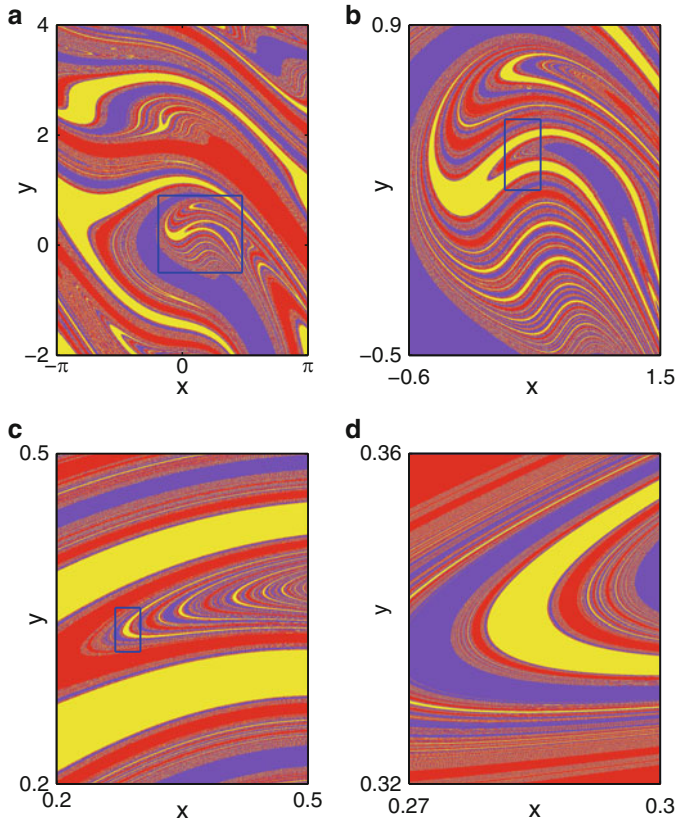
Fig. 5.14 Wada basin boundary for the forced damped pendulum $\gamma = 0.2, f_0 = 1.66$ in (5.2), on the stroboscopic section $(x, y \equiv \dot{x})$. At these parameters, three attracting limit cycles coexist. Panels (**b, c, d**) are successive magnifications of boxes in (**a, b, c**), respectively (Figure by Y. Do)

Fig. 5.15 Schematic illustration of the setting for establishing the Wada property. See text for details

the stable manifold of $\mathbf{p}$ and therefore be in $C_\varepsilon(\mathbf{x})$ [547]. Thus, the boundary of B_1 must be the boundaries of all other basins. Since $W^s(\mathbf{p})$ is dense in each of the basin boundaries, all boundaries are common to all basins, and hence the Wada property is fulfilled.
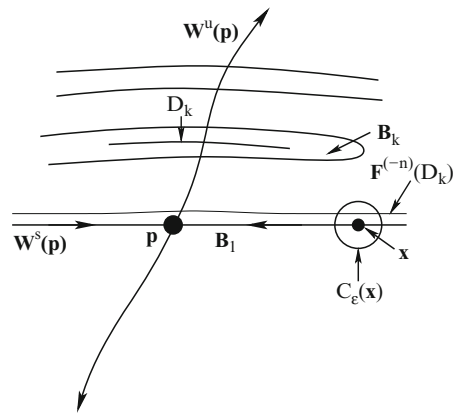
Computationally, to verify condition (1), one can plot a piece of the unstable manifold, trace it under the dynamics, and determine whether it intersects all basins of interest. Condition (2) is more difficult to verify from numerical traces of the stable manifold. To overcome these difficulties, Nusse and Yorke proposed the construction of *basin cells*, which leads to numerically verifiable conditions guaranteeing that the boundary of a basin is a Wada basin boundary [559, 560].

To explain the idea of basin cells, consider an invertible dissipative map $\mathbf{f}$ in the plane. Traditionally, the basin of attraction of an attractor is defined to be the set of points that approach the attractor asymptotically. Since there has been no rigorous way to determine whether an attractor is chaotic or whether there are multiple coexisting attractors, this concept of "basin" is in principle ill defined. Nusse and Yorke redefined a "basin" as the set of points that enter a trapping region [559, 560]. A compact region Q is a *trapping region* if $\mathbf{f}(Q) \in Q$ and $\mathbf{f}(Q) \neq Q$. These two conditions guarantee that a trajectory entering a trapping region does not leave the region, and there must then be at least one attractor inside. The basin of the trapping region Q is the set of points that map into the interior of Q. A trapping region may contain invariant sets such as chaotic saddles; that is, there can be points in the region whose trajectories do not converge to an attractor. Trapping regions of practical importance are those having piecewise smooth boundaries that consist of finitely many smooth curve segments. If a trapping region Q is constructed such that (1) there is an unstable periodic orbit on its boundary and (2) the boundary consists of pieces of the stable and the unstable manifolds of the periodic orbit, then Q is a *basin cell*. Although there is an infinite number of unstable periodic orbits on a fractal basin boundary, only a few may be "qualified" to generate a basin cell. Thus, in order to have a basin cell, the unstable periodic orbit on the cell boundary needs to be chosen carefully [559, 560].

Figure 5.16 illustrates two types of basin cells that are topologically equivalent to some basin cells that can be explicitly constructed from the system of forced damped pendulum in parameter regions with Wada basin boundaries shown in Fig. 5.14a–d. Let $\mathbf{P}$ denote the unstable periodic orbit that generates a basin cell C_P. As shown in Fig. 5.16, for a periodic point $\mathbf{p}$ of $\mathbf{P}$, its unstable manifold can form an *arc* that starts from $\mathbf{p}$ and ends at a corner point, an intersection point between the stable and the unstable manifolds of $\mathbf{p}$. Such an arc is outside the basin cell (except the endpoints). The union of all supporting arcs, one for each periodic point $\mathbf{p}$ of $\mathbf{P}$, is called the *scaffolding* of the basin cell C_P [559, 560]. For instance, for the cell in Fig. 5.16a, the scaffolding consists of the union of two supporting arcs, while in Fig. 5.16b, the scaffolding is the union of three supporting arcs. With such a geometric construction, Nusse and Yorke proved the result that if the scaffolding of C_P intersects at least two other basins, the boundary of the basin cell C_P is a Wada basin boundary. This result is remarkable because all the quantities and conditions
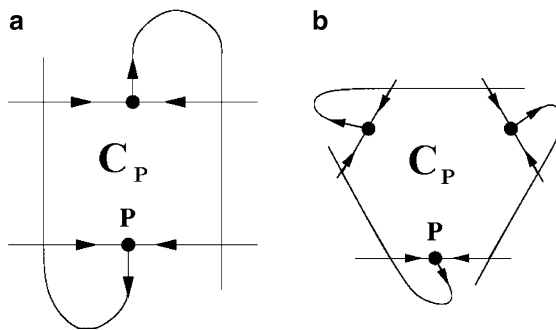
Fig. 5.16 Schematic illustration of two types of basin cells that can be constructed from three-dimensional flows with Wada basin boundaries. In (**a**), the basin cell is generated by an unstable periodic orbit of period 2. In (**b**), the cell-generating periodic orbit has period 3. See [559, 560]

are numerically verifiable. Using this result, one can prove that the basin boundaries such as those in the forced Duffing's oscillator (Fig. 5.13) and in the forced damped pendulum (Fig. 5.14) are Wada basin boundaries [559, 560].

A natural question is how Wada basin boundaries can arise as a system parameter changes. One route was discovered by Nusse et al. [558], which is by a saddle-node bifurcation on a fractal basin boundary. Specifically, if the system under consideration already has two coexisting attractors with a fractal basin boundary, then a saddle-node bifurcation on the boundary can create a third attractor and a third basin of attraction. In this case, if a basin cell can be constructed that contains the third attractor and if the scaffolding of an unstable periodic orbit on the boundary of the cell intersects the original two basins, the fractal basin boundary becomes Wada.

Saddle-node bifurcation on a fractal basin boundary can in fact result in an extreme form of indeterminacy in dynamical systems, as pointed out by Thompson [780–782], who asked what happens to an orbit initially placed on a periodic attractor (node) when it is destroyed via slow variation of a parameter through a saddle-node bifurcation. He discovered that if there are at least two other attractors (in addition to the periodic attractor to be destroyed through the saddle-node bifurcation) with a fractal basin boundary between their basins of attraction, and if the saddle is located on the boundary (in fact Wada), then the bifurcation can be *indeterminate* in the following sense. After the system drifts through the bifurcation, to which attractor the orbit goes depends sensitively on small effects such as noise, computer roundoff, and the way the parameter is changed. From our discussion, we see that this extreme type of indeterminacy is closely related to the occurrence of a Wada basin boundary. In particular, say μ is the bifurcation parameter, and as μ is decreased through the critical value μ_0, a saddle-node bifurcation occurs. Assume that two other attractors exist in a parameter interval about μ_0 with a fractal basin boundary. Thus for $\mu_0 - \varepsilon_1 < \mu < \mu_0$ there are three attractors with a Wada basin boundary, where $\varepsilon_1 > 0$ is a small constant. Now imagine that μ increases from this situation through μ_0. For $\mu_0 < \mu < \mu + \varepsilon_2$, where $\varepsilon_2 > 0$ is small, there are only two attractors with a fractal basin boundary. Thompson's result

indicates that in a situation in which random perturbations or computational errors are present, as μ adiabatically increases through μ_0, it is fundamentally impossible to determine where an orbit placed on the node (attractor) for $\mu_0 - \varepsilon_1 < \mu < \mu_0$ would go.

5.6   Sporadically Fractal Basin Boundaries

Sporadically fractal basin boundaries have the character of a bounded curve, say $y = g(x)$, such that $g(x)$ is a differentiable (or smooth) function except for a set of x values of zero measure. Furthermore, the nondifferentiable set of x values is a fractal set with dimension less than one. The curve thus has a dimension between one and two. This type of basin boundary was discovered by Rosa et al. [651, 652] and was subsequently analyzed rigorously by Hunt et al. [346]. It was conjectured that sporadically fractal basin boundaries exist in typical dynamical systems of phase-space dimension at least two for noninvertible maps, at least three for invertible maps (thus at least four for flows).

In order to highlight the relevance of sporadically fractal basin boundaries to physical situations, in what follows we describe the occurrence of this type of boundary in the context of chaotic phase synchronization in systems described by differential equations. We then discuss a mathematical model to understand the dynamical origin and properties of these exotic basin boundaries.

5.6.1   Chaotic Phase Synchronization

Chaotic phase synchronization was discovered by Rosenblum, Pikovsky, and Kurths in 1996 [653] and has since become an active area of research (see [80, 602]). If one examines a chaotic attractor from a three-dimensional flow, such as the Rössler oscillator, one finds that trajectories on the attractor exhibit rotation-like motions around the z-axis, as shown in Fig. 5.17. The motions have a well-defined center of rotation and a unique direction (counterclockwise in Fig. 5.17b). Using the center of rotation and an arbitrary reference line, a rotational angle ϕ can be defined, as shown schematically in Fig. 5.18.

For the Rössler attractor in Fig. 5.17, it is convenient to use cylindrical coordinates: $(x, y, z) \rightarrow (r, \phi, z)$, where $r = \sqrt{x^2 + y^2}$ and $\phi = \tan^{-1}(y/x)$ (within one rotation). For a chaotic trajectory, from a reference point corresponding to the initial condition, the phase variable $\phi(t)$ is a monotonically increasing function of t. In cylindrical coordinates, the Rössler equations can be conveniently written as $d\mathbf{x}/dt = \mathbf{R}(\mathbf{x})$, where $\mathbf{x} \equiv (r, \phi, z)$. The question Rosa et al. asked [652] was whether the phase variable can be locked with respect to an external periodic driving. One can imagine that if the periodic driving is weak, the phase will be chaotic, but under strong driving, it is likely that the chaotic rotation would follow more or less that of the external periodic pattern. In this case the phase variable of the chaotic oscillator
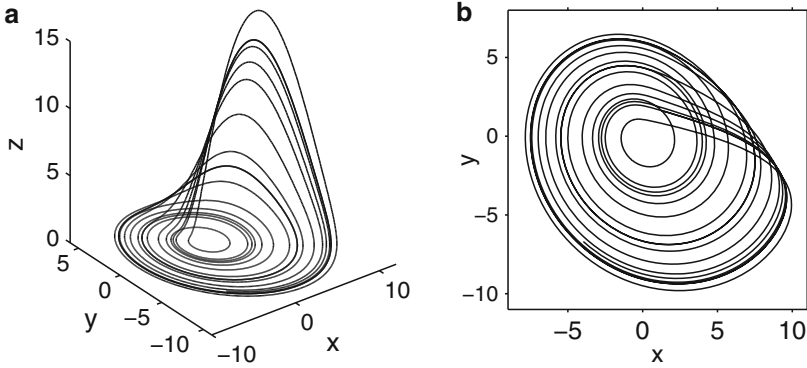
Fig. 5.17 (**a**) Chaotic attractor from the Rössler oscillator: $\dot{x} = -(y+z)$, $\dot{y} = x + 0.25y$, and $\dot{z} = 0.9 + z(x - 6.0)$, in the three-dimensional phase space. (**b**) Projection of the attractor on the (x, y)-plane. A chaotic trajectory exhibits a rotation-like motion

Fig. 5.18 Definition of phase variable ϕ for a chaotic rotation
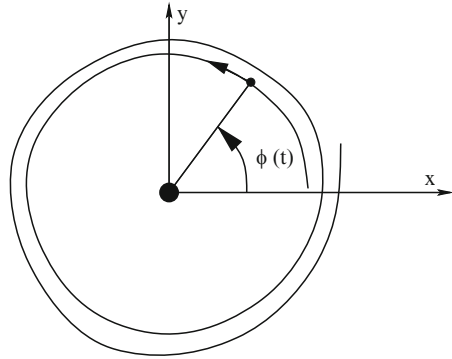
is said to have been synchronized (paced) with the phase of the external periodic signal. To address this question, consider the following general system:

$$\frac{d\mathbf{x}}{dt} = S(\mathbf{x}, s)\mathbf{R}(\mathbf{x}) + A\mathbf{P}(t), \tag{5.19}$$

where $S(\mathbf{x}, s) = 1 + s(r^2 - \bar{r}^2)$, $\mathbf{P}(t) = [0, \sin(2\pi t/T), 0]$, s and $\bar{r}$ are parameters of the modulating function $S(\mathbf{x}, s)$ ($\bar{r}$ can be chosen to be the average value of $r(t)$ for $s = 0$ and $A = 0$), and A is the amplitude of the external periodic driving. To search for synchronization, it is convenient to use $\theta = \phi(t) - 2\pi t/T$, the phase difference between the chaotic oscillator and the external periodic signal. Phase synchronization is defined by the locking of θ within 2π: $-\pi < \theta < \pi$. For a given T, phase synchronization was found to occur for sufficiently large values of A [652]. In fact, there is a region of finite area in the two-dimensional parameter space (T, A) in which phase synchronization occurs. To understand the fundamental dynamical mechanism for the synchronization, Rosa et al. suggested to define the angle variable θ on the

real line, $-\infty < \theta < +\infty$, rather than on the circle, $-\pi \leq \theta \leq \pi$. The angle thus becomes *lifted*. The phase-synchronized state corresponds to an attractor confined within $-\pi < \theta < \pi$. The attractor is chaotic because the amplitude dynamics remains chaotic even when its phase is locked. Due to the invariance of the system under the transformation $\theta \rightarrow \theta \pm 2\pi$, there is an infinite array of such attractors spaced by 2π in θ.

Imagine for a fixed T, as A increases through a critical value A_c, phase synchronization occurs so that for $A > A_c$, an infinite array of attractors is formed. For $A < A_c$, there is no phase locking so that θ cannot be confined in any of the 2π intervals. A trajectory can thus move across the entire θ-axis. However, for A slightly below A_c, the trajectories will be confined within one of the 2π intervals for long time before moving to an adjacent 2π interval. There is thus *transient chaos* corresponding to the temporal phase locking. The time it takes for a trajectory to escape an attractor and to move to an adjacent one is typically much smaller than the time that the trajectory stays on the attractor. What can be expected is thus the confinements of θ values within 2π for long stretches of time and rapid jumps of magnitude 2π amid the long confinements. This 2π-jump phenomenon has indeed been observed numerically and experimentally [80]. The point is that the transition to chaotic phase synchronization can be regarded as crisis-like transition whereby isolated chaotic attractors are formed from transient chaos.

Rosa et al. found that after the onset of phase synchronization, the basin boundaries between the chaotic attractors in two adjacent 2π cells are sporadically fractal. The boundaries are in fact similar to those from the two-dimensional map (5.5), as shown in Fig. 5.4.

5.6.2 Dynamical Mechanism

To understand how sporadically fractal basin boundaries can arise in dynamical systems, Hunt et al. [346] proposed a class of two-dimensional maps (5.5), where the *x*-dynamics is governed by the following one-dimensional map:

$$f(x) = \begin{cases} 9x/(4-5x), & \text{for } x \leq 0, \\ 9x/4, & \text{for } 0 \leq x \leq 4/9, \\ (81/4)(x - x^2), & \text{for } 4/9 \leq x \leq 5/9, \\ (9/4)(1-x), & \text{for } x \geq 5/9, \end{cases} \tag{5.20}$$

as shown in Fig. 5.19.

This map has two invariant sets: a stable fixed-point attractor at $x = -1$ with a negative Lyapunov exponent and a "middle ninth" Cantor set in $0 \leq x \leq 1$, the set of initial conditions in the unit interval that do not approach the attractor. The Cantor set is in fact a repeller with a positive Lyapunov exponent $\ln(9/4)$ because the
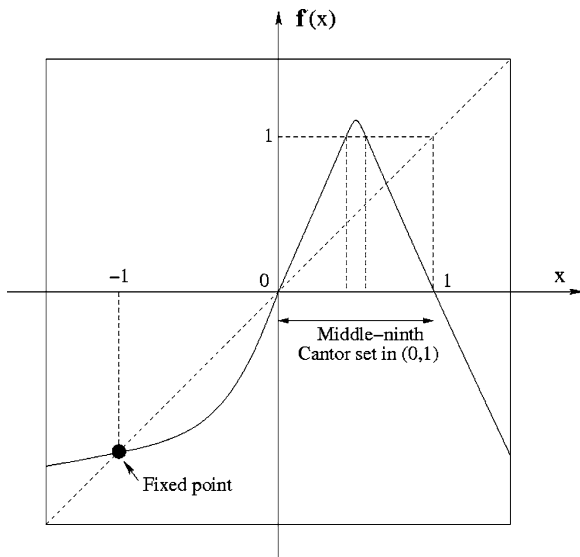
Fig. 5.19 One-dimensional map (5.20) as $f(x)$ in (5.5)

slopes of the map about the Cantor set are $\pm 9/4$. For the two-dimensional map (5.5), at each iterate every vertical line segment is expanded by the factor $\lambda > 1$. Thus almost all initial conditions approach asymptotically either $y = +\infty$ or $y = -\infty$, which can be regarded as the two attractors of the system. The boundary between the two basins of attraction is a function $y = g(x)$, the dynamics on which are determined by $f(x)$. Since $f(x)$ has two invariant sets and since the y-dynamics is unstable, on the basin boundary there are two invariant sets as well: a saddle point (at $x = -1$) with one positive and one negative Lyapunov exponent, and a chaotic repeller with two positive Lyapunov exponents. Numerical experiments revealed that $g(x)$ is smooth for almost all x values but nondifferentiable for a set of x values constituting the middle-ninth Cantor set in the one-dimensional map $f(x)$. The box-counting dimension of the curve $y = g(x)$ turns out for $\lambda = 1.1$ to be $D_{b0} \approx 1.75$ [346].

How is it that the basin boundary curve can be smooth at all x except for a set of measure zero, yet has a box-counting dimension greater than 1? To understand this property, Hunt et al. [346] considered the Hölder exponent $H(x)$ at x of the function $g(x)$: $|\Delta y| \sim |\Delta x|^{H(x)}$, where Δx is infinitesimal and $\Delta y = g(x+\Delta x) - g(x)$. If $H(x) < 1$, $g(x)$ is not differentiable at x, but if $g(x)$ is differentiable at x, then $H(x) = 1$. Points on $y = g(x)$ with $H(x) < 1$ exhibit a cusplike, spiked behavior. Now consider two nearby points (x_0, y_0) and $(x_0 + \Delta x_0, y_0 + \Delta y_0)$ on the basin boundary and iterate them n times under the map (5.5). Since they are on the basin boundary, their images (x_n, y_n) and $(x_n + \Delta x_n, y_n + \Delta y_n)$ must also be on the basin boundary. For n not too large, Δx_n and Δy_n can still be regarded as small quantities. Since the nth iterate of the map (5.5) provides a smooth transformation of the neighborhood of (x_0, y_0) to the neighborhood of (x_n, y_n), the Hölder exponents are

the same for (x_0, y_0) and (x_n, y_n): $|\Delta y_0| \sim |\Delta x_0|^H$ and $|\Delta y_n| \sim |\Delta x_n|^H$. From (5.5), we have $\Delta x_n \sim \exp(\lambda_1 n)\Delta x_0$, where λ_1 is the Lyapunov exponent of the one-dimensional map $f(x)$. If $H < 1$, $|\Delta y|$ is much greater than $|\Delta x|$, so the effect of Δx on the y-dynamics is negligible. We have $\Delta y_n \sim \exp(\lambda_2 n)\Delta y_0$, where $\lambda_2 = \ln\lambda$. The Hölder exponent is thus given by $H = \lambda_2/\lambda_1$ if $\lambda_1 > \lambda_2$. Otherwise, we have $H = 1$ because the assumption $H < 1$ is contradicted. Since there are two possible values for the Lyapunov exponent λ_1 in the one-dimensional map $f(x)$ (correspond-ing to the two invariant sets), and particularly $\lambda_1 = \ln(9/4)$ for trajectories on the middle-ninth Cantor set, we see that $H < 1$ if $\lambda < 9/4$. For randomly chosen x on the basin boundary (with Lebesgue measure one), the trajectory goes to the attractor at $x = -1$ that has $\lambda_1 < 0$. For these points $H = 1$, and the boundary is smooth.

The relationship between the Hölder exponent and the Lyapunov exponents can be used to obtain the box-counting dimension of the basin boundary curve $y = g(x)$. Suppose we cover the (x, y)-plane with square boxes of linear size $\varepsilon \ll 1$. If the boundary curve contained in a column of width ε is smooth, i.e., no points of the middle-ninth Cantor set lie in it ($H = 1$), the number of boxes required to cover the curve segment is of order 1. If the boundary curve in a column of boxes contains points of the Cantor set so that $H < 1$, the variation of the curve in the y-direction is $|\Delta y| \sim \varepsilon^H$ (because $\Delta x = \varepsilon$). The number of boxes required to cover the boundary curve in this column is thus of order $\varepsilon^H/\varepsilon = \varepsilon^{H-1}$. Since the total number of boxes needed to cover the Cantor set (the chaotic repeller of $f(x)$) of dimension D_x is ε^{-D_x}, the number of boxes necessary to cover the spiked parts of the basin boundary curve is $\varepsilon^{-(1+D_x-H)}$. This implies that the box-counting dimension of the chaotic repeller embedded in the basin boundary is $D_0 = 1 + D_x - H$. Taking into account the fact that the number of boxes required to cover the smooth parts of the boundary is of order ε^{-1}, we see that if $1 + D_x - H < 1$, then ε^{-1} is much greater than $\varepsilon^{-(1+D_x-H)}$, so in this case the number of boxes needed to cover the whole boundary curve is of order ε^{-1}. Conversely, this number is of order $\varepsilon^{-(1+D_x-H)}$ if $1 + D_x - H > 1$. These estimates yield the box-counting dimension of the boundary curve $y = g(x)$ as

$$D_{b0} = \max\{1, 1 + D_x - H\}. \tag{5.21}$$

An interesting observation is that the basin boundary's being spiky, i.e., $H < 1$, is not sufficient to make $D_{b0} > 1$, i.e., to make the boundary sporadically fractal. To have $D_{b0} > 1$ requires $H < D_x$, i.e., that the dimension D_0 of the repeller be larger than 1. This means that the spiked behavior should be sufficiently intense for sporadically fractal boundaries to arise. The uncertainty exponent is thus

$$\alpha = 2 - D_{b0} = 1 - D_x + H = 2 - D_0 < 1. \tag{5.22}$$

For the model described by (5.5) and (5.20), we have $D_x = \ln 2/\ln(9/4)$ and $H = \ln\lambda/\ln(9/4)$, so $D_{b0} = D_0 = 2 - \alpha = 1 + \ln(2/\lambda)/\ln(9/4) > 1$ for $\lambda < 2$ and $D_{b0} = \alpha = 1, D_0 < 1$, for $\lambda > 2$.

5.7 Riddled Basins

We have seen up to now several types of complicated basins. Despite differences, a common feature among them is open sets (volumes) contained in a basin. In this section we discuss riddled basins, basins that do not contain any open sets but nonetheless have a positive Lebesgue measure. Because a riddled basin has no open sets, for every initial condition that approaches the attractor with a riddled basin asymptotically, there are initial conditions *arbitrarily nearby* that go to another coexisting attractor. Thus, an arbitrarily small uncertainty in the initial condition can lead to a completely different attractor. Riddled basins are therefore space-filling. In a D-dimensional phase space, $D_{b0} = D$, riddled basins are *fat fractals* [234, 564, 773]. In fact, the uncertainty exponent associated with a riddled basin is close to zero, which means that a vast reduction in the error in specifying the initial conditions results in hardly any improvement in one's ability to predict the final attractor. As a consequence, prediction of attractors for specific initial conditions and parameters becomes practically impossible. Because of this serious consequence, there has been much effort devoted to riddled basins (for a review and historical comments, see [7]).

The dynamical conditions for riddling to occur were first described by Alexander et al. [11]. They offered the following definition for a riddled basin: *The basin of attraction of an attractor is riddled if its complement intersects every disk in a set of positive measure*. Roughly, the term "disk" here refers to D-dimensional phase-space volumes of all sizes. In order to argue that the basin of a chaotic attractor is riddled, the following two conditions need to be established: (1) a set of positive measure is attracted to the attractor; and (2) sufficiently many points near the attractor are repelled from it. In particular, to prove condition (1), one can compute the transverse Lyapunov exponent (to be defined below) and show that it is negative [11]. To prove condition (2), it is necessary to show that there exists an open *dense* set near the attractor where points approach another coexisting attractor. In contrast, a fractal basin is open and it is defined with respect to the basin boundary: a basin is fractal if its boundary is a fractal set. The mathematical feature that distinguishes a riddled basin from a fractal one is then that the former is a closed set of positive measure, while the latter is open.

A necessary condition for riddling is the existence of an *invariant subspace*, which often results from a symmetry of the system. An example is the following system of N coupled chaotic oscillators:

$$\frac{d\mathbf{x}_i}{dt} = \mathbf{F}_i(\mathbf{x}_i) + K \sum_j \mathbf{H}(\mathbf{x}_i - \mathbf{x}_j), \quad i = 1, \ldots, N, \tag{5.23}$$

where $\mathbf{F}_i(\mathbf{x}_i)$ is the velocity of oscillator i when uncoupled, and the coupling is represented by strength K and the function $\mathbf{H}(\mathbf{x}_i - \mathbf{x}_j)$ that satisfies the condition $\mathbf{H}(\mathbf{0}) = \mathbf{0}$. When the individual oscillators are identical, i.e., $\mathbf{F}_i = \mathbf{F}_j$, the

synchronous state $\mathbf{x}_i(t) = \mathbf{x}_j(t)$ $(i, j = 1, \ldots, N)$ is a solution to (5.23). In this case, the dynamical equations are identical for each oscillator, so oscillators starting synchronized remain so forever. The subspace defined by $\mathbf{x}_i(t) = \mathbf{x}_j(t)$ $(i, j = 1, \ldots, N)$ is therefore invariant. The existence of such an invariant subspace was the starting point for analyzing the dynamics of coupled chaotic oscillators in most existing works in the area of chaotic synchronization [602, 711]. In fact, the first experimental evidence for riddled basins was found in this context (see Fig. 1.18).

5.7.1 Riddling Bifurcation

How does a riddling bifurcation occur that creates a riddled basin? The answer was provided in [455]. In a two-dimensional phase space, the invariant subspace is a line. In this case, the onset of riddling is determined by a saddle-repeller bifurcation [294, 295]. In particular, the chaotic attractor $\mathscr{A}$ in the invariant subspace is one-dimensional. Before the bifurcation, $\mathscr{A}$ attracts all points in some neighborhood of itself, and all the periodic orbits embedded in the chaotic attractor are saddles in the full phase space. At the riddling bifurcation, one of the periodic orbits, usually of low period, becomes transversely unstable. Since this periodic orbit is already unstable in the attractor, it becomes a repeller in the two-dimensional phase space. To be concrete, let $\mathbf{x}_p$ be an unstable fixed point embedded in the chaotic attractor in the invariant subspace. The point is stable transversely to this subspace for $p < p_c$, as shown in Fig. 5.20a. Riddling occurs when $\mathbf{x}_p$ loses its transverse stability as a parameter p passes through a critical value p_c. For such systems, the loss of transverse stability is induced by the collision at $p = p_c$ of two point repellers $\mathbf{r}_+$ and $\mathbf{r}_-$, located symmetrically with respect to the invariant subspace, with the saddle at $\mathbf{x}_p$ (a saddle-repeller bifurcation). These two repellers exist only for $p \leq p_c$, as shown in Fig. 5.20a. For $p > p_c$, the saddle $\mathbf{x}_p$ becomes a repeller, and the two repellers $\mathbf{r}_+$ and $\mathbf{r}_-$ off the invariant subspace no longer exist.

Due to nonlinearity, a "tongue" opens at $\mathbf{x}_p$, allowing trajectories near the invariant subspace to escape for $p > p_c$, as shown in Fig. 5.20b. Each preimage of $\mathbf{x}_p$ also develops a tongue simultaneously. Since preimages of $\mathbf{x}_p$ are dense in the invariant subspace, an infinite number of tongues open up simultaneously at $p = p_c$, indicating that initial conditions arbitrarily close to the invariant subspace can go to another attractor.

At the riddling bifurcation a single periodic orbit becomes transversally unstable. As the parameter p is increased further, more and more periodic orbits become unstable until, for another critical parameter $p_c^0 (> p_c)$, the full attractor in the invariant subspace becomes transversely unstable. This occurs when the average transverse Lyapunov exponent λ_T becomes positive. This bifurcation is called the *blowout bifurcation* [30, 435, 727].

Fig. 5.20 Riddling
bifurcation at p_c. (**a**) Unstable
saddle fixed point in the
invariant subspace and two
repellers off the invariant
subspace for $p < p_c$ (before
the saddle-repeller
bifurcation). (**b**) Tongue
structure formed for $p > p_c$,
after the onset of riddling.
Trajectories originated from
initial conditions inside the
tongues escape the invariant
subspace to $+\infty$ [455]
(Copyright 1996, the
American Physical Society)
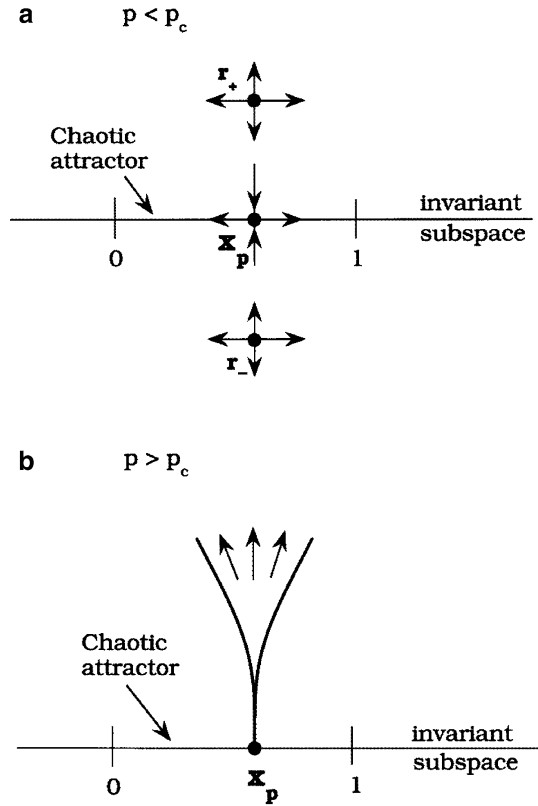
5.7.2 An Example

To make these ideas more concrete, we use the following map [455]:

$$x_{n+1} = 4x_n(1 - x_n), \tag{5.24}$$

$$y_{n+1} = pe^{-b(x_n - x_p)^2} y_n + y_n^3,$$

where $y = 0$ defines the invariant subspace as a trajectory with $y_0 = 0$ will have
$y_n = 0$ and $b > 0$ is a parameter. In this system, $\mathscr{A}$ is the fully developed chaotic
attractor of the logistic map, and $x_p = 3/4$ denotes the nontrivial unstable fixed point
of the logistic map.

The two eigenvalues of the unstable fixed point $\mathbf{x}_p = (x_p = 3/4, y = 0)$ are
$(\Lambda_x, \Lambda_y) = (-2, p)$. Thus, $\mathbf{x}_p$ is stable in the y direction for $p < 1$ and unstable for
$p > 1$. This fixed point is a saddle for $p < 1$. For $p < 1$, there are two other unstable
fixed points located at $\mathbf{r}_\pm \equiv (x_p, \pm\sqrt{1 - p})$, which have eigenvalues $(-2, 3 - 2p)$,
both being repellers for $p < 1$, as shown in Fig. 5.20a. The repellers collide with
each other and with the saddle at $p = p_c = 1$ in a saddle-repeller bifurcation, and

they do not exist for $p > 1$. Thus, beyond the riddling bifurcation (for $p > 1$), two tongues, symmetrically located with respect to the invariant subspace, open up at $x = x_p$, allowing trajectories near $y = 0$ to escape to $|y| = \infty$. Observe that the cubic term in the y-dynamics guarantees that if $|y_n| > 1$, then $|y_{n+1}| > |y_n| > 1$. Once a trajectory reaches $|y| = 1$, its y value tends to infinity rapidly. As a result, $y = \pm\infty$ can be regarded as coexisting attractors, $A_\pm$, of (5.24) with $\mathscr{A}$, fulfilling the condition for riddling.

The transverse Lyapunov exponent is the average of the logarithms of the stretching rates of the y-dynamics at $y = 0$ along a trajectory of the x-dynamics. That is,

$$\lambda_T = \left\langle \ln \left| \frac{\mathrm{d}y_{n+1}}{\mathrm{d}y_n} \right| \right\rangle_{|y=0}, \tag{5.25}$$

where the angled brackets denote an average taken with respect to the natural measure of the attractor $\mathscr{A}$. Since $\mathrm{d}y_{n+1}/\mathrm{d}y_n = p \exp[-b(x_n - x_p)^2]$ at $y = 0$, we have $\lambda_T = \ln p - b(\langle x^2 \rangle - 2\langle x \rangle x_p + x_p^2)$. Substituting the averages for the chaotic attractor of the x-dynamics, we obtain

$$\lambda_T = \ln p - 3b/16. \tag{5.26}$$

The blowout bifurcation takes place at $p_c^0 = \exp(3b/16) > 1$.

5.7.3 Scaling Relation

A quantity characterizing the degree of riddling of a basin is the ratio between the sizes of the basins of the attractors A_+ (or A_-) and $\mathscr{A}$, which can be computed as follows. Take a line parallel to the invariant subspace at distance $y_0 \ll 1$ and determine the fraction $F(y_0)$ of the length of this line in the basin of A_+ or (A_-). The fraction typically obeys the following scaling law [567]:

$$F(y_0) \sim |y_0|^\eta, \tag{5.27}$$

where η is a positive exponent. As $y_0 \to 0$, the fraction of the basin of $A_\pm$ approaches zero, but for any finite $|y_0|$ this fraction is nonzero. For p values close to the blowout bifurcation point p_c^0, a stochastic model by Ott et al. [567] predicts the exponent η to be

$$\eta = \frac{|\lambda_T|}{Q}, \tag{5.28}$$

where Q represents the diffusion coefficient characterizing the variance of the finite-time transverse Lyapunov exponents (the analogue of Q_2 introduced in Sect. 2.2.2 and in Appendix A). Close to but below the blowout bifurcation point, λ_T is negative and small.

Another measurable quantity is the uncertainty exponent α, defined by $f(\varepsilon) \sim \varepsilon^\alpha$, where $f(\varepsilon)$ is the probability of finding two points within distance ε along a line at distance y_0 from the invariant plane, which belong to different basins

(to those of $\mathscr{A}$ and of A_+ (or A_-)). The stochastic theory predicts, for p close to p_c^0, that

$$\alpha = \frac{\lambda_T{}^2}{4Q\lambda_1},\tag{5.29}$$

where λ_1 is the Lyapunov exponent of attractor $\mathscr{A}$. Since λ_T is small, the uncertainty exponent is small, signifying a fundamental obstacle to prediction. Due to the fat-fractal nature of the boundary (5.12) does not hold. In this case, we have $D_{b0} = D$ but $\alpha \neq 0$.

5.8 Catastrophic Bifurcation of a Riddled Basin

While symmetry and invariance are common in mathematical models of physical systems, the notion of symmetry and invariance is *nongeneric*, because in physical reality, imperfections or perturbations that destroy system symmetry are always present. In the coupled-oscillator system (5.23), a typical type of imperfection is parameter mismatches among oscillators. The presence of heterogeneity among the vector fields $\mathbf{F}_i$, no matter how small, immediately destroys the originally invariant subspace defined by the synchronous state. A key question is thus, can a riddled basin be physically observed? Investigation along this line [438, 441] has indicated that riddling is typically destroyed by symmetry-breaking perturbations and is converted into a fractal basin, no matter how small the perturbations are. This has been called *catastrophe of riddling* [438]. However, for small perturbations, the resulting fractal basin may appear similar to a riddled one.

5.8.1 An Example

We consider the following noninvertible two-dimensional map [441]:

$$x_{n+1} = T(x_n) = \begin{cases} 2x_n, & 0 \leq x < 1/2, \\ 2(1 - x_n), & 1/2 \leq x \leq 1, \end{cases}\tag{5.30}$$

$$y_{n+1} = f(x_n, y_n) = \begin{cases} px_n y_n + \varepsilon, & |y| < 1 \\ \lambda y_n, & |y| \geq 1, \end{cases}$$

where $T(x)$ is the tent map, p and $\lambda > 1$ are parameters, and ε is the symmetry-breaking parameter. The phase-space region of interest is $\{0 \leq x \leq 1, -\infty < y < \infty\}$. For $\varepsilon = 0$, the system possesses a one-dimensional invariant subspace $y = 0$, which is caused by the reflection symmetry $y \to -y$. Because $\lambda > 1$, the map has two other attractors: $A_\pm$ at $y = \pm\infty$. The chaotic attractor $\mathscr{A}$ of the tent map in $y = 0$ can be the

third attractor of the full system if it is transversely stable. Since $\mathrm{d}y_{n+1}/\mathrm{d}y_n = px_n$ at $y = 0$, we have $\lambda_T = \ln p + \langle \ln x \rangle = \ln p - 1$. A blowout bifurcation occurs at $p_c^0 = e$.

As ε is increased from zero, no matter how little, the chaotic attractor of the tent map is no longer an attractor of the whole system. A catastrophe of riddling occurs for $p < p_c^0$ as $|\varepsilon|$ is increased from zero, in which the riddled basin of $\mathscr{A}$ for $\varepsilon = 0$ is replaced by the fractal basin either of A_+ or of A_-, depending on the sign of ε. For $p > p_c^0$, the basins of the $y = \pm\infty$ attractors are $y > 0$ and $y < 0$, respectively if $\varepsilon = 0$. In this case, as $|\varepsilon|$ is increased from zero, a smooth-to-fractal basin boundary metamorphosis occurs because the two simple basins ($y > 0$ and $y < 0$) are replaced by fractal ones. Because of the simplicity of (5.30), these bifurcations can in fact be understood analytically to a certain extent.

The replacement of the riddled basin by a fractal one in the presence of a symmetry-breaking perturbation can be seen qualitatively as follows. As discussed above, for $\varepsilon = 0$, the basin of the chaotic attractor $\mathscr{A}$ is a closed set with positive measure, which is the complement of two symmetric open dense sets belonging to the attractors $A_\pm$, respectively. While initial conditions with $y_0 > 0$ or $y_0 < 0$ can go to $\mathscr{A}$, they cannot cross the invariant line $y = 0$. For $\varepsilon \neq 0$, the dense set of unstable periodic orbits originally embedded in $\mathscr{A}$ in $y = 0$ spread out in the vicinity of $y = 0$, converting $\mathscr{A}$ into a nonattracting chaotic set. Because of this spread of unstable periodic orbits, a trajectory initiated in $y > 0$ can penetrate the originally invariant line $y = 0$ and go to the $y = -\infty$ attractor, and vice versa. The basin of the $y = -\infty$ attractor in $y > 0$ must be open and therefore is fractal.[3] The same holds for the basin of the $y = +\infty$ attractor in $y < 0$. Thus, as soon as ε becomes nonzero, the riddled basin of $\mathscr{A}$ is destroyed, and simultaneously, two fractal basins arise. In what follows we analyze how unstable periodic orbits embedded in the original chaotic attractor in $\mathscr{A}$ are perturbed by the symmetry-breaking, based on which we can establish the existence of open, but not dense, sets that belong to the basins of the attractors at infinities.

For concreteness, we consider the map (5.30) with $\varepsilon < 0$ around the blowout bifurcation, i.e., for p less than but close to p_c^0. Since unstable periodic orbits are structurally stable, we expect that they shift to a small neighborhood about the originally invariant subspace $y = 0$ for $\varepsilon \neq 0$. For example, the original fixed point $\mathbf{x}_p = (x_p, 0)$ (a repeller with an unstable direction in both x and y, where $x_p = 2/3$ is the nontrivial unstable fixed point of the tent map) is shifted to (x_p, y_p), where y_p is

$$y_p = \frac{-|\varepsilon|}{1 - px_p}. \tag{5.31}$$

---

[3] Consider an open neighborhood $\mathscr{B}$ of one of the attractors at infinity. Choose a point p in its basin and evolve it forward in time. Eventually, the resulting trajectory will approach the attractor, which means that at some finite time, the trajectory will enter $\mathscr{B}$, say at point p'. The point p' in $\mathscr{B}$ must then have an open neighborhood. Since p' is iterated from p in finite time, p must also have an open neighborhood in the basin.

For $p \approx p_c^0$, we have $px_p \approx 2e/3 > 1$ and hence $y_p > 0$. The eigenvalues of the perturbed fixed point (x_p, y_p) are $\Lambda_x = -2$ and $\Lambda_y = px_p > 1$. Thus, under the symmetry-breaking perturbation, the shifted fixed point is still a repeller. Consider now the period-2 orbit of the tent map: $(x_1^{(2)} = 2/5, 0)$ and $(x_2^{(2)} = 4/5, 0)$. The eigenvalues of the twice iterated map at these points are $\Lambda_x = -4$ and $\Lambda_y = p^2 x_1^{(2)} x_2^{(2)}$. The latter is smaller than unity for $p < 1.77$. The two-cycle is then a saddle in the full phase space. For $\varepsilon \neq 0$, the y-coordinates of the orbit become

$$y_1^{(2)} = \frac{-|\varepsilon|(px_2^{(2)} + 1)}{1 - p^2 x_1^{(2)} x_2^{(2)}} \quad \text{and} \quad y_2^{(2)} = \frac{-|\varepsilon|(px_1^{(2)} + 1)}{1 - p^2 x_1^{(2)} x_2^{(2)}}.$$

Altogether, we observe that (1) an orbit is shifted upward (downward) from $y = 0$ if it is a repeller (saddle), and (2) the eigenvalues of the orbit remain unchanged. In general, this is valid for any periodic orbit. Since all repellers are located in $y > 0$, a trajectory starting in $y < 0$ cannot cross $y = 0$, but since all saddles are located in $y < 0$, a trajectory starting in $y > 0$ can move across the x-axis and go to the $y = -\infty$ attractor. Thus, due to the symmetry-breaking, the $y = -\infty$ attractor acquires a basin in $y > 0$.

The picture depicted above, i.e., saddles shifted downward and repellers upward, is specific to the system (5.30) for the case of $\varepsilon < 0$. For $\varepsilon > 0$, saddles will shift upward and repellers downward. In general, in two dimensions we expect to observe saddles and repellers on both sides of the originally invariant subspace when there is a symmetry-breaking. As a result, there will be fractal basins both above and below the originally invariant subspace. In higher dimensions, unstable periodic orbits with different unstable dimensions – a type of nonhyperbolicity known as *unstable dimension variability* (see also Sect. 4.4.2), – which are originally all located in the invariant subspace, will be shifted to its neighborhood under a symmetry-breaking perturbation.

For $\varepsilon = 0$, the "roots" of the open set, i.e., the fixed point $(x_p, 0)$ and all its preimages, are located in the invariant subspace $y = 0$ and are dense (see Fig. 5.21a). As we have seen, for $\varepsilon \neq 0$, these "roots" are shifted and are distributed in the two-dimensional phase-space region about $y = 0$, as shown in Fig. 5.21b. Thus, the open set is no longer dense. The set of initial conditions in the unit square $0 \leq (x, y) \leq 1$ that go to the $y = -\infty$ attractor is now open. In fact, it is straightforward to see that the region bounded by the curve $xy < |\varepsilon|/p$ in the unit square maps to $y < 0$ after one iteration. The basin of the $y = -\infty$ attractor in $0 \leq (x, y) \leq 1$ thus consists of this bounded region and all its preimages. The boundaries separating the basins of the $y = \pm\infty$ attractors are fractal. We remark, however, that in this case, the basin in $y > 0$ of the $y = -\infty$ attractor may appear indistinguishable from that of a riddled basin because unstable periodic orbits in the originally invariant subspace are perturbed only slightly.

We thus see that for $p < p_c^0$ and $\varepsilon \neq 0$, persistent chaos in the invariant subspace, together with its riddled basin for $\varepsilon = 0$, is replaced by a chaotic transient and fractal basins of the attractors at infinities, respectively.
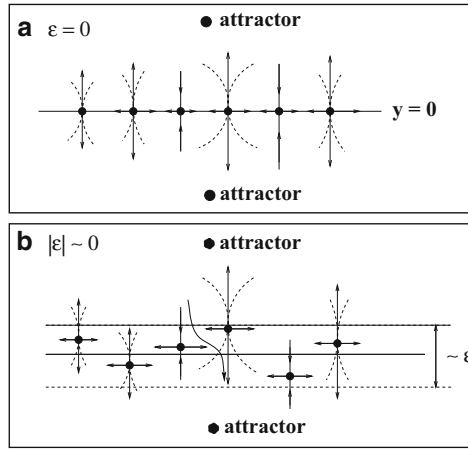
Fig. 5.21 Schematic illustrations of the dynamics of unstable periodic orbits: (**a**) for $\varepsilon = 0$, $y = 0$ is invariant and the roots of the tongues are dense in $y = 0$, creating a riddled basin; (**b**) for $\varepsilon \neq 0$, $y = 0$ is no longer invariant, the locations of the periodic orbits are shifted about $y = 0$, and the roots of the tongues are no longer dense, leading to fractal basins [438] (Copyright 1999, the American Physical Society)

5.8.2 Critical Behavior and Scaling Laws

We have seen that the presence of a small amount of symmetry-breaking causes a spread of unstable periodic orbits in a neighborhood of size about ε in the vicinity of the originally invariant subspace. The dynamics outside the neighborhood can be approximately described by that of a random process. To see this, we rewrite (for $y_n > 0$) the y-equation in (5.30), as follows:

$$-\ln y_{n+1} = -\ln y_n - \ln(px_n + \varepsilon/y_n).$$

Letting $Y_n \equiv -\ln y_n$, we obtain

$$Y_{n+1} = Y_n + v_n, \tag{5.32}$$

where $v_n = -\ln(px_n + \varepsilon/y_n)$ is a random variable because x_n comes from a chaotic process. For $\varepsilon \sim 0$, v_n is approximately independent of y_n most of the time (except when y_n gets close to the original invariant subspace). Equation (5.32) thus describes a random walk. If the average drift $v \equiv \langle Y_{n+1} - Y_n \rangle = \langle v_n \rangle$ is small, the random-walk model can be solved using the diffusion approximation, from which various scaling relations can be derived. Specifically, since v is small, the evolution of the probability as a function of discrete time n can be approximated as an evolution in continuous time t. Let $P(Y,t)\mathrm{d}Y$ be the probability of finding the walker in the interval $[Y, Y + \mathrm{d}Y]$ at time t. Then $P(Y,t)$ obeys the following diffusion equation [237]:

$$\frac{\partial P}{\partial t} + v \frac{\partial P}{\partial Y} = Q \frac{\partial^2 P}{\partial Y^2}, \tag{5.33}$$

where Q is the diffusion coefficient, defined as

$$2nQ = \left\langle (Y_n - n\nu)^2 \right\rangle. \tag{5.34}$$

Adopting the above diffusive picture, we see that ν and Q are the two key parameters that determine the dynamics. In fact, the average drift $-\nu$ and Q are analogous respectively to the transverse Lyapunov exponent λ_{T} (which can be defined only when $\varepsilon = 0$) and the diffusion coefficient Q characterizing the degree of the fluctuations of the finite-time transverse Lyapunov exponent, used in Sect. 5.7.3. In the simple model (5.30), $\nu < 0$ for $p > p_{\mathrm{c}}^0$ and $\nu > 0$ for $p < p_{\mathrm{c}}^0$. Thus, we have

$$\nu \sim (p_{\mathrm{c}}^0 - p). \tag{5.35}$$

When there is a symmetry-breaking so that the notions of invariant subspace and transverse Lyapunov exponent no longer hold, we can still use ν and Q to characterize the dynamics in the vicinity of the original invariant subspace. In particular, regarding the ε-neighborhood of the original invariant subspace as a *pseudoinvariant manifold* under a symmetry-breaking, the stability of this manifold can be quantified by ν and Q. Defining the *pseudotransverse Lyapunov exponent*

$$\Lambda_{\mathrm{T}} \equiv -\nu, \tag{5.36}$$

we see that if $\Lambda_{\mathrm{T}} > 0$ ($\nu < 0$), the pseudoinvariant manifold is transversely unstable because a trajectory leaves the pseudoinvariant manifold exponentially rapidly. If, however, $\Lambda_{\mathrm{T}} < 0$ ($\nu > 0$), a trajectory can spend a long time near the pseudoinvariant manifold, although the trajectory will eventually leave it. In this sense, the manifold is *quasistable* with respect to transverse perturbations. Introducing the pseudotransverse Lyapunov exponent, with the parameter Q characterizing its finite-time fluctuations, thus enables us to quantify the dynamical property of the pseudoinvariant manifold [441].

A detailed discussion about the validity of the diffusion approximation near the transition point to a chaotic attractor with a riddled basin, at which the average drift (or the transverse Lyapunov exponent) is nearly zero, can be found in [565, 567]. Here, because of the symmetry-breaking, the range for the validity of the diffusion approximation is limited. In particular, we note that a trajectory cannot enter the ε-neighborhood of the original invariant subspace $y = 0$. However, for $|y| > |\varepsilon|$, the trajectory experiences both repulsion from and attraction toward the ε-neighborhood of $y = 0$ due to the existence of periodic orbits with different unstable dimensions, namely, repellers and saddles. If $\nu \approx 0$, the amount of repulsion is approximately equal to that of attraction, and hence we expect the diffusion picture to be valid for $|\varepsilon| < |y| < 1$. This corresponds to the range $Y \in (0, \overline{\varepsilon})$, where $\overline{\varepsilon} = -\ln|\varepsilon| \gg 1$. For clarity of the presentation, we consider the case $\varepsilon < 0$, so that the symmetry-breaking-induced basin of the $y = -\infty$ attractor lies in $y > 0$.

We fix a line segment $0 \le x \le 1$ at $y = y_0$, $0 < y_0 \ll 1$, and uniformly choose a large number of initial conditions from it, which leads to the following initial condition for the diffusion equation (5.33):

$$P(Y,0) = \delta(Y - Y_0), \tag{5.37}$$

where $Y_0 = -\ln y_0$. Since a trajectory reaching $y = 1$ quickly goes to the $y = +\infty$ attractor, we have the following absorbing boundary condition at $Y = -\ln 1 = 0$:

$$P(0,t) = 0. \tag{5.38}$$

Roughly, a trajectory entering the $|\varepsilon|$-neighborhood of $y = 0$ is lost to the basin of the $-\infty$ attractor. A realistic picture is that the Y-location of the absorbing boundary depends on x. For instance, from the model (5.30), we see that a trajectory goes to the $y = -\infty$ attractor whenever $p x_n y_n < |\varepsilon|$. Insofar as x_n is not too small, this happens when $y_n < |\varepsilon|/p x_n \sim |\varepsilon|$. Thus, as a crude approximation, we impose another absorbing boundary at $\bar{\varepsilon}$:

$$P(\bar{\varepsilon},t) = 0. \tag{5.39}$$

Let $F(|\varepsilon|, y_0)$ be the fraction of initial conditions from the line segment at y_0 that go to the $y = -\infty$ attractor A_-. As $|\varepsilon|$ is increased, we expect $F(|\varepsilon|, y_0)$ to increase. For small $|\varepsilon|$, the diffusion equation (5.33) together with the initial and the boundary conditions (5.37)–(5.39) can be solved to yield the following scaling law [441]:

$$F(|\varepsilon|, y_0) = \frac{y_0^{\nu/Q} - 1}{|\varepsilon|^{\nu/Q} - 1}. \tag{5.40}$$

If $\nu > 0$, we have $|\varepsilon|^{\nu/Q} - 1 \approx -1$ for $|\varepsilon| \ll 1$ and hence $F \approx 1 - y_0^{\nu/Q} = $ constant, a behavior drastically different from that of the symmetric case (5.27) and (5.28). For $\nu < 0$, $|\varepsilon|^{\nu/Q} - 1 \approx |\varepsilon|^{\nu/Q}$, and hence for any fixed y_0, we have

$$F(|\varepsilon|, y_0) \sim |\varepsilon|^{-\nu/Q} = |\varepsilon|^{|\nu|/Q} \quad \text{for } \nu < 0. \tag{5.41}$$

We see that in the parameter regime where $\nu \approx 0$, the fraction remains roughly constant, regardless of the amount of symmetry-breaking. This also implies the catastrophic nature of the symmetry-breaking: riddling is destroyed and a fractal basin component is immediately induced as the system deviates from the symmetric one, no matter how small the deviation is.

Consider a trajectory originated from the symmetry-breaking-induced fractal basin of the $y = -\infty$ attractor in $y > 0$. After it falls into the negative vicinity of $y = 0$, it typically experiences a chaotic transient. In particular, if $\nu < 0$ ($\Lambda_T > 0$), the transient time is short. If, however, $\nu > 0$ ($\Lambda_T < 0$), the time can be extraordinarily long [441].

To assess the dimensionality of the boundary between the basin of the $y = +\infty$ attractor and the symmetry-breaking-induced basin, we fix a line segment at $y = y_0$,

where $| \varepsilon | \ll y_0 < 1$, and examine the set of intersecting points with it of the basin boundary. Let d_0 be the box-counting dimension of this set. We expect $0 < d_0 \leq 1$ and the dimension of the boundary to be $D_{b0} = 1 + d_0$ in the two-dimensional phase space. For a riddled basin, D_{b0} is the phase-space dimension. Here, despite the presence of a small amount of symmetry-breaking, D_{b0} is still close to 2. *Thus, in a practical sense, the symmetry-breaking-induced fractal basin resembles a riddled one.*[4]

It can be shown, utilizing the solution to the diffusion equation (5.33) [441, 565, 567], that the uncertainty exponent is independent of the symmetry-breaking parameter ε and is given by

$$\alpha = \frac{v^2}{4Q\lambda_1}, \tag{5.42}$$

where λ_1 is the Lyapunov exponent on the original attractor $\mathscr{A}$ in the invariant subspace. Thus, in the regime where $v \approx 0$ (but $v \neq 0$), so that the diffusion approximation is valid, we expect $\alpha \approx 0$ and hence $d_0 \approx 1$, leading to

$$D_{b0} = 2 - \frac{v^2}{4Q\lambda_1}.$$

A fractal basin boundary with dimension close to that of the phase space (or a near-zero uncertainty exponent) means that the uncertainty probability remains approximately constant, regardless of how accurately we can specify the initial condition. Thus, realistically, it is impossible to predict, from a given initial condition, the asymptotic attractor. This fundamental obstacle to prediction is common for riddled basins and persists even when the riddled basin is replaced by a fractal one due to symmetry-breaking.

---

[4] Since very close to a boundary arises the chaotic saddles's stable manifold is nearly space-filling, the set of initial conditions leading to long transients also exhibits riddled-like behavior [834]

Chapter 6
Chaotic Scattering

Scattering is a fundamental tool for probing many physical and chemical processes. In a scattering experiment, particles are injected into the system and their characteristics after the scattering are recorded, from which many properties of the system can be revealed. In a general sense, scattering can be defined as a problem of obtaining various relations between some output variables characterizing the particles after the scattering versus some input variables characterizing the particles before the scattering. The relations are called *scattering functions*. In a regular scattering process, the functions are typically smooth, examples of which can be found in textbooks of classical mechanics. It has been realized, however, that there can be situations in which a scattering function may contain an uncountably infinite number of singularities. Near any of the singularities, an arbitrarily small change in the input variable can cause a large change in the output variable. This is a sensitive dependence on initial conditions that signifies the appearance of chaos. Scattering in this case is chaotic.

Dynamically, chaotic scattering is due to the existence of chaotic saddles in the Hamiltonian phase space. Incoming particles move toward the scattering region in which a chaotic saddle resides along its stable manifold. They then wander chaotically near the saddle, but only for a finite amount of time, because the saddle is nonattracting. Finally, they exit the scattering region along the unstable manifold. The particle trajectories are thus transiently chaotic, with the sensitivity to initial conditions originating from the chaotic nature of the saddle. It is generally understood now that chaotic scattering is the physical manifestation of transient chaos in Hamiltonian systems.

After reviewing a broad range of applications of chaotic scattering, we will explore a system of three-disk billiard scatterers, which is perhaps the simplest system exhibiting chaotic scattering. A question of interest concerns how chaotic scattering arises as a system parameter changes. Two basic routes to chaotic scattering will be analyzed using a system of three and four "soft" circular potential hills. In Hamiltonian systems, nonhyperbolicity can arise whereby a chaotic saddle is adjacent to stable regions (also called the Kolmogorov–Arnold–Moser (KAM) tori). A distinct feature of nonhyperbolic chaotic scattering is that particles can spend a long time in the vicinity of KAM tori, leading to a long-term algebraic decay of the survival probability, in contrast to the exponential decay for hyperbolic chaotic

scattering, where all periodic orbits are unstable. We will show that the asymptotic algebraic decay associated with nonhyperbolic chaotic scattering is often preceded by an intermediate-time exponential decay. The effect of small dissipation will also be discussed. As an application, the ray dynamics in deformed optical microcavities will be studied. The properties of scattering cross section in chaotic cases are discussed in Appendix D.

6.1 Occurrence of Scattering

Chaotic scattering can occur in applications from many disciplines (for reviews, see [7, 201, 257, 411, 568]). We shall give a few representative examples.

- *Astronomy.* The three-body problem provides an example of an open Hamiltonian system, for which Poincaré [608] predicted the existence of complicated trajectories. For a simplified three-body system, Sitnikov proved that the motion of the third body is generally chaotic [533] before escape takes place. The structure of the underlying chaotic saddle, however, has been described only recently [417]. Petit and Hénon considered another class of restricted three-body problems: two small bodies moving about a massive one [326, 594], which is relevant to the motions of the moons of large planets or of particles in planetary rings (e.g., the rings of Saturn). They demonstrated that chaotic scattering can occur in the case of close encounters of the small bodies. Chaotic scattering has also been identified in a model of the motion of an incoming star toward a binary [97], during which gravitational energy is effectively converted into kinetic energy. The escape of stars from galaxies has also been investigated [719, 736], as well as the problem of light rays around black holes [168, 169], the escape from galactic halos [169], and chaos in cosmological models [536].
- *Chemical reaction dynamics.* The observable signature of classical chaotic scattering, namely complicated and discontinuous behavior in the scattering functions, had been noticed by Rankin and Miller [622] in their study of atom–diatom collisions, before the concept of chaos became widespread. In classical models of chemical reactions [42, 257, 420], the average lifetime of chaotic trajectories can often be interpreted as the average lifetime of intermediate complexes. A central problem is the study of complex barriers separating reacting and non-reacting trajectories, as determined by the stable and the unstable manifolds of the underlying chaotic saddle [421, 806, 829].
- *Transport processes.* Diffusion and other transport phenomena can be regarded as consequences of chaotic scattering, as pointed out first by Gaspard and Nicolis [258]. This deterministic way of describing transport phenomena in a single particle picture is based on the idea of an open but finite Hamiltonian system with a large size in a certain direction. The phase space is low-dimensional but of large linear size. The escape rate from some underlying chaotic saddle can then be calculated, which can be related to the transport coefficients [201, 257, 258, 399, 802]. Consider, for example, the problem of electric

conduction where a diffusive current is also present. Microscopically, random walks take place in the scattering region, which correspond to a scattering process subject to a bias, leading to a nonzero average velocity. In the framework of the escape-rate formalism one finds that the escape rate can be expressed by the drift coefficient (to which the electric current is proportional), the diffusion coefficient, and the length of the system [778]. The escape is in fact responsible for two different types of transport, drift and diffusion, but generalizations to other transport coefficients also hold [201, 257, 802]. So far it has been understood that other characteristics of chaotic scattering such as the Lyapunov exponents cannot be expressed solely by macroscopic parameters. It is the escape rate alone that has a well-defined thermodynamic limit [804].

- *Optical processes in microcavities.* A promising area of application of chaotic scattering is optical processes in microcavities. This has been a subject of intense study due to its potential implications for the design of novel microlasers [34, 176, 509, 570]. An interesting feature of optical dielectric cavities is that they can support whispering-gallery (WG) modes, defined as the situation in which light rays circulate almost tangent to the surface of the cavity via total internal reflection, suffering minimal losses caused by evanescent leakage and scattering due to surface roughness [34, 176, 481, 509, 618]. If there are no deformations in the cavity geometry from the ideal shape of cylinder or sphere, in a practical sense light can be trapped in the cavity indefinitely. In order for a cavity to be useful, the directionality of laser emission is important, which cannot be achieved if the cavity is perfectly circular. A simple solution is to apply smooth deformations from the circular symmetry, resulting in so-called asymmetric resonant cavities [265, 552, 553]. Due to symmetry-breaking, the condition of total internal reflection cannot be satisfied indefinitely for classical light rays, the escaping dynamics of which can in fact be cast as a chaotic-scattering problem. This classical approach has proven to be quite useful, particularly considering the fact that it is difficult to study cavities with large deformations, since the modes of highly deformed cavities are not perturbatively related to those of the circular cavities [265, 519, 552–554]. We will discuss the classical approach in Sect. 6.7.

- *Hydrodynamic processes.* In two-dimensional incompressible fluid flows, the advective dynamics are Hamiltonian. If the geometry of the flow is open, such as the setting where the flow is around an obstacle, the dynamics of particles advected by the flow can be regarded as those from a scattering problem where particles coming toward the obstacle are "scattered" away, as illustrated by the experiment in Fig. 1.19. Indeed, chaotic scattering can occur commonly in the advective dynamics of passive particles (Lagrangian chaos). A detailed treatment of this topic will be presented in Chap. 10.

- *Electronic transport in nanostructures.* A fundamental structure in modern semiconductor devices is mesoscopic junction systems for electronic transport, such as quantum dots [238]. At the mesoscopic scale, the wavelength of the electrons is small but cannot be neglected, so both the classical and quantum dynamics are relevant. In the classical picture, electrons can be regarded as point

particles moving through the junction, which is equivalent to an open billiard system in which chaotic scattering can occur generically. At the quantum-mechanical level, the most studied phenomenon is conductance fluctuations, which are observed commonly in quantum dots. To explain the fluctuations, it is necessary to consider the quantum manifestations of classical chaotic scattering. In particular, the elements of the quantum scattering matrix exhibit fluctuations in their dependence on the energy, and the origin of the quantum fluctuations can be attributed to the occurrence of chaotic scattering when the system is in the classical regime, as the experiment in Fig. 1.20 illustrates. Quantum chaotic scattering will be treated in Chap. 7.

The problem of chaotic scattering is related to that of chaotic transients in dissipative dynamical systems. In particular, since the interest is in the different final outcomes from the scattering process, one can define different *exit basins*, each being a region of the phase space where particles exhibit qualitatively similar asymptotic behavior. The exit basin associated with exit route n is the set of initial conditions that lead to an escape from the scattering region via the route. Although attractors do not exist, the exit basins play similar roles to those of basins of attractions. Analysis tools and methods suitable for basin boundaries can therefore be applied to chaotic scattering [164]. For example, the portion of uncertain initial regions can be determined and the uncertainty exponent (Sect. 5.3) can be calculated, which determines the box-counting dimensions associated with the underlying chaotic saddle. If the number of exit basins exceeds two, the basins often exhibit the Wada property [6, 164, 613, 614, 668]. In addition, leaking (Sect. 2.7) any closed Hamiltonian systems leads effectively to a scattering problem.

6.2 A Paradigmatic Example of Chaotic Scattering

A simple model of chaotic scattering is the three-disk system introduced by Eckhardt, Gaspard, and Rice [210, 260] (for a review see [257]). The system consists of three hard circular disks of identical radii R in the two-dimensional plane, as shown in Fig. 6.1, and can also be considered a "classical pinball machine." The distances between the individual disks are all a, and the disks are located at $x = -a\sqrt{3}/6$, $y = a/2$ (disk 1), $x = a\sqrt{3}/3$, $y = 0$ (disk 2), and $x = -a\sqrt{3}/6$, $y = -a/2$ (disk 3). Since the disks are hard, a particle will bounce off a disk upon collision. The reflection and incident angles with respect to an individual disk are equal for a bounce, as shown in Fig. 6.1. As such, a particle coming from far away to the left can experience bounces between the hard disks (the scattering region) and, after spending a finite amount of time there, exits to infinity with an angle ϕ, where ϕ is defined counterclockwise with respect to the x-axis, as shown in Fig. 6.2. Since energy is conserved, the velocity of the particle is constant and chosen to be unity: $v = 1$. Let the incident particle trajectory be parallel to the x-axis with an impact parameter b. The deflection angle with which the particle exits the scattering region depends on the value of the impact parameter: $\phi = \phi(b)$. Moreover, the time
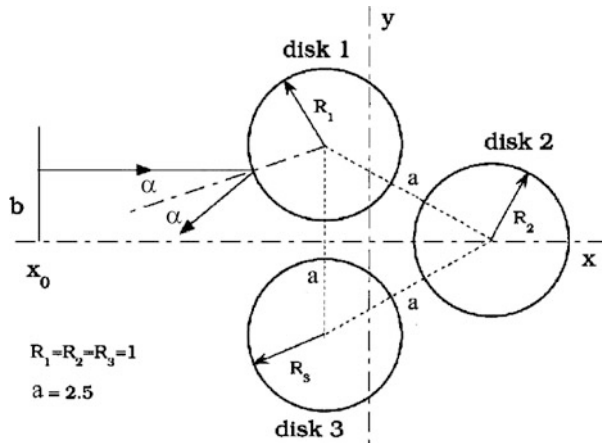
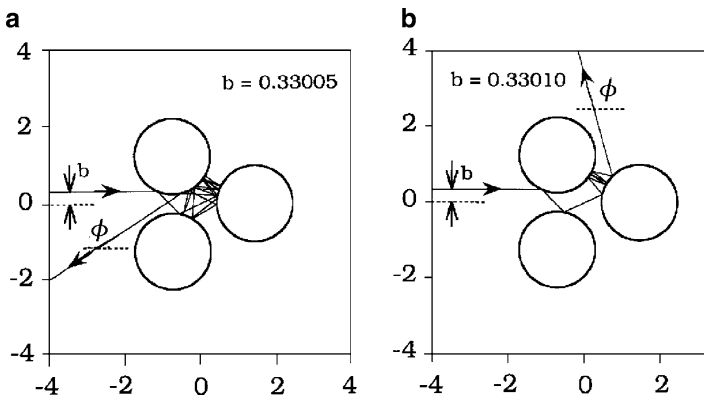**Fig. 6.1** The three-disk scattering system [838] (copyright 1995, the American Institute of Physics)

Fig. 6.2 Two particle trajectories for $a = 2.5$ and $R = 1$ with impact parameters (**a**) $b_1 = 0.33005$ and (**b**) $b_2 = 0.33010$ [838] (copyright 1995, the American Institute of Physics)

$T(b)$ that the particle spends in a region that contains the scattering region before exiting, referred to as the delay time, also depends on the impact parameter b. Both the deflection angle and the delay time are examples of scattering functions.

Figure 6.2a,b show two particle trajectories with close impact parameters: $|b_2 - b_1| = 5 \times 10^{-4}$. However, the difference in the deflection angles for the two trajectories is of order π. Such a large difference is also reflected in the delay time, the time by which the particles stay within, say, distance $d = 10 (\gg R, a)$ of the origin. Since particle 1 experiences substantially more bounces in the scattering region than particle 2, we have $T(b_1) > T(b_2)$. Thus, about the impact parameter $b \approx b_1$ (or b_2), a small difference in the initial condition causes a large difference in the outcome of the trajectories, the hallmark of chaos.
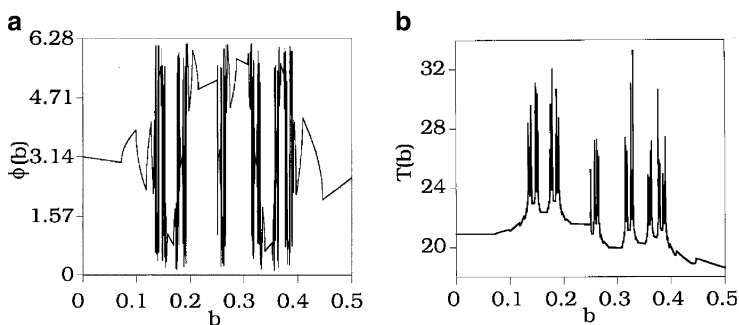
Fig. 6.3 The deflection function (**a**) and the delay-time function (**b**) for $a/R = 2.5$ [838] (copyright 1995, the American Institute of Physics)

The sensitive dependence on initial conditions occurs commonly at many impact parameters (in fact, at an infinite number of them). This can be seen in Fig. 6.3a,b, plots of the deflection function $\phi(b)$ and the delay-time function $T(b)$, respectively. The delay-time function is analogous to the lifetime function in the dissipative cases, as shown, e.g., in Fig. 1.5. It is apparent that these plots contain both smooth and wild oscillating parts. The mixture of smooth and wild oscillating parts in $\phi(b)$ and $T(b)$ repeats itself on smaller scales. In fact, there exists a Cantor set of an uncountably infinite number of b values at which $\phi(b)$ and $T(b)$ have singularities. A b-interval between two neighboring singularities is called the interval of continuity.

An efficient method for computing the box-counting dimension d_s of the set of singularities, which is particularly convenient for chaotic scattering, is the uncertainty algorithm described in Sect. 5.3. For an arbitrary location on the left of the scattering region (e.g., $x_0 = -10$ in Fig. 6.1), an initial condition (impact parameter) b is chosen randomly. A small perturbation is applied, yielding a nearby initial condition $b + \varepsilon$. The scattering trajectories originated from these two initial conditions are computed. If the numbers of bounces in the scattering region experienced by the two particles are the same, the first initial condition is called "certain" against small perturbation. This will occur if the initial condition is chosen in the range where the scattering functions are smooth. If the initial conditions lead to trajectories with different numbers of bounces in the scattering region, they are "uncertain" with respect to the perturbation ε. The fraction of uncertain initial conditions $f(\varepsilon)$ can then be computed from many randomly chosen initial-condition pairs. As ε is decreased, $f(\varepsilon)$ will decrease as ε^{α} (see (5.7)), where α is the uncertainty exponent and $d_s = 1 - \alpha$ is the box-counting dimension of the set of singularities. With the parameters of Fig. 6.3, the uncertainty exponent is estimated to be $\alpha \approx 0.39$, indicating $d_s \approx 0.61$. The procedure described above is effective when the value of d_s is not close to zero. For situations in which the dimension value is arbitrarily small, special care needs to be exercised in implementing the uncertainty algorithm [162].

That a chaotic saddle contains an infinite number of unstable periodic orbits can be seen physically using the three-disk system, where periodic orbits are the particle trajectories that repeat themselves after a certain number of bounces between the hard disks, and hence these trajectories are permanently trapped in the scattering

Fig. 6.4 Three unstable period-2 orbits, one unstable period-3 orbit, and their symbolic representations [838] (copyright 1995, the American Institute of Physics)
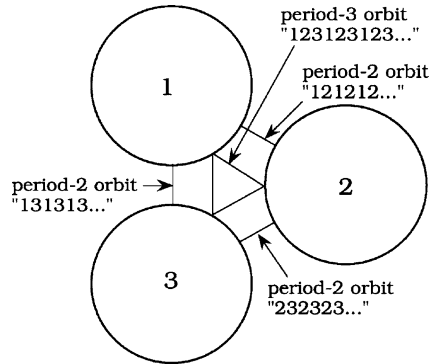
region. Figure 6.4 shows some examples of periodic orbits. The orbits are all unstable (hyperbolic): typical perturbations to the orbit, no matter how small, will result in deviations away from the orbit and exit of the particle from the scattering region. For the three-disk system, every periodic orbit can be represented by a symbolic sequence. For example, each bounce can be denoted by the label (1, 2, or 3) of the disk on which it occurs, and a particle trajectory can be encoded as

$$S_1 S_2 S_3 \cdots S_{n-1} S_n S_{n+1} \cdots , \tag{6.1}$$

where $S_i = 1, 2, 3$ depending on whether the particle bounces off disk $1, 2$, or 3 at the ith bounce, respectively. Since a typical scattering trajectory eventually exits the scattering region, the corresponding symbolic representation has only a finite number of symbols. Periodic orbits are represented by a string of infinite symbols consisting of repetitions of a finite number of symbols. As the period m increases, the number N_m of periodic orbits increases exponentially, since the number of possibilities of representing a string of length m increases exponentially as a function of m. How N_m grows can be assessed by noting that, since two or more identical symbols in a sequence are forbidden (a particle cannot hit the same disk two or more times consecutively), the number of nonrepetitive symbolic sequences of length m is $3 \times 2^{m-1}$. The definitions (1.25), (1.26) of the topological entropy K_0 lead to the value $K_0 = \ln 2$. The scattering process is thus equivalent to a Bernoulli process on two symbols.

Besides periodic orbits, there are also trajectories that wander in the scattering region forever but never repeat themselves, as can be seen again via the symbolic representation (6.1). There is in fact an uncountably infinite number of such aperiodic or chaotic trajectories. These, together with the infinite number of unstable periodic orbits, make up the chaotic saddle. Since all periodic orbits are hyperbolic, the chaotic saddle and the scattering process are also hyperbolic.[1] To visualize the chaotic saddle, one can define a discrete-time map from the scattering dynamics. For example, the incident angle α_n (see Fig. 6.1) at bounce n can be taken as

---

[1] In hyperbolic chaotic scattering, all periodic orbits are unstable, while in nonhyperbolic chaotic scattering, there are stable or neutrally stable periodic orbits and quasiperiodic orbits, which will be treated in Sects. 6.3 and 6.4.

Fig. 6.5 Chaotic saddle in the phase space of the three-disk scattering system for $a/R = 2.5$
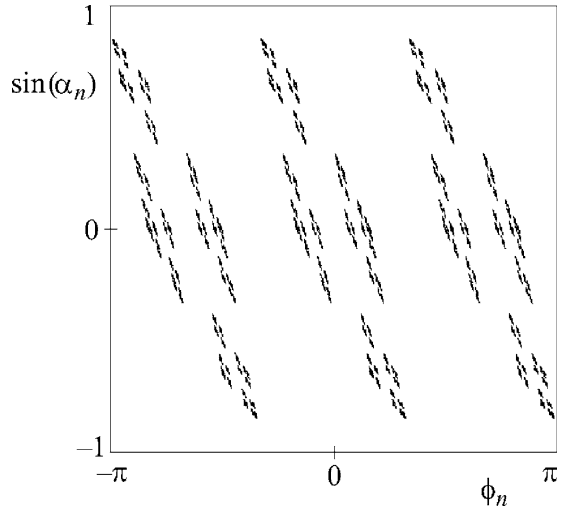
a dynamical variable, in terms of the angle ϕ_n of the incident trajectory defined counterclockwise with respect to the x-axis. (For the last bounce N, ϕ_{N+1} is identical to the deflection angle ϕ of the trajectory plotted in Fig. 6.3.) Figure 6.5 shows the chaotic saddle in the two-dimensional phase space $(\phi_n, \sin\alpha_n)$.

Saddles in Hamiltonian systems have a special property: stable and unstable directions are equivalent, (2.82),

$$D_{s,i} = D_{u,i}, \tag{6.2}$$

and therefore in the two-dimensional phase spaces the partial dimensions coincide:

$$D_i^{(1)} = D_i^{(2)} = D_i/2, \tag{6.3}$$

where $i = 0, 1$ and D_0 and D_1 denote the box-counting and the information dimensions, respectively, of the entire saddle. This symmetry is visible in Fig. 6.5. The scattering singularities correspond to intersections of the stable manifold with a line of initial conditions. The dimension d_s of the set of scattering singularities is then the same as the partial box-counting dimension along the stable or unstable direction:

$$d_s = D_{s,0} - 1 = D_0^{(1)}, \tag{6.4}$$

which implies that the box-counting dimension $D_0 = 2d_s$ of the chaotic saddle can be expressed by means of the uncertainty exponent $\alpha = 1 - d_s$ as $D_0 = 2(1 - \alpha)$. The escape rate κ of the saddle can be obtained by launching many particles with different impact parameters toward the scattering region and examining the number of particles remaining in the region with time. The exponential decay can be followed both in continuous time and in the discrete time of the Poincaré map. For example, for $a/R = 2.5$, one obtains in continuous time $\kappa \approx 0.74$. The average Lyapunov

exponent can be estimated from the general relation (2.76) and the fact that the box-counting dimension is close to the information dimension, which leads to

$$\lambda_1 \approx \frac{\kappa}{1 - d_s} = \frac{\kappa}{\alpha}. \tag{6.5}$$

This relation is valid both in continuous and in discrete time. For example, for $\kappa \approx 0.74$ and $\alpha \approx 0.39$, the dimensionless continuous-time Lyapunov exponent is $\lambda_1 \approx 1.9$.

In the special arrangement of infinitely many aligned hard disks of decreasing radius, the scattering function was found [364] to be nearly as irregular as in chaotic cases, although the system is integrable. There is an infinite number of periodic orbits, but there are no higher-order cycles and heteroclinic connections. This example implies that in order to establish that a scattering process is chaotic, it is necessary to demonstrate the positivity of the topological entropy (or the Lyapunov exponent of the chaotic set).

6.3 Transitions to Chaotic Scattering

The hard-disk scattering system discussed in Sect. 6.2 exhibits hyperbolic chaotic scattering. In Hamiltonian systems, hyperbolicity of the chaotic saddle occurs only if the dynamics can be described by a complete set of symbolic sequences (e.g., in the Hénon map for $a > a_h(b)$; cf. Fig. 3.9). Hyperbolic scattering can therefore be called in such a case *fully developed chaotic scattering* [74, 194]. A basic question is how hyperbolic chaotic scattering arises as a system parameter changes. This *transition* issue can be addressed by considering scattering in Hamiltonian systems of smooth potentials $V(\mathbf{r})$. The equations of motion for a particle of unit mass are given by

$$\ddot{\mathbf{r}} = -\text{grad}\,V(\mathbf{r}). \tag{6.6}$$

This is a time-independent Hamiltonian problem, and hence the particle's total energy E is conserved. The transition scenario is schematically illustrated in Fig. 6.6, where E is regarded as a bifurcation parameter, and E_c is a critical parameter value. For $E > E_c$, the scattering dynamics is either regular or chaotic but nonhyperbolic (to be discussed in Sect. 6.4). Hyperbolic chaotic scattering occurs for $E < E_c$. Here we address possible types of bifurcations to hyperbolic chaotic scattering.

In two-degree-of-freedom time-independent Hamiltonian systems, there are two known routes to hyperbolic chaotic scattering. The first is the *abrupt bifurcation* in
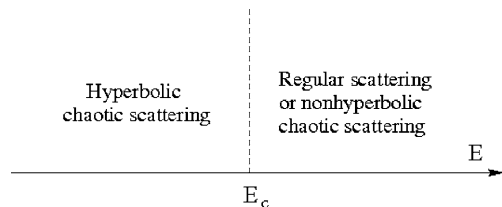

Fig. 6.6 Schematic illustration of bifurcation to hyperbolic chaotic scattering

which the scattering is regular for $E > E_c$, but as soon as E is decreased through E_c, hyperbolic chaotic scattering occurs [74, 436]. Accordingly, the number of unstable periodic orbits associated with the scattering dynamics is zero or finite for $E > E_c$ (corresponding to zero topological entropy), but immediately becomes infinite for $E < E_c$ ($K_0 > 0$). In the second route, the creation of periodic orbits is not abrupt but through the *saddle-center* and period-doubling bifurcations.[2] The existence of the center after a saddle-center bifurcation implies that there are surrounding KAM tori. In this case, when chaotic scattering appears, it is nonhyperbolic. (At a lower energy, E_c, it might, however, become hyperbolic.)

6.3.1 Scattering from a Single Hill

It is useful to review the dynamics of scattering from a single potential hill. Consider the localized potential:

$$V(x,y) = \begin{cases} E_m\left[1 - \frac{x^2+y^2}{R^2}\right], & x^2 + y^2 \le R^2, \\ 0, & x^2 + y^2 > R^2. \end{cases} \tag{6.7}$$

The quadratic form is prototypical for any circularly symmetric potential around its hilltop of height E_m. The equation of motion (6.6) within the disk of radius R is therefore $\ddot{\mathbf{r}} = s^2\mathbf{r}$ with

$$s = \frac{\sqrt{2E_m}}{R}, \tag{6.8}$$

which has the solution

$$\mathbf{r}(t) = \frac{s\mathbf{r}_0 + \mathbf{v}_0}{2s}e^{st} + \frac{s\mathbf{r}_0 - \mathbf{v}_0}{2s}e^{-st} \tag{6.9}$$

under the initial condition $\mathbf{r}(0) = \mathbf{r}_0$ and $\mathbf{v}(0) = \mathbf{v}_0$.

Consider now the case in which a particle approaches the scattering region (circle of radius R) from a large distance along the x-axis. The particle speed is v_0 and the impact parameter is b. The incident angle θ defined by Fig. 6.7 is zero. Upon entering the scattering region, the position is $\mathbf{r}_0 = (-\sqrt{R^2 - b^2}, b)$. For sufficiently large R (small b), the particle spends a long time within the scattering region, so that $st \gg 1$. The second term in (6.9) is then negligibly small when the particle leaves the circle. The velocity components at the time of exit are $v_x = [(v_0 - s\sqrt{R^2 - b^2})/2]\exp(st)$ and $v_y = (sb/2)\exp(st)$. The angle that the scattered trajectory makes with the x-axis is $\tan\phi = v_y/v_x$. Since $E = v_0^2/2$, the deflection function is, using (6.8),

---

[2] A saddle-center bifurcation in a Hamiltonian system is equivalent to a saddle-node bifurcation in dissipative systems that is responsible, for instance, for the creation of periodic windows in a chaotic parameter regime.

Fig. 6.7 Schematic illustration of a scattering trajectory. The incoming particle before the scattering is characterized by two initial variables: the impact parameter b and the incident angle θ. The outgoing particle after the scattering is characterized by the deflection angle ϕ
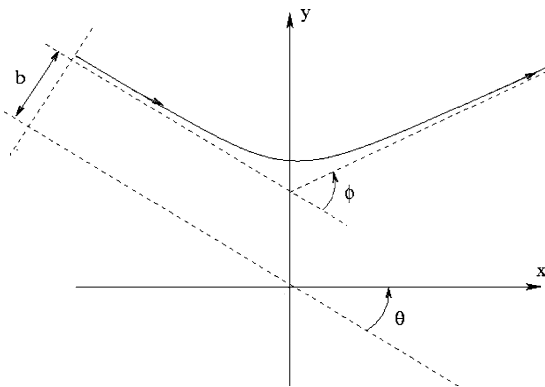
$$\tan \phi(b) = \frac{b/R}{\sqrt{E/E_m} - \sqrt{1 - (b/R)^2}}. \tag{6.10}$$

The maximal deflection angle ϕ_m occurs at $b = R\sqrt{(E - E_m)/E}$ and is given by

$$\tan \phi_m = \sqrt{E_m/(E - E_m)}, \quad E \geq E_m. \tag{6.11}$$

Above the hilltop energy, i.e., for $E > E_m$, the maximum deflection angle is $\phi_m < \pi/2$. As $E \to E_m$ from above, the maximum angle approaches 90°. Below the hilltop energy, the deflection angle can take on *any* value: $0 \leq \phi \leq 180°$. (For $b \to 0$ backscattering occurs, i.e., $\phi \to 180°$.)

## 6.3.2 Abrupt Bifurcation to Chaotic Scattering

6.3.2.1 Basic Phenomenon

A prototypical example to illustrate the abrupt route to chaotic scattering is the planar potential scattering system introduced in [74]. The potential is given by

$$V(x,y) = x^2 y^2 \exp\left[-(x^2 + y^2)\right], \tag{6.12}$$

as shown in Fig. 6.8, where there are four potential hills located at $(x,y) = (\pm 1, \pm 1)$ of identical height $E_m = \mathrm{e}^{-2} \approx 0.13533$. Particle motion is governed by (6.6) with $\mathbf{r} = (x,y)$. Because of the conservation of energy, there are only three independent first-order differential equations, so the phase-space dimension is three. Now suppose that particles of energy E and impact parameter b are launched toward the scattering region where the value of $V(x,y)$ is appreciable (e.g., $R = \sqrt{x^2 + y^2} \leq 5.0$). Since the maximum of the potential hills is locally quadratic, the results from Sect. 6.3.1 can be applied. For $E > E_m$, particle trajectories can reach any point of the plane. While the trajectories are typically deflected

Fig. 6.8 Surface plot of the
four-hill potential $V(x,y)$
defined by (6.12) [74] (with
kind permission from
Elsevier Science)
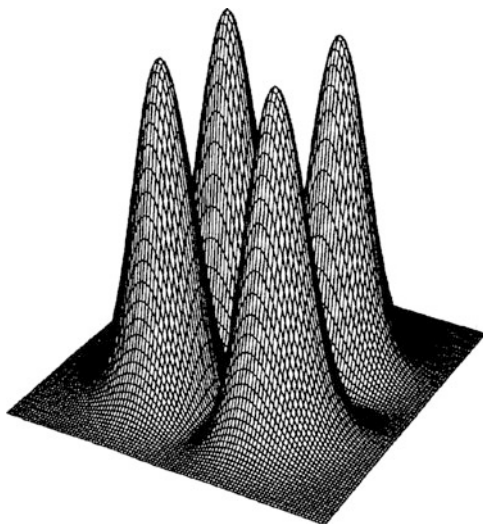
by the potential, the deflection angle from a single potential hill is less than $90°$,
(6.11), and hence particles cannot bounce back and forth between any pair of po-
tential hills. In this case, no periodic orbit can be formed. If, however, the particle
energy is smaller than the height of the potential hill, $E < E_m$, trajectories cannot
penetrate the region of the hill where the values of the potential function are larger
than E. As a result, the deflection angle from any single potential hill can reach
$180°$, making possible bounces among the hills and consequently periodic motions
in the scattering region. In this case, qualitatively, the system is similar to the
hard-disk scattering system discussed in Sect. 6.2, and we expect hyperbolic chaotic
scattering to occur for $E < E_m$. Indeed, the deflection and the delay-time functions
exhibit features similar to those in Fig. 6.3a,b. Bifurcation to chaotic scattering is
abrupt in the sense that chaos arises immediately as the particle energy is decreased
through the critical value $E_c = E_m$.

For E slightly below E_m, trajectories can be confined in the scattering region,
experiencing backscattering, or bouncing among the potential hills. Unstable peri-
odic orbits can then exist, as shown in Fig. 6.9, where several orbits are indicated
schematically. In addition, an uncountably infinite number of aperiodic orbits exist
that traverse among the hills in any order. These periodic and aperiodic orbits can
be determined by utilizing symbolic dynamics, as in the hard-disk scattering system
treated in Sect. 6.2. In particular, four distinct symbols, say $S_i = 0, 1, 2$, and 3, can be
associated with each hill, as shown in Fig. 6.9. Since no symbol can repeat consec-
utively in any sequence, the number N_m of distinct periodic sequences of period m
increases exponentially with m, $N_m \sim 3^m$, implying that no periodic orbit is missing.
The topological entropy is then $K_0 = \ln 3 > 0$, ensuring the existence of a chaotic
saddle. Since every orbit is unstable, scattering is hyperbolic. Explicit numerical
computations using this definition confirm the discontinuous change is the topolog-
ical entropy from 0 to $\ln 3$ when the system exhibits an abrupt bifurcation to chaotic
scattering [191].

Fig. 6.9 Representative
unstable periodic orbits of
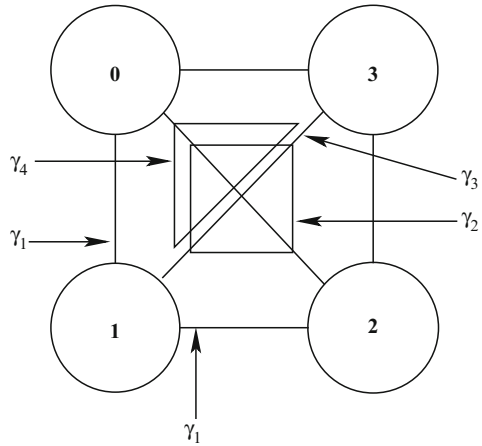low periods in the four-hill
scattering system

Fig. 6.10 Scattering region
bounded by four distinct
periodic orbits of period 2
and a crossing orbit. The
existence of such an orbit
implies a heteroclinic tangle
of intersections between the
stable and the unstable
manifolds of the
corresponding pair of
periodic orbits that are not
located at opposite sides of
the bounding region
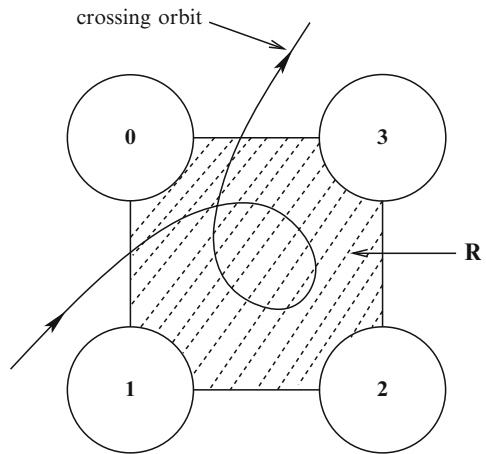
Here we briefly describe the rigorous results [138, 139, 643] that imply the existence of a chaotic saddle for $E < E_m$. Mathematically, for $E < E_m$, the topology of the energy surface is characteristically different from that for $E > E_m$. Specifically, for $E < E_m$, there are four regions in the (x,y)-plane, determined by $V(x,y) > E$, into which classical trajectories are forbidden. There are then four unstable periodic orbits of period 2 along segments of the straight lines $x = \pm 1$ and $y = \pm 1$ (the four γ_1 orbits in Fig. 6.9), which are the boundaries of the scattering region R, as shown in Fig. 6.10. Orbits leaving R never return. The analyses in [138, 643] indicate that if there is a trajectory that enters R through one of the bounding periodic orbits and leaves through another, but nonopposite, bounding periodic orbit, the corresponding two bounding periodic orbits have a heteroclinic tangle of intersections of their stable and unstable manifolds. Such a trajectory is called a "crossing-orbit," as schematically illustrated in Fig. 6.10. By symmetry, the
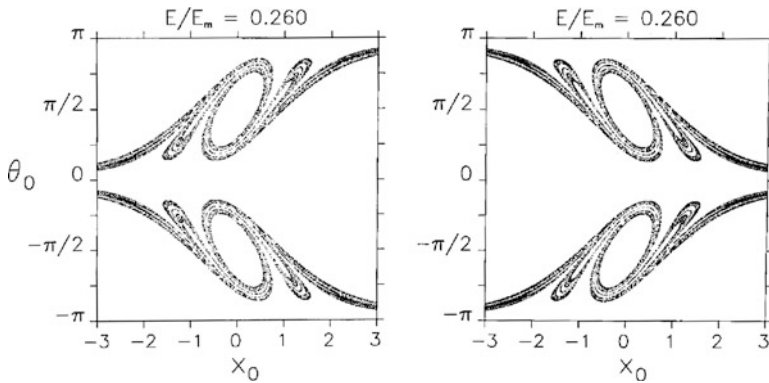
Fig. 6.11 Stable (*left*) and unstable (*right*) manifolds of the chaotic saddle for $E = 0.260E_m$ [74] (with kind permission from Elsevier Science)

existence of a crossing orbit for any pair of nonopposite sides implies the existence of crossing orbits for all four pairs of nonopposite sides. A heteroclinic tangle of stable and unstable manifolds implies the existence of a chaotic saddle in R. The problem of demonstrating hyperbolic chaotic scattering in this case thus reduces to the straightforward task of finding crossing orbits, which are indeed found in numerical experiments [74].

The saddle and its stable and unstable manifolds can be visualized conveniently on a proper Poincaré surface of section. Recall that the phase-space dimension is three, so any three independent variables can be utilized to represent the dynamics. One can choose, for instance, (x, θ, y) (for the choice of θ, see Fig. 6.7). Choosing the surface of section defined by $y = 0$ and computing the intersecting points of trajectories with the two-dimensional plane (x, θ) for $\dot{x} > 0$, the authors in [74] obtained the stable and unstable manifolds of the chaotic saddle, as shown in Fig. 6.11 for $E = 0.26E_m$. The intersecting points between the stable and unstable manifolds constitute the chaotic saddle itself, which can also be obtained via the PIM-triple method (Sect. 1.2.2.4), as shown in Fig. 6.12. Note that the x, y coordinates of points on the saddle are contained completely in the region R.

6.3.2.2   Scaling of Dynamical Invariants with Energy

While the transition to chaotic scattering is abrupt, the dimension of the set of singularities in the scattering function changes continuously from zero as E is decreased from E_m. To obtain the scaling of the box-counting dimension with the energy difference $(E - E_m)$, an insightful approach is to construct a model scattering system with self-similarity in the underlying fractal set. Consider the system of three symmetric hills of identical height E_m, as shown in Fig. 6.13a. In order for the potential hills to be equivalent to hard disks, the sizes of the cross sections of the hills should

Fig. 6.12 For $E = 0.260 E_m$, the chaotic saddle responsible for the observed hyperbolic chaotic scattering [74] (with kind permission from Elsevier Science)
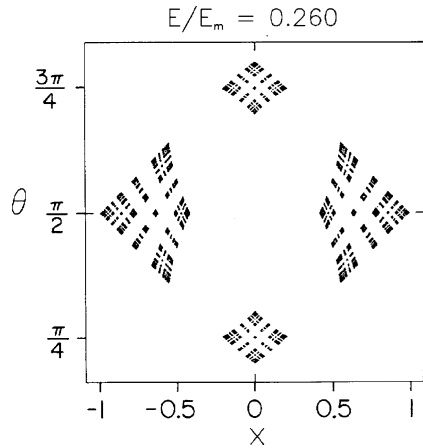

Fig. 6.13 For a scattering system of three identical hills (**a**), the corresponding cantor-set construction (**b**)
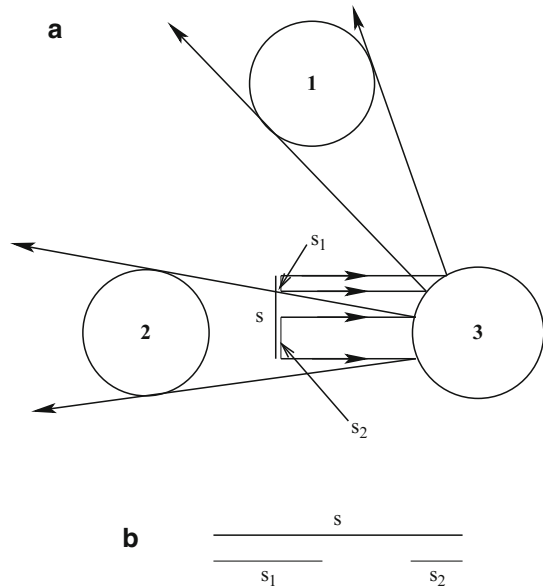
be small. This stipulates that the energy be close to E_m. In the "hard-disk" range of each hill, the deflection angle satisfies $|\tan\phi| \sim O(1)$. It can be seen from (6.10) that this holds in the range $b \sim (E_m - E)$. For the potential configuration in Fig. 6.13a, deflection angles near 180° and 120° are relevant because the corresponding trajectories are reflected by the hills and are likely to stay in the scattering region for a relatively long time. Effectively, a reflection occurs when a particle is within a distance of order $(E_m - E)$ of any peak. The potential hills in Fig. 6.13a can thus be considered hard disks of radii on the order of $(E_m - E)$.

Suppose now that particles are launched along the *x*-direction from a vertical line segment located between hills 2 and 3. Let the interval s correspond to initial conditions that reflect from hill 3. The subintervals $s_1 \subset s$ and $s_2 \subset s$ correspond to initial conditions that reflect from hill 3 and then from hills 1 and 2, respectively. Figure 6.13b shows the first stage of the construction of a Cantor set. The sizes of interval s and subintervals $s_{1,2}$ satisfy

$$s \sim E_m - E, \quad \text{and} \quad s_{1,2} \sim (E_m - E)^2. \tag{6.13}$$

Since the relation of interest is how the box-counting dimension of the Cantor set scales with the energy, the Cantor set can be regarded as if it were exactly self-similar. For such a Cantor set whose first stage of construction is as indicated in Fig. 6.13b, the dimension d_s of the set of singularities is determined by the following transcendental equation, (1.20):

$$\left(\frac{s_1}{s}\right)^{d_s} + \left(\frac{s_2}{s}\right)^{d_s} = 1, \tag{6.14}$$

which yields, as a consequence of (6.13),

$$(E_m - E)^{d_s} \sim \text{constant}.$$

The scaling law of the box-counting dimension near the abrupt bifurcation to chaotic scattering is then given by

$$d_s = \frac{D_0}{2} \sim \frac{1}{\ln\left[(E_m - E)^{-1}\right]}. \tag{6.15}$$

It can be seen that $d_s \to 0$ as $E \to E_m$, which is consistent with the physical picture that the scattering is regular for $E > E_c = E_m$.

The dynamics on the interval s is analogous to that of the open one-dimensional tent map treated in Chap. 2. The escape rate and the Lyapunov exponent are given by $\kappa = -\ln(s_1/s + s_2/s)$ and $\lambda_1 = -[s_1 \ln(s_1/s) + s_2 \ln(s_2/s)]/(s_1 + s_2)$, (2.28) and (2.30), respectively. Using (6.13), one can find that [768]

$$\kappa = -\ln(E_m - E) + C_0, \quad \lambda_1 = -\ln(E_m - E) + C_1, \tag{6.16}$$

where C_0 and C_1 are constants. The divergence at E_m implies that all bounded orbits are infinitely unstable when they appear at $E_c = E_m$, and consequently, the escape from the entire saddle is infinitely fast. The orbits become less unstable when the energy decreases, but the saddle remains ratified as reflected by the scaling of the dimension (6.15). Deviations from the circular symmetry have also been considered, such as potential hills with elliptical tops [772]. Abrupt bifurcation thus appears to be a generic route to chaotic scattering.

6.3.3 Saddle-Center Bifurcation to Chaotic Scattering

Besides the abrupt bifurcation route, in two-degree-of-freedom Hamiltonian systems there is another generic route to chaotic scattering, which is similar to the period-doubling route to chaos in dissipative dynamical systems [235, 236]. In this route [74, 194], when scattering first becomes chaotic, it is typically nonhyperbolic in the sense that there are coexisting KAM tori in the phase space. As the bifurcation parameter is varied further, hyperbolic chaotic scattering arises.

A paradigm for understanding the saddle-center route to chaotic scattering, relative to the abrupt bifurcation route, is the general scattering configuration consisting of three asymmetric potential hills [74, 194] of heights E_{m1}, E_{m2}, and E_{m3}, where $E_{m1} \leq E_{m2} \leq E_{m3}$. Depending on the relative positions of the three hills, there are two situations of interest, as shown in Fig. 6.14, where the distances between the centers of the hills are much larger than the effective radii of the hills. The hills are denoted by dots located at 1, 2, and 3. In case (a), the hill of the lowest maximal energy (hill 1) is outside the circle whose diameter is the line joining the two hills with larger maximal energy values (hills 2 and 3). In case (b), hill 1 is inside the circle.

Consider the first case (a). In order to have a trapped orbit, the minimally required deflection angle ϕ_{m*} by hill 1 for particles coming from hill 2 or hill 3 should be greater than $90°$. If the particle energy is greater than E_{m1} but smaller than E_{m2}, this condition cannot be satisfied, and hence there are no bounded orbits reflecting from hill 1. In this case, the only allowed periodic orbit is the one bouncing back and forth between hills 2 and 3. Scattering is thus not chaotic for $E > E_{m1}$. As E is lowered through E_{m1}, the deflection angle at hill 1 can immediately reach $180°$, as seen in Sect. 6.3.1. Consequently, as E is decreased through E_{m1}, unstable periodic orbits of all possible sequences of visits to all three hills can exist, which is analogous to the three hard-disk scattering system treated in Sect. 6.2. There is then an abrupt bifurcation to chaotic scattering.

Now consider case (b) with energy in the range $E_{m1} < E < E_{m2} \leq E_{m3}$. The deflection angles by hills 2 and 3 can be as high as $180°$. Let $\phi_{m1}(E)$ be

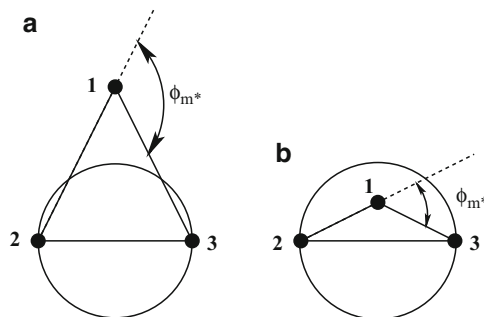**Fig. 6.14** Scattering configurations of three nonidentical potential hills: the abrupt-bifurcation route occurs in case (**a**), and the saddle-center-bifurcation route can occur in case (**b**). The heights of the hills are ordered as $E_{m1} \leq E_{m2} \leq E_{m3}$, and ϕ_{m*} denotes the deflection angle required by an orbit coming from hill 2 to be reflected by hill 1 toward hill 3

the maximum deflection angle by hill 1, and let E_{m*} denote the energy at which the maximum deflection angle is ϕ_{m*}. From Sect. 6.3.1, we know that $\phi_{m1}(E_{m2}) < 90°$ and $\phi_{m1}(E_{m1}) = 90°$. Since hill 1 is now inside the circle, the maximal deflection angle required for an orbit to be trapped is $\phi_{m*} < 90°$. There are then two situations: $\phi_{m1}(E_{m2}) > \phi_{m*}$ and $\phi_{m1}(E_{m2}) < \phi_{m*}$. As the maximum deflection angle increases with decreasing energy, (6.11), these situations correspond to $E_{m*} > E_{m2}$ and $E_{m*} < E_{m2}$, respectively.

In the first case, the maximum deflection angle from hill 1 is greater than ϕ_{m*} because for $E < E_{m2}$, we have $\phi_{m1}(E) > \phi_{m1}(E_{m2}) > \phi_{m*}$. Thus, as in case (a) in Fig. 6.14, periodic orbits of all possible sequences of visits to three hills can exist. There is then an abrupt bifurcation to chaotic scattering as E is decreased through $E_c = E_{m2}$.

The characteristically distinct route to chaotic scattering occurs when the system configuration is such that $E_{m*} < E_{m2}$, i.e., $\phi_{m1}(E_{m2}) < \phi_{m*}$. In this case, for E smaller than but close to E_{m2}, there is no chaos. As E is decreased, $\phi_{m1}(E)$ will increase until $E = E_{m*}$, where the maximum deflection angle is equal to ϕ_{m*}. For smaller values of E, $E_{m1} < E < E_{m*}$, there can then be orbits traversing back and forth between hills 2 and 3 through hill 1 with symbol sequences such as $\ldots 2131213\ldots$ that do not contain subsequences 23 and 32, as shown in Fig. 6.15. This situation is completely different from abrupt bifurcation, where periodic orbits of all orders of three symbols are possible. Here, as the energy is decreased from E_{m*}, there will eventually be unstable periodic orbits made up of all possible combinations of the symbols, leading to hyperbolic chaotic scattering at some energy $E = E_c < E_{m*}$.

As E is decreased from E_{m*} to E_c, an infinite number of unstable periodic orbits is created. In contrast to the case of abrupt bifurcation, where the infinite set of unstable periodic orbits is created as a result of a sudden change in the topology of the energy surface, here the creation of the periodic orbits is a continuous and smooth process, involving no change in the topology of the energy surface. In smooth Hamiltonian systems of two degrees of freedom, a generic mechanism for generating periodic orbits is saddle-center bifurcations.[3] For saddle-center bifurcations, the centers are stable elliptic orbits surrounded by KAM tori.
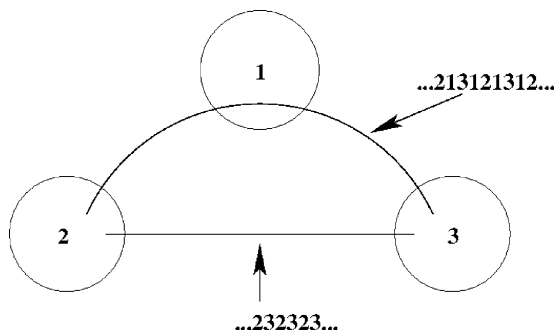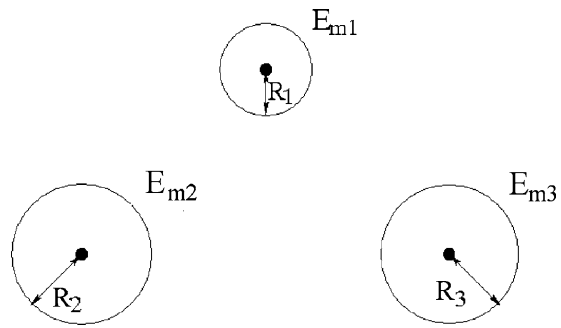

Fig. 6.15 Two distinct types of periodic orbits, and the corresponding symbol sequences, in the saddle-center route to chaotic scattering in the case $E_{m1} < E \leq E_{m*} < E_{m2}$, where $\phi_{m1}(E_{m*}) = \phi_{m*} < 90°$

...213121312...

...232323...

---

[3] See footnote 2.

Fig. 6.16 Schematic illustration of the scattering system consisting of three localized quadratic potential hills, as in (6.17), situated at (x_i, y_i)

The centers can undergo period-doubling cascades. Typically, there can be KAM tori coexisting with chaotic saddles, leading to nonhyperbolic chaotic scattering. When the processes of saddle-center bifurcations followed by period-doubling cascades are completed, all elliptic orbits are destroyed and all periodic orbits are unstable, giving rise eventually to hyperbolic chaotic scattering.

The particular way that the infinite number of unstable periodic orbits for hyperbolic chaotic scattering are created was investigated by Ding et al. [194]. For numerical convenience, they chose a combination of localized potentials. The potential function of the system is

$$V(x,y) = V_1(x,y) + V_2(x,y) + V_3(x,y), \tag{6.17}$$

where each V_i is of the form (6.7) with hill height E_{mi}, radius R_i, and centered at (x_i, y_i). Potentials V_2 and V_3 were chosen to be identical and arranged in a symmetric fashion, as shown in Fig. 6.16. The particle energy E was fixed, and the height E_{m1} of the potential hill 1 was chosen to be the bifurcation parameter. The heights of hills 2 and 3 satisfy $E_{m2} = E_{m3} \gg E$. Decreasing E, as we have discussed in the preceding paragraph, is equivalent to increasing E_{m1}. Figure 6.17a–c show schematically the possible periodic orbits of the system together with their stable and unstable manifolds respectively before, at, and after the saddle-center bifurcation at $E_{m1} = E_{m*}$.

Before the saddle-center bifurcation (Fig. 6.17a), there is only one periodic orbit (denoted by π_1), the one bouncing back and forth between hills 2 and 3. At the bifurcation (Fig. 6.17b), a saddle (denoted by π_3) and a center (denoted by π_2) are born, and they coincide at the bifurcation. After the bifurcation, the saddle and the center are separated, as shown in Fig. 6.17c. Because of the symmetry of the system with respect to $x = 0$, it is convenient to choose the Poincaré surface of section to be $x = 0$. The dynamical variables on the Poincaré section can be chosen to be (v_y, y). The KAM tori surrounding the center π_2 can be obtained numerically [194], as shown in Fig. 6.18. The period-doubling bifurcation of the center can also be computed, as shown in Fig. 6.19, where the center π_2 is already unstable and a new center of period 2 exists.

As E_{m1} is increased further, a cascade of period-doubling bifurcations occurs, which becomes completed at a large enough value $E_{m1} = E_c$. Here, the stable and
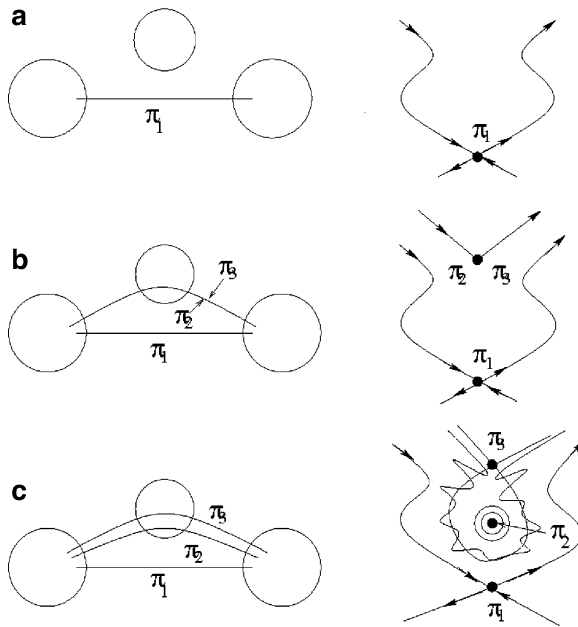
Fig. 6.17 Schematic illustration of periodic orbits in the configuration space (*left*) and in the phase space (*right*), together with their stable and unstable manifolds, before (**a**), at (**b**), and after (**c**) the saddle-center bifurcation [194] (copyright 1990 by the American Physical Society)
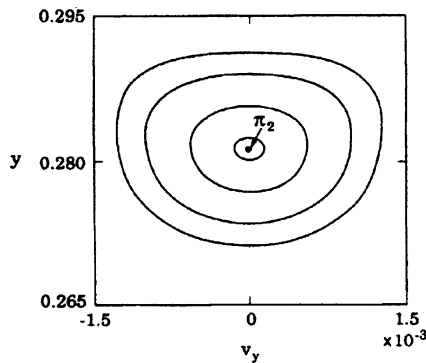
Fig. 6.18 KAM tori surrounding the center π_2 immediately after the saddle-center bifurcation that occurs at $E_{m1} = E_{m*} = 0.187$. Here $E_{m1} = 0.195$, $E = 1$, and other parameters are $x_1 = 0$, $y_1 = 2.2$, $x_2 = -x_3 = 6$, $y_2 = y_3 = 0$, $R_1 = 2$, $R_2 = R_3 = 3$, and $E_{m2} = E_{m3} = 10$ [194] (copyright 1990, the American Physical Society)

the unstable manifolds of the unstable periodic orbits π_1, π_2, and π_3 can have an intricate tangle of heteroclinic intersections. A horseshoe (Sect. 1.2.2.1) of complete symbolic dynamics with $K_0 = \ln 2$ is then formed. For $E_{m1} > E_c$, chaotic scattering is hyperbolic.

Fig. 6.19 New center
of period 2 and its
accompanying KAM tori,
after the period-doubling
bifurcation of π_2, for
$E_{m1} = 0.207$. Other
parameters are the same
as in Fig. 6.18 [194]
(copyright 1990, the
American Physical Society)
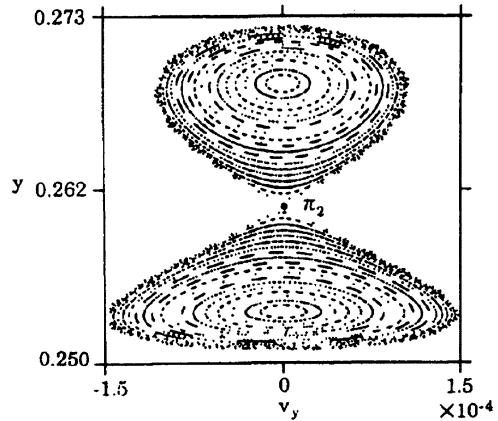
6.3.4 Abrupt Bifurcation to Chaotic Scattering with Discontinuous Change in Dimension

A feature in the abrupt bifurcation discussed in Sect. 6.3.2 is that the dimension d_s of the set of singularities in the scattering functions changes continuously through the bifurcation. In particular, it can be seen from (6.15) that although the bifurcation is considered abrupt, the box-counting dimension d_s is still continuous at the bifurcation (where it takes on the value $d_s = 0$). There exists, in fact, a different type of abrupt bifurcation to chaotic scattering in two-degree-of-freedom Hamiltonian systems for which the box-counting dimension changes *discontinuously* through the bifurcation point [436]. To explain this bifurcation, let the particle energy E be the bifurcation parameter and let E_0 be a bifurcation point. Before the bifurcation ($E < E_0$), there exists a *bounded* chaotic region in the phase space surrounded by forbidden potential barriers. The bounded chaos is typically developed through the destruction of a hierarchy of KAM tori. Particles from outside cannot enter this bounded chaotic region, so that the scattering dynamics is regular. At E_0, the barriers disappear, and the bounded Hamiltonian chaos becomes transient, allowing scattering particles to access the previously forbidden region. Scattering then becomes chaotic for $E > E_0$. The key difference between this scenario to chaotic scattering and that discussed in Sect. 6.3.2 is that here, the change in the dimension of the set of singularities in the scattering function is due to the sudden access of scattering trajectories to *an already developed chaotic set*.

This type of abrupt bifurcation to chaotic scattering can be demonstrated by considering the physically realistic situation whereby particles are scattered by molecules. Assume that there are three molecules located at vertices $\mathbf{x}_j \equiv (x_j, y_j)$ ($j = 1, 2, 3$) of a regular triangle of unit side length. For each molecule, its interaction with a scattering particle can be modeled by the Morse potential, a paradigm for studying various phenomena in chemical and atomic physics [323, 495, 496]. The dimensionless potential function of the scattering system can be written as

$$V(\mathbf{x}) = \sum_{j=1}^{3} V_M(\mathbf{x}, \mathbf{x}_j), \tag{6.18}$$

where

$$V_M(\mathbf{x}, \mathbf{x}_j) = \frac{1}{2}\left[1 - e^{-\alpha(r_j - r_e)}\right]^2, \tag{6.19}$$

and $r_j = \sqrt{(x - x_j)^2 + (y - y_j)^2}$ ($j = 1, 2, 3$) is the distance from vertex j, r_e is the effective range of the potential hill, and α determines the steepness of the potential. Each Morse hill is spherically symmetric and has a repulsive region surrounded by an attractive region. The potential is highly localized, and the region about $(x, y) = (0, 0)$, where $V(x, y)$ is appreciable, can be regarded as the scattering region. The difference between this scattering model and the one in Sect. 6.3.2 is that the height of the potential is large ($E_m \approx V_M(\mathbf{x}_j, \mathbf{x}_j) \gg 1$), so that the potential hills are classically impenetrable. As a result, the abrupt bifurcation here occurs at low energies when the energy is *increased* through a critical value, in contrast to the case treated in Sect. 6.3.2.

In a physically realistic energy regime, the particle energy is much smaller than the height of the potential hills: $E \ll E_m$. Figure 6.20a,b show the contours of the potential for $E = 1$ and 4, respectively, where for $E = 1$, the region enclosed between the inner and outer closed curves is the classically forbidden one, and for $E = 4$, the regions enclosed by the three somewhat circular closed curves are the classically forbidden regions. Thus, for $E = 1$, particles coming from afar cannot enter the scattering region, and they simply are bounced back from the potential. In this case, the scattering is regular. However, for $E = 4$, the potential configuration is similar to that of three hard disks for which the scattering is chaotic. Figure 6.21 shows the scattering functions for $E = 1$ and $E = 4$. For $E = 4$, scattering becomes chaotic, since
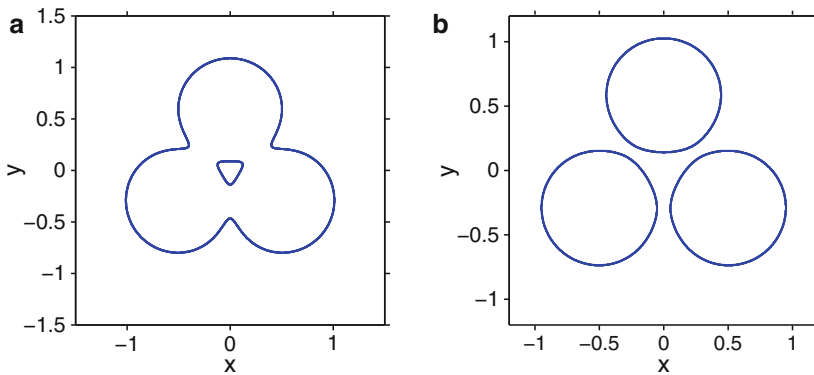

Fig. 6.20 Contour plots of the Morse potential (6.18) configuration for (**a**) $E = 1$ and (**b**) $E = 4$. Other parameters are $\alpha = 6$ and $r_e = 0.68$. The locations of the vertices of the triangle are $(x_1, y_1) = (1/2, -1/(2\sqrt{3}))$, $(x_2, y_2) = (-1/2, -1/(2\sqrt{3}))$, and $(x_3, y_3) = (0, \sqrt{1/3})$ [436] (copyright 1999, the American Physical Society)
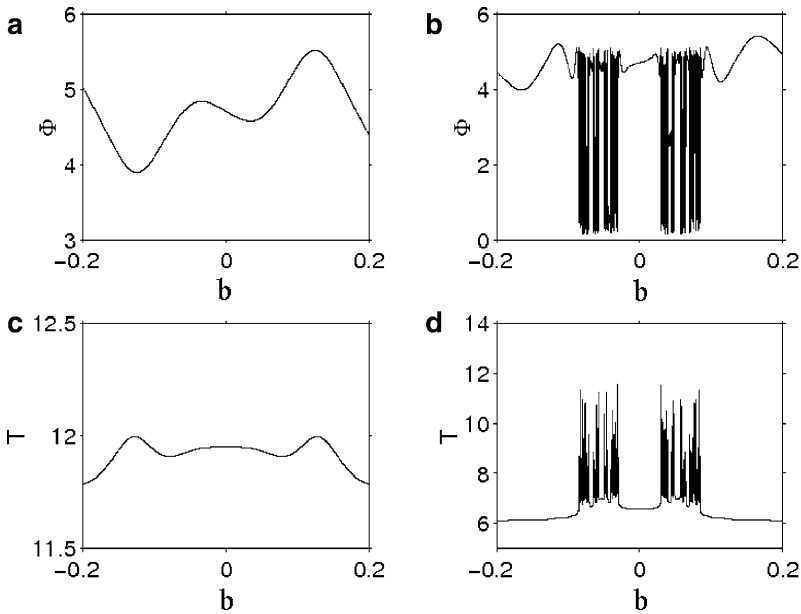
Fig. 6.21 Scattering functions: (**a**), (**b**) Deflection functions $\phi(b)$ for $E = 1$, and $E = 4$, respectively. (**c**), (**d**) Delay-time functions $T(b)$ for $E = 1$ and $E = 4$, respectively. Parameters are the same as in Fig. 6.20 [436] (copyright 1999, the American Physical Society)

there are an infinite number of singularities in the scattering function. Figure 6.21c,d show the corresponding delay-time plots for $E = 1$ and $E = 4$, respectively.

The absence and presence of chaotic scattering at $E = 1$ and $E = 4$, respectively, suggest that there is a bifurcation to chaotic scattering as E is increased from 1 to 4. It can be argued that this bifurcation is abrupt. In particular, for $E = 1$, there is a small triangular-like area in the center of the scattering region (Fig. 6.20a) in which the value of the potential is actually lower than E, and hence this area is allowed for particle trajectories. This region, however, is *inaccessible* to scattering particles from outside, because it is enclosed by a larger forbidden region. Dynamics inside the triangular-like potential region can be chaotic. For $E = 1$, the phase space contains both KAM tori and Hamiltonian chaotic seas, as shown in Fig. 6.22a, where the x-coordinate and the x-component of the particle velocity are plotted on the Poincaré surface of section defined by $y = 0$. Chaos in this case is bounded. As E is increased, the triangular-like area enlarges and the phase-space structure inside also evolves. In particular, KAM tori are destroyed and the chaotic sea is enlarged, as shown by the phase-space structure on the Poincaré surface of section in Fig. 6.22b for $E = 2.5$. At some critical energy value E_0 where the inner allowed region connects with the outside one, the previously bounded chaotic sea becomes a chaotic saddle because trajectories can escape through one of the openings (Fig. 6.20b). Now particles coming from outside can access the transienting chaotic region, so that the scattering becomes chaotic. The appearance of chaotic scattering is abrupt, because for $E < E_0$, the scattering dynamics is smooth, while it is chaotic for $E > E_0$.
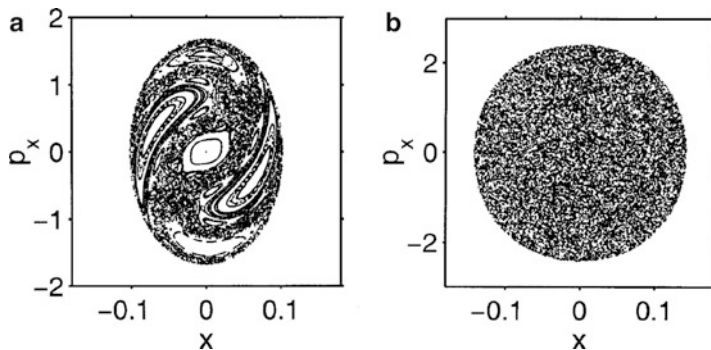
Fig. 6.22 Phase-space structure on a Poincaré surface of section of the classically allowed region that is inaccessible to scattering particles for (**a**) $E = 1$, and (**b**) $E = 2.5 < E_0$. There are both KAM tori and bounded chaotic seas for $E = 1$. For $E = 2.5$, all KAM tori have disappeared. Parameters are the same as in Fig. 6.20 [436] (copyright 1999, the American Physical Society)

The critical energy E_0 can be estimated as follows. For each individual potential hill, the radius $r > r_e$ of the classically forbidden spherical region is

$$r = r_e - \frac{1}{\alpha} \ln \left(1 + \sqrt{2E} \right).$$

If there is no overlapping between the potentials, two adjacent potentials touch each other at $r = 1/2$. Thus, E_c is approximately determined by

$$r_e - \frac{1}{\alpha} \ln \left(1 + \sqrt{2E_0} \right) \approx 1/2.$$

For $r_e = 0.68$, $\alpha = 6$, this gives $E_0 \approx 1.9$. Due to the overlapping among potentials, the actual value of E_0 is somewhat larger than the estimated one. It was found numerically [436] that $E_0 \approx 2.55$.

In this route to chaotic scattering, depending on whether there are still KAM tori left for E slightly above E_0, the scattering can be either hyperbolic or non-hyperbolic. For the scattering configuration described, abrupt bifurcation leads to *hyperbolic chaotic scattering*. An alteration in the scattering configuration can lead to abrupt bifurcation to nonhyperbolic chaotic scattering. For instance, when the Morse molecule on the y-axis is pulled closer to the pair in the x-direction, say at $y_3 = 0.45$, there are still KAM tori left in the scattering region after the bifurcation that connects the inner and outer allowed regions.

The major physically measurable consequence of the abrupt bifurcation to chaotic scattering described above is that there is a discontinuous change in the dimension d_s of the set of singularities in the scattering function. From Fig. 6.21a–d, it is apparent that for $E < E_0$ (before the bifurcation), both the scattering and the delay-time functions are smooth, and hence, $d_s = 0$. For $E > E_0$ (after the bifurcation), the scattering and the delay-time functions suddenly contain a Cantor set

Fig. 6.23 Box-counting
dimension d_s of the set of
singularities in the scattering
function versus E. There is a
jump in d_s at E_0, the abrupt
bifurcation point to chaotic
scattering with discontinuous
change [436] (copyright
1999, the American Physical
Society)
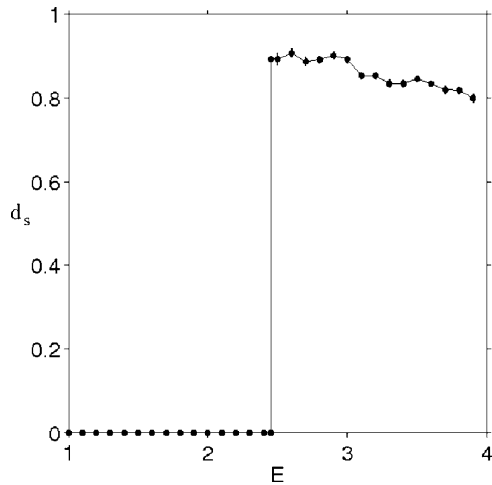
of singularities with $d_s > 0$. Figure 6.23 shows d_s versus E for $1.0 \le E \le 4.0$. Theoretically, for E immediately above E_0 when the bounded chaotic sea in the scattering region just becomes transient, the value of d_s is unity because by continuity, the box-counting dimension of the chaotic saddle for E slightly above E_0 is the same as that of the Hamiltonian chaotic sea for E slightly below E_0, which is the phase-space dimension. Numerically, it was found that $d_s \approx 0.9$ for $E = 2.6 > E_0$. This discontinuous change in the box-counting dimension is the key ingredient that distinguishes this abrupt route to chaotic scattering from the one discussed in Sect. 6.3.2.

6.4 Nonhyperbolic Chaotic Scattering

6.4.1 Algebraic Decay

In general, Hamiltonian systems arising in situations of physical interest permit three types of dynamics: regular (integrable), completely chaotic (hyperbolic), and nonhyperbolic, where regular and hyperbolic dynamics correspond somewhat to the two oppositely extreme situations, and nonhyperbolic dynamics lies somewhere in between them. Thus, in open Hamiltonian systems, while hyperbolic scattering can be expected, a more common situation has chaotic saddles encircling KAM tori in the phase space, for which the scattering is nonhyperbolic. Indeed, as we have seen, in the saddle-center route to hyperbolic scattering, there exists a wide parameter interval for which the scattering is nonhyperbolic.

A fundamental issue in nonhyperbolic chaotic scattering concerns the impact of the presence of KAM surfaces on particle motions. In this regard, one generally observes that, if a particle enters a chaotic region near some KAM surface, the particle wanders close to that surface for a long time. This is called the *stickiness* effect of

KAM tori. The origin of this stickiness effect can be understood by the following simple observation. Take two nearby points on a given KAM surface and observe their evolution. What one typically finds is that the distance between the two points hardly changes with time, because the Lyapunov exponents in the directions along the KAM surface are zero (i.e., the motion is quasiperiodic). The symplectic nature of the Hamiltonian dynamics stipulates that the Lyapunov spectrum be organized in pairs of exponents with equal values but opposite signs. An orbit on a KAM surface there has zero Lyapunov exponents in directions both along and perpendicular to the surface. Now consider a particle initialized in the chaotic region. Due to ergodicity, this particle will come arbitrarily close to some KAM surface bordering the chaotic region. When this occurs, the effective, finite-time Lyapunov exponents become nearly zero, leading to slow divergence of the particle trajectory from the KAM surface. The role of the KAM surfaces is similar to that of a marginally stable fixed point in one-dimensional nonhyperbolic transient chaos, as described in Sect. 2.4.

The main consequence of the stickiness effect on chaotic scattering is that the probability (density) $p(t)$ of escaping at time t is asymptotically algebraic, and hence the long-time behavior of the survival probability $P(t)$ is also algebraic:

$$p(t) \sim t^{-z-1}, \quad P(t) \sim t^{-z}, \quad \text{for large } t, \tag{6.20}$$

where z is an algebraic-decay exponent [136, 137, 315, 388, 513–515], in contrast to exponential decay in hyperbolic chaotic scattering or associated with chaotic transients in dissipative systems.

The algebraic-decay exponent, as defined by (6.20), in fact characterizes scattering situations, i.e., situations in which the initial conditions are chosen *far away* from KAM surfaces. There exists a distinct type of initial conditions, e.g., those chosen in the sticking region, for which the exponent is different. Following the escape process of these initial conditions is called the transient-chaos approach to chaotic scattering [603]. The corresponding escape time and survival probability distributions $p_{tr}(t)$ and $P_{tr}(t)$, respectively, obey the law

$$p_{tr}(t) \sim t^{-z_{tr}-1}, \quad P_{tr}(t) \sim t^{-z_{tr}}, \quad \text{for large } t, \tag{6.21}$$

with a different decay exponent z_{tr}. Pikovsky pointed out [603] that a larger number of trajectories are held up in the transient case than in the scattering case and the exponent z_{tr} is smaller than z with unit difference:

$$z_{tr} = z - 1. \tag{6.22}$$

A derivation of this rule will be given in Sect. 6.4.5.

The escape-time distribution of the transient case is thus proportional to the survival probability of the scattering case:

$$p_{tr}(t) \sim P(t). \tag{6.23}$$

As a consequence of the algebraic decay, the escape rate from regions around KAM surfaces tends to zero, $\kappa \to 0$, implying, according to (2.76), that the chaotic saddle is locally space-filling:

$$D_0 = D_1 = 2. \tag{6.24}$$

A detailed discussion about the dimensionality will be given in Sect. 6.4.3.[4]

Theoretical models [144,315,514,515] have been proposed to explain the numerically observed algebraic-decay law. A fundamental assumption of these models is that a particle in the phase space executes a random walk between families of self-similar chains of islands. Besides yielding the algebraic scaling law, these models also predict the values of the algebraic-decay exponent based on the number of self-similar families of KAM islands included in the calculation. It should be pointed out, however, that chaotic systems with no KAM surfaces may also exhibit an algebraic-decay behavior, reflecting some long-term correlation among orbits. One example of such systems is the Bunimovich stadium, in which the dynamics is completely chaotic. The origin of the long-term correlation in this system is due to the existence of an infinite class of neutrally stable periodic orbits in the phase space [473, 801].

As a system parameter is changed, if observations are made over *finite times*, the resulting algebraic-decay exponent can exhibit large fluctuations [286, 445]. The dynamical mechanism underlying the fluctuations will be treated in Sect. 6.5. The rest of this section will be devoted to the development of horseshoe structure in nonhyperbolic chaotic scattering, the box-counting dimension, the intermediate-time behavior, and the relationship between scattering and leaked dynamics.

6.4.2 Development of Horseshoe Structure in Nonhyperbolic Chaotic Scattering

As a parameter changes, the saddle underlying nonhyperbolic chaotic scattering can undergo structural changes before it becomes a fully developed hyperbolic saddle with a complete grammar. It was pointed out by Jung and coworkers that a parameter can be introduced to characterize the development of the underlying horseshoe structure [362, 657], which measures the penetration depth of the tendrils into the interior of the fundamental area of the horseshoe.

To be specific, we consider here the case of a binary horseshoe characterized by the existence of two fixed points on a Poincaré map. One of the fixed points is hyperbolic for any parameter values, and it lies inside the scattering region. Its invariant manifolds trace out the horseshoe. The stability of the other fixed point depends on the parameter values. Initially, this inner fixed point is stable and surrounded by

---

[4] The algebraic-decay law holds not only for two-degree-of-freedom Hamiltonian systems, but also for higher-dimensional systems [192, 381].
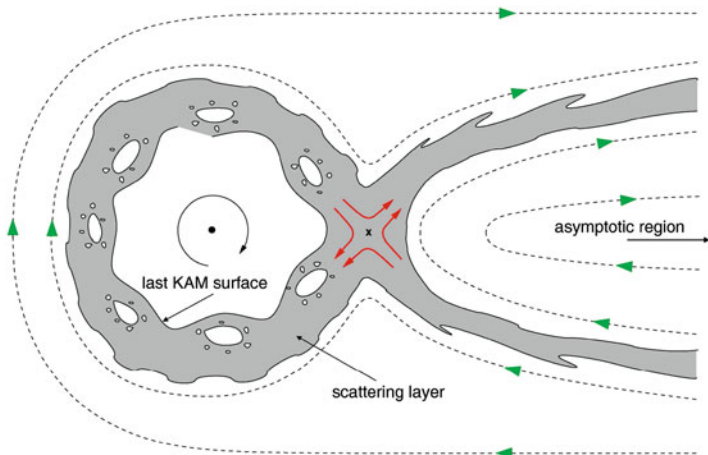
Fig. 6.24 Poincaré section of a scattering system described by a binary horseshoe when the inner fixed point (*black dot*) is elliptic. The arrows indicate the flow of trajectories about the hyperbolic fixed point and outside the scattering layer [363] (with kind permission from the Institute of Physics)

KAM surfaces. As a system parameter is changed, the KAM surfaces break into chains of secondary islands and chaotic layers, which eventually fuse into a fully developed horseshoe. Figure 6.24 is a schematic representation of the case in which a large primary island exists and encloses the inner fixed point.

The development parameter α defined in [362, 657] takes on specific values for certain configurations of the stable and the unstable manifolds of the hyperbolic fixed point. To visualize such a situation, consider Fig. 6.25, which shows the topology of the horseshoe at a somewhat initial stage of its development. The first intersection of the stable and the unstable manifolds, the primary intersection point, is denoted by P. This point, together with the hyperbolic point H and the manifolds passing through them, defines a rectangular domain, the fundamental area of the horseshoe. Tendrils of positive labels are defined as arcs of the manifolds lying within the fundamental area, where labeling starts at P. The tendrils are images or preimages of each other, a property that allows one to define tendrils with negative labels, too. The development parameter takes on values $\alpha = 2^{-m}$ if the first tendril of one of the invariant manifolds is intersected by the tip of the mth tendril of the other manifold at two points only. Figure 6.25 illustrates the case of $m = 4$. It can be seen that the tendrils of levels 2 and 3 also intersect at two points only. In general, the tips of the primary tendrils of the invariant manifolds penetrate into areas that are free of manifolds. As a result, homoclinic bifurcations cannot occur under small changes of the parameters.

When α reaches the values $\alpha = 1/8$, $1/4$, and $1/2$, consecutively, the tendrils become longer, as suggested by Fig. 6.25. The horseshoe becomes more developed and the stability island shrinks during this process. According to the definition in
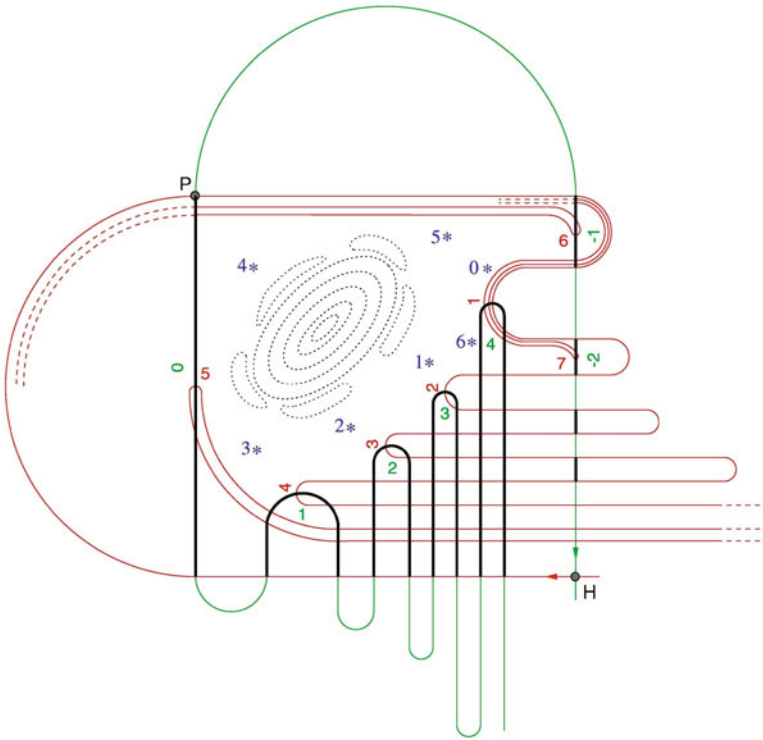
Fig. 6.25 Schematic diagram illustrating the topology of an incomplete binary Hamiltonian horse-shoe for development parameter $\alpha = 1/16$, where H and P denote the hyperbolic fixed point and the primary intersection point, respectively. Tendrils of the stable manifold have been emphasized (*in black*). Stars mark the subsequent images of the point labeled by 0 [363] (with kind permission from the Institute of Physics)

[362,657], α can take on any values $r2^{-m}$ with $r = 1, 2, \ldots, 2^m - 1$ at any fixed level m. For example, $\alpha = 3/4$ corresponds to the case that tendril 2 crosses the fundamental area, turns back into it, and the first tendril of the other manifold becomes intersected again by this long tendril at two points only. The limit $\alpha \to 1$ corresponds thus to a fully developed binary horseshoe with $K_0 = \ln 2$ ($\alpha = 0$ describes an integrable homoclinic loop).

The topology of the horseshoe for any α is unique. In fact, there is a one-to-one correspondence between the topological entropy K_0 and the development parameter:

$$e^{K_0} = g(\alpha), \tag{6.25}$$

where $g(0) = 1$ and $g(1) = 2$. The explicit from of the function $g(\alpha)$ is not known, but its value can be determined [657] for certain values of α, as illustrated in Table 6.1. Relation (6.25) is universal. The dependence of α on system parameters is, however, not universal. Thus the relation between the topological entropy and some system parameter depends on system details.

Table 6.1 Relation between the development parameter α and function $g = \exp(K_0)$ at a few points

α	0	0.25	0.50	0.75	1
$g(\alpha)$	1	1.54	1.71	1.91	2

The ideas can be generalized straightforwardly to ternary horseshoes [362]. The development parameter is then denoted by β, and its typical values are $\beta = 3^{-m}$. An experiment with ternary horseshoes will be presented in Sect. 7.6 in the quantum-mechanical context.

A careful investigation of the geometry of incomplete horseshoes can lead to a detailed understanding of their topological features [361, 527]. The rules that describe how tendrils are mapped onto each other are sometimes called lobe dynamics, and play an important role in the context of fluid transport (Sect. 10.3.3).

6.4.3 Dimension in Nonhyperbolic Chaotic Scattering

An important result in nonhyperbolic chaotic scattering concerns the box-counting dimension of the set of singularities in the scattering function. Lau et al. [470] argued, with numerical support, that the dimension is $d_s = 1$. This unity of the dimension is a direct consequence of the algebraic-decay law associated with nonhyperbolic chaotic scattering, which can be seen intuitively by considering a measure-zero Cantor set that has $d_s = 1$, through the following construction [470]. Start with the unit interval $[0, 1]$, remove the open middle third interval. From each of the two remaining intervals remove the middle fourth interval. Then from each of the four remaining intervals remove the middle fifth, and so on. At the nth stage of the construction, there are $N = 2^n$ subintervals, each of length $\varepsilon_n = [2/(n+2)]2^{-n}$. The total length of all subintervals $\varepsilon_n N \approx 2/n$ goes to zero *algebraically* for $n \to \infty$. For $n \gg 1$, we have $\varepsilon_n \approx 2^{1-n}/n$, and hence $n \approx \ln \varepsilon_n^{-1}/\ln 2$. In order to cover the set with intervals of size ε_n, the required number of intervals is $N(\varepsilon) \approx 2/(\varepsilon n)$, which depends on ε as

$$N(\varepsilon) \approx \frac{2\ln 2}{\varepsilon \ln \varepsilon^{-1}}.$$

The box-counting dimension d_s of the set is then obtained as the limit of

$$\frac{\ln N(\varepsilon)}{\ln \varepsilon^{-1}} = 1 - \frac{\ln \ln \varepsilon^{-1}}{\ln \varepsilon^{-1}} + \frac{\ln(2\ln 2)}{\ln \varepsilon^{-1}}.$$

Note that for $\varepsilon \to 0$ this yields $d_s = 1$. The weak logarithmic dependence does not contribute to the asymptotic dimension value. However, it is the logarithmic term that is responsible for ensuring that the total length (measure) is zero: $\varepsilon N(\varepsilon) \sim (\ln \varepsilon^{-1})^{-1} \to 0$ as $\varepsilon \to 0$.

From a more general standpoint, if at each stage a fraction $\eta_n = \alpha/(n+c)$, where α and c are constants, is removed from the middle of each of the 2^n remaining intervals, then

$$N(\varepsilon) \sim \frac{1}{\varepsilon} \left(\ln \frac{1}{\varepsilon} \right)^{-\alpha}. \tag{6.26}$$

An observation is that the slope of the curve $\ln N(\varepsilon)$ versus $\ln \varepsilon^{-1}$, which is $\mathrm{d} \ln N(\varepsilon)/\mathrm{d}(\ln \varepsilon^{-1})$, is always less than 1 for small ε, but it approaches 1 logarithmically as $\varepsilon \to 0$. Thus, the result $d_s = 1$ still holds. A practical implication is that for fractals whose general characters are similar to those for this example, an accurate numerical estimation of the dimension will require going to infinitesimally small scales, and as such, any numerical estimation of the dimension over a finite range of scales will be an underestimate. As the scale is decreased, the numerically determined value of the dimension will increase toward 1.

The relevance of the above construction of the Cantor set to chaotic scattering can be argued as follows [470]. Consider particles launched from a line segment straddling the stable manifold of the chaotic saddle. There is an interval in the values of some input variables that lead to trajectories remaining in the scattering region for at least a duration of time T_0. By time $2T_0$ a fraction η of these particles will have left. If the initial conditions of these escaping particles are all located in the middle of the original interval, there are then two equal-length subintervals of the input variable that lead to trajectories that remain for at least time $2T_0$. By time $3T_0$ an additional fraction η of the particles whose initial conditions are located in the middles of the two subintervals remaining at time $2T_0$ escape. There are then four subintervals, particles initiated from which can remain in the scattering region for time at least $3T_0$, and so on. The resulting set is a Cantor set of measure zero on which particles never escape. The box-counting dimension of the Cantor set is given by

$$d_s = \frac{\ln 2}{\ln \left[2/(1-\eta) \right]}.$$

For hyperbolic chaotic scattering, particles escape exponentially from the scattering region: $P(t) \sim e^{-\kappa t}$, where $P(t)$ is the survival probability and the escape rate is determined by the fraction η as $\kappa = T_0^{-1} \ln (1-\eta)^{-1}$. For nonhyperbolic dynamics, because of the algebraic decay $P(t) \sim t^{-z}$, the fraction η is no longer a constant: it varies at each stage of the construction of the Cantor set. At the nth stage, i.e., for times $(n-1)T_0 < t < nT_0$ (n large), the fraction η_n is approximately given by $\eta_n \approx -T_0 P^{-1} \mathrm{d}P/\mathrm{d}t \approx z/n$, which yields (6.26) and hence a Cantor set with dimension 1, where α in (6.26) is identified to be the algebraic-decay exponent z.

To provide support for the above heuristic argument, Lau et al. [470] conducted numerical experiments utilizing a two-dimensional scattering map (see Sect. 6.4.4). Evidence of the box-counting dimension's approaching unity as the length scale is reduced is apparent even in the plot of a scattering function: one observes an apparent increase in the density of the singularities. Computations indicate that the dimension indeed approaches unity as finer and finer scales are examined [470]. The signature of the unit box-counting dimension has also been identified in the classical model of two-electron atoms [313].

6.4.4 Intermediate-Time Exponential Decay

In spite of the asymptotic algebraic decay, on *intermediate times* the decay of the survival probability can be exponential in nonhyperbolic chaotic scattering. Its occurrence depends on the choice of the initial distribution of particles used to obtain the survival probability. For initial conditions far away from KAM tori the exponential decay is generically present.

The two-dimensional area-preserving map utilized by Lau et al. to establish the unity of the box-counting dimension in nonhyperbolic chaotic scattering [470] provides a convenient numerical model for observing as well the intermediate-time exponential decay:

$$M\begin{pmatrix} x \\ y \end{pmatrix} = \begin{cases} \lambda[x - (x+y)^2/4] \\ \lambda^{-1}[x + (x+y)^2/4] \end{cases}, \tag{6.27}$$

where $\lambda > 1$ is a parameter. Utilizing a discrete-time map (instead of a continuous-time flow) makes high-precision computation feasible. For the map (6.27), almost all orbits starting from negative values of y are scattered to infinity. The dynamics is nonhyperbolic for $\lambda < 6.5$ and hyperbolic for $\lambda > 6.5$. In the nonhyperbolic regime there is a major KAM island in the phase space that leads to an asymptotically algebraic decay.

The survival probability $P(n)$ of a particle in the scattering region can be approximated by the fraction of a large number of particles still remaining in the scattering region (defined by $\sqrt{x^2 + y^2} < r$) at time n. In [534], $r = 100$ is fixed and initial conditions are chosen from the horizontal line at $y_0 = -2$. The decay of $P(n)$ with time is exponential for intermediate n values, and algebraic for larger times, as shown in Fig. 6.26. For $\lambda = 4.0$, the exponential decay $P \sim e^{-\kappa n}$ holds up to $n = 250$, after which the algebraic decay law $P(n) \sim n^{-z}$ takes over, where $\kappa \approx 0.08$ and $z \approx 1$. This suggests that there is a time-scale separation in the system: up to a certain multiple of $1/\kappa$ the behavior is different from that in the long-time limit.

To explain this time-scale separation, the following picture has been proposed [13, 18, 370]. The entire chaotic saddle can be effectively *split into two components*: a hyperbolic one lying outside the KAM surfaces and a nonhyperbolic component
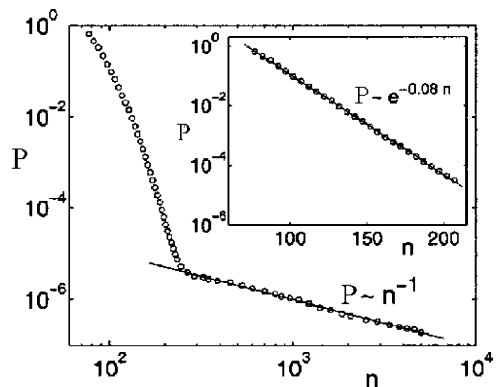

Fig. 6.26 Survival probability $P(n)$ for the map (6.27) for $\lambda = 4.0$. The inset illustrates exponential decay on intermediate time scales [534] (copyright 2002, the American Physical Society)

located around the KAM tori. Particles starting far from the KAM surfaces and having intermediate lifetimes have no chance to come close to the nonhyperbolic region, because of the stickiness of the KAM tori. The relaxation to the non-hyperbolic behavior occurs after most particles have approached the hyperbolic component. Since the dwelling around the hyperbolic component is sufficiently long, the intermediate-time dynamics can be characterized by a well-defined escape rate, a positive Lyapunov exponent, and dimension d_s that is strictly less than unity. The full escape-time distribution can thus be written, after short-time fluctuations occurring up to time n^*, as

$$p(n) \approx \begin{cases} a e^{-\kappa n} & \text{for } n^* < n < n_{nh}, \\ a e^{-\kappa n} + b(\kappa n)^{-z-1} & \text{for } n > n_{nh}, \end{cases} \qquad (6.28)$$

where n_{nh} is the time when the contribution of the nonhyperbolic component becomes first observable, and therefore $a e^{-\kappa n_{nh}} \gg b(\kappa n_{nh})^{-z-1}$.

It should be emphasized that the development-parameter approach of Sect. 6.4.2 characterizes the hyperbolic component of the saddle only. In a realistic scattering experiment most particles move along trajectories that stay in the scattering region for a short time only. They do not have the time necessary for penetrating into the nonhyperbolic component around the KAM surfaces. In this sense knowledge about the hyperbolic properties is highly experimentally relevant.

6.4.5 Relation to Poincaré Recurrences

The behavior of intermediate-time exponential decay is also present in generic leaked area-preserving maps **f**, when the leak is far away from any KAM tori. The arguments provided in Sect. 2.7 to compare leaked with closed systems can be applied, which lead to the conclusion that the intermediate-time relaxation of the Poincaré recurrence distribution $p_r(n)$ and of the escape-time distribution $p(n)$ of the corresponding leaked problem are proportional to each other: $p_r(n) \sim p(n)$ for any n with $p(n)$ given by (6.28). In particular, (2.104) holds, where γ is the relaxation rate of the Poincaré recurrence-time distribution (on intermediate time scales). Furthermore, with initial condition (2.105), the entire distributions coincide. In area-preserving cases, ρ_r is a uniform distribution over the image **f**(I) of the leak. These features can be illustrated by the standard map whose phase space is shown in Fig. 6.27(a). Chaotic trajectories tend to stay for a long time near the hierarchical border of the KAM island, shown in the center of the figure, which constitutes the nonhyperbolic component of the chaotic saddle. The exponential decay is governed by the hyperbolic component, whose unstable manifold is shown in Fig. 6.27b for a specific leak. The distributions of the escape and the recurrence times are shown in Fig. 6.28. As in the case of dissipative systems (Fig. 2.21), short-time oscillations and an intermediate-time exponential decay are present. However, in this case an algebraic decay is observed
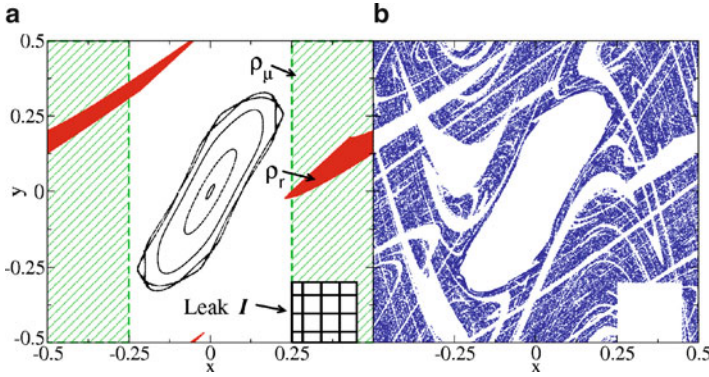
Fig. 6.27 (**a**) Phase space of the standard map given by $y_{n+1} = y_n - 0.52\sin(2\pi x_n)$ and $x_{n+1} = x_n + y_{n+1}$, peridoic in $|x, y| \geq 0.5$, with a leak defined by $I = [0.25 < x < 0.45, -0.5 < y < -0.03]$. The nonhyperbolic component of the chaotic saddle about the KAM island is in the center of the figure. The support of ρ_r (see (2.105)) at $\mathbf{f}(I)$ for which $p_r(n) = p(n)$ is marked as the dark-gray region. (**b**) The unstable manifold of the hyperbolic component of the saddle
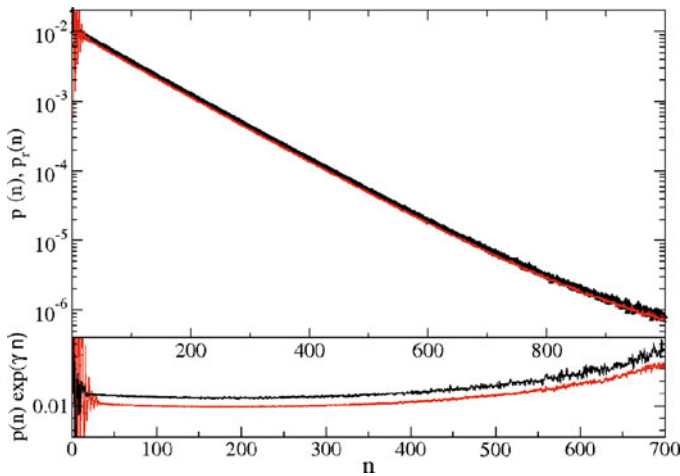

Fig. 6.28 Recurrence $p_r(n)$ and escape $p(n)$ time distributions in the leaked standard map, as shown in Fig. 6.27. Both functions decay exponentially over intermediate times with exponent $\gamma = \kappa$. For $p_r(n)$ (lower curve) a single initial condition is followed over 10^{11} steps. For $p(n)$ (upper curve) ρ_0 is a homogeneous distribution ρ_μ for $|x| > 0.25$. *Lower panel*: Distributions multiplied by $\exp(\kappa n)$, where $\gamma = \kappa \approx 0.011$

for times $n > n_{nh} \approx 300$. This provides additional support for the picture that the initial density ρ_0 quickly converges to the hyperbolic component of the saddle, and that the nonhyperbolic component is approached afterward. The transition of a typical trajectory from the hyperbolic to the nonhyperbolic components of the saddle is illustrated in Fig. 6.29. By increasing the number n_0 of iterations over which trajectories that have not escaped are monitored when applying the sprinkler method of Sect. 1.2.2.3, the nonhyperbolic component appears with an increasing weight.
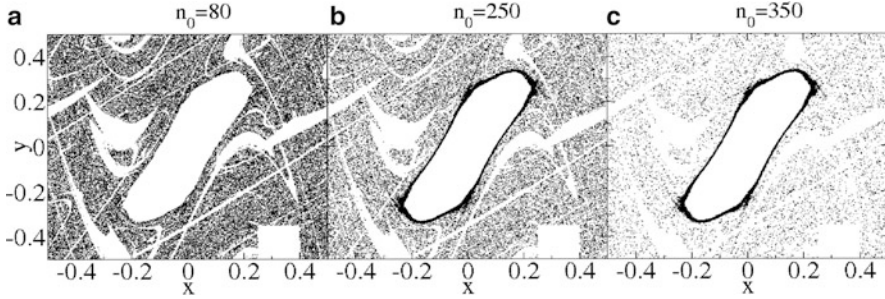
Fig. 6.29 Saddles characterizing the dynamics at different time n_0 obtained by the sprinkler method. For $n_0 \ll n_{nh} \approx 300$ in (**a**), the hyperbolic component is disjoint from the region containing the KAM island. In (**b**) and (**c**) the nonhyperbolic component becomes more and more apparent

Quantitatively, the crossover time $n_c > n_{nh}$ between the exponential decay and the algebraic decay can be defined as

$$a e^{-\kappa n_c} = b(\kappa n_c)^{-(z+1)}, \tag{6.29}$$

which is the time when the contributions from the hyperbolic and the nonhyperbolic components are of *equal* importance. The crossover time has been found [18] (as also can be seen from (6.29) under the assumption that b/a depends at most weakly on κ) to be proportional to the reciprocal of the escape rate from the leaked system:

$$n_c \sim 1/\kappa. \tag{6.30}$$

This scaling implies that the exponential decay dominates for small recurrence/leak regions.

The similarity between scattering dynamics and Poincaré recurrences can be used to explain the difference between the long-term algebraic-decay exponents for scattering and transient chaos as described in Sect. 6.4.1. Here we follow the argument of Altmann et al. [17]. Consider first initial conditions around the sticking region (the case of transient chaos) and examine the time a trajectory takes to escape to a region far away from the sticking region. The distribution $P_{tr}(\tau)$ of escape times longer than time $\tau \gg 1$ is proportional to the natural measure $\mu(\tau)$ of the region of the phase space to which the trajectories stick for a time longer than τ. Due to ergodicity, we have

$$P_{tr}(\tau) \sim \mu(\tau) = \frac{n_\tau}{n}, \tag{6.31}$$

where n_τ is the total time spent inside the sticking region and $n \gg 1$ is the total time of observation.

For the recurrence problem with a single trajectory of length n initialized far away from the sticking region, the cumulative probability $P_r(\tau)$ to find recurrence times larger than τ can be expressed as

$$P_r(\tau) = \frac{N_\tau}{N} \sim P(\tau), \tag{6.32}$$

where N_τ is the number of recurrences with recurrence times larger than τ and N is the total number of recurrences observed in the time interval n. The right-hand side expresses the observation that the recurrence-time statistics are proportional, also for long times, to the lifetime distribution $P(\tau)$ of the scattering problem for initial conditions far away from any sticking region. Since the total observation time can be estimated as N times the mean recurrence time τ_r, (2.103), we have $n \sim N\tau_r$. Similarly, the total time spent inside the sticking region is approximately the number N_τ of recurrences with times longer than τ multiplied by τ: $n_\tau \sim N_\tau\tau$. Since τ_r is a constant, independent of τ, these allow us to write

$$P(\tau) \sim \frac{N_\tau}{N} \sim \frac{n_\tau/\tau}{n/\tau_r} = \frac{n_\tau\tau_r}{n\tau} \sim \frac{P_{\text{tr}}(\tau)}{\tau}, \qquad (6.33)$$

from which the shift of algebraic decay exponent by one (6.22) immediately follows from (6.20) and (6.21).

6.5 Fluctuations of the Algebraic-Decay Exponent in Nonhyperbolic Chaotic Scattering

Consider the two-dimensional setting in which the phase space contains a central KAM island encircled by some outermost KAM surface. There is a chaotic region outside the KAM surface, which contains smaller island chains. For particles initialized in the chaotic region, their escape process takes place on a wide range of time scales. For intermediate times (e.g., $t < t_1$), the decay is exponential. For particles that stay a long but finite time in the region, their corresponding trajectories spend substantial amounts of time near some accessible KAM surfaces, leading to an algebraic decay in the survival probability. From an observational point of view, the more dominant the island chains are in the chaotic region, the more time the particles spend near them, the slower the escape process is. The "slowness" can be quantified by the algebraic decay exponent z in (6.20), where a smaller value of z corresponds to a "slower" escape process over the period of observation. This intuition is consistent with the theoretical picture [514, 515] where the value of the decay exponent decreases as the number of island chains included in the calculation increases.

When some KAM surfaces undergo transformations from being absolute barriers to partial barriers called Cantori [498], an entire new region of the phase space becomes accessible to the chaotic orbits. The decay exponent z drops drastically after this point. After the breakup of the outermost KAM surfaces surrounding the central island, another time scale $t_2 > t_1$ becomes important for the system. For particles that have escaped in the time interval $t_1 < t < t_2$, their trajectories lie entirely outside the newly created Cantori. Therefore, the exponent z measured over this time interval is still roughly the same as that before the breakup of the corresponding KAM surfaces. The particles that stay longer than t_2, however, will explore the region enclosed by the newly created Cantori, thereby causing the exponent z to be markedly smaller than the one measured over the interval $t_1 < t < t_2$.

Thus the curve $P(t)$ versus t exhibits two scaling regions with different algebraic decay exponents. The time scale at which this crossover takes place coincides with the typical time for a chaotic trajectory to penetrate the newly created Cantori. This consideration can be repeatedly applied as the parameter further increases, suggesting fluctuations in the exponent z. As the system approaches hyperbolicity, the interval $0 < t < t_1$ becomes larger and larger, reflecting the fact that the island structures in the phase space become less and less significant.

An acknowledged notion is that the algebraic decay in the presence of KAM surfaces should be a universal phenomenon with a single exponent. This notion is partly derived from the numerical work of Karney [388], Chirikov and Shepelyansky [136], and of Cristadoro and Ketzmerick [144]. While this may indeed be the case given the hierarchical island structure in the phase space, to attain such a universal exponent one needs a prohibitively long time to perform the needed numerical calculations. In the case of actual experiments, the required long period of time of observation becomes even more unrealistic. This notwithstanding, the algebraic-decay behavior itself is found to occur on relatively short time scales. The value of the decay exponent measured over a *finite time interval* accessible to numerical experiments is influenced by the presence of some dominant island structures. In this regard the variations of the exponent can, in fact, be utilized to reflect the major qualitative changes in the system.
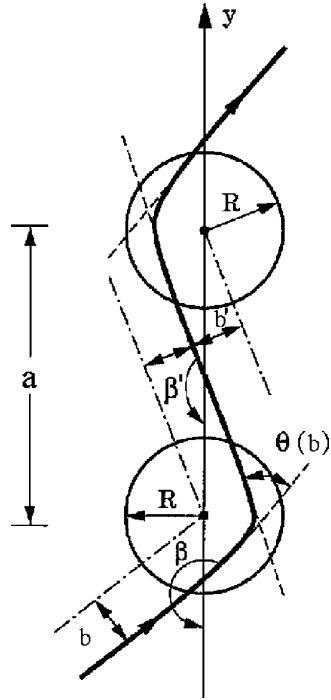
6.5.1 Numerical Model

The chaotic-scattering system introduced by Troll and Smilansky [790] is convenient for illustrating the phenomenon of algebraic-decay exponent fluctuations. In the system, particles are scattered by an infinite array of nonoverlapping elastic scatterers, as shown in Fig. 6.30, which are placed in the plane at constant intervals a along the y-axis. Each scatterer is represented by a circularly symmetric potential $V(r)$ that vanishes for $r > R$, where $R < a/2$ (nonoverlapping). To have chaos, it is necessary for the potential $V(r)$ to be *attractive*, because if $V(r)$ is repulsive, only trivial invariant orbits can be formed in the scattering region.

The nonoverlapping condition entails that particle trajectories be straight lines in the region between potential wells and suffer a deflection when they enter some scatterer. Let $\theta(b)$ be the deflection angle of a particle trajectory from an individual scatterer. In general, $\theta(b)$ is a monotonically decreasing function of the impact parameter b (at least near $b = 0$). Due to the finite range of each scatterer, $\theta(b) = 0$ for $|b| > R$. For a particle of unit mass, $u = \sqrt{2E}$ is the constant particle velocity during its free motion. For a particle moving toward any of the scatterers with impact parameter b and velocity $\mathbf{u}$, its new velocity $\mathbf{u}'$ after the scattering has the same magnitude (u) as $\mathbf{u}$ but assumes a different direction. Let β and β' be the angles of the velocity vectors relative to the $-y$-axis when the particle is in regions where the potential is negligible. From Fig. 6.30, we have

$$\beta' = \beta - \theta(b).\qquad(6.34)$$

Note that $\theta(b) < 0$ for $b > 0$. Now the particle may either collide with the scatterer
above (if $u'_y = -u\cos\beta' > 0$) or with the scatterer below (if $u'_y < 0$). In either case,
scattering is determined by the value of the impact parameter b' relative to the new
scatterer. A geometric argument gives

$$b' = b - a\,\mathrm{sgn}[\cos\beta']\,\sin\beta'. \tag{6.35}$$

The next scattering takes place only if $|b'| < R$. Otherwise, the particle will continue
to move along a straight-line trajectory, leaving the system. Such particles will be
regarded as having escaped the scattering region.

Symbolically, the two-dimensional map (6.34) and (6.35) can be represented as

$$(\beta', b') = M(\beta, b). \tag{6.36}$$

The phase space for M is defined by the domain $[0, 2\pi) \times [-R, R]$, which is a cylin-
der. It can be verified that M is area-preserving.

In the Troll–Smilansky system, chaotic scattering can arise via the saddle-center
bifurcation route. This can be seen as follows. For a given physical potential $V(r)$,
the deflection angle $\theta(b)$ is a monotonically decreasing function of b for values of

b near $b = 0$, and $\theta(0) = 0$. Suppose $\theta(b) = -kb$, where k is a positive constant measuring the local slope of the deflection function. The scattering map becomes

$$\beta' = \beta + kb, \tag{6.37}$$

$$b' = b - a \, \text{sgn}[\cos(\beta')] \sin(\beta'). \tag{6.38}$$

This map has fixed points at $(\beta, b) = (0,0)$ and $(\beta, b) = (\pi, 0)$, corresponding to orbits traveling along the negative and positive y-axis, respectively. Due to the symmetry of the system, it is necessary to analyze the linear stability of only one of the fixed points, say $(\pi, 0)$. Near $(\pi, 0)$ the linearized mapping has the eigenvalues

$$\lambda_\pm = [(2 - ak) \pm \sqrt{a^2 k^2 - 4ak}]/2. \tag{6.39}$$

For $k = 0$, which corresponds to $V(r) = 0$ in the potential, we have $\lambda_\pm = 1$. For $0 < k < 4/a$, however, the eigenvalues $\lambda_\pm$ are complex and the fixed point is elliptic. For a nonintegrable system, an elliptic fixed point is surrounded by layers of quasiperiodic orbits, other elliptic points, and hyperbolic points whose stable and unstable manifolds form intricate homoclinic tangles, signifying the existence of chaotic invariant sets. In this sense, transition to chaos occurs as soon as k becomes nonzero. In physical terms, chaotic scattering takes place immediately after an array of attractive potentials is placed in the plane, regardless of the depth of each individual potential. For k slightly above zero, chaotic regions are exponentially small, and they exist between and outside the KAM tori. Beyond the initial bifurcation to nonhyperbolic chaotic scattering, the phase space contains a mixture of KAM surfaces and chaotic components. Further increase in k leads to complete hyperbolic scattering dynamics.

6.5.2 Decay-Exponent Fluctuations

To demonstrate the dependence of the decay exponent on system parameters, it is convenient to choose $V(r)$ to be a localized quadratic potential given by [445]

$$V(r) = -V_0[1 - (r/R)^2], \quad \text{for } r \leq R, \tag{6.40}$$

where $V(r) = 0$ for $r > R$, and $V_0 \geq 0$ measures the depth of the potential well. A calculation similar to that of Sect. 6.3.1 yields the following expression for the deflection angle:

$$\tan \theta(b) = \frac{-2b\sqrt{R^2 - b^2}}{R^2(E + V_0)/V_0 - 2b^2}, \tag{6.41}$$

where E is the particle energy. The coefficient k in (6.37) is then $k = 2V_0/(R(E + V_0))$. For $V_0 = 0.2$, $E = 0.5$, $R = 1.0$, and $a = 3.7$, the decay exponent of the survival

Fig. 6.31 Algebraic decay
exponent z as a function of
parameter a for the
Troll–Smilansky scattering
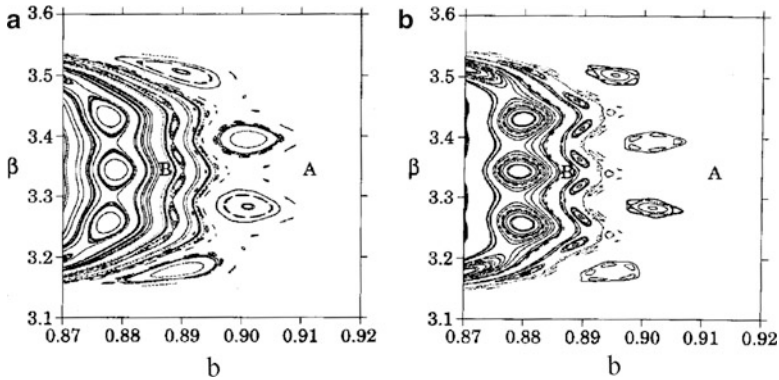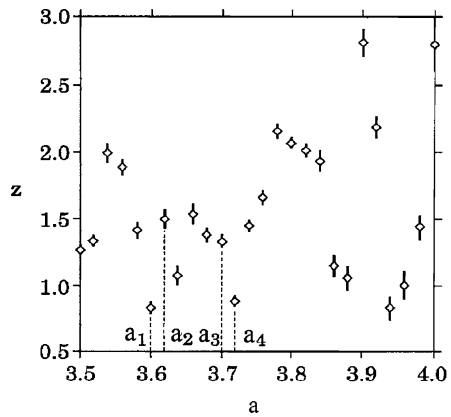map [445] (copyright 1992,
the American Physical
Society)

Fig. 6.32 Phase-space plots for (**a**) $a_1 = 3.60$ and (**b**) $a_2 = 3.62$ [445] (copyright 1992, the
American Physical Society)

probability $P(t)$ for particles initiated far away from KAM islands is found to be
$z \approx 1.32$. As the parameter a varies, the decay exponent z fluctuates, as shown in
Fig. 6.31. For larger values of a, there are no KAM surfaces, and particles appear to
escape from the scattering region exponentially.

The dynamical mechanism responsible for the fluctuations in the algebraic-decay
exponent z can be seen by examining the phase-space structure. For example, one
can choose two representative pairs of parameter values from Fig. 6.31: $a_1 = 3.60$,
$a_2 = 3.62$ and $a_3 = 3.70$, $a_4 = 3.72$, and explore the topology of the KAM sur-
faces and chaotic sets for each parameter value. Specifically, for the first pair a_1 and
a_2, the decay exponent increases, $z_2 > z_1$, while for the second pair the exponent de-
creases, $z_4 < z_3$. The phase-space structures corresponding to a_1 and a_2 are shown in
Fig. 6.32a,b. For clarity, only trajectories on KAM surfaces are plotted. A noticeable
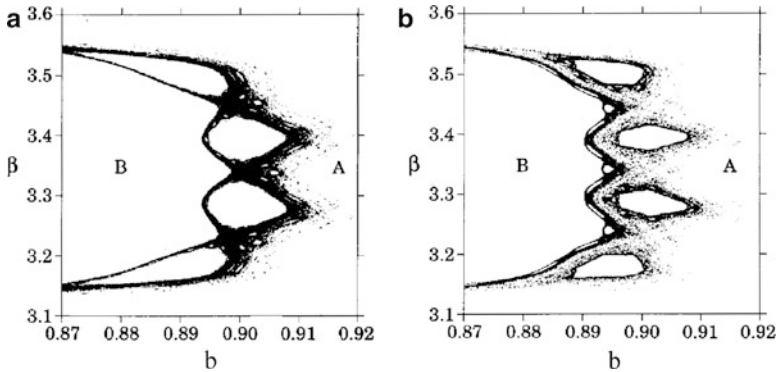
Fig. 6.33 Long trajectories on the nonhyperbolic chaotic saddles for (**a**) $a_1 = 3.60$ and (**b**) $a_2 = 3.62$ [445] (copyright 1992, the American Physical Society)

feature common to both parameter values is that the phase space is divided into two distinct regions by KAM surfaces: region B enclosed within the KAM surfaces and region A that lies outside. As a result of this phase-space partitioning, particles launched from outside visit only region A before exiting the potential. Region B in this case plays the role of the central island. The particle decay dynamics for both a_1 and a_2 are thus determined by the structures present in region A. As a is increased from a_1 to a_2, the boundary between the two regions deforms slightly but otherwise remains essentially intact. In contrast, the area occupied by islands undergoes a reduction. The effect of this reduction can be further demonstrated by plotting in its entirety the connected chaotic component in region A. Figure 6.33a,b, obtained using the PIM-triple procedure (Sect. 1.2.2.4), displays two such long chaotic trajectories. Evidently, the sum of blank pockets in region A that represent areas occupied by islands is markedly smaller in Fig. 6.33b than in Fig. 6.33a. The implication in physical terms is that particles exit the potential faster for $a_2 = 3.62$ than for $a_1 = 3.60$, thereby furnishing an explanation to the observed relationship $z_2 > z_1$.

For the second parameter pair a_3 and a_4, for which the algebraic-decay exponent actually decreases, the corresponding phase-space topologies are quite different, as shown in Fig. 6.34a,b. In particular, while the two regions A and B in Fig. 6.34a are still visibly separated by KAM surfaces, the boundary between the two regions in Fig. 6.34b has been destroyed. This situation entails that the chaotic component previously enclosed in region B is now accessible to particles initialized in region A. In geometric terms, the two chaotic regions lying on different sides of the KAM surfaces have been combined into a single connected chaotic set. The latter point can be seen in Fig. 6.35a,b, a long trajectory on the chaotic saddle for a_3 and a_4, respectively.

It is known that Cantori created immediately after the breakup of KAM surfaces serve as effective barriers to particle transport [498]. The typical time for a particle to penetrate the Cantori thus constitutes a new time scale n_2 in the system.
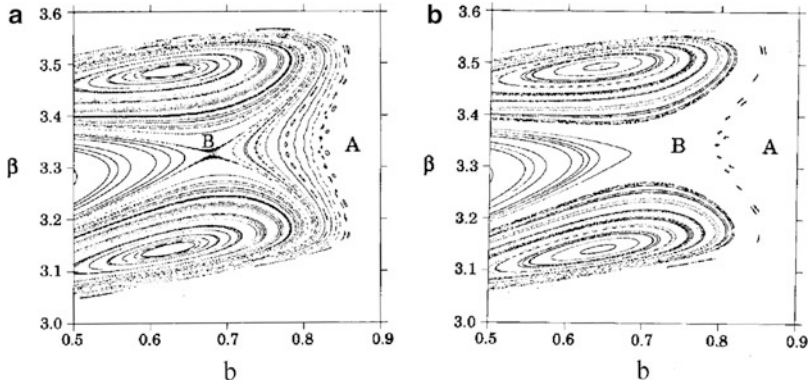
Fig. 6.34 Phase-space plots for (**a**) $a_3 = 3.70$ and (**b**) $a_4 = 3.72$ [445] (copyright 1992, the American Physical Society)
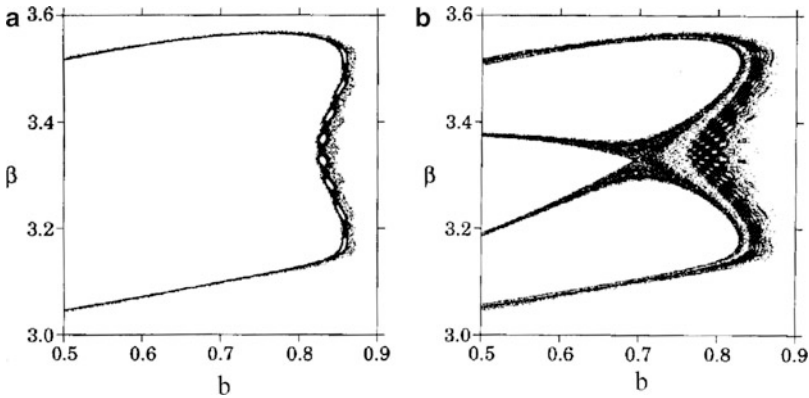
Fig. 6.35 Long trajectories on the nonhyperbolic chaotic saddles for (**a**) $a_3 = 3.70$ and (**b**) $a_4 = 3.72$ [445] (copyright 1992, the American Physical Society)

The presence of this new time scale leads to observable consequences. For particles that exit the potential in time less than $n = n_2$, the corresponding trajectories lie entirely outside the newly created cantori. This implies that the exponent measured over some time interval $n_1 < n < n_2$ should be roughly the same as that before the breakup of KAM surfaces. Particles that stay longer than $n = n_2$, however, are likely to penetrate the Cantori and explore the chaotic component previously enclosed within the KAM surfaces. Reflected in the decay dynamics, this corresponds to a slower escape process, thus a smaller decay exponent measured over the interval $n > n_2$. The numerical result for a_4 is shown in Fig. 6.36, where two regions of distinct slopes can be seen. The exponent measured over the first interval of scaling behavior $n < n_2$ is $z \approx 2.27$, while that measured over the remaining interval $n > n_2$

Fig. 6.36 Crossover behavior in the algebraic-decay law for $a_4 = 3.72$ [445] (copyright 1992, the American Physical Society)

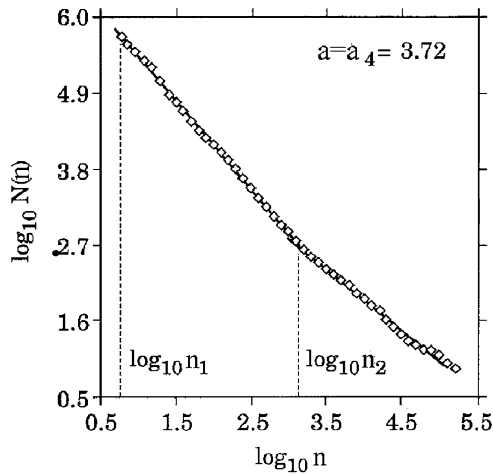is $z \approx 1.88$, confirming the consideration given above. The crossover time $n = n_2$ in Fig. 6.36 is roughly $1,200$ iterates. As indicated, this time represents the number of iterates for a typical trajectory to penetrate the Cantori.[5]

The discussions above indicate that a sudden structural change, or a metamorphosis, in the phase space, as exemplified by the destruction of KAM surfaces and subsequent exposure of a new layer of KAM islands, can manifest itself through variations in the decay exponent. Conversely, this relationship can be used to interpret unexpected findings in physical systems. One such example is the study reported in [450] in which a theoretical model of microwave ionization of hydrogen Rydberg atoms was considered. The results indicate that contrary to naive intuition, the ionization rate, analogous to the decay exponent z, is not a monotonically increasing function of the field strength. In many instances the increment of the field strength actually leads to a decline of the ionization rate. The reasons behind the finding are precisely what has been described above, namely the complicated metamorphosis patterns in the phase space.

---

[5] In higher-dimensional scattering systems, the energy surface is no longer isolated into regions enclosed by KAM surfaces. The chaotic set in this case forms a single integrated component on which a typical particle can execute Arnol'd diffusion. If the energy surface is unbounded, the particle decay still obeys the algebraic law [192]. The characteristic behavior of Arnol'd diffusion in which a particle hops from one well-defined region in the phase space to another closely resembles the penetration of Cantori in two-dimensional systems. This is expected to lead to multiple decay exponents measured over short intervals of time.

6.6 Effect of Dissipation and Noise on Chaotic Scattering

An aspect of chaotic scattering concerns about the effect of weak dissipation [534, 702, 704]. The influence of dissipation can be quite different for hyperbolic and nonhyperbolic chaotic scattering. In particular, weak dissipations have negligible effect on the physical observables in hyperbolic chaotic scattering, such as scattering functions, since hyperbolic dynamics are structurally stable (Chap. 1). For nonhyperbolic dynamics, qualitatively different behavior can arise due to weak dissipation. For instance, marginally stable periodic orbits in KAM islands can become stable attractors, turning their nearby phase-space regions into the respective basins of attraction [239, 240]. This means that part of phase-space region that contains the previous chaotic saddle now becomes part of the basins of the attractors. For scattering dynamics, the converted subset contains orbits of the previous invariant set in the neighborhood of the KAM islands. Due to the existence of dense orbits in the original chaotic saddle, the invariant set remains in the basin boundaries of the periodic attractors. Consequently, the new invariant set is the asymptotic limit of the boundaries between scattered and *captured* orbits. Chaos thus occurs on a *dissipative* chaotic saddle whose stable manifold becomes the boundary separating the basins of the attractors and those of the scattering trajectories. This reasoning suggests that the structure and the meaning of the Cantor set of singularities is fundamentally altered: in successive steps, a *constant* instead of a decreasing fraction in the middle of each interval is removed (Sect. 6.4.3). As a result, the scattering dynamics becomes *hyperbolic* with exponential decay. The dimension of the Cantor set immediately decreases from unity as a dissipation parameter is turned on. The appearance of attractors accompanied by such a metamorphosis of the chaotic saddle can occur for arbitrarily small dissipation.

The following dissipative version of the map given by (6.27) has been useful for providing insights into the effect of weak dissipation on chaotic scattering [534]:

$$M\begin{pmatrix} x \\ y \end{pmatrix} = \begin{cases} \lambda[x - (x+y)^2/4 - \nu(x+y)] \\ \lambda^{-1}[x + (x+y)^2/4] \end{cases}, \qquad (6.42)$$

where $\nu \geq 0$ is the dissipation parameter. Figure 6.37a shows the stable manifold of the nonhyperbolic saddle in the scattering region. When weak dissipation is present ($\nu > 0$), the fixed point in the center of the island becomes an attractor. The basin of attraction of this attractor "captures" the island itself and orbits close to the stable manifold of the previously existing chaotic saddle, as shown in Fig. 6.37b. The intricate character of the basin of attraction with apparent fractal boundaries comes from the points of the invariant set that are arbitrarily close to the island for $\nu = 0$. The newly created basin of attraction contains these points and hence all their preimages as well. These preimages extend in the phase space along the original stable manifold of the chaotic saddle, leading to the large-scale structure of the boundary that mimics the original stable manifold (Fig. 6.37a versus Fig. 6.37b). Because of this similarity, delay-time functions, which are physically measurable, *resemble* each other in both the conservative and the weakly dissipative cases, as
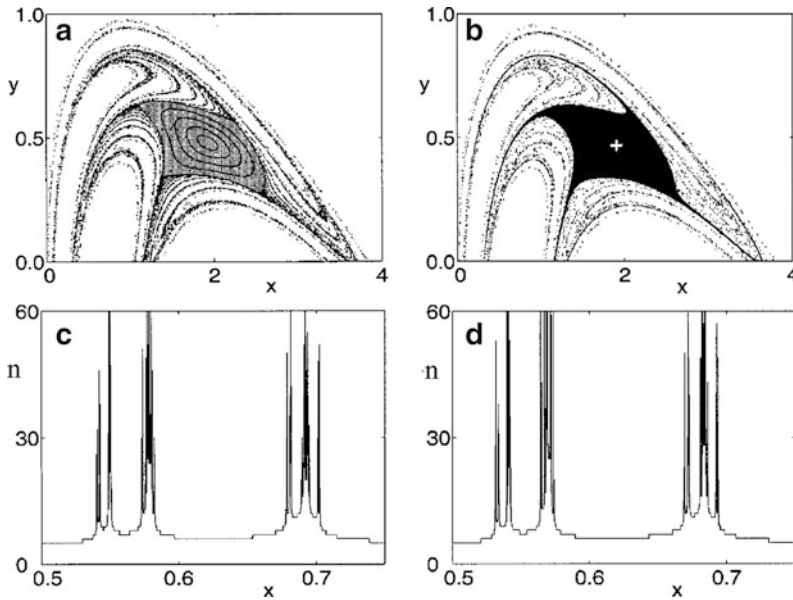
Fig. 6.37 For the scattering map (6.42) for $\lambda = 4.0$, phase-space structure and delay-time function: (**a**) for $\nu = 0$, KAM island (*gray*), scattered orbits (*blank*), and the stable manifold of the nonhyperbolic chaotic saddle (*black*); (**b**) for $\nu = 0.01$, captured orbits (*black*) and scattered orbits (basin of allocation) (*blank*). The plus sign represents the fixed-point attractor. (**c**), (**d**) Delay-time function in the conservative and dissipative cases (**a**) and (**b**), respectively, where n is the time taken by particles to reach $\sqrt{x^2 + y^2} \geq 100$ [534] (copyright 2002, the American Physical Society)

Fig. 6.38 Survival probability $P(n)$ for the map (6.42) for $\lambda = 4.0$, $\nu = 0.001$ in the interval $[x_0, x_0 + 10^{-7}]$, $y_0 = -2$, $x_0 = 0.5760006$ [534] (copyright 2002, the American Physical Society)

$$P \sim e^{-0.08\,n}$$
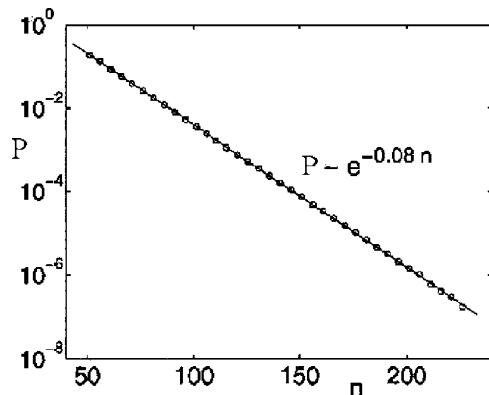
shown respectively in Fig. 6.37c,d, where the delay times of particles launched from the horizontal line $y = -2$ toward the scattering region are plotted against their x-coordinates on the line [534].

In the presence of a weak dissipation, the decay becomes *strictly* exponential, as shown in Fig. 6.38. The escape rate is the same as that of the intermediate-time decay in the conservative case: $\kappa \approx 0.08$. The original algebraic decay in the

conservative case is destroyed by the dissipation because orbits with points close to the island, which otherwise would be stuck, are captured by the periodic attractor. The escape rate in general changes under further increases of the dissipation. (In the hyperbolic region ($\lambda \geq 6.5$) the decay is always exponential. For $\lambda = 8.0$, for example, κ remains essentially constant and is equal to 0.9 in the range $0 \leq \nu \leq 0.01$ [534].)

The uncertainty algorithm can again be used to compute the box-counting dimension d_s of the set of singularities in the scattering functions. In Sect. 6.4.3, we have argued that $d_s = 1$ when the map (6.42) is nonhyperbolic and conservative. A technical point about the numerical evaluation of the dimension in this case, as discussed in Sect. 6.4.3, is that the result converges *slowly* to unity. When a small amount of dissipation is present, $d_s + 1$ is the dimension of the boundary between the scattered and captured dynamics. The numerical convergence of d_s is in this case *faster* and essentially independent of the resolution. For example, for $\lambda = 4.0$ and $\nu = 0.01$, the dimension is found to be $d_s \approx 0.8$ [534], a well-convergent value as the length scale is reduced over six orders of magnitude. As the dissipation parameter is increased, the rate of decrease in the dimension is relatively large initially, but as the parameter passes through a small critical value ν_c, the rate is reduced significantly, and becomes nearly zero for $\nu > \nu_c$. This crossover behavior appears quite general [704]: as the dissipation parameter is increased from zero, attractors are constantly created as the system becomes more dissipative (for closed systems see [239]). When most of the attractors that the system is capable of having have already been created as the critical dissipation value is approached, the decrease in the dimension slows.

The addition of weak noise has a qualitatively similar effect on nonhyperbolic scattering to that of dissipation. Very weak noise leads to a slower algebraic decay than in the deterministic case [20]. Stronger noise destroys KAM islands and stickiness is no longer present. As a result, the asymptotic decay law changes from algebraic to exponential [705]. The escape rate has been found in such situations to increase with the noise amplitude [644,703], preceded in some cases by a local minimum [20]. All these studies suggest that the algebraic decay law, regarded to hold universally in nonhyperbolic chaotic scattering, is apparently structurally unstable against dissipation and noise.

6.7 Application of Nonhyperbolic Chaotic Scattering: Dynamics in Deformed Optical Microlasing Cavities

Optical processes in microcavities occur in important applications such as microdisk semiconductor lasers [119] and optical fiber communication [570], in which total internal reflection of light is exploited to achieve nearly perfect mirror reflectivity. Dielectric cavities (cylinders or spheres) are a common type of optical microcavity. In such a situation, ideally the surface of the cavity confines certain modes of the electromagnetic field, such as the "whispering gallery" (WG) modes [176,509,618], defined as the state in which light circulates almost tangent to the surface of the

cavity via total internal reflection, suffering minimal loss caused by evanescent leakage and scattering due to surface roughness. The *ray dynamics* inside dielectric cavities is governed by the laws of geometric optics: upon collision with the boundary a ray generally splits into a reflected ray and a transmitted ray.

A fundamental quantity characterizing a microcavity is the quality factor, or the Q-value, defined as $Q = \omega\tau$, where ω is the frequency of the resonant mode and τ is its lifetime in the cavity [265, 519, 552, 789]. If there are no deformations in the cavity geometry from the ideal shape of cylinder or sphere, in a practical sense light in WG modes can be trapped in the cavity for arbitrarily long time, making the Q-value of the cavity high. This is the principle on which the world's smallest lasers were fabricated [176, 509].

While a circular symmetry allows WG modes to have high Q-values, it prevents the laser emission from having a good directionality. Asymmetric resonant cavities (ARCs) with smooth deformations from the circular symmetry were then suggested [265, 519, 552]. Such deformations can be quite large, ranging from 1 to 50% with respect to the corresponding circular geometry. Although WG modes of a spherical or of a cylindrical cavity can be treated analytically and the effect of small deformations can be analyzed using the traditional wave-perturbation theory, it is difficult to study cavities with large deformations, since the modes of highly deformed cavities are not perturbatively related to those of the circular cavities. A question is then whether high-Q modes exist in highly deformed cavities. The pioneering works in [265, 519, 552] showed that for dielectric materials with low index of refraction ($n < 2$, such as glass fibers or cylindrical dye jets, assuming that the surrounding medium has $n_0 = 1$), if the cavity surface remains convex, high-Q WG modes can still exist. This important result is obtained by studying chaotic dynamics resulting from classical ray tracing. Specifically, by treating waves propagating in ARCs as light rays bouncing within the cavity, the problem of ARCs becomes that of classical billiards. Far-field emission was found to be peaked in specific directions even in cavities where the reflected rays have uniformly chaotic dynamics; see Fig. 1.21. It was demonstrated that the Q-value and the directionality of an ARC can be computed directly from properties of *open* chaotic ray dynamics, such as the decay law, which are found to be in good agreement with experimental measurements [265, 519, 552]. It was also demonstrated both experimentally and computationally that for high-index semiconductor materials (index of refraction $n > 2$), WG modes may not be relevant to the lasing properties of the cavities [265]. Instead, resonant modes of "bow-tie" shapes are found to be responsible for the laser performance in the presence of large geometric deformations.

The scope of discussion here will be restricted to low-index dielectric lasing cavities, for which the relevant dynamics is that of WG modes. To illustrate the role of nonhyperbolic chaotic scattering, we shall focus on the following question: in order to achieve both high-Q values and a good directionality, what is the maximally allowed amount of deformation from circular symmetry? The question is particularly relevant to the practical design of microdisk semiconductor lasers, where it is desirable to know the upper bound of the allowed deformation. It is convenient to choose the well-studied example of a two-dimensional (cylindrical) resonator with quadrupolar deformation from the circular boundary, and investigate the ray

dynamics in the resonator from the standpoint of chaotic scattering by focusing on the decay property of trajectories in the phase space. Here, decay is due to the fact that light can be refracted, and then it leaves the cavity. The WG modes thus correspond to chaotic-scattering trajectories in the phase space.

6.7.1 Dynamical Criterion for High-Q Operation

Qualitatively, the interplay between the amount of deformation and the algebraic-decay exponent can be seen as follows. For a given value of the refraction index n and circular symmetry, the WG-mode operation stipulates that the angle α of incidence (Fig. 6.39) satisfy $\sin\alpha < \sin\alpha_c$, where α_c is a critical angle. For cavities with small deformations, the range of the angle α is small as the corresponding ray circulates near the boundary, and hence it is relatively easy for the condition $\sin\alpha < \sin\alpha_c$ to be satisfied, leading to a high probability of light rays being trapped inside the cavity. The decay exponent z is expected to be small in such cases. Large deformations from the circular symmetry give rise to a large range of the angle α, and consequently, it is more likely for the condition of total internal reflection to be violated, leading to large values of z. Let ε be the parameter characterizing the amount of deformation. The algebraic-decay exponent z is a nondecreasing function of ε. A criterion to determine the maximally allowed amount of deformation can be derived by noting that the average lifetime τ of very long lived trajectories can be written as

$$\tau \sim \int_{t_c}^{\infty} t p_{\text{tr}}(t) \mathrm{d}t \sim \begin{cases} t_c^{2-z}, & \text{if } z > 2, \\ \infty, & \text{if } z < 2, \end{cases} \tag{6.43}$$

where $p_{\text{tr}}(t)$ is the escape-time distribution (6.21) for particles initiated around KAM tori and t_c is the time of the onset of the algebraic decay. If $z < 2$, the average lifetime diverges asymptotically, indicating that in any practically long time scales, a
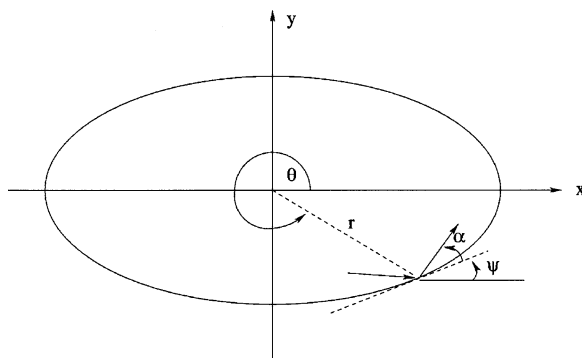

Fig. 6.39 Variables for constructing a Poincaré section for tracing ray dynamics in a two-dimensional cavity [486] (copyright 2002, the American Physical Society)

high value of Q can be expected. If in the corresponding range of deformation, a high directionality can be maintained (to be discussed below in numerical experiments), then the criterion for determining the upper bound of ε can be set as $\varepsilon < \varepsilon_c$, where $z(\varepsilon_c) = z_c = 2$.

6.7.2   A Numerical Example

The following class of two-dimensional cavities, expressed in polar coordinates (r, θ) with quadrupolar deformation characterized by ε, was considered in [486]:

$$r(\theta) = \frac{1 + \varepsilon \cos 2\theta}{\sqrt{1 + \varepsilon^2/2}}. \tag{6.44}$$

Classical ray tracing can be done using the Poincaré map defined with respect to the angles [59] ψ, α, and θ, as shown in Fig. 6.39. The map can be written in the following implicit form, relating the dynamical variables at successive total internal reflections off the boundary of the cavity:

$$\tan(\psi_t + \alpha_t) = \frac{(1 + \varepsilon \cos 2\theta_{t+1}) \sin \theta_{t+1} - (1 + \varepsilon \cos 2\theta_t) \sin \theta_t}{(1 + \varepsilon \cos 2\theta_{t+1}) \cos \theta_{t+1} - (1 + \varepsilon \cos 2\theta_t) \cos \theta_t},$$

$$\tan \psi_{t+1} = \frac{2\varepsilon \sin \theta_{t+1} \sin 2\theta_{t+1} - \cos \theta_{t+1}(1 + \varepsilon \cos 2\theta_{t+1})}{\sin \theta_{t+1}(1 + \varepsilon \cos 2\theta_{t+1}) + 2\varepsilon \cos \theta_{t+1} \sin 2\theta_{t+1}},$$

$$\alpha_{t+1} = \psi_{t+1} - \psi_t - \alpha_t, \tag{6.45}$$

where t is the discrete-time index denoting the event of bounce of a light ray off the cavity boundary. In numerical experiments, the critical angle of incidence is fixed to be $\alpha_c = 47.3$ degrees, which corresponds to cavities with refraction index $n \approx 1.475$ ($\cos \alpha_c = 1/n$). Figure 6.40a shows, for $\varepsilon = 0.1$, a representative phase-space structure of the map in (6.45). There are both KAM tori and chaotic regions. While the map in (6.45) describes the dynamics of particles in a closed billiard, imposing the threshold line at α_c makes the system effectively open (a leaked billiard). Figure 6.40b shows, in the two-dimensional physical space (x, y), a typical scattering trajectory in a WG mode and its escape from the cavity after about 1,000 bounces. Figure 6.40c shows the delay time T measured in the number of reflections of light rays in the cavity as a function of the initial angle of incidence α_0. If the trajectory lives on a KAM torus, the time is infinite, and if the ray is in a chaotic region, it will eventually escape but the time it stays in the cavity can be long. Since WG modes correspond to trajectories in the open chaotic region above the binding KAM tori, the Q-value of the cavity in the WG modes is determined by motions of rays in the chaotic region. The emission of light rays in the WG modes apparently has a high degree of directionality, as shown in Fig. 6.40d, a histogram of the emission angle θ_{out}, where θ_{out} is defined to be the angle of the refracted exiting light ray with respect to the x-axis.
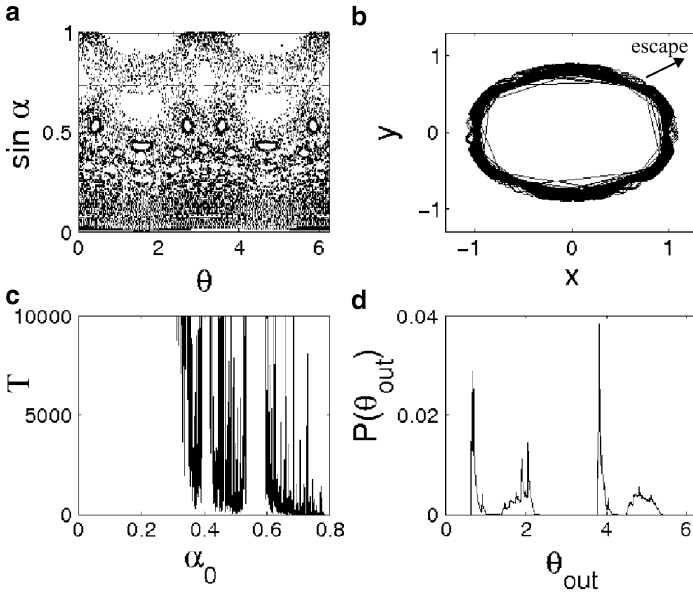
Fig. 6.40 For a dielectric cavity of refraction index $n \approx 1.475$ with quadrupolar deformation of $\varepsilon = 0.1$: (**a**) phase-space structure with perfect internal reflection (the *dashed horizontal line* indicates the value of $\sin \alpha_c$; points above this line are considered to have escaped), (**b**) behavior of light ray (in a WG mode) and its escape from the cavity, (**c**) delay time of light rays versus the initial angle of incidence, and (**d**) histogram of the emission angle θ_{out}. The highly localized pattern in the histogram indicates a high degree of directionality of the emitting light. A set of 1,000 initial conditions chosen uniformly from $\alpha_0 \in [0.05, \pi/4]$ were utilized [486] (copyright 2002, the American Physical Society)

In the presence of deformation, the probability for a light ray to survive in the scattering region decays algebraically with time, and the value of the decay exponent z of the probability density $p(t)$ increases as the deformation becomes large. Figure 6.41a shows that the algebraic exponent increases monotonically as the deformation parameter ε is increased. For $\varepsilon < \varepsilon_c \approx 0.22$, the exponent remains below the critical value $z_c = 2$, indicating that for $0 < \varepsilon < \varepsilon_c$, the average lifetime of light rays in the cavity diverges and the Q-value of the cavity is high in a statistical sense. In contrast, for $\varepsilon > \varepsilon_c$, the algebraic-decay exponent is above 2, implying relatively low Q-values. Thus, in order to achieve a high-Q operation, the amount of deformation should not exceed the value of about 0.2.

While high-Q operation of the cavity is desired, an equally important measure is the directionality of light emission. To quantify this, consider the worst case, in which light is emitted equally probably in all directions. The probability distribution $P(\theta_{out})$ of the emission angle of the exiting light ray is thus $P(\theta_{out}) = 1/(2\pi)$ for $0 \le \theta_{out} \le 2\pi$. For the computed distribution as in Fig. 6.40d, the height of the distribution $P(\theta_{out})$ can be normalized to $1/(2\pi)$ and the total area under the distribution curve is

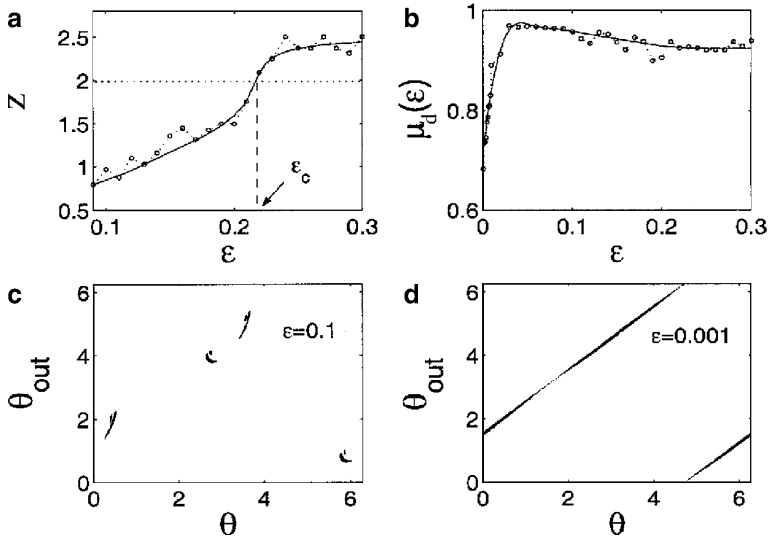$$A(\varepsilon) = \int_0^{2\pi} P(\theta_{out}) d\theta_{out},$$

Fig. 6.41 For a cavity of refractive index $n \approx 1.475$ with quadrupolar deformation, (**a**) algebraic-decay exponent z versus the deformation parameter ε. High-Q lasing operation can be expected for $\varepsilon < \varepsilon_c \approx 0.22$, (**b**) Measure μ of directionality versus ε. Apparently, a high degree of directionality can be maintained in the range of high-Q operation. (**c**), (**d**) position angle θ versus the emission angle θ_{out} for $\varepsilon = 0.1$ and 0.001, respectively [486] (copyright 2002, the American Physical Society)

where a unit area indicates uniform emission. The following measure of directionality can then be defined:

$$\mu_d(\varepsilon) = 1 - A(\varepsilon), \qquad (6.46)$$

where a high value of μ_d signifies a high degree of directionality (for uniform emission, $\mu_d = 0$). Figure 6.41b shows, for the particular cavity in (6.44), μ_d versus ε. Apparently, in the range of high-Q operation ($\varepsilon < \varepsilon_c$), $\mu_d \approx 1$, indicating a high degree of directionality. It was also found [486] that in the range of the deformation parameter where light emissions possess a high degree of directionality, the rays appear to exit the cavity at only a few locations on the boundary. At each exiting point, the range of the emission angle θ_{out} is highly localized. This behavior is shown in Fig. 6.41c, where the angle θ that defines the position of a boundary point (position angle) versus the emission angle θ_{out} is plotted for the escaping light rays for $\varepsilon = 0.1$. In contrast, when the deformation is near zero, light rays can exit from almost anywhere on the boundary ($0 \leq \theta < 2\pi$), which means that for the WG-mode operation, light can be emitted in almost every possible direction: $0 \leq \theta_{\text{out}} < 2\pi$, as shown in Fig. 6.41d. That high-Q operation and high degrees of directionality can be realized simultaneously in deformed cavities can be potentially useful for practical design and fabrication of microlasing cavities [183, 474, 660, 699].

In generic situations the phase space is mixed and also contains hyperbolic regions. If the region where emissions take place, i.e., the leak region from the point of view of energy loss, happens to fall far from large KAM surfaces, the total energy $E(t)$ inside the cavity decays exponentially over intermediate time scales. After some short time t^* one can write $E(t) \sim (1-r)^t$, where r is the leakage rate, i.e., the emitted energy per unit time. The energy decay rate κ_E governing the law

$$E(t) \sim e^{-\kappa_E t} \tag{6.47}$$

can then be expressed as

$$\kappa_E = -\ln(1-r). \tag{6.48}$$

The leakage rate has recently been shown by Altmann [15] to be the integral of the emission rate $\mathscr{T}$ of the light ray over the leak region taken with respect to the *conditionally invariant measure* of the leaked billiard dynamics:

$$r = \int_I \mathscr{T} \mathrm{d}\mu_c. \tag{6.49}$$

Relations (6.48) and (6.49) are analogous to relation (2.98), which determines the escape rate of leaked dynamical systems. The crossover to the algebraic decay takes over at some time t_c, which is expected to scale with the reciprocal of the decay rate κ_E, in analogy with (6.30). A detailed investigation also shows [15] that the localization of the far-field emission in specific directions is related to the unstable manifold of the chaotic saddle in the leaked system. The energy inside the cavity is distributed according to the c-measure, which is nonzero along the unstable manifold of the chaotic saddle. Strong intensity can therefore be observed only in points along the perimeter of the cavity that are on the unstable manifold of the leaked problem. For long times, the exponential decay crosses over to a power-law decay governed by the nonhyperbolic component of the chaotic saddle, but the directionality does not change qualitatively. The reason is that rays escape the non-hyperbolic component through the hyperbolic regions. The unstable manifold of the nonhyperbolic component of the chaotic saddle therefore follows closely that of the hyperbolic component [19].

Chapter 7
Quantum Chaotic Scattering and Conductance Fluctuations in Nanostructures

This chapter is devoted to the manifestation of classical chaotic scattering in the quantum world. The major characteristic that distinguishes a quantum system from its classical counterpart is that in quantum mechanics, the system is characterized by a nonzero value of the Planck constant. Let $\hbar$ denote the Planck constant nondimensionalized by normalizing to characteristic length and momentum values, so that $\hbar \to 0$ corresponds to the classical limit, $\hbar \ll 1$ to the semiclassical regime, and $\hbar \sim 1$ to the fully quantum-mechanical regime. To study the quantum manifestation of classical Hamiltonian chaos, the semiclassical regime is of particular importance because this is the regime in which both quantum and classical effects are relevant. In particular, we shall be interested in signatures of chaotic scattering when the same system is treated quantum-mechanically in the semiclassical regime. The mathematical methods needed to study the semiclassical regime differ from those used so far. This chapter is therefore of different character than the others. Our aim is to flesh out the most important phenomena only, where fingerprints of the classical transient chaos appear at the semiclassical level, motivating the reader to pursue more detailed studies.

The fundamental quantity characterizing a quantum scattering system is the scattering matrix, or the S-matrix, whose elements are the transition probabilities between quantum states of the system before and after the scattering. The formulation of the S-matrix in terms of classical quantities had been of great interest in chemical physics even before chaos started attracting wide attention. The seminal contribution by Miller [525], who obtained a formula for S-matrix elements in terms of purely classical quantities in the semiclassical regime for reactive scattering systems, becomes the fundamental tool in the study of quantum chaotic scattering. Given a system that exhibits chaotic scattering in the classical limit, the S-matrix elements in the semiclassical regime exhibit random fluctuations as some physical parameters of the system, such as the energy of the scattering particles or the strength of some externally applied magnetic field, change in a classically small but quantum-mechanically large range. We shall see that depending on whether the classical scattering is hyperbolic or nonhyperbolic, the statistical properties of the fluctuations in the S-matrix elements can be quite distinct.

An important class of systems in which the semiclassical theory of chaotic scattering finds direct application is semiconductor nanostructures, and particularly

quantum dots. In such a system, electrons are restricted to a plane near the interface between two different semiconductors. Applying voltage to contact gates deposited above the junction allows for the construction of submicron-sized, two-dimensional cavities in which electrons are scattered. Furthermore, at millikelvin temperatures, in such a system the mean free path and the coherence length are typically much larger than the cavity length. For low currents, the transport characteristics are determined by the approximately ballistic and coherent motion of electrons in the cavity. As a result, one can expect that the classical orbital dynamics of electrons, whether regular or chaotic, will play a major role in the transport. Indeed, for a two-dimensional electron-gas quantum dot that exhibits hyperbolic chaotic scattering classically, important physical properties of the system, such as various conductances, show random fluctuations that are absent when the underlying classical dynamics is regular.

Realistic quantum dots have nonhyperbolic classical scattering dynamics with chaotic sets coexisting with nonescaping KAM islands surrounding stable orbits in the phase space. For such a system, the conductances show strong *regular* fluctuations as some external parameter is varied. The origin of the regular conductance fluctuations is quantum-dynamical tunneling into the KAM islands, and the dominant frequency of the fluctuation pattern can be predicted by the semiclassical theory of tunneling. Dynamical tunneling has in fact become an active area of research not only in condensed-matter physics, but also in atomic and optical physics, which is illustrated by the example of scattering echoes. Leaked quantum systems are also discussed.

The materials of this chapter require preliminary knowledge about quantum mechanics. The semiclassical treatment of scattering processes is reviewed in Appendix C, while the concept of scattering cross sections is discussed in Appendix D.

7.1 Quantum Manifestation of Chaotic Scattering

The S-matrix elements characterize the transition probabilities between two asymptotic states. We consider the fluctuations of the S-matrix elements with energy. The treatment here follows that of Blümel and Smilansky [76,77]. For convenience, let I and I' be a pair of initial and final states (action variables) of the scattering process. The energy fluctuations of the S-matrix elements can be examined by the following autocorrelation function:

$$C_{II'}(\varepsilon) = \langle S_{II'}^*(E)S_{II'}(E+\varepsilon)\rangle_E, \tag{7.1}$$

where $S_{II'}(E)$ and $S_{II'}(E+\varepsilon)$ are the S-matrix elements between the initial and the final states at energy E and $E+\varepsilon$ (ε small compared with E), respectively, the asterisk represents the complex conjugate, and the average is over a classically small but quantum-mechanically large energy interval ΔE. Miller's theory

(see Appendix C, (C.1)) expresses the semiclassical S-matrix elements in the action-angle representation as

$$S_{II'} \equiv \langle I'|S|I \rangle = \left(\frac{1}{2\pi} \right)^{1/2} \sum_s \left| \frac{\partial I'}{\partial \theta} \right|_{(s)}^{-1/2} \exp \left[\frac{i\bar{\Phi}^{(s)}(I',I)}{\hbar} - i\nu_s \frac{\pi}{2} \right], \qquad (7.2)$$

where $\bar{\Phi}^{(s)}(I',I)$ is the dimensionless classical action along paths s, and ν_s is the Maslov index (Sect. C.2). The action variable I itself is also dimensionless. The quantity $|2\pi \partial I'/\partial \theta|_{(s)}^{-1}$ is the classical transition probability $p_{I,I'}^{(s)}$ for trajectories with initial and final action-angle variables I, θ and I', θ' (C.2). Substituting (7.2) into (7.1), concentrating on the energy-dependence of the action, and approximating

$$\bar{\Phi}^{(s)}(E + \varepsilon) \approx \bar{\Phi}^{(s)}(E) + \varepsilon \partial \Phi^{(s)}/\partial E, \qquad (7.3)$$

we obtain

$$C_{II'}(\varepsilon) \sim \left\langle \sum_s p_{II'}^{(s)}(E) \exp \left[\frac{i\varepsilon}{\hbar} \frac{\partial \bar{\Phi}^{(s)}}{\partial E} \right] \right\rangle_E + \left\langle \sum_{s \neq s'} [p_{II'}^{(s)}(E) p_{II'}^{(s')}(E)]^{1/2} \right.$$

$$\left. \exp \left\{ \frac{-i}{\hbar} [\bar{\Phi}^{(s)}(E) - \bar{\Phi}^{(s')}(E + \varepsilon)] + \frac{i\pi(\nu_s - \nu_{s'})}{2} \right\} \right\rangle_E. \qquad (7.4)$$

The phase factor in the second term in (7.4) is mainly determined by the differences in the classical actions $\bar{\Phi}^{(s)}$ from different trajectories s and s'. Since the energy interval ΔE over which the summations are carried out is chosen to be quantum-mechanically large, in the semiclassical regime ($\hbar \ll 1$) the double summation in the second term is essentially zero. The summation in the first term in (7.4) involves the partial derivative of the classical action with respect to the energy, $\partial \bar{\Phi}^{(s)}/\partial E$, which is the time it takes for a trajectory to travel from the initial to the final state. This time is in fact the delay time $t^{(s)}$ associated with this trajectory:

$$\frac{\partial \bar{\Phi}^{(s)}}{\partial E} = t^{(s)}. \qquad (7.5)$$

Thus the summation in the first term of (7.4) can be regarded as being with respect to this time. For chaotic scattering the distribution of the delay time can essentially be from zero to infinity. It is thus reasonable to replace the summation by an integral with respect to the delay time. This gives

$$C_{II'}(\varepsilon) \approx \int dt \langle p_{II'}(E,t) \rangle_E \exp \left(\frac{i\varepsilon t}{\hbar} \right), \qquad (7.6)$$

which is the Fourier transform of the classical probability $p_{II'}(E,t)$ that a transition $I \rightarrow I'$ occurs when the delay time of the trajectory is in the interval $[t, t+dt]$. This is, however, the escape-time distribution (Sect. 1.2.1)

$$p_{II'}(E,t) \sim p(t) \qquad (7.7)$$

at constant energy E. The main features of the autocorrelation function are thus independent of I, I', and we can suppress these indices in $C_{II'}(\varepsilon)$.

7.2 Hyperbolic Chaotic Scattering

7.2.1 Autocorrelation of the S-Matrix Elements

As discussed in Chap. 6, for hyperbolic chaotic scattering, the probability $p_{II'}(E,t)$ is independent of the initial and the final states I and I', and it decays exponentially with the escape rate κ at energy E:

$$p_{II'}(E,t) \sim \exp[-\kappa t].$$

Since the energy range ΔE is chosen to be classically small, the escape rate $\kappa(E)$ can be regarded as constant in ΔE. Substituting $p_{II'}(E,t)$ into (7.6) gives

$$C(\varepsilon) = \frac{C(0)\kappa}{\kappa - i\varepsilon/\hbar}. \tag{7.8}$$

The magnitude squared of the autocorrelation function is a Lorentzian of width $\hbar\kappa$:

$$|C(\varepsilon)|^2 = \frac{|C(0)\hbar\kappa|^2}{(\hbar\kappa)^2 + \varepsilon^2}. \tag{7.9}$$

It is thus the classical escape rate that determines the half-width of the semiclassical autocorrelation function of the S-matrix elements. As a consequence,

$$\left.\frac{d|C(\varepsilon)|^2}{d\varepsilon}\right|_{\varepsilon=0} = 0, \tag{7.10}$$

that is, the autocorrelation function is flat near $\varepsilon = 0$, indicating that the statistical fluctuations of the S-matrix elements with energy are relatively mild. The Lorentzian form of the autocorrelation function of the S-matrix elements has been evidenced in several cases. An example is shown for the microwave experiment of Doron, Smilansky, and Frenkel (see inset of Fig. 1.20 in Chap. 1), where the Lorentzian curve with the predicted width is displayed. More recent experiments with microwaves [427, 493, 576] found and even better agreement between the observed data and the semiclassical theory.

7.2.2 S-Matrix in the Time Domain

Instead of considering the scattering process as a wave phenomenon of fixed energy E, one can consider a narrow wave packet and follow its motion in time. The two approaches are related: the S-matrix $S(t)$ in the time domain is the Fourier transform of $S(E)$.

Consider the magnitude squared of the Fourier transform $S(t)$ of $S(E)$:

$$| S(t) |^2 = \left\langle \left| \int dE S_{II'}(E) e^{-iEt/\hbar} \right|^2 \right\rangle_{II'}, \tag{7.11}$$

where the average is taken over the matrix elements of the S-matrix. Using (7.2) and expressing the magnitude squared of the integral in (7.11) as a double integral, we have

$$\left| \int dE S_{II'}(E) e^{-iEt/\hbar} \right|^2 = \int dE dE' \sum_{s,s'} [p_{II'}^{(s)}(E) p_{II'}^{(s')}(E')]^{1/2}$$

$$\exp\left\{ i \left[\frac{\bar{\Phi}^{(s)}(E) - \bar{\Phi}^{(s')}(E')}{\hbar} - \pi\frac{v_s - v_{s'}}{2} - t\frac{E - E'}{\hbar} \right] \right\}.$$

When averaging over many matrix elements in the semiclassical regime, the double sum with off-diagonal elements $s \neq s'$ is essentially zero, so we can concentrate on the diagonal elements

$$\int dE dE' \sum_s p_{II'}^{(s)}(E) \exp\left\{ i \left[\frac{\bar{\Phi}^{(s)}(E) - \bar{\Phi}^{(s)}(E')}{\hbar} - t\frac{E - E'}{\hbar} \right] \right\}. \tag{7.12}$$

Since the dominant contribution comes from the regime in which $E - E'$ is small, we use (7.3) and (7.5) again to obtain

$$\int dE dE' \sum_s p_{II'}^{(s)}(E) \exp\left[i(t^{(s)} - t)(E - E')/\hbar \right], \tag{7.13}$$

where $t^{(s)}$ is the delay time for trajectory s. The integral over $E - E'$ is proportional to $\delta(t - t^{(s)})$. We have

$$| S(t) |^2 \sim \langle p_{I,I'}(E,t) \rangle_{II'}. \tag{7.14}$$

The magnitude squared of the Fourier transform of $S(E)$ with respect to the energy is proportional to the escape time distribution, and decays as $\exp(-\kappa t)$, with κ being the classical escape rate at energy E. This property has also been demonstrated in the microwave experiment shown in Fig. 1.20.

7.2.3 Relation to Orthogonal Ensemble of Random Matrices

Another correlation function is

$$F_{II'}(\eta) = \langle S_{II'}^*(E) S_{I(I'+\eta)}(E) \rangle_{\{I\}}, \tag{7.15}$$

where η denotes the action difference in two final states at energy E and $\langle \cdot \rangle_{\{I\}}$ is the average over a classically small but quantum-mechanically large domain of the initial and final states. Utilizing similar reasoning as for the energy autocorrelation function and making use of the fact that the partial derivative of the classical action integral $\bar{\Phi}^{(s)}$ with respect to I is the angle variable, Blümel and Smilansky obtained [76, 77]

$$F_{II'}(\eta) \sim \left\langle \sum_s p_{II'}^{(s)} \exp\left[\frac{i\eta}{\hbar} \frac{\partial \bar{\Phi}^{(s)}}{\partial I} \right] \right\rangle_{\{I\}} \sim \int d\theta \langle p_{II'}(E, \theta) \rangle_{\{I\}} \exp\left(\frac{i\eta\theta}{\hbar} \right),$$

(7.16)

where θ is the classical angle between the incoming and outgoing scattering trajectories, i.e., the deflection angle, and $p_{II'}(E, \theta)$ is the probability that the angle is in a small range $[\theta, \theta + d\theta]$ for energy E. For hyperbolic chaotic scattering, $p_{II'}(E, \theta)$ typically peaks at some mean angle θ_0 and decays exponentially as θ deviates from θ_0:

$$p_{II'}(E, \theta) \sim \exp(-\alpha|\theta - \theta_0|),$$

and it is independent of I and I'. These considerations lead to

$$F(\eta) = \frac{F(0)}{1 - i\eta/(\hbar\alpha)},$$

(7.17)

indicating that the magnitude squared of $F(\eta)$ also has a Lorentzian shape.

Since η is the difference between the action variables of final states after the scattering, in quantum mechanics it is an integer multiple of the Planck constant $\hbar$. In a classically small but quantum-mechanically large range, the integer $\eta/\hbar$ can be large. Thus, if α is not too large we have $|F(\eta)| \sim 0$, indicating that the S-matrix elements are *uncorrelated* with respect to the final state. Since the S-matrix is unitary and symmetric, its properties are completely determined by those of Dyson's orthogonal ensemble of random matrices [76, 77, 208]. Some important properties of the ensemble are the following:

(a) The nearest-neighbor distribution of the eigenvalues of the S-matrix on the unit circle is a Wigner distribution.
(b) At a given energy, the distribution of the magnitude squared of the S-matrix elements is Poissonian.
(c) Because of (b), i.e., the probability of $S_{II'}$ being small is large, the energy dependence of the scattering cross section $\sigma_{II'}(E)$ (for a given transition) exhibits a characteristic fluctuation pattern: the Ericson fluctuations [224].
(d) Because of the Lorentzian autocorrelation function of the S-matrix elements, the autocorrelation function of the scattering cross section $\langle \sigma_{II'}(E)\sigma_{II'}(E+\varepsilon) \rangle_E$ should also be a Lorentzian of the same width $\hbar\kappa$, set by the classical escape rate.

These properties have been verified in several studies (see, e.g., [75, 76]).

7.3 Nonhyperbolic Chaotic Scattering

We have seen in Chap. 6, (6.20), that for classical nonhyperbolic chaotic scattering,

$$p_{II'}(E,t) \sim t^{-(z+1)}, \quad \text{for large } t, \tag{7.18}$$

where the constant z is the algebraic-decay exponent, and the form is independent of I and I'. A natural question is how nonhyperbolic chaotic scattering manifests itself quantum-mechanically. This question was addressed [442] with the result that the fine-scale semiclassical quantum fluctuations of the S-matrix with energy can be *enhanced* in the nonhyperbolic case as compared to the hyperbolic case.

In the semiclassical regime, the energy autocorrelation function and the particle decay probability are Fourier-transform pairs, (7.6), regardless of the nature of classical scattering (i.e., hyperbolic versus nonhyperbolic). Since the algebraic decay law is valid for large t, to obtain the energy autocorrelation function of the S-matrix elements, we rewrite $p_{II'}(E,t)$ as

$$p(E,t) = \begin{cases} g(t), & 0 \le t \le T, \\ at^{-(z+1)}, & t > T, \end{cases} \tag{7.19}$$

where T is a large fixed value and $g(t)$ is a smooth function. Substituting (7.19) into (7.6) yields

$$
\begin{aligned}
C(\varepsilon) &\sim \int_0^T g(t) \exp\left(\frac{i\varepsilon t}{\hbar}\right) dt + \int_T^\infty at^{-(z+1)} \exp\left(\frac{i\varepsilon t}{\hbar}\right) dt \\
&= \frac{\hbar}{\varepsilon}\left[\int_0^{\bar{x}} g(x\hbar/\varepsilon)e^{ix}dx + a\int_{\bar{x}}^\infty \left(\frac{x\hbar}{\varepsilon}\right)^{-(z+1)} e^{ix}dx\right] \\
&= C_0 + C_1 \varepsilon^z,
\end{aligned}
\tag{7.20}
$$

where the change of variable $\varepsilon t/\hbar = x$ ($\bar{x} \equiv \varepsilon T/\hbar$) and the fact that $\bar{x}$ is small for small ε have been used, and $C_0 = C(0)$ and C_1 are constants. This form of the energy autocorrelation function is characteristically different from the Lorentzian function in (7.9). In particular, the derivative of $C(\varepsilon)$ with respect to the energy variation ε is

$$\frac{dC(\varepsilon)}{d\varepsilon} \sim \varepsilon^{z-1}. \tag{7.21}$$

In two-degree-of-freedom Hamiltonian systems, the classical algebraic-decay exponent z may fall in the range below 1 (see Fig. 6.31). In these cases (7.21) implies that the derivative $dC(\varepsilon)/d\varepsilon$ can be arbitrarily large for arbitrarily small values of ε. That is, for nonhyperbolic chaotic scattering, the energy autocorrelation function can exhibit a cusp for small energy difference ε. As ε is increased, $C(\varepsilon)$ decreases rapidly from C_0.

The above argument for the cusp behavior in $C(\varepsilon)$ cannot be valid for infinitesimal values of ε because this corresponds to the infinite time limit of the semiclassical approximation. Strictly speaking, the cusp behavior holds only in the range $\varepsilon_{max} > \varepsilon > \varepsilon_{min}$, where $\varepsilon_{max} \sim \hbar/T$ and T is the classically determined time in (7.19). The cutoff of the cusp behavior at small energy difference ε_{min} occurs because the semiclassical approximation breaks down for large times $t > t_{max}$, which corresponds to $\varepsilon_{min} \sim \hbar/t_{max}$. This can be understood by noting that the algebraic decay results from particle orbits that spend long stretches of time near KAM surfaces. Orbits contributing to longer times penetrate more deeply into the sticky region near a KAM surface. At finite wavelengths, there comes a time past which the phase space structures resolved by classical orbits still in the scattering region are quantum-mechanically not resolved. This determines the crossover time t_{max}.[1] Thus, the algebraic-decay exponent appearing in (7.21) is the one characterizing long but finite time intervals. As Fig. 6.31 shows, this exponent can take on different values.

The cusp behavior in the energy autocorrelation function for nonhyperbolic chaotic scattering can be numerically verified [442] by the Troll–Smilansky model defined by (6.34) and (6.35), with the potential function $V(r)$ chosen as the Woods–Saxon potential

$$V(r) = -\frac{V_0}{1 + \exp[(r - R_0)/c]}, \tag{7.22}$$

where $V_0 > 0$ and R_0 and c are constants. For the fixed set of parameters $V_0 = 10$, $R_0 = 1$, $c = 0.1$, and $a = 4$, the nonoverlapping condition for adjacent potentials is satisfied because $V(r = a/2)/V_0 \sim 10^{-5}$. When the particle energy is large, the phase space consists of KAM islands and chaotic regions for $E = 10$, and the decay of particles from the scattering region is well fit by an algebraic dependence. As the particle energy decreases from $E = 10$ to $E = E_{crit}$, where $1 < E_{crit} < 10$, the KAM surfaces are destroyed. At lower values of E, there are no KAM surfaces, and the decay of particles from the scattering region becomes exponential.

Quantum-mechanically, the effect of any single scatterer is completely specified once the phase shifts are given. Because of the discrete translational symmetry of the system in the y direction, the wave function satisfies $\psi^{(\alpha)}(x,y) = \exp(i\alpha y)\varphi^{(\alpha)}(x,y)$, where $\varphi^{(\alpha)}(x,y)$ is periodic with period a in y. So we have $\psi^{(\alpha)}(x,y + na) = \exp(in\alpha a)\psi^{(\alpha)}(x,y)$. Thus the y component of the momentum q_n is quantized: $q_n = \alpha + 2n\pi/a$. By the conservation of energy $q_n^2 \leq k^2$, where k is the wave number ($E = \hbar^2 k^2/2$), there exists a maximum integer N_B (maximum number of open channels) above which q_n is not allowed, which corresponds to evanescent waves.

To compare the quantum calculation with the semiclassical predictions, it is necessary to use sufficiently small values of Planck's constant $\hbar$, so that there is a large number of waves on the scale of the system's spatial period a. For the nonhyperbolic

---

[1] It has been shown that this time scales with the Planck constant algebraically [242,460]. The scaling law of the crossover time with the Planck constant is fundamental for semiclassical treatment of classically chaotic systems.

Fig. 7.1 Magnitude squared of S-matrix autocorrelation functions (*diamonds* for the nonhyperbolic case ($E = 10$) and *triangles* for the hyperbolic case ($E = 1$)) and the corresponding semiclassical predictions (*thick solid curves*) [442] (copyright 1992, the American Physical Society)
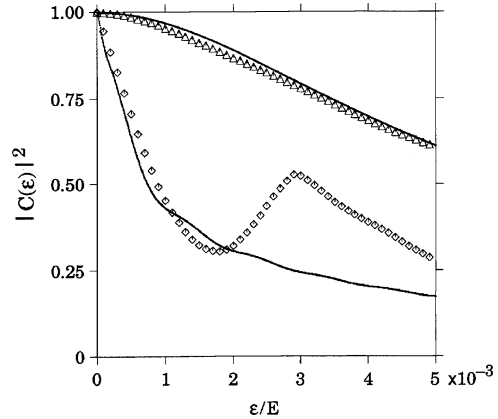
case $E = 10$, $\hbar^2/2 = 10^{-3}$ was chosen [442], so that the corresponding wave vector is $k_0 = 100$ and there are 127 open channels ($128 > 2a/\lambda > 127$). For the case of hyperbolic scattering at $E = 1$, $\hbar^2/2 = 10^{-4}$ was chosen ($k_0 = 100$), so the number of open channels is the same as that in the nonhyperbolic case. The autocorrelation function $C(\varepsilon)$ was computed using an energy width $\Delta E/E \approx 0.1$. As a function of energy, an S-matrix element contains both a smooth part and a fluctuating part. To compare with the semiclassical theory, the smooth part was subtracted off and only the fluctuating part was kept. Figure 7.1 shows the magnitude squared of the quantum autocorrelation functions $|C(\varepsilon)|^2$ for both the $E = 10$ case (nonhyperbolic, plotted as diamonds) and the $E = 1$ case (hyperbolic, plotted as triangles), where an average was performed with respect to a small block of matrix elements. The $C(\varepsilon)$ curves are, however, essentially independent of the particular matrix block chosen in the averaging process [442]. Also shown in Fig. 7.1 are the semiclassical predictions from (7.20); the lower thick solid curve corresponds to $E = 10$, and the upper thick solid curve corresponds to $E = 1$. To calculate the semiclassical correlation functions, the classical decay data were substituted directly into (7.6). For both the hyperbolic and the nonhyperbolic cases, Fig. 7.1 suggests that the quantum calculation is consistent with the semiclassical theory for small ε. The energy autocorrelation function appears to follow the predicted cusp behavior near $\varepsilon = 0$ for nonhyperbolic scattering. This means that in comparison with the hyperbolic-scattering case, the fine-scale fluctuations of the matrix elements with energy are greatly enhanced in the nonhyperbolic case.

7.4 Conductance Fluctuations in Quantum Dots

One important area in which the semiclassical theory of quantum chaotic scattering finds application is electronic transport in semiconductor nanostructures. In semiconductor nanodevices, a basic component is mesoscopic junctions,

or *quantum dots*, which connect a number of quasi-one-dimensional electronic wave guides and control the electronic transport. The size of the junctions is usually appreciable on quantum scales but small on classical scales, so electron motions are coherent and *ballistic*. A mesoscopic junction system is thus equivalent to an open billiard system, for which chaotic scattering dynamics can be expected. However, quantum effects are also important. Predictions from the semiclassical theory of quantum chaotic scattering are then expected to be useful and experimentally observable. In particular, because of the fine-scale fluctuations of the S-matrix elements with energy (or magnetic field), various conductances measured from the junction system can exhibit fluctuations as well. Conductance fluctuations in mesoscopic junction systems have been an active area of research (for reviews, see [39, 40, 46, 68, 501]), which has recently been extended to the relativistic quantum regime in graphene dots [342, 343].

Here, we give a brief introduction to this vast area of research. In particular, we introduce the basic physics of quantum dots, describe the Büttiker–Landauer formula, which relates conductances to transmission probabilities (S-matrix elements), and discuss random conductance fluctuations in dots for which the classical scattering dynamics are hyperbolic. The case of conductance fluctuations in typical, nonhyperbolic junction systems, for which dynamical tunneling into KAM surfaces becomes important, will be addressed in Sect. 7.5.

7.4.1 Basic Physics of Quantum Dots

We use the GaAs/AlGaAs heterojunction to illustrate the basic physics associated with two-dimensional electron gas semiconductor quantum dots. In such a junction, material GaAs is made as pure as possible, but typically it is a weak p-type of semiconductor. AlGaAs has a wider band gap, so it is effectively an insulator. Modern molecular-beam epitaxy techniques enable atomically sharp interfaces between these two materials to grow [238], which are heterojunctions. The two materials have approximately the same lattice and dielectric constants. It is possible to have a GaAs layer followed by an almost perfectly matched layer of AlGaAs. The energy bands of the two materials, before any interactions occur, are shown in Fig. 7.2.

The AlGaAs is doped as n-type. Electrons in the conduction band migrate to fill the few holes in the top of the GaAs valence band, but most of them end up in states near the bottom of the GaAs conduction band, as shown in Fig. 7.3. Positive charges associated with donor impurities attract these electrons to the interface and consequently bend the energy bands on both sides of the interface in the interaction process. This is the source of an electrical field in the system. The transfer of electrons from AlGaAs to GaAs continues until a dipole layer, formed of the positive donors and the negative inversion layer, is sufficiently strong. The dipole layer gives rise to a discontinuity in the potential that forces the Fermi levels of GaAs and AlGaAs to be equal, as shown in Fig. 7.3. Because of this, electrons will be confined in a two-dimensional sheet within about 100 Å of the interface, and consequently, electron motions in the junction are effectively two-dimensional.

Fig. 7.2 Energy-band structure of the GaAs/AlGaAs interface before any electronic interactions
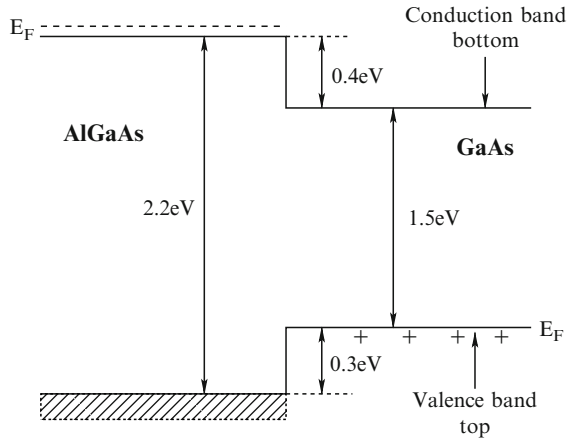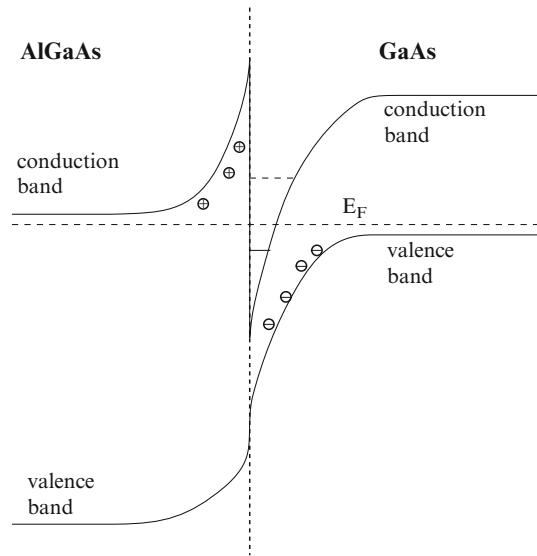

Fig. 7.3 Electron energy-level diagram of a GaAs/AlGaAs heterojunction device. Donor electrons occupy the first conduction subband of the potential well. The two-dimensional electron sheet is confined to within about 100 Å of the interface

The GaAs/AlGaAs heterojunction can be patterned by electron-beam lithography and low-energy ion exposure into miniature wires and junctions [238]. The junction can be designed and fabricated to have different geometric shapes in a controllable manner. The width of the wire is on the order of a few micrometers and the electron mobility is typically larger than $10^6 \, cm^2/V \cdot s$ at millikelvin temperatures. As a consequence of this high mobility, the mean distance l_e between elastic collision events due to crystal imperfections and impurities can exceed most experimentally accessible channel lengths L, so electrons travel from an entrance of the junction to an exit with a minimal number of collisions. The electron motion in the junction system can then be regarded as ballistic with conserved momentum. The quantum-dot systems, besides their importance in nanoscience and technology, are an ideal test bed for the semiclassical theory of quantum chaotic scattering.

7.4.2 Büttiker–Landauer Formula

The Büttiker–Landauer formula relates various transmission probabilities (S-matrix elements) of electronic transport in a quantum dot to physically measurable conductances [107, 108, 468]. (For a comprehensive treatment, see [46, 155].) Consider a junction of arbitrary shape with four terminals. Under the assumption that electrons move ballistically through the junction, phase-destroying events do not occur. For generality, assume that an external magnetic field is present so that there is an Aharonov–Bohm flux ϕ through the system, as shown in Fig. 7.4. Thus the conductances of the junction are functions of the magnetic field. Alternatively, one can imagine that the energy of the electrons can be varied, and in this case, the conductances are functions of the electron energy. The leads to the junction being connected to reservoirs at chemical potentials $\mu_1, \ldots, \mu_4$, which serve as sources and sinks of electrons and energy. In particular, at zero temperature a reservoir of chemical potential μ_i feeds the connected lead with electrons up to kinetic energy μ_i ($i = 1, \ldots, 4$). Every electron coming through the junction and reaching another reservoir is absorbed by it, regardless of the energy and the phase of the electron. It is convenient to assume that the wires connecting the junction and reservoirs are perfect, i.e., they are strictly one-dimensional quantum channels with two states at the Fermi energy: one with positive velocity (taken to be the direction away from a reservoir and toward the junction) and another with negative velocity. Scattering in the junction is elastic, and inelastic events occur only in the reservoirs.

The elastic scattering properties of the junction are characterized by the probabilities $T_{ij}(\phi)$ for electrons incident in lead j to be transmitted into lead i, and $R_{ii}(\phi)$, the probabilities that electrons coming into lead i are reflected back into the same lead. Current conservation and time-reversal invariance in the presence of a magnetic flux imply $R_{ii}(\phi) = R_{ii}(-\phi)$ and $T_{ii}(\phi) = T_{ii}(-\phi)$. The potentials μ_i are rather arbitrary within a small range at the Fermi energy. Let $\mu_0 \leq \min\{\mu_i\}$ ($i = 1, \ldots, 4$). Thus, below the potential μ_0, states with positive and negative velocities are filled and there is no net current flow in each lead. It is necessary to consider only the energy range $\Delta\mu_i = \mu_i - \mu_0$ above μ_0. Reservoir i injects a current $ev_i\rho_i\Delta\mu_i$ into lead i, where v_i is the electron velocity at the Fermi energy, and $\rho_i = 1/(hv_i)$ is the density
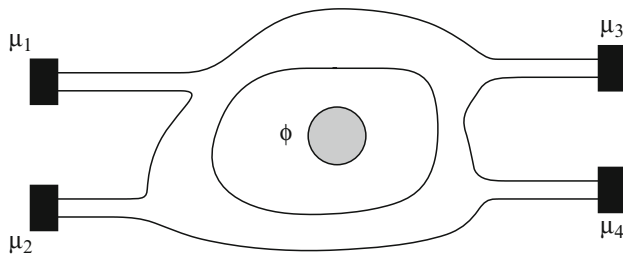

Fig. 7.4 A general junction of four terminals connected to four reservoirs at chemical potentials μ_1, μ_2, μ_3, and μ_4, respectively. An Aharonov–Bohm flux ϕ is applied through the junction

of states in lead i. The current injected by reservoir i is thus $(e/h)\Delta\mu_i$. To be concrete, consider the current in one of the leads, say lead 1. A current $(e/h)R_{11}\Delta\mu_1$ is reflected back to reservoir 1. Each of the reservoirs 2, 3, and 4 contributes a current $-(e/h)T_{1j}\Delta\mu_j$ $(j=2,3,4)$ to the total current in lead 1. We thus have

$$I_1 = \frac{e}{h}\left[(1-R_{11})\mu_1 - \sum_{j\neq 1} T_{1j}\mu_j\right].$$ (7.23)

Because of the charge conservation

$$1 = R_{ii} + \sum_j T_{ij}$$ (7.24)

for any i, the reference potential μ_0 is canceled in (7.23). In general, the net current in any lead i can be written as

$$I_i = \frac{e}{h}\left[(1-R_{ii})\mu_i - \sum_{j\neq i} T_{ij}\mu_j\right].$$ (7.25)

As an example, we consider the Hall resistance in the presence of a strong magnetic field B for a symmetric four-disk billiard junction, as shown in Fig. 7.5. Because of the surfaces of negative curvature in the junction, classical dynamics can be chaotic, so this junction system provides a paradigmatic system for studying quantum manifestations of chaotic scattering. Because of the symmetry, the transmission probabilities are $T_{41} = T_{34} = T_{23} = T_{12} \equiv T(B)$ for large B, while all other
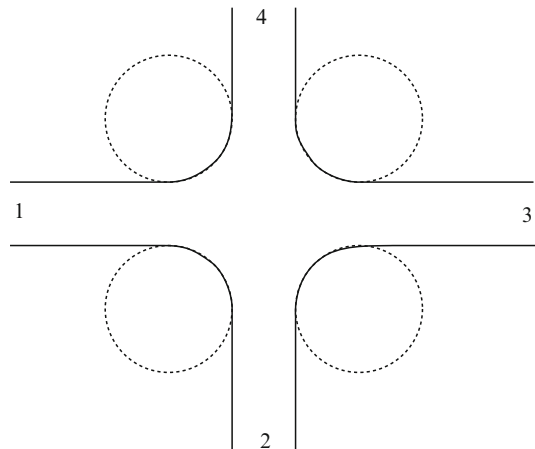

Fig. 7.5 A symmetric, four-disk junction from which Hall conductance can be measured

transmission probabilities are zero. From (7.24) one finds that $1 - R_{ii} = T(B)$ for any i. The currents in (7.25) are

$$I_1 = \frac{e}{h}T(B)[\mu_1 - \mu_2],$$

$$I_2 = \frac{e}{h}T(B)[\mu_2 - \mu_3],$$

$$I_3 = \frac{e}{h}T(B)[\mu_3 - \mu_4],$$

$$I_4 = \frac{e}{h}T(B)[\mu_4 - \mu_1]. \tag{7.26}$$

In a typical four-terminal experiment, only two of the potentials are measured. Suppose current flows from lead 1 to lead 3. The potentials measured are $\mu_2 = eV_2$ and $\mu_4 = eV_4$ under the condition that the currents I_2 and I_4 are zero. Equation (7.26) then implies that $\mu_1 = eV_4$, $\mu_3 = eV_2$, and

$$I_1 = \frac{e^2}{h}T(B)[V_4 - V_2] = -I_3. \tag{7.27}$$

The Hall conductance is defined as

$$G_{\mathrm{H}} = \frac{I_1}{V_4 - V_2}, \tag{7.28}$$

which is obtained in this particular setting as

$$G_{\mathrm{H}}(B) = \frac{e^2}{h}T(B). \tag{7.29}$$

The Hall conductance is proportional to the single nonzero transmission probability.

7.4.3 Conductance Fluctuations as Quantum Manifestation of Chaotic Scattering

One of the first studies on conductance fluctuations in quantum dots was carried out by Jalabert, Baranger, and Stone [355] (see also [656]). They considered the conductance for an open-stadium junction with two leads, and the symmetric four-disk junction system in Fig. 7.5. For the open-stadium system the conductance is directly proportional to the transmission probability, since there are only two leads connected to the junction, one for the incoming and another for the outgoing electrons. The width of each channel is denoted by W. For both junction systems, the classical scattering dynamics are chaotic and hyperbolic. Quantum-mechanical calculations

Fig. 7.6 (**a**) Hall resistance $R_H \equiv 1/G_H$ versus the magnetic field strength B for a four-disk junction defined by the geometric parameters $R/W = 4$ (*inset*). (**b**) For an open-stadium billiard junction of width $W = 1,000$ Å, the transmission probability $T(B)$ versus the magnetic field strength [355] (copyright 1990, the American Physical Society)
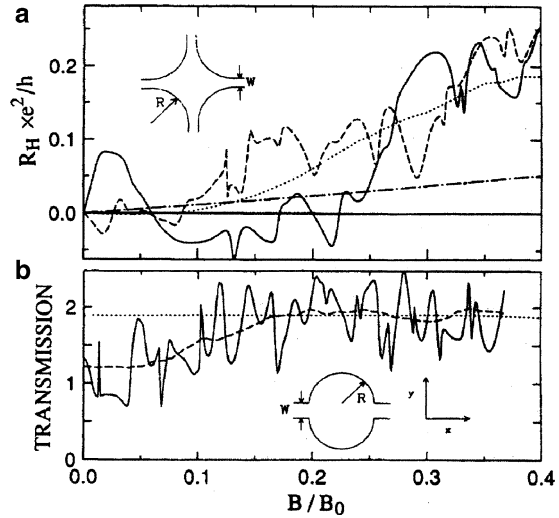
of the resistance as a function of the external magnetic field showed significant random fluctuations, as shown in Fig. 7.6. In Fig. 7.6a, the fluctuating curves are from two quantum calculations with slightly different Fermi energies E_F. In particular, the solid fluctuating curve is for $k_F W/\pi = 4.3$, and the dashed curve is for $k_F W/\pi = 4.4$, where k_F is the wave number at the Fermi energy. The existence of these fluctuations is consistent with observation (c) in Sect. 7.2.3. The dotted curve, which does not exhibit fluctuations, is from a purely classical calculation. The dashed-dotted curve is the result of quantum calculation for a square junction, in which the classical scattering dynamics is regular. In Fig. 7.6b, the solid, fluctuating curve is the quantum result for the transmission probability $T(B)$ with $k_F W/\pi = 4.5$, and the dashed curve is the smoothed average $\langle T(B) \rangle$ used for computing the magnetic-field autocorrelation function $C(\Delta B)$. The dotted line is the purely classical result. Fluctuations are thus absent in a purely classical calculation of the scattering matrix (as done by Beenakker and van Houten [47]), or for regular cavities where there is no classical chaotic scattering. These indicate that the origin of the fluctuations is quantum-mechanical and classical chaos is also relevant. Jalabert, Baranger, and Stone performed a semiclassical analysis of the S-matrix elements with predictions that appear to agree with the quantum calculations. The analysis is similar to that described in Sect. 7.2, except that the electron energy is replaced by the magnetic field strength B. An example of the magnetic field correlation function of the transmission probability $T(B)$ is shown in Fig. 7.7, which corresponds to the open-stadium junction in Fig. 7.6b. For small magnetic field strength, the correlation is Lorentzian, as predicted by the semiclassical theory. The half-width is given again by a classical quantity, similar to the parameter α in (7.17).
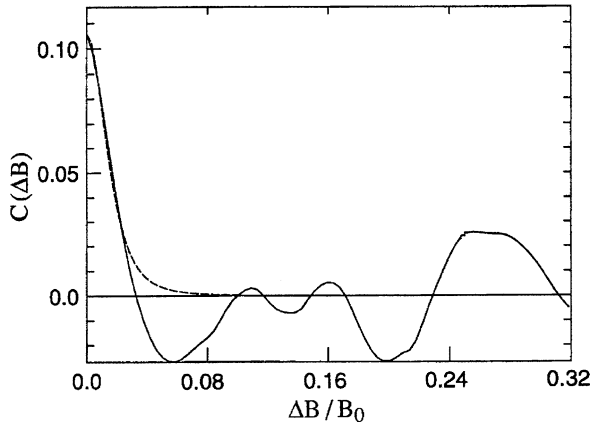
Fig. 7.7 Magnetic field correlation function $C(\Delta B)$ (*continuous line*) from the *dashed smoothed curve* of $\langle T(B) \rangle$ in Fig. 7.6b. The *dashed curve* is the Lorentzian semiclassical prediction [355] (copyright 1990, the American Physical Society)

7.5 Dynamical Tunneling in Nonhyperbolic Quantum Dots

A tacit assumption in the study of conductance fluctuations in quantum dots, as discussed in Sect. 7.4, is that the underlying classical dynamics is hyperbolic. In such an idealized case, the random-matrix theory is applicable. We have seen in Sect. 7.2 that this approach predicts universal conductance fluctuations with a Lorentzian type of correlation functions. A fundamental difficulty with the random-matrix-theory-based approach is that many experimental results have suggested that hyperbolicity is in fact an unusual dynamical feature in quantum dots (see e.g., [10, 345, 523].) Thus, for typical dots, the observed properties of the transport simply cannot be explained by the random-matrix theory. It is of interest to study the effect of nonhyperbolicity on conductance fluctuations [68, 166].

In a typical nonhyperbolic quantum-dot system, the conductance exhibits strong *regular* fluctuations as the gate voltage (or the magnetic field) is varied, as opposed to random fluctuations [67, 69]. An example of the measured fluctuations is shown in the lower left inset of Fig. 7.8. It was argued in [166] that in order to explain these results, it is necessary to take into account quantum-mechanical tunneling of electrons through the KAM islands (*dynamical tunneling*), which corresponds to classically forbidden trajectories that are not taken into account in the usual semiclassical approach.

For the quantum-dot system considered in [166], the self-consistently computed potential profile is shown in the upper right inset in Fig. 7.8 (for more details, see [69]). For the range of voltages studied, the profile remains basically the same. For higher voltages, the potential is more confining, and the two openings become smaller. The low-temperature electron and density mobility of this dot are 4×10^{15} m^{-2} and 70 m^2/V · s [69], respectively, with the corresponding Fermi
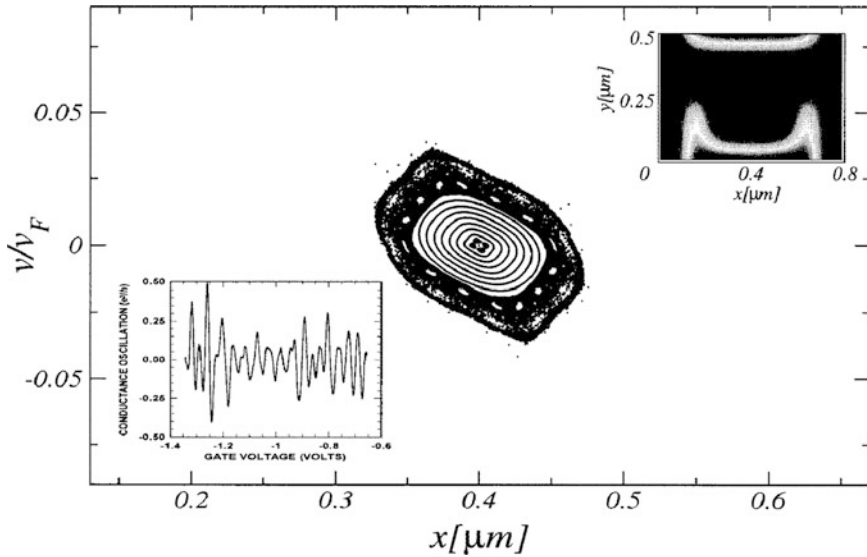
Fig. 7.8 A nonhyperbolic quantum dot. The *upper right inset* shows the electrostatic potential profile (as a gray-scale plot) of the dot at the gate voltage of $V_g = 0.6$ V. *Main panel*: Poincaré section of the corresponding classical scattering process with $E = E_F = 14.3$ mV, where v is the x-component of the velocity, given in units of the Fermi velocity. The "chaotic sea" surrounding the island is the plot of a single trajectory that stays a long time near the island before escaping. The phase-space area of the island is about $\hbar$. The *lower left inset* shows the measured conductance fluctuations observed by varying the gate voltage [69] (copyright 2002, the American Physical Society)

energy of 14.3 meV. Each gate voltage corresponds to a different shape of the electrostatic potential that can be computed self-consistently on a grid using a Poisson solver. The transmission of electrons can be described as a scattering process in the dot. The classical scattering dynamics can be studied by simulating the motion of electrons at the Fermi energy in the underlying potential. The phase-space structure can be visualized using a proper Poincaré surface of section. Figure 7.8 indicates that the classical dynamics is nonhyperbolic, with a large KAM island dominating the phase space. This island is centered on a period-1 orbit that bounces back and forth vertically through the center of the dot, the so-called *bouncing-ball orbit*. It is apparent that the usual random-matrix approach cannot be applied to this system.

We have seen in Sect. 7.3 that the semiclassical theory of nonhyperbolic chaotic scattering predicts stochastic conductance fluctuations with different statistical properties from those in the hyperbolic case. The theory does not predict the regular fluctuations seen in experiments. This is because the usual semiclassical theory considers only the interferences between the classically allowed trajectories, and hence ignores the possibility of electron tunneling into the KAM island (corresponding to diffraction in optics). This effect is negligible only if the de Broglie wavelength λ_e of the electron is much smaller than the cavity size. For typical dots of size $1\,\mu m$, λ_e is about one-tenth of the cavity length, and therefore tunneling

cannot be neglected. Nonetheless, since λ_e is small enough, semiclassical concepts such as the Bohr–Sommerfeld quantization of periodic orbits can still be applied. Conductance measurements reveal that these regular oscillations have only a few dominant frequencies [69]. It was argued [166] that these peaks are due to dynamical tunneling [701, 783]: there is a probability that an incoming electron tunnels into the KAM island. If the electron energy and the system parameters are such that the semiclassical quantization condition (see below) is satisfied for a low-period stable periodic orbit within the island, there is a resonance with a sharp decrease in the transmission. As the system's parameters change, these resonances occur with the period given by the position of the peaks in the Fourier transform of the conductance fluctuations. As a matter of fact, dynamical tunneling is of great importance in many fields, e.g., in cold-atom physics [327, 735] and in atomic optical billiard [385]. The semiclassical theory of dynamical tunneling can be relevant for such systems as well.

Because KAM surfaces are classically impenetrable, the classical dynamics restricted to the island shown in Fig. 7.8 is that of a closed system. For closed systems, the Gutzwiller trace formula stipulates that each *stable* orbit generates a series of delta functions in the density of states, at energies for which the resonance condition holds [301, 525],

$$S_{\text{eff}} = S + \frac{\Omega}{2\pi}\left(m + \frac{1}{2}\right) + \frac{\nu}{4\pi} = n, \tag{7.30}$$

where $S = \frac{1}{\hbar}\int p \cdot \mathrm{d}q$ is the action along the periodic orbit in units of Planck's constant, S_{eff} is an effective action, Ω is a quantity that characterizes the stability of the orbit, and ν is the Maslov index; $m, n = 0, 1, 2, \ldots$. The quantum-dot system under consideration is open. Just as an incoming electron can tunnel in, an electron within the island is in a *metastable* state, and can "decay" by escaping. This causes the peaks in the density of states to broaden, and their width is inversely proportional to the average time it takes for an electron to tunnel out of the island. If this time is not too short, the peaks will be sharp enough to be resolved, and their positions are determined by (7.30).

Consider first the case $m = 0$. Note that n is the *longitudinal quantum number*, which counts the number of nodes in the "eigenfunction" along the orbit. Within the island of Fig. 7.8 there are infinitely many periodic orbits, but only the lowest-period ones are expected to be resolved.[2] The most important orbit in the island is the period-one bouncing-ball orbit corresponding to the fixed point at the center of the island in Fig. 7.8. Moura et al. calculated [166] numerically S_{eff} in (7.30) as a function of the gate voltage V_g for this island, and compared it with the experimental results, as shown in Fig. 7.9. It can be seen that the points fall reasonably well on a straight line, which corresponds to a periodic recurrence of the resonance. Since a resonance occurs each time S_{eff} goes through an integer, the absolute value

---

[2] High-period orbits generate peaks that are too closely spaced to be resolved, even more so with the broadening of the levels caused by the quantum metastability of the system.
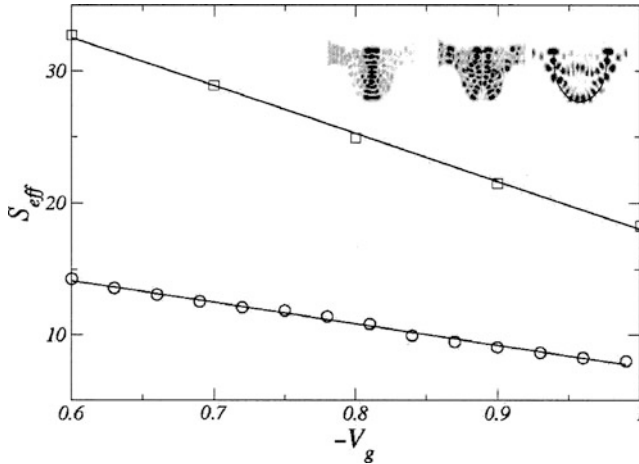
Fig. 7.9 Effective action S_{eff} versus the gate voltage, for the stable (*circles*) and unstable (*squares*) orbits. The *inset* shows a pair of closely spaced concentrated wave functions corresponding to the stable bouncing-ball orbit (*left* and *center images*), and a scar due to the unstable orbit (*right image*) along with its corresponding classical orbit, obtained by a full quantum-mechanical simulation of the open system [166] (copyright 2002, the American Physical Society)

of the slope of the straight line gives the semiclassical prediction for the frequency of the *conductance oscillations*. This frequency was found to be $16.4\,\text{V}^{-1}$, in remarkable agreement with the measured value of $15\,\text{V}^{-1}$ [69], suggesting that this peak corresponds to recurring tunneling resonances. This is reinforced by a fully quantum simulation of the *open* system [69]. In particular, concentrations of wave functions (the insets of Fig. 7.9, each corresponding to a different value of the gate voltage) computed from the technique in [796] show a recurrent pattern. The recurrence frequency of the concentrated wave function was determined to be [166] $16\,\text{V}^{-1}$, in agreement with the semiclassical prediction and with the experimental result. Since this orbit is classically inaccessible from outside, the results represent direct evidence of dynamical tunneling is nonhyperbolic quantum dots.

In a general case, i.e., when m is any positive integer, the second term in S_{eff} in (7.30) represents the quantization of the component of the motion transverse to the periodic orbit. This means that for each n there is actually an infinite set of resonances, labeled by m, similar to a vibrational band in a molecule. Assuming that S_{eff} changes linearly with the gate voltage V_g, one can estimate the separation ΔV_g between two resonances with consecutive transverse quantum numbers:

$$\Delta V_g \approx \frac{\Omega}{2\pi \left| dS_{\text{eff}}/dV_g \right|}, \tag{7.31}$$

where it is assumed that Ω does not change much between two successive resonances. Although Ω depends on n, its values were found [166] to lie in the range between 1 and 2 rads. Using the value of $\left| dS_{\text{eff}}/dV_g \right|$ derived from Fig. 7.9, one obtains that ΔV_g is between 1×10^{-2} and $2 \times 10^{-2}\,\text{V}$. Just as n counts the number of

nodes along the orbit, m counts the number of nodes across it, so we expect that for each n, there is a set of concentrated wave functions having $0, 1, 2, \ldots$ transverse nodes, separated by the gate voltage interval ΔV_g. Such recurring pairs of concentrated wave functions were observed in the quantum-mechanical simulation for the bouncing-ball orbit, separated by a gate voltage difference of about $2 \times 10^{-2}\,\mathrm{V}$, which agrees well with the prediction. One pair is shown in Fig. 7.9 (left and center images of the inset). It can be seen that they correspond to $m = 0$ and $m = 1$. They are also found for other values of n, and they recur at the *same* period, as predicted. It was emphasized [166] that this phenomenon cannot be explained without taking the mechanism of tunneling into account, since it requires electrons to access the stable orbit that is classically forbidden. The concentrated wave functions corresponding to higher values of m ($m = 2, 3, \ldots$) were not resolved by the simulation, because of their short lifetime.

Although the discussion so far has been focused on the stable orbits, unstable orbits are also present in the system, and they contribute to the density of states. The concentrated wave function corresponding to the main unstable orbit is displayed in the upper right inset in Fig. 7.9. A classical trajectory analysis suggests that the orbit giving rise to this whispering-gallery scar is guided by the soft walls around the perimeter of the lower section of the dot, bouncing from the upper wall at two points, located close to the two lead openings. The resonant condition for unstable periodic orbits is given by (7.30) without the Ω term [301]. This means that unstable periodic orbits do not give rise to the subband of resonances associated with m. In the Fourier transform of the conductance oscillations, a peak was observed at $V_g \approx 37\,\mathrm{V}$, corresponding to an unstable periodic orbit of period 1. Figure 7.9 also shows a plot of S_{eff} versus V_g for this orbit, and from the slope we get a recurrence frequency of $36.3\,\mathrm{V}^{-1}$, again in good agreement with the experimental result. The concentrated wave functions related to these resonances were seen in the quantum-mechanical simulation, but no subband was observed. The other main periodicities found in the conductance correspond to harmonics of the main stable and unstable resonances studied above. Note that in [345], isolated resonances were predicted to arise from the chaotic part of the phase-space outside the islands (see Fig. 7.8), but these can be detected for smaller values of $\hbar$ only, i.e., for larger quantum dots.[3]

We thus see that the usual semiclassical approach is not enough to explain the transport characteristics of typical semiconductor nanostructures, and the quantum-mechanical tunneling of the electron through KAM islands has to be taken into account. Tunneling resonances caused by stable and unstable periodic orbits of low periods within the KAM islands cause regular oscillations of the conductance. These results are expected to hold for all quantum-dot systems [166]. The general standpoint is that tunneling plays a fundamental role in mesoscopic transport.

---

[3] In contrast to [345], $\hbar$ is of the size of the island and therefore the hierarchical part of the phase space surrounding the island is not resolved quantum-mechanically. That is why the resonances due to the hierarchical states are not observed. Note, however, that these are always *broader* than those due to the stable island.

7.6 Dynamical Tunneling and Quantum Echoes in Scattering

As pointed out by Jung, Mejia-Monasterio, and Seligmann [363, 365], echoes can occur in classical and quantum chaotic scattering. In the classical context, echoes occur in nonhyperbolic systems when the chaotic saddle is in such a stage of development that the stable island associated with the inner periodic orbit is relatively large. Quantum-mechanically, a short pulse in the incoming wave can then lead to periodic pulses in the outgoing wave.

To describe the classical phenomenon, let us recall the form of the Poincaré section of a binary horseshoe as illustrated by Fig. 6.24. When incoming scattering trajectories approach the central region along the stable manifold, they rotate around the stable island and return to the vicinity of the hyperbolic fixed point. Depending on the initial conditions, some of the trajectories leave the hyperbolic point along its unstable manifold. The remaining trajectories continue to rotate to complete a second revolution. By reaching the hyperbolic fixed point again, some trajectories exit the central region around the island, and the process continues. The asymptotic outgoing flux resulting from a narrow packet of incoming trajectories therefore exhibits intensity oscillations in time. These oscillations are the scattering echoes.

The time between successive maxima of the outgoing flux corresponds to the mean period of rotation around the island. This time can be expressed by the development parameter introduced in Sect. 6.4.2. Based on Fig. 6.25, which illustrates a binary horseshoe for development parameter $\alpha = 2^{-m}$ with $m = 4$, we can estimate the mean period of rotation. Consider a point (star marked by 0) lying close to the unstable tendril 1. Since the unstable tendril of level n is the image of tendril $(n-1)$ on the Poincaré section, the nth image of the starting point will be close to the unstable tendril $(n+1)$. The revolution is almost completed after the $(m+1)$th iteration, when the point is around the tip of the unstable tendril $m+2$ (tendril 6 in Fig. 6.25). After another step, the trajectory completes a bit more than one revolution. The period on the Poincaré map can thus be estimated as $T = m + 3/2$. In terms of the development parameter α, we have

$$T = -\log_2 \alpha + 3/2. \tag{7.32}$$

In continuous time the period can be expressed as

$$T = t_0(-\log_2 \alpha + 3/2), \tag{7.33}$$

where t_0 is the average return time to the Poincaré section. For ternary horseshoes one obtains [363]

$$T = t_0(-2\log_3 \beta + 3/2), \tag{7.34}$$

where the factor 2 is a consequence of the fact that there are two hyperbolic fixed points associated with a ternary horseshoe. The development parameter alone thus determines the classical winding period, which is the pulsation period of the scattering echoes.

At the quantum level, the echoes are of a similar origin, and arise if the system is excited with a short pulse. A new feature is that the quantum wave function can penetrate the classical KAM surfaces and reach the inner region of the classical island. This dynamical tunneling effect results in rotation of the quantum probability around the island at small distances from the center with a small average speed. The classical result in (7.34) is thus an upper bound for the quantum pulsation period. In a measurement of the quantum echoes one is able to extract information from regions of the phase space that are inaccessible to classical scattering trajectories.

Such experiments were performed in Darmstadt by Dembowski and coworkers [175], who used open microwave billiards both at room temperature and in a superconducting state. The data were taken for continuous input of microwaves of different frequencies, and the response to a short incoming pulse was obtained by Fourier transform. The S-matrix elements S_{ij} between antennas i and j (lying outside the scattering region) were evaluated in the time domain. The phenomenon of pulsation in the transmission probabilities can be seen in Fig. 7.10. Numerical simulations of the classical open billiard used in the experiment reveals that the horseshoe is ternary, and its development parameter is $\beta = 3^{-8}$. The classical formula (7.34) yields $T = 4.67$ ns as the pulsation time. The microwave experiments show that the period T of the echoes gets shorter with time. Initially, $T = 4.2$ ns; then T decreases and stabilizes about $T = 3.3$ ns. This can be explained by the fact that the wave packet needs time to penetrate into the region of the classical KAM island. With time, echoes from deeper layers inside the island are received. The initial response originates from the chaotic layer, and is close indeed to the classical result.
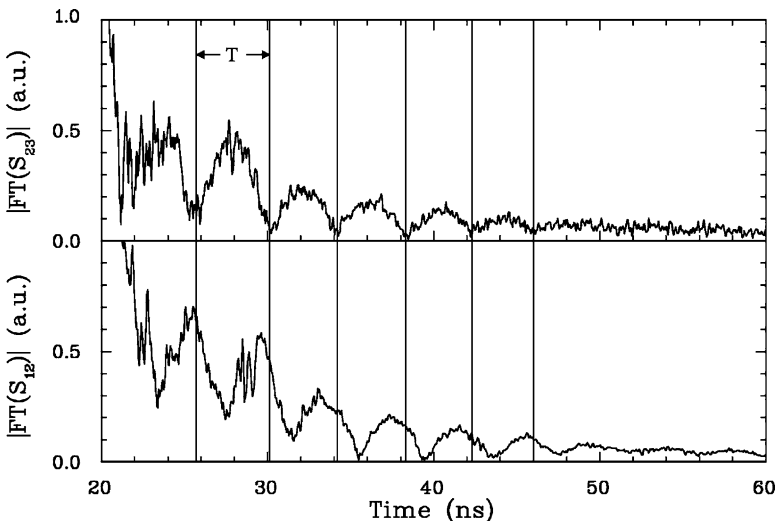

Fig. 7.10 Transmission probabilities between antennas 2 and 3 (*top*) and between 1 and 2 (*bottom*) in the scattering echo experiment by Dembowski and coworkers. Since the classical horseshoe is at its initial stage of development, periodicity is observed in the decay process. Period T marks the classical value given by (7.34) [175] (copyright 2004, the American Physical Society)

After T is stabilized, one observes dynamical tunneling from a fixed penetration depth of the island. The same data reveal an overall exponential decay with time, an indication of the tunneling effect.

After a metal disk is introduced into the inner part of the billiard, the echoes disappear. This can be explained by the destruction of the central integrable island in the phase space, which is the theoretical basis for the echoes.

The phenomenon of scattering echoes provides an example of the *inverse* chaotic scattering problem. From a measured quantity one can extract information about the structure of the underlying chaotic saddle. It is remarkable in the Darmstadt experiment that it is achieved in a regime far from the semiclassical limit (as shown by the deep tunneling). Nevertheless, from the initial period T the development stage of the underlying classical chaotic saddle and its dynamical invariants such as the topological entropy can be assessed, at least approximately. Recent numerical studies indicate that the quantum echoes can also be observed in the conductance fluctuations of semiconductor nanostructures [472].

7.7 Leaked Quantum Systems

Open quantum systems can arise beyond the scattering context. For example, *absorbing regions* can play an important role in quantum mechanics corresponding to the existence of a classical leak. The quantum dynamics is governed then by a nonunitary evolution operator, and the system has properties different from those of closed quantum systems. Study of the open kicked rotator leads to the observation that *quantum fractal eigenstates* exist, which reflect the pattern of the underlying chaotic saddle [116]. In particular, the long-lived eigenstates concentrate on fractal trapped sets. The left and right eigenstates of the nonunitary propagator concentrate in the limit of $\hbar \to 0$ on the stable and unstable manifolds of the chaotic saddle, respectively [403], as can be seen from the example of the quantized open baker map. The quantized version of the leaked baker map of Sect. 2.7.1 was studied in [226, 587].

A related problem is the analysis of the statistical properties of energy levels. The well-known Weyl law states that the number $N(k)$ of levels with wave number smaller than k grows with a power of k. For two-dimensional systems, the exponent is 2. The extension to open systems is that the number $N(k)$ of resonances with wave numbers of real part smaller than k scales as

$$N(k) \sim k^{\alpha} \tag{7.35}$$

with

$$\alpha = 1 + \frac{D_0}{2} = 1 + D_0^{(1)}, \tag{7.36}$$

where D_0 is the box-counting dimension of the underlying classical are preserving chaotic saddle on a properly chosen Poincaré map, and $D_0^{(1)} = D_0^{(2)}$ is the partial

box-counting dimension (see Sect. 2.6.2). This is the *fractal Weyl law* [209, 225, 414, 494, 556, 620, 712, 732, 825]. These properties apply also to the microlasing cavities described in Sect. 6.7. The ray dynamics presented there correspond in a first-order approximation to geometrical optics. The second-order approximation is a semi-classical wave dynamics, which is analogous to semiclassical quantum mechanics [695, 825].

The problem of quantum Poincaré recurrences has also been studied [117]. The short-time behavior is that of the classical problem, and after a crossover time that depends on the value of $\hbar$, an algebraic decay sets in both in classically hyperbolic and nonhyperbolic cases. Quantum effects are thus able to convert the classical exponential behavior into a power law, and also to change the algebraic-decay exponent. The integrated return probability $P_r(t)$, i.e., the probability of returning to the given region after time t, was found to decay universally as $P_r(t) \sim 1/t$, which corresponds to a decay of the recurrence time distribution , defined in Sect. 2.7.2, as $p_r(t) \sim 1/t^2$.

Another phenomenon through which the effect of leaking can be observed is *Loschmidt echo*. Since there are no trajectories in quantum systems, the chaoticity of the system can be checked, as suggested by Peres [593], by evolving a wave packet under two slightly modified Hamiltonians and measuring how they differ in time. In Loschmidt echoes, the wave packet evolves forward in time with a Hamiltonian up to time t, and then evolves backward in time with a slightly modified Hamiltonian over the same period t. The overlap between the initial and final wave packets is measured as a function of t. Goussev and Richter [277] considered a billiard, and the difference in the two Hamiltonians is due to a change in the shape of the billiard in a small region I. The decay of the echo was found to be governed by the classical escape rate characterizing the billiard with a leak in region I. These observations indicate that within the field of quantum chaos, there is an increasing recent interest in open systems. These, in the semiclassical limit, reflect properties of the underlying classical transient chaos.

Part III
High-Dimensional Transient Chaos

Chapter 8
Transient Chaos in Higher Dimensions

This chapter is devoted to transient chaos in higher-dimensional dynamical systems. The defining characteristic of high-dimensional transient chaos is that the underlying chaotic set has unstable dimension more than one, in contrast to most situations discussed in previous chapters, where chaotic sets have one unstable dimension. We shall call nonattracting chaotic sets with one unstable dimension *low-dimensional*, while those having unstable dimension greater than one *high-dimensional*. The increase in the unstable dimension from one represents a highly nontrivial extension in terms of what has been discussed so far about transient chaos. For instance, the PIM-triple algorithm, which is effective for finding an approximate continuous trajectory on a low-dimensional chaotic saddle, is generally not applicable to high-dimensional chaotic saddles. In a scattering experiment in high-dimensional phase space, the presence of a chaotic saddle cannot guarantee that chaos can be physically observed. In particular, if the box-counting dimension of the chaotic saddle is low, its stable manifold may not intersect a set of initial conditions prepared in the corresponding physical space; only when the dimension is high enough can chaotic scattering be observed.

First we present a prototypical example, the three-dimensional baker map, for which a basic property of high-dimensional hyperbolic systems can be seen explicitly: different numbers of the expanding and the contracting dimensions. Next we show how the escape rate and the metric entropy can be expressed in terms of the Lyapunov exponents in high-dimensional maps, present derivations for the dimension formulas of the stable and the unstable manifolds for high-dimensional chaotic saddles, and address their applicability and the concept of typicality using particular examples. An efficient algorithm, the stagger-and-step method, is then described for computing high-dimensional chaotic saddles. Chaotic scattering in three-degree-of-freedom systems is presented, the conditions for the observability of chaotic scattering are formulated, and new features of the scattering dynamics are discussed. The phenomenon of superpersistent chaotic transients and applications are also treated in this chapter.

8.1 Three-Dimensional Open Baker Map

Three-dimensional invertible maps arise on stroboscopic or Poincaré sections of
four-dimensional flows. There are two classes of hyperbolic maps: (1) maps with
one unstable and two stable directions (type I) and (2) maps with two unstable and
one stable direction (type II). The escape dynamics in these two cases are generally
different.

The open three-dimensional baker map is the spatial extension [165] of the pla-
nar baker map treated in Sect. 2.5. Because of the odd dimensionality of the map,
the number of unstable directions is different from that of stable directions. Con-
sequently, such maps, even if they preserve volume, cannot describe Hamiltonian
systems. Nonetheless, in the volume-preserving case they can be used to model the
advection by three-dimensional time-periodic flows (see [165] and Chap. 10). The
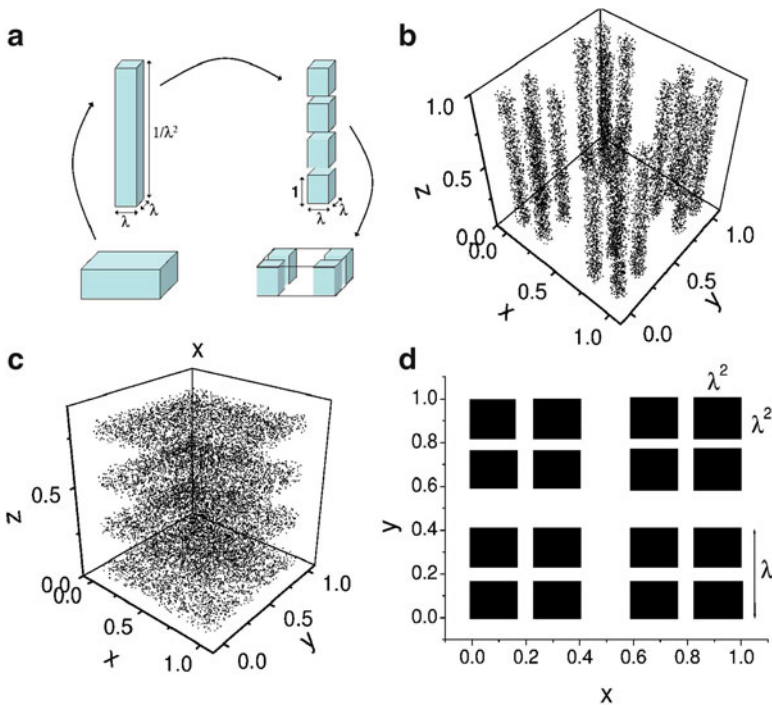map, denoted by M, is defined on the unit cube, and its action is shown in Fig. 8.1a.

Fig. 8.1 (**a**) Illustration of the action of one iteration of the three-dimensional open baker map
M on the unit cube (the restraining region Γ) for type-I dynamics. For simplicity the parameters
are chosen to be $b = c \equiv \lambda$ and $a = 1/\lambda^2$ (volume-preserving case). Note that the drawing is not
to scale. (**b**) For $\lambda = 0.35$, surviving points after two iterations of the map with initial conditions
chosen randomly from the cube. (**c**) The same as (**b**), but for the inverse map M^{-1} (type-II dynam-
ics). (**d**) For $\lambda = 0.35$, intersection with a horizontal plane of the set of surviving points after two
iterations of the map [771] (with kind permission from Elsevier Science)

One iteration of the map consists of two actions. Firstly, the x and y directions are contracted by factors b and c, respectively, where $b, c < 1/2$, while the z direction undergoes an expansion by a factor $a > 4$. Under the transformation, the cube turns into a long, thin rectangular slab with its long edge along the z-axis, as shown in Fig. 8.1a. Secondly, four pieces of unit height of this slab are selected and placed in the four corners of the cube. The pieces of the slab that are not selected are discarded and are regarded as having escaped (Fig. 8.1a). The map has two contracting directions and one expanding direction, and is therefore of type I. For the inverse map M^{-1}, stable directions turn into unstable ones, and vice versa. As a result, M^{-1} has one stable and two unstable directions, and is of type II. The two generic types of three-dimensional hyperbolic maps can thus be conveniently studied using the baker map. Since hyperbolic systems are structurally stable, generality is not lost by assuming any particular form for M.

Because the contracting and the expanding directions of M (and also M^{-1}) are aligned with the x-, y-, and z-axes, it is not difficult to visualize the stable and the unstable manifolds: the stable manifold of M is a Cantor set of planes parallel to the horizontal (x, y)-plane, and the unstable manifold is a Cantor set of vertical segments. We can visualize these manifolds by iterating M forward a given number of times for many initial conditions chosen randomly within the unit cube. The distribution of points that have not escaped approximate the unstable manifold of M, which is the stable manifold of M^{-1}. Conversely, iterating backward (or iterating M^{-1} forward) in time gives the stable manifold of M (or the unstable manifold of M^{-1}). These results are shown in Fig. 8.1b, c.

Consider now the unstable manifold of M, as shown in Fig. 8.1b. Since it is made up of vertical line segments, and since the expansion and the contraction rates are uniform, we can restrict attention to the intersection of the unstable manifold with a horizontal plane. This is depicted in Fig. 8.1d, where the intersection of the set of surviving points after two iterations of M with a horizontal plane is shown. In the limit of an infinite number of iterations, a double Cantor set in the plane is formed with partial box-counting dimensions $D_0^{(2)} = \ln 2 / \ln (1/b)$ and $D_0^{(3)} = \ln 2 / \ln (1/c)$ along the stable manifolds. The unstable manifold is the product of this Cantor set and a one-dimensional line segment; its dimension is

$$D_{u,0} = 1 + \ln 2 \left(\frac{1}{\ln (1/b)} + \frac{1}{\ln (1/c)} \right). \tag{8.1}$$

Similar reasoning can be applied to the stable manifold. The partial box-counting dimension along the unstable direction is set by the stretching factor a. Since in each step a factor $1/a$ of the slab remains in the unit cube, we have $D_0^{(1)} = \ln 4 / \ln a$. The stable manifold is the product of this Cantor set with a plane. We obtain

$$D_{s,0} = 2 + \frac{\ln 4}{\ln a}. \tag{8.2}$$

The manifold dimensions satisfy

$$1 < D_{u,0} < 3, \quad 2 < D_{s,0} < 3. \tag{8.3}$$

The chaotic saddle is the intersection of the stable and the unstable manifolds, and its box-counting dimension is

$$D_0 = \sum_{j=1}^{3} D_0^{(j)} = D_{u,0} + D_{s,0} - 3. \tag{8.4}$$

The baker map has one positive Lyapunov exponent $\lambda_1^+ = \ln a$ and two negative ones of magnitudes $\lambda_1^- = \ln(1/b)$ and $\lambda_2^- = \ln(1/c)$. The escape rate is $\kappa = \ln(a/4)$, and the topological entropy is $K_0 = \ln 4$.

The inverted map has two positive Lyapunov exponents, $\lambda_1^+ = \ln(1/b)$ and $\lambda_2^+ = \ln(1/c)$, and a negative exponent of magnitude $\lambda_1^- = \ln a$. The topology of the escaping process in the inverted map is different from that of M, which is also reflected by the difference in the values of the escape rate (for the inverted map it is $\kappa = -\ln(4bc)$). The manifold dimensions can be obtained from (8.1) and (8.2) by interchanging the indices u and s.

In general, the structures of the stable and the unstable manifolds for the two types of generic maps are topologically similar to those shown in Fig. 8.1. In particular, for type-I maps, the stable manifold is a Cantor set of surfaces, and the unstable manifold is a Cantor set of one-dimensional curves (vice versa for type-II maps). Also, the inequalities (8.3) hold in general for type-I maps.

Based on (8.3), we observe that for type-II maps, the dimension $D_{s,0}$ of the stable manifold may be less than 2. In this case, the stable manifold has generically a null intersection with a one-dimensional curve (see (8.52)), and thus the lifetime distribution along a line is a smooth function, even though there is a fractal invariant set. For $D_{s,0} > 2$, however, a typical lifetime function has a fractal set of singularities that is similar to that in Fig. 1.5. The transition point defined by $D_{s,0} = 2$ is given for the map M^{-1} by the condition $1/\ln b + 1/\ln c = -1/\ln 2$. If the map is of type I, however, this transition does not occur. This is a nontrivial difference between the dynamics of the two types of map. We will consider a similar problem in the context of high-dimensional chaotic scattering in Sect. 8.5.1.

8.2 Escape Rate, Entropies, and Fractal Dimensions for Nonattracting Chaotic Sets in Higher Dimensions

8.2.1 Escape Rate and Entropies

Consider an open dynamical system described by an N-dimensional map. For a general chaotic saddle in the N-dimensional phase space, there are U positive and

S negative average Lyapunov exponents, where $U + S = N$. The exponents can be ordered as follows

$$\lambda_U^+ \geq \lambda_{U-1}^+ \geq \cdots \geq \lambda_1^+ > 0 \geq -\lambda_1^- \geq \cdots \geq -\lambda_{S-1}^- \geq -\lambda_S^-. \tag{8.5}$$

Thus all quantities $\lambda_j^{+,-}$ are positive, and smaller values of the subscripts j correspond to Lyapunov exponents that are closer to zero in magnitude. Analogous to the low-dimensional cases, one can define partial box-counting and information dimensions $D_0^{(j)}$ and $D_1^{(j)}$, respectively, for any direction j along which an average Lyapunov exponent exists. The total dimension D_i ($i = 0, 1$) of the nonattracting set is the sum of the partial dimensions:

$$D_i = \sum_j D_i^{(j)}, \quad i = 0, 1. \tag{8.6}$$

General expressions for the escape rate and the metric entropy follow from the extension of the information-theoretic arguments in Sect. 2.6.3 for two-dimensional maps [380].

Along the stable directions particles cannot escape. Along an unstable direction, they cannot escape either if the partial information dimension is $D_1^{(j)} = 1$ (more precisely, the escape is slower than exponential). Exponential escape is possible only along unstable directions for which $D_1^{(j)} < 1$. Since escapes in different directions j are independent of each other, and the mean velocity of the information flow is λ_j^+, the escape rate is the sum of contributions from all unstable directions:

$$\kappa = \sum_{j=1}^U \lambda_j^+ (1 - D_1^{(j)}). \tag{8.7}$$

The metric entropy, as discussed in Sect. 2.6.3, is the rate at which information stored in the insignificant digits of the initial condition flows toward the significant ones. This flow occurs along the unstable directions only. Since the information dimension and the Lyapunov exponent characterize the density of information and the mean velocity of the flow, respectively, we have

$$K_1 = \sum_{j=1}^U \lambda_j^+ D_1^{(j)}. \tag{8.8}$$

Using (8.7), one can write K_1 as

$$K_1 = \sum_{j=1}^U \lambda_j^+ - \kappa. \tag{8.9}$$

This relation implies that the degree of unpredictability of the dynamics on the nonattracting set, measured by K_1, is only a fraction of the total flux $\sum_{j=1}^U \lambda_j^+$ of digits, because of the loss of information due to escape. Formula (8.9) is an extension

of Pesin's relation [564], according to which the metric entropy is the sum of all positive Lyapunov exponents for closed N-dimensional maps.

In invertible systems, the same amount of information flows in along the stable directions as the amount flowing out along the unstable directions, i.e.,

$$\sum_{j=1}^{S} \lambda_j^- D_1^{(j)} = \sum_{j=1}^{U} \lambda_j^+ D_1^{(j)}. \tag{8.10}$$

A special case of this rule has been observed in (2.80) for two-dimensional maps.

The relations (8.7), (8.8), and (8.9) are valid for noninvertible and nonhyperbolic cases as well. For example, two-dimensional maps with two positive Lyapunov exponents are covered by these formulas, such as the repellers of the complex quadratic map, the Julia sets shown in Fig. 1.3b, which are topologically a circle. Due to the symmetry, both Lyapunov exponents and both partial information dimensions are equal. Equations (8.7) and (8.8) then imply, with the notation $\lambda_1^+ = \lambda_2^+ \equiv \lambda$, that

$$\kappa = \lambda (2 - D_1), \quad K_1 = \lambda D_1. \tag{8.11}$$

Since the natural measure of the connected Julia set is known to have information dimension $D_1 = 1$ [84], we have $\kappa = \lambda = K_1$. This is to be contrasted with the properties of isolated repeller points of the complex quadratic maps for which $D_1 = 0$ and hence, $\kappa = 2\lambda$ with $K_1 = 0$.

Obtaining an expression for the topological entropy is more complicated. As generalizations of (2.22) and (2.81), we have [380]

$$K_0 = \sum_{j=1}^{U} \lambda_j^+ - \kappa + \frac{1}{2} \sum_{j,k}^{U} Q_{2,j,k}^+ + \cdots \tag{8.12}$$

and

$$\kappa = \sum_{j=1}^{U} \lambda_j^+ (1 - D_0^{(j)}) + \frac{1}{2} \sum_{j,k}^{U} (1 - D_0^{(j)})(1 - D_0^{(k)}) Q_{2,j,k}^+ + \cdots, \tag{8.13}$$

where $Q_{2,j,k}^+$ represents the cumulant of the Lyapunov exponents from expanding directions j and k [380].

8.2.2 Dimension Formulas for High-Dimensional Chaotic Saddles

For high-dimensional chaotic saddles, dimension formulas for the entire stable and unstable manifolds can be derived. Our treatment here follows that of Hunt et al. [347]. Imagine normalizing the size of the chaotic saddle so that it can be enclosed

by a cube of unit length. This cube is considered the restraining region. For a hyperbolic saddle, the cube can be regarded as having edges parallel to directions of stretching and contraction as defined by the Lyapunov exponents λ_j^+ and $-\lambda_i^-$. Now uniformly sprinkle a large number of points in the cube and iterate them forward n times. The resulting trajectory points will be distributed to slabs within the cube of dimensions

$$1 \times 1 \times \cdots \times 1 \times e^{-\lambda_1^- n} \times e^{-\lambda_2^- n} \times \cdots \times e^{-\lambda_S^- n}, \tag{8.14}$$

where there are U slab edges of unit length in the U unstable directions. Let $N^{(\mathrm{sl})}(n)$ be the number of slabs at time n. Since trajectory points within these slabs remain in the cube for at least n iterates, the total content of the slabs is proportional to $\exp(-\kappa n)$, where κ is the escape rate from the chaotic saddle. Since the density of points has increased by a factor of $\exp\left[\left(\sum_{j=1}^S \lambda_j^- - \sum_{j=1}^U \lambda_j^+\right)n\right]$, we have

$$N^{(\mathrm{sl})}(n)e^{-\lambda_U^+ n} \times e^{-\lambda_{U-1}^+ n} \times \cdots \times e^{-\lambda_1^+ n} = N^{(\mathrm{sl})}(n)\exp\left(-\sum_{j=1}^U \lambda_j^+ n\right) \sim \exp(-\kappa n). \tag{8.15}$$

Using (8.9), we see that (8.15) implies

$$N^{(\mathrm{sl})}(n) \sim e^{K_1 n}. \tag{8.16}$$

Since at time n, trajectory points that have not left the restraining region are distributed in the vicinity of the unstable manifold, we need to examine the set of $N^{(\mathrm{sl})}(n)$ in (8.14). Say we wish to cover them using small N-dimensional cubes. A natural choice for the edge length of such a cube is that set by the contraction of the dynamics. Since there are several contracting directions, we have different choices. Take

$$\varepsilon_i = \exp(-\lambda_{i+1}^- n) \tag{8.17}$$

with index i between 0 and $S-1$. The required number of cubes is then

$$N^{(u)}(\varepsilon_i) = \left(\frac{1}{\varepsilon_i}\right)^U \left(\frac{e^{-\lambda_1^- n}}{\varepsilon_i}\right)\left(\frac{e^{-\lambda_2^- n}}{\varepsilon_i}\right)\cdots\left(\frac{e^{-\lambda_i^- n}}{\varepsilon_i}\right)N^{(\mathrm{sl})}(n) \tag{8.18}$$

$$\sim \left(\frac{1}{\varepsilon_i}\right)^{U+i}\exp[-(\lambda_1^- + \lambda_2^- + \cdots + \lambda_i^-)n + K_1 n],$$

where (8.16) has been used.

The information dimension of any invariant measure can be considered as the box-counting dimension of regions containing most of the measure, i.e., regions covering typical sets taken with respect to the measure (see, e.g., [773]). Applying

this to the c-measure of the unstable manifold, represented by the slabs at time n, we find an approximation to the information dimension of the unstable manifold for large n:

$$D_{u,1}(i) = \frac{\ln N^{(u)}(\varepsilon_i)}{\ln(1/\varepsilon_i)} = U + i + \frac{K_1 - (\lambda_1^- + \lambda_2^- + \cdots + \lambda_i^-)}{\lambda_{i+1}^-}. \tag{8.19}$$

The covering by the set of ε_i-cubes may not be optimal, so $D_{u,1}(i)$ is an upper bound of $D_{u,1}$: $D_{u,1} \leq D_{u,1}(i)$. It is thus necessary to minimize $D_{u,1}(i)$ over i to obtain the true dimension. A convenient way to find the minimum of $D_u(i)$ is to examine the quantity $D_{u,1}(i+1) - D_{u,1}(i)$, which is

$$D_{u,1}(i+1) - D_{u,1}(i) = \left(\frac{1}{\lambda_{i+1}^-} - \frac{1}{\lambda_{i+2}^-}\right) \times [(\lambda_1^- + \lambda_2^- + \cdots + \lambda_i^- + \lambda_{i+1}^-) - K_1].$$

Since $\lambda_{i+1}^- \leq \lambda_{i+2}^-$, we see that $D_{u,1}(i+1) - D_{u,1}(i)$ is positive (negative) if the term in the square brackets is positive (negative). Thus, if there exists a value I of i such that

$$\lambda_1^- + \lambda_2^- + \cdots + \lambda_I^- + \lambda_{I+1}^- \geq K_1 \geq \lambda_1^- + \lambda_2^- + \cdots + \lambda_I^-, \tag{8.20}$$

then $D_{u,1}(I+1) - D_{u,1}(I)$ is positive or zero but $D_{u,1}(I) - D_{u,1}(I-1)$ is negative or zero. That is, we have $D_{u,1}(I) \leq D_{u,1}(I+1)$ and $D_{u,1}(I) \leq D_{u,1}(I-1)$ simultaneously, indicating that the value of I chosen in (8.20) is the optimal choice of the index i that yields the true dimension $D_{u,1}$:

$$D_{u,1} = U + I + \frac{K_1 - (\lambda_1^- + \lambda_2^- + \cdots + \lambda_I^-)}{\lambda_{I+1}^-}, \tag{8.21}$$

where I is the largest index for which the numerator of (8.21) is still positive.

The information dimension of the natural measure of the stable manifold can be obtained in a similar manner. To see where the slabs of size (8.14) (whose number is $N^{(sl)}(n)$) come from within the cube, we iterate them backward n times and obtain $N^{(sl)}(n)$ slabs of initial conditions, each of dimension

$$e^{-\lambda_U^+ n} \times e^{-\lambda_{U-1}^+ n} \times \cdots \times e^{-\lambda_1^+ n} \times 1 \times \cdots \times 1, \tag{8.22}$$

where for each slab there are S edges of unit length. Since initial conditions leading to trajectories that remain in the restraining region for at least n iterates are found in the slabs of size given by (8.22), we can cover them by small cubes of properly chosen edge length $\varepsilon_j = \exp(-\lambda_{j+1}^+ n)$ and obtain an upper bound $D_{s,1}(j)$ for the true dimension $D_{s,1}$. Reasoning similar to that in the derivation of $D_{u,1}$ yields the following optimal choice of the index J:

$$\lambda_1^+ + \lambda_2^+ + \cdots + \lambda_J^+ + \lambda_{J+1}^+ \geq K_1 \geq \lambda_1^+ + \lambda_2^+ + \cdots + \lambda_J^+, \qquad (8.23)$$

which gives

$$D_{\mathrm{s},1} = S + J + \frac{K_1 - (\lambda_1^+ + \lambda_2^+ + \cdots + \lambda_J^+)}{\lambda_{J+1}^+}, \qquad (8.24)$$

where J is the largest index for which the numerator of (8.24) is still positive.

The information dimension of the chaotic saddle, which is the intersection of its stable and unstable manifolds, is

$$D_1 = D_{\mathrm{u},1} + D_{\mathrm{s},1} - N = (I + J) + \frac{K_1 - \sum_{i=1}^I \lambda_i^-}{\lambda_{I+1}^-} + \frac{K_1 - \sum_{j=1}^J \lambda_j^+}{\lambda_{J+1}^+}. \qquad (8.25)$$

This is a generalization of (8.4) for the information dimension of the invariant set to any N-dimensional map.

In the case of a chaotic attractor, we have $\kappa = 0$, so K_1 is the sum of all positive Lyapunov exponents. This leads to the information dimension D_1 of the attractor, since $D_1 = D_{\mathrm{u},1}$ with (8.21), which is the Kaplan–Yorke formula in higher dimensions [564]. Note that the index I in $D_{\mathrm{u},1}$ is then such that $(\sum_{j=1}^U \lambda_j^+ - \sum_{i=1}^I \lambda_i^-)$ is positive but $(\sum_{j=1}^U \lambda_j^+ - \sum_{i=1}^{I+1} \lambda_i^-)$ is negative. Furthermore, from (8.23) we see that $J = U - 1$ and thus $D_{\mathrm{s},1} = S + U = N$, i.e., the stable manifold is space-filling, as it should for a basin of attraction.

A special case is high-dimensional maps derived from Hamiltonian flows. Due to the symplectic structure of the dynamics, positive and negative Lyapunov exponents arise in pairs: $\lambda_j^+ = \lambda_j^-$. The manifold dimensions in Hamiltonian systems therefore coincide:

$$D_{\mathrm{u},1} = D_{\mathrm{s},1} = (D_1 + N)/2. \qquad (8.26)$$

For a chaotic saddle of a two-dimensional map with one positive Lyapunov exponent $\lambda_1 \equiv \lambda_1^+ > 0$ and one negative exponent $\lambda_2 \equiv -\lambda_1^- < 0$, we have $U = 1$ and $S = 1$. In dissipative or area-preserving systems, we have $\lambda_1 + \lambda_2 \leq 0$. As a result, $\lambda_1 + \lambda_2 - \kappa < 0$. Thus $K_1 \leq |\lambda_2|$, and we have $I = 0$ and $J = 0$, which leads to the corresponding formulas derived in Sect. 2.6.2.

Readers should keep in mind that the dimension formulas (8.21), (8.24), and (8.25) are derived heuristically under the assumption that the chaotic saddle is hyperbolic. While there is numerical evidence for a class of open systems (see, e.g., [745, 746]) with nonhyperbolic high-dimensional chaotic saddles, there has been no systematic numerical study to validate these formulas, although they are conjectured to apply to *typical* systems [347]. This can be seen heuristically by noting that for such a system, small perturbations cannot change its properties and dynamical invariants. Atypical systems, on the other hand, are those whose dynamical invariants change under small perturbations. In the next section we will consider specific examples to contrast typical versus atypical systems with respect to their dimensions.

8.3 Models Testing Dimension Formulas

Because of the heuristic nature in the derivation of the dimension formulas, it is insightful to examine representative models for which the quantities involved in the formulas can be obtained analytically or numerically. The following two models, due to Sweet and Ott [746], will be used: (1) an analytic two-dimensional, noninvertible expanding map, and (2) a three-dimensional billiard scatterer.

8.3.1 Two-Dimensional Noninvertible Map Model

8.3.1.1 Natural Measure and Lyapunov Exponents

The map is of the form

$$x_{n+1} = 2x_n \bmod(1), \tag{8.27}$$
$$y_{n+1} = \alpha(x_n)y_n + \frac{\eta}{2\pi} \sin(2\pi x_n),$$

where $\alpha(x) > 1$ and the map is defined in the region $-\infty \le y \le +\infty$ and $0 \le x \le 1$. The variable x can be considered as an angle-like variable, so the map is defined on a cylinder. The following piecewise constant function was chosen for $\alpha(x)$:

$$\alpha(x) = \begin{cases} \alpha_1, & 0 < x < 1/2, \\ \alpha_2, & 1/2 < x < 1, \end{cases} \tag{8.28}$$

where $1 < \alpha_1 \le \alpha_2$. Because $\alpha(x) > 1$, almost all initial conditions go either to $y = +\infty$ or to $y = -\infty$, which can be regarded as two attractors, and there is a boundary between the two basins of attraction near $y = 0$. The boundary is an invariant set, which is ergodic because of the chaotic dynamics in x. In fact, the invariant set is a chaotic repeller with two positive Lyapunov exponents. The Jacobian matrix of (8.27) is

$$J(x) = \begin{bmatrix} 2 & 0 \\ \eta \cos(2\pi x) & \alpha(x) \end{bmatrix}, \tag{8.29}$$

so the two Lyapunov exponents of the chaotic repeller are

$$\lambda_a = p\ln\alpha_1 + (1-p)\ln\alpha_2 \quad \text{and} \quad \lambda_b = \ln 2, \tag{8.30}$$

where p is the measure of the region $x < 1/2$. Note that for the one-dimensional map $x_{n+1} = 2x_n \bmod(1)$ alone, we have $p = 1/2$ because a random initial condition leads to a trajectory that visits the intervals $[0, 1/2]$ and $[1/2, 1]$ with equal probabilities. However, the presence of the y-dynamics changes the natural measure

of the x-intervals. To calculate p, consider the strip $-K \leq y \leq K$ on the cylinder and sprinkle a large number of initial conditions uniformly in the strip with density ρ_0. A vertical line segment of length $2K$ at $x = x_0$ and centered at $y_0 = 0$ iterates to $x = x_1$, and its center will be at $y_1 = (\eta/2\pi)\sin(2\pi x_0)$. This line segment will at the same time be stretched vertically by a factor of $\alpha(x_0)$. The endpoints of the segment will then be at $(\eta/2\pi)\sin(2\pi x_0) \pm \alpha(x_0)K$. In order for the segment to span the initial strip $-K \leq y \leq K$, it is necessary to choose K such that $(\eta/2\pi)\sin(2\pi x_0) - \alpha(x_0)K < -K$ (if $y_1 > 0$) or $(\eta/2\pi)\sin(2\pi x_0) + \alpha(x_0)K > K$ (if $y_1 < 0$). In either case, it is necessary to have

$$K > (\eta/2\pi)|\sin(2\pi x_0)|/[\alpha(x_0) - 1],$$

which can be satisfied if we choose

$$K > (\eta/2\pi)/(\alpha_1 - 1).$$

Since the map stretches a region uniformly in the x-direction by a factor of two and in the y-direction by a factor of either α_1 or α_2, after one iterate the density will still be uniform in the initial strip, and it is $\rho_1 = [(\alpha_1^{-1} + \alpha_2^{-1})/2]\rho_0$. After n iterations, the density in the strip becomes

$$\rho_n = \left[\frac{1}{2}(\alpha_1^{-1} + \alpha_2^{-1})\right]^n \rho_0,$$

which decays exponentially with time ($\rho_n = \rho_0 \exp(-\kappa n)$) with escape rate

$$\kappa = \ln \frac{2\alpha_1\alpha_2}{\alpha_1 + \alpha_2}. \tag{8.31}$$

Since both Lyapunov exponents are positive, the chaotic repeller formally coincides with its stable manifold. It suffices thus to calculate the natural measure of the stable manifold. To do so, note that in the x-direction, an interval of length 2^{-n} maps to the unit interval after n iterates. It is thus useful to divide the initial strip $-K \leq y \leq K$ into 2^n vertical substrips. In substrip i, we have $x \in s_i^{(n)} = [(i-1)/2^n, i/2^n]$ ($i = 1, \ldots, 2^n$). For a uniform distribution of $N_0 = 2K\rho_0$ points in the strip $-K \leq y \leq K$, $N_0/2^n$ will be in $s_i^{(n)}$ and we ask how many of those there are whose trajectories do not leave the strip at time n. Assume that in n iterates, the substrip $s_i^{(n)}$ experiences $n_1(i)$ and $n_2(i)$ vertical stretches by α_1 and α_2, respectively, where $n_1(i) + n_2(i) = n$. The initial subregion in $s_i^{(n)}$ that can survive at least n iterates has vertical height $2K\alpha_1^{-n_1(i)}\alpha_2^{-n_2(i)}$. There are then

$$\frac{2K\alpha_1^{-n_1(i)}\alpha_2^{-n_2(i)}}{2K} \cdot \frac{N_0}{2^n} = 2^{-n}\alpha_1^{-n_1(m)}\alpha_2^{-n_2(m)}N_0$$

such initial conditions. The measure of the stable manifold in $s_i^{(n)}$ is

$$\mu_i^{(n)} = \frac{2^{-n} \alpha_1^{-n_1(i)} \alpha_2^{-n_2(i)} N_0}{\rho_n 2K} = \frac{2^{-n} \alpha_1^{-n_1(i)} \alpha_2^{-n_2(i)} N_0}{[(1/2)(\alpha_1^{-1} + \alpha_2^{-1})]^n N_0} = \frac{\alpha_1^{n_2(i)} \alpha_2^{n_1(i)}}{(\alpha_1 + \alpha_2)^n}. \quad (8.32)$$

We have

$$\mu([0,1]) = \sum_{i=1}^{2^n} \mu_i^{(n)} = 1.$$

The measures of the intervals $[0, 1/2]$ and $[1/2, 1]$ are given by

$$p = \mu_1^{(1)} = \frac{\alpha_2}{\alpha_1 + \alpha_2}, \quad 1 - p = \mu_2^{(1)} = \frac{\alpha_1}{\alpha_1 + \alpha_2}, \quad (8.33)$$

which gives

$$\lambda_a = \frac{\alpha_2}{\alpha_1 + \alpha_2} \ln \alpha_1 + \frac{\alpha_1}{\alpha_1 + \alpha_2} \ln \alpha_2. \quad (8.34)$$

It can be checked that

$$\lambda_a \leq \kappa, \quad (8.35)$$

where the equality holds if the vertical stretching is uniform across the unit interval in x: $\alpha_1 = \alpha_2$.

8.3.1.2 Dimension Formulas

For a general two-dimensional map with two positive Lyapunov exponents, $0 < \lambda_1^+ \leq \lambda_2^+$, we have, from Sect. 8.2.2, $U = 2 = N$, $I = 0$, and $S = 0$, so that $D_{u,1} = 2$ and $D_{s,1} = D_1$. Depending on the value of κ relative to those of λ_2^+ and λ_1^+, there are two cases in which the dimension formula for D_1 is different. The first case is $\lambda_1^+ < K_1 < \lambda_2^+$, so $J = 1$ and we have

$$D_1 = D_{s,1} = 1 + \frac{K_1 - \lambda_1^+}{\lambda_2^+} = 2 - \frac{\kappa}{\lambda_2^+}. \quad (8.36)$$

The second case is $K_1 < \lambda_1^+$, so $J = 0$. In this case, the dimension is

$$D_1 = D_{s,1} = \frac{K_1}{\lambda_1^+} = 1 + \frac{\lambda_2^+}{\lambda_1^+} - \frac{\kappa}{\lambda_1^+}. \quad (8.37)$$

Because of the inequality (8.35), there are three distinct cases: (i) $\lambda_b > \kappa > \lambda_a$, (ii) $\kappa > \lambda_b > \lambda_a$, and (iii) $\kappa > \lambda_a > \lambda_b$, which should be treated separately. For illustrative purpose, we set $\alpha_2 = r\alpha_1$ and calculate how the dimension D_1 varies with the parameter α_1. We have

$$\kappa = \ln 2 + \ln \alpha_1 - \ln (1 + r^{-1}),$$
$$\lambda_a = \ln \alpha_1 + (1 + r)^{-1} \ln r,$$
$$\lambda_b = \ln 2. \tag{8.38}$$

For case (i), the condition $\lambda_b > \kappa > \lambda_a$ stipulates that $\ln \alpha_1 < \ln (1 + r^{-1}) \equiv \ln \alpha_a$. The order of the Lyapunov exponents is then $\lambda_2^+ = \lambda_b > \lambda_1^+ = \lambda_a$. We have $\lambda_1^+ < K_1 < \lambda_2^+$ so that $J = 1$. Application of formula (8.36) gives

$$D_1 = 1 + \frac{\ln (1 + r^{-1}) - \ln \alpha_1}{\ln 2}, \quad \text{for } \alpha_1 < \alpha_a. \tag{8.39}$$

For case (ii), the defining condition $\kappa > \lambda_b > \lambda_a$ is equivalent to $\ln \alpha_a < \ln \alpha_1 < \ln 2 - (1 + r)^{-1} \ln r \equiv \ln \alpha_b$. The order of the Lyapunov exponents is the same as in case (i). However, we now have $K_1 = \lambda_2^+ + \lambda_1^+ - \kappa < \lambda_1^+$ so that $J = 0$. The corresponding formula (8.37) thus gives

$$D_1 = \frac{(1 + r)^{-1} \ln r + \ln (1 + r^{-1})}{\ln \alpha_1 + (1 + r)^{-1} \ln r}, \quad \text{for } \alpha_a < \alpha_1 < \alpha_b. \tag{8.40}$$

For case (iii), we have $J = 0$ and $\ln \alpha_1 > \ln \alpha_b$. The order of the Lyapunov exponents is $\lambda_2^+ = \lambda_a > \lambda_1^+ = \lambda_b$, and (8.37) yields

$$D_1 = \frac{\ln (1 + r^{-1}) + (1 + r)^{-1} \ln r}{\ln 2}, \quad \text{for } \alpha_1 > \alpha_b. \tag{8.41}$$

Results (8.39), (8.40), and (8.41) are summarized schematically in Fig. 8.2. We see that $D_1 > 1$ for $\alpha_1 < \alpha_a$ but $D_1 < 1$ for $\alpha_1 > \alpha_a$. In fact, for $\alpha_1 < \alpha_a$, the chaotic repeller, which is the basin boundary between the $y = \pm\infty$ attractors, is a fractal curve, as shown in Fig. 8.3. Numerical computation indicates [746] that for the repeller,
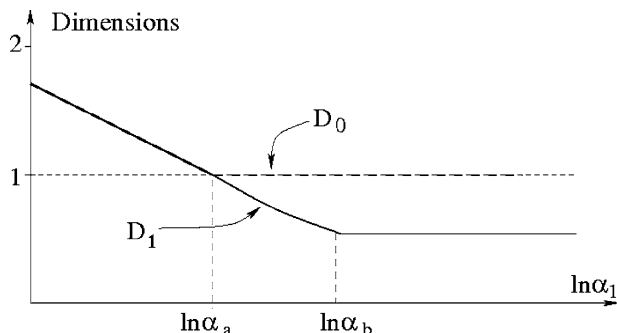
Fig. 8.2 For map (8.27), dimension of the chaotic repeller versus parameter α_1. For $\alpha_1 < \alpha_a$, the information dimension D_1 and the box-counting dimension D_0 of the chaotic repeller are greater than 1 and are equal. For $\alpha_1 > \alpha_a$, $D_1 < 1$, but $D_0 = 1$. Geometrically, there is a transition from a fractal to a nonfractal behavior in the basin boundary as α_1 is increased through α_a
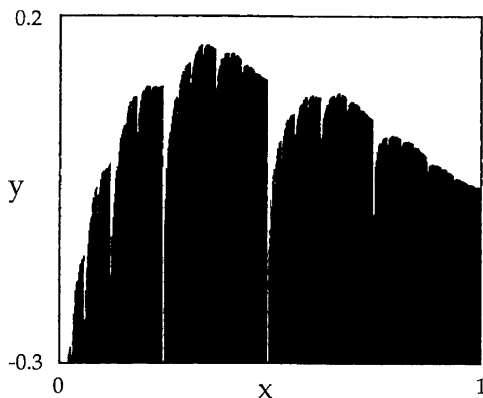
Fig. 8.3 For map (8.27), basins of attraction of the $y = +\infty$ (*blank*) and $y = -\infty$ (*black*) attractors for $\alpha_1 = 1.1$ and $r = 3$. The basin boundary, a chaotic repeller, is apparently a fractal curve. Both its box-counting and information dimensions are $D \approx 1.28$ [746] (with kind permission from Elsevier Science)

the box-counting dimension D_0 and the information dimension D_1 are equal. For $\alpha_1 > \alpha_a$, however, the repeller is a smooth curve with $D_0 = 1$. Geometrically, there is thus a transition from fractal to nonfractal behavior as α_1 is increased through α_a. Numerically obtained values of the information dimension of the repeller agree with those predicted by the formulas (8.40)–(8.41) [746]. For $\alpha_1 > \alpha_a$ the natural measure is rather irregular in spite of the fact that the support of the measure is a smooth curve.

8.3.1.3 The Issue of Typicality

The dimension formulas (8.21)–(8.25) were conjectured to apply for *typical* systems [347]. The two-dimensional map (8.27) provides a good example through which the notions of typicality and atypicality can be understood. In particular, consider $\eta = 0$. In this case, the line $y = 0$ is invariant in that a trajectory starting from this line remains on it forever. This invariant subspace, which is the x-axis, is the basin boundary in which the chaotic repeller resides. The natural measure is thus distributed on the x-axis. Dividing the x unit intervals into 2^n subintervals of width 2^{-n}, the measure contained in each subinterval is given by $\mu_i^{(n)}$ in (8.32). The information dimension of the natural measure for large n is (see (1.22))

$$D_1 = \frac{\sum_{i=1}^{2^n} \mu_i(n) \ln 1/\mu_i^{(n)}}{\ln 2^n}. \tag{8.42}$$

Utilizing (8.32) and the fact that for large n, the typical (most probable) values of n_1, n_2 are

$$\frac{n_1}{n} = \frac{\alpha_2}{\alpha_1 + \alpha_2}, \quad \frac{n_2}{n} = \frac{\alpha_1}{\alpha_1 + \alpha_2}, \tag{8.43}$$

we obtain the same expression for D_1 as in case (iii), (8.41). Thus for $\eta = 0$, the information dimension is a constant for all α_1 and $\alpha_2 > 1$. The dimension formulas yield, however, different results for different ranges of α_1. In particular, for $\lambda_a < \lambda_b$, they provide larger values than the exact information dimension (8.41). The situation $\eta = 0$ is thus *atypical*. However, as soon as we set $\eta \neq 0$, no matter how small, the dimension formulas are recovered and (8.41) becomes valid for $\alpha_1 > \alpha_b$ only. This is so because the value of $\eta \neq 0$ can always be scaled to one by the change of variable $y \rightarrow y/\eta$.

8.3.2 A Chaotic Billiard Scatterer

We consider a three-dimensional billiard scattering system with dynamics similar to those seen in the map example in the preceding discussion. As shown in Fig. 8.4a, the system consists of an ellipsoid placed in an infinite tube in the z-direction with cross section as shown in Fig. 8.4b. A free particle moving in the tube experiences elastic bounces off the walls of the tube and off the surface of the ellipsoid as well. Depending on the initial position and the initial velocity of the particle, it approaches either $z = +\infty$ or $z = -\infty$. The boundaries between these two exit basins are located near $z = 0$. Since the particle motion has three degrees of freedom, which corresponds to a phase-space dimension of five (due to energy conservation), the system represents a physical example in which high-dimensional chaotic scattering can arise and the dimension formulas can be tested in the typical setting whereby the ellipsoid is tilted slightly with respect to the z-axis. The symmetric system, in which the major axis of the ellipsoid is the z-axis, represents an atypical situation
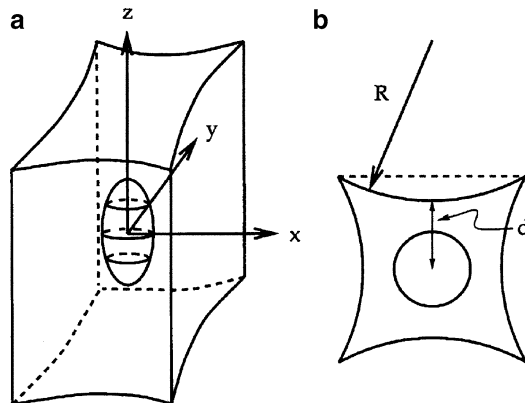
Fig. 8.4 (**a**) Billiard system consisting of an ellipsoid placed at $z = 0$ in an infinite tube in the z-direction. (**b**) Cross sections of the tube and of the billiard at $z = 0$. The parameters are $R = 25$, $d = 10$, and the radius of the ellipsoid at $z = 0$ is 5 [745, 746] (with kind permission from Elsevier Science)

whereby the dimension formulas could fail. This billiard system thus also represents an example in which the mathematical notions of typicality versus atypicality can be understood intuitively in physical terms.

To study the scattering dynamics, it is convenient to focus on bounces from the ellipsoid. Setting particles at the unit speed and utilizing cylindrical coordinates (z, ϕ) and (v_z, v_ϕ), Sweet and Ott derived a four-dimensional map relating these coordinates at a bounce to the previous one from the ellipsoid [745, 746]. If the particle goes over the top (bottom) of the ellipsoid with $v_z > 0$ $(v_z < 0)$, it continues toward $z = +\infty$ $(z = -\infty)$. Due to the inward wall curvature of the tube, there is a sensitive dependence on initial conditions in the particle dynamics, signifying chaotic scattering. This can be seen explicitly by considering the symmetric case in which there is an invariant manifold Λ defined by $z = 0$ and $v_z = 0$ in the four-dimensional phase space, since particles started in Λ never leave it. The dynamics in the invariant manifold Λ is that of a two-dimensional billiard shown in Fig. 8.4b, which is hyperbolic and ergodic in the sense that almost every orbit comes arbitrarily close to any point in the phase space. The invariant set Λ is nonattracting in the four-dimensional phase space because almost all initial conditions in the vicinity of Λ lead to trajectories that go to $z = \pm\infty$. In particular, if a cloud of initial conditions is sprinkled in a region containing Λ, the fraction of trajectories that remain in this region up to n bounces decreases exponentially with time as $\sim \exp(-\kappa n)$, where κ is the escape rate. For typical trajectories with respect to the natural measure on Λ, there are two pairs of Lyapunov exponents, $\pm\lambda_\phi$ and $\pm\lambda_z$, which characterize motions on the chaotic set and toward or away from it, respectively. The scattering dynamics is thus chaotic with two positive Lyapunov exponents, and numerically the inequality $\lambda_\phi > \lambda_z$ has been found [745, 746]. In this special configuration, the full manifold Λ is a chaotic saddle.

For the case in which the ellipsoid is slightly tilted, the saddle survives, but its geometry becomes more complicated. The Lyapunov exponents for typical trajectories with respect to the natural measure on the saddle are, however, approximately the same as those in the untilted case.

The stable manifold of the saddle is physically important because it separates the space of initial conditions into two regions that yield trajectories approaching $z = \pm\infty$, respectively. These regions, the exit basins, can be determined numerically, as shown in Fig. 8.5a, b for the untilted and slightly tilted cases, respectively, which represent two-dimensional cross sections in the four-dimensional map. A straightforward application of the dimension formulas (8.21) and (8.24) with $U = S = 2$ in this typical case yields

$$D_{s,1} = D_{u,1} = 4 - \frac{\kappa}{\lambda_\phi}, \quad D_1 = 4 - 2\frac{\kappa}{\lambda_\phi}, \quad \text{for } \lambda_\phi > \kappa, \tag{8.44}$$

where $J = 1$. For $\lambda_\phi < \kappa$ so that $J = 0$, we have

$$D_{s,1} = D_{u,1} = 3 - \frac{\kappa - \lambda_\phi}{\lambda_z}, \quad D_1 = 2 - 2\frac{\kappa - \lambda_\phi}{\lambda_z}. \tag{8.45}$$
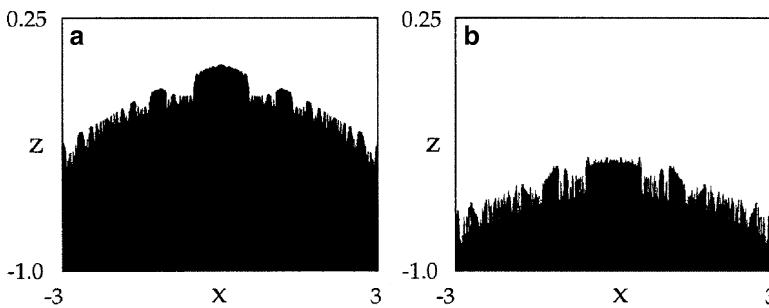
Fig. 8.5 Examples of regions of initial conditions (*exit basins*) that yield trajectories to $z \to +\infty$ (*white*) and $z \to -\infty$ (*black*) in the two-dimensional cross section (x,z) defined by $y = 5.1$, $v_x = 0$, and $v_z = 0.1$ for (**a**) the untilted case and (**b**) a small tilt of $2\pi/100$ [745,746] (with kind permission from Elsevier Science)

Note that in this second case the information dimension of the manifold (saddle) is less than 3 (2). When plotting these dimensions as a function of κ/λ_ϕ one would see a break at 3 (2), similar to that seen in Fig. 8.2 at α_a.

For the untilted (atypical) case, a detailed analysis [746] gives that the dimension is

$$D_{s,1} = D_{u,1} = 4 - \frac{\lambda_z + \kappa}{\lambda_\phi}, \quad D_1 = 4 - 2\frac{\lambda_z + \kappa}{\lambda_\phi}, \quad \text{for } \lambda_\phi > \lambda_z + \kappa. \quad (8.46)$$

The meanings and relationship between the above two dimension formulas can be understood as follows. Suppose one uses some algorithm to compute the dimension with refining accuracy ε. Then for an infinitesimal amount of tilt the true value of the dimension as given by (8.44) can be obtained only when ε is small, e.g., for $\varepsilon < \varepsilon_*$. For resolution size greater than ε_*, the small amount of tilt has no effect, so that the value of the dimension extracted for $\varepsilon > \varepsilon_*$ would agree with that given by (8.46). Around ε_*, the scaling with ε is expected to show a crossover from the form given by (8.46) to that given by (8.44). In a physical experiment with a finite resolution of distance scales, if the amount of tilt is small, the measured dimension may be that given by (8.46). The true dimension can be recovered only in the $\varepsilon \to 0$ limit.

Note that since the stable manifold of the saddle divides the four-dimensional phase space, its *box-counting* dimension is at least three. Numerically, it was found [746] that in the tilted and untilted configurations the stable manifold's box-counting dimensions are close to the information dimensions predicted by formulas (8.44) and (8.46), respectively, insofar as these dimensions are larger than 3, as shown in Fig. 8.6. Otherwise, the box-counting dimensions were found to remain at 3. The two dimensions deviate here drastically, similar to the situation in the $\alpha > \alpha_a$ range of Fig. 8.2.
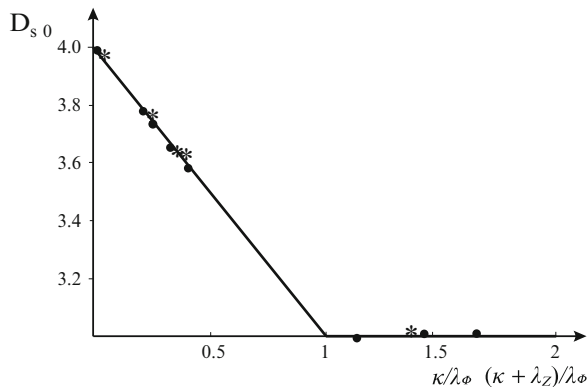
Fig. 8.6 Numerical verification of the stable manifold's dimension for the tilted case (variable κ/λ_ϕ) and the untilted case (variable $(\kappa+\lambda_z)/\lambda_\phi$). The linear curve corresponds to formulas (8.44) and (8.46) for $D_{s,1} > 3$. Dots (*stars*) represent numerically determined values of the box-counting dimension $D_{s,0}$ for the tilted (*untilted*) case

8.4 Numerical Method for Computing High-Dimensional Chaotic Saddles: Stagger-and-Step

8.4.1 Basic Idea

In applications involving transient chaos, it is often useful and desirable to detect and compute chaotic saddles. Several methods have been described in Chap. 1, but they are applicable to systems with *one unstable direction only*. To numerically construct chaotic saddles in higher dimensions with more than one unstable direction, two methods are presently available. One is the "PIM-simplex" method by Moresco and Dawson [529] and another is the "stagger-and-step" method by Sweet et al. [744]. The PIM-simplex method is relatively sophisticated, and its applicability is somewhat limited [529, 744]. The stagger-and-step method is, however, relatively straightforward to implement and it is generally applicable to chaotic saddles that are unstable in several dimensions. Here we focus on this method.

Consider an N-dimensional continuous map $\mathbf{f}$, where $N \geq 2$, and assume that a chaotic saddle exists within a restraining region Γ that does not contain any attractor. The transient lifetimes for initial conditions in Γ can be defined as follows. For initial condition $\mathbf{x}$, the escape time $T(\mathbf{x})$ is the minimum $n \geq 0$ for which the nth iterate is in Γ but the $(n+1)$th iterate of $\mathbf{x}$ is not in Γ. For points $\mathbf{x}$ on the stable manifold of the chaotic saddle in Γ, the escape time is $T(\mathbf{x}) = \infty$. If $T(\mathbf{x})$ is finite but large, $\mathbf{x}$ is close to the stable manifold. That is, all points with escape time at least n, where n is large, belong to a small neighborhood of the stable set. This observation is the main idea behind the stagger-and-step method.

A *stagger* is a perturbation $\mathbf{r}$ to a point $\mathbf{x}$ that results in a new point $\mathbf{x}+\mathbf{r}$ such that $T(\mathbf{x}+\mathbf{r}) > T(\mathbf{x})$. The stagger method generates sequences $\{\mathbf{x}_n\}$ of the form

$\mathbf{x}_{n+1} = \mathbf{x}_n + \mathbf{r}_n$, where $\mathbf{r}_n$ is a stagger, such that $T(\mathbf{x}_{n+1}) > T(\mathbf{x}_n)$. Such sequences are called stagger trajectories. The purpose is to find a point or a small set of points that are sufficiently close to the stable manifold. To do so, one can specify some relatively large $\delta > 0$. Starting from $n = 0$, for each n, random perturbations $\mathbf{r}$ of magnitude less than δ are repeatedly chosen using some specified probability distribution until one with $T(\mathbf{x}_n + \mathbf{r}) > T(\mathbf{x}_n)$ is found. One can then set $\mathbf{r}_n = \mathbf{r}$. The process stops as soon as $T(\mathbf{x}_{n+1}) > T^*$, where T^* is a predetermined (large) time. Sometimes δ may be too small so that no stagger can be found. In this case, one should increase δ.

In order to guarantee that stagger trajectories can be found in an efficient way, the probability distribution from which $\mathbf{r}$ is chosen is important. A uniform distribution, for instance, is not a good choice because the fraction of perturbations that are staggers goes to zero exponentially fast as the escape time increases. This is a consequence of the general exponential decay of transiently chaotic systems. To overcome this difficulty, Sweet et al. suggested using an "exponential stagger distribution" for choosing $\mathbf{r}$, which can be realized as follows. Write $10^{-a} = \delta$ and let s be a uniformly distributed random variable between a and b, where 10^{-b} is the accuracy of double precision in digital computers (typically $b = 15$). The choice of $\mathbf{r}$ is thus $\mathbf{r} = 10^{-s}\mathbf{u}$, where $\mathbf{u}$ is a random directional unit vector. In so doing, the fraction of staggers decreases much more slowly than exponentially, and hence the probability of finding a stagger can be enhanced significantly as compared with the case of uniform distribution, thereby reducing the computation time.

After a stagger trajectory is found, a point $\mathbf{x}_0$ can be picked up for which $T(\mathbf{x}_0) > T^*$. One can then generate a trajectory $\{\mathbf{x}_n\}$ using the map $\mathbf{f}$. The basic idea is to apply the map only when $\mathbf{x}_n$ has escape time $T(\mathbf{x}_n) > T^*$. If $T(\mathbf{x}_n) \leq T^*$, then one finds a nearby stagger point $\mathbf{x}_n + \mathbf{r}_n$ with a higher escape time using $\delta = \varepsilon$ (say 10^{-10}). The trajectory $\{\mathbf{x}_n\}$ is of the form

$$\mathbf{x}_{n+1} = \begin{cases} \mathbf{f}(\mathbf{x}_n) & \text{if } T(\mathbf{x}_n) > T^* \text{ (a step)}, \\ \mathbf{f}(\mathbf{x}_n + \mathbf{r}_n) & \text{if } T(\mathbf{x}_n) \leq T^* \text{ ($\mathbf{r}_n$ is a stagger)}, \end{cases} \qquad (8.47)$$

where $|\mathbf{r}_n| \leq \varepsilon$ and $T(\mathbf{x}_n + \mathbf{r}_n) > T(\mathbf{x}_n)$. (Note that $T[\mathbf{f}(\mathbf{x}_n)] = T(\mathbf{x}_n) - 1$.) Such a trajectory is called a *stagger-and-step* trajectory. By construction, any stagger-and-step trajectory $\{\mathbf{x}_n\}$ satisfies $|\mathbf{f}(\mathbf{x}_n) - \mathbf{x}_{n+1}| < \varepsilon$, so that $\{\mathbf{x}_n\}$ is a numerical trajectory with precision of order $\varepsilon = 10^{-10}$, and it is close to the chaotic saddle after a few iterates. From a stagger-and-step trajectory, dynamical invariants such as the Lyapunov exponents of the saddle can be computed.

To give an example, Sweet et al. [744] considered the following four-dimensional map:

$$\begin{aligned} x_{n+1} &= A - x_n^2 + By_n + k(x_n - u_n), \\ y_{n+1} &= x_n, \\ u_{n+1} &= C - u_n^2 + Dv_n + k(u_n - x_n), \\ v_{n+1} &= u_n, \end{aligned} \qquad (8.48)$$
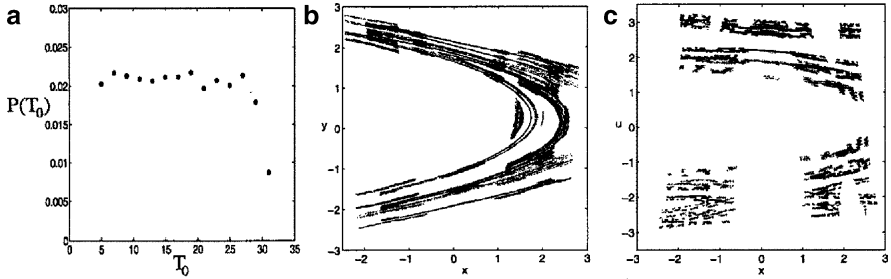
Fig. 8.7 Stagger-and-step method. (**a**) An example of the probability of finding a stagger versus the escape time, (**b**, **c**) projections of a trajectory of 10^5 points of the chaotic saddle, for the four-dimensional map (8.48) at the set of parameter values given in the text [744] (copyright 2001, the American Physical Society)

where A, B, C, D, and k are parameters. For $A = 3.0$, $B = 0.3$, $C = 5.0$, $D = 0.3$, and $k = 0.4$, there is transient chaos. The restraining region Γ was chosen to be $(-4,4) \times (-4,4) \times (-4,4) \times (-4,4)$ and δ to be the length of the diagonal of Γ ($\delta = 16$). To find a stagger required about 50 choices of perturbed points $\mathbf{r}$, the probability of which is approximately 0.02, at least for a range of the escape time, as shown in Fig. 8.7a. It can be seen that for escape time T_0 between 5 and 29, this probability is indeed approximately constant. The projections of a stagger-and-step trajectory of 10^5 points on the chaotic saddle in the (x,y)-plane and in the (x,u)-plane are shown in Fig. 8.7b and c, respectively, where $\varepsilon = 10^{-10}$ and $T^* = 30$. From this trajectory the Lyapunov exponents of the chaotic saddle were computed to be $\lambda_2^+ \approx 1.33$, $\lambda_1^+ \approx 0.77$, $\lambda_1^- \approx 1.97$, and $\lambda_2^- \approx 2.54$.

The stagger-and-step method slows down with increasing dimensionality due to the exponential growth of phase-space volume with dimension. A recent method due to Bollt [87] replaces the random choice by a deterministic search for larger life-times. To this end, one determines the lifetime function in the phase space. For any point one can then find the direction along which the lifetime increases the fastest. This gradient-search algorithm leads to solving an ordinary differential equation, which essentially follows the unstable foliation toward the stable manifold of the chaotic saddle. The method has been shown to be efficient for maps of dimension at least eight.

8.4.2 Invariant Sets Constrained to Slow Manifolds

In high-dimensional systems one is often faced with the problem of the separation of time scales. In such multiscale systems the fast, high-frequency components damp out rapidly due to dissipation, and the dynamics becomes restricted to a lower-dimensional manifold embedded in the full phase space. This manifold is called the *slow manifold*, the dynamics on which may turn out to be transiently chaotic. Morgan, Bollt, and Schwartz [530] worked out a method to determine invariant sets in slow manifolds.

A paradigmatic form of multiscale systems is given by the differential equations

$$\dot{\mathbf{x}} = \mathbf{F}(\mathbf{x}, \mathbf{y}; \mu),$$
$$\mu \dot{\mathbf{y}} = \mathbf{G}(\mathbf{x}, \mathbf{y}; \mu), \tag{8.49}$$

where $\mu \ll 1$ is a small parameter characterizing the separation in time scales, and the vector $\mathbf{y}$ denotes the fast variables. In the limit of extreme separation, $\mu = 0$, (8.49) reduces to an algebraic constraint: $\mathbf{G}(\mathbf{x}, \mathbf{y}, 0) = 0$. Solving the constraint for $\mathbf{y}$ yields an expression $\mathbf{y} = \mathbf{H}_0(\mathbf{x})$. The graph of $\mathbf{H}_0$ is the slow manifold in this limit, assumed to be single-valued for simplicity. The dynamics on the slow manifold is obtained from (8.49) as

$$\dot{\mathbf{x}} = \mathbf{F}[\mathbf{x}, \mathbf{H}_0(\mathbf{x}); 0]. \tag{8.50}$$

For nonzero but small values of μ, the slow manifold is expected to persist. It is given by the graph of a function labeled as $\mathbf{y} = \mathbf{H}_\mu(\mathbf{x})$, which can be obtained as an expansion in powers of μ starting with $\mathbf{H}_0(\mathbf{x})$. The dynamics on this slow manifold can also be obtained from a perturbation expansion starting with (8.50). For a suitably defined map, the full dynamics can be written as $(\mathbf{x}_{n+1}, \mathbf{y}_{n+1}) = \mathbf{f}(\mathbf{x}_n, \mathbf{y}_n)$, and the form of the slow manifold is $\mathbf{y}_n = \mathbf{H}_\mu(\mathbf{x}_n)$.

In order to construct the chaotic saddle on the slow manifold, Morgan et al. [530] applied the stagger-and-step method with the following modifications. The restraining region Γ is chosen as a neighborhood of the slow manifold. Since orbits can enter this region, one looks for the first escape time from Γ. The step-and-stagger iterations are chosen as

$$(\mathbf{x}_{n+1}, \mathbf{y}_{n+1}) = \begin{cases} \mathbf{f}[\mathbf{x}_n, H_\mu(\mathbf{x}_n)] & \text{(a step)}, \\ \mathbf{f}[\mathbf{x}_n + \mathbf{r}_n, H_\mu(\mathbf{x}_n + \mathbf{r}_n)] & \text{(a stagger)}, \end{cases} \tag{8.51}$$

and the iterate $\mathbf{y}_{n+1}$ is projected back onto the slow manifold, so that the resulting stagger-and-step trajectory lies near the slow manifold. In addition, since the slow manifold is determined with finite precision (typically a power of μ), the parameter δ that sets the modulus of the stagger perturbation cannot be chosen to be less than this accuracy.

The method has been successfully applied to a structural mechanical system in [530] with two slow variables ψ_1, ψ_2. Figure 8.8 shows the chaotic saddle projected on the plane of the slow variables.

A more complete picture can be obtained by plotting the slow manifold along with the stable and unstable foliations on it. In the spirit of the sprinkler method (Sect. 1.2.2.3), an approximation of these manifolds can be obtained by searching for trajectories that remain near the slow manifold (and do not approach any attractor) for sufficiently long times. The initial points of such trajectories approximate the stable manifold. The unstable manifold can be obtained, e.g., by applying the same procedure to the time-reversed dynamics. The algorithm is called the constrained invariant-manifold method. Figure 8.9 shows a case in which for simplicity, there is
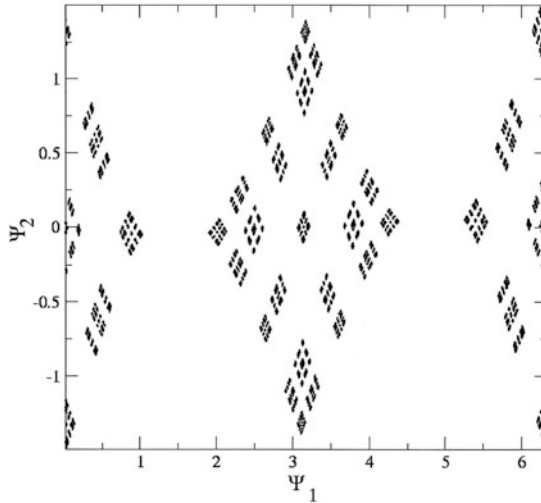
Fig. 8.8 Result of the modified stagger-and-step algorithm (8.51) applied to the problem of a pendulum coupled to a viscoelastic rod. The chaotic saddle is shown on a stroboscopic map in the plane of the slow variables ψ_1, ψ_2. The time-scale parameter is $\mu = 0.05$, and the slow manifold is specified with an accuracy of μ^2 [530] (copyright 2003, the American Physical Society)
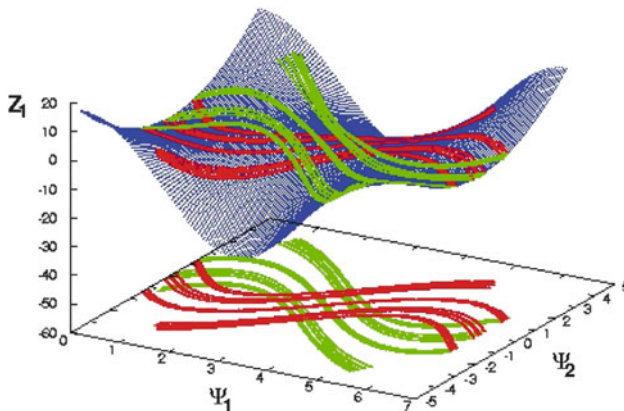

Fig. 8.9 The slow manifold $z_{1,n} = H_\mu(\psi_{1,n}, \psi_{2,n})$ (*blue*) in the problem of a pendulum coupled to a viscoelastic rod as it appears on a stroboscopic map at the parameters of Fig. 8.8. The stable (*unstable*) manifold is plotted in *green* (*red*) [530] (copyright 2003, the American Physical Society)

a single fast variable z_1. The slow manifold is a smooth surface in the phase space of one fast and two slow variables. The invariant manifolds are given both in the slow manifold and in the plane of the slow variables.

8.5 High-Dimensional Chaotic Scattering

As a physical manifestation of high-dimensional transient chaos, we discuss a class of three-degree-of-freedom, time-independent open Hamiltonian systems that exhibit chaotic scattering. Issues to be addressed are the dimension requirement for chaotic scattering to be physically observed and the topology of high-dimensional chaotic scattering. While there have been attempts to address chaotic scattering in higher-dimensional systems [124, 366, 444, 745–748, 829], the topic is relatively unexplored and much research is needed.

8.5.1 Dimension Requirement for Chaotic Saddles to be Observables

Due to the high dimensionality of the phase space, an issue of concern is whether chaotic scattering can be observed even if there is a chaotic saddle of low dimension in the scattering region. In particular, suppose in a scattering experiment, one measures a scattering function for particles launched from a one-dimensional line segment. If the dimension of the chaotic saddle is not sufficiently high, its stable manifold may not have generic intersections with the line. Such intersections, and consequently a set of singularities in the scattering function, can be observed only when the dimension of the chaotic saddle is sufficiently high.

   To address this observability issue, we recall a basic mathematical statement concerning the dimension of the intersection between two sets. Let S_1 and S_2 be two subsets of an N-dimensional manifold with dimensions $D(S_1)$ and $D(S_2)$, respectively. The dimension of the set of intersection between S_1 and S_2 is denoted by $D(S_1 \bigcap S_2)$. The question is whether the sets S_1 and S_2 intersect generically in the sense that the intersection cannot be removed by small perturbations. The natural approach is to look at the dimension D_I:

$$D_I = D(S_1) + D(S_2) - N.$$

If $D_I \geq 0$, the intersection is generic, and the dimension of the set of intersection is [232]

$$D(S_1 \bigcap S_2) = D_I = D(S_1) + D(S_2) - N. \tag{8.52}$$

If D_I is negative, then S_1 and S_2 do not have a generic intersection. For example, consider the intersection between two one-dimensional curves in a two-dimensional plane: $D(S_1) = D(S_2) = 1$ and $N = 2$. We obtain $D_I = 0$, which means that the intersecting set consists of points, and the intersections are generic because small perturbations cannot remove them. If, however, $N = 3$, then $D_I < 0$, which means that two one-dimensional curves do not intersect generically in a three-dimensional space. If they intersect at a point, small perturbations in the positions of the lines typically remove the intersection. These two cases, together with an additional one
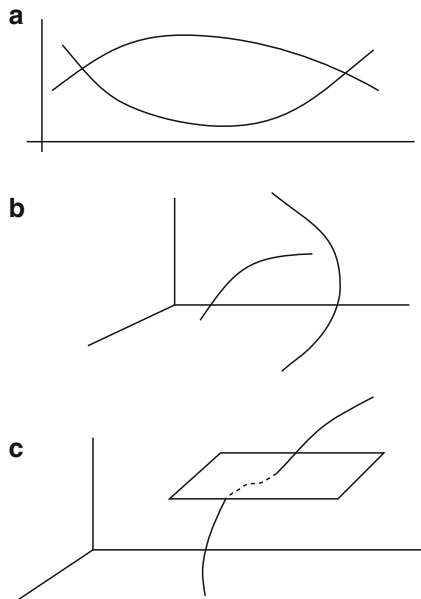
Fig. 8.10 Illustration of generic and nongeneric intersections of simple geometric sets: (**a**) $D_1 = D_2 = 1$ and $N = 2$ (generic intersection), (**b**) $D_1 = D_2 = 1$ and $N = 3$ (nongeneric intersection), and (**c**) $D_1 = 1$, $D_2 = 2$, and $N = 3$ (generic intersection)

($D(S_1) = 1$, $D(S_2) = 2$, and $N = 3$), are illustrated in Fig. 8.10. It can also be said that the codimension $D - N$ is additive for generically intersecting sets. Formula (8.52) is valid for both the box-counting and the information dimensions.

To apply these arguments to chaotic scattering, we consider a continuous-time autonomous scattering system of phase-space dimension $N + 2$. Due to energy conservation, the corresponding continuous-time flow is $(N + 1)$-dimensional, so the scattering map is N-dimensional. The box-counting dimensions of the stable and the unstable manifolds in the map are denoted by $D_{s,0}$ and $D_{u,0}$. The symplectic nature of the dynamics stipulates $D_{u,0} = D_{s,0}$. The box-counting dimension of the chaotic saddle is

$$D_0 = D_{s,0} + D_{u,0} - N = 2D_{s,0} - N, \tag{8.53}$$

since dynamically, the chaotic saddle is the intersecting set between the stable and the unstable foliations. Let $0 < d_s \le 1$ be the box-counting dimension of the singularities probed by a scattering function. This is the set of intersecting points between the stable manifold of dimension $D_{s,0}$ and a one-dimensional line segment from which particles are initiated in the N-dimensional map. Equation (8.52) implies

$$d_s = D_{s,0} + 1 - N, \tag{8.54}$$

or $D_{s,0} = d_s + N - 1$. Utilizing (8.53) gives the following formula relating the dimension of the chaotic saddle to d_s:

$$d_s = \frac{D_0 - N + 2}{2}. \tag{8.55}$$

Scattering singularities can be seen if $d_s > 0$, which is fulfilled only if

$$D_0 > N - 2. \tag{8.56}$$

For a two-degree-of-freedom autonomous Hamiltonian system, one obtains a two-dimensional map, $N = 2$, so the condition is always satisfied. In contrast, in a three-degree-of-freedom system, $N = 4$, and D_0 must be larger than 2 for chaotic scattering to be observable. In this case, if the box-counting dimension of the saddle in the map is smaller than 2, the set of singularities will not be observable, and as a result, any measured scattering function will typically exhibit only smooth features. This implies that by examining the scattering functions only, no chaotic behavior can be revealed, even when there is a chaotic saddle in the phase space and the scattering dynamics is chaotic.

8.5.2 Normally Hyperbolic Invariant Manifolds in High-Dimensional Chaotic Scattering

For high-dimensional scattering systems, hyperbolic periodic orbits and their stable and unstable manifolds often do not have the necessary dimensionality to partition the phase space on the energy shell. In search of higher-dimensional structures with features of periodic orbits of low-dimensional scattering, Wiggins and coworkers [808, 811, 829] suggest the geometrical objects of *normally hyperbolic invariant manifolds* [828]. On such a manifold, the expansion and contraction rates for the invariant motion are dominated by those transverse to the manifold. Like a saddle point, a normally hyperbolic invariant manifold has its own stable and unstable manifolds. In Hamiltonian systems, normally hyperbolic invariant manifolds can exist about equilibrium points of saddle-center-$\cdots$-center type. In an n-degree-of-freedom time-continuous system, such an equilibrium point possesses a pair of real eigenvalues of opposite signs (say $\pm\lambda$) and $2n - 2$ purely imaginary eigenvalues occurring in complex conjugate pairs ($\pm i\omega_j$, $j = 2, \ldots, n$). In the $(2n - 1)$-dimensional energy shell, the normally hyperbolic invariant manifold is a $(2n - 3)$-dimensional sphere around the saddle-center-$\cdots$-center type of fixed point.

Normally hyperbolic invariant manifolds are typical in systems with internal degrees of freedom where some basic "transformation" can take place during the scattering process. Chemical reactions provide a natural example in this context. The basic transformation is then that reactants form products. The normally hyperbolic invariant manifold is the energy surface of an unstable invariant subsystem

with one degree of freedom less than that of the full system. In the terminology of chemistry, this subsystem is an activated complex, or an unstable supermolecule [808]. This unstable subsystem is thus a proper generalization of the basic hyperbolic periodic orbits in two-degree-of-freedom systems (e.g., the orbits bouncing between two disks in the three-disk scattering system; see Fig. 6.4). The activated complex or the normally hyperbolic invariant manifold is located between reactants and products. More precisely, around the normally hyperbolic invariant manifold the phase space has the "bottleneck" property that facilitates the construction of a dividing surface. This surface has the property of "no-recrossing" and therefore separates the phase-space region of reactants and products. The dividing surface is of dimension $2n - 2$ and contains as an invariant set the intermediate complex.

The stable and the unstable manifolds of the intermediate complex are $(2n-2)$-dimensional, which is one dimension less than that of the energy surface. These manifolds can therefore act as *separatrices*, i.e., they enclose volumes of the energy shell. Their key dynamical significance is that the only way for trajectories to lead to reactions is for them to be in certain volumes enclosed by the stable and the unstable manifolds. Note that any Poincaré section of the continuous dynamics in the $(2n-1)$-dimensional energy shell defines an $(N = 2n - 2)$-dimensional map. The normally hyperbolic invariant manifold is an $(N-2)$-dimensional object in this map. Its stable and unstable manifolds have dimension $N - 1$.

The stable and the unstable manifolds of the intermediate complex can cross each other. The homoclinic and heteroclinic intersections, as well as such intersections of subsets of the normally hyperbolic invariant manifolds, can then form a high-dimensional chaotic saddle.

If the chaotic saddle is formed by the intersections of the separatrix manifolds of the intermediate complex, the scattering functions are similar to those in low-dimensional systems. The locally $(N-1)$-dimensional manifolds have, with finite probability, intersections with any line of initial conditions: applying (8.52) with $D(S_1) = N - 1$, $D(S_2) = 1$ to get $D(S_1 \bigcap S_2) = 0$, we see that the typical intersections are points. Furthermore, in such cases the chaotic saddle's full stable (unstable) manifold has box-counting dimension $> N - 1$. As a consequence, the saddle, that is the intersection of these manifolds, is of dimension $D_0 > N - 2$. Equation (8.55) gives then $d_s > 0$, implying that *the set of singularities is always observable* if the saddle is formed by normally hyperbolic invariant manifolds. The intersections of the stable manifold with a line yield the endpoints of intervals of continuity in the scattering function. They can thus be used to define scattering cross sections (Appendix D).

Besides chemical reactions, normally hyperbolic invariant manifolds have been applied to problems of celestial mechanics [806, 807] and to escape problems from multidimensional potential wells [809]. It is likely that the concept can have a broad range of potential applications in other contexts. A recent review of both the classical and quantum aspects of such transition-state theories can be found in [810].

8.5.3 *Metamorphosis in High-Dimensional Chaotic Scattering*

A prototype system for investigating high-dimensional chaotic scattering is the configuration in which scattering centers are located at the vertices of a regular tetrahedron [124, 444, 747, 748]. When the centers are hard-wall spheres [58, 124, 415, 535, 817], the problem corresponds to a light beam bouncing back and forth among reflecting balls that can be found, for instance, in holiday decorations. This type of chaotic scattering can be readily observed, and experiments have been carried out, generating fractal images [747, 748]. While the hard-wall system is illuminating for demonstrating the fractal structure associated with chaotic scattering in high dimensions, the topology of the scattering is fixed, analogous to the planar three-hard-disk scattering system. Basic issues such as bifurcations cannot be addressed using the hard-wall systems.

Because of this difficulty, scattering systems consisting of physically realistic *soft* potentials were considered [421, 444], which are relevant to the scattering of particles by molecules in the three-dimensional physical space. It was found [444] that (1) the chaotic-scattering topology can undergo a sudden change (*metamorphosis*) as a system parameter (e.g., energy) changes continuously, (2) at the metamorphosis, the behavior of the box-counting dimension of the chaotic saddle changes characteristically, and (3) chaotic scattering can occur in energy regimes for which it is not possible in the corresponding planar scattering system. An exemplar system consists of four potential hills located at the four vertices of a regular tetrahedron of unit side length, as shown in Fig. 8.11. To mimic physical situations such as particle scattering by nonrotating diatomic molecules, the Morse potential was chosen for each hill [444]. The total potential of the scattering system is

$$V(\mathbf{x}) = \sum_{j=1}^{4} V_M(\mathbf{x}, \mathbf{x}_j), \tag{8.57}$$
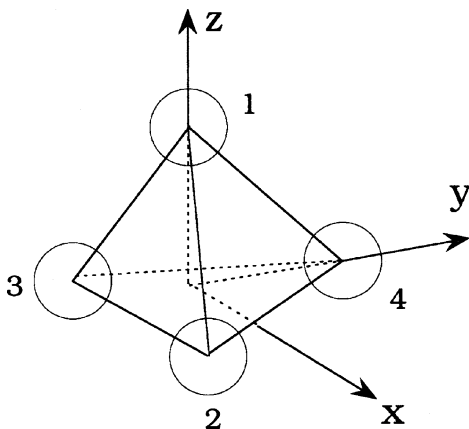
Fig. 8.11 A schematic illustration of the scattering system: four Morse potential hills located at the vertices of a regular tetrahedron [444] (copyright 2000, the American Physical Society)
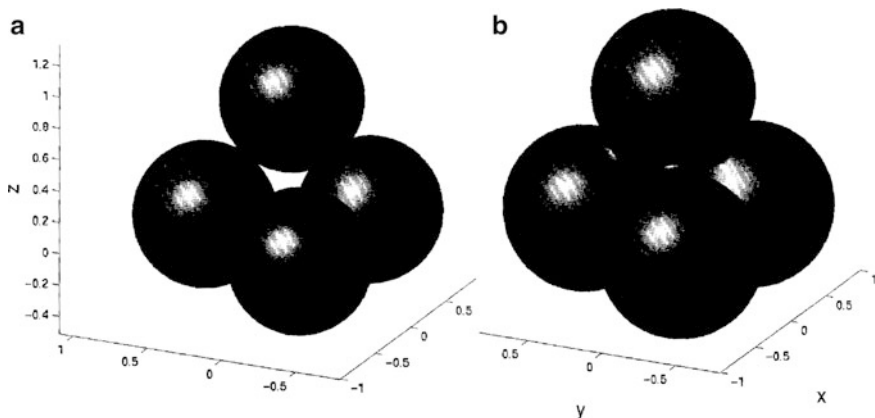
Fig. 8.12 Surfaces of equal energy for potential (8.57), for energies above and below the critical energy E_c. (**a**) Isoenergy surface for $E = 4$ ($E > E_c$); (**b**) Isoenergy surface for $E = 1$ ($E < E_c$) [444] (copyright 2000, the American Physical Society)

where $V_M(\mathbf{x}, \mathbf{x}_j)$ is given by (6.19), $\mathbf{x}_j$ ($j = 1, \ldots, 4$) denote the vertices of the tetrahedron, and $r_j = \sqrt{(x - x_j)^2 + (y - y_j)^2 + (z - z_j)^2}$ is the distance to vertex j. The particle energy E is a convenient bifurcation parameter.

The region of the three-dimensional physical space classically inaccessible to particles of energy E is given by $V(\mathbf{x}) > E$. In order to have chaotic scattering, the particle energy needs to be below the maximum energy E_m of the potential hills. For energy values larger than a critical energy E_c (and lower than E_m), the inaccessible part of the physical space consists of four disconnected regions, each surrounding one vertex of the tetrahedron, as shown in Fig. 8.12a. The regions are approximately spherical in shape, but are not perfectly spherical because their shapes are distorted by the other hills. As the energy decreases toward E_c, the inaccessible regions grow in radius, and for $E = E_c$, the previously disconnected regions begin to connect with each other. For $E \leq E_c$, the inaccessible regions are thus fully connected, as shown in Fig. 8.12b. As E is decreased from E_c, a whole family of orbits in the invariant set is destroyed. These are orbits that bounce back and forth between each pair of forbidden regions an arbitrary number of times, including the six unstable periodic orbits that connect each pair of hills existing for $E > E_c$. As these orbits are destroyed, however, another family of orbits is created at $E = E_c$; these orbits bounce off the newly created forbidden regions connecting each pair of hills. This topological change in the dynamics of the system at E_c can cause a metamorphosis in the scattering dynamics [444].

The basic physics associated with the topological metamorphosis can be understood in terms of the structural change in the "holes" on each side plane of the tetrahedron potential configuration as the particle energy is decreased. Each side plane of the tetrahedron potential (see Fig. 8.13) is similar to the two-dimensional
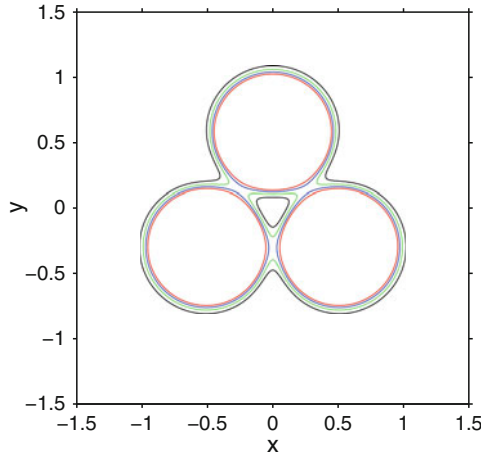
Fig. 8.13 Energy contours of the Morse potential in the (x, y)-plane at $z = 0$. The contours belong to the energy values $E = 4$ (*red*), $E = 3$ (*blue*), $E = 2$ (*green*), and $E = 1$ (*black*). Other parameters are $\alpha = 6$ and $r_e = 0.68$. The value of the critical energy is $E_c = 2.25$ [444] (copyright 2000, the American Physical Society)

system treated in Sect. 6.3.4. The critical energy E_c is close to the value of E_0 determined in the two-dimensional case. It was found numerically [444] that $E_c \approx 2.25$. For $E < E_c$, the forbidden regions are connected, and an incoming particle can penetrate the interior of the tetrahedron only through the holes on the side planes. The holes in the central regions of the side planes are always present, because of the attractive parts of each Morse hill. This allows particles to enter the scattering region inside the tetrahedron at low energies. For E slightly below E_c, the holes are relatively large, and hence the range of initial conditions with which particles can enter the holes are appreciable. The holes, however, become smaller as E is decreased further from E_c. For E slightly below E_c, the size of the hole can be estimated as

$$s \approx s_0 - C(E_c - E), \tag{8.58}$$

where $s_0 = (\sqrt{3} - 1)/2$ is the size for $E = E_c$ and C is a positive constant. Thus, to observe chaotic scattering at low energies in an experimental setting, initial conditions have to be prepared carefully so that particles can enter the holes, since the scattering will not be chaotic if the particles do not enter the holes. In fact, no unstable periodic orbit can be formed outside the holes for $E < E_c$.

To explore the scattering function, we note that, since the physical space is three-dimensional, there are two angles characterizing the momentum of a scattering particle: the azimuthal angle ϕ and the polar angle θ. Figure 8.14a, b show, for $E = 4$ and $E = 1$ respectively, ϕ after the scattering versus b, where particles are launched upward with $v_{x0} = v_{y0} = 0$, $v_{z0} = \sqrt{2E}$ from $z_0 = -10.0$, and the deflection angle $\phi(x_0)$ is recorded when the particles exit the scattering region. A Cantor set of singularities in the scattering dynamics implies the presence of a chaotic saddle whose
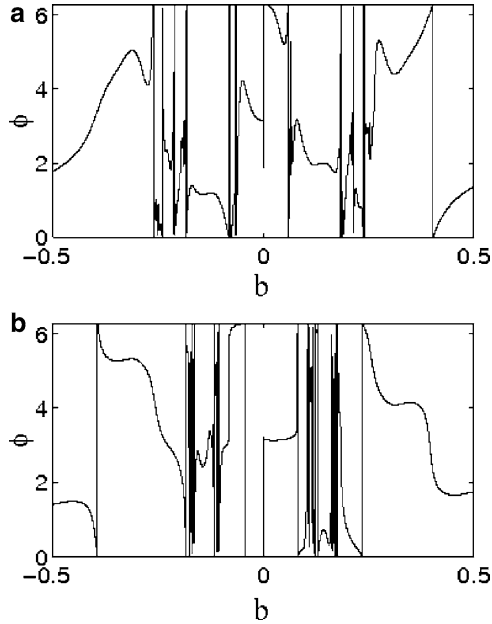
Fig. 8.14 Deflection function: azimuthal angle ϕ as a function of the impact parameter for (**a**) $E = 4$, and (**b**) $E = 1$ [444] (copyright 2000, the American Physical Society)

box-counting dimension in the underlying four-dimensional map is larger than two. The dynamical and physical natures of the scattering observed at these energies are, however, quite different, because of the topological change in the structure of the invariant set. A computation of the dimension d_s of the set of singularities in the scattering function leads, by (8.55) to the box-counting dimension D_0 of the chaotic saddle. It was found [444] that for $E = 4$, the dimension is $D_0 = 3.33 \pm 0.02$, and for $E = 1$, $D_0 = 2.83 \pm 0.02$. Figure 8.15 shows the dimension D_0 of the saddle versus E for $1 \leq E \leq 4$. For $E > E_c$, the dimension remains roughly constant. This is due to the structural stability of the chaotic saddle in this energy regime, where the potential hills remain isolated and hence there is no exponential change in the number of unstable periodic orbits. For $E < E_c$, D_0 appears to decrease as E is lowered from E_c.

The reason that the box-counting dimension decreases as the energy is decreased from E_c can be understood heuristically as follows. Consider initial conditions on a line that contains a Cantor set of singularities. The Cantor set corresponds to particle trajectories that can enter the holes in the side planes of the tetrahedron and stay in the scattering region forever. Those that cannot enter the holes or enter the holes but escape in finite time correspond to gaps, also called intervals of continuity, between points in the Cantor set. Decreasing the size of the holes is equivalent to enlarging these gaps. For a binary self-similar Cantor set of primary gap size Δ, its box-counting dimension is
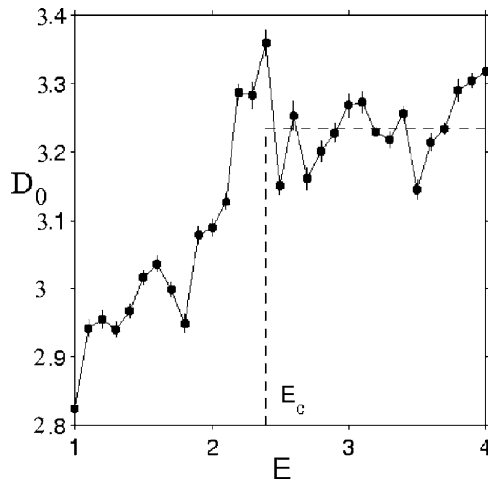
Fig. 8.15 Box-counting dimension D_0 of the chaotic saddle versus the energy E. The dimension remains practically constant for $E > E_c$ and decreases as E is decreased through $E_c \approx 2.25$ [444] (copyright 2000, the American Physical Society)

$$d_s = \frac{\ln 2}{\ln 2 - \ln (1 - \Delta)}.$$

Assuming that $1 - \Delta$ is proportional to s, the size of the holes, we obtain, using (8.58),

$$d_s \sim [A - B \ln (s_0 - C(E_c - E))]^{-1}, \tag{8.59}$$

for E slightly below E_c, where A and B are positive constants. This scaling relation indicates that the dimension of the chaotic saddle decreases as the energy E is decreased from the critical value E_c, due to the shrinkage of the holes in the side planes of the potential configuration.

Notice that for energies about $E < E_0 \approx E_c$, chaotic scattering does not occur if the system has only two degrees of freedom, due to the fact that the inaccessible regions are connected. Thus, for two-degree-of-freedom Hamiltonian systems (corresponding to two-dimensional area-preserving maps), no particle coming from outside the scattering region can enter the bounded, triangular-like region formed at the center of the potential hills. The dynamics in the bounded triangular-like region is typically made up of chaotic seas mixed with KAM tori. Although there is bounded chaos in this case, it is not accessible to particles from outside, and hence there is no chaotic scattering (Fig. 6.20a). In the case of three-degree-of-freedom systems (four-dimensional maps), in the same energy range, the corresponding classically allowed bounded region in the center of the potential hills is accessible to scattering particles coming from outside. Chaotic scattering is thus possible, which for this class of scattering systems is uniquely a high-dimensional phenomenon.

8.5.4   Topological Change Accompanying the Metamorphosis

The topology of chaotic scattering can be studied by examining the structure of *exit basins*. For the tetrahedron configuration, there are four side planes through which particles can exit. Suppose a large number of particles is launched toward the scattering region from a two-dimensional area in an $(x$-$y)$-plane at some large negative z position. After the scattering, the particles in the initial plane can be color-coded, depending on through which side plane they exit the system. Figure 8.16a shows, for $E = 4$, the basin structure in the area defined by $(-0.4 \leq x_0, y_0 \leq 0.4)$ in the
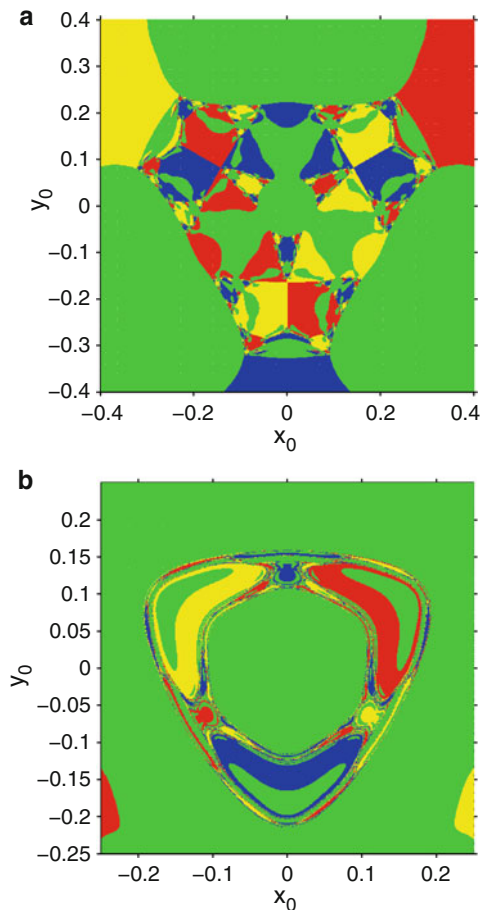
Fig. 8.16 Exit basins of scattering trajectories for (**a**) $E = 4$, and (**b**) $E = 1$. In (**a**), the basin boundaries common to the four colors consist of completely isolated points only. In (**b**), the part of the basin boundary common to the four colors is connected and it is Wada. See text for the meaning of the color coding [444] (copyright 2000, the American Physical Society)

plane located at $z_0 = -10.0$, where 500×500 particles uniformly distributed in the initial area are launched toward the scattering region along the $+z$-direction [444]. If a particle exits through the plane defined by vertices $(1,2,4)$ shown in Fig. 8.11 (or $(1,3,4)$, or $(1,2,3)$, or $(2,3,4)$), its location in the initial two-dimensional area is marked by red (or yellow, or blue, or green). As can be seen from Fig. 8.16a, the boundary contains isolated points where the four colors meet, but for almost all points on the boundary only two colors meet. The basin boundary is the set of intersecting points between the stable manifold of the chaotic saddle with the initial plane. For this energy, then, the common boundary points with different colors are isolated. As the energy is lowered, the previously classically forbidden regions become connected, and extended parts of the basin boundary points are now common to the four colors, as shown in Fig. 8.16b for $E = 1$. This is the Wada property of basins (Sect. 5.5). The topology of the basin undergoes a sudden change (metamorphosis) from being disconnected to being Wada at the critical energy value E_c.

For $E > E_c$, when the forbidden regions are disconnected (Fig. 8.12a), a scattering trajectory will typically enter the scattering region, bounce off the forbidden regions a number of times, and leave. As the particle leaves the scattering region, it crosses one of the side planes shown in Fig. 8.11. For typical trajectories, one can continuously change the initial conditions so as to cause a continuous change in the trajectory (this is not true if the initial condition lies on the stable manifold of the saddle, but such points have zero measure in the phase space). That is, there are paths in the space of initial conditions for which the escape parameters (such as escape angles, lifetime, etc.) change continuously, and these paths contain all initial conditions except for a set of measure zero. Now consider a subspace M in the full space of initial conditions, which can be chosen to have dimension two or higher. Consider one such path, denoted by C, that connects two points a and b in M belonging to two different escape basins, denoted by S_1 and S_2. Distinct side planes defining the different escapes are separated by segments that connect two adjacent triangular faces (Fig. 8.11). For $E > E_c$, parts of these segments lie outside the forbidden regions. Therefore, the path C in M can be chosen such that the corresponding trajectories go from one escape to a neighboring one continuously, without going through any other escape; in other words, all points in C belong to either S_1 or S_2. This corresponds to a basin boundary that separates only two escapes, and therefore to a non-Wada basin.

The picture described above completely changes when the energy goes below E_c. The forbidden regions are now connected into one single region, and the boundaries between the side planes that define the different escapes lie entirely within it. One can no longer go smoothly from one escape to another by a continuous change of initial conditions, due to the presence of forbidden regions separating the escape routes.

The change in the topological structure of the escape basin described above is possible only in three-dimensional physical space: it does not happen for two-degree-of-freedom systems, in which the basin boundaries in systems with three or more escapes typically have the Wada property (Sect. 5.5). The reason is that the forbidden regions separating distinct escapes can never be bypassed from one escape channel to another.

8.6 Superpersistent Transient Chaos: Basics

The type of transient chaos discussed so far, such as that induced by a boundary crisis, is characterized by the familiar algebraic scaling law (3.2) of its escape rate κ as a function of parameter variations in p. There exists, however, another distinct class of transient chaos: superpersistent transient chaos, characterized by the following scaling law:

$$\kappa \sim \exp\left[-C(p - p_c)^{-\chi}\right], \quad p > p_c, \tag{8.60}$$

where $C > 0$ and $\chi > 0$ are constants. As p approaches the critical value p_c from above, the transients become superpersistent in the sense that the exponent in the average transient lifetime

$$\tau \approx \frac{1}{\kappa} \sim \exp\left[C(p - p_c)^{-\chi}\right], \quad p > p_c,$$

diverges in an exponential-algebraic manner. This type of transient chaos is quite common in high-dimensional systems. Its origin can, however, be understood in simple models. For illustrative purposes we therefore shall again use here low-dimensional maps.

Superpersistent transient chaos was conceived to occur through the dynamical mechanism of unstable–unstable pair bifurcations. The same mechanism causes a riddling bifurcation that creates a riddled basin, so superpersistent chaotic transients can be expected at the onset of riddling [711]. It was shown that noise can also induce superpersistent chaotic transients under certain conditions. For a recent review, see [440].

8.6.1 Unstable–Unstable Pair Bifurcation

Unstable–unstable pair bifurcation represents a generic mechanism for superpersistent chaotic transients [294, 295, 455]. One can imagine two unstable periodic orbits of the same period, one on the chaotic attractor and another on the basin boundary, as shown in Fig. 8.17a. As a bifurcation parameter p reaches a critical value p_c, the
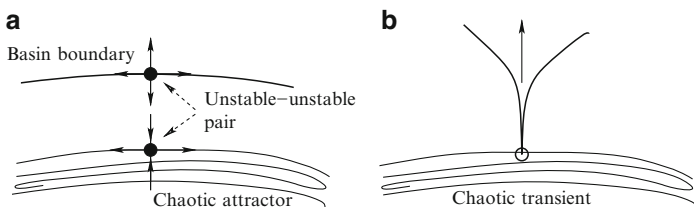
Fig. 8.17 Schematic illustration of an unstable–unstable pair bifurcation. (**a**) Invariant sets for $p < p_c$: a chaotic attractor, the basin boundary, and the pair of unstable periodic orbits. (**b**) For $p > p_c$, an escaping channel is created by an unstable–unstable pair bifurcation that converts the originally attracting motion into a chaotic transient

two orbits *coalesce* and disappear simultaneously, leaving behind a "channel" in the phase space through which trajectories on the chaotic attractor can escape, as shown in Fig. 8.17b. The chaotic attractor is thus converted into a nonattracting chaotic set, but the channel created by this mechanism is typically supernarrow [294, 295, 455]. Suppose that on average, it takes time $T(p)$ for a trajectory to travel through the channel in the phase space. We expect the tunneling time $T(p)$ to be infinite for $p = p_c$, but for $p > p_c$, the time becomes finite and decreases as p is increased from p_c. For p above but close to p_c, the tunneling time can be long.

From Fig. 8.17a, we see that if the phase space is two-dimensional, the periodic orbit on the attractor is a saddle and that on the basin boundary is a repeller. This can arise only if the map is noninvertible. Thus, the unstable–unstable pair bifurcation can occur in noninvertible maps of at least dimension two, or in invertible maps of at least dimension three (or in flows of dimension at least four).

Let $\lambda_1 > 0$ be the largest average Lyapunov exponent of the chaotic attractor. After an unstable–unstable pair bifurcation the opened channel is locally transverse to the attractor. A trajectory that spends time $T(p)$ in the channel opened up at an unstable periodic orbit on the attractor, the *mediating orbit* involved in the unstable–unstable pair bifurcation, must come to within distance of about $\exp[-\lambda_1 T(p)]$ from this orbit. The probability for this to occur is proportional to $\exp[-\lambda_1 T(p)]$. The average time for the trajectory to remain on the earlier attractor, or the average transient lifetime, can be related to the tunneling time as

$$\tau(p) \sim \exp[\lambda_1 T(p)],$$

or equivalently,

$$\kappa(p) \sim \exp[-\lambda_1 T(p)]. \tag{8.61}$$

The tunneling time thus determines the scaling of the escape rate with the parameter variation.

Since the escaping channel is extremely narrow, the dynamics in the channel is approximately one-dimensional along the direction from the mediating periodic orbit to the orbit on the basin boundary, as schematically shown in Fig. 8.17. The basic dynamics can be captured through the following simple one-dimensional map:

$$x_{n+1} = x_n^{k-1} + x_n + p, \tag{8.62}$$

where x denotes the dynamical variable in the channel, $k \geq 3$ is an odd integer to generate two real fixed points, and p is a bifurcation parameter with critical point $p_c = 0$. For $p < p_c = 0$, the map has a stable fixed point $x_s = -|p|^{1/(k-1)}$ and an unstable fixed point $x_u = |p|^{1/(k-1)}$, which collide at p_c and disappear for $p > p_c$, mimicking an unstable–unstable pair bifurcation. Since for $0 < p \ll 1$, $T(p)$ is large (see Sect. 2.4), the map (8.62) can be approximated by the following differential equation:

$$\frac{dx}{dt} = x^{k-1} + p. \tag{8.63}$$

Suppose the root of the channel is $x = 0$ and its length is l. The tunneling time is then

$$T(p) \approx \int_0^l \frac{dx}{x^{k-1} + p} \sim p^{-\frac{k-2}{k-1}}. \tag{8.64}$$

Substituting (8.64) into (8.61) gives

$$\kappa(p) \sim \exp\left(-Cp^{-\frac{k-2}{k-1}}\right), \tag{8.65}$$

where $C > 0$ is a constant. We see that as p approaches the critical value $p_c = 0$ from above, the average transient lifetime diverges in an exponential-algebraic way, giving rise to superpersistent transients. The exponent χ in the scaling law (8.60) thus assumes the value $(k-2)/(k-1) < 1$.

To give a concrete example, we use the class of noninvertible two-dimensional maps considered by Grebogi, Ott, and Yorke [294, 295]:

$$\theta_{n+1} = 2\theta_n \bmod 2\pi, \quad z_{n+1} = az_n + z_n^2 + \beta \cos \theta_n, \tag{8.66}$$

where a and β are parameters. Because of the z_n^2 term in the z-equation, for large z_n we have $|z_{n+1}| > |z_n|$. There is thus an attractor at $z = +\infty$. Near $z = 0$, depending on the choice of the parameters, there can be either a chaotic attractor or none. For instance, for $0 < \beta \ll 1$, there is a chaotic attractor near $z = 0$ for $a < a_c = 1 - 2\sqrt{\beta}$, and the attractor becomes a chaotic repeller for $a > a_c$ [294]. The chaotic attractor, its basin of attraction, and part of the basin of the infinity attractor are shown in Fig. 8.18.
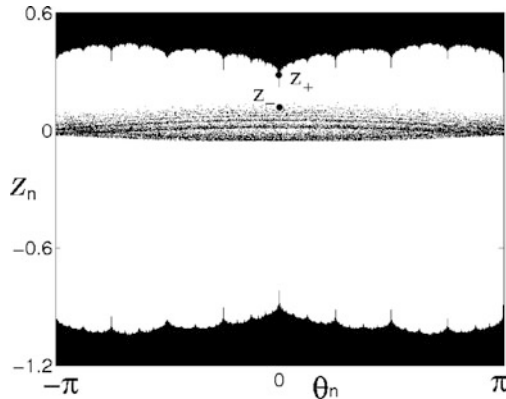
Fig. 8.18 Phase space of the two-dimensional map model (8.66): a chaotic attractor near $z = 0$ (*black*), its basin of attraction (*blank*), and the basin of the attraction of the attractor at $z = +\infty$ (*black*) for $a = 0.5$ and $\beta = 0.04$, before the unstable–unstable pair bifurcation ($a_c = 0.6$). The fixed points $z_\pm$ are marked [294] (copyright 1983, the American Physical Society)

Following the argument leading to the scaling law (8.65), one can see that the map (8.66) allows for superpersistent transients for $a > a_c$. In particular, for $a < a_c$ there are two fixed points: $(0, z_+)$ and $(0, z_-)$, where $z_{\pm} = \left(1 - a \pm \sqrt{(1-a)^2 - 4\beta}\right)/2$, on the basin boundary and on the chaotic attractor, respectively. They coalesce at $a = a_c$. For $a > a_c$, a channel is created through which trajectories on the original attractor can escape to the attractor at infinity. At the location of the channel where $\theta = 0$, the z-mapping becomes

$$z_{n+1} = az_n + z_n^2 + \beta.$$

Letting $\delta = z - z_*$, where $z_* = (1-a)/2$, we obtain

$$\delta_{n+1} = \delta_n^2 + \delta_n + b, \tag{8.67}$$

with $b = \sqrt{\beta}(a - a_c) - [(a - a_c)/2]^2$. For $a \approx a_c$, we have $b \approx \sqrt{\beta}(a - a_c)$. Equation (8.67) is identical to (8.62) with $k = 3$. The integral (8.64) then yields $T \approx \pi b^{-1/2}/2$. The Lyapunov exponent is determined by the θ-dynamics: $\lambda_1 = \ln 2$. Using (8.61), we obtain the scaling of the escape rate for $a > a_c$ as

$$\kappa(a) \sim e^{-T \ln 2} \approx e^{(-\pi \ln 2/2)b^{-1/2}} \approx e^{-C(a-a_c)^{-1/2}}, \tag{8.68}$$

where $C = \pi(\ln 2)\beta^{-1/4}/2$ is a positive constant.

8.6.2 Riddling Bifurcation and Superpersistent Chaotic Transients

In Sect. 5.7, the phenomenon of riddling, or riddled basins in dynamical systems with symmetry, is described. The presence of symmetry often leads to an invariant subspace. In the absence of symmetry-breaking or random perturbations, a trajectory originated in the invariant subspace remains there forever. Situations can also be expected whereby a chaotic attractor lies in the invariant subspace. As discussed, one such example is the system of coupled, identical chaotic oscillators. The synchronization manifold is naturally a low-dimensional invariant subspace in the full phase space that can be high-dimensional if the number of oscillators is large. If another attractor exists outside the invariant subspace, riddling can occur in the sense that the basin of the chaotic attractor in the invariant subspace is riddled with holes of all sizes that belong to the basin of the other attractor. Imagine the situation in which all unstable periodic orbits embedded in the chaotic attractor are stable with respect to perturbations in the direction transverse to the invariant subspace. In this case, almost all initial conditions in the vicinity of the invariant subspace lead to trajectories that end up asymptotically on the chaotic attractor. Riddling bifurcation refers to the situation in which when a system parameter changes, an unstable periodic orbit

(usually of low period) embedded in the chaotic attractor becomes transversely unstable. An immediate physical consequence of the riddling bifurcation is that when there is a small amount of symmetry-breaking, an extraordinarily low fraction of the trajectories in the invariant subspace diverge, as shown in Fig. 5.21.

Due to nonlinearity, a "tongue" opens at $\mathbf{x}_\mathrm{p}$, allowing trajectories near the invariant subspace to escape for $p > p_\mathrm{c}$, as shown in Fig. 5.20b. Each preimage of $\mathbf{x}_\mathrm{p}$ also develops a tongue simultaneously. Since preimages of $\mathbf{x}_\mathrm{p}$ are dense in the invariant subspace, an infinite number of tongues open up simultaneously at $p = p_\mathrm{c}$, indicating that initial conditions arbitrarily close to the invariant subspace can approach another attractor. Trajectories in the chaotic attractor remain there even for $p > p_\mathrm{c}$, since the subspace in which the chaotic attractor lies is invariant and each tongue has zero width there. But trajectories near the chaotic attractor have a finite probability of being in the open and dense set of tongues. Trajectories having initial conditions in the tongues approach asymptotically the other attractor. The basin of attraction of the chaotic attractor is thus a Cantor set of leaves of positive Lebesgue measure (a fat fractal), signifying riddling. Physically, since the onset of riddling induces the creation of these supernarrow tongues near the invariant subspace, it leads to superpersistent chaotic transient behavior in the vicinity of the chaotic attractor. For points chosen at random at a small distance d from the attractor, the probability of not being attracted depends on the distance d as

$$P(d) \sim \exp[-Kd^{-\gamma}], \qquad (8.69)$$

where $\gamma > 0$ is a positive exponent, and $K > 0$ is a constant. In the presence of symmetry-breaking as characterized by the parameter ε, a similar argument leads to the escape rate

$$\kappa(\varepsilon) \sim \exp[-K\varepsilon^{-\gamma}], \qquad (8.70)$$

for initial conditions in the original invariant subspace.

To make these ideas more concrete, it is convenient to use the following extension of the noninvertible two-dimensional map (5.24) [455]:

$$\begin{aligned}
x_{n+1} &= rx_n(1-x_n), & (8.71)\\
y_{n+1} &= \varepsilon + pe^{-b(x_n-x_\mathrm{p})^2}y_n + y_n^3,
\end{aligned}$$

where for $\varepsilon = 0$, $y = 0$ defines the invariant subspace, r, $b > 0$ are parameters, and p is the bifurcation parameter. The broken symmetry is with respect to $y \to -y$. The dynamics in the invariant subspace is described by the logistic map $x_{n+1} = rx_n(1-x_n)$, for which chaotic attractors can arise.

In the symmetric case ($\varepsilon = 0$), the two eigenvalues of the unstable fixed point $\mathbf{x}_\mathrm{p}$ ($x_\mathrm{p} = 1 - 1/r$, $y = 0$) are $(2-r, p)$. Thus, $\mathbf{x}_\mathrm{p}$ is stable in the y direction for $p < 1$ and unstable for $p > 1$. This fixed point is a saddle for $r > 3$ and $p < 1$. For $p < 1$, there are two other unstable fixed points located at $\mathbf{r}_\pm \equiv (x_\mathrm{p}, \pm\sqrt{1-p})$. These two fixed points have eigenvalues $(2-r, 3-2p)$, both pure repellers for $r > 3$ and $p < 1$, as

shown in Fig. 5.20a. The two repellers collide with each other and with the saddle at $p = p_c = 1$ in a saddle-repeller bifurcation. They do not exist for $p > 1$. Thus, for $p > 1$, two tongues, symmetrically located with respect to the invariant subspace, open up at $x = x_p$, allowing trajectories near $y = 0$ to escape to $|y| = \infty$, since the cubic term in the y−dynamics guarantees that if $|y_n| > 1$, then $|y_{n+1}| > |y_n| > 1$. Once a trajectory reaches $|y| = 1$, its y value approaches infinity rapidly. So $|y| = \infty$ can be regarded as the second attractor of (8.71) besides the chaotic attractor in the $y = 0$ plane (invariant subspace), which exists for $r > 3.6$.

When there is symmetry-breaking ($\varepsilon > 0$), trajectories can leave the original chaotic attractor at $y = 0$ ($y = 0$ is no longer an invariant subspace), and hence the attractor is converted into a chaotic saddle. Simulation of (8.71) showed that only an exceedingly small fraction of the points at $y = 0$ diverges toward the $|y| = \infty$ attractor. The transient time can easily be longer than, say, 10^5 iterations even for $\varepsilon = 0.014$. To obtain the scaling of the escape rate with the symmetry-breaking parameter, the first step is to estimate, for $\varepsilon \geq 0$, the size δ of the tongue at $y = 0$ for a trajectory of transient time $T(\varepsilon)$. Since the $y = 0$ attractor is chaotic, its maximum Lyapunov exponent λ_1 is positive. Let $L_u = e^{\lambda_1} > 1$, which is the stretching factor for an infinitesimal vector in the x direction. That the transient time, the time needed to reach a distance of order unity, is T implies $\delta L_u^T \approx 1$, which gives

$$\delta \approx L_u^{-T}. \tag{8.72}$$

The next step is to examine the probability that a trajectory falls into the tongue of size δ at $y = 0$ for $\varepsilon \geq 0$, which is proportional to δ. The average time for a trajectory to fall into the tongue is

$$\tau \sim \delta^{-1} \approx L_u^T = \exp(\lambda_1 T). \tag{8.73}$$

The final step is to evaluate T, the time it takes for the trajectory to exit once it has fallen into the tongue. Near x_p, we have $\exp[-b(x_n - x_p)^2] \approx 1$. For initial conditions chosen at $y_0 = 0$, the trajectory satisfies $y_n \geq \varepsilon$ for $n \geq 1$. For small ε it takes many iterations for a trajectory to reach $y = 1$. Thus, the y-dynamics within the tongue can be approximated by the differential equation

$$\frac{dy}{dt} = \varepsilon + y^3.$$

This gives

$$T = \int_0^1 \frac{dy}{\varepsilon + y^3} = \varepsilon^{-2/3} \int_0^{\varepsilon^{-1/3}} \frac{dz}{1 + z^3}. \tag{8.74}$$

For $\varepsilon \to 0$ the integral converges to $C = \pi/3^{3/2}$. Substitution of this expression into (8.73) and using $\kappa \approx 1/\tau$ yields the following scaling of the escape rate:

$$\kappa \sim \exp[-C\lambda_1 \varepsilon^{-2/3}], \tag{8.75}$$
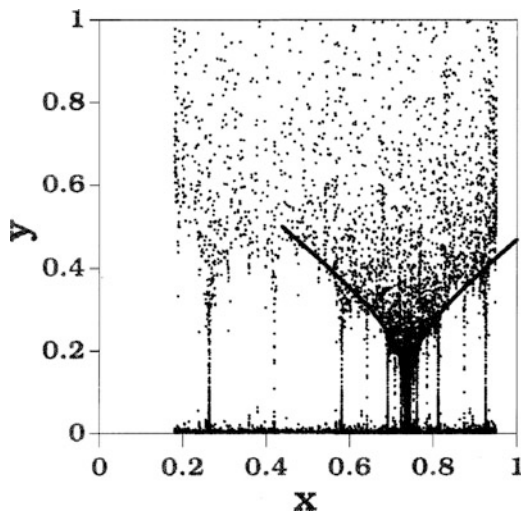
Fig. 8.19 Mushroom-shaped phase-space regions (tongues) through which trajectories escape the $y = 0$ chaotic attractor ($r = 3.8$) at $p = 1.18 > p_c = 1$ and $\varepsilon = 0.005$ in (8.71) [455] (copyright 1996, the American Physical Society)

which is the scaling law (8.70) with $K \equiv C\lambda_1$. In (8.75), the exponent $2/3$ is a consequence of the y^3 term in the y-dynamics. If this term is replaced by, say, a y^2 term, the exponent will be $1/2$. Thus, the exponent $2/3$ in (8.75) is specific to the two-dimensional map model (8.71). However, the scaling relation (8.70) is general, with the exponent γ being positive.

The escaping behavior of trajectories, once they have fallen into the tongue, can be seen by monitoring their traces in the phase space before they reach $y = 1$. Since the tongues are supernarrow at $p = p_c$, it is numerically convenient to examine the case of $p > p_c$, but for p close to p_c. Figure 8.19 shows the last 50 points of 600 trajectories before they reach $y = 1$. There is a "mushroom-shaped" (tongue) crowd of trajectory points in the phase space located above the fixed point $x_p \approx 0.7368$. The solid curves in Fig. 8.19 indicate the envelope of the tongue, which can be derived analytically by considering the escaping dynamics in the vicinity of x_p. Specifically, after a trajectory falls into the escaping channel located at x_p, its dynamics can be approximated by

$$(x_{n+1} - x_p) \approx (2 - r)(x_n - x_p), \quad y_{n+1} \approx \varepsilon + py_n + y_n^3.$$

By introducing $z_n \equiv |x_n - x_p|$, the x-dynamics becomes $z_{n+1} = |2 - r|z_n = (r - 2)z_n$. For p close to p_c and ε small, it takes an extremely large number of iterations for a typical trajectory to escape due to the long chaotic transient. We thus have

$$\mathrm{d}z/\mathrm{d}t = (r - 3)z, \quad \mathrm{d}y/\mathrm{d}t = \varepsilon + (p - 1)y + y^3. \tag{8.76}$$

This implies that for $\varepsilon \approx 0$, we have $dz/dy = (r-3)z/[(p-1)y+y^3]$, which leads to

$$z(y) = \left(\frac{y}{\sqrt{(p-1)+y^2}} \right)^{(r-3)/(p-1)} , \quad \text{for } p > p_c = 1. \quad (8.77)$$

The solid curves in Fig. 8.19 are $[x_p \pm z(y)]$, respectively. They represent the envelope of the tongue reasonably well.

8.7 Superpersistent Transient Chaos: Effect of Noise and Applications

8.7.1 Noise-Induced Superpersistent Chaotic Transients

In the general setting, in which an unstable–unstable pair bifurcation can occur, noise can induce superpersistent transients *preceding* the bifurcation. Consider, in the noiseless case, a chaotic attractor in its basin of attraction ($p < p_c$). When noise is present, there can be a nonzero probability that two periodic orbits, one belonging to the attractor and the other to the basin boundary, can get close and coalesce *temporally*, giving rise to a nonzero probability that a trajectory on the chaotic attractor crosses the basin boundary and moves toward the basin of another attractor. Transient chaos thus arises even for $p < p_c$. Due to weak noise, the channels through which trajectory escapes the chaotic attractor open and close intermittently in time. Escaping through the channel requires the trajectory to stay in a small vicinity of the opening of the channel for a finite amount of time, which occurs with extremely small probability. The creation of the channel by noise and the noisy dynamics in the channel are thus the key ingredients to the noise-induced transient behavior.

For a two-dimensional phase space, the situation described above is schematically illustrated in Fig. 8.17a, b for the cases in which noise is respectively absent and present. If the attractor is close to the basin boundary, noise of strength σ can induce an unstable–unstable pair bifurcation, creating a narrow channel through which trajectories can escape, as shown in Fig. 8.17b even for $p < p_c$. As (8.61) suggests, the escape rate can be expressed in terms of the tunneling time $T(p,\sigma)$ as

$$\kappa(p,\sigma) \sim \exp[-\lambda_1 T(p,\sigma)], \quad (8.78)$$

where $\lambda_1 > 0$ is the largest Lyapunov exponent of the original chaotic attractor. Again, since the escaping channel is extremely narrow, for $T(p,\sigma)$ large, the dynamics is approximately one-dimensional in the channel along which the periodic orbit on the attractor is stable but the orbit on the basin boundary is unstable for $p < p_c$ (Fig. 8.17a). This feature can thus be captured through the stochastic version of the map (8.62):

$$x_{n+1} = x_n^{k-1} + x_n + p + \sigma \xi_n, \quad (8.79)$$
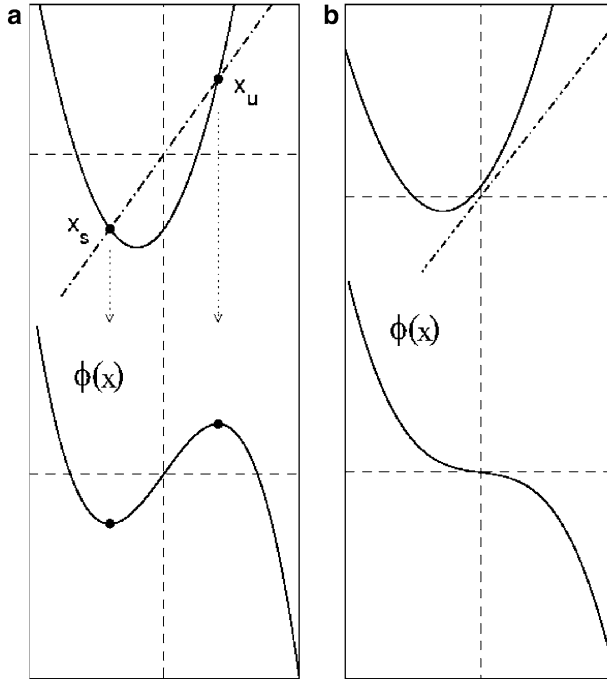
Fig. 8.20 Dynamics of the map (8.79), for $k = 3$ (**a**) in the subcritical cases ($p < 0$), and (**b**) in the supercritical case ($p > 0$). *Upper graph*: deterministic map ($\sigma = 0$), *lower graph*: quasipotential $\Phi(x)$

where $\sigma \ll 1$ is the noise amplitude and ξ_n is a Gaussian random variable of zero mean and unit variance. For $T \gg 1$, (8.79) can be approximated by the Langevin equation

$$\frac{\mathrm{d}x}{\mathrm{d}t} = x^{k-1} + p + \sigma\xi(t) \equiv -\frac{1}{2}\frac{\mathrm{d}\Phi}{\mathrm{d}x} + p + \sigma\xi(t), \qquad (8.80)$$

where the function

$$\Phi(x) = -2(x^k/k + px) \qquad (8.81)$$

is the associated quasipotential of the one-dimensional problem (see Sect. 4.2). For $p < 0$, the underlying deterministic system for (8.80) has a stable fixed point $x_\mathrm{s} = -|p|^{1/(k-1)}$ and an unstable fixed point $x_\mathrm{u} = |p|^{1/(k-1)}$. For $p > 0$, there are no fixed points, as shown in Fig. 8.20. It is convenient to define the opening x_r of the channel at the stable fixed point $x_\mathrm{r} = x_\mathrm{s}$ when it exists, i.e., for $p < 0$, and set $x_\mathrm{r} = 0$ otherwise. A properly formulated first-passage-time problem for this one-dimensional stochastic process can yield the scaling of $T(p, \sigma)$ [198, 199] as follows.

Let $P(x,t)$ be the probability density function of the stochastic process described by (8.80) that satisfies the Fokker–Planck equation:

$$\frac{\partial P(x,t)}{\partial t} = -\frac{\partial}{\partial x}[(x^{k-1} + p)P(x,t)] + \frac{\sigma^2}{2}\frac{\partial^2 P}{\partial x^2}. \qquad (8.82)$$

Let l be the effective length of the channel in the sense that a trajectory with $x > l$ is considered to have escaped the channel. The tunneling time $T(p,\sigma)$ required for a trajectory to travel through the channel is equivalent to the mean first passage time from the opening x_r of the channel to l. For an escaping trajectory, once it falls into the channel through x_r, it will eventually exit the channel at $x = l$ without even going back to the original chaotic attractor. This is so because the probability for a trajectory to fall into the channel and then to escape is already exponentially small, (8.78), and hence the probability for any "second-order" process to occur, whereby a trajectory falls into the channel, moves back to the original attractor, and falls back in the channel again, is negligible. For trajectories in the channel there is thus a reflecting boundary condition at $x = x_r$,

$$\left[(x^{k-1} + p)P(x,t) - \frac{\sigma^2}{2}\frac{\partial P}{\partial x}\right]\Big|_{x=x_r} = 0, \qquad (8.83)$$

and an absorbing boundary condition at $x = l$,

$$P(l,t) = 0. \qquad (8.84)$$

Assuming that trajectories initially are near the opening of the channel (but in the channel), we have the initial condition

$$P(x,x_r) = \delta(x - x_r^+). \qquad (8.85)$$

Under these boundary and initial conditions, the solution to the Fokker–Planck equation yields the following mean first-passage-time [256, 640] for the stochastic process (8.80):

$$T(p,\sigma) = \frac{2}{\sigma^2}\int_{x_r}^{l} dy \exp\left[\frac{\Phi(y)}{\sigma^2}\right]\int_{x_r}^{y}\exp\left[\frac{-\Phi(y')}{\sigma^2}\right]dy'. \qquad (8.86)$$

The double integral in (8.86) can be carried out [198, 199] for the three distinct cases critical ($p = 0$), supercritical ($p > 0$), and subcritical ($p < 0$).

In the weak-noise regime ($\sigma \ll \sigma_c \sim |p|^{k/(2(k-1))}$), the results can be summarized as

$$T(p,\sigma) \sim \begin{cases} p^{-(k-2)/(k-1)}, & p > 0, \\ \sigma^{-(2-4/k)}, & p = 0, \\ |p|^{-(k-2)/(k-1)}\exp\left(|p|^{k/(k-1)}/\sigma^2\right), & p < 0. \end{cases} \qquad (8.87)$$

These laws imply the following scaling laws for the escape rate of the chaotic transients in various regimes (substituting the expressions of $T(p, \sigma)$ in (8.78)):

$$\kappa(p, \sigma) \sim \begin{cases} \exp\left[-Cp^{-(k-2)/(k-1)}\right], & p > 0, \\ \exp\left[-C\sigma^{-(2-4/k)}\right], & p = 0, \\ \exp\left(-C|p|^{-(k-2)/(k-1)}\exp[|p|^{k/(k-1)}/\sigma^2]\right), & p < 0. \end{cases} \qquad (8.88)$$

The general observation is that different behaviors arise depending on the bifurcation parameter p: independent of noise for the supercritical regime, normally superpersistent for the critical case, and extraordinarily superpersistent for the subcritical regime in the sense of scaling in (8.88) (for $p < 0$). Numerical support for these distinct scaling behaviors was obtained [198, 199].

8.7.2 Application: Advection of Inertial Particles in Open Chaotic Flows

We will see in Chap. 10 that the inertia of the advective particles alters the advective dynamics, and the underlying dynamical system becomes dissipative so that attractors can arise, and hence particles can be trapped permanently in some region in the physical space. The possibility that toxin particles can be trapped in physical space is particularly worrisome. It is thus interesting to study the structural stability of such attractors. In particular, can chaotic attractors so formed be persistent under small noise? It was found [197] that in general, the attractor is destroyed by weak noise and replaced by a chaotic transient, which is typically superpersistent. For weak noise, the extraordinarily long trapping time makes the transient particle motion practically equivalent to an attracting motion with similar physical or biological effects.

Noise in the context of particle advection can be due, for example, to the diffusivity of the advected particles [143]. Diffusion can be generated by, e.g., microscopic interactions (molecular diffusion). The dimensionless equation of motion of an inertial particle will be detailed in Chap. 10. The noisy version of this equation in a two-dimensional incompressible flow $\mathbf{u}(x, y, t)$ in the horizontal plane is

$$\ddot{\mathbf{r}}(t) = A\left[\mathbf{u}(\mathbf{r}(t), t) - \dot{\mathbf{r}}(t)\right] + \frac{3}{2}R\frac{d}{dt}\mathbf{u}(\mathbf{r}(t), t) + \sigma\boldsymbol{\xi}(t), \qquad (8.89)$$

where $\boldsymbol{\xi}(t) = (\xi_x(t), \xi_y(t))$, and $\xi_x(t)$ and $\xi_y(t)$ are independent Gaussian random variables of zero mean and unit variance, and σ is the noise amplitude. Parameters A and R are the inertial parameter and the density ratio, respectively, as defined in (10.29). The noise-free dynamics in a given time-periodic flow, the so-called

von Kármán vortex street around a cylinder, will be described in Sect. 10.7. There
are three attractors [53]: two chaotic ones about the cylinder and a regular one at
$x = \infty$. We present here the main effect due to noise because of its close relation to
superpersistent chaotic transients.

Because of the explicit time dependence in the flow velocities, the attractors
and their basins move oscillatorily around the cylinder. The remarkable feature is
that in the physical space, there are time intervals during which the attractors come
close to the basin boundaries. Thus, under noise, we expect permanently trapped
motion on any one of the two chaotic attractors to become impossible. In particular,
particles can be trapped near the cylinder, switching intermittently on the two origi-
nally chaotic attractors, but this can last only for a finite amount of time: eventually
all trajectories on these attractors escape and approach the $x = \infty$ attractor. That is,
chaos becomes transient if one takes into account the effect of noise, or equivalently,
of diffusivity.

To understand the nature of this noise-induced transient chaos, one can distribute
a large number of particles in the original basins of the chaotic attractors and ex-
amine the channel(s) through which they escape to the $x = \infty$ attractor under noise.
Figure 8.21a–c show, for three dimensionless instants of time (1, 1/4, and 1/2 mod
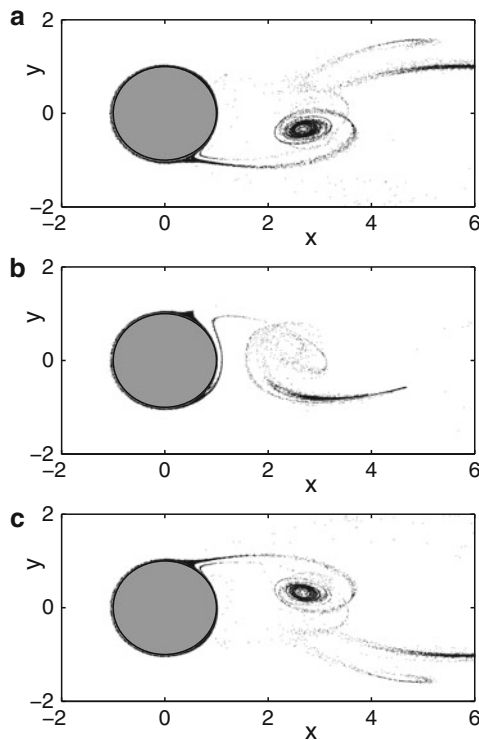
Fig. 8.21 (**a**)–(**c**) At three different instants of time, $1/4$ time units apart, locations of the tem-
porally trapped and escaping inertial particles in the von Kármán vortex street in the presence of
noise [197] (copyright 2000, the American Physical Society)

(1), respectively), locations of an ensemble of particles in the physical space. While there are particles still trapped in the original attractors, many others are already away from the cylinder. Since this is a two-dimensional projection of the full particle dynamics, some fractal-like features overlap. The escaping channels through which particles escape form a set of thin openings surrounding the cylinder and extending to one of the von Kármán vortices in the flow. After wandering near the vortex, particles go to the $x = \infty$ attractor. In the physical space the locations of these openings vary in time, but the feature that they are narrow is common.

For a fixed noise amplitude, the lifetimes of the particles near the cylinder obey an extremely slow decaying distribution. A least-squares fit gives [197] the escape rate as a function of the noise amplitude σ as

$$\kappa \approx \frac{1}{\tau} \approx \exp\left(-3.3\sigma^{-0.55}\right). \tag{8.90}$$

Note that for $\sigma = 0$, there is an attracting motion, so that κ vanishes. The way that κ goes to zero follows the superpersistent transient scaling law as σ is decreased.

Theoretically, the observed noise-induced superpersistent chaotic transient behavior can be explained using the approach in Sect. 8.7.1. The result implies that it may be possible to observe superpersistent chaotic transients in physical space. The flow system used for experimental study of advective chaotic scattering by Sommerer and coworkers (Fig. 8.19) is a possible candidate.

Chapter 9
Transient Chaos in Spatially Extended Systems

Chaos is not restricted to systems without any spatial extension: it in fact occurs commonly in spatially extended dynamical systems that are most typically described by nonlinear partial differential equations (PDEs). If the patterns generated by such a system change randomly in time, we speak of spatiotemporal chaos, a kind of temporally chaotic pattern-forming process. If, in addition, the patterns are also spatially irregular, there is fully developed spatiotemporal chaos. In principle, the phase-space dimension of a spatially extended dynamical system is infinite. However, in practice, when a spatial discretization scheme is used to solve the PDE, or when measurements are made in a physical experiment with finite spatial resolution, the effective dimension of the phase space is not infinite but still high.

Transient chaos is common in dissipative spatiotemporal systems. The basic reason is that spatial coupling is typically diffusive. The asymptotic attractors are therefore often temporally periodic, or even time-independent. It is the approach toward these attractors that is chaotic. In this sense, spatiotemporal chaos often collapses after some time, and a regular behavior then takes over. If the lifetime increases rapidly with the system size, the transients are *supertransients*. An important physical context in which supertransients arise is fluid dynamical turbulence in pipe flows, where the well-known stationary laminar solution is the only asymptotic attractor, and the observed turbulent behavior appears to be a kind of transient chaos only. Motivated by this example, we shall sometimes call the fully developed chaotic behavior of other spatiotemporal systems "turbulent."

In systems exhibiting supertransients, a general picture emerges: In a large system, it is not possible to determine whether the observed "turbulence" is transient unless an asymptotic time regime is reached. If the transient time is much longer than any physically realizable time, the system is effectively "turbulent," regardless of the nature of the asymptotic attractor. The transients mask in this case the real attractor, and pose a fundamental difficulty for observing the asymptotic state of the system. In this sense, attractors are irrelevant to "turbulence." Supertransients are thus perhaps the most surprising applications of the concept of transient chaos to high-dimensional dynamical systems.

In this chapter, we first introduce several paradigmatic models of spatially extended dynamical systems and discuss supertransients in different models. Scaling laws with the system size are derived. We then address the effect of noise

and of nonlocal couplings on supertransients, discuss various crisis phenomena in spatially extended systems, and characterize the fractal properties of supertransients. Finally, turbulence in pipe flows, which represents an important physical situation in which supertransients can be observed experimentally, is discussed.

9.1   Basic Characteristics of Spatiotemporal Chaos

9.1.1   Paradigmatic Models

There are several classes of models of spatially extended systems that can be used to study transient spatiotemporal chaos [775].

Coupled map lattices (CML), introduced by Kaneko [378], provide the simplest models for spatiotemporal dynamics of continuous variables. In a CML, the local building blocks of the dynamics are in the form of low-dimensional maps, and they are coupled to their neighbors according to some rule with a coupling of strength ε. In this model, both time and space are discrete, but the dynamical variables are continuous. The dynamics does depend on the boundary conditions. Often periodic boundary conditions are assumed, but absorbing boundary conditions have also been used. In one dimension, the typical form of a CML defined on N sites with diffusive local coupling is

$$x_{n+1}^i = (1-\varepsilon)f(x_n^i) + \frac{\varepsilon}{2}\left[f(x_n^{i+1}) + f(x_n^{i-1})\right], \quad i = 0,\ldots,N-1, \qquad (9.1)$$

where x is the dynamical variable, $f(x)$ is a map describing the local dynamics, and n and i denote discrete time and space, respectively. For periodic boundary conditions we have $x_n^0 = x_n^{N-1}$, while for absorbing boundary conditions we have $x_n^0 = x_n^{N-1} = 0$ for any time instant n. The size of the system is N.

In a *cellular automaton* (CA) [833] even the dynamical variable is discrete. By coarsening the x variable of a CML, the dynamics is mapped onto that of a CA [609]. If, for example, the new variable is chosen to be 0 (1) for x smaller (larger) than a threshold, a two-state CA is obtained from (9.1).

The Kuramoto–Shivashinsky (KS) equation is a simple PDE exhibiting interesting spatiotemporal dynamics. It was derived to describe propagating patterns in plasmas, in chemistry and in cellular flames [85]. The KS equation governs the dynamics of a continuous scalar field $u(x,t)$ according to a nonlinear equation whose dimensionless form can be written as

$$\frac{\partial u}{\partial t} = -u\frac{\partial u}{\partial x} - \frac{\partial^2 u}{\partial x^2} - \frac{\partial^4 u}{\partial x^4}. \qquad (9.2)$$

It is remarkable that there are no free parameters in the model, and hence the system size L serves as the only control parameter. Alternatively, one can fix the size and, after appropriate rescaling, convert (9.2) to

$$\frac{\partial u}{\partial t} = -u\frac{\partial u}{\partial x} - \frac{\partial^2 u}{\partial x^2} - v\frac{\partial^4 u}{\partial x^4}, \tag{9.3}$$

where $v \sim L^{-2}$ is a dimensionless parameter.

The complex Ginzburg–Landau (cGL) equation governs the spatiotemporal evolution of a complex field $\psi(\mathbf{r},t)$. It is the normal form of spatiotemporal systems in the vicinity of Hopf bifurcations [85]. In its most commonly used two-dimensional version, the cGL equation is

$$\frac{\partial\psi}{\partial t} = \mu\psi - (1+i\alpha)\Delta\psi + (1+i\beta)|\psi|^2\psi, \tag{9.4}$$

where Δ denotes the Laplacian. The system has three dimensionless parameters: μ, α, and β. When the dimensionless system size is fixed, the parameter μ characterizes the size dependence.

Reaction–diffusion (RD) equations describe the coupled dynamics of chemical concentrations, or interacting populations. Their general form for two concentrations $a(\mathbf{r},t)$ and $b(\mathbf{r},t)$ is

$$\frac{\partial a}{\partial t} = r_a(a,b) + \Delta a, \quad \frac{\partial b}{\partial t} = r_b(a,b) + \delta\Delta b, \tag{9.5}$$

where the functions r_a, r_b govern the nonlinear reaction equations in the homogeneous case, and the dimensionless parameter

$$\delta = D_b/D_a$$

is the ratio of the diffusion coefficients.

The Navier–Stokes (NS) equation describes the dynamics of the velocity and the pressure fields, $\mathbf{v}(\mathbf{r},\mathbf{t})$ and $p(\mathbf{r},t)$, respectively, of a viscous fluid. For incompressible flows not subject to any external force the dimensionless form of the NS equation is

$$\frac{\partial\mathbf{v}}{\partial t} + \mathbf{v}\nabla\mathbf{v} = -\nabla p + \frac{1}{Re}\Delta\mathbf{v}, \quad \nabla\cdot\mathbf{v} = 0, \tag{9.6}$$

where Re is the Reynolds number. Note that there is no dynamical equation for the pressure. It is the incompressibility equation $\nabla\cdot\mathbf{v} = 0$ that provides a condition of self-consistency to make the pressure unique.

Figure 9.1 presents several typical complex patterns in spatiotemporal systems.

9.1.2 Phase Spaces of Spatiotemporal Systems

The phase space of a spatiotemporal system is high-dimensional. In a CML, it is spanned by all the variables x^i at different sites $i = 0,\ldots,N-1$. In a system described by nonlinear PDEs, the infinite-dimensional phase space is spanned by the set of all possible spatial distributions of the fields, compatible with a given boundary condition. In the KS and cGL equations, these are the functional spaces $u(x)$
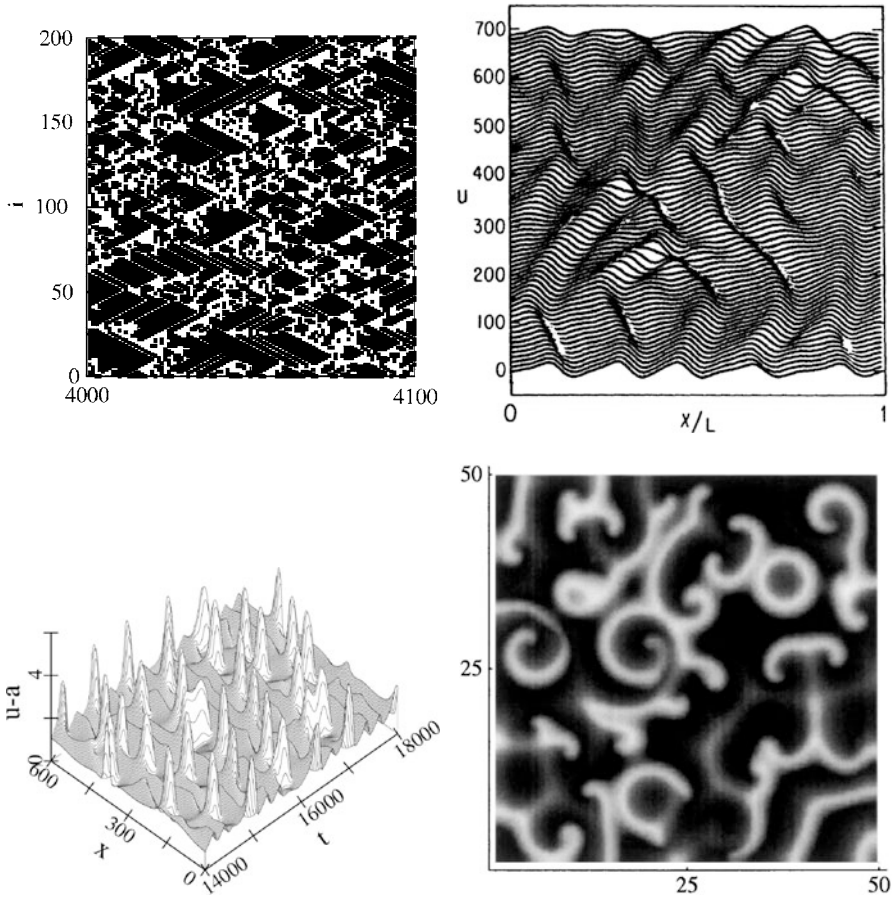
Fig. 9.1 *Upper left*: space-time diagram of a CML. Black (*white*) dots correspond to sites in a laminar (chaotic) regime. Horizontal (vertical) axis represents time (space) [797] (with kind permission from Elsevier Science). *Upper right*: space-time diagram of a solution of the KS equation (9.2). The distribution of the field variable $u(x)$ is plotted at an instant of time [715] (copyright 1986, the American Physical Society). *Lower left*: space-time diagram of an RD problem in one spatial dimension. The third axis represents the difference between the two concentrations [812] (with kind permission from the Institute of Physics). *Lower right*: instantaneous spatial pattern of an excitable medium in two dimensions. *Shading* corresponds to the concentration of one substance. The pattern is similar to that from the cGL equation [741] (copyright 1998, the American Physical Society)

and $\psi(\mathbf{r})$ respectively. In RD problems and fluid dynamics, two functions define the phase space: the set of all possible concentrations $a(\mathbf{r})$ and $b(\mathbf{r})$ for the former and the set of all possible velocity and pressure fields $\mathbf{v}(\mathbf{r})$ and $p(\mathbf{r})$ for the latter, where the forms of the functions are determined by the boundary conditions. For example, for a fluid system described by the NS equation, all velocity fields vanish on walls at rest but take on the values of the velocities of moving walls.

A given spatial distribution of the field variable represents a point of the phase space. Any of them can be a possible initial condition. The time evolution of the system corresponds to a motion among different phase-space points, and traces out a continuous curve emanating from the point representing the initial state. The time evolution is unique, and the phase-space description is thus complete.

A convenient way of representing an infinite-dimensional phase space is to expand the field variable(s) in terms of a complete set of orthonormal basis functions. The expansion coefficients a_i, $i = 1, \ldots$, can also be considered phase-space variables. This expansion can be truncated at some index N if variables a_i with $i = N+1, N+2, \ldots$ are negligible with respect to global dynamics. Thus, even systems described by PDEs can be represented as high-dimensional systems with a finite number of degrees of freedom. In a finite-dimensional phase space, stationary solutions correspond to fixed points of the phase space. Stable stationary solutions are thus fixed-point attractors. Homogeneous periodic solutions or waves correspond to limit cycles. Complicated chaotic solutions can be associated with chaotic attractors or chaotic saddles. The phenomenon of long transients is naturally related to situations in which the chaotic set is a saddle, and in addition, this saddle is rather dense (although not entirely space-filling) in the phase space.

9.1.3 Spatiotemporal Intermittency

There is a large literature on the phenomenon of spatiotemporal intermittency (STI) [120, 121, 375, 376, 378, 379, 404]. Here we briefly review this phenomenon, in order to distinguish it from concepts appearing later in this chapter. The concept of STI applies to spatiotemporal systems in which any space-time point can be classified as either *laminar* or *turbulent*. By "laminar" we mean a regular pattern (whose temporal dynamics might be both regular and chaotic), while "turbulent" regions have no apparent regularity either in space or in time. Spatiotemporal intermittency implies that there are intervals in both space and time in which one of the phases dominates. Domains of a given type of behavior have well-defined boundaries. An example is provided by the upper left panel of Fig. 9.1. There were many experiments on STI (for recent examples, see [269, 478, 659]).

Spatiotemporal intermittency is not the only possible manifestation of spatiotemporal chaos, but it is certainly a typical one. It can be considered as state of transition between laminar and fully turbulent phases. This does not imply that STI must evolve to be more and more complicated. Spatiotemporal intermittency can very well provide an asymptotic state, a spatiotemporally chaotic attractor. The usual statistical measures of STI consider long-time averages of spatial characteristics, such as the distributions of the size of laminar regions and of the "turbulent" regions [120, 121]. In a spatiotemporally intermittent state both distributions are exponentially decaying. The decay constants are related to the sizes of the average laminar or turbulent phases. A difference between the characters of these distributions typically

appears at the onset of STI. Here the distribution of the laminar domains follows a power law, indicating the lack of any characteristic sizes. The onset is, therefore, similar to a phase transition.

We wish to emphasize that STI can also characterize long transients [376, 619, 831]. In fact, many transients in spatiotemporal systems are of this type. We shall see that the lifetime can be sufficiently long to make statistical properties stationary (similar to, e.g., the statistics needed to determine the average Lyapunov exponent on a chaotic saddle in low-dimensional systems).

9.2 Supertransients

9.2.1 Transient Chaos in Coupled Map Lattices

Perhaps the first indication of complex spatiotemporal patterns appearing as long-lived transients was found in the thermal convection experiments by Ahlers and Walden, as early as 1980 [9]. For a detailed investigation of these transients, however, CMLs have proven to be convenient model systems, initiated by the seminal paper of Crutchfield and Kaneko [146].

The CML (9.1) has been studied extensively for different types of map f. The initial conditions are most frequently taken as random numbers at each site. When the map is strictly contracting, the asymptotic behavior is always spatially regular and temporally periodic (often homogeneous and steady). The transients toward this state are, however, typically chaotic. For map f that produces transient chaos on its own with positive topological entropy but possesses periodic attractors, the asymptotic behavior can often be spatially regular and temporally periodic. The CML built on the map f with chaotic attractors generates permanent spatiotemporal chaos if the coupling is weak, but transient chaos leading to a simple attractor is common for intermediate and strong couplings [831]. These results are summarized in Table 9.1. An observation is that diffusive coupling can generate chaos even from nonchaotic maps, and it often converts permanent local chaos into global transients.

A question is how the average transient lifetime $\tau \approx 1/\kappa$ depends on the system size L. For weak coupling $\varepsilon < \varepsilon_0$, practically no size-dependence is found. For slightly stronger coupling, however, the lifetime increases rapidly with the

Table 9.1 Dynamics of the map f and of the corresponding CML

Map f	CML
Nonchaotic	Transiently chaotic [146, 228, 387, 487, 609, 610]
Transiently chaotic	Transiently chaotic [377]
Permanently chaotic	Transiently chaotic [465, 619, 831]
	Permanently chaotic [619, 831]
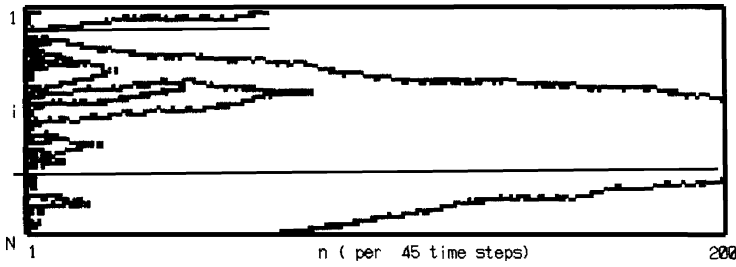
Fig. 9.2 Typical space-time pattern of type-I supertransients [377] (with kind permission from Elsevier Science)

system size. These are the *supertransients* [146]. There are two distinct types of supertransients. *Type-I supertransients* are characterized by a power-law scaling

$$\kappa(L) \sim L^{-\beta} \tag{9.7}$$

with a positive exponent β. *Type-II supertransients* are characterized by an exponential scaling:

$$\kappa(L) \sim \exp(-aL^\gamma), \tag{9.8}$$

where γ is a positive exponent and the coefficient a in general depends on the system parameters.

The patterns associated with the two types of supertransients are qualitatively different. For type-I supertransients, the basic features are defects whose density decreases gradually with time, as shown in Fig. 9.2. This can also be considered as a kind of aging process. Correspondingly, dynamical invariants such as the Lyapunov exponents and entropies also decrease with time.

Type-II supertransients are, in contrast, statistically steady over a long period of time, i.e., averages are time-independent in the chaotic state, and the transition to an attractor is rather abrupt, as exemplified by Fig. 9.3. If the maximum Lyapunov exponent is positive, a chaotic saddle is expected to exist in the high-dimensional phase space.

9.2.2 Origin of Supertransient Scaling

The different scaling rules can be traced back to the different patterns that are characteristic of the two classes of supertransients.

Type-I supertransients: The dominant process is that the defects, as indicated in Fig. 9.2, undergo a kind of random walk, and when they meet, they annihilate. For an anomalous random walk, the variance of the displacement scales with time as $t^{1/\beta}$, where β is a positive number ($\beta = 2$ corresponds to normal diffusion). Estimating
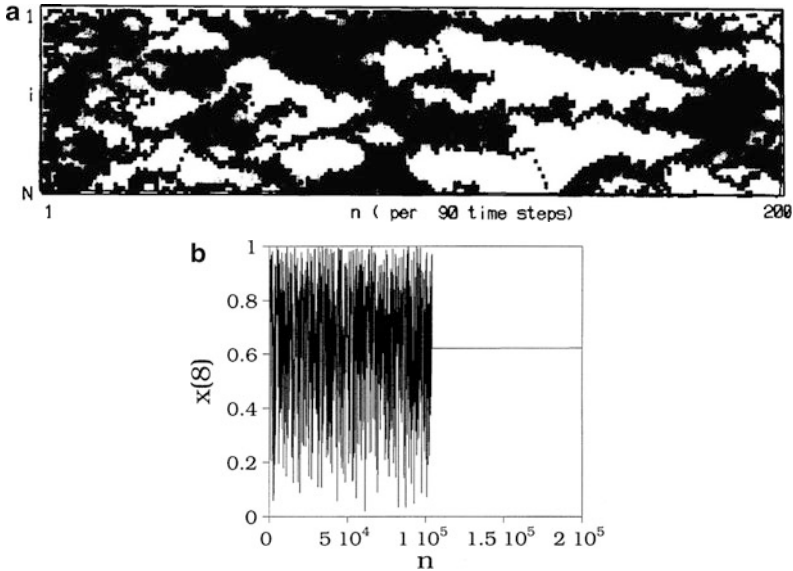
Fig. 9.3 (**a**) Typical space-time pattern of type-II supertransients. From [377] (with kind permission from Elsevier Science). (**b**) Time-dependence at a single site illustrating that the crossover to the nonchaotic behavior is abrupt [465] (copyright 1995, the American Physical Society)

the average lifetime τ as the time needed to reach a displacement variance of the order of the system size, we obtain $\tau \sim L^\beta$, which is equivalent to (9.7).

Type-II supertransients: Let $x^*(i)$ denote the coordinate corresponding to the regular spatiotemporal attractor at site i. A basin size r can be found that is much smaller than the system size in the following sense: if $|x_0(i) - x^*(i)| < r$ for *all* sites, the system reaches the attractor without chaotic excursions, but if the difference is larger than r, irregular transients appear. This basin size is a measure of the extension of the attractor's basin, restricted to a single dimension. The probability P that a randomly chosen initial condition at some of the sites falls within the basin size is proportional to this size: $P \sim r \ll 1$.

The following intuitive argument can be used to explain the scaling with the system size [228, 377, 619, 812]. In a spatially extended system there exists a correlation length ξ, within which neighboring sites move in a coherent manner. Conversely, only sites farther apart than ξ move independently. The system can thus be divided into L/ξ subunits that behave independently. For a random initial condition, the probability Π of falling into all the local basins is P raised to the power of the number of independent units, i.e., $\Pi \sim P^{L/\xi}$. Time needed to reach the hole is the phase space of the basin size is proportional to $1/\Pi$, and thus the average lifetime is estimated as

$$\tau(L) \sim \Pi^{-1} \sim P^{-L/\xi} \sim r^{-L/\xi} \sim \mathrm{e}^{aL}, \tag{9.9}$$

where $a = (\ln 1/r)/\xi$ is a positive constant. Here we have assumed that the basin size is independent of the system size. A strong dependence of r on L can modify the result. If, for example, $r = r(L) \sim \exp(-L^{\gamma-1})$, we have $\tau(L) \sim \exp(L^{\gamma}/\xi)$ (cf. (9.8)). Numerical computations often support, however, a linear length-dependence in the exponent, indicating a weak dependence of the basin size on L.

Finally, we note that the problem of supertransients is effectively the high-dimensional analogue of chaos in well-stirred chemical reactions in *closed* containers. In the absence of any material flux, the final state can be only in thermal equilibrium governed by a fixed-point attractor. With initial conditions far away from the thermal equilibrium, one brings the system into a regime whereby long chaotic transients can arise, as pointed out by Scott, Showalter, and coworkers (see Fig. 1.15). The novel feature in spatiotemporal systems is that nearly all initial conditions are far away from the attractor, since the probability of falling into the basin of attraction is extremely small.

9.2.3 Supertransients with Exponentially Long Lifetimes in Other Systems

It is remarkable that supertransients, mainly of type II, appear in a large number of systems other than CMLs. Typically, the lifetime scales with the system size as

$$\kappa(L) \sim \exp(-aL). \tag{9.10}$$

Evidence for this behavior has been found in a number of systems, as follows.

Kuramoto–Shivashinsky equation. The investigations of Shraiman [715] and of Hyman, Nicolaenko, and Zalesky [348] on phase turbulence in the one-dimensional KS equation (9.2) provided the first examples of supertransients in a PDE system, discovered earlier than those in CMLs. The upper right panel of Fig. 9.1 shows a typical transient pattern.

Complex Ginzburg–Landau equation. After a detailed numerical analysis of long-lasting spatiotemporal turbulence in the two-dimensional cGL equation by Bohr and coworkers [85, 86, 344], Braun and Feudel [98] and Houghton and coworkers [340] provided numerical evidence for an exponential scaling of the average transient lifetime with the system size.

Reaction–diffusion systems. The first example of type-II supertransients in RD systems of the type (9.5) in one spatial dimension was found by Wacker, Bose, and Schöll [812]. A typical concentration distribution in the transient phase can be seen in the lower left panel of Fig. 9.1. A decomposition of patterns during the transients into eigenmodes indicates that there exist no preferred modes [516–518]. Transient patterns are thus shown to be uncorrelated, a feature underlying the argument leading to type-II supertransient scaling. The study of RD systems was extended by Wackerbauer, Showalter, and coworkers [813–815, 842].

Two-dimensional excitable medium. The model investigated by Strain and Greenside [741] differs slightly in structure from (9.5), but exhibits similar dynamical behavior, although with different types of patterns in two dimensions (lower right panel of Fig. 9.1). This is the first PDE model in which the fractal properties of a high-dimensional chaotic saddle were investigated (Sect. 9.5).

Complex networks. An observation of Zumdieck, Timme, Geisel, and Wolf [858] was that in a randomly diluted set of coupled oscillators, the transients toward a limit-cycle attractor are chaotic and exhibit the scaling (9.10), with the number of oscillators replacing the length *L*. The average lifetime of the transients depends also on the network connectivity, and reaches a maximum at as intermediate level of dilution. Irregular and exponentially long transients were also observed in different neural network models [178, 428, 855, 856]. Supertransients with exponentially long lifetimes were also observed in social networks [51, 52].

Turbulent shear flow. The Theoretical work of Eckhardt and coworkers (see, e.g., [229, 231]) based on the Navier–Stokes equation (9.6) predicted the long-lived transient nature of turbulence in pipes. Recent experiments by Hof et al. [334, 336] provided evidence for a type-II (or even stronger) supertransient scaling, where the quantity in (9.10) is replaced by the Reynolds number (for more detail see Sect. 9.6).

9.2.4 Stable Chaos

A peculiar feature of type-II supertransients is that the maximum Lyapunov exponent is in certain cases negative even *during the transients*, although the transient patterns are as irregular as otherwise. This phenomenon has been called stable chaos [609, 610] and provides an example whereby linear stability can coexist with nonlinear instability in the transient phase. Following the definition of Politi and coworkers [856], stable chaos means transients that (1) have a negative or zero maximum Lyapunov exponent and (2) appear stationary for long times, the average of which scales with the system size exponentially. The phenomenon is robust also in the sense that it can be present in finite regions of the parameter space [609].

Stable chaos was first found in CMLs for which the local map *f* is piecewise linear, is discontinuous at certain points, and possesses a simple periodic attractor. The map *f* can be contracting [146, 228, 857] or can have expanding pieces [62, 148, 609]. The transients are in any case random, illustrated by an exponential decay in both the temporal and the spatial correlations. These features are not due to the discontinuity in *f*, because a continuous variant of the map, in which the discontinuity is replaced by a steep continuous line, has been shown to exhibit the same behavior [228, 609]. The supertransients as such maps are nonchaotic in the sense of sensitive dependence on initial conditions, but are chaotic in the sense of positive topological entropy.

The irregular behavior of stable chaos cannot be related to a local production of information, due to the lack of a positive Lyapunov exponent. Investigations [118, 264, 610, 784] led to the conclusion that the irregularity associated with stable

chaos is produced by transport, i.e., by the nonlinear propagation of finite disturbances. The so-called *damage spreading* analysis [833] can therefore be used to understand the phenomenon of stable chaos. In particular, one is interested in the effect produced by finite localized perturbations. Indeed, in systems exhibiting stable chaos [118, 264, 610, 784], initially perturbed regions in space spread with a *constant* front velocity v. Disturbances can thus travel through the system without damping. It is this velocity that plays in some sense the role of a positive Lyapunov exponent.

Stable chaos often appears in a certain range of a control parameter, e.g., the coupling constant ε in (9.1). Outside this range, there are no long transients and the system rapidly reaches a synchronized, periodic state, in which the front velocity v is zero. The transition is, however, not a single point in the parameter space. It occurs in an extended interval [118], where ordered and chaotic dynamics characterized by $v = 0$ and $v \neq 0$, respectively, alternate in a quite irregular manner.

Stable chaos is not restricted to CMLs. Bonaccini and Politi [91] considered coupled nonchaotic oscillators in continuous time. The oscillators are subject to a synchronous periodic forcing over a period T, which is suddenly changed to an unforced state of length T', and this mechanism is repeated periodically. For sufficiently rare active driving where T/T' small, the largest Lyapunov exponent of the coupled-driven system is negative, and the system exhibits properties of stable chaos. The diluted neural network model [856] mentioned in Sect. 9.2.3 was shown to follow the scaling (9.10) in a certain range of parameters, where all Lyapunov exponents are negative during the transients.

In all the continuous-time examples, the dynamics is associated with the presence of discontinuities, or with being close to such singularities. In the oscillator model there is a sudden change in the driving mechanism, and in the neural-network model the discontinuity is connected with changes in the spike ordering. Thus one can conclude [172, 856] that discontinuities or rapid changes in the dynamical equations are a necessary condition for the onset of stable chaos. A detailed review of stable chaos can be found in [611], which also presents an additional realistic system with stable chaos: a diatomic gas of hard-point particles.

9.3 Effect of Noise and Nonlocal Coupling on Supertransients

Numerical results on the effect of noise on supertransients in spatially extended dynamical systems were obtained in [433] for a CML system. The diffusive coupling constant ε in (9.1) was replaced by a random variable $\varepsilon \to \varepsilon + \sigma \xi_n$, where ξ_n is a random number taken at time instant n, and σ represents the noise intensity. This choice of noise is homogeneous over the full system, i.e., ξ_n does not depend on the site index i. The average lifetime was found to depend little on the noise intensity σ in the weak-noise regime, suggesting that supertransients are robust [850].

A more recent investigation of Wackerbauer and Kobayashi [814] considered the effect of spatially inhomogeneous noise as well. They studied an RD system (9.5)

in one spatial dimension with periodic boundary condition. The continuous space dependencies in the concentrations $a(x,t)$ and $b(x,t)$ are approximated by a discrete set $[a^{(i)}(t), b^{(i)}(t)]$ of variables for $N \gg 1$ sites ($i = 1, \ldots, N$). Correspondingly, the diffusive coupling term is also discretized. This chain of variables can be considered to be arranged around a circle. Additive noise $\sigma \xi^{(i)}(t)$ is included in the chemical kinetic equation governing the concentration $b^{(i)}$. The chain is divided into k blocks such that N/k neighboring sites are subject to the same realization of noise. The noise terms acting on neighboring blocks are chosen to be independent. Any value $k > 1$ corresponds to a spatially inhomogeneous noise – the more inhomogeneous, the larger the value of k. The results show that spatially inhomogeneous weak noise tends to decrease the escape rate of supertransients up to a certain strength at which a minimum of the escape rate is reached, as shown in Fig. 9.4. The effect intensifies with the degree of the inhomogeneity parameter k. The scenario is similar to what occurs in a class of low-dimensional systems (Fig. 4.2). Qualitatively, weak inhomogeneous noise makes the system more random and reduces the chance of finding the small basin of the attractor. In this model, homogeneous noise ($k = 1$) has a destructive effect on the transients: it leads to a monotonic increase in the escape rate for increasing noise strength. However, type-II supertransient scaling remains valid in that the lifetime increases exponentially with the size even in the presence of noise.

In search of a method to control the length of supertransients, an approach is to investigate the effect of nonlocal coupling in the noise-free problem. Yonker and Wackerbauer [842] studied the consequence of adding a few nonlocal connections (shortcuts). At sites coupled not only to the nearest neighbors but to a third, more distant, site, they modified the discrete Laplacian so that all three sites are included in a way that ensures the same perturbation, the same as in the locally coupled model. The length s of the shortcuts is a basic parameter, which is defined as the minimal number of sites between the two end sites of the shortcut divided by the number N of sites in the ring. The longest shortcut connecting two opposite sites along the circle corresponds to length $s = 1/2$. For a single shortcut of small length,
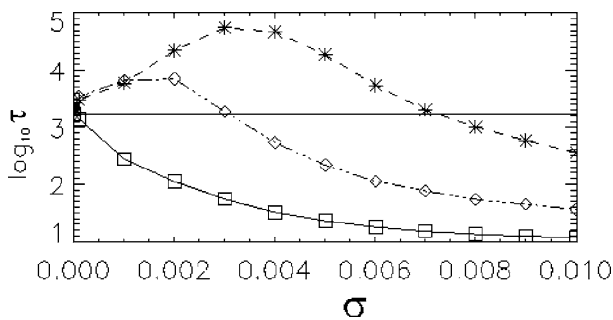
Fig. 9.4 Dependence of the average lifetime τ on the noise intensity σ in an RD system. The degree of spatial noise inhomogeneity k decreases from $k = 20$ (*stars*) to $k = 4$ (*diamonds*) to spatially homogeneous noise $k = 1$ (*squares*) [814] (copyright 2007, the American Physical Society)

the average lifetime increases, reaches a maximum at about $s = 0.05$, then decreases, finally leading to a reduced lifetime compared to that in the locally coupled system. The overall dependence is similar to that of the upper curves in Fig. 9.4. In any case, the type-II supertransient scaling remains valid for any s with a slightly s-dependent prefactor $a(s)$ in (9.10).

Adding more shortcuts can have a drastic effect on the transients. For example, two can have the local effect of stabilizing spatiotemporal chaos for arbitrarily long times, effectively preventing its collapse. Whether this can actually happen depends on the locations of the shortcuts and the initial conditions. For example, in a large ensemble of cases with randomly chosen shortcut locations, the probability for spatiotemporal chaos to be permanent is about 70%. Three shortcuts can increase the likelihood of permanent chaos even more. A further increase in the number of shortcuts, however, seems to weaken the effect, and the likelihood of transient chaos increases again.

Control of spatiotemporal transients via nonlinear feedback was suggested in [619], where it was demonstrated for a CML system that proper control can shorten the lifetime of the transients by several orders of magnitude. These developments illustrate that adding weak noise, or taking over methods from the physics of networks, has the potential to provide some effective ways to harness transient chaos in spatially extended systems.

9.4 Crises in Spatiotemporal Dynamical Systems

9.4.1 Boundary Crises: Supertransients Preceding Asymptotic Spatiotemporal Chaos

When there is an asymptotic spatiotemporal chaotic attractor, or asymptotic "turbulence," long chaotic transients typically occur in a parameter range preceding the permanently chaotic regime. Suppose the latter is in the parameter range $p > p_1$. Chaotic transients are then present for $p < p_1$. Intuitively, their average length should increase on approaching the critical value p_1. For supertransients, one expects a power-law divergence in the exponent of the average lifetime, i.e., a decay of the escape rate as

$$\kappa(p, L) \sim \exp[-c(L)(p_1 - p)^{-\delta}], \tag{9.11}$$

where $\delta > 0$ and the coefficient $c > 0$ depends on the system size L. Combining this with the size dependence of (9.8) or (9.10), we see that the coefficient a changes with the parameter p as

$$a(p) \sim (p_1 - p)^{-\delta}. \tag{9.12}$$

A detailed investigation of the two-dimensional cGL equation (9.4) led to the conclusion [85, 86, 344] that permanent spatiotemporal chaos is present in a region of the parameter plane (α, β) (μ fixed). When approaching the boundary of this

Fig. 9.5 For the cGL
equation (9.4), the largest
average Lyapunov exponent
λ_1 of the chaotic sets as a
function of the parameter α.
Spatiotemporal chaos is
permanent for $\alpha > \alpha_1$.
For $\alpha_c < \alpha < \alpha_1$, only
chaotic transients are present
[86] (copyright 1990, the
American Physical Society)
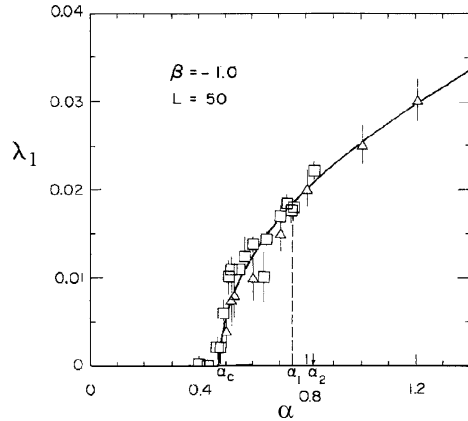
region from outside, the scaling relation (9.11) was found with exponent $\delta = 2$, which is similar to that for low-dimensional supertransient systems (cf. (8.60)), but here the exponent δ is larger than unity, and a size-dependence is also present.

When the largest average Lyapunov exponent λ_1 of the attractor is plotted as a function of the parameter $p \equiv \alpha$, it is positive in the range $\alpha > \alpha_1$. This curve can be merged smoothly with the curve of the Lyapunov exponent for the transient regime, as shown in Fig. 9.5, illustrating that the spatiotemporal chaotic saddle is converted at α_1 into a chaotic attractor. The critical parameter value α_1 can thus be viewed as a point of crisis in the cGL system. The Lyapunov exponent vanishes at some $\alpha < \alpha_c$, so the transients are not chaotic for $\alpha < \alpha_c$. For α slightly larger than α_c, the exponent scales as $\lambda_f(\alpha) \sim (\alpha - \alpha_c)^{1/2}$ [85, 86].

9.4.2 Interior Crises in Spatially Coherent Chaotic Systems

An investigation of different types of crisis phenomena in the KS equation was carried out by Chian, Rempel, and coworkers [126, 631, 632, 634]. These authors used the form (9.3) of the equation in which the length is fixed but the parameter ν contains the size of the original system. A parameter range was chosen for which the dynamics is chaotic in time but remains coherent in space. A Fourier decomposition of (9.3) with $N = 16$ modes appeared to be sufficient to illustrate the crisis phenomenon. In particular, in a parameter range of ν, a periodic window was found, as seen by plotting the long-time values of the sixth Fourier component a_6 as a function of ν. The window is bounded by an interior crisis and a saddle-node bifurcation at its two ends (Fig. 9.6a). Inside the window the attractor is a period-3 orbit or is localized in three narrow bands. In both cases it is surrounded by an extended chaotic saddle. The concept of basic components, introduced in Sect. 3.3 to characterize low-dimensional crises, thus becomes applicable to high-dimensional problems. This *surrounding chaotic saddle* (SCS) was determined by the PIM-triple method (Sect. 1.2.2.4), and its projection on the a_6 variable is also
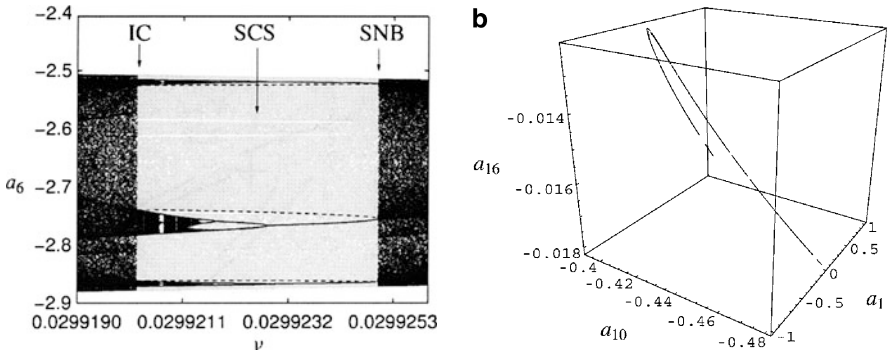
Fig. 9.6 Interior spatiotemporal crisis. (**a**) Bifurcation diagram of mode amplitude a_6 as a function of parameter v in the KS equation (9.3). *Gray dots* indicate points on the surrounding chaotic saddle (SCS). IC and SNB denote interior crisis and saddle-node bifurcation, respectively. (**b**) A three-dimensional projection of the SCS for $v = 0.029925$ [631] (with kind permission from Elsevier Science)

Fig. 9.7 Part of the phase space projected on the (a_5, a_6)-plane for $v = 0.0299211$, before interior crisis (IC). CA: chaotic attractor, SM: stable manifold of the mediating period orbit denoted by a *cross*. *Gray dots* mark the stable manifold of the SCS [631] (with kind permission from Elsevier Science)
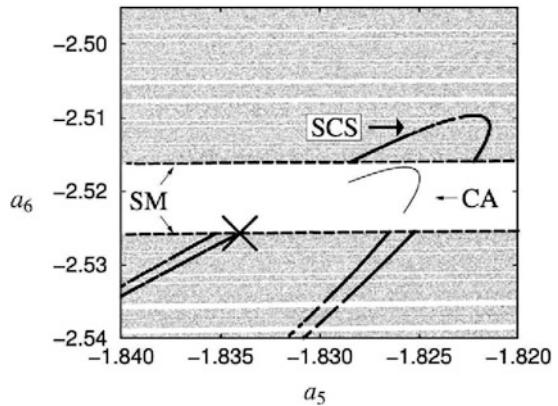
shown in the bifurcation diagram. In the full phase space the chaotic saddle turns out to be extended but low-dimensional, as can be seen in a three-dimensional projection close to the saddle-node bifurcation, where no chaotic attractor exists. The saddle is practically a single line segment, but gaps are visible along this line (Fig. 9.6b).

In the middle of the window the attractor undergoes a period-doubling bifurcation, after which a small-size chaotic attractor (CA), the three-band attractor, appears. The surrounding chaotic saddle, SCS, coexists now with the chaotic attractor. In a projection onto the plane of two Fourier components, the stable manifold of the mediating periodic orbit separating the attractor from the saddle can be seen, as shown in Fig. 9.7. The saddle's stable manifold appears to be dense.

At the crisis, the small-size chaotic attractor collides with the mediating orbit or with its stable manifold, and thus with the chaotic saddle as well (Fig. 9.8a).
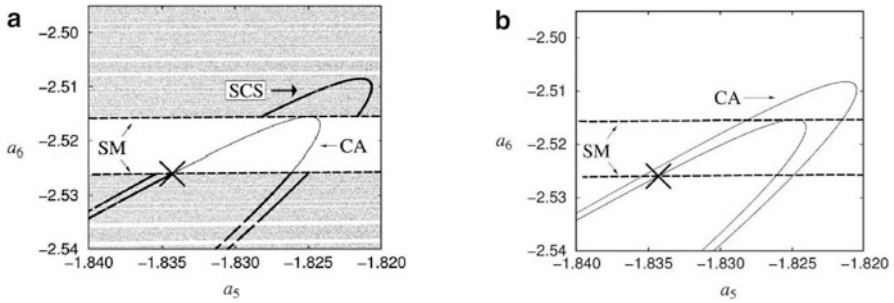
Fig. 9.8 Phase-space projection on the (a_5, a_6)-plane at IC, $v = 0.02992021$ (**a**), and slightly beyond crisis (**b**) [631] (with kind permission from Elsevier Science)
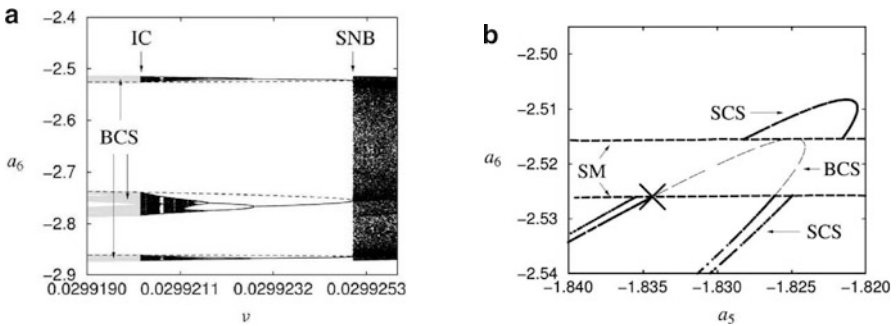
Fig. 9.9 (**a**) Bifurcation diagram as in Fig. 9.6 containing only the band chaotic attractor, which is converted into a band chaotic saddle (BCS, plotted in *gray*) beyond the interior crisis. (**b**) Chaotic saddles forming the backbone of the extended chaotic attractor projected on the (a_5, a_6)-plane at the postcrisis parameter value $v = 0.02992006$ [631] (with kind permission from Elsevier Science)

The large gaps present along the surrounding saddle just before the crisis become filled up by the newly generated orbits (see Sect. 3.4), and the extended chaotic attractor to appear contains the previous attractor, the saddle, and the filled-up gaps (Fig. 9.8b). After the crisis, points of the extended attractor that remain forever on the three bands occupied by the small attractor in the precrisis regime are connected to a saddle situated in this region, the *band chaotic saddle* (BCS). This saddle can be represented both on the bifurcation diagram (Fig. 9.9a) and on a projection of the plane of two variables (Fig. 9.9b). Similarly, points never leaving the region of the former surrounding chaotic saddle form a postcrisis chaotic saddle (SCS) that can be considered the continuation of the precrisis SCS. These two saddles are the main building blocks of the extended chaotic attractor arising from the interior crisis. The situation is thus similar to that for low-dimensional maps (Chap. 3).

9.4.3 Crises Leading to Fully Developed Spatiotemporal Chaos

In another series of papers, Rempel, Chian, and coworkers [633, 638] aimed to understand crises underlying spatiotemporal inhomogeneities [320]. For this purpose they used a one-dimensional PDE model of regularized long waves for a field $\phi(x,t)$ driven sinusoidally both in space and time. With all other parameters fixed, the main control parameter is the driving amplitude f. A Fourier decomposition of $\phi(x,t)$ into $N = 32$ spatial modes was used. As f is changed, the dynamics exhibit three qualitatively different types of behavior. For the lowest value of f the pattern is regular in space and quasiperiodic in time (Fig. 9.10a). For higher values of f, spatial regularity remains but the pattern becomes temporally chaotic (Fig. 9.10b), as indicated by the appearance of a positive Lyapunov exponent. The corresponding attractor is called a temporally chaotic attractor (TCA). A further increase in f leads to the appearance of fully developed spatiotemporal chaos (Fig. 9.10c). This occurs suddenly and is accompanied by an increase in the maximum Lyapunov exponent to a much larger value. The new attractor is a spatiotemporally chaotic attractor (STCA) that possesses a larger dimension value than the previous one (the TCA).

To follow these changes in the phase space, Rempel and Chian projected the invariant sets on the plane defined by the real parts of the second and the third Fourier modes, after taking an appropriate Poincaré map. The quasiperiodic torus attractor appears to be associated with a few closed curves (Fig. 9.11a). The authors
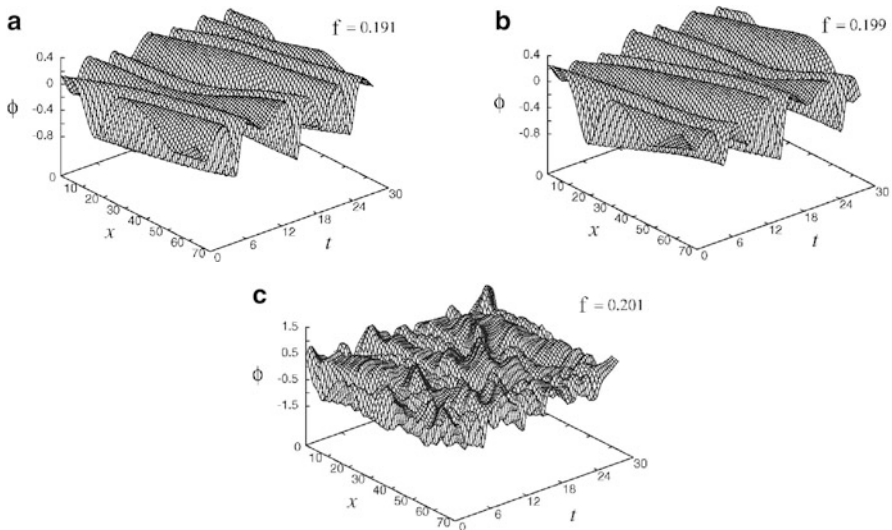
Fig. 9.10 Spatiotemporal patterns of the field ϕ for different values of the driving amplitude f: (**a**) spatially regular, temporally quasiperiodic; (**b**) spatially regular, temporally chaotic; and (**c**) spatially irregular, temporally chaotic [633] (copyright 2007, the American Physical Society)
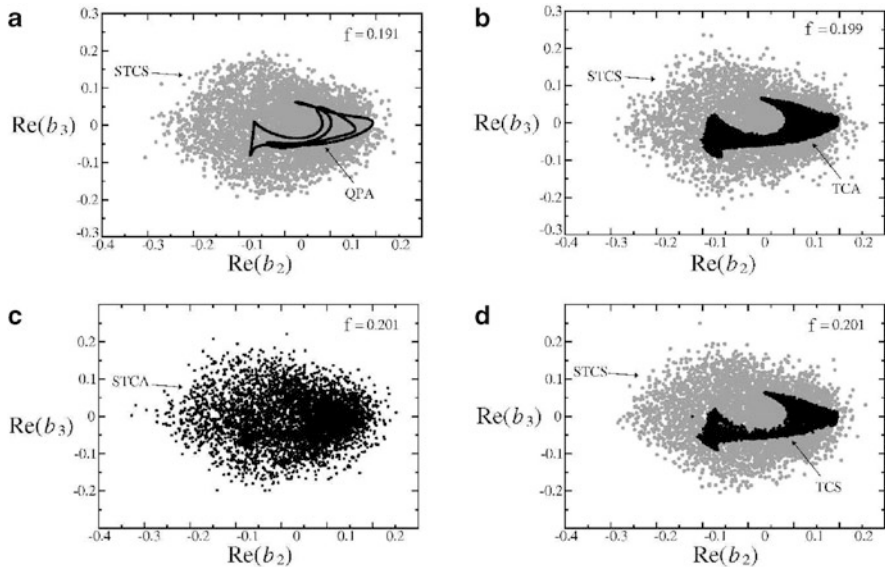
Fig. 9.11 Phase-space projection of various invariant sets on the plane of two modes. (**a**) A quasiperiodic attractor (QPA, *black*) and a spatiotemporally chaotic saddle (STCS, *gray dots*), (**b**) Temporally chaotic attractor (TCA), (**c**) a spatiotemporally chaotic attractor (STCA) after crisis, which occupies the regions where the former STCS and TCA reside, and (**d**) decomposition of STCA into a postcrisis STCS and a temporally chaotic saddle TCS after the crisis [633] (copyright 2007, the American Physical Society)

pointed out that already here an extended chaotic saddle exists surrounding the attractor. The corresponding transients carry irregular spatiotemporal patterns, and therefore the saddle is called the spatiotemporally chaotic saddle (STCS). When the spatially regular dynamics becomes chaotic, the torus attractor breaks, but the new temporally chaotic attractor (TCA) remains localized around the former torus (Fig. 9.11b). The TCA is area-filling in the projection, but is of small size. The surrounding saddle, STCS, does not change appreciably. When permanent spatiotemporal chaos occurs, the chaotic attractor suddenly broadens and becomes a spatiotemporally chaotic attractor (STCA); Fig. 9.11c. It is remarkable that the extension of the STCA is practically the same as that of the spatiotemporal saddle (STCS) earlier. At this crisis the temporally chaotic attractor collides with the surrounding saddle, and the latter becomes embedded in the new attractor. In this postcrisis regime, Rempel and Chian were also able to identify a chaotic saddle in the region occupied by the temporal attractor earlier. This saddle is called the temporally chaotic saddle (TCS); Fig. 9.11d. In the projection, it fills a slightly smaller area than the TCA.

If a trajectory on the extended attractor comes to the vicinity of the TCS, a regular pattern appears in the space, which changes chaotically in time. After some time, the trajectory deviates from this saddle, and comes close to the chaotic saddle that exists outside the TCS, a postcrisis STCS that governs the spatiotemporally chaotic

dynamics. After escaping from the STCS, the trajectory returns to the vicinity of the TCS and the pattern becomes regular again, etc. The average lifetime of the spatially regular phases can, in principle, be estimated as the average lifetime on the TCS. The full process is intermittent [131], and the situation is the high-dimensional analogue of crisis-induced intermittency discussed in Sect. 3.3. A similar phenomenon was observed in the damped KS equation [635].

The spatiotemporal intermittency (STI) mentioned in Sect. 9.1.3 is not the kind of intermittency treated here, since regular and irregular phases extend in STI over finite regions of the real space only. It may be useful to study spatiotemporal intermittency in terms of the underlying chaotic saddles. At present, little is known about the scaling with system size of the lifetimes associated with the intermittent dynamics discussed here.

9.5 Fractal Properties of Supertransients

9.5.1 Dimensions

Supertransients have specific fractal properties, as emphasized in [462–465]. It has been observed that chaotic saddles underlying long transients typically have a stable manifold whose dimension is close to that of the phase space. The basin of attraction of the regular asymptotic attractor can be determined on a plane of initial conditions of just a few variables (Fig. 9.12a). In a long observation time only a few points converge to the attractor; the others remain away from it. These points represent initial conditions that stay close to the chaotic saddle's stable manifold. Alternatively, in a
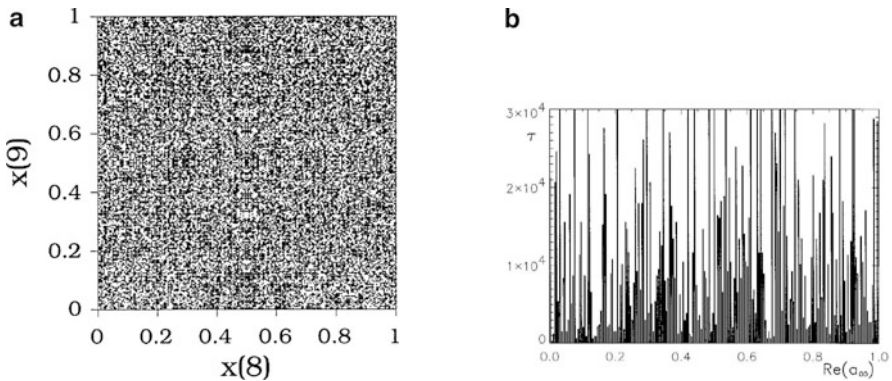
Fig. 9.12 (**a**) Stable manifold of a chaotic saddle (*black dots*) in the plane of two variables of a CML described by (9.1) [465] (copyright 1995, the American Physical Society). (**b**) Transient lifetime as a function of the initial condition taken from a one-dimensional line in the phase space of the cGL equation in its supertransient state [98] (copyright 1996, the American Physical Society). The dimension of the set of points with long lifetimes is denoted by d_s

plot of the lifetime function, the lifetimes needed to reach the attractor as a function of a single initial coordinate also appear to be dense (Fig. 9.12b). It is useful to introduce, as in scattering problems (Sect. 6.2), the box-counting dimension d_s as the dimension of the set of points where the lifetime is formally infinite along such a segment. Since infinite lifetime values belong to the stable manifold of the saddle, this d_s is the dimension of the intersection of a line with the stable manifold of the saddle.

As a quantitative measure of the fractality, the uncertainty exponent (Sect. 5.3) can be determined. The numerical value of α was found to be as small as 10^{-3} (cf. Fig. 9.13), indicating that d_s is quite close to unity. It was also shown [462–464] that the largest Lyapunov exponent computed at fixed finite time is extremely sensitive to small changes in the parameters. Supertransients are thus characterized by riddled structures in the parameter space.

A simple formula for the partial dimension d_s was conjectured in [465]. In particular, escape occurs mostly along the direction of the largest positive Lyapunov exponent λ_{max}. The system is therefore expected to behave effectively as a two-dimensional system with positive Lyapunov exponent λ_{max}. Utilizing the Kantz–Grassberger relation (2.76), one obtains the following information dimension $d_{s,1}$ of the set of singularities:

$$d_{s,1}(L) = 1 - \frac{\kappa(L)}{\lambda_{max}}. \tag{9.13}$$

Taking into account that the dimension of a set resulting from the intersection of two sets follows from the rule according to which the codimensions are additive, (8.52), one finds for an N-dimensional map that the information dimension $D_{s,1}$ of the stable manifold is given by

$$D_{s,1}(L) = N + d_s - 1 = N - \frac{\kappa(L)}{\lambda_{max}}. \tag{9.14}$$

Fig. 9.13 Plot of the fraction of uncertain initial conditions $f(\varepsilon)$ versus uncertainty ε. With the value of the uncertainty exponent α, the box-counting dimension d_s is $d_s = 0.9985$, a quantity that is hardly distinguishable from unity [465] (copyright 1995, the American Physical Society)
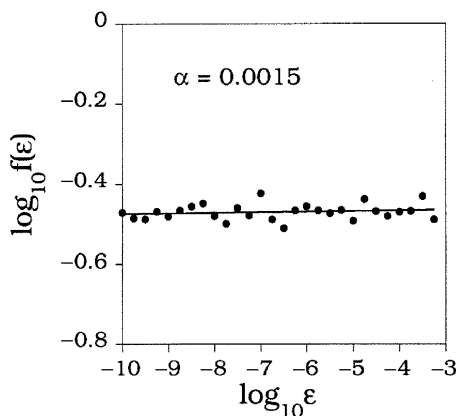
We see that since κ is small, the dimension of the stable manifold is close, for type-II supertransients exponentially close, to the dimension of the phase space.

Equation (9.14) in fact follows directly from the general dimension formulas in Sect. 8.2.2. In particular, consider an $(N \gg 1)$-dimensional map with a small escape rate. When κ is nearly zero, the only possibility for the left-hand side of (8.23) to be larger than K_1 is that all the positive Lyapunov exponents appear on the right-hand side, i.e., $J + 1 = U$. The numerator in the ratio in (8.24) then contains $\lambda_U^+ - \kappa = \lambda_{\max} - \kappa$. Since $S + J = S + U - 1 = N - 1$, we recover (9.14).

The dimension formula (8.21) for the unstable manifold can also be applied. For spatiotemporal systems with small escape rate, observe first that the condition (8.20) requires that the sum of all Lyapunov exponents (with signs taken into account) up to index I be greater than κ, but up to index $I + 1$ be smaller than κ. For near-zero values of κ, the sums should practically be positive and negative, respectively. This is the condition in the Kaplan–Yorke formula (see (8.21) with $\kappa = 0$)

$$D_1 = U + I + \frac{\lambda_1^+ + \cdots + \lambda_U^+ - (\lambda_1^- + \cdots + \lambda_I^-)}{\lambda_{I+1}^-} \tag{9.15}$$

for chaotic attractors. One can then imagine a chaotic attractor with the same Lyapunov exponent spectrum as the saddle, and denote its information dimension by $D_{\mathrm{attr},1}$. Given a discrete set of Lyapunov exponents, a small κ does not change the value of I, and we can write

$$D_{\mathrm{u},1}(L) = D_{\mathrm{attr},1} - \frac{\kappa(L)}{\lambda_{I+1}^-}. \tag{9.16}$$

For the saddle's dimension we then obtain, from (9.14),

$$D_1(L) = D_{\mathrm{attr},1} - \kappa(L) \left(\frac{1}{\lambda_{\max}} + \frac{1}{\lambda_{I+1}^-} \right) = D_{\mathrm{u},1}(L) - \frac{\kappa(L)}{\lambda_{\max}}. \tag{9.17}$$

Equations (9.14), (9.16), and (9.17) illustrate that a supertransient chaotic saddle is a *quasiattractor* in the sense that its dimension is close to that of an attractor (with almost identical Lyapunov spectrum), its stable manifold is nearly space-filling (close to forming a basin of attraction), and its unstable manifold has nearly the same dimension as the chaotic saddle (for an attractor, $D_{\mathrm{u},1}$ and D_1 coincide). These observations indicate that the dimension of supertransient chaotic saddles can be approximated by the Kaplan–Yorke formula, and explain why statistical averages are so well defined on supertransient chaotic saddles. The validity of relations (9.14) and (9.16) was recently illustrated for various high-dimensional reaction–diffusion systems [734].

It is worth mentioning that although the stable manifold is nearly space-filling, the unstable manifold's dimension can take on any value. It is the number U of positive Lyapunov exponents and the index I that essentially determine the value of $D_{\mathrm{u},1}$. In principle, it can assume a small value even in a high-dimensional phase space.

9.5.2   Dimension Densities

In high-dimensional systems it is useful to define dimension densities [85,487,831], i.e., quantities expressing the dimension falling on a single degree of freedom. For supertransients, the dimension density $\delta_s \equiv D_s/N$ of the stable manifold is close to unity. Little is known, however, about the dimension densities $\delta_u = D_{u,1}/N$ and $\delta = D_1/N$ of the unstable manifold and of the saddle, respectively. The question so far has been addressed in a few cases only. In particular, for a model of excitable media, Strain and Greenside [741], and for different RD systems, Stahlke and Wackerbauer [734], found the dimension density of the chaotic saddle to be of order a few percent. This is also consistent with the observation [516] that the number of positive Lyapunov exponents is small even in large systems (although the number increases with the system size).

An important dynamical property in high-dimensional systems is the existence of a Lyapunov density [85]. It implies that the set of the Lyapunov exponents $\lambda_j^\pm$, defined by (8.5), as a function of $x \equiv j/N$ converges for $N \rightarrow \infty$ to a well-defined function $\Lambda^\pm(x)$, as exemplified by Fig. 9.14. In such a case the number U of positive (or negative) Lyapunov exponents scales with the dimension of the phase space, and U/N converges to a constant. As a result, the metric entropy (8.9) can be written as

$$K = \int_0^{U/N} \Lambda^+(x)\mathrm{d}x - \kappa. \tag{9.18}$$

Similarly, the sums defining the indices J and I, (8.23) and (8.20), more precisely the ratios J/N and I/N, can also be expressed as integrals, which depend on the value of the escape rate. For small escape rates, however, the dependencies are weak, and
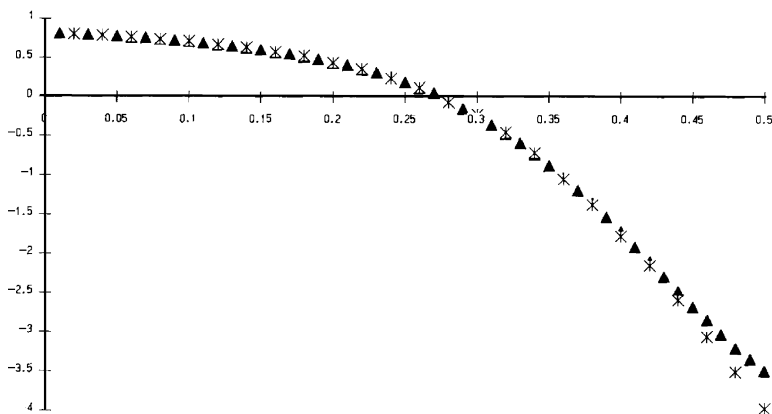
Fig. 9.14 Spectrum of Lyapunov exponents λ_j associated with chaotic transients for a CML of size $N = 50$ (*crosses*) and $N = 100$ (*triangles*), as a function of $x = j/N$. The convergence to a limiting Lyapunov density can be seen [487] (with kind permission from Elsevier Science)

we have $J/N = (U-1)/N \to U/N$. Since the fraction appearing in the general expression of $D_{s,1}$ and $D_{u,1}$ is always less than one, it does not contribute to the dimension density. Supertransients are thus characterized by the following dimension densities:

$$\delta_s = \frac{S+U}{N} = 1, \quad \delta = \delta_u = \frac{U+I}{N}. \tag{9.19}$$

It is worth defining the signed Lyapunov density $\Lambda(x)$, as shown in Fig. 9.14. Since, as stipulated by (8.5), $\Lambda(x) = \Lambda^+(U/N - x)$ for $0 \le x \le U/N$ and $\Lambda(x) = -\Lambda^-(x - U/N)$ for $1 \ge x \ge U/N$, the nontrivial dimension density $\delta_u = \delta$ also satisfies the equation

$$\int_0^{\delta_u} \Lambda(x)\,\mathrm{d}x = 0. \tag{9.20}$$

When considering the integral of the signed Lyapunov density between zero and some value x, the dimension density is the x value for which the integral vanishes. In fact, (9.20) is valid for spatiotemporal chaotic attractors as well [262]. We conclude that the picture based on the Lyapunov and dimension densities suppresses the role of the finite lifetime of chaos, and emphasizes the quasiattractor character of supertransients.

The problem of stable chaos (Sect. 9.2.4) deserves special attention. Although these systems appear to exhibit fractal features, dimension formulas (8.21) and (8.24) are not applicable. In fact, these relations are valid for generic chaotic saddles, but that is not the case here. There is a possibility for strange nonchaotic saddles to arise in analogy with strange nonchaotic attractors [241]. (For strange nonchaotic repellers of one-dimensional maps, see Sect. 2.4.) A strange nonchaotic spatiotemporal saddle might have a box-counting dimension that does not increase linearly with the system size, i.e., with a density $\delta_u = \delta = 0$.

9.6 Turbulence in Pipe Flows

9.6.1 Turbulence Lifetime

The transition to turbulence in pipe flows has long been a fascinating problem in fluid dynamics (for reviews, see [216, 217, 299]). Investigations of the phenomenon began in the second part of the nineteenth century with the milestone experiments of Reynolds in 1883. He pointed out that in a pipe of fixed length the flow changes from smooth (laminar) to irregular (turbulent) at sufficiently large flow velocities. A good dimensionless measure of the flow velocity is the Reynolds number $Re = UD/\nu$, with U and D chosen as the mean flow speed across the pipe and the diameter, respectively. When the flow velocity slowly increases in a given setting, the transition from laminar flow to turbulence occurs abruptly at a critical Reynolds number Re_c of order 2,000. Early experiments indicated, however, that under controlled conditions the laminar flow can be maintained up to Reynolds numbers much larger

than 2,000. It was recognized later that the roughness of the wall's surface plays an important role: the rougher the wall, the smaller the critical Reynolds number. More recent investigations have led to the observation that perturbations to the laminar flow such as those caused by surface roughness are needed to trigger turbulence, and the critical Reynolds number Re_c depends on the type and the strength of the perturbation. Thus the onset of turbulence is determined not only by the Reynolds number but also by the perturbation. To trigger turbulence, the flow has to be sufficiently fast and the perturbation has to be sufficiently strong. The required perturbation is, however, smaller for larger values of the Reynolds number. Therefore, in any experimental setting in which small perturbations cannot be avoided, turbulence will always appear at sufficiently large values of the Reynolds number.

The steady laminar solution, such as the parabola profile in a pipe of circular cross section, is linearly stable for *all* Reynolds numbers [299]. In dynamical-system terms, this implies the existence of a fixed-point attractor in the infinite-dimensional phase space, with a relatively small basin of attraction. In addition, there is no evidence for the existence of any stable state with simple spatial or temporal pattern, e.g., traveling waves, which would be the analogues of limit cycle attractors. The turbulent state can be considered a high-dimensional chaotic state associated with either a chaotic attractor or a chaotic saddle.

The first indication of the transient character of pipe turbulence appeared about 20 years ago [99, 299], based on investigations of the stability of the laminar profile. There has been increasing experimental evidence since then indicating that even if the turbulent state is established for not too large Reynolds numbers, this state can suddenly decay, without any apparent precursor, toward the laminar state. This implies that the chaotic sets for not too large values of the Reynolds number are nonattracting. Research has then been concentrated on the average lifetime τ of the chaotic saddle. The classical experiments suggest that the lifetime is rather large, for otherwise, the turbulence would not have appeared to be permanent to earlier investigators. The use of long pipes and efficient numerical methods have made more detailed investigations possible. Figure 1.23 shows the experimental findings of Peixinho and Mullin on the exponential decay in time. The value of the escape rate appears to be *independent* of the details of the initial perturbation, but depends on the Reynolds number only. The exponential decay sets in only after some time t_0 in any experimental run.

When plotting the actual lifetime as a function of the perturbation amplitude A to trigger the turbulence in numerical simulations, a more detailed picture can be obtained. A slight change in the amplitude can lead to drastically different lifetimes if the amplitude is above a threshold (Fig. 9.15). The irregular part of the lifetime distribution is fractal. Furthermore, the average Lyapunov exponent during the turbulent phase was shown to be strictly positive [231]. These features indicate that the high-dimensional saddle underlying the turbulence has all the characteristics of low-dimensional chaotic saddles and of transient chaos in many other spatiotemporal systems.

A basic question is the dependence of the turbulent escape rate on the Reynolds number. In the class of functions exhibiting a rapid decrease with the Reynolds
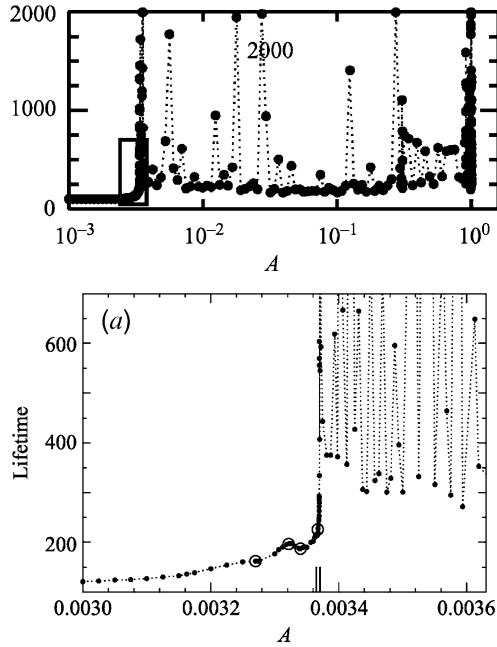
Fig. 9.15 Turbulence lifetime versus perturbation amplitude A in a pipe at Reynolds number $Re = 2{,}000$ obtained numerically. The *bottom panel* is a magnification of the box indicated in the *top panel*. At the edge of chaos, at the value marked by two *vertical bars*, the function turns from smooth to fractal-like, indicating that chaotic transients are triggered by sufficiently large amplitudes [231] (with kind permission from Cambridge University Press)

number, a choice is some functions that approach zero for a finite value of Re. This form can retain one aspect of the original picture, namely that beyond a threshold Reynolds number, permanent turbulence can be present. The laminar fixed-point attractor would then coexist with the chaotic attractor of the turbulence. Another choice is some monotonically decreasing functions of Re with nonzero values for any Re. Using a pipe of length 30 m, experiments by Hof, Westerweel, Schneider, and Eckhardt [336] provided a firm answer to the question. In a set of experiments covering more than two decades of lifetimes, they showed that the escape rate is nonzero up to large values of Re. This suggests that *turbulence remains a transient*, a feature also observed in superfluid turbulence [693] and magneto hydrodynamical turbulence [639]. By measuring time in units of D/U, the dimensionless escape rate was found in [160, 217, 336] to scale with Re as

$$\kappa(Re) = a\mathrm{e}^{-bRe} \tag{9.21}$$

with parameter b between 0.03 and 0.04 (see Fig. 9.16). According to this rule, any increase in the Reynolds number by 100 implies a multiplication of the escape rate by a factor of $1/33$. Thus, pipe turbulence is a kind of type-II supertransient (with system size replaced by the Reynolds number).
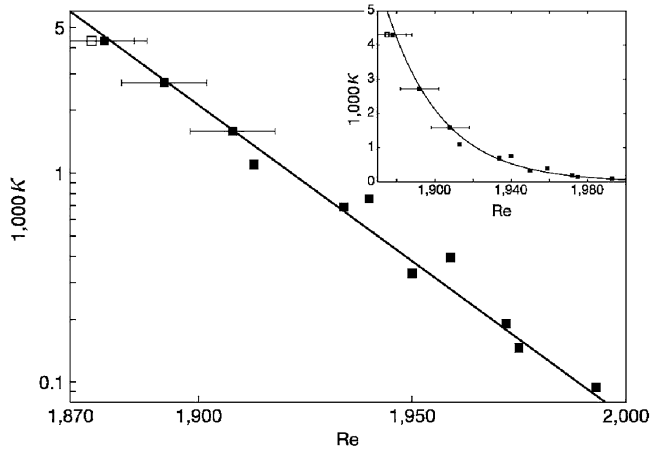
Fig. 9.16 Escape rate as a function of the Reynolds number in the experiment by Hof et al. The *straight-line* fit corresponds to formula (9.21). The *inset* shows the same data on a linear scale to illustrate that the escape rate is asymptotic to zero rather than crossing the horizontal axis at a finite value of *Re* [217] (with kind permission from Annual Reviews)

A recent experimental study by Hof, de Lozar, Kuik, and Westerweel [334] extended the range of turbulent lifetimes by six orders of magnitude by collecting data from four pipe setups with significantly reduced statistical errors. The extended data set (which contains, as a subset, the points of Fig. 9.16) suggests a superexponential scaling with the Reynolds number in the form of

$$\kappa(Re) = \exp\left[-\exp\left(c_1 Re + c_2\right)\right] \tag{9.22}$$

with $c_1 = 0.0057$, $c_2 = -8.7$. This fit is valid in the Reynolds-number range $(1670, 2040)$, where the dimensionless κ changes between 0.2 and 10^{-8}. Note that a further extension of these results is hardly possible, since due to the rapid increase in the lifetime, the measurement at $Re = 2,100$ would already require an estimated time of 46 years [334, 663].

Due to extended and improved numerical methods, the range of Reynolds numbers and sample sizes of experiments have become accessible in computer simulations. The results of [33] were in close quantitative agreement with the form of (9.22). Similar superexponential scaling of lifetimes was reported in a Taylor–Couette flow [95].

A possible theoretical explanation of the superexponential scaling was provided by Goldenfeld and coworkers [267]. The authors argued that the determining factor for the suppression of a puff is the probability that the largest velocity fluctuations fall below some threshold value. These large-amplitude events follow extremal statistics. From general results on such statistics the superexponential form of (9.22) can be derived.

9.6.2   Other Aspects of Hydrodynamical Supertransients

An interesting feature of the lifetime distribution versus perturbation amplitude, as shown in Fig. 9.15, is that slowly varying regions are interwoven with intervals of rapid change. In the smooth regions the transients are short and nonchaotic. The transition (indicated by two bars in Fig. 9.15) between the extended smooth region at small amplitudes and the region with fractal fluctuations is rather abrupt. This point on the border between laminar and chaotic regions is called the *edge of chaos* [691, 720], which separates initial conditions that decay directly to the laminar attractor and those that come close to the chaotic saddle first, i.e., exhibit turbulence. Trajectories starting from the edge of chaos move in a region intermediate between laminar and turbulent dynamics. The results of [409, 520, 691, 720, 803] suggest that the edge of chaos lies, for any Reynolds number, in the stable manifold of an invariant object, the edge state that resides in the phase space between the fixed point and the chaotic saddle. The stable manifold is thus a kind of basin boundary between the laminar and the turbulent dynamics. The latter, of course, cannot have a real basin of attraction, but only one that appears to be so in finite-time observations (the quasiattractor character discussed in Sect. 9.5). The dynamics restricted to the edge of chaos converges to a chaotic state, the edge state, and numerical simulations in pipe flows indicated that it corresponds indeed to an irregular wavy motion along the pipe, which is, however, less energetic than the turbulent dynamics itself [691]. This attractor is only a relative attractor, since it is unstable with respect to perturbations perpendicular to the edge of chaos.

Low-dimensional chaotic saddles contain an infinite number of unstable periodic orbits (Sect. 2.6.4). In an analogous way, the chaotic saddle underlying pipe turbulence is expected to contain coherent structures. Both in theory and experiments, they were shown to be regular traveling waves [229, 335], all *unstable*, corresponding to hyperbolic states in the high-dimensional phase space. Currently, there is an intensive search underway for such coherent structures (spatiotemporal patterns) [213, 263, 303, 690, 800] about which chaos is organized. Over a long-time observation of turbulence one expects to see different coherent states in different time intervals. This kind of approach may eventually lead to a periodic-orbit expansion [153] of the chaotic saddle, in full analogy with low-dimensional problems (see Appendix A). There is then hope that the statistical properties of the turbulent flow can be expressed in terms of the properties of the coherent structures.

Finally, we mention that there are other hydrodynamical situations in which the onset of turbulence is similar to that in pipe flows. Notable examples are plane Poiseuille flows (pressure-driven flows between two large parallel plates) [816] and Couette flows (driven by a moving wall) [215, 686, 692]. The common feature in these shear flows is that the laminar profile is stable.[1] One expects therefore in these situations that turbulence is not permanent and decays eventually toward

---

[1] Plane Poiseuille flows are linearly unstable, but the critical Reynolds number is much above the value at which turbulence transition occurs [217].

a laminar profile. Shear-flow turbulence is thus a case of its own, and is present in the form of high-dimensional chaotic transients. We are thus currently witnessing the appearance of concepts of transient chaos in the study of classical turbulence.

9.7 Closing Remarks

In this chapter we have focused on supertransients. Although they are quite common, there are cases in which the distribution of transient lifetimes is not exponential, or if it is, the average lifetime does not grow rapidly with the system size. It may, e.g., become saturated (for examples, see [252] and [831]). The type of coupling plays an important role [797]. It is, nevertheless, an open question at present whether one can decide from first principles if a system exhibits super-transients. In fact, the question of how to decide whether a spatiotemporal system possesses a chaotic attractor has not been answered. A systematic application of nonlinear stability analysis to different possible asymptotic patterns [517] may provide insights. A recent investigation [813] showed that the master-stability function [583], a central tool in the theory of synchronization in dynamical systems, can successfully be applied as an indicator for transient versus permanent spatiotemporal chaos.

A somewhat analogous phenomenon to supertransients was found in Hamiltonian systems with many degrees of freedom. Any isolated macroscopic system should eventually relax to a state of thermal equilibrium in which any macroscopic variable is independent of time. Nevertheless, in systems with global (mean field) coupling, long relaxations were found whose average time diverges with the number of components [14, 21, 607, 839]. More recently, a metastable state was discovered [531], as characterized by periodic or quasiperiodic oscillations of macroscopic variables about mean values that are different from the respective equilibrium values. The lifetime of the metastable state was found to increase linearly with the number of degrees of freedom. The underlying microscopic dynamics is chaotic, but must have different characters in the metastable and equilibrium states. Both examples can be considered as type-I supertransients, which last long in the thermodynamic limit.

In some spatiotemporal problems the linear size may not be freely chosen. Long transients may, nevertheless, be present (see, e.g., [188, 841]), but it is not apparent whether they scale at all with some parameter of the problem. It is useful to find a scaling parameter in such cases and check whether the dependence is power-law or exponential. In the case of time-delayed systems [841], a natural candidate for some scaling parameter is the delay time.

It is worth pointing out a difference between the shear-turbulence problem and the supertransient phenomena in spatially extended systems other than pipe flows. The scaling in turbulence is not with respect to the length of the pipe, but rather with the diameter D in the Reynolds number. It would be interesting to understand this difference better.

The concept of unstable coherent structures as building blocks for a periodic-orbit type of expansion of the chaotic saddle, or those of the edge of chaos and the invariant sets associated with it, can be applied to all systems exhibiting supertransients. It is quite remarkable that problems ranging from fluid dynamics and chemistry to population dynamics and biology with quite different underlying mathematical structures all share similar features, dominated by long-lasting chaotic transients. A unified understanding of the physics underlying this phenomenon deserves further efforts.

Part IV
Applications of Transient Chaos

Chapter 10
Chaotic Advection in Fluid Flows

The advection of tracer particles in hydrodynamical flows represents one of the successful applications of chaos theory. The basic observation is that molecular diffusion is negligible on the typical time scale of the flow.[1] As a result, in the absence of any diffusion-enhancing mechanism such as hydrodynamical turbulence, advection dominates. Indeed, the main physical mechanism for fluid stirring is advection, whose efficiency can be enhanced greatly by chaotic dynamics. The spreading of pollutants on large scales is also dominated by advection. Potential applications of chaotic advection range from laboratory investigations of fluid dynamics to the study of large-scale environmental flows. From the point of view of dynamical systems, an appealing feature of the passive advection problem is that its phase space coincides with the physical space of the fluid, rendering possible direct experimental observation and characterization of fractal structures associated with chaotic dynamics.

This chapter is devoted to transiently chaotic advective dynamics in hydrodynamical flows. If a fluid system is open, as schematically shown in Fig. 10.1, transient chaos can arise. More precisely, a flow is open if there is a net current flowing through the region of observation. A typical example is the flow around a fixed obstacle, such as a cylinder placed in a channel. In environmental science, flows around an island or a peninsula can generate transiently chaotic advection. In an open flow, the dynamical trajectories of advective particles are typically unbounded in the sense that nearly all particles escape the region where strong stirring takes place in a finite time. The dynamical invariant sets responsible for such chaotic advective dynamics are chaotic saddles. Because of the coincidence of the phase space with the physical space, chaotic saddles and their invariant manifolds are effectively hydrodynamical observables. In the context of the spreading of materials in flows, of interest is not a single-particle trajectory but rather the motions of an ensemble of trajectories

---

[1] In particular, if the length and velocity scales are L and U, respectively, the typical hydrodynamical time scale is L/U and the diffusive time scale is L^2/D_{diff}, where D_{diff} is the diffusion coefficient, whose typical value for water and most tracer substances is of order 10^{-8} m^2/s. Suppose $L = 1$ m and $U = 0.1$ m/s. The hydrodynamical and the diffusive time scales are thus ten seconds and one thousand days, respectively, rendering physically irrelevant any diffusive processes in the flow.
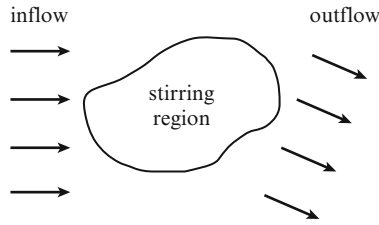
Fig. 10.1 Schematic diagram illustrating an open flow that generates transiently chaotic advective dynamics. The flow can be time-dependent and relatively complicated in a bounded region, the stirring region, while the incoming and outgoing flows far away from the region can be simple

originated from a dye droplet. Spreading of substances such as pollutants in a flow can therefore occur along fractal patterns determined by the unstable manifold of the chaotic saddle associated with the flow.

This chapter is organized, as follows. After establishing the analogy between advection in open incompressible flows and chaotic scattering, we consider two paradigmatic time-periodic flows and treat the dynamics of dye droplets, transport properties (lobe dynamics), and the fractality of dye boundaries. We then consider aperiodic or chaotically time-dependent flows and address the problem of coherent structures. The effect of artificial leaking of the advective dynamics of closed flows will be shown to reveal useful information via the transients caused by the leak. The advective dynamics of finite-size particles will also be considered. Finally, how chemical or biological reactions take place in open flows with chaotic advective dynamics will be considered, which is of interest in fields ranging from chemical reactions and combustion to atmospheric chemistry and the population dynamics of plankton.

10.1 General Setting of Passive Advective Dynamics

For an idealized particle of zero size and zero mass, its velocity $\dot{\mathbf{r}}$ is the flow velocity $\mathbf{u}(\mathbf{r},t)$ at any time instant. In the theory of advection, the velocity field is assumed to be known and the advective dynamics, or the *Lagrangian dynamics*, are described by

$$\dot{\mathbf{r}}(t) = \mathbf{u}[\mathbf{r}(t),t]. \tag{10.1}$$

The solution to this equation is the path $\mathbf{r}(t)$ of the particle. Because of the explicit time dependence, (10.1) consists of three first-order ordinary differential equations that can be nonautonomous and nonlinear. Chaos can then arise, leading to chaotic advection [26]. Note that the main phase-space variables are the components of $\mathbf{r}$ that specify the position of the particle in the actual physical space.

Advection in *two-dimensional*, *incompressible* flows specified by $\mathbf{r} = (x,y)$ and $\mathbf{u} = (u_x, u_y)$ is especially interesting because of its equivalence to motion in one-degree-of-freedom Hamiltonian systems. In particular, the condition of

incompressibility implies the existence of some stream function [429] $\psi(x,y,t)$ that determines the velocity components of flow as

$$u_x(x,y,t) = \frac{\partial \psi(x,y,t)}{\partial y}, \quad u_y(x,y,t) = -\frac{\partial \psi(x,y,t)}{\partial x}. \tag{10.2}$$

Incompressibility is ensured because

$$\mathrm{div}\mathbf{u} = \partial u_x/\partial x + \partial u_y/\partial y = 0.$$

The streamlines $y(x)$, the tangent lines to the local velocity $\mathbf{u}$ at point (x,y), satisfy the equation

$$\frac{\mathrm{d}y}{\mathrm{d}x} = \frac{u_y}{u_x} \tag{10.3}$$

at any instant of time. As a consequence, we have $u_y\,\mathrm{d}x - u_x\,\mathrm{d}y = 0$, which implies that $\mathrm{d}\psi(x,y,t) = 0$ according to (10.2). The streamlines are thus contour lines of the stream function. Equations of motion for the advective dynamics are

$$\dot{x} = \frac{\partial \psi(x,y,t)}{\partial y}, \quad \dot{y} = -\frac{\partial \psi(x,y,t)}{\partial x}, \tag{10.4}$$

which are equivalent to Hamilton's equations of motion [268] in classical mechanics under the "Hamiltonian" $\psi(x,y,t)$. In the Hamiltonian formulation, the coordinate variables x and y in the physical space correspond to the generalized position and momentum variables. Consequently, in the (x,y) plane, we obtain area-preserving tracer dynamics.

Depending on whether the flow is steady or unsteady, the tracer dynamics can be simple or complex. In particular, for steady flows, the stream function is time-independent: $\psi = \psi(x,y)$. Equations (10.4) are thus a set of two autonomous first-order differential equations. The total time derivative of ψ along a tracer trajectory is

$$\frac{\mathrm{d}\psi(\mathbf{r}(t))}{\mathrm{d}t} = \frac{\partial \psi}{\partial x}\dot{x} + \frac{\partial \psi}{\partial y}\dot{y} = 0, \tag{10.5}$$

indicating that the trajectory actually coincides with a streamline. The dynamics is integrable, since there exists a conserved quantity, ψ, the analogue of the energy of conservative motion of a point particle in one dimension. However, when the stream function depends explicitly on time, the advective dynamics is described by a time-dependent Hamiltonian function that effectively has one and a half degrees of freedom. In this case, trajectories do not coincide with the streamlines, and in fact, they can be much more complicated than the streamlines. Even if the streamlines are smooth time-dependent curves, which arise when no turbulence is present in the flow field, the particle trajectories can be quite complex. Indeed, motions of tracer particles can typically be chaotic even for simple time-periodic flows. Chaos associated with tracer dynamics is sometimes called Lagrangian turbulence.

In the past three decades, a great amount of knowledge about advective dynamics has been obtained both for closed [27, 569, 826] and for open flows [394].

For open two-dimensional incompressible flows with asymptotic simplicity, i.e., situations in which there is a central stirring region, and the incoming and the outgoing flows far away from the region are simple and stationary (see Fig. 10.1), time-dependence is important, but only for the stirring region. The asymptotic dynamics are then simple, and the tracer motion can be considered a scattering process with characteristics of *chaotic scattering* (Chap. 6), where the stirring region plays the role of the scattering region.

10.2 Passive Advection in von Kármán Vortex Streets

10.2.1 Flow Model

Flow around an obstacle is a classical problem in fluid mechanics [206, 429]. We consider a viscous, incompressible flow around a long cylinder of radius R_0. Far away from the obstacle, the flow is uniform. For convenience, we can label the longitudinal flow direction x and the transverse direction y. Let U be the flow velocity for $x \to \pm\infty$. The Reynolds number is defined as

$$Re = 2R_0U/\nu, \tag{10.6}$$

where ν is the kinematic viscosity of the fluid. For sufficiently small values of Re, the flow is stationary. As Re is increased through a critical value $Re_c \approx 80$ [206,429], the stationary solution of the Navier–Stokes equation becomes unstable, and the flow becomes time-periodic of with period T:

$$\mathbf{u}(\mathbf{r}, t + T) = \mathbf{u}(\mathbf{r}, t). \tag{10.7}$$

In this case, vortices are created in the wake of the cylinder, detach from it, and drift downstream. They gradually lose strength because of viscosity and typically die out after some distance. New vortices are shed from the cylinder surface at intervals of half a period $T/2$, alternating above and below the middle of the cylinder, as shown in Fig. 10.2. This process generates a *von Kármán vortex street* behind the cylinder. In the following, for simplicity we assume that at any instant there are at most two vortices in the flow. That is, the lifetime of each detached vortex is equal to one period T.

The flow associated with the von Kármán vortex street was studied by direct numerical simulation of the Navier–Stokes equation for $Re = 250$ under the usual no-slip boundary conditions on the surface of the cylinder [371], based on which an analytical model for the time-periodic flow was proposed [370, 854]. In the analytic model, the stream function ψ is given by

$$\psi(x, y, t) = f(x, y)g(x, y, t), \tag{10.8}$$
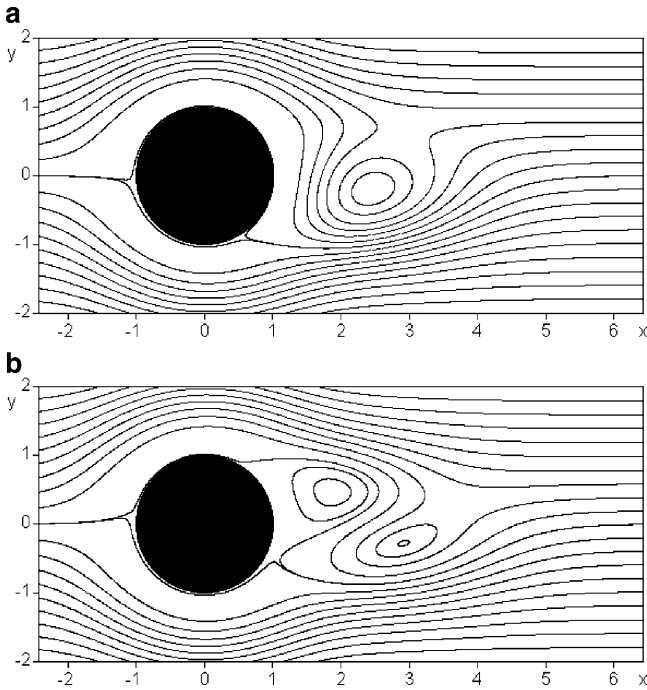
Fig. 10.2 Streamlines of the von Kármán flow (10.8) around a cylinder at two different instants (**a,b**) of time, separated by one quarter of the full period of the flow. The flow is from left to right. The vortex shedding can be seen, and this process sets the stirring region to be approximately $1 < x < 4$, $|y| < 1$ [771] (with kind permission from Elsevier Science)

where the factor

$$f(x,y) = 1 - \exp\{-a[(x^2 + y^2)^{1/2} - 1]^2\} \tag{10.9}$$

guarantees the no-slip boundary condition at the surface of the cylinder whose radius is chosen to be unity $R_0 = 1$ (equivalently, the radius R_0 is taken to be the length unit of the system). The quantity $a^{-1/2}$ plays the role of the width of the boundary layer. The time unit is chosen to be the period of the flow: $T = 1$. The function $g(x,y,t)$ in (10.8) is

$$g(x,y,t) = -Wh_1(t)g_1(x,y,t) + Wh_2(t)g_2(x,y,t) + u_0ys(x,y), \tag{10.10}$$

where the first two terms describe the alternating birth and the subsequent death of the vortices, respectively. The maximum vortex amplitude is W, with time-dependence described by

$$h_1(t) = |\sin(\pi t)|, \quad h_2(t) = h_1(t - 1/2). \tag{10.11}$$

The vortices are of Gaussian shape of characteristic linear size $r^{-1/2}$, so the functions $g_1(x,y,t)$ and $g_2(x,y,t)$ are given by

$$g_i(x,y,t) = \exp\left(-r\left\{[x - x_i(t)]^2 + \alpha^2[y - (-1)^{i-1}y_0]^2\right\}\right), \quad i = 1, 2, \quad (10.12)$$

whose centers move downstream at constant velocity:

$$x_1(t) = 1 + l_0\,[t \bmod 1]; \quad x_2(t) = x_1(t - 1/2), \quad (10.13)$$

where y_0 is the distance of the vortex centers from the x-axis. The last term in (10.10) arises from the background flow, and the screening factor

$$s(x,y) = 1 - \exp\left[-(x-1)^2/\alpha^2 - y^2\right] \quad (10.14)$$

ensures that the effect of the background flow of dimensionless velocity $u_0 = UT/R_0$ is reduced in the wake. The parameters were set as $a = 1$, $\alpha = 2$, $r = 0.35$, $l_0 = 2$, $y_0 = 0.3$, $u_0 = 14$, and $W = 24$ to fit the direct numerical solution to that of the Navier–Stokes equation [370]. In fact, results obtained from the analytic model are robust with respect to the dynamics under study, so the exact values of the parameters are not so important. Only in the wake of the cylinder is the flow nontrivial, being time-dependent because of the vortex shedding. As a result, the stirring region is the time-dependent part of the flow, situated within an area of finite extension (of length about l_0 along the x-direction) in the wake. The model thus serves as a paradigm for a large class of open chaotic flows and has been used widely in the studies of various aspects of transient chaotic advection [61, 664, 665, 669, 670, 682] A generalization of these ideas led to the conclusion that the chaotic motion of particles transported by blood can play an important role in the development of certain circulatory diseases [681]. An extension of the model to more than two vortices in the wake has recently been worked out [835].

10.2.2 Advection and Droplet Dynamics

The motions of passively advected particles can be determined by integrating (10.4) with the stream function (10.8). The chaotic nature of particle motions in the flow can be seen from Fig. 10.3, where trajectories originated from two nearby initial conditions are shown. The trajectories separate from each other quickly, indicating a sensitive dependence on initial conditions, the hallmark of chaos. In both the far upstream and the far downstream regions, particles move along straight lines. However, in the wake, there is a chaotic saddle (Fig. 10.4), whose invariant manifolds play a determining role in particle advection.

The role of the unstable manifold of the chaotic saddle can be assessed by placing a dye droplet of a continuum of particles upstream into the flow and monitoring the deformation of the shape of this droplet, the droplet dynamics (the role of the stable
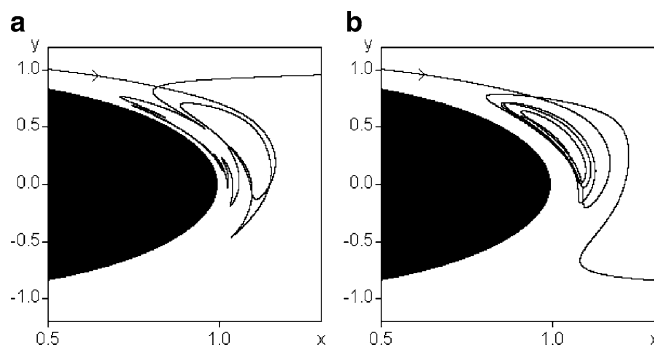
Fig. 10.3 For the von Kármán flow (10.8), two representative (**a,b**) trajectories originated from a pair of nearby initial conditions. The black region is the cylinder that appears to have an elliptical shape due to the different scales in the x- and y-directions in the plot. Sensitive dependence on initial conditions can be seen

manifold will be discussed in Sect. 10.4). If the initial droplet is situated about the x-axis, it overlaps with the stable manifold of the saddle. Particles exactly on the stable manifold approach the saddle and never leave it. Neighboring particles approach the saddle but they typically stay in the vicinity of the saddle for a finite amount of time before exiting the wake along the unstable manifold of the saddle. This suggests that *the unstable manifold is traced out* by particles that stay in the region of observation in the wake for a relatively long time. The unstable manifold of the chaotic saddle arising in advection in open flows can be regarded as the main transport route of the tracer dynamics: particles accumulate on it while being advected away.

In numerical simulations with a finite number of particles, the manifold serves as a periodically moving template that will eventually be emptied. Figure 10.5 shows the evolution of a droplet in the von Kármán flow. The droplet first becomes stretched and folded. It then traces out a moving fractal object, the unstable manifold. The fact that the region is not uniformly emptied in the last panel and particles are still visible around the cylinder suggests a type of dynamics similar to nonhyperbolic chaotic scattering dynamics (Sect. 6.4). In fact, the hyperbolic component (of structures resembling the direct product of two Cantor sets) lies outside the boundary layer and is responsible for an exponential decay of particles, and the nonhyperbolic component is located close to the smooth cylinder surface, which determines the long-time behavior of particle decay from the wake [370]. The different patterns of these two components can be distinguished in Fig. 10.4.

These numerical investigations led Sommerer and coworkers [725] to an experimental investigation of passive advection in the wake of a cylinder. They demonstrated that dye droplets trace out the unstable manifold of the chaotic saddle in the wake, as shown in Fig. 1.19. They also determined the escape rate and the Lyapunov exponent of the transiently chaotic dynamics as well as the asymptotic box-counting dimension of the dye droplet. For a related experiment, see [276].

The von Kármán vortex street is in fact not a particular property of flows with a cylindrical obstacle. Approximately, most two-dimensional flows past an obstacle
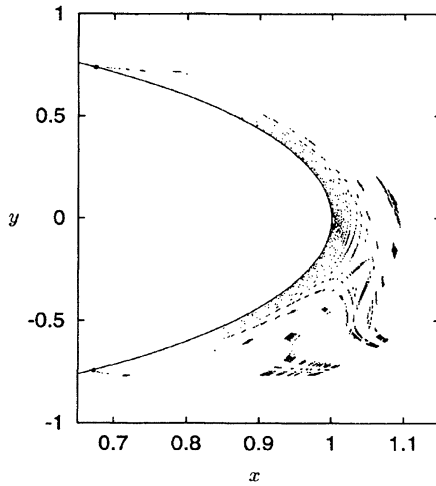
Fig. 10.4 Chaotic saddle in the von Kármán flow obtained by the PIM-triple method. The set of black points represents initial conditions of tracers belonging to a certain time instant ($t = 0.3\mathrm{mod}1$), which do not escape the wake either forward or backward in time. In the advection problem the chaotic saddle appears in the space of the fluid, and it can also be considered the set of never-escaping fluid elements [592] (copyright 1995, the American Physical Society)
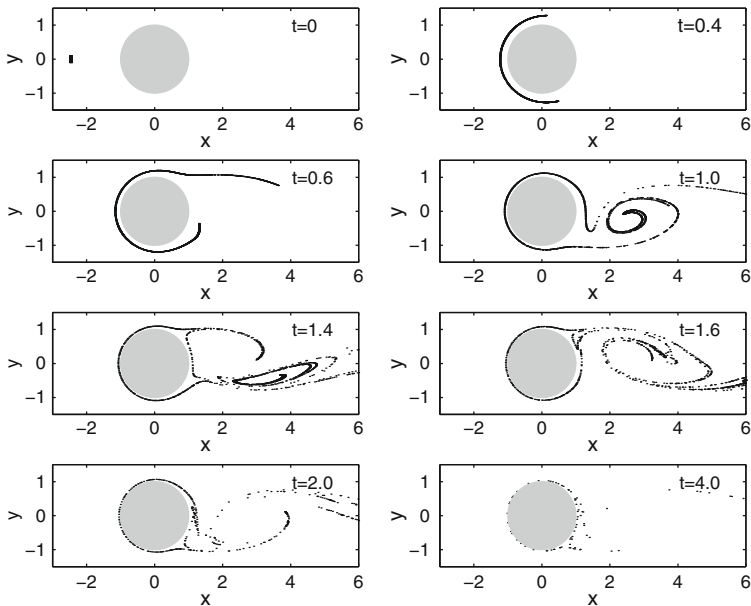
Fig. 10.5 Droplet dynamics: time evolution of a droplet of 20,000 tracers in the von Kármán flow shown at different dimensionless time instants [774] (copyright 2000, the American Institute of Physics)
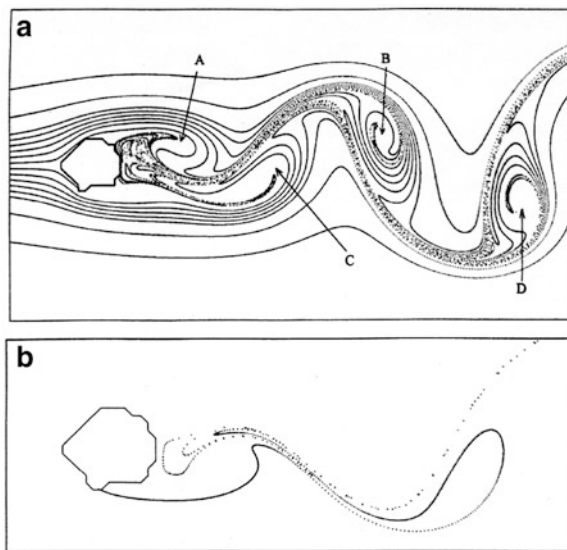
Fig. 10.6 Patterns of a sea current around the Gran Canaria island. Black lines are numerically obtained streaklines, i.e., traces of continuously injected dye from localized point sources. Several streaklines are shown in *panel* (**a**), and a single streakline is shown in *panel* (**b**). Many of the streaklines trace out a fractal pattern, the unstable manifold of the chaotic saddle in the wake of the island [28] (with kind permission from Elsevier Science)

have this property, provided that their Reynolds numbers are in an appropriate range. As a result, von Kármán vortices are found in many realistic situations. For example, Fig. 10.6 shows the dye patterns obtained from a simulation of the sea current around the island of Gran Canaria [28]. Fractal filaments generated by the von Kármán vortices are visible and pronounced.

10.3 Point Vortex Problems

10.3.1 Vortex Dynamics

The dynamics of point vortices in two-dimensional or of parallel vortex lines in three-dimensional *ideal incompressible fluids* is another classical problem in hydrodynamics. It has long been known [412, 467, 549, 662] that the equations of motion of a system of *n* such vortices can be cast into a canonical form. The Hamiltonian is

$$H(\{x_i, y_i\}) = -\frac{1}{\pi} \sum_{i<j} \Gamma_i \Gamma_j \ln r_{i,j}, \qquad (10.15)$$

where (x_i, y_i) stands for the position of vortex i of strength Γ_i ($i = 1, \ldots, n$) in the (x, y)-plane, and $r_{i,j}$ is the distance between vortices i and j. The value E of the Hamiltonian is constant in time and is thus effectively the energy of the vortex system. The equations of motion are determined by the corresponding Hamilton equations [412, 467, 549, 662]:

$$\Gamma_i \dot{x}_i = \frac{\partial H}{\partial y_i}, \quad \Gamma_i \dot{y}_i = -\frac{\partial H}{\partial x_i}. \tag{10.16}$$

The equations can be made dimensionless by the transformations

$$(x, y) \rightarrow (Lx, Ly), \quad t \rightarrow \frac{\pi L^2}{\Gamma} t, \quad H \rightarrow \frac{\Gamma^2}{2\pi} H, \tag{10.17}$$

where Γ is a preselected vortex strength and L denotes a characteristic length scale.

The vortex dynamics possesses conserved quantities. An example is the coordinates of the center of vorticity: $\bar{x} = \sum_i \Gamma_i x_i / \sum_i \Gamma_i$ and $\bar{y} = \sum_i \Gamma_i y_i / \sum_i \Gamma_i$. Besides energy conservation, there are four more conservative constraints. Thus, out of the $2n$ coordinates of the n-vortex problem, only $2n - 5$ are independent. Nonintegrability and chaos require at least three independent nonlinear equations, and hence *the dynamics of four or more vortices can be chaotic.*

An interesting example is the collision of vortex pairs. When two vortex pairs encounter each other, they interact and exchange partners for a finite amount of time. The new couples strongly perturb each other, until a new collision leads to an exchange again. The two original vortex pairs are recovered, and they separate along a straight line from each other. The role of chaos in this scattering process was pointed out by Eckhardt and Aref [214].

An isolated vortex of strength Γ generates at distance r from its center a circulational flow with a velocity field proportional in modulus to Γ/r. The stream function $\psi(x, y)$ is $-(\Gamma/\pi) \ln r$. In a system of n vortices these contributions are superimposed, yielding

$$\psi(x, y, t) = -\sum_j \frac{\Gamma_j}{\pi} \ln r_j(t), \tag{10.18}$$

where $r_j(t)$ is the distance of point (x, y) from vortex j. Because the vortices follow their own dynamics, the distances $r_j(t)$, and consequently the stream function, are time-dependent. For a particle advected by the vortices, the equation of motion is given by (10.4) with the stream function $\psi(x, y, t)$ of (10.18). It is worth noting that the advection problem in the field of n vortices can also be considered as a special $(n+1)$-vortex problem in which one of the vortices is of vorticity zero. This special vortex does not have any feedback on the flow, and hence its motion corresponds to that of a tracer particle. Thus, the passive advection in the field of *three or more vortices is typically chaotic.*

A condition for a vortex flow to be *open* is that the total vortex strength vanish:

$$\sum_i \Gamma_i = 0. \tag{10.19}$$

In this case the center-of-vorticity coordinates are formally infinite, and there is no constraint on the vortices to remain bounded to a finite fluid domain. What happens is that the four vortices can remain close to each other but their geometric center moves ahead in a certain direction. Far from the vortices, the streamlines are straight lines along which the vortices can be approached (for $\sum_i \Gamma_i \neq 0$, the streamlines far from the vortices are closed curves).

10.3.2 Advection by Leapfrogging Vortex Pairs

Consider an example of open flow of four vortices whereby two vortex pairs of equal strengths $(\Gamma_1 = \Gamma_2 = -\Gamma_3 = -\Gamma_4 \equiv \Gamma)$ move in the same direction along a symmetry axis, the x-axis. The Hamiltonian of the system is [590] (for notation see Fig. 10.7)

$$H(x_1, x_2, y_1, y_2) = \frac{\Gamma^2}{2\pi}(-2\ln r_{1,2} + 2\ln r_{2,4} + \ln r_{1,4} + \ln r_{2,3})$$

$$= \frac{\Gamma^2}{2\pi}\ln\left(4y_1 y_2 \frac{(x_1 - x_2)^2 + (y_1 + y_2)^2}{(x_1 - x_2)^2 + (y_1 - y_2)^2}\right) = E. \quad (10.20)$$

Since the geometric center of the x-coordinates, $x_0 \equiv (x_1 + x_2)/2$, does not appear in H, the conjugate variable

$$2y_0 \equiv (y_1 + y_2) = \text{const} \quad (10.21)$$

is conserved during the motion, where $2y_0$ can be considered as the average width of the vortex pairs. It is convenient to choose $2y_0$ as the characteristic length $L = 2y_0$ and then to rescale the equations of motion according to (10.17). The following variables, besides the center-of-mass coordinates, can then be used:

$$x_r \equiv x_2 - x_1, \quad y_r \equiv y_2 - y_1. \quad (10.22)$$
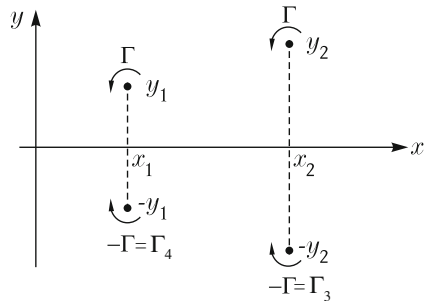
Fig. 10.7 Arrangement of the four vortices in the leapfrogging problem

Energy conservation enables us to obtain an explicit formula for trajectories in the relative coordinates:

$$\frac{1}{1-y_r^2} - \frac{1}{1+x_r^2} = \mathrm{e}^{-E}. \tag{10.23}$$

Bounded trajectories are present for energy values $E > E_s \equiv 0$, where no real solution y_r exists for $x_r \rightarrow \infty$. This corresponds to a strictly periodic motion of the vortex pairs, called *leapfrogging* [206, 709]. Since the Hamiltonian depends on x_r and y_r only, the vortex dynamics is integrable. The equations of motion can be solved by direct numerical integration, which yields the time-dependence of the vortex-center coordinates $x_i(t)$ and $y_i(t)$ ($i = 1, 2$).

The dimensionless stream function (10.18) of the advection problem takes the form

$$\psi(x,y,t) = \ln\left(\frac{r_3(t)\, r_4(t)}{r_1(t)\, r_2(t)}\right), \tag{10.24}$$

where $r_i(t)$ denotes the distance of the advected particle at (x,y) from the center of vortex i at time t. The mixing region can be conveniently chosen as a circle containing all vortices in a frame *comoving* with the geometric center $[x_0(t) = (x_1(t) + x_2(t))/2, y = 0]$ along the x-axis. Individual trajectories are again typically transiently chaotic. A representative chaotic saddle responsible for transient chaos is shown in Fig. 10.8. We note that the saddle is quite dense and can be regarded as consisting of a hyperbolic component (the direct product of two Cantor sets) and a
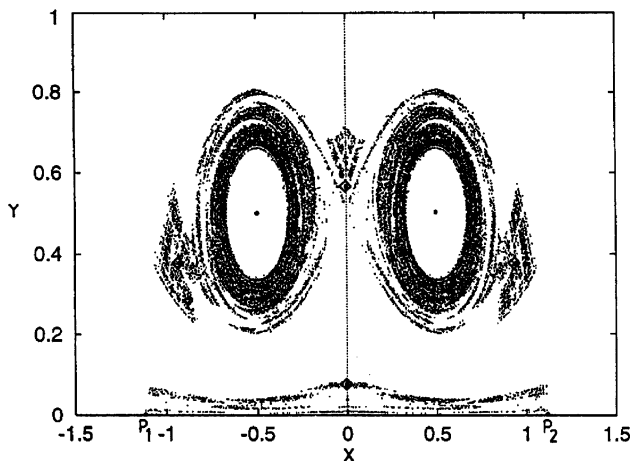
Fig. 10.8 The chaotic saddle of the leapfrogging problem for $y > 0$ in the comoving frame on a stroboscopic map at $t = 0$, obtained by means of the PIM-triple algorithm. The full chaotic saddle is obtained by mirroring this set to the x-axis. Points $P_{1,2}$ denote fixed points along the x-axis. The vortex centers are marked by dots. The value of energy is $E = \ln 2$ (with kind permission from the institute of physics)

nonhyperbolic one located about the ellipsoidal regions containing the vortices that are not accessible by scattering trajectories. These are the regions where the effect of one vortex is more pronounced than that of any other and can therefore be called the *vortex core* for the Lagrangian dynamics. Inside this core the effects of other vortices can be regarded as a weak perturbation, and the conditions of the KAM theory are thus fulfilled [430, 431], where the boundary of the core is a KAM torus. In fact, KAM tori surrounding vortices are present in the advection induced by any number of vortices [35].

For the advection problem defined by (10.24), the unstable manifold of the chaotic saddle is shown in Fig. 10.9, which is typically traced out by particle droplets. It is quite remarkable that this unstable manifold is similar to the pattern obtained from an experiment of three-dimensional smoke rings [206, 710], as shown in Fig. 10.10. In the experiment, the smoke itself plays the role of the dye. This example shows that experimentally visualizable flow patterns, such as streakline patterns, are in fact unstable manifolds of chaotic saddles. The occurrence of fractal streakline patterns thus provides evidence of transient chaos in the advection problem.

The leapfrogging vortex rings can be considered as building blocks of turbulent jets [278]. The particle transport in such a flow thus gives hints about the entrainment of ambient fluid by jetlike flows such as cumulus clouds [133].

A dye pattern (an unstable manifold) similar to that of Fig. 10.9 was observed in a recent experiment on open flow advection by Gouillart et al. [276], who used two rotating rods to stir dye in a channel of slowly moving viscous flow.
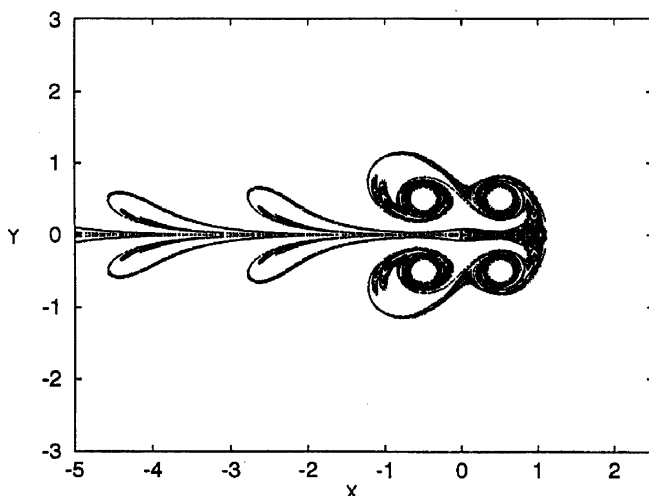
Fig. 10.9 For the advective dynamics of the leapfrogging problem determined by (10.24), the unstable manifold of the full chaotic saddle [590] (with kind permission from the Institute of Physics)
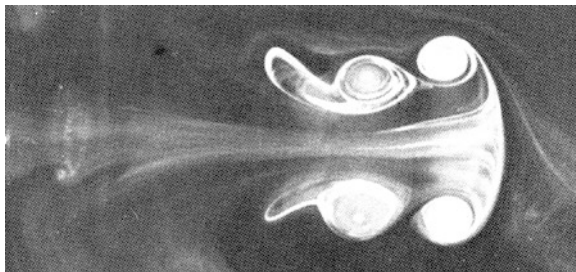
Fig. 10.10 Photograph of a planar cross section through two leapfrogging smoke rings from the 1978 experiment of Yamada and Matsui [206] (with kind permission from the Parabolic Press)

10.3.3 Lobe Dynamics

Examining the lobe dynamics is a technique for quantifying transport due to chaotic advection, as pioneered by Rom-Kedar, Leonard, Wiggins, and coworkers [48, 647] (for a recent review, see [499]). The method is based on the observation that invariant manifolds govern the motion of fluid regions, called lobes, which are formed by segments of the stable and the unstable manifolds. Lobes can transport fluid between regions of qualitatively different flow characters.

The general idea of lobe dynamics can be conveniently illustrated by the example of leapfrogging vortex pairs. In particular, the advective dynamics has two hyperbolic fixed points, P_1 and P_2, along the axis of symmetry (x) in the comoving frame, which are elements of the chaotic saddle (see Fig. 10.8). The stable and the unstable manifolds emanating from the symmetry axis are denoted by W_1^s and W_2^u, respectively. Figure 10.11 illustrates, schematically, some important topological features, for simplicity on one half-plane only. One can define an interaction region S, a subset of the stirring region, bounded by segment P_2P of W_2^u and segment P_1P of W_1^s, where P is the primary intersection point of the manifolds. Lobes formed by W_2^u and the boundary of the interaction region are denoted by E_i (D_i) with $i > 0$ if they are fully or partially inside (fully outside) S. The advective dynamics transforms each lobe E_i (D_i) into E_{i+1} (D_{i+1}) after one flow period, where the convention is that the first (last) lobe that lies inside the interaction region has label $i = 0$. These rules define lobes with negative i. Due to the incompressibility of the flow, the areas of all lobes are equal. Numerically computed manifold branches, however, show that the actual topological pattern is much more complex than in the schematic diagram, as shown in Fig. 10.12. For example, due to the strong stretching and folding inside the interaction region, lobe E_0 has a strange shape and intersects with lobe D_0 at six points (in contrast to Fig. 10.11, where the number of intersecting points is two).

The idea of lobe dynamics can be applied to any Hamiltonian (volume-preserving) problem (see, e.g., Fig. 6.25). In the hydrodynamical context, lobes are relevant because they connect fluid regions of different characters: outside the interacting region S the overall flow surrounds the vortices and moves to the left in the comoving frame, while fluid inside the interaction region tends to remain in the
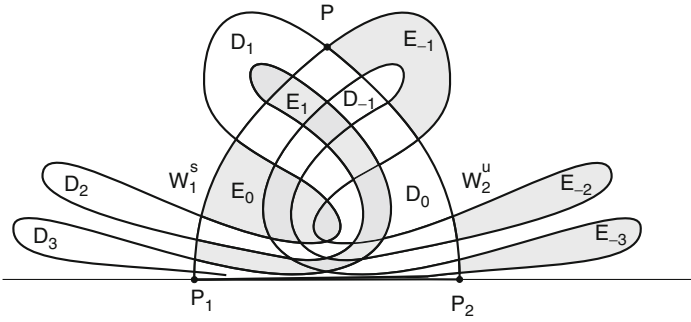
Fig. 10.11 Schematic diagram of the stable manifold W_1^s of the fixed point P_1 and the unstable manifold W_2^u of the fixed point P_2 on a stroboscopic map taken at integer multiples of the period of the flow, shown above the axis of symmetry $x = 0$, where P represents the primary intersection point. Lobes E_i and D_i are indicated for a few values of i
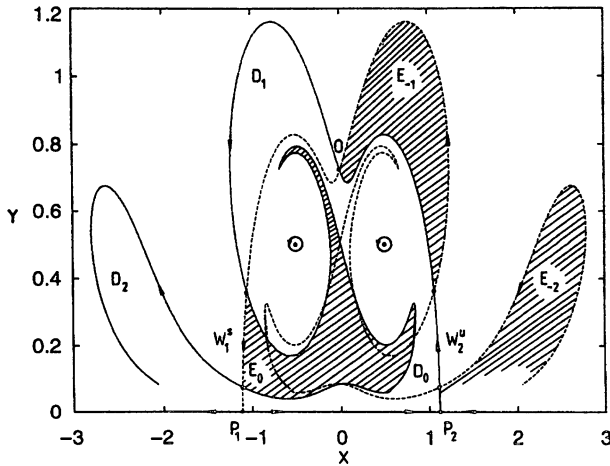
Fig. 10.12 Branches of the numerically determined manifolds W_1^s and W_2^u and the corresponding lobes in the leapfrogging problem (with kind permission from the Institute of Physics)

vicinity of the vortices. Lobe E_{-1} is transformed in one time unit into E_0, i.e., the fluid area of E_{-1} is transported from the ambient region into a region close to the vortices. While there is a tendency for fluid to be trapped by the vortices, permanent trapping is impossible due to escape. The same area flows out of the interaction region via the lobe transformation $D_0 \rightarrow D_1$. Dividing the area of one lobe by the period of the flow, one obtains the average material *flux* inside (and outside) the interaction region. This is the Lagrangian background of the *entrainment* in fluid mechanics [133].

The lobe dynamics can be used to trace out the *escape-time distribution* in the interacting region. For example, points escaping the interaction region S in one time unit, regardless of when they entered the region, lie in D_0. Those spending just
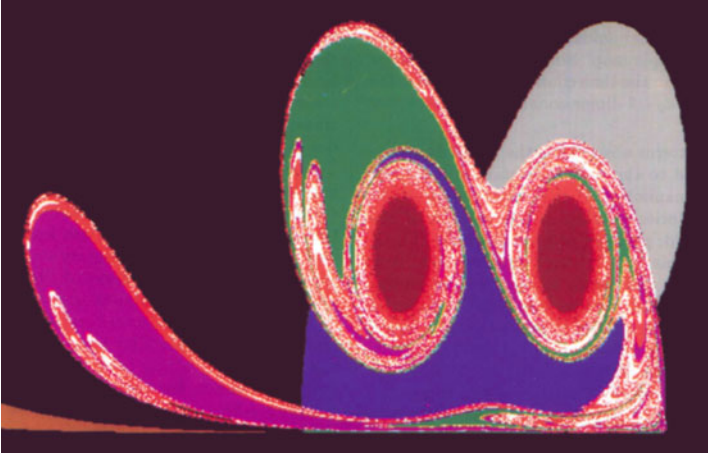
Fig. 10.13 Images E_i of lobe E_{-1} in different colors: $i = -1$: *gray*; 0: *blue*; 1: *green*; 2 *magenta*; 3, 4: *white*. Lobes with $i \geq 5$ are marked by light red. They contain points entering the interaction region more than five time units earlier and approximate the unstable manifold [591] (with kind permission from World Scientific Publishing Co.)

one time unit inside lie in $E_0 \cap D_0$. Points from $E_i \cap D_j$ spend $i - j + 1$ time units in the interaction region. Assuming exponential decay of particles from the interaction region, one can estimate the escape rate as the logarithm of the area ratio between S and $S - D_0$. This is, however, typically a poor estimate, since the exponential decay is an asymptotic property that sets in with good accuracy only after some time (see (1.6)).

Lobes in general possess a convoluted structure, as shown in Fig. 10.13, where images of lobe E_{-1} (gray) over several periods are displayed. The first image E_0 (blue) is mapped onto E_1 (green), which is so strongly elongated that it does not appear to be connected (although it is). A considerable part of this lobe is already outside S. Higher-order lobes become more and more convoluted.

10.4 Dye Boundaries

We have seen that dye particles trace out the unstable manifold of an underlying chaotic saddle in a generic open flow. It is natural to ask how boundaries between *different* dyes behave [407, 592, 670, 787], which are defined as the borderlines between different colors injected into the flow somewhere in the inflow region. In particular, imagine that particles are injected continuously far upstream at $x = x_{in}$ so that the colors above and below a critical value y_c are different. We can focus on how the boundary between these two colors evolves over time. On a stroboscopic map taken with respect to the period of the flow, the boundary pattern will stabilize after some time. If the stable manifold of the chaotic saddle intersects the region

of both colors at x_{in}, both types of dyes tend to trace out the unstable manifold asymptotically, implying that the stabilized boundary between the two colors contains a fractal part, the unstable manifold of the chaotic saddle, or a fractal subset of it. The dye boundary contains a nonfractal part as well. The particular shape of the boundary depends on the value of x_{in} and y_c, but the box-counting dimension is independent of such details [592] and coincides with the box-counting dimension $D_{u,0}$ of the unstable manifold. An example from the von Kármán flow is shown in Fig. 10.14.

Dye *exit* boundaries can be obtained by sprinkling particles in a domain containing the stirring region. Particles are followed until they cross a line x_{out} far away downstream. Their initial coordinates are colored depending on whether after crossing $x = x_{out}$ on a stroboscopic map they lie above or below a preselected value y_c. These boundaries are analogues of exit basin boundaries in chaotic scattering (and are also similar to fractal basin boundaries), the fractal part of which contains the stable manifold of the chaotic saddle, as shown in Fig. 10.15.
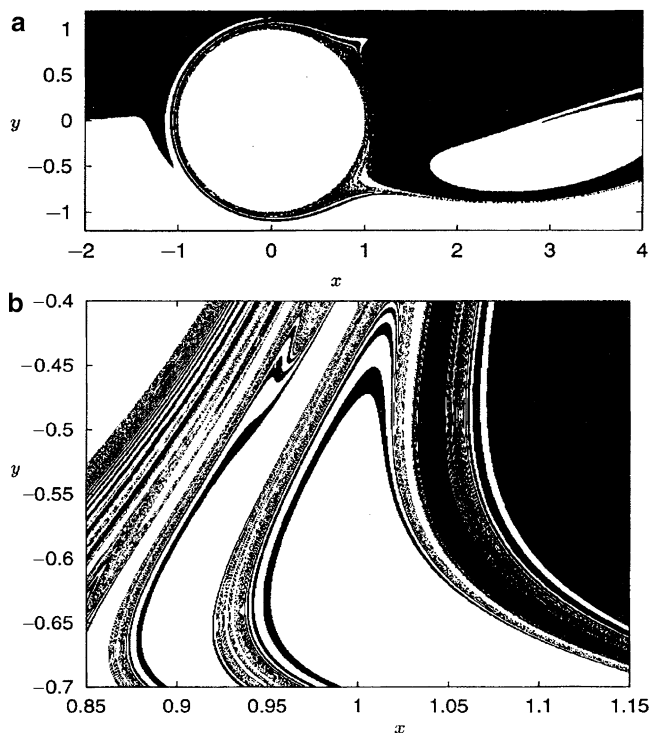
Fig. 10.14 Dye boundary in the von Kármán flow. Shown is the boundary between *black* and *white* dyes injected from $x_{in} = -6$ with $y_c = 0$ on a stroboscopic map (taken at time $t = 0.3 \mathrm{mod} 1$). Particles with initial coordinates $x_{in}, y \geq 0$, are *black*. (**a**) Global pattern and (**b**) enlargement of a part of (**a**). The fractal part contains the unstable manifold [592] (copyright 1995, the American Physical Society)
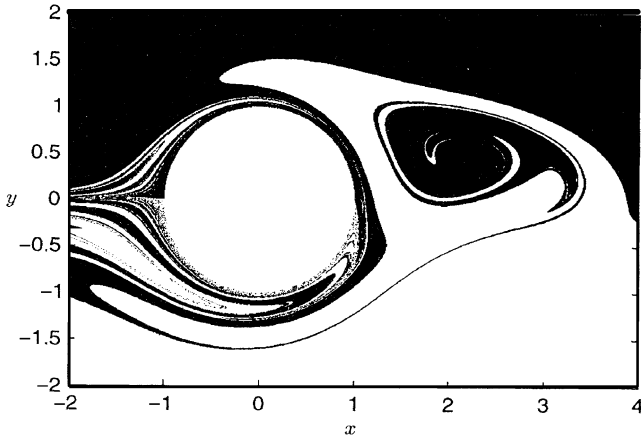
Fig. 10.15 Dye exit boundary in the von Kármán flow. Initial conditions are labeled *black* or *white*, depending on whether after crossing the $x = x_{out} = 6$ line on the stroboscopic map (taken at time $t = 0.3 \bmod 1$), they lie in the half-plane $y \geq 0$ or $y < 0$, respectively. The fractal part contains the stable manifold of the chaotic saddle [592] (copyright 1995, the American Physical Society)

To illustrate a general property of dye boundaries, imagine that the flow in the far upstream region is separated into bands perpendicular to the inflow velocity whose length is exactly the distance that the fluid traverses over one full period. Color this infinite set of bands periodically with at least three colors. As the fluid enters the stirring region, some part of each region of color becomes trapped around the chaotic saddle and flows away slowly from there. So there is time for the next color to come close to the previous one around the unstable manifold. The dye boundary will then have smooth and also fractal components, and the latter have the *Wada* property (Sect. 5.5). In the neighborhood of any point on the fractal part of the boundary, particles of all colors are present, as shown in Fig. 10.16.

The Wada property can be understood as follows. Consider the motion of a dye droplet in the time-reversed dynamics. If it overlaps initially with the unstable manifold, it traces out the stable manifold more and more accurately with time. The stable manifold stretches up to infinity in the upstream region. Unavoidably, it crosses an infinite number of colored bands. When following the dynamics of particles very close to the stable manifold under the again reversed, i.e., forward, dynamics, we see that they all end up in a small droplet about a point of the chaotic saddle, where all the colors accumulate. The points of the droplet on the unstable manifold flow along the manifold much more slowly than those outside the manifold. These points have thus in their arbitrarily small neighborhoods all the colors. This observation shows that not only the chaotic saddle, but also the neighborhood of its unstable manifold is *strongly stirred* in open chaotic flows. The argument indicates that Wada dye boundaries can be expected in all flows where the stable manifold of the entire chaotic saddle stretches over regions of infinitely many different colors. Note that for dye boundaries, it is the *unstable* manifold that may exhibit the Wada property, not the stable manifold as in basin boundaries (see Sect. 5.5). The argument also
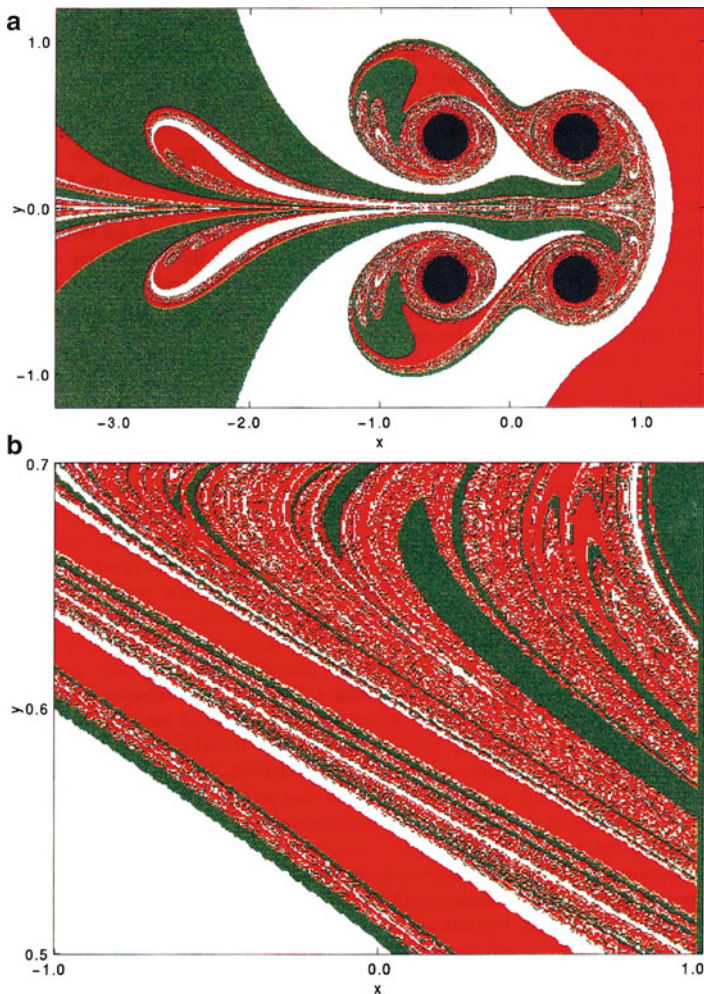
Fig. 10.16 Wada dye boundaries in the leapfrogging flow. The dye distribution is shown around the leapfrogging vortex pairs swimming in a fluid colored bandwise in *red*, *white*, and *green* on a stroboscopic map. The lower panel is a magnification of a small region in the upper panel, which illustrates the Wada property [787] (with kind permission from Elsevier Science)

indicates that the boundaries between particle ensembles of different behaviors are stable or unstable manifolds. The boundaries are material lines, and therefore the fluid flux across them is zero. In chaotic flows they nevertheless provide a mechanism (e.g., via the lobe dynamics) for material exchange between different regions.

For three-dimensional flows, many of the above phenomena persist. A basic new feature (see Chap. 8) is that manifolds can be either locally one-dimensional or locally two-dimensional, depending on the details of the dynamics. For chaotic dynamics both the stable and the unstable manifolds are fractal, indicating the presence of a chaotic saddle in the flow.
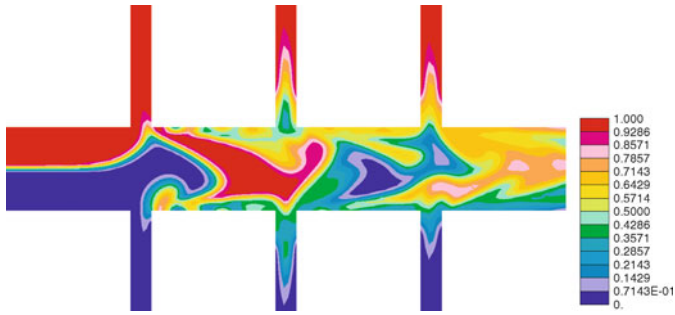
Fig. 10.17 Concentration distribution of a passive scalar (*red*: full concentration; *dark blue*: zero concentration) in a micromixer. The flow in the main channel is stationary and is manipulated by time-periodic flows in the secondary channels. Varying the frequencies of these perturbations can enhance mixing. (Picture by I. Mezić.)

One area in which the observations of this chapter are relevant is microfluid devices. Recent technological advances have made the fabrication of microchannels of a few hundred micrometers in cross section possible [96, 140, 389, 733]. These devices are used in printers and biomedical instruments. At this scale, fluid viscosity dominates, turbulence cannot be present, and diffusion is often negligible. As a result, the only source of effective stirring is chaotic advection. A typical microfluid arrangement is a channel, along which fluid moves due to a pressure gradient. It is often perturbed time-periodically by flows from secondary channels to generate stirring regions around such junctions, as shown in Fig. 10.17. In this case, chaotic saddles provide the dynamical mechanism for efficient stirring.

10.5 Advection in Aperiodic Flows

In this section we address the question of how passive advective dynamics change in the realistic situation in which the temporal behavior of the flow field is more complicated than periodic. Periodic flows have the special feature that the asymptotic time-dependence can be recovered from finite-time velocity samples. This feature is the basis for the use of stroboscopic maps. Aperiodic flows, however, cannot be reconstructed for all times from a one-period velocity sample. In such a case, velocity data are available only over *finite-time* intervals. Chaotic-like dynamics of advected particles is then unavoidably of a transient character. Stroboscopic maps are, however, no longer available and the concepts of hyperbolic orbits, and stable and unstable manifolds, cannot be directly applied. Nonetheless, analogues of these quantities can be defined, and certain features such as the fractality of tracer patterns can be robust even in open aperiodic flows.

10.5.1 Coherent Structures in Aperiodic Flows

Coherent structures are well known to characterize turbulent velocity fields, or flows of general time-dependence. They can be defined as fluid regions exhibiting coherent behavior over long periods of time (see, e.g., [504]). Different criteria based on the instantaneous velocity field, i.e., the Eulerian frame, have been proposed, but they all have the drawback of being reference-frame-dependent. It has been accepted that a proper definition of coherent structures should be established in the particle-based, i.e., the Lagrangian, framework. In particular, coherent structures are distinguished sets of fluid particles. This change of view was due to a series of works by Wiggins, Jones, Haller, and coworkers (see, e.g., [307, 310, 499, 524]), and can be interpreted as the increasing use of dynamical-system concepts in fluid dynamics.

Examples of coherent structures are material filaments and vortex cores of finite lifetime. We have seen in Sects. 10.3.3 and 10.4 that such structures in time-periodic flows are related to the invariant manifolds of hyperbolic orbits and to KAM tori, respectively. Both types of structures are special material lines that enhance or inhibit stirring. The definition of Lagrangian coherent structures in general aperiodic flows thus requires a proper generalization of these concepts to situations in which no stroboscopic repetition is present.

An earlier approach to studying coherent structures was based on finding stagnation points (hyperbolic points in the Eulerian frame) of the flow and searching for such points associated with finite-time Lagrangian stable and unstable manifolds [307, 524]. In this setting the analogue of the lobe dynamics can be worked out, and material transport can be quantified (for a recent review see [499]).

A more general approach due to Haller and coworkers [298, 304, 305, 310, 707] is applicable regardless of whether the flow has Eulerian stagnation points. The basic idea is to examine the *stretching* and the distribution of future or past stretchings assigned to any point in the fluid. The stretchings constitute the stretching field. Haller and coworkers obtained rigorous results on the characterization of stretching around material lines of aperiodic flows defined over finite intervals. They pointed out that the analogue of the stable manifold exists in the form of material surfaces of *large future stretchings*. These surfaces are also called repelling surfaces, since particles on both sides of them depart in opposite directions and have qualitatively different future behaviors. Regions of large past stretchings correspond to the unstable manifold (called attracting material surfaces). Special intersections between the repelling and the attracting surfaces or lines form hyperbolic cores, the analogues of hyperbolic orbits. Due to the finite-time observation of aperiodic flows, the hyperbolic manifolds are not unique, but for sufficiently long time intervals they appear to be locally unique up to the numerical precision [310]. Dominant hyperbolic coherent structures turn out to be *maximizing surfaces* (ridges) of the stretching field. The maxima of large past stretchings correspond to unstable manifolds of strongly hyperbolic orbits. Indeed, contours of constant dye concentrations were found in experiments [805] to align with lines of large past stretchings. This is analogous to the observation in Sect. 10.4 according to which dye boundaries contain unstable manifolds. The maxima of large future stretchings separate regions of qualitatively

different tracer dynamics. This is a generalization of the statement in Sect. 10.4, according to which dye exit boundaries contain stable manifolds. Elliptic coherent structures, or finite-time vortex cores, are defined as regions in which both the future and past stretchings are weak.

A convenient measure to characterize the stretching field is Lyapunov exponents. There are two types of such exponents. The first type is *finite-time* Lyapunov exponents, the instantaneous growth rates over a finite interval τ of the separation distance D between two nearby trajectories starting from some point $\mathbf{x}$, which are defined as [597]

$$\lambda(\tau, \mathbf{x}) = \lim_{D_0 \to 0} \frac{1}{\tau} \ln \frac{D(\tau)}{D_0}, \tag{10.25}$$

where the time interval τ is chosen to be shorter than or equal to the interval over which the aperiodic fluid flow is defined. The values of the finite-time Lyapunov exponents are distributed about the average Lyapunov exponent λ_1. They also depend on the time instant t when the two nearby trajectories are initiated.

The second type of measure is *finite-size* Lyapunov exponents, which characterize the local amplification rates of a separation distance of size δ for a trajectory starting from point $\mathbf{x}$ until the separation reaches an amplified value $r\delta$, where $r > 1$. These exponents are defined as [31, 82]

$$\lambda(\delta, r, \mathbf{x}) = \frac{1}{\tau(\delta, r, \mathbf{x})} \ln r, \tag{10.26}$$

where $\tau(\delta, r, \mathbf{x})$ is the time needed for the separation to reach $r\delta$. If the time is longer than the interval over which the fluid flow is defined, no finite-size Lyapunov exponent can be assigned to the given point $\mathbf{x}$. The exponents also depend on the time instant t when the separation distance is set to δ. Since taking the limit $\delta \to 0$ is not necessary, finite-size Lyapunov exponents are easier to determine in numerical simulations than finite-time Lyapunov exponents. Typically, the two Lyapunov-exponent fields are not identical, since they also depend on parameters τ, δ, and r. Their extrema appear, however, to coincide. It can therefore be said that hyperbolic Lagrangian coherent structures are maxima (ridges) of both the finite-time and the finite-size Lyapunov-exponent fields. Elliptic coherent structures, i.e., vortex cores, are assigned to near-zero values of these fields.

As an example, Fig. 10.18 shows the finite-size Lyapunov-exponent field in a square-shaped lake of linear size 2 km. The flow is generated by wind and is obtained as a numerical solution to the shallow-water equations [579]. Initially, a wind of strength 14 m/s blows from the northwest; then it changes abruptly but continuously to northeast, and after some time it changes back again, etc. The period over which the wind direction is constant is not fixed. The period in fact changes *randomly* from an ensemble with a mean value given as 8 h. The maximum deviation is ± 2 h. The flow field was determined over the period of about 60 changes in the wind direction. The largest values of the finite-size Lyapunov exponent (largest stretching) in forward time are marked by red. They represent the stable manifolds. The largest values in backward time are marked by blue, and they trace out the unstable
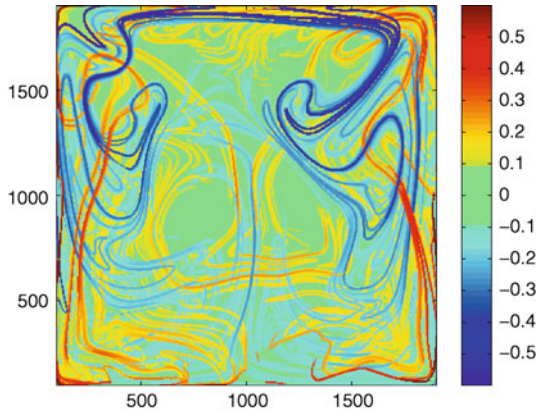
Fig. 10.18 Finite-size Lyapunov-exponent field in an aperiodically wind-driven lake at an instant of time, where the change in the wind direction occurs in an aperiodic manner at the average of 8 h. Color coding indicates the values of the finite-size Lyapunov exponent in units of 1/h. Length is measured in meters. Computational parameters are $\delta = 7$ m and $r = 50$. (Picture by M. Pattantyús-Ábrahám.)

manifolds. Several intersections can be seen, which correspond to periodic orbits, homoclinic and heteroclinic intersections. Light gray marks near-zero values of the Lyapunov field and indicates elliptic coherent structures (vortex cores). The overall picture changes with time, but the main topological features remain unchanged over the period of investigation.

An aspect that makes the concept of Lagrangian coherent structures relevant is that being material lines or surfaces, they prohibit fluid flux across themselves. They are *barriers to transport*. Unstable manifolds thus trap fluid, a property important in the context of spreading of pollutants. Applications of coherent structures are therefore particularly important in environmental flows or in geophysical fluid dynamics [142, 413, 477, 827], ranging from oceanic upwelling regions [655] to jetstreams [760]. Unstable manifolds are not only convenient observables; they may also have biological relevance [374]. For example, top marine predators, such as frigate birds, have been found to track Lagrangian coherent structures in their effort to locate food patches. For a recent review of Lagrangian coherent structures, see [580].

A different type of problem of engineering importance is the *separation profile* of the boundary layer over obstacles merged in uniform flows, a classical phenomenon in fluid dynamics. Traditional approaches were based on Eulerian concepts [429], but recent work by Haller and coworkers [306, 743] indicated that the proper view for understanding this unsteady process should be Lagrangian. The separation profile turns out to be a coherent structure of filamentary shape. Such a profile can be thought of as a material line that attracts and ejects particles near the (time-dependent) separation point. The profile behaves thus as an unstable manifold. A new feature is that, due to the degeneracy of fixed points on no-slip boundaries, the manifold is nonhyperbolic. It corresponds nevertheless to a ridge in the past stretching field, as shown in Fig. 10.19. The theory predicts separation points and
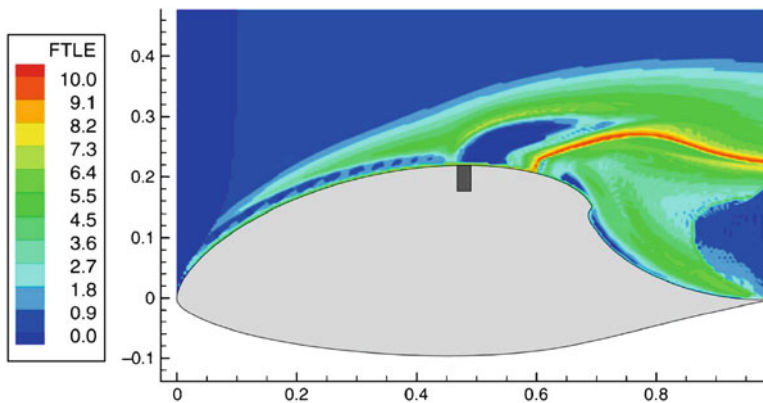
Fig. 10.19 Finite-time Lyapunov-exponent field, computed from integrating backward in time, in an aperiodic flow around an airfoil at an instant of time. The color bar marks the nondimensionalized finite-time Lyapunov-exponent values. The separation profile which separates the free stream flow from the wake appears as a line with the highest value of the finite-time Lyapunov exponent [707] (with kind permission from Elsevier Science)

separation angles in unsteady flows, and hence it is of use in monitoring and controlling the separation process, which has far-reaching consequences for aerodynamic properties such as lift and drag.

An alternative method to determine coherent structures is based on the concept of *almost invariant sets* mentioned briefly in Sect. 2.6. In the context of advection, these are regions where fluid is trapped, regions that hardly mix with their neighborhood, i.e., coherent structures. One should then consider the Frobenius–Perron (or transfer) operator, defined by (2.67), and apply it to the advection problem. In an incompressible flow the advective dynamics is area-preserving ($J \equiv 1$). For practical purposes, one can partition a closed fluid region into boxes and determine the transition probabilities among all the boxes, in order to approximate the operator by a linear matrix whose entries are the transition probabilities [173, 248–251]. The largest eigenvalue of the matrix is unity, as it should be in a closed system, and the eigenfunction is constant in chaotic regions. The second eigenvalue, provided that it lies close to unity, appears to have an eigenfunction that concentrates on almost invariant sets (coherent structures) only. The coherent structures obtained in this way practically agree with the ridges of the finite-time or finite-size Lyapunov exponent fields [248]. As pointed out by Pikovsky and coworkers [600, 601], an analogous method can be applied to the problem of passive scalars in the presence of diffusion, where the "noisy" version of the transfer operator should be considered.

10.5.2   Open Aperiodic Flows

In open flows of aperiodic time-dependence, analogues not only of hyperbolic orbits but also of chaotic saddles exist. The key observation is that there are orbits that

never escape the mixing region of interest. Particles on these bounded orbits are never able to reach the upstream or the downstream region. In particular, irregular flows can have some kind of *topological stability*, meaning that they preserve some topological properties of the flow, such as the number of dominant vortex cores. If the flow is defined over a sufficiently long time interval, the flow pattern may repeat the same qualitative features a large number of times. In such cases a *multiplicity of nonescaping orbits* can be present in the mixing region, and this set appears to be fractal numerically [352, 544]. Because the orbits are unstable, their union can be regarded as a *chaotic saddle*. As an extension of the concept of hyperbolic material lines of Sect. 10.5.1, we can then speak of fractal manifolds of this saddle.

To see these features, we present here an example, which is the generalization of the leapfrogging problem treated in Sect. 10.3.2. Breaking the symmetry of the leapfrogging problem leads to a type of vortex dynamics characterized by the asymptotic formation of two noninteracting vortex pairs. If, however, the vortex strengths are also changed so that no pairs can be formed but the resulting vorticity is still zero, i.e., $\sum_{i=1}^{4} \Gamma_i = 0$, one obtains a long-term aperiodic vortex motion. The average distance among the vortices remains bounded, but their geometric center moves in a certain direction. The stirring region can be any region enclosing all four vortices in a comoving frame. The stable manifold can be studied by monitoring the delay times (escape times) from the mixing region. Using tracer trajectories, we can obtain the time spent in the stirring region for each initial condition. The spatial distribution of delay times for the four vortices is shown in Fig. 10.20a. It can be seen that, besides the vortex cores, points with large escape times lie on a filamentary structure. Examples of magnifications are shown in Fig. 10.20b, where it can be seen that the complex patterns are present on all smaller scales. One can also construct a set corresponding to the time-reversed tracer dynamics starting from the same set of initial conditions, which is the unstable manifold that exhibits similar patterns, as shown in Fig. 10.20c. The set of intersections of these two foliations has the property that trajectories starting from it never leave the mixing region either under the forward or the backward dynamics. It is thus a natural generalization of a chaotic saddle, as shown in Fig. 10.20d, although the flow is aperiodic.

An efficient way of visualizing the unstable manifold is to follow a droplet of dye injected into the mixing region. Snapshots taken at different times are shown in Fig. 10.21. It can be seen that the ensemble tends to produce a complicated filamentary structure. In contrast to the periodic generation of identical lobes (cf. Fig. 10.9), here the emerging patterns continuously change their form and size due to the aperiodic motion of the vortices driving the flow. By investigating *several* tracer ensembles, one finds on average an exponential decay $N(t)/N_0 \sim \exp(-\kappa t)$ in the dimensionless time t with escape rate $\kappa = 3.0$. The average Lyapunov exponent measured along several orbits of long escape times is estimated to be $\lambda_1 \approx 55$.

The fractal properties of the stable foliations can be extracted by covering the singularities in the delay-time function as in any chaotic scattering process, using boxes of size ε. The slope of the $\log N(\varepsilon)$ versus $\log \varepsilon$ plot yields, after averaging over several ensembles, a well-defined value $D_0^{(1)} = 0.95$ for the partial box-counting dimension, in agreement with the formula $D_0^{(1)} \approx 1 - \kappa/\lambda_1$.
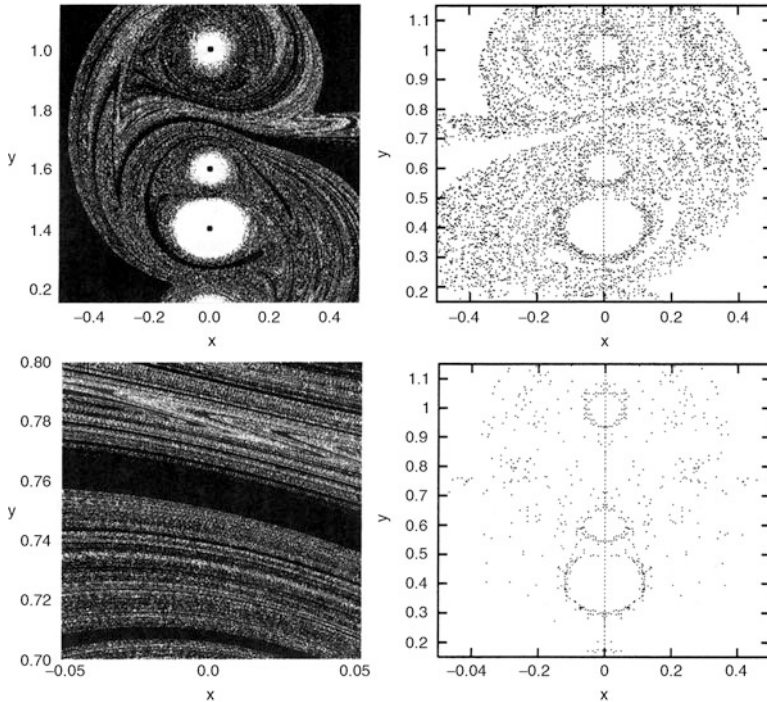
Fig. 10.20 Advection in an aperiodic four-vortex problem ($\Gamma_1 = \Gamma_2 = \Gamma_3 = 1$, $\Gamma_4 = -3$). (**a**) Delay time from the stirring region, represented on a *gray scale*, as a function of the initial position of 160,000 tracers distributed uniformly in a frame comoving with the four vortices. Coordinates are measured in nondimensionalized units. Brighter points correspond to larger escape times, distributed in the interval $[0.18, 1.2]$ in dimensionless time. (**b**) Magnification of part of (**a**). (**c**) Dots representing initial conditions whose escape times are larger than 1.2 under the backward dynamics, which form approximately the unstable manifold. (**d**) Dots representing initial positions whose escape times are larger than 1.2 under both the forward and the backward dynamics. These dots thus represent approximately the underlying chaotic saddle [544] (copyright 1998, the American Physical Society)

While it seems surprising that the tracer dynamics possesses a well-defined escape rate and average Lyapunov exponent, and exhibits a pronounced fractal structure although the flow is temporally irregular, theoretically these features can be understood in the framework of *random maps* (Sect. 4.6). In particular, one can observe the motion of a particle advected by an aperiodically time-dependent flow at integer multiples of a preselected time lag t_0 and define a sequence of "stroboscopic" maps that connect the coordinates at $t = nt_0$ with those at $t = (n+1)t_0$. In contrast to periodic flows, this map does depend on the time at which the snapshot is taken. As a result, following a trajectory in discrete times requires the application of a sequence of *different* maps. The actual form of these maps is not known a priori in general. If, however, the flow preserves some qualitative features, e.g., it is topologically stable, the map can be assumed to have the form (4.49), in which the *parameters* are n-dependent. For sufficiently complex flows and not very short time
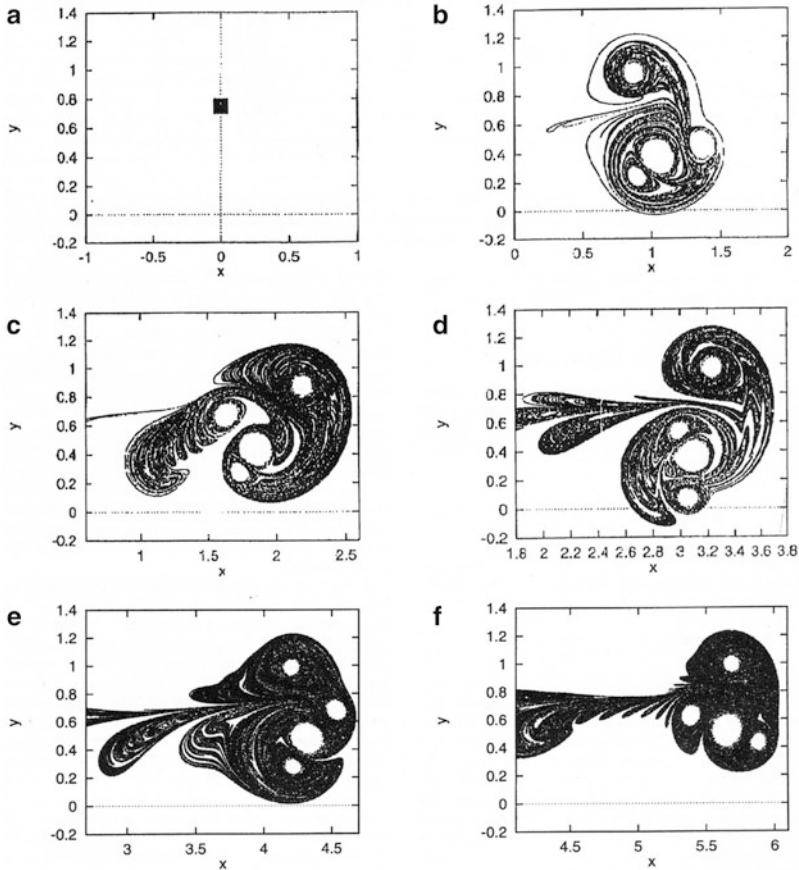
Fig. 10.21 Temporal evolution of an ensemble of 160,000 particles initially placed on a square. Snapshots are taken at dimensionless times (**a**) $t = 0$, (**b**) $t = 0.1$, (**c**) $t = 0.2$, (**d**) $t = 0.3$, (**e**) $t = 0.4$, and (**f**) $t = 0.5$ [544] (copyright 1998, the American Physical Society)

lags, the n-dependence might be so irregular that subsequent maps correspond to *independent* choices. This means that on each iterate n, the map (more precisely, the set of its parameters) is randomly chosen with respect to a stationary distribution. The chaotic saddle of Fig. 10.20d is thus a fluid-dynamical example of a snapshot chaotic saddle (see Sect. 4.6.1). If the nonrandom version of the map is chaotic, the random map is expected to be chaotic, too, although with different dynamical invariants for the respective chaotic processes. The requirement of topological stability of the flow is reflected by the feature that the *topological entropy* of the map is *positive* for each fixed realization of the parameter ensemble, and does not exhibit significant fluctuations.

For incompressible two-dimensional open flows, their random-map advection models are area-preserving two-dimensional maps with open phase spaces. As shown in Appendix B (see also [352, 544]), random maps possess *well-defined*

dynamical averages. Moreover, the dimension formulas (e.g., (4.51)) remain valid. These relations also imply that if a tracer pattern (such as one in Fig. 10.21) is found to have a well-defined fractal or information dimension, it *cannot depend on the time at which the snapshot is taken*, although the actual shapes of the pattern can be quite different at different times. This indicates that the dynamical-system approach to characterizing and understanding chaotic advection in aperiodic flows can be effective.

10.6 Advection in Closed Flows with Leaks

Chaotic advection in closed flows is characterized by space-filling stable and unstable manifolds. One can get insight into these foliations by leaking a closed flow in the sense that whenever a particle enters a preselected region, the leak, it is considered to have escaped. This process will not alter the fluid flow, and the leaked advective dynamics is transiently chaotic. Points never escaping the complement of the leak, both forward and backward in time, form a chaotic saddle. The manifolds of this saddle are subsets of the closed system's manifolds, since the advective dynamics outside the leak are exactly the same as in the closed system.

The idea of leaked advection dates back to Pierrehumbert [598], who proposed the *resetting mechanism* as a simple model of certain chemical reactions. Whenever a tracer enters a preselected region, a given property of the tracer, such as the concentration, is reset to a value associated with that region, regardless of its previous value. This mimics the situation in which dye is introduced by diffusion from a solid surface and is maintained at the saturation concentration in a diffusive boundary layer. In the case of two or more resetting regions, tracers of different concentrations come close to each other along fractal-like boundaries. An example of two concentrations is shown in Fig. 10.22. Note that the black (white) dots can be obtained by iterating trajectories backward in time until they reach the black (white) resetting band and then coloring the corresponding initial locations. This is exactly the dye exit boundary problem treated in Sect. 10.4 under the time-reversed dynamics. Since such boundaries contain the stable manifold of a chaotic saddle, the concentration boundaries generated by resetting contain the *unstable* manifold of the leaked advective dynamics followed in forward time. The resetting pattern is thus a fingerprint of the chaotic saddle underlying the leaked dynamics, where the leak is the union of the resetting regions. The resetting patterns are thus the analogues of the dye-boundary patterns in open flows. The basic difference is that the resetting regions are set at will, and the advective dynamics is thus artificially opened. General properties of leaked systems (Sect. 2.7) hold for the resetting problem.

A direct analogue of dye exit boundaries in the context of leaked flows is the following. Consider a subregion, a region of observation, of the closed flow problem that is to be partitioned according to what happens to the tracers outside this region. Define target regions outside the region of observation and color the initial locations according to the first arrival at these regions. The problem is relevant to

Fig. 10.22 Tracer distribution in the presence of resetting in a closed time-periodic flow. The upper (*lower*) resetting band sets a concentration value marked by black (*white*). These two concentrations come arbitrarily close to each other along a filamentary pattern [542] (copyright 2000, the American Institute of Physics)
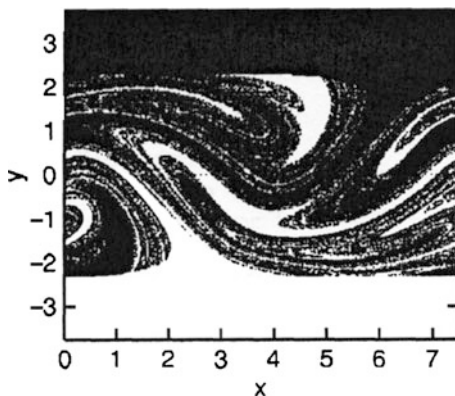
Fig. 10.23 Tracer initial conditions in a central square of the problem of the aperiodically wind-driven lake in Fig. 10.18, colored according to which of the target regions, bands along the shores (also colored), any specific tracer is advected. The initial conditions of tracers that do not reach any of the bands along the shores over the period of observation are left blank. (Picture by M. Pattantyús-Ábrahám.)
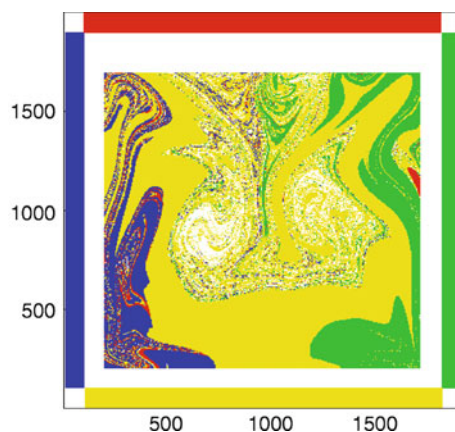
the prevention of environmental pollution. In particular, imagine that a pollutant is released in an extended region within the flow. By determining to which boundary region the different pollutant particles are advected, one can learn which parts along the boundary are most likely to be affected by the pollution release.

Figure 10.23 shows an example from the problem of the wind-driven lake in Sect. 10.5.1. The region of observation is a large rectangle in the middle of the lake. Each point is distinguished according to which of the bands (of width 100 m) along the four shores will be reached by the particle first. The result indicates that the pollutants released in the rectangle are most dangerous for the southern shore. The western shore is somewhat less polluted than the eastern one. The northern coast is hardly affected. The boundaries between different colors contain the stable manifold of the chaotic saddle residing in the region of observation. A comparison with Fig. 10.18 shows that the ridges of the finite-size Lyapunov-exponent field run parallel to these boundaries in accordance to the observations that large future stretchings belong to the stable manifold and that the stable manifold of the leaked system is a subset of the closed system's stable manifold.
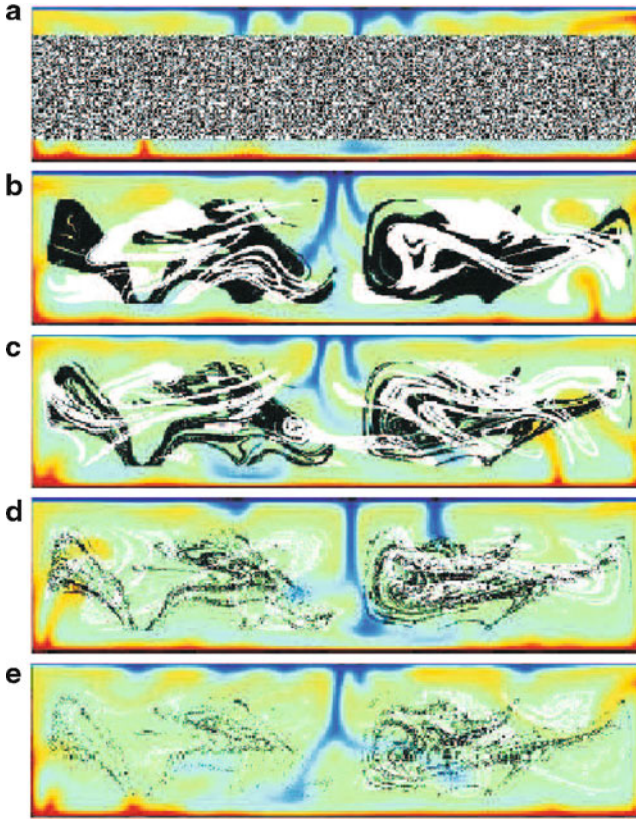
Fig. 10.24 Snapshots of the tracer distribution in a domain within two convection cells in a numerical simulation of Earth's mantle. The region of observation is the dotted subregion in panel (**a**). The actual positions of the nonescaped tracers in white and the initial positions in black after 2, 6, 14, and 17 average overturns are shown in panels (**b**), (**c**), (**d**), and (**e**), respectively. Color coding corresponds to dimensionless temperature differences (*dark blue*: 0, *red*: 1) [689] (copyright 2007, the American Institute of Physics)

The leaking method has been applied to visualizing the foliations of three-dimensional flows [793], and it also has applications in geophysics [687,689]. As an example we present the results for the convective flow in Earth's mantle [689], which is strongly aperiodic. The region of observation is the dotted rectangle within the flow, as shown in Fig. 10.24. A large number of particles are initiated in this region, and trajectories staying within the region are followed up to dimensionless time t. The initial (final) points of these trajectories are denoted black (white). Both the black and the white regions become more and more ramified with time. The black points converge to a stationary, fractal-like pattern, which is the stable manifold of the saddle in the region of observation. The white points trace out a moving foliation, the unstable manifold, at time t. In fact, these manifolds belong to a snapshot chaotic saddle. The loss of detail is due, for large times, to the escape

of tracers. It can be seen, nevertheless, that in certain small regions the particle distribution remains dense, which can be interpreted as a sign of poor stirring due to the existence of elliptic Lagrangian coherent structures. Time is measured here in average overturn times within a convective cell. Due to the high viscosity of the mantle material, this time is about $4 \cdot 10^8$ years. The full lifetime of Earth is thus about 10 overturns, and the time instant in panel (d) of the figure corresponds approximately to the age of Earth. This is consistent with the observation that the current state of Earth's mantle is heterogeneous, i.e., not (yet) uniformly stirred.

10.7   Advection of Finite-Size Particles

So far, we have assumed that particles are passively advected by the fluid in that the particle motion follows exactly that of the flow, which can occur for idealized particles of zero size and zero inertia. Finite-size particles, however, *cannot* adjust their velocities instantaneously to variations of the flow velocity. They are therefore also called inertial particles. As a result, in general, the particle velocity $\mathbf{v} = \dot{\mathbf{r}} \equiv d\mathbf{r}/dt$ will differ from the fluid velocity $\mathbf{u}$.

The equation of motion for the dynamics of a small rigid spherical particle of radius a, density ρ_p, and mass m_p in a fluid of density ρ_f is given by [32, 506]

$$m_p \dot{\mathbf{v}} = m_f \frac{d}{dt} \mathbf{u}(\mathbf{r}(t),t) - \frac{1}{2} m_f \frac{d}{dt} [\mathbf{v} - \mathbf{u}(\mathbf{r}(t),t)]$$
$$- 6\pi a \rho_f \nu [\mathbf{v}(t) - \mathbf{u}(\mathbf{r}(t),t)] + (m_p - m_f)\mathbf{g}, \qquad (10.27)$$

where m_f is the mass of the fluid displaced by the particle, ν is the kinematic viscosity, and $\mathbf{g}$ is the gravity vector. The first term on the right-hand side is the acceleration of the fluid element at position $\mathbf{r}(t)$ and at time t, which represents the force exerted on the particle by the undisturbed fluid. The derivative $d\mathbf{u}/dt = \partial\mathbf{u}/\partial t + (\mathbf{u} \cdot \nabla)\mathbf{u}$ is the total hydrodynamical derivative taken along the trajectory of a fluid element. The second, the third, and the fourth terms represent the added-mass effect, the Stokes drag, and the buoyancy-reduced weight, respectively. The so-called history term [506, 522] is neglected here, which models the slow diffusion of vorticity. Equation (10.27) is valid for low particle Reynolds number $Re_p = 2a \, | \, \mathbf{v} - \mathbf{u} \, | \, /\nu$ when the drag is proportional to the velocity difference. This requires that the initial velocity difference be small as well.

Using dimensionless variables defined by

$$\mathbf{r} \rightarrow \mathbf{r}L, \quad \mathbf{v} \rightarrow \mathbf{v}U, \quad \mathbf{u} \rightarrow \mathbf{u}U, \quad t \rightarrow \frac{L}{U}t,$$

where L and U are the typical length and velocity scales of the flow, we obtain the following dimensionless equation of motion:

$$\ddot{\mathbf{r}}(t) = A\left[\mathbf{u}(\mathbf{r}(t),t) - \dot{\mathbf{r}}(t)\right] + \left(1 - \frac{3R}{2}\right)\frac{gL}{U^2}\mathbf{n} + \frac{3}{2}R\frac{d}{dt}\mathbf{u}(\mathbf{r}(t),t). \qquad (10.28)$$

In (10.28), **n** is a vertical unit vector pointing downward, and the dimensionless parameters are

$$A = \frac{9}{2} \frac{L\nu}{Ua^2} R, \quad R = \frac{2\rho_f}{2\rho_p + \rho_f}, \tag{10.29}$$

where A is the *inertial parameter*, which can be interpreted as a dimensionless relaxation rate toward the flow velocity. The limit $A \to \infty$ corresponds to the case of point particles of zero inertia, where the passive advection equation (10.1) holds. The parameter R is the density ratio, where $R < 2/3$ corresponds to aerosols (heavier than the fluid), and $R > 2/3$ to bubbles (lighter than the fluid).

The general inertial dynamics (10.28) possesses a four-dimensional phase-space (x, y, v_x, v_y) even for planar stationary flows. What can be seen in the fluid is a projection of the phase-space objects onto the configuration space. The inertial dynamics is dissipative even for incompressible flows, and the phase-space volume contracts at the positive rate of $2A$. The dissipative character of the inertial dynamics implies that *attractors* can arise in the phase space. Indeed, the existence of attractors, regular or chaotic, corresponds to *accumulation* of particles in the configuration space. This is the phenomenon of *preferential concentration*, which occurs often in reality. In general, the dynamics of inertial particles are relevant to a number of phenomena ranging from sedimentation [845–847] and cloud physics [233] to engineering [522] and environmental applications like hurricanes [673] (for a review see [115]). In what follows we shall focus on the question of how the dynamics of advective particles change in open flows as a result of inertia.

In the flow model of the von Kármán vortex street of Sect. 10.2, attractors can be formed in the bubble regime $2/3 < R < 2$. Light particles can thus *become trapped* in the wake forever. For example, for $R = 1.47$ and $A = 30$, there are three attractors [50, 53, 197]: two chaotic and one at $x = \infty$. The chaotic attractors are located near the cylinder (but not stuck on it): one in the upper half-plane $y > 0$ and another in the lower half-plane $y < 0$. The basins of these attractors can be calculated by distributing a large number of particles in a region overlapping with the cylinder, setting the initial velocities equal to the flow velocity and then computing toward which attractor every initial particle is attracted. Figure 10.25 shows an example, a two-dimensional slice of the basin structure in the full phase space. It can be seen that near the cylinder, the basin boundaries among the three attractors are apparently fractal.[2] It is not only the dynamics on the attractor that is chaotic; there are actually *dissipative* chaotic saddles on the basin boundaries, and they ensure that the approaches toward the attractors, including the escape from the wake (the approach toward the attractor at $x = \infty$) are transiently chaotic processes.

Chaotic saddles of the inertial dynamics also exist in parameter regions where attractors are not present. A systematic investigation of the escape rate $\kappa(A)$ from

---

[2] Note that Fig. 10.25 represents a plot of initial conditions. For both ideal (Hamiltonian) and inertial particles, those with long lifetimes belong to the stable foliation of the nonattracting chaotic set. It is known that for a general Hamiltonian system, under weak dissipation, the stable foliations are converted into the basin boundaries between the coexisting attractors [534], which are fractals.
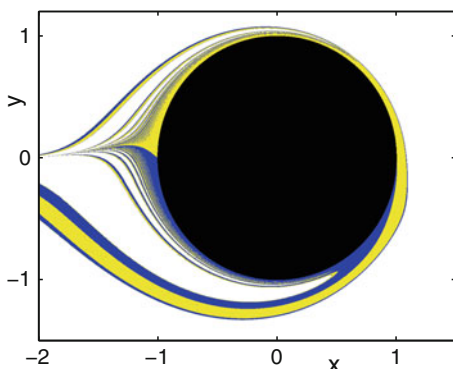
Fig. 10.25 Finite-size particle (*bubble*) advection in the von Kármán flow for particle parameters $A = 30$ and $R = 1.47$ ($g = 0$). Basins of attraction of two chaotic attractors (*light blue* and *yellow*, respectively) in the plane of the fluid at $t = 0.3 \mathrm{mod}1$ are shown. The blank region denotes the basin of the attractor at $x = \infty$ [197] (copyright 2003, the American Physical Society)
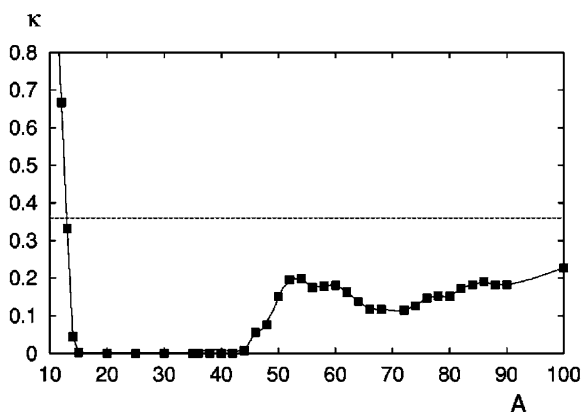
Fig. 10.26 Escape rate as a function of the inertial parameter in the bubble regime ($R = 1.7$). The horizontal line is the escape rate for passive tracers [50] (copyright 2003, the American Physical Society)

the hyperbolic components of these saddles shows that the escape rate is *below* the escape rate of fluid parcels or passive tracers in the full range $A > 12$, as shown in Fig. 10.26. This indicates that bubbles spend much more time in the wake than fluid particles. In the interval $14 < A < 45$, the escape rate vanishes, indicating the presence of attractors. For A between 33 and 45 these attractors are chaotic. Beyond 45 the escape rate is positive, and it approaches for large A the value of ideal tracers.

The tendency is opposite for aerosol particles. The escape rate is *above* the escape rate of fluid particles for any value of A, i.e., heavy particles spend much less time in the wake than fluid particles (Fig. 10.27).
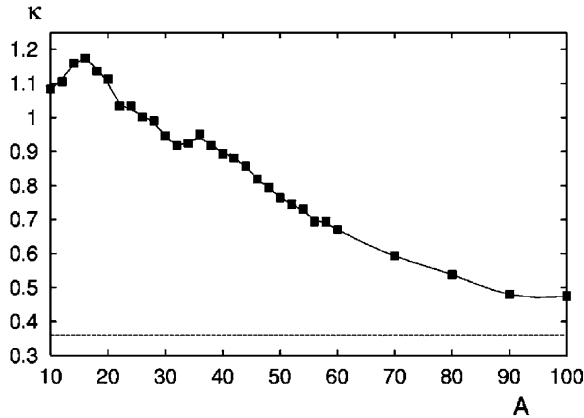
Fig. 10.27 Escape rate as a function of the inertial parameter in the aerosol regime ($R = 0.5$). The horizontal line is the escape rate for passive tracers [50] (copyright 2003, the American Physical Society)

A qualitative argument to explain why bubbles tend the form attractors, or escape much more slowly than aerosols, is as follows. Particles advected by the fluid are typically subject to the influence of local vortices. The centrifugal force on a particle comoving with a vortex is proportional to the density difference $\rho_p - \rho_f$. For heavy particles this force pushes particles outward, but for light ones it attracts particles toward the vortex center. The presence of this "anticentrifugal" force is the main reason for the existence of bubble attractors.

An interesting approach to the advection of finite-size particles was due to Haller and coworkers [308, 672]. They show that for small particle sizes, i.e., for large inertial parameters $A \gg 1$, the dynamics of a finite-size particle can be approximated by the dynamics on a low-dimensional inertial manifold, which can be calculated explicitly from a given velocity field. After a short transient time the equation of motion of such small particles can be well approximated by a first-order differential equation, called the inertial equation. The advantage of this equation becomes apparent when one traces particles in backward time. Finding a localized source of particle release is often of central relevance. Such a source-inversion problem appears, for example, in locating a source of air-transported contaminant particles. The approach based on the time-reversed integration of (10.28) leads to an unavoidable numerical instability due to an exponential growth of the type $\exp(At)$. In contrast, the inertial equation is free from such instabilities. It can be solved readily in backward time, too, and this procedure provides with good accuracy the initial spatial coordinates of inertial particles, as demonstrated the example of bubbles in the von Kármán flow [308, 309] and by other advection problems [674, 759].

In spite of the repelling centrifugal force for heavy particles, Vilela and Motter showed that aerosols can also be trapped by open flows [799]. Such aerosol attractors can arise as a result of the interactions between two or more vortices.
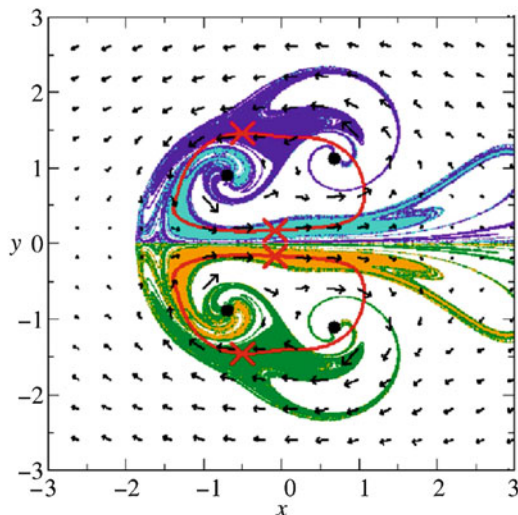
Fig. 10.28 For finite-size particle advection in the leapfrogging vortex problem for parameters $A = 50$ and $R = 0$ ($g = 0$), basins of attraction of four regular attractors (*red crosses*) at time $t \bmod T = 0.8$. *Black arrows* mark the fluid velocity vectors at this instant. The closed red curves display the attracting orbits in the comoving frame, projected onto the plane of the fluid [799] (copyright 2007, the American Physical Society)

An example is shown in Fig. 10.28, where periodic aerosol attractors in the leapfrogging problem of Sect. 10.3.2 are demonstrated. Note that the structure of the basin boundary is qualitatively similar to the stable manifold of the chaotic saddle in the passive tracer problem.

The case of neutrally buoyant particles, $R = 2/3$, is special [36, 758]. In an open chaotic flow, the effect of inertia is to cause a dispersion of particles around the chaotic saddle that exists for perfect tracers [798]. The main result is that inertia causes the fractal structure of the chaotic set to be lost in the configuration space, so, below a certain scale determined by the inertial parameter, the spatial distribution becomes smooth. In the slow manifold approach of Haller and coworkers, the slow dynamics coincides with that of infinitesimally small ideal tracers: $\dot{\mathbf{r}}(t) = \mathbf{u}$. Therefore the particle dynamics should synchronize with the Lagrangian tracer motion. It was shown [672], however, that the slow manifold has domains that repel nearby trajectories, which explains the numerical findings in [36, 798].

10.8 Reactions in Open Flows

Chemical or biological reactions often occur in fluid flows. Such processes are of interest in fields ranging from chemical reactors and combustion to atmospheric chemistry and the population dynamics of plankton. We shall present the basic

understanding of reaction outcomes in the theoretical framework of transient chaos. Without loss of generality, we restrict our discussion to two-dimensional flows and specifically consider autocatalytic reactions as a pedagogical model, which in fact occur commonly in nature [223]. They are generic models of infection-like processes. To be concrete, the model describes the penetration of a stable phase B into an unstable one A. The reaction scheme is

$$A + B \rightarrow 2\,B. \tag{10.30}$$

Consider discrete particles advected by the flow, which upon collision can change their properties [521, 786] but do not affect the underlying flow. Component A is assumed to be uniformly distributed, and hence a single seed of B is sufficient to trigger an extended reaction. In a closed container, B spreads until it eventually takes over all the available space. In an open flow, however, particles are transported away by the outflow, and in a fixed region of observation, product (B) particles can accumulate in a nontrivial pattern. If two particles of different types come closer than a threshold distance, they then react. This distance is called the *reaction range*, denoted by σ. It is convenient to assume that reactions occur at certain times only, and that they take place instantaneously. The time interval between two successive reactions is τ. At integer multiples of τ, the autocatalytic activities of B-particles convert all the A-particles within σ into B particles. During a period of length τ between two successive reactions, the particles are passively advected by the flow of given velocity field **u**. In the limit $\tau \rightarrow 0$, the reaction velocity $\sigma/\tau = v$ remains finite. In what follows we shall study the continuous-time model.

10.8.1 Heuristic Theory

Consider a droplet of B-particles that initially intersects the stable manifold of the chaotic saddle. As we have seen (e.g., Sects. 10.2 and 10.4), the material of the droplet will be distributed in the stirring region along filaments, in bands along the unstable manifold. In the presence of reactions, the loss due to escape is countered by the production of new B-particles. As a result, these particles will be distributed in bands of finite width along the branches of the unstable manifold. The widths are approximately the same along all branches, and we let $\delta(t)$ denote the average B-bandwidth at time t.

There are two mechanisms for $\delta(t)$ to change. Firstly, it decreases at the rate $-\lambda_1 \delta$. This is due to the exponential stretching along the unstable manifold with an average Lyapunov exponent λ_1 of the passive advective dynamics, which is accompanied, because of incompressibility, by a contraction of strength $-\lambda_1$. Secondly, the bandwidth increases due to the reaction, and the rate of increase is given by $2v$, since the reaction front propagates on both sides of the band. We thus have

$$\dot{\delta} = -\lambda_1 \delta + 2v. \tag{10.31}$$

On any filamentary segment, infinitely many other segments accumulate, since they form a fractal set. The total B-distribution, covering the unstable manifold, appears thus to be a fractal on length scales *above* $\delta(t)$, but it is two-dimensional below this scale.

Consider a region of observation of linear size L that contains the B-bands of average width $\delta(t)$ about the unstable manifold. The smallest box size where fractal scaling can be observed is the average bandwidth $\varepsilon = \delta$. The number of boxes of size ε needed to cover the populated filaments in the region of observation is $N(\delta) \sim \delta^{-D_{u,1}}$, where $D_{u,1}$ is the information dimension of the unstable manifold. The distribution of material B within the band is continuous, and the density is approximately the same in each band. The total area covered by material B in the observation region is therefore $N(\delta)$ times the area δ^2 of a single box, $\delta^2 N(\delta)$, which is proportional to the number concentration c of the B-particles in the total region of observation:

$$c \sim \left(\frac{\delta}{L}\right)^{2-D_{u,1}}. \tag{10.32}$$

The time derivative of the total number of B-particles is

$$\dot{c} \sim L^{D_{u,1}-2}(2 - D_{u,1})\delta^{1-D_{u,1}}\dot{\delta}. \tag{10.33}$$

By substituting $\dot{\delta}$ from (10.31), we obtain, after using the Kantz–Grassberger formula (2.76),

$$\dot{c} = -\kappa c + q\kappa \frac{v}{\lambda_1 L}c^{-\beta}, \tag{10.34}$$

where q is a dimensionless factor, and the exponent β is a constant:

$$\beta \equiv \frac{D_{u,1} - 1}{2 - D_{u,1}}. \tag{10.35}$$

The first term on the right-hand side of (10.34) describes the escape of B-particles due to the outflow. The second term is the *production term*, that is, the rate of production of B due to the autocatalytic reaction. The exponent $-\beta$ in the production term is *always* negative, since the dimension of the unstable manifold in open flows satisfies the relation $1 < D_{u,1} < 2$. This implies that the smaller the number of B-particles, the greater the production, and the productivity diverges as c approaches zero.

The basic rate equation (10.34) contains a single chemical parameter, the reaction velocity. All other parameters of the equation are parameters of the passive advection problem in open flows. It is striking to see that the quantities λ_1 and $D_{u,1}$ (or κ) associated with transient chaos *play an essential role in the chemical dynamics*, indicating that reactions in open flows can have different outcomes from those in well stirred containers.

Equation (10.34) describes the competition of two effects: outflow and production. As a result of the balance between these factors, a *steady state* sets in after
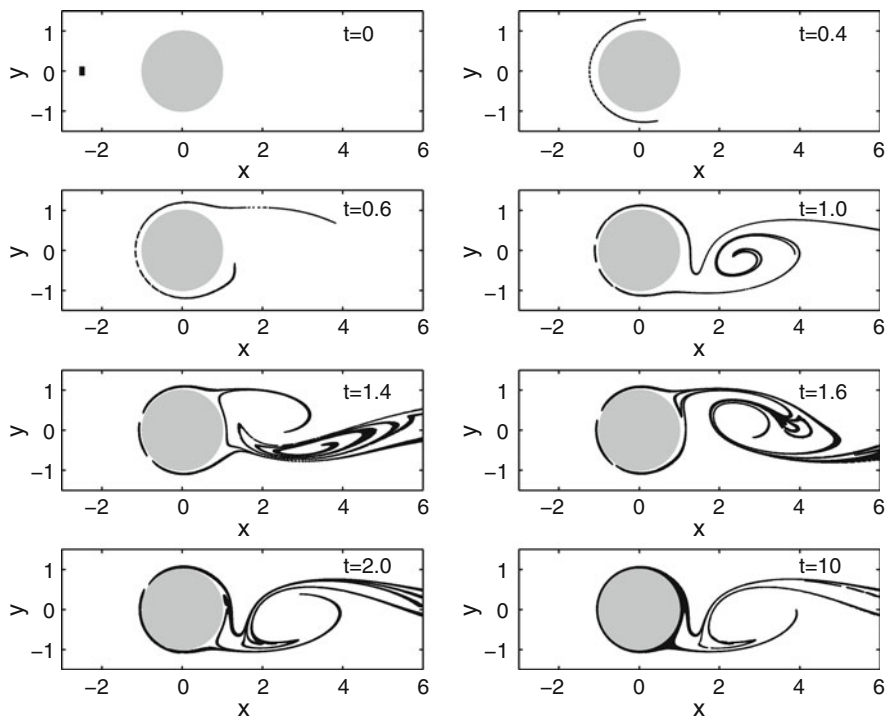
Fig. 10.29 Evolution of a chemical steady state of B-particles in an autocatalytic reaction taking place in the von Kármán vortex flow. After a few time units, the pattern no longer changes on a stroboscopic map [774] (copyright 2000, the American Institute of Physics)

sufficiently long time in the observational region. This can be seen in numerical simulations, as shown in Fig. 10.29, where a droplet of B-particles in the sea of A-particles is stretched and folded as a passive droplet initially, but the B-area increases subsequently. In fact, an accumulation takes place along the unstable manifold. However, in contrast to passive advection (e.g., Fig. 10.5), here the population is not emptied but approaches a steady state. The distribution is in dynamical equilibrium since there is a flux of B-particles permanently leaving the region, but exactly the same amount of new chemicals is produced on average. The process is thus dissipative, converging toward a *chemical attractor*. In continuous time, the attractor is a limit cycle in time-periodic flows. In this sense we can say that reactions become synchronized to the flow.

This heuristic theory has been generalized to cover different types of reactions in open flows, for example, acid–base reactions [392], reactions with inertial particles [537, 550, 551], flames and other fronts [410, 742], and reactions in three-dimensional flows [165]. The basic ideas also contribute to a better understanding of the properties of chemical transients toward equilibrium in closed flows [390, 395, 396]. Further details can be found in the reviews [545, 771].

10.8.2   Biological Activities

The temporal evolution of populations can be considered as a reaction between individuals and the available resources (food). In this context, the singular production term in the rate equation (10.34) reflects the principle of *advantage of rarity*. In particular, a state with a smaller number of organisms will grow *faster* than another one with more individuals. This is due to the fact that a smaller population covers the unstable manifold with a smaller area but with a longer perimeter. One consequence of the advantage-of-rarity principle is the existence of a nontrivial steady state in which the population never dies out.

A particularly important example is plankton dynamics [391, 502, 543, 545], where several competing species can often coexist. Traditional theoretical and empirical investigations show that the number of coexisting species in a given ecosystem is limited by the number of different resources for which the species are competing. In a well-stirred environment, only those species are able to survive which are best adapted to the use of at least one of the limiting resources [223]. This result is based on the hypothesis that the competing species are homogeneously stirred in their habitat. Observation shows, however, that a large number of species can coexist in a single ecosystem while competing for the same limiting resources. This contradiction of competitive exclusion with observations is common in the plankton communities, and is known as the *paradox of plankton*.

In plankton dynamics, the condition of open flow is often fulfilled, since a fluid element escaping the region of observation has no chance to return within the biological time scale. Thus the advantage of rarity principle applies, a mechanism that favors the survival of all the species that are about to become extinct. Figure 10.30 provides numerical evidence for the coexistence of two species in the presence of a single resource in the wake of a cylinder. The theory of reactions in open flows thus provides one possible resolution to the paradox of plankton. The theory can be used to study other ecosystem-related problems, such as the transport of plankton across island wakes [664, 666], plankton blooms in vortices [665], prebiotic evolution [682], and metabolic networks [393].

10.8.3   Reactions in Open Aperiodic Flows

The observations in Sect. 10.5.2 indicate that the particles of a B-droplet are distributed in bands along the unstable manifold of a chaotic saddle. The key feature in deriving (10.34) is that the dimension of the saddle is time-independent. It is thus plausible that the picture would essentially be the same for aperiodic flows. In particular, the relevant dimension is that of the aperiodic flow's unstable manifold. It can indeed be shown [397] that for random maps with weak parameter variations, (10.34) remains valid with the exponent β determined the same way by the dimension as in (10.35), except that $D_{u,1}$ is replaced by the dimension of the unstable manifold of the snapshot chaotic saddle. Numerical simulations show that chemical
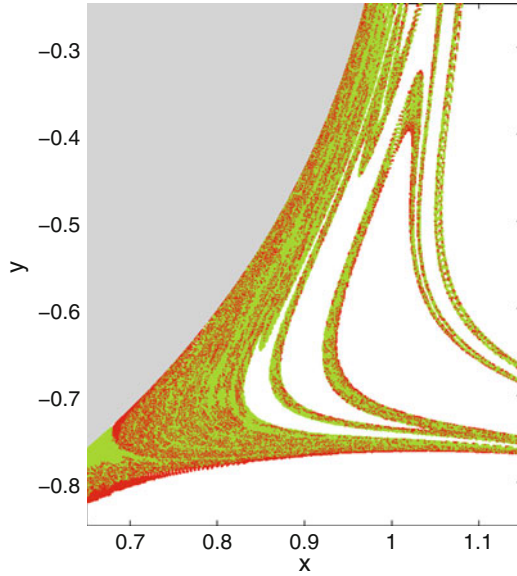
Fig. 10.30 Coexistence of two species in the von Kármán vortex street flow. Shown is population distribution close to the cylinder, after a steady state has settled in. The two species are green and red. Resource material is white [391] (with kind permission from the National Academy of Sciences of the United States)
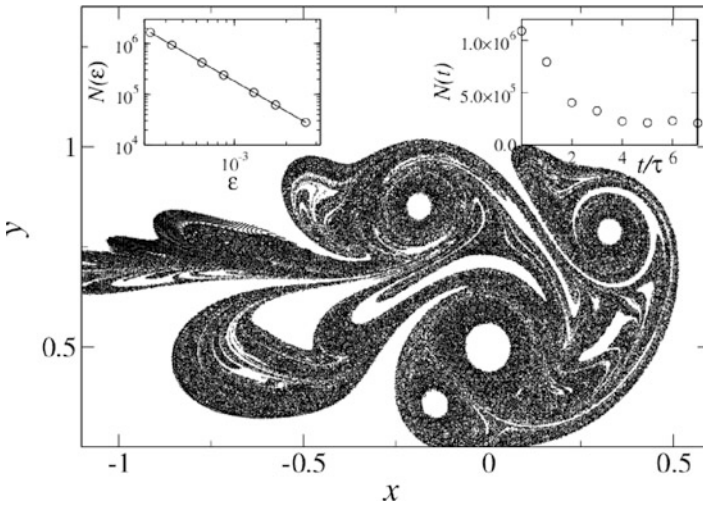
Fig. 10.31 Autocatalytic reaction in the aperiodic four-vortex flow. The main figure shows the B-distribution at dimensionless time 14. *Right inset*: Number of B-particles versus time. *Left inset*: Fractal scaling coinciding with that of the unstable manifold of the snapshot chaotic saddle in the reaction-free problem [397] (copyright 2004, the American Physical Society)

processes can reach an asymptotic state in such flows, too. An example is given in Fig. 10.31, where the B-distribution of an autocatalytic reaction in the four-vortex problem treated in Sect. 10.5.2 is shown at dimensionless time $t = 14$. By this time the system is in a "steady state." Because of the flow's aperiodicity, the number of B-particles does not stay constant in time, but fluctuates randomly, as shown in the right inset of Fig. 10.31. It can also be seen that the B-distribution is filamentary. The product particles accumulate along the unstable manifold of the snapshot chaotic saddle in this aperiodic flow. The box-counting dimension of the product is therefore the same as that of the unstable manifold in the passive advective dynamics (left inset of Fig. 10.31).

This observation shows that the appearance of transiently chaotic advective dynamics in reactive systems is a robust phenomenon.

Chapter 11
Controlling Transient Chaos and Applications

Besides the occurrence of chaos in a large variety of natural processes, chaos may also occur because one may wish to design a physical, biological, or chemical experiment, or to project an industrial plant to behave in a chaotic manner. That chaos may indeed be desirable is further evidenced by the fact that it can be controlled using small perturbation of some accessible parameter or dynamical variable of the system.

The key ingredient for the control of chaos is the observation that any chaotic set has embedded within it a large number of unstable periodic orbits of low periods. Because of ergodicity, the trajectory visits or accesses the neighborhood of each one of these periodic orbits. Some of these periodic orbits may correspond to desired system performance according to some criterion. The second ingredient is the realization that chaos, while signifying sensitive dependence on small changes to the current state, thereby rendering the system state unpredictable over long times, implies that the system's behavior can be altered using small perturbations. The accessibility of the chaotic system to many different periodic orbits combined with its sensitivity to small perturbations allows for the control and manipulation of the chaotic process. Specifically, the Ott–Grebogi–Yorke (OGY) approach [566] is as follows. One first determines some of the unstable low-period periodic orbits that are embedded in the chaotic attractor. One then examines the locations and the stabilities of these orbits and chooses one that yields the desired system performance. Finally, one applies small controls to stabilize this desired periodic orbit. A particularly appealing feature of the OGY approach is that control can be achieved based on data using nonlinear time series analysis for the observation and understanding of the system. This is important, since chaotic systems can be complicated and equations of the process are often unknown.

Since the seminal paper on the OGY paradigm there has been a tremendous amount of research on controlling chaos. The focus of this chapter is on *controlling transient* chaos. We shall present the basic idea and methodology of controlling the dynamics on nonattracting chaotic sets. The existence of transient chaos makes a new type of control possible, i.e., to convert *transient chaos into permanent chaos* via small and infrequent perturbations. The methods of maintaining chaos will be reviewed. We will then consider applications: voltage collapse and prevention,

and how to prevent species extinction. An algorithm for maintaining chaos in the presence of noise will also be presented, as well as a method of encoding digital information using transient chaos.

11.1 Controlling Transient Chaos: General Introduction

11.1.1 Basic Idea and Method

It is possible to control motion on a nonattracting chaotic set to convert transiently chaotic dynamics into periodic dynamics by stabilizing one of the infinite number of unstable periodic orbits embedded in the set. The feature of this type of control is that it stabilizes an orbit that is *not* on the actual attractor of the system. One thus selects an *atypical behavior* that cannot be revealed by a long-time observation of the unperturbed motion. This type of control is effectively *stabilizing a metastable state*. To be specific, we shall discuss the control method in the OGY paradigm [566] because it leads to an algorithm capable of carrying out the finest possible selection of the target orbit to be stabilized and applying the weakest possible perturbation. Other methods [79, 123, 667, 694, 785], e.g., the delayed feedback-control method of Pyragas [617], are also applicable. To be concrete, we focus on invertible dynamical systems.

To achieve control of transient chaos, one has to use an *ensemble* of trajectories [767] because any randomly chosen initial point leads to a trajectory that escapes any neighborhood of the saddle in finite time. This ensemble is typically chosen to start from a compact region having intersections with the stable manifold of the chaotic saddle. One also selects a target region *I* containing a predetermined unstable periodic orbit on the chaotic saddle. Then the ensemble of trajectories start to evolve, and one waits until a trajectory enters the target region to activate control. The control perturbation is adjusted with time so as to stabilize the periodic orbit. Only small local perturbations are allowed, smaller in size than some value δ, the maximum allowed perturbation. In general, δ is proportional to the linear extension of the target region [566].

To illustrate the OGY method, we shall use a two-dimensional map with p as an externally accessible control parameter [767]. We restrict parameter perturbations to be small, i.e., $|p - \overline{p}| < \delta$, where $\overline{p}$ is some nominal parameter value, and $\delta \ll 1$ defines the range of parameter variation. We wish to program the parameter p so that a chaotic trajectory is stabilized when it enters an ε-neighborhood of the target periodic orbit. Without loss of generality, we assume that the target orbit is an unstable fixed point embedded in the chaotic saddle, denoted by $\mathbf{x}_F(\overline{p})$. The location of the fixed point in the phase space depends on the control parameter p. Upon application of a small perturbation Δp, we have $p = \overline{p} + \Delta p$. Since Δp is small, we expect $\mathbf{x}_F(p)$ to be close to $\mathbf{x}_F(\overline{p})$, and write

$$\mathbf{x}_F(p) \approx \mathbf{x}_F(\overline{p}) + \mathbf{g}\Delta p, \tag{11.1}$$

where **g** is a vector given by

$$\mathbf{g} \equiv \frac{\partial \mathbf{x}_F}{\partial p}\bigg|_{p=\overline{p}} \approx \frac{\mathbf{x}_F(p) - \mathbf{x}_F(\overline{p})}{\Delta p}. \tag{11.2}$$

The vector **g** needs to be determined before a control law can be applied to stabilizing the fixed point $\mathbf{x}_F(\overline{p})$.

To formulate a control law, we make use of the fact that the dynamics of any smooth nonlinear system is approximately linear in a small neighborhood of a fixed point. Thus, near $\mathbf{x}_F(\overline{p})$, we have

$$\mathbf{x}_{n+1} - \mathbf{x}_F(p) \approx \mathbf{J}[\mathbf{x}_F(p)] \cdot (\mathbf{x}_n - \mathbf{x}_F(p)), \tag{11.3}$$

where $\mathbf{J}[\mathbf{x}_F(p)]$ is the 2×2 derivative matrix of the map $\mathbf{f}(\mathbf{x}, p)$ evaluated at the fixed point $\mathbf{x}_F(p)$, defined as

$$\mathbf{J}[\mathbf{x}_F(p)] = \frac{\partial \mathbf{f}}{\partial \mathbf{x}}\bigg|_{\mathbf{x}_F(p)} \approx \mathbf{J}[\mathbf{x}_F(\overline{p})] + \frac{\partial \mathbf{J}}{\partial p}\bigg|_{p=\overline{p}} \Delta p. \tag{11.4}$$

Note that $\Delta p \sim \varepsilon$ and $|\mathbf{x}_n - \mathbf{x}_F(p)| \sim \varepsilon$, where ε is the size of the small neighborhood in which the linear approximation (11.3) is valid. Substituting (11.1) and (11.4) into (11.3), and keeping only terms that are of first order in ε, we obtain

$$\mathbf{x}_{n+1} - \mathbf{x}_F(\overline{p}) \approx \mathbf{g}\Delta p + \mathbf{J}[\mathbf{x}_F(\overline{p})] \cdot [\mathbf{x}_n - \mathbf{x}_F(\overline{p}) - \mathbf{g}\Delta p]. \tag{11.5}$$

Since $\mathbf{x}_F(\overline{p})$ is embedded in the chaotic saddle, it has one stable and one unstable direction. Let $\mathbf{e}_s$ and $\mathbf{e}_u$ be the stable and the unstable unit eigenvectors at $\mathbf{x}_F(\overline{p})$, respectively, and let $\mathbf{f}_s$ and $\mathbf{f}_u$ be two unit vectors that satisfy $\mathbf{f}_s \cdot \mathbf{e}_s = \mathbf{f}_u \cdot \mathbf{e}_u = 1$ and $\mathbf{f}_s \cdot \mathbf{e}_u = \mathbf{f}_u \cdot \mathbf{e}_s = 0$ (relations by which the vectors $\mathbf{f}_s$ and $\mathbf{f}_u$ can be determined from the eigenvectors $\mathbf{e}_s$ and $\mathbf{e}_u$), which are the contravariant basis vectors associated with the eigenspaces $\mathbf{e}_s$ and $\mathbf{e}_u$ [566]. The derivative matrix $\mathbf{J}[\mathbf{x}_F(\overline{p})]$ can then be written as

$$\mathbf{J}[\mathbf{x}_F(\overline{p})] = \lambda_u \mathbf{e}_u \mathbf{f}_u + \lambda_s \mathbf{e}_s \mathbf{f}_s, \tag{11.6}$$

where λ_s and λ_u are the stable and the unstable eigenvalues in the eigendirections $\mathbf{e}_s$ and $\mathbf{e}_u$, respectively.

When the trajectory point $\mathbf{x}_n$ falls into the small ε-neighborhood of the desired fixed point $\mathbf{x}_F(\overline{p})$, (11.3) becomes valid. A small parameter perturbation Δp_n can there be applied at time n to make the fixed point shift slightly so that at the next iteration $(n+1)$, $\mathbf{x}_{n+1}$ falls on the stable direction of $\mathbf{x}_F(\overline{p})$:

$$\mathbf{f}_u \cdot [\mathbf{x}_{n+1} - \mathbf{x}_F(\overline{p})] = 0. \tag{11.7}$$

For sufficiently small $\mathbf{x}_n - \mathbf{x}_F(\overline{p})$ we can substitute (11.5) into (11.7) to obtain $\Delta p_n = c_n$, where c_n is given by

$$c_n = \frac{\lambda_u \mathbf{f}_u \cdot [\mathbf{x}_n - \mathbf{x}_F(\overline{p})]}{(\lambda_u - 1)\mathbf{f}_u \cdot \mathbf{g}} \equiv \mathbf{C} \cdot [\mathbf{x}_n - \mathbf{x}_F(\overline{p})]. \tag{11.8}$$

We assume in the above that the generic condition $\mathbf{g} \cdot \mathbf{f}_u \neq 0$ is satisfied, so c_n can be calculated. Once $\mathbf{x}_{n+1}$ falls on the stable direction of $\mathbf{x}_F(\overline{p})$, we can set the control perturbation to zero, and the trajectory for subsequent time will approach the fixed point at the geometrical rate λ_s.

   The considerations above apply only to a local small neighborhood of $\mathbf{x}_F(\overline{p})$. Globally, one can specify the parameter perturbation Δp_n by setting $\Delta p_n = 0$ if $|c_n|$ is too large, since the range of the parameter perturbation is limited to be small. Thus, practically, we have

$$\Delta p_n = \begin{cases} c_n, & \text{if } |c_n| < \delta, \\ 0, & \text{if } |c_n| \geq \delta. \end{cases} \tag{11.9}$$

In this way, in the definition of c_n in (11.8), it is unnecessary to restrict the quantity $|\mathbf{x}_n - \mathbf{x}_F(\overline{p})|$ to be small.

   Figure 11.1 shows an example [767] of controlling a fixed point on the Hénon chaotic saddle in comparison with the uncontrolled trajectory. We see that the controlled motion is not a part of the asymptotic dynamics [605, 606, 792].

11.1.2 Scaling Laws Associated with Control

There are scaling laws characterizing the ensemble of trajectories in the limit of a small allowed perturbation δ. Many of the trajectories approach the asymptotic attractor before entering the target region enclosing the periodic orbit to be stabilized on the chaotic saddle. Short transients are therefore irrelevant for the controlling process, but trajectories with lifetimes significantly larger than $1/\kappa$ are unprobable. As a result, the average time τ_c needed to achieve control is independent of δ and is limited from above by the chaotic lifetime $\tau \approx 1/\kappa$ for some values of δ:

$$\tau_c \leq 1/\kappa. \tag{11.10}$$

Because of the escape, only a small portion of all trajectories can be controlled. When the target region is a disk, the number of controlled trajectories $N(\delta)$ decreases with decreasing δ according to the power law [767]:

$$N(\delta) \sim \delta^{\gamma(\kappa)}, \tag{11.11}$$

where the exponent $\gamma(\kappa)$ depends on the escape rate of the saddle. The number of controlled trajectories is proportional to the c-measure $\mu_c(I)$ of the target region I. The c-measure is smooth along the unstable direction, so the measure μ_c of a region
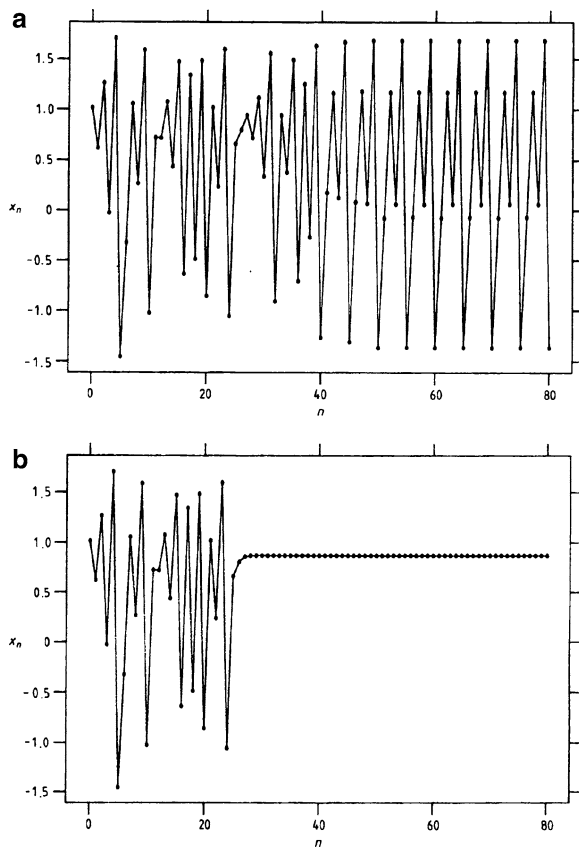
Fig. 11.1 For the Hénon map at parameters $a = 1.45$, $b = 0.2$, where the attractor is a period-5 cycle, (**a**) a transiently chaotic time series. The trajectory ceases to be chaotic at about the 38th time step, where it enters the neighborhood of the period-5 attractor. (**b**) Controlled signal started from the same initial point. The Hénon map has the form given in the caption of Fig. 5.9 with $a = 1.45 + p_n$, $J = -b$, where the maximum allowed perturbation is $\delta = 0.1$. The fixed point is at $x_F = y_F = 0.868858$. Control sets in at the 26th step, and the fixed point on the saddle is stabilized [767] (with kind permission from Institute of Physics)

of size l_1 and l_2 along the unstable and the stable direction, respectively, scales according to (2.89). For $l_1 \sim l_2 \sim \delta$, the scaling exponent is given by

$$\gamma(\kappa) = 1 + \alpha_2(\kappa), \tag{11.12}$$

where $\alpha_2(\kappa)$ is the crowding index along the stable direction. In the particular case in which the target region contains a fixed point, the exponent $\gamma(\kappa)$ is (2.91):

$$\gamma(\kappa) = 1 + \frac{\lambda_1^* - \kappa}{|\lambda_2^*|}, \tag{11.13}$$

where λ_i^* $(i = 1, 2)$ are the local Lyapunov exponents of the fixed point to be stabilized $(\lambda_{1(2)}^* = \ln |\lambda_{u(s)}|)$.

When applying the OGY method to controlling permanent chaos, the scaling properties of an ensemble of N_0 trajectories are different. The average time τ_c needed to achieve control is a function of the linear size of the target region, which is proportional to the maximum allowed perturbation δ. It was pointed out [566] that $\tau_c(\delta)$ increases algebraically as δ is decreased,

$$\tau_c(\delta) \sim \delta^{-\gamma}, \quad \text{for} \quad \delta \ll 1, \tag{11.14}$$

where $\gamma > 0$ is a characteristic exponent. This scaling law shows that the dynamics of reaching the target region is itself a kind of transient chaos. The process of control can be interpreted as leaking a closed chaotic system at the target region (Sect. 2.7). The time needed to achieve control is thus the average lifetime of the invariant chaotic saddle of the leaked system. For small leak sizes the lifetime scales as the inverse of the natural measure μ of the leak. We have

$$\gamma = 1 + \alpha_2, \tag{11.15}$$

where $\alpha_2 = \lambda_1^* / |\lambda_2^*|$ is the crowding index along the stable direction of the chaotic set in the closed system.[1] However, the number $N(\delta)$ of controlled trajectories is fixed, $N(\delta) = N_0$, since all N_0 trajectories of the ensemble are controlled sooner or later.

The scaling laws in the control of permanent and transient chaos thus appear to be the two extremes of a general process, where for the former, $N(\delta)$ is constant, but for the latter, $\tau_c(\delta)$ is constant. There exists a unifying relation between $N(\delta)$ and $\tau_c(\delta)$ that holds in both cases [769]. The key observation is that the number of controlled trajectories in the entire process is proportional to the average number of trajectories controlled *per unit time* multiplied by the average time needed to achieve control. The average number of trajectories controlled per time step is proportional to the probability of falling in the target region. For small regions this is proportional to the c-measure of the target region in the uncontrolled system. Since the latter scale as δ^γ or $\delta^{\gamma(\kappa)}$, the number of trajectories controlled per time step follows the scaling law

$$\frac{N(\delta)}{\tau_c(\delta)} \sim \delta^{\gamma(\kappa)}, \tag{11.16}$$

which is valid for both permanent ($\kappa = 0$) and transient ($\kappa > 0$) chaos.

---

[1] For a larger target region, the exponent γ depends strongly on the location of I even if $\mu(I)$ is kept constant [101, 103, 571, 572, 574]. From the general theory of leaked systems (cf. Sect. 2.7), this can be understood as being due to the complicated overlap of the leak with its preimages.

11.1.3 Remarks

11.1.3.1 Controlling Fractal Basin Boundaries

An immediate application is the control of motions on a fractal basin boundary [418, 434, 706], which contains a chaotic saddle whose stable manifold constitutes the boundary. One can then control a desirable periodic orbit in the saddle. By applying weak control perturbations, a hyperbolic orbit on the basin boundary can be converted into an attracting orbit [418]. The methodology is potentially important in applications where periodic driving can result in a catastrophic failure of the system. A particular example is ship capsizing, where the method of controlling motion on fractal basin boundaries was computationally tested to prevent chaos-induced ship capsizing even in cases where the driving due to environmental influences (e.g., waves) is not periodic but has a substantially irregular (chaotic) component [195].

An alternative method for steering most trajectories to a desirable attractor is to build a hierarchy of paths to it and then stabilize trajectories around one of the paths in the hierarchy [434]. A pronounced improvement in the probability for a random trajectory to approach a desirable attractor can be achieved when there are fractal basin boundaries or riddled basins.

11.1.3.2 Controlling Chaotic Scattering

A feature of chaotic saddles in Hamiltonian systems is that they typically contain a nonhyperbolic component where the local Lyapunov exponents are arbitrarily close to zero (Sect. 6.4). A problem is to investigate the influence of the nonhyperbolic component on the control process. If one selects a periodic orbit close to a KAM surface, the time to achieve control is usually long due to the stickiness effect. Numerical investigation showed [453] that the average time to achieve control could be an order of magnitude longer than the average chaotic lifetime on the hyperbolic component.

In general, controlling a collisional scattering process means *stabilizing the intermediate complexes* of a reaction that would otherwise be of finite lifetime. Although KAM surfaces can be important for the controlling process, the qualitative behavior of the controlled ensemble is similar to that of a fully hyperbolic system.

11.1.3.3 Improved Method of Controlling a Chaotic Saddle

As we have seen, a major difference between stabilizing unstable periodic orbits embedded in a chaotic attractor and in a chaotic saddle is that for the attractor, the probability that a chaotic trajectory enters the neighborhood of the desired unstable periodic orbit is one, while for transient chaos, only a small set of initial conditions can be controlled, since most trajectories will have already left the chaotic saddle before entering the neighborhood of the target periodic orbit. An issue is how to maximize this probability of control of transient chaos. A useful observation is that there exists a dense chaotic orbit in the saddle *that comes arbitrarily close to any*

target unstable periodic orbit. Such a dense orbit is the complement of the set of all unstable periodic orbits in the saddle, and can be numerically obtained by the PIM-triple method (Sect. 1.2.2.4). The probability that a trajectory approaches this orbit can be significantly larger than the probability that the trajectory enters the neighborhood of the target unstable periodic orbit, if the reference orbit is long. By stabilizing a trajectory about the reference orbit first, and then switching to stabilize it about the target periodic orbit after the trajectory comes close to it, we can increase substantially the probability that a trajectory can be controlled [447, 461]. This can indeed be achieved, since there exist stable and unstable directions at each point of the reference orbit on the chaotic saddle. Hence in principle, controlling a trajectory near the reference orbit is equivalent to stabilizing a long unstable periodic orbit. The longer the length of the reference orbit, the larger the probability of controlling periodic orbits.

11.2   Maintaining Chaos: General Introduction

The conversion of transient chaos into permanent chaos is called chaos maintenance or preservation, and the basic ideas date back to the work of Yang et al. [840], Schwartz and Triandaf [697], and Kapitaniak and Brindley [383]. The term partial control of chaos is also in use [849], since the algorithms do not determine exactly where the trajectory goes around a nonattracting chaotic set. The practical relevance of this approach is due to the fact that there are systems that require chaos in order to function properly. Notable examples are mechanical systems in which the avoidance of resonance via chaos is desirable [697], advection in fluids where complete stirring can be achieved only via permanent chaos (cf. Chap. 10), and biological systems in which the disappearance of chaos may signal pathological phenomena (see point (2) of Sect. 4.4.3). Under certain conditions, simple regular attractors may appear, and it is then important to intervene in order to maintain chaos. Later in this chapter we shall investigate two examples in detail in which maintenance of chaos is useful: preventing voltage collapse (Sect. 11.3) and species extinction (Sect. 11.4).

11.2.1   Basic Idea

The aim is to intervene the dynamics in such a way as to keep chaotic behavior alive in situations in which it would naturally be absent. In fact, stabilizing a trajectory about a reference orbit on a chaotic saddle, which can enhance the probability of converting a transiently chaotic behavior into a periodic one, as described in the last subsection, can be considered as an attempt to maintain chaos if the reference orbit is long. Other types of algorithms are based on the observation that systems exhibiting transient chaos have special regions in their phase spaces, called loss regions or *escape regions*. They are identified by the property that after the orbit enters such

a region, it immediately ceases its chaotic motion, i.e., it is rapidly drawn to some simple attractor. Examples of loss regions are the primary escape interval I_0 of open one-dimensional maps (see Fig. 2.1) and the area bounded by the outermost branch of the chaotic saddle's unstable manifold and the outermost branch of its stable manifold (cf. the shaded area AB in Fig. 3.12).

The strategy can be formulated straightforwardly for map $\mathbf{f}(\mathbf{x}_n, p)$, where p denotes the parameter whose temporal change will be used to maintain chaos. After identifying a loss region L, one considers the preimages L_m of this region under the unperturbed map $\mathbf{f}(\mathbf{x}_n, \bar{p})$, where $\bar{p}$ is the nominal parameter value. The set L_m is thus the set of points mapped onto the loss region in m iterates, and the width of L_m decreases exponentially along the unstable direction(s) as m increases. Yang et al. [840] suggested the following approach. Pick a large value M of m and consider the preimages of the loss region up to level $M + 1$. If the unperturbed orbit lands in L_{M+1} on iterate n, one applies a control parameter p_n (different from $\bar{p}$) in order to kick the orbit out of L_M on the next iterate. Since L_M is thin, the required change $\Delta p_n = p_n - \bar{p}$ is small. After the orbit is kicked out of L_M, it is likely to execute a chaotic motion. Due to the fractal structure of the nonattracting set, the orbit falls with probability one outside this chaotic set, i.e., in a region L_r with $r > M$. Long chaotic sequences are expected if r happens to be much larger than M. After some time, the orbit falls again in L_{M+1} when a small control is activated, and so on.

The amount of the control parameter shift Δp_n at the nth step can be estimated by using the sensitivity vector (11.2) evaluated in the loss region and its preimages. By assuming that this vector is approximately a constant $\bar{\mathbf{g}}$ over these regions, and using the maximum width d_M of region L_M, one finds that

$$\Delta p_n \approx \frac{d_M}{|\bar{\mathbf{g}}|}, \tag{11.17}$$

which is a small number for $M \gg 1$. These ideas were successfully applied to maintaining chaos in different models [840], and also in an experiment in which the intermittent signal of a megnetomechanical ribbon [350] was converted into a nonintermittent chaotic signal. This means that chaos was maintained on a chaotic saddle lying outside a marginally stable periodic orbit.

11.2.2 Maintaining Chaos Using a Periodic Saddle Orbit

The method proposed by Schwartz and Triandaf [697] (see also [698]) can be applied to situations in which the chaotic attractor of an invertible system has been destroyed in a crisis (Chap. 3). (The parameter whose change leads to crisis is not necessarily the same as the parameter p that will be used in the control process.) The system may then exhibit transient chaos until it reaches the periodic saddle point mediating the crisis. If the trajectory happens to fall on one side of the stable manifold of this mediating orbit, it directly approaches a periodic attractor. On the

other side of the stable manifold, however, it has chances to return to the chaotic saddle appearing there as the remnant of a former chaotic attractor. We shall call this side of the manifold the chaotic side. Once the trajectory enters a neighborhood of the saddle orbit, a small perturbation in parameter p is applied to ensure that the trajectory falls on the chaotic side in the next step.[2] To optimize chaos maintenance, one can use the distribution of lifetimes to select a target point $\mathbf{x}_{tar}$ lying close to the mediating orbit with a particularly long lifetime, which ensures that perturbations should be applied only rarely.

In a two-dimensional map, the local dynamics around a saddle point can be approximated by equations (11.5) and (11.6). Note, however, that the hyperbolic fixed point $\mathbf{x}_F$ is now the mediating orbit and not an unstable point inside the saddle as in Sect. 11.1. The required amount of control Δp_n at time instant n when the trajectory happens to be close to the mediating orbit can be obtained from these equations by requiring $\mathbf{x}_{n+1} = \mathbf{x}_{tar}$. After a multiplication of (11.5) by $\mathbf{f}_s$, one obtains

$$\Delta p_n = \frac{\mathbf{f}_s \cdot [\lambda_s(\mathbf{x}_n - \mathbf{x}_F(\overline{p})) - (\mathbf{x}_{tar} - \mathbf{x}_F(\overline{p}))]}{(\lambda_s - 1)\mathbf{f}_s \cdot \mathbf{g}}. \tag{11.18}$$

The required control is thus proportional to $\lambda_s[\mathbf{x}_n - \mathbf{x}_F(\overline{p}) - (\mathbf{x}_{tar} - \mathbf{x}_F(\overline{p}))]$.

The method can be extended to higher dimensions and has successfully been applied by In et al. [351] to maintain chaos in a magnetoelastic ribbon experiment, as shown in Fig. 1.22. The perturbation leads to permanent chaos in a system in which the natural attractor would be periodic.

11.2.3 Practical Method of Control

In [185], a practical method was suggested for converting transient chaos into sustained chaos, based on measured time series. In contrast to the situation of chaotic attractors, these time series consist of short segments of chaotic oscillations exhibiting a number of local maxima and minima. Let e_n $(n = 1, \ldots, L)$ be the set of extrema (maxima or minima) from one measured segment of one dynamical variable $x(t)$. In order to detect the underlying dynamics, an ensemble of transient chaotic trajectories from a large number of random initial conditions can be used, each yielding a number of points in the e_{n+1} versus e_n plot. As a crude approximation, the dynamics of the underlying system can be represented by a map $e_{n+1} = M(e_n)$, where if the underlying dynamics is approximately one-dimensional, $M(e)$ is a one-dimensional smooth curve. For higher-dimensional dynamics, the plot $M(e)$ typically exhibits some complicated structure. It is possible to identify regions of the plane $\mathbf{e}_n = (e_n, e_{n+1})$ in which the chaotic saddle lies, and a loss region where

---

[2] If the perturbation is chosen so that the trajectory falls on the other side, one can speed up the escape process to the simple attractor and can *reduce* the average lifetime of chaos [383].

escape from the chaotic saddle occurs. Thus, by applying a small perturbation to an accessible set ($\{e_n\}$) of dynamical variables at a time when the trajectory is in the escape region, chaotic motion can also be maintained for a finite period of time. The difference between this approach and that of the previous subsections is that the region is identified here only in the two-dimensional plane (e_n, e_{n+1}), and not in the full phase space. Because of this, information about target points in this method is incomplete. The situation can be improved if more dynamical variables are experimentally accessible [185].

11.3   Voltage Collapse and Prevention

We present an example of application of maintaining chaos: voltage collapse in electrical power systems and prevention. We shall describe a model system and demonstrate that voltage collapse is typically preceded by transient chaos. A practical control method will then be discussed to convert transient chaos into sustained chaos, thereby preventing voltage collapse while at the same time *preserving the natural dynamics* of the system.

11.3.1   *Modeling Voltage Collapse in Electrical Power Systems*

Electrical power systems are essentially nonlinear dynamical systems. Most major power-system failures in the past were reported to be caused by the dynamic response of the system to disturbances [132, 200]. Voltage collapse occurs when the system is heavily loaded. In such a case, dynamical variables of the system, such as various voltages, fluctuate randomly for a period of time before collapsing to zero suddenly, leading to a complete blackout of the system. Due to an ever-increasing demand for electrical power, there is an interest in operating the power system near the edge of its stability boundary. As a consequence, the system becomes highly nonlinear and can exhibit chaotic behaviors. One possible mechanism for voltage collapse is then as follows. The system operates in a parameter region where there is a chaotic attractor. A disturbance or a temporal overload causes a shift in a system parameter so that a boundary crisis occurs, after which the system exhibits transient chaos, leading to a voltage collapse. To understand the phenomenon of voltage collapse, Dobson and Chiang [132, 200] introduced a model power system consisting of a generator, an infinite bus, a nonlinear load, and a capacitor in parallel with the nonlinear load. Subsequently, Wang and Abed pointed out that the presence of the capacitor could cause an increase in the reactive power demand of the load to almost practically unreachable values even in normally encountered parameter regimes. A modified model was proposed [818, 819], which is mathematically described by the following set of differential equations:

$$\dot{\delta}_m = \omega, \tag{11.19}$$
$$0.01464\dot{\omega} = -0.05\omega + 1.0 - 5.25V\sin(\delta_m - \delta),$$
$$-0.03\dot{\delta} = -2.1V^2 + 2.8V + Q(\delta_m, \delta, V) - 0.3 - Q_1,$$
$$-0.0765\dot{V} = 0.84V^2 - 1.204V - 0.03\left[P(\delta_m, \delta, V) - 0.6\right]$$
$$-0.4[Q(\delta_m, \delta, V) - 0.3 - Q_1],$$

where the dynamical variables δ_m, ω, δ, and V are from circuit analysis, Q_1, the load, is a bifurcation parameter, and $P(\delta_m, \delta, V)$ and $Q(\delta_m, \delta, V)$ are the real and reactive powers supplied to the load by the network, which are nonlinear functions of their variables [818, 819]. A bifurcation analysis indicated [185] that there is a period-doubling cascade to chaos, and a crisis occurs at $Q_{1c} \approx 2.56037833$, after which the chaotic attractor is converted into a chaotic saddle. The range for the attractor is relatively small. Suppose the system operates at some value of Q_1 before the crisis. A small change in Q_1 can push the system over the crisis where there is transient chaos. A voltage collapse can then occur. Figure 11.2 shows a time series $V(t)$ for $Q_1 = 2.5603784 > Q_{1c}$, where $V(t)$ goes to zero suddenly after about 80 time units.

How to prevent voltage collapse? A possible approach is to reduce the load Q_1 to bring the system back into the parameter regime where there is an attractor. In a practical situation, however, it may not be feasible to change the load of an electrical power system in a relatively short time. One viable strategy is then to control transient chaos.
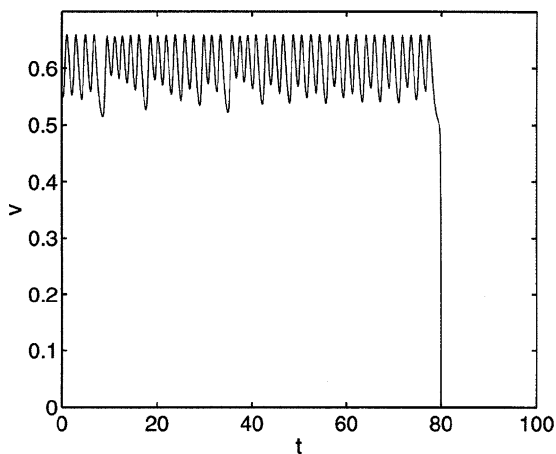
Fig. 11.2 A typical example of voltage collapse in the power system (11.19) [185] (copyright 1999, the American Physical Society)

11.3.2 Example of Control

Figure 11.3a shows the return map obtained from the local minima of $V(t)$ for $Q_1 = 2.5603784 > Q_{1c}$. There is a primary escape interval below which $V(t)$ goes to zero quickly, as shown in Fig. 11.3b. The vertical lines denote the regions from which target points are chosen. The escape interval corresponds to an escape region on the chaotic saddle. In contrast, before the crisis, there is no such gap in the return map. To achieve control in the regime of transient chaos, a set of 3,000 target points was selected [185] in the vicinity of the escape interval with long lifetime. Figure 11.4 shows the lifetime versus the value of local minima. The plot is not smooth and contains an infinite number of singularities corresponding to points on the stable manifold of the chaotic saddle. This singular structure renders selection of desired target points possible. Each target point contains the
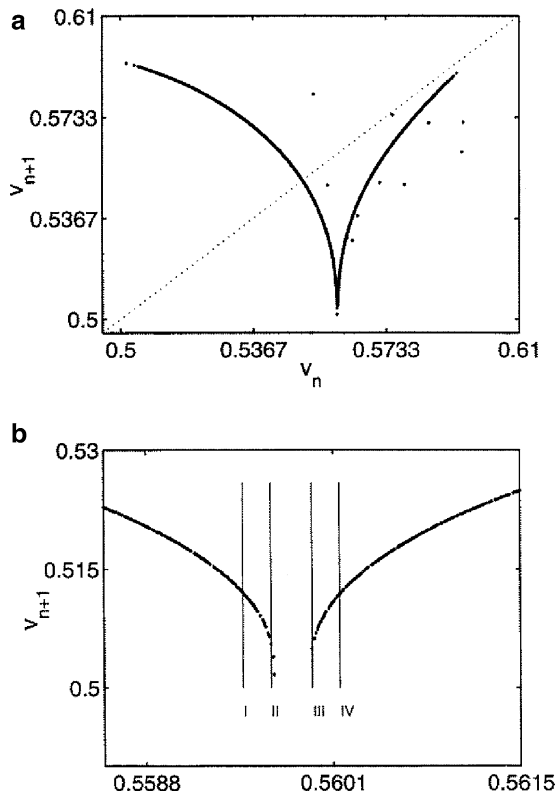
Fig. 11.3 Return map constructed from the local minima of $V(t)$: (**a**) after the crisis for $Q_1 = 2.5603784$; and (**b**) a magnification of part of (**a**) near the cusp. There is a primary escape interval, enclosed between lines II and III, through which a trajectory approaches asymptotically the state with $V = 0$ (voltage collapse). Two regions to the *left* (I – II) and to the *right* (III – IV) of the gap are the regions from which target points can be chosen for control [185] (copyright 1999, the American Physical Society)
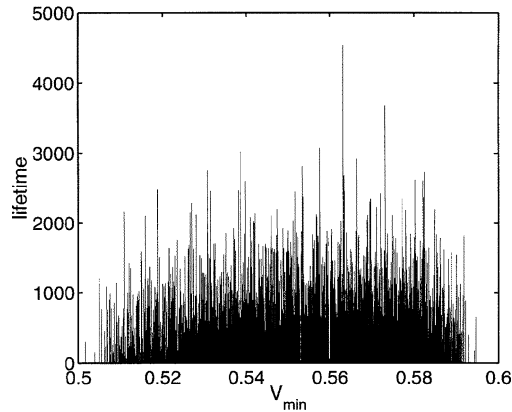
Fig. 11.4 Lifetime versus the local minima of $V(t)$ in the return map. The plot contains an infinite number of singularities corresponding to points on the stable manifold of the chaotic saddle [185] (copyright 1999, the American Physical Society)

values of the four dynamical variables in (11.19), although $V(t)$ is always at a local minimum. The set of target points is then stored for computing the control perturbation. When an actual trajectory falls into the escape interval, the computer selects a target point such that the required perturbation to kick the trajectory onto the target point is minimal. Perturbations can be applied to the dynamical variables **x** directly. Or if there is an accessible system parameter p that can be adjusted, perturbations can be applied to the parameter based on the difference between the trajectory point in the escaping window and the target point: $\Delta p = (\partial \mathbf{x}/\partial p)|_{\text{target}} \Delta \mathbf{x}$. In the power-system model (11.19), since all four dynamical variables can be perturbed, it is convenient to apply control directly to these variables. An example of control is shown in Fig. 11.5a, a controlled voltage signal $V(t)$. The required control perturbations are shown in Fig. 11.5b. In the time interval shown, only four small perturbations are required to sustain transient chaos. In general, the average time interval for applying perturbations is approximately the average lifetime of the chaotic saddle. Perturbations are required only when the system drifts into the regime of transient chaos, since transient chaos is the culprit of voltage collapse.

A key question in any scheme of controlling transient chaos concerns the probability of a typical trajectory being controlled.[3] Since the system performs normally before the collapse and since control is activated only when $V(t)$ falls into the escape

---

[3] We address initial conditions only in the original basin of the attractor because, before the collapse, the system performs normally and operates in the precrisis regime. We are not concerned with initial conditions outside the basin, although they usually yield trajectories leading to $V = 0$. A voltage collapse can thus be regarded as a catastrophic event. Our control method is applicable to preventing this type of catastrophe.
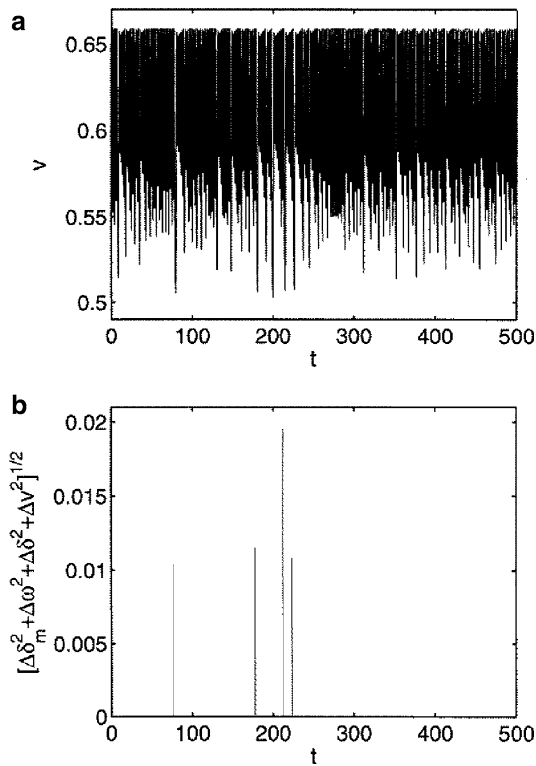
Fig. 11.5 An example of controlling transient chaos to prevent voltage collapse: (**a**) a controlled time series $V(t)$; and (**b**) required control perturbations. Apparently, only infrequent perturbations are needed to prevent voltage collapse [185] (copyright 1999, the American Physical Society)

interval, almost all trajectories can be controlled [185]. This implies that voltage collapse can be effectively prevented by controlling transient chaos.

11.4 Maintaining Chaos to Prevent Species Extinction

We consider the problem of species extinction in ecological systems, which can occur as a consequence of deterministic transient chaos even in the absence of external disturbances. Controlling transient chaos by applying small, ecologically feasible perturbations to the populations at appropriate but rare times thus provides a possibility for preventing species extinction.

11.4.1 Food-Chain Model

Extinction of species has been a mystery in nature [604]. A common belief about local extinction is that it is typically caused by external environmental factors such as sudden changes in climate. For a species of small population size, small random changes in the population (known as "demographic stochasticity") can also lead to extinction. How species extinction occurs is extremely complex, since each species typically lives in an environment that involves interactions with many other species (e.g., through competition for common food sources, predator–prey interactions, etc.) as well as physical factors such as weather and environmental disturbances. From a mathematical point of view, a dynamical model for the population size of a species is complex, involving temporal and spatial variations, external driving, and random perturbations. Such a system should, in general, be modeled by nonlinear partial differential equations with random and/or regular external driving forces. A difficulty associated with this approach is that the analysis and numerical solution of stochastic and/or driven nonlinear partial differential equations present a challenging problem.

Nonetheless, in certain situations the mathematical model for species extinction can become simpler. For example, it was suggested by McCann and Yodzis [510] that deterministic chaos in simple but plausible ecosystem models, mathematically described by coupled ordinary differential equations, can provide a hint as to how local species extinction can arise without the necessity of considering temporal or spatial variations and external factors. The key observation is that the population dynamics of a large class of ecosystems can be effectively modeled by deterministic chaotic systems [317, 339, 507, 508]. It was shown [510] that transient chaotic behavior responsible for species extinction can indeed occur in a simple three-species food-chain model that incorporates biologically reasonable assumptions about species interactions [316]. The model involves a resource species, a prey (consumer), and a predator [510], and is given by

$$\frac{\mathrm{d}R}{\mathrm{d}t} = R\left(1 - \frac{R}{K}\right) - \frac{x_C y_C C R}{R + R_0}, \tag{11.20}$$

$$\frac{\mathrm{d}C}{\mathrm{d}t} = x_C C\left(\frac{y_C R}{R + R_0} - 1\right) - \frac{x_P y_P P C}{C + C_0},$$

$$\frac{\mathrm{d}P}{\mathrm{d}t} = x_P P\left(-1 + \frac{y_P C}{C + C_0}\right),$$

where R, C, and P are the population densities of the resource, the consumer, and the predator, respectively; K is the resource carrying capacity; and x_C, y_C, x_P, y_P, R_0, and C_0 are parameters.

The biological assumptions of the model are as follows: (1) the life history of each species involves continuous growth and overlapping generations, with no age structure, permitting the use of differential equations; (2) the resource population R grows logistically; (3) each consumer species (immediate consumer C,

predator P) without food dies off exponentially; (4) each consumer's feeding rate, e.g., $x_C y_C R / (R + R_0)$, saturates at high food levels. The resource population R, growing alone, equilibrates at its carrying capacity K. The resource population and the intermediate consumer, without the predator, either settles to a stable equilibrium or a stable limit cycle, a kind of "biological oscillator." The oscillations are generated by the saturating feeding response, which permits the resource to periodically "escape" control by the consumer. With the top predator, there are in a sense two coupled oscillators in the food chain. A system of coupled oscillators can typically give rise to chaotic dynamics.

11.4.2   Dynamical Mechanism of Species Extinction

How species extinction can occur in the model can be revealed by a bifurcation analysis [510]. In particular, a chaotic attractor can arise via the period-doubling route and is then destroyed through boundary crisis, say at $K = K_c$. None of the populations corresponding to trajectories on the chaotic attractor is extinct, because the attractor is located in a phase-space region away from the origin, $(R, C, P) = (0, 0, 0)$. In this parameter range, however, there is also a limit-cycle attractor, located in the plane $P = 0$, which coexists with the chaotic attractor. Trajectories on the limit-cycle attractor correspond to the situation in which the predator population is extinct. For K slightly less than K_c, depending on the choice of the initial condition, the system either approaches the chaotic attractor or the limit cycle with $P = 0$. For K slightly below K_c, there is still a finite distance from the tip of the chaotic attractor to the basin boundary. Thus, for any initial condition chosen in the basin of the chaotic attractor, the population of the predator $P(t)$ behaves chaotically in time but never decreases to zero, because the attractor lives in a region where $P(t) \neq 0$. In this case, the predator never becomes extinct.

As the carrying capacity K increases through the critical value K_c, the predator will eventually become extinct for almost all initial conditions. This is quite counterintuitive, but it can be understood from the dynamics. At $K = K_c$, the tip of the chaotic attractor touches the basin boundary (as in Fig. 3.2), creating "holes" on the basin boundary through which trajectories can now leak and enter the basin of the limit-cycle attractor with $P = 0$. Species extinction can thus occur as the result of transient chaos.

11.4.3   Control to Prevent Species Extinction

One way to prevent extinction is to decrease the resource carrying capacity K so that the sustained chaotic motion on the attractor is restored. But ecologically, it may not be feasible to adjust the carrying capacity of an environment, and even if this can be done, it may take some time to accomplish after detecting that the

predator population is in danger. The predator may already have become extinct before the carrying capacity can be changed. An alternative approach was proposed to restore sustained chaotic motions without the need to vary the carrying capacity of the environment but instead, by making use of the idea of maintaining chaos via small feedback controls (Sect. 11.2).

One can identify the "dangerous" escape regions surrounding the collision points between the chaotic attractor and the basin boundary by monitoring the populations of R, C, and P. If it is determined that the populations are close to a dangerous region, small but judiciously chosen perturbations tos the populations are applied to guarantee that no immediate exit from the hole occurs. By targeting a set of points in the escape region for which the trajectory maps back to the region of recurrent chaotic motion, one can compute the required perturbations. Usually the perturbations need to be applied only rarely. This technique may be of practical use: by applying small but occasional adjustments to the population at appropriate times estimated from time series, species extinction can be prevented. From an ecological point of view, it may be more feasible to make small adjustments to the local *populations* than to change the carrying capacity of the environment.

A potential problem in designing the control algorithm based on the map derived from a Poincaré surface of section is that a substantial fraction of trajectories escape and approach the limit cycle at $P = 0$ without even being controlled. The reason is that it usually takes a long time for a trajectory to return to the surface of section. In the case of transient chaos, a trajectory, because of its finite lifetime, may never pierce through the surface of section before exiting. The following approach was proposed [716] to maintain sustained chaotic motion for almost all transient chaotic trajectories. A critical two-dimensional plane in the three-dimensional phase space (R, C, P) is identified: $P = P_{crit} = $ constant, which separates the region of recurrent chaotic motions from the region in which the dynamics is such that the population $P(t)$ goes directly to zero. This plane need not be the basin boundary, nor is it a Poincaré surface of section. The criteria for choosing this plane are these: (1) ecologically, it is chosen with respect to the population that can become extinct; and (2) dynamically, it should be sufficiently close to the originally recurrent chaotic region. *The plane $P = P_{crit}$ thus represents a critical level of the endangered population at which human intervention must be introduced to prevent the extinction of the species P.* The concept of a "threshold population size" may provide a useful rule of thumb for manipulating the dynamics, and similar ideas were actually used in conservation theory [270]. That the critical plane is chosen close to the recurrent chaotic region indicates that arbitrarily close to but above the critical plane, there exists an infinite number of points in the phase space, trajectories starting from which can resume recurrent chaotic motions for at least a finite amount of time. These considerations are illustrated [716], for example, in Fig. 11.6, where the lifetime span is plotted for trajectories resulting from a grid of 500×500 points chosen from a two-dimensional region in the (R, P) plane at $C = 0.5$. Here, the lifetime is defined to be the time that the trajectory spends in the phase-space region with $P(t) > P_{crit}$. For this example, a simple search procedure leads to the choice of a critical plane at $P_{crit} = 0.57$. In Fig. 11.6, the yellow and red spots represent points with greater
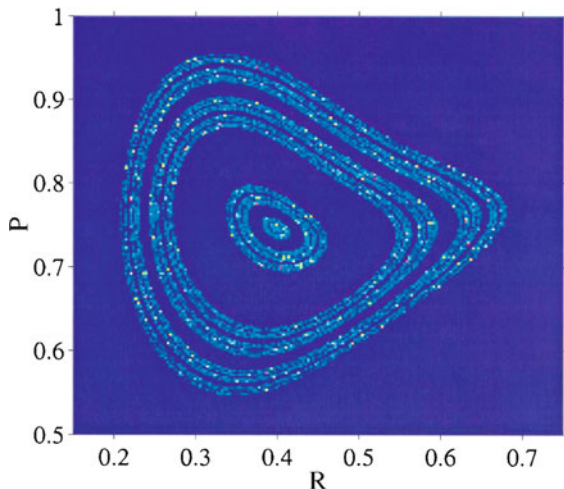
Fig. 11.6 Lifetime plot of trajectories resulting from a grid of 500×500 points chosen from a two-dimensional region in the (R,P) plane at $C = 0.5$, where the lifetime is defined to be the time that the trajectory spends in the phase-space region with $P(t) > P_{\text{crit}} = 0.57$. *Brighter colors* indicate longer lifetime. Model parameters are $x_C = 0.4$, $y_C = 2.009$, $x_P = 0.08$, $y_P = 2.876$, $R_0 = 0.16129$, and $C_0 = 0.5$ [510]. The bifurcation parameter is set to be $K = 1.02 > K_c$ so that there is transient chaos [716] (with kind permission from Elsevier Science)

lifetimes than the blue spots. It can be seen that the distribution of the lifetime is highly nonuniform, due to the fractal structure of the natural measure of the chaotic saddle.

The setting of a critical plane and the fact that there exists an infinite number of "hot" spots with long chaotic lifetimes provide us with a feasible way to design intervention or control. Say the population $P(t)$ falls slightly below the critical level at time t. Let (R_-, C_-, P_-) be the values of the state variables at this time, where P_- is slightly less than P_{crit}, and let (R_+, C_+, P_+) be the values of the state variables a little before t, where P_+ is slightly above P_{crit}. At time t, arbitrarily small random adjustments $[\delta R(t), \delta C(t), \delta P(t)]$ are made to *all* the populations in the phase space within a small neighborhood centered at (R_+, C_+, P_+), so that the trajectory collapses to a point. With a nonzero probability, the trajectory will be close to one of the hot spots contained in the neighborhood so that chaotic motion can occur for a finite amount of time. Note that it is not meaningful to kick the trajectory back directly to the point (R_+, C_+, P_+), since this point maps to (R_-, C_-, P_-) immediately. Figure 11.7a shows a controlled population $P(t)$ for $K = 1.02$, which indicates a sustained, sizable population of the predator through a long time. Figure 11.7b shows the magnitude of the applied perturbations $\delta X(t) \equiv \sqrt{[\delta R(t)]^2 + [\delta C(t)]^2 + [\delta P(t)]^2}$ versus time. It can be seen that the required perturbations $[\delta R(t), \delta C(t), \delta P(t)]$ are indeed small ($\delta X(t) < 0.04$, compared with the size of the population, which is about one) and rare (only about 100 perturbations
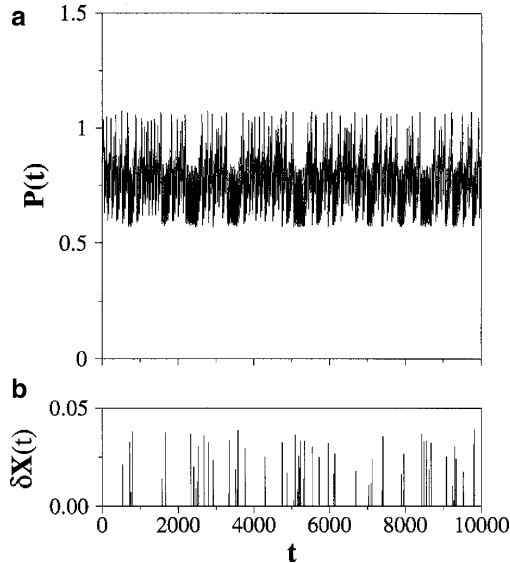
Fig. 11.7 (**a**) A controlled population $P(t)$ for $K = 1.02$, which indicates a sustained, sizable population of the predator through a long time. (**b**) Magnitude of the applied perturbations $\delta X(t)$ versus time [716] (with kind permission from Elsevier Science)

are applied in a time interval of $(0, 10000)$). Numerical computations reveal [716] that the chaotic population $P(t)$ can be maintained practically indefinitely through the use of occasional and small adjustments to all the populations, for almost all initial conditions chosen in the original basin of the chaotic attractor.

An issue of practical interest is how often small adjustments need to be applied so that finite species populations can be maintained. To address this question, we observe that the time intervals for successive adjustments of the populations are in fact the times that the trajectory stays in the region where $P > P_{\text{crit}}$. Their average is the average lifetime τ of the chaotic saddle. For the parameter setting in Fig. 11.6, it was found [716] that $\tau \approx 209$, which means that roughly 50 adjustments to the populations need to be made in a time interval of length of $10,000$. This estimate is consistent with the result in Fig. 11.7b.

The model discussed has incorporated within itself biologically and ecologically reasonable assumptions [510]. Even then, the neglected degrees of freedom would show up as small corrections, and there is always random noise present in any environment. It thus becomes important to assess the influence of random noise. The simplicity embedded in the control method makes it evident that control is robust against the influence of weak noise. The reason is that in the algorithm, deliberate effort is made to avoid the need to utilize detailed and more accurate information about the dynamics, such as the derivative matrices and the stable and the unstable eigenvalues associated with target points. As such, if deterministic transient chaos is the main culprit for the extinction of a species for a particular system, it is possible to control transient chaos to effectively prevent

extinction even in noisy environments, regardless of the details of the system dynamics. This may be of value to the important environmental problem of species preservation.

11.5 Maintaining Chaos in the Presence of Noise, Safe Sets

The presence of weak environmental noise may drastically decrease the efficiency of the algorithms used to maintain chaos. The dynamics is then described by the stochastic map $\mathbf{x}_{n+1} = \mathbf{f}(\mathbf{x}_n, p_n) + \sigma\boldsymbol{\xi}_n$, where σ is the noise amplitude, and we assume that p_n is chosen according to one of the chaos-maintaining scenarios described in the previous sections. The destructive effect of noise can be weakened or even eliminated by introducing an *additional* control variable $\mathbf{r}_n$, applied under the influence of noise. The overall dynamics is then described as

$$\mathbf{x}'_{n+1} = \mathbf{f}(\mathbf{x}_n, p_n) + \sigma\boldsymbol{\xi}_n,$$
$$\mathbf{x}_{n+1} = \mathbf{x}'_{n+1} + \mathbf{r}_n. \tag{11.21}$$

We assume that the noise is bounded, $|\boldsymbol{\xi}_n| \leq 1$, and weak, $\sigma \ll 1$. An interesting question is how the magnitude r of the control variable should be chosen in order to ensure maintenance of chaos despite the presence of noise.

The presence of noise implies that trajectories fall, in general, a distance of order σ away from points with long-lived chaotic transients. The amount of control needed to compensate this shift is therefore at least $r = \sigma$. This strategy therefore does not work for a control weaker than the noise amplitude: $r < \sigma$. A remarkable recent observation of Sanjuán, Yorke, and coworkers [4,661,848,849] was that there is a strategy for maintaining chaos even if the original control parameter p is unchanged (it is kept at its nominal value $\bar{p}$) and even if noise is *stronger* than control.

The problem can also be considered as a mathematical game between two players called the "protagonist" and the "adversary." The adversary chooses the amount $\boldsymbol{\xi}_n$ of noise, knowing x_n and the map $\mathbf{f}(\mathbf{x}) \equiv \mathbf{f}(\mathbf{x}, \bar{p})$. The protagonist's goal is to survive around the chaotic saddle, and he/she can choose the response to the adversary's action, namely the amount $\mathbf{r}_n$ of control. The initial condition can also be chosen by the protagonist. This game was also called Yorke's game of survival [4]. The probability that the protagonist will survive in the vicinity of the chaotic saddle is zero, even without noise, because of escape. This fact makes the survival of the protagonist nontrivial, in particular if the adversary is allowed to act more strongly than the protagonist: $r < \sigma$.

The idea ensuring survival is based not directly on the chaotic saddle, but rather on a related concept, the existence of a horseshoe map (cf. Sect. 1.2.2.1) around it. The action of this map implies that there is a particular set of points, the *safe set*, that lies outside but close to the saddle, and the strategy ensures that points of the map (11.21) remain on the safe set forever.
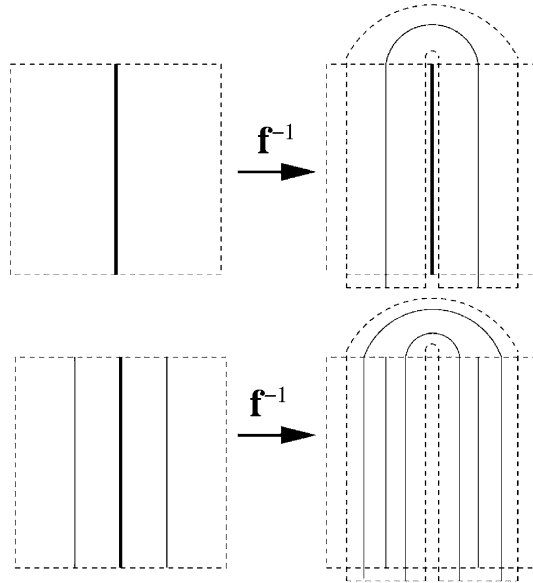
Fig. 11.8 Schematic diagram showing the construction of safe sets S^k. The set S^0 (*thick line*) consists of a vertical segment that divides Q into two halves and lies outside the horseshoe shape of $\mathbf{f}^{-1}(Q)$, marked by *dashed lines*. Safe sets S^1 (*thin black line*) and S^2 (*thin gray line*) are the preimages of S^0 and S^1, respectively [849] (copyright 2008, the American Physical Society)

Different safe sets are needed for different values of σ. Therefore, a family of safe sets $\{S^j\}$ is defined based on the horseshoe construction. Figure 11.8 shows how these sets are generated on a topological square, denoted by Q, containing the chaotic saddle. The action of the inverse map $\mathbf{f}^{-1}$ deforms this square into a horseshoe. The safe set S^0 of level 0 is chosen as a vertical line segment that divides the square Q into two halves. Points of S^0 are in the primary escape region of Q, i.e., they leave the square in one iteration. The preimage of S^0 within Q contains two vertical segments. They form the safe set S^1 of level 1. Following this procedure, one defines the set S^k for any $k > 1$ as the preimage of S^{k-1} in Q (see Fig. 11.8).

Thus the safe set S^k of level k has the following properties:

- S^k consists of 2^k vertical segments.
- Any vertical segment of S^k has two adjacent segments of S^{k+1} that are closer to it than any other segments of S^k.
- The maximum distance, denoted by δ_k, between any of the 2^k segments of S^k and its adjacent segments of S^{k+1} goes to zero as $k \to \infty$.

The safe set is thus always outside the chaotic saddle, but it is close to the saddle for $k \gg 1$. The key idea of the strategy for ensuring survival, and thus maintaining chaos, is to place the initial condition on one segment of an adequate safe set S^k. Then one just has to apply the control $\mathbf{r}_n$ to make point $\mathbf{x}_{n+1}$ of (11.21) lie on the original segment or another segment of S^k.

The adequate safe set S^k corresponds to a level k for which $\delta_{k-1} < \sigma$. For small σ, k is always large. If the initial condition $\mathbf{x}_0$ is on such an S^k, its unperturbed image $\mathbf{f}(\mathbf{x}_0)$ lies on a segment of S^{k-1} that has two adjacent segments of S^k. The perturbation $\boldsymbol{\xi}_0$ due to noise leads to a point $\mathbf{x}_1' = \mathbf{f}(\mathbf{x}_0) + \sigma\boldsymbol{\xi}_0$. If this point lies in the region between the aforementioned two segments of S^k, there exists a control variable $\mathbf{r}_0$, smaller than or equal to $\delta_{k-1} < \sigma$ in modulus, which puts the trajectory on a segment of S^k. If point $\mathbf{x}_1'$ is outside the region between the two curves of S^k, its distance from the segment of S^{k-1} is at most σ, and a perturbation smaller than σ can put the point on the closest segment of S^k. Thus, the image point $\mathbf{x}_1$ lies on a segment of S^k. The same strategy can be applied at any iteration step. One thus always finds a constant r such that with $|\mathbf{r}_n| \leq r < \sigma$ the trajectory $\mathbf{x}_n$ for any n lies on S^k (with the same k as the initial condition), and the system is maintained to remain close to the chaotic saddle forever. The lower bound for the ratio r/σ was shown [4, 848, 849] to be $1/2$, which means that in some cases, chaos can be maintained with a control as weak as half of the strength of noise. Whether this optimal limit can be reached depends on the noise amplitude and the properties of the original map $\mathbf{f}$.

11.6 Encoding Digital Information Using Transient Chaos

Developments in nonlinear dynamics and chaos have led to the idea of encoding digital information using chaos [88–90, 318, 319, 354, 650]. In particular, it was demonstrated both theoretically and experimentally by Hayes et al. [318, 319] that a chaotic system can be manipulated, via arbitrarily small time-dependent perturbations, to generate controlled chaotic orbits whose symbolic representations correspond to the digital representation of a desirable message. Imagine a chaotic oscillator that generates a large-amplitude signal consisting of an apparently random sequence of positive and negative peaks. A possible way to assign a symbolic representation to the signal is to associate a positive peak with a one, and a negative peak with a zero, thereby generating a binary sequence. The use of small perturbations to an accessible system parameter or variable can then cause the signal to follow the orbit whose binary sequence encodes a desirable message that one wishes to transmit. One advantage of this type of message-encoding strategy is that the nonlinear chaotic oscillator that generates the waveform for transmission can remain simple and efficient, while all the necessary electronics controlling the encoding of the signal can remain at a low-powered microelectronic level.

The basic principle that makes the above scheme of digital encoding with chaos possible lies in the link between chaos and information (Sects. 2.6.3, 8.2.1). The fundamental unpredictability of chaos implies that chaotic systems can be regarded as sources that naturally generate digital communication signals. By manipulating a chaotic system in an intelligent way, digital information can be encoded. A central issue in any digital communication scheme is *channel capacity* [71, 708], a quantity that measures the amount of information that can be encoded. For a chaotic system,

channel capacity is equivalent to the *topological entropy* (Sect. 1.2.3.3) because it defines the rate at which information is generated by the system.

In a digital communication scheme, it is desirable to have the channel capacity as large as possible to maximize the amount of information that can be encoded. For nonlinear digital communication, it is generally advantageous to use transient chaos as information sources from the standpoint of channel capacity. The orbital complexity associated with trajectories on a chaotic saddle can be greater than that of trajectories on a chaotic attractor, because crisis is generally a complexity-increasing event (Sect. 3.1.1). For a symbolic dynamics of two symbols, the maximally allowed value of the topological entropy, $\ln 2$, is often realized in a parameter regime in which there is transient chaos (see, e.g., Fig. 3.10). Thus, it is desirable to design a chaotic system operating in a transient chaotic regime for digital encoding.

11.6.1 The Channel Capacity

For illustrative purpose, we demonstrate how transient chaos can be utilized to encode digital information using the one-dimensional logistic map $x_{n+1} = f(x_n) = rx_n(1 - x_n)$. A symbolic dynamics for the logistic map can be defined by setting the symbolic partition at the critical point $x_c = 0.5$. A trajectory point x bears the symbol **0** if $x < x_c$ and the symbol **1** if $x > x_c$. A trajectory in the phase space thus corresponds to a sequence in the symbolic space. The topological entropy K_0 quantifies how random such a symbol sequence can be. Its value is obtained from the number Ω_m of possible symbol sequences of length m as given by (1.25). In practice, one can plot $\ln \Omega_m$ versus m for, say, $1 \leq m \leq 16$. The slope of such a plot is approximately K_0.

As r is increased toward $r_c = 4$, the topological entropy K_0 continuously increases from zero to $\ln 2$ except when r falls in one of the infinite number of periodic windows. The topological entropy of the chaotic repeller remains constant in the window, where the constant is the value of K_0 at the beginning of the window. Since $\ln 2$ is the maximally realizable value of the topological entropy for a symbolic dynamics of two symbols, and since a crisis occurs at r_c, the entropy remains at $\ln 2$ for $r > r_c$, as shown in Fig. 11.9. This can be advantageous because message encoding becomes quite straightforward for hyperbolic transient chaos, since there are no forbidden words associated with the symbolic dynamics. In the communication terminology, such a channel is unconstrained.

11.6.2 Message Encoding, Control Scheme, and Noise Immunity

To encode an arbitrary binary message into a trajectory that lives on a nonattracting chaotic set, it is necessary to use small perturbations to an accessible system parameter or a dynamical variable. For the logistic map we choose to perturb the state
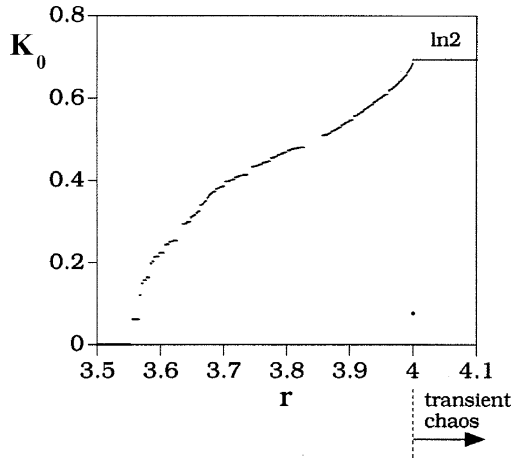
Fig. 11.9 For the logistic map, the topological entropy K_0 versus r for $3.5 < r < 4.1$. After the devil-staircase, for $r > 4$, K_0 remains at $\ln 2$, the maximum possible value for a symbolic dynamics of two symbols [439] (with kind permission from World Scientific Publishing Co)

variable x. Say we wish to apply only small perturbations of order 2^{-m}. A viable procedure is as follows. First, we convert the message into a binary sequence using the ASCII code and store the sequence in a symbol register. Next, we choose an initial condition whose trajectory stays near the chaotic repeller for a certain number n_c ($n_c > m$) of iterations. This is practically feasible, since one can run the system and predetermine the phase-space regions where initial conditions yield trajectories whose lifetimes are at least n_c. We then determine all m symbols corresponding to m points on the trajectory starting from x_0 and check to see whether the mth symbol agrees with the first message bit in the symbol register. If yes, we iterate x_0 once to get x_1 and determine the mth symbol from x_1 (equivalently, the $(m+1)$th symbol from x_0) to see whether it matches the second message bit in the symbol register. If not, we apply a small perturbation to x_0 so that the mth symbol from it matches the first message bit. This process continues until all the message bits in the symbol register are encoded into the chaotic trajectory.

The required parameter perturbation can be computed using the *coding function* [318, 319]. First divide the unit interval in x into N bins of size $\delta x = 1/N$, where $\delta x \ll 1/2^m$ and $1/2^m$ is the maximally allowed perturbation. We then choose a point from each bin, iterate it m times, and determine the corresponding symbol sequence of length m: $S_1 S_2 \ldots S_m$, where S_i can be either zero or one. Any point leaving the unit interval in fewer than m iterations is disregarded. For those points x for which a symbol sequence of length m can be defined, the following is computed:

$$R = \sum_{i=1}^{m} S_i / 2^i, \tag{11.22}$$
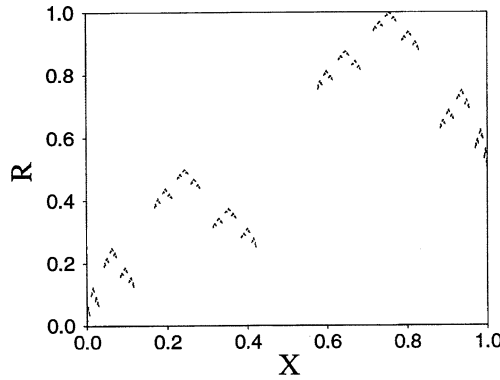
Fig. 11.10 Coding function $R(x)$ for the logistic map at $r = 4.1$, where R can assume any value between 0 and 1, but there are many gaps on the x-axis, due to the fact that the chaotic repeller is a fractal Cantor set [439] (with kind permission from World Scientific Publishing Co)

where $0 \leq R \leq 1$. This gives the value of the coding function $R(x)$ for points on the chaotic repeller. Since the chaotic repeller has topological entropy $\ln 2$, R can in principle have any value between 0 and 1. Figure 11.10 shows the coding function for the logistic map at $r = 4.1$, where $\delta x = 2 \times 10^{-4}$.

With the coding function, the determination of the state perturbations becomes straightforward. Let the natural m-bit symbol sequence from x_0 be $a_1 a_2 \ldots a_{m-1} a_m$ (produced by iterating the map directly) and let the first message bit to be encoded be b_1. We compare the natural symbol sequence $a_1 a_2 \ldots a_{m-1} a_m$ with the desirable symbol sequence $a_1 a_2 \ldots a_{m-1} b_1$ and compute $\delta R = (a_m - b_1)/2^m$. From the coding function $R(x)$, we can then compute the perturbation δx. This is done by locating pairs of points with the same value of δR in the computer representation of the coding function $R(x)$ and choosing the one that yields the smallest value of δx. Thus, by applying δx to the initial condition x_0, the trajectory point after m iterations is associated with the symbol that is the first message bit. Note that if a_m is identical to the message bit b_1, no perturbation is necessary. To encode the next message bit, we iterate the perturbed initial condition once to obtain x_1. Let $x'_0 = x_1$. The natural m-bit symbol sequence of x'_0 is $a'_1 a'_2 \ldots b_1 a'_m$, where $a'_1 = a_2$, $a'_2 = a_3$, $\ldots$, and a'_m is the binary symbol corresponding to the trajectory point $f^{(m)}(x'_0)$. We now compare a'_m and b_2 to determine the next perturbation to be applied to x'_0. Continuing this procedure, we can encode an arbitrary message into the chaotic trajectory $\{x_n\}$.

An example of encoding a specific piece of information [439] is shown in Fig. 11.11a, where the English word "TIGER" is encoded into a trajectory on the chaotic repeller of the logistic map for $r = 4.1$. The binary (ASCII) representation of the word is shown at the top of the figure. Assuming that perturbations of magnitude 2^{-8} are to be applied, we generate a set of initial conditions whose lifetimes in the unit interval under the map are at least 8. Shown in Fig. 11.11a is a time series for which the first binary bit of the message is encoded into the trajectory at $n = 8$. Time-dependent perturbations are applied at subsequent iterations so that the entire
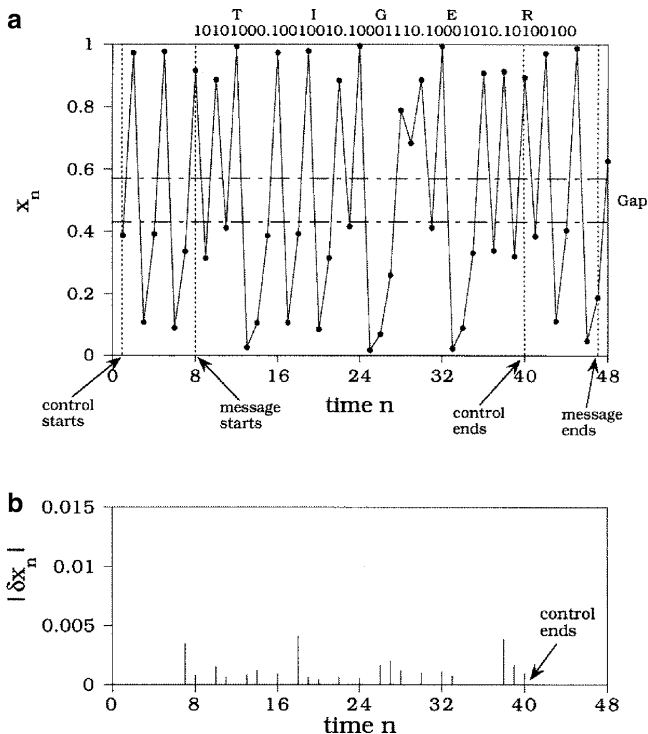
Fig. 11.11 Encoding the English word "TIGER" into a trajectory on the chaotic repeller at $r = 4.1$ for the logistic map. The binary representation of the word is shown at the top of the figure. Shown in (**a**) is a time series where small control is initiated at $n = 1$ and the first binary bit of the message is encoded into the trajectory at $n = 8$. The *dashed–dotted lines* represent the endpoints of the primary escape interval. Time-dependent perturbations are applied at subsequent iterations so that the entire message "TIGER" can be encoded into the trajectory. The magnitudes of the control perturbations required are shown in (**b**) [439] (with kind permission from World Scientific Publishing Co)

message "TIGER" can be encoded into the trajectory. Figure 11.11b shows the magnitude of the control perturbations applied at different time steps. We see that the perturbations required are small. No control perturbation is required for the first six time steps because for this initial condition, the natural symbols corresponding to the trajectory points from $n = 8$ to $n = 13$ happen to coincide with the first six bits of the message.

Some features of the control scheme are as follows. Since the channel capacity of the chaotic repeller is $\ln 2$, there are no forbidden symbol sequences. Thus, in the encoding scheme, any binary sequences can be produced by a typical trajectory near the chaotic repeller. Since we use the coding function $R(x)$ to compute the perturbation δx, once the perturbation is turned on, the trajectory is automatically confined in the vicinity of the chaotic repeller because the coding function is defined with respect to trajectories on the repeller. Suppose that small perturbations on the order of 2^{-m} are to be applied. To encode a message, we need only identify a set of

initial conditions that can stay near the chaotic repeller for m iterations. Since the typical value of m is, say, 10, it is fairly straightforward to identify a large number of such initial conditions. In practice, before encoding, we can run the system to produce a set of initial conditions whose lifetimes are greater than m. Together with the coding function that also needs to be determined beforehand, one can in principle encode any binary sequence into a dynamical trajectory on the chaotic repeller.

Besides possessing the maximum topological entropy $\ln 2$, the chaotic repellers of the logistic map for $r > 4$ also have the property of strong noise immunity. To see this, we contrast a chaotic repeller with the chaotic attractor at $r = 4$. For the chaotic repeller, we see that there is a primary escape interval of size $\sim \sqrt{s}$, where $s = r/4 - 1$, about the partition point $x_c = 1/2$. For the chaotic attractor there is no such gap. A trajectory on the chaotic attractor can then come arbitrarily close to the partition point. In a noisy environment, this may cause a bit error. Say the trajectory point is to the immediate right of x_c. This point thus has the symbol 1. Due to noise, the trajectory can be kicked through x_c, and it thus assumes the wrong symbol 0. For a trajectory on the chaotic repeller, this situation is improved. Insofar as the noise amplitude is smaller than the size of the primary escape interval across the partition point x_c, the symbolic dynamics is immune to noise. This may be of value to practical implementation of communication with chaos [89, 90].[4]

Since all chaotic repellers for $r > 4$ in the logistic map have the same topological entropy $\ln 2$, it appears that it is more advantageous to use chaotic repellers at large r because they possess larger gaps across x_c, and thus their corresponding symbolic dynamics are more robust against noise. However, as r increases, the average lifetime of transient chaos decreases. In general, in choosing an optimal chaotic repeller for digital encoding, there is a trade-off between the ease of generating a trajectory near the chaotic repeller and the noise immunity [89, 90].

Although our discussion has been focused on one-dimensional maps, similar ideas apply to transient chaos in two-dimensional maps [443].

---

[4] The stability of transient chaos against noise has been discussed in Chap. 4.

Chapter 12
Transient Chaotic Time-Series Analysis

Parallel to the rapid development of nonlinear dynamics, there has been a tremendous amount of effort devoted to data analysis. Suppose an experiment is conducted and some time series are measured. Such a time series can be, for instance, a voltage signal from a physical or a biological experiment, or the concentration of a substance in a chemical reaction, or the amount of instantaneous traffic at a point in the Internet, and so on. The general question is this: what can we say about the underlying dynamical system that generates the time series if the equations governing the time evolution of the system are unknown and the only available information about the system is a set of measured time series?

The purpose of this chapter is to introduce the delay-coordinate embedding technique for transient chaotic time-series analysis. The method has proven effective, particularly for time series from low-dimensional, deterministic dynamical systems under the influence of weak noise. That is, for situations in which the dynamical invariant set responsible for the behavior of the measured time series is low-dimensional and the noise amplitude is relatively small, the delay-coordinate embedding method can yield reliable information about the underlying dynamical system.

The mathematical foundation of the delay-coordinate embedding technique was laid by Takens in 1980 [756]. He proved that under fairly general conditions, the underlying dynamical system can be faithfully reconstructed from time series in the sense that a one-to-one correspondence can be established between the reconstructed and the true but unknown dynamical systems. Based on the reconstruction, quantities of importance for understanding the system can be estimated, such as the relative weights of determinism and stochasticity of the underlying system, its dimensionality, the Lyapunov exponents, and unstable periodic orbits that constitute the skeleton of the invariant set responsible for the observed dynamics.

There exists a large body of literature on the application of the delay-coordinate embedding technique to dynamical systems with chaotic attractors. Time series obtained from permanently chaotic systems can in principle be arbitrarily long. For transient chaos, a measured signal exhibits a random behavior only for a finite amount of time before settling into an asymptotic state. For data analysis, conventional wisdom may be simply to disregard the transient portion of the data and to concentrate on the final state. By doing this, however, information about the system

may be lost, because the irregular part of the data is likely to contain important information about the system dynamics. Analyzing transient chaotic time series is thus necessary.

Pertinent issues in the data analysis of transient chaotic systems include reconstructing the chaotic saddle, detecting unstable periodic orbits, estimating the correlation dimension, and computing the Lyapunov exponents. We shall demonstrate in this chapter that many of the standard algorithms that are used to estimate dynamical invariants from time series of sustained chaotic processes can be applied to *ensembles* of transient chaotic time series. That is, instead of constructing a single long time series from a set of shorter ones, one can consider a collection of transient time series, starting from different initial conditions.

12.1 Reconstruction of Phase Space

Let $u_i(t)$ $(i = 1,\ldots,l)$ be a set of l measurements from an underlying dynamical system that evolves the state variable in time according to a set of deterministic rules represented, e.g., by a set of differential equations. The phase-space dimension can in general be quite large. However, it often happens that the asymptotic evolution of the system occurs on a dynamical invariant set of a much smaller dimension only. A realistic assumption is that the details of the system equations in the phase space and of the asymptotic invariant set that determines what can be observed through experimental probes are unknown. The task is to estimate, *based solely on one or a few time series*, statistical quantities characterizing the invariant set. The delay-coordinate embedding technique established by Takens [756] provides a practical solution to this task [382, 575]. In particular, Takens's embedding theorem guarantees that a phase space topologically equivalent to that of the unknown dynamical system can be reconstructed from time series, on the basis of which characteristics of the dynamical invariant set can be assessed.

Takens's delay-coordinate embedding method can be described as follows. From each measured time series $u_i(t)$ $(i = 1,\ldots,l)$, the following vector quantity of q components is constructed:

$$\mathbf{u}_i(t) = \{u_i(t), u_i(t+\tau_d), \ldots, u_i[t+(q-1)\tau_d]\},$$

where τ_d is the *delay time*. Since there are l time series, a vector of $m \equiv ql$ components can be constructed as follows:

$$\begin{aligned}
\mathbf{x}(t) &= \{\mathbf{u}_1(t), \mathbf{u}_2(t), \ldots, \mathbf{u}_l(t)\} \\
&= \{u_1(t), u_1(t+\tau_d), \ldots, u_1[t+(q-1)\tau_d], \\
&\qquad u_2(t), u_2(t+\tau_d), \ldots, u_2[t+(q-1)\tau_d], \\
&\qquad \ldots, u_l(t), u_l(t+\tau_d), \ldots, u_l[t+(q-1)\tau_d]\}.
\end{aligned} \qquad (12.1)$$

The quantity m is called the embedding dimension. The delay time τ_d and the embedding dimension m are the two fundamental parameters in Takens's method.

1. *Delay time τ_d.* In order for the time-delayed components $u_i(t + j\tau_d)$ ($j = 1, \ldots, q - 1$) to serve as independent variables, the delay time τ_d needs to be chosen properly. If τ_d is too small, adjacent components $u_i(t)$ and $u_i(t + \tau_d)$ will be too correlated to serve as independent coordinates. If τ_d is too large, neighboring components are too uncorrelated for the purpose. Empirically, one can examine the autocorrelation function of $u_i(t)$ and determine a proper delay time [779]. In particular, for a time series of zero average, $\langle u_i(t) \rangle = 0$, one computes

$$c(\tau_d) \equiv \frac{\langle u_i(t) u_i(t + \tau_d) \rangle}{\langle u_i^2(t) \rangle},$$

where $\langle \cdot \rangle$ stands for time average. The delay time τ_d can be chosen to be the value of τ_d such that $c(\tau_d)/c(0) \approx e^{-1}$.

There exist various alternative empirical methods for choosing a proper delay time [109, 405, 484, 485, 654], all of which yield similar results. A firmer theoretical foundation can be established by exploring the statistics for testing continuity and differentiability from chaotic time series, as proposed by Pecora and coworkers [271, 582, 584–586].

2. *Embedding dimension m.* In order to have a faithful representation of the true dynamical system, the embedding dimension m should be sufficiently large. Takens's theorem [756] provides a lower bound for m. In particular, suppose the dynamical invariant set lies in a D-dimensional smooth subspace in the phase space (D is an integer). One can ask whether the dynamical invariant set will intersect itself in the reconstructed phase space. In order to obtain a one-to-one correspondence between points on the invariant sets in the actual and reconstructed phase spaces, self-intersection should not occur. Recall condition (8.52) for the generic intersection between two sets. Applying this for two identical sets $S_1 = S_2$, $D(S_1) = D(S_2) = D$, in the phase space of dimension $N = m$, no self-intersection requires $D_I < 0$, which implies $m > 2D$. Then, if $m > 2D$, the m-dimensional reconstructed vectors $\mathbf{x}(t)$ have a one-to-one correspondence with the vectors in the true dynamical system.

While Takens's theorem assumes that the relevant dimension D of the set is that of the manifold in which the set lies, this dimension can be significantly larger than the dimension of the set itself which is physically more relevant. The work by Sauer, Yorke, and Casdagli [679] extended Takens's theorem to relax the dimension requirement: the dimension D can in fact be the box-counting dimension D_0 of the invariant set. For a faithful reconstruction of an invariant set of box-counting dimension D_0, the embedding dimension m should be at least $2D_0$: $m > 2D_0$.

Since D_0 is not known a priori, a practical criterion is needed for a proper choice of the embedding dimension m. The method of *false neighbors* (for a review see the book by Kantz and Schreiber [382]) provides such a criterion. The aim is to find points that are neighbors in the m-dimensional embedding space but are not neighbors in reality. Such false neighbors are mapped far away from their real neighbors

after one time step τ_d. For $m \ll 2D_0$ the proportion of false neighbors is large, but for $m \approx 2D_0$ it becomes small. Numerical algorithms for determining the proportion of false neighbors are available [324].

12.1.1 Reconstruction of Invariant Sets

For the reconstruction of a chaotic saddle from time series of a single variable, a method was proposed by Jánosi et al. [356, 357]. It is based on the creation of a long artificial signal and consists of the following steps:

(a) Take an ensemble of time series containing long irregular transients to an attractor (either simple or chaotic).
(b) Locate the attractor of the dynamics from the dynamical variable of interest and separate the transient part.
(c) Construct truncated time series by disregarding points that belong to the transition periods both from the initial point to the saddle and from the vicinity of the saddle to the attractor. The length distribution of the truncated time series follows an exponential decay, from which the escape rate can be determined.
(d) By means of some simple matching procedure (e.g., matching the dynamical variable and its derivative), "glue" the truncated signals together into a long signal. Apply the delay-coordinate embedding method to determine the chaotic saddle in the reconstructed phase space.

This method was applied to the NMR laser experiment described in Sect. 1.3. In particular, the control parameter was kept at a value below an interior-crisis point at which a sudden attractor enlargement takes place. Long chaotic transients wander in the region of the postcrisis attractor (Sect. 3.2) before settling into the small attractor. Transient signals are thus characterized by large oscillations compared to the signals on the attractor. The gluing procedure was based on the observation that the laser action between subsequent pulses is nearly zero. It is with respect to this practically constant laser background level that different transient pieces can be glued together. The laser output was recorded as a normalized, dimensionless scalar time series $\{u_i\}_{i=1}^{1024}$ ($0 < u_i < 1$) at the sampling rate of $1/2,500$ s.

The particular realization of steps (a)–(d) was as follows:

(a) An ensemble of nearly 10^4 short records of length 0.4096 s was generated, which is about four times the average lifetime of transients. This was compared with a long record on the chaotic attractor. Figure 12.1a, b show a typical segment of the permanently chaotic signal and the transient signal, respectively. (The last two-thirds of the transient signal is very close to the attractor.) Note that between the large peaks of the transient part there are no peaks of intermediate height characterizing the motion on the attractor.
(b) The maximum amplitude of oscillations on the attractor can be determined, and all signals having a peak larger than this were considered to be away from the attractor. To separate the transient part, the last peak larger than the attractor maximum was identified and the segment ending with this peak and a short piece at the laser background level was kept.
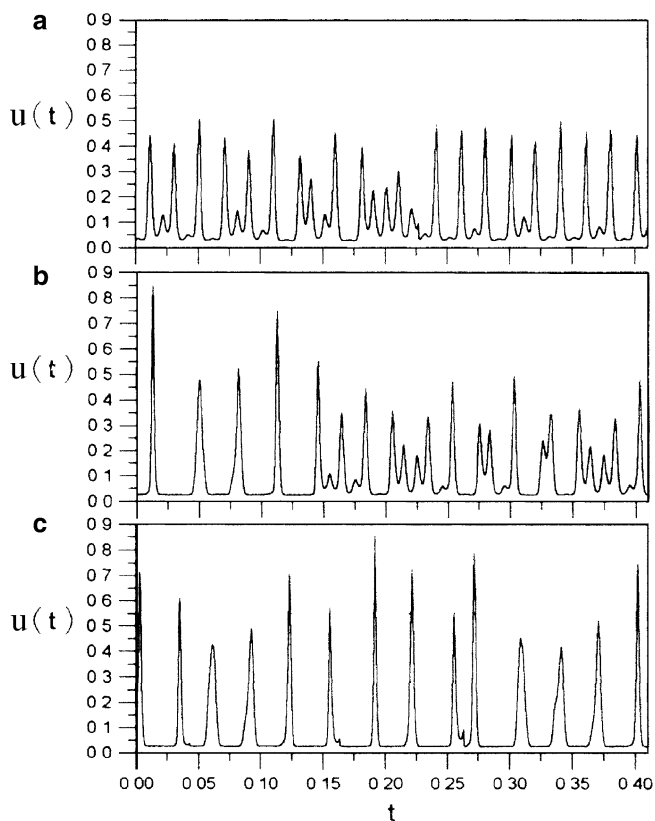
Fig. 12.1 Normalized time series $u(t)$ from the NMR laser experiment of [356]: (**a**) signal characterizing the chaotic attractor, (**b**) signal of a typical transient to the attractor, and (**c**) part of the long artificial time series representing motion near the chaotic saddle (copyright 1994, the American Physical Society)

(c) It was observed that the transitions to the saddle were short, rendering it sufficient to discard short segments of the time series before the first large peak is reached. The escape rate was estimated to be $\kappa = 9.3 \pm 0.06\,\mathrm{s}^{-1}$.

(d) To decrease the error related to the gluing procedure, truncated signals shorter than $1/\kappa$ were discarded. The remaining 5600-plus time series were glued together at the laser background level. A segment of the glued time series is shown in Fig. 12.1c. The difference between the dynamics on the attractor and the transient dynamics can be seen. A single peak consists of typically 20–30 data points, indicating that the correlation is high between consecutive data points, according to which the delay time $\Delta n = 5$ ($\tau_\mathrm{d} = 5/2{,}500\,\mathrm{s}$) was chosen. Figure 1.16a and b show the reconstructed chaotic saddle and the coexisting chaotic attractor, respectively. It can be seen that the saddle is more extensive in the phase space than the attractor.

The main advantage of constructing a long, artificial signal from a set of transiently chaotic time series is that the methods applicable to sustained chaotic time series can be applied straightforwardly. For example, for the laser experiment described above, embedding up to dimension 10 leads to a largest Lyapunov exponent 225 (1/s) for the chaotic saddle, which is about twice as large as that of the attractor. The partial information dimension $D_1^{(1)}$ along the unstable manifold (2.76) was estimated to be about 0.96. Its closeness to unity explains the lack of large holes along the reconstructed saddle in Fig. 1.16a.

The stable and unstable manifolds can also be reconstructed from the time series of a single variable representing an experimentally accessible system. A variant of the sprinkler method (Sect. 1.2.2.3) was proposed by Triandaf, Bollt, and Schwartz [788]. They suggested defining a restraining region Γ not containing any attractor in the m-dimensional delay-coordinate space of a single scalar variable u. One picks an initial condition within this space and follows the dynamics up to time $t = n_0 \tau_d$, $n_0 \gg 1$. If the entire trajectory remains within Γ, then record both the initial and final points in a file. Repeat this for a large number of initial conditions. The set of all initial (final) points of the trajectories kept reconstruct the stable (unstable) manifold in the delay-coordinate space. An example with three delay coordinates I_0, I_1, I_2 of a laser system is shown in Fig. 12.2.
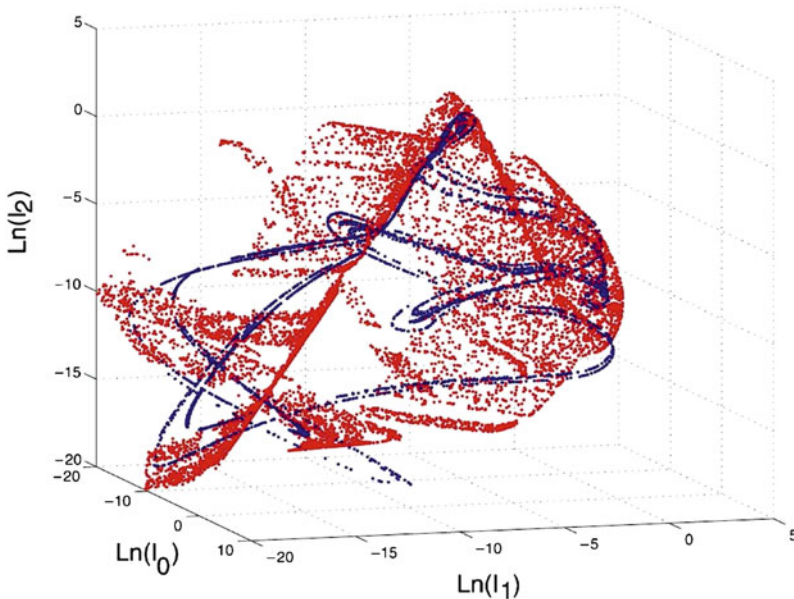
Fig. 12.2 Stable (*red*) and unstable (*blue*) manifolds of a laser system producing transient chaos. The embedding space is three-dimensional. Variables I_0, I_1, I_2 are intensity delay coordinates, and the restraining region is the box defined by the axis segments shown. The stable (unstable) manifolds are obtained as initial and final points of trajectories remaining in the box for $n_0 = 200$ times the delay time [788] (copyright 2003, the American Physical Society)

12.1.2 Reconstructing Invariant Sets of Delay-Differential Equations

A special class of high-dimensional problems is provided by systems in which the rate of change of the system's state depends explicitly on the state at some past time. Such problems are described by delay-differential equations [227,737], which serve as prototypical dynamical systems of infinite dimension. For these, both numerical and analytical methods are intermediate in complexity between ordinary and partial differential equations. A paradigmatic form of such equations describing a single variable $x(t)$ is

$$\frac{\mathrm{d}x(t)}{\mathrm{d}t} = F\left[x(t), x(t-\tau)\right], \tag{12.2}$$

where $\tau > 0$ is a time delay. The solution to this equation is unique for all $t \geq 0$ if initial data are given for all times in the interval $-\tau \leq t \leq 0$. Since (12.2) is translationally invariant in time, the continuation of a solution for $t > t_0 > 0$ is uniquely determined by its history on the interval $[t_0 - \tau, t_0]$. The delay-differential equation (12.2) can therefore be regarded as a dynamical system acting on the infinite-dimensional space of continuous functions defined on the delay interval $[-\tau, 0]$.

Transient chaos in delay-differential equations had long been identified in the form of fractal basin boundaries (see Chap. 5) as in [8,492]. The identification of the underlying chaotic saddle was much more recent and was due to Taylor and Campbell [761]. They apply the delay-coordinate embedding method to functions defined on the interval $[-\tau, 0]$ by discretizing this interval into an integer number $m-1$ of equal subintervals. In the notation of Sect. 12.1, this corresponds to choosing the delay time as $\tau_{\mathrm{d}} = \tau/(m-1)$, and m is the embedding dimension. After choosing a suitable restraining region in the m-dimensional space, a long chaotic trajectory can be found by means of the stagger-and-step method (Sect. 8.4). A three-dimensional projection of the saddle can be visualized in the space of $x(t), x(t-\tau/2), x(t-\tau)$, as shown in Fig. 12.3.

A Poincaré section can be defined by intersecting the saddle trajectory of Fig. 12.3 with a plane $x(t) = x^*$. The obtained section through the saddle shown in Fig. 12.4 has the structure that resembles the product of two Cantor sets, which is typical in low-dimensional systems. There are a few regions, however, in which points overlap, indicating that the reconstruction of the saddle in Fig. 12.3 is faithful outside these regions only. A computation of the correlation dimension yields the value $D_2 = 2.2 \pm 0.1$ [761]. Assuming the box-counting dimension to be close to this value, the condition for a faithful embedding requires the embedding dimension to be larger than 4.4 ± 0.2. The three-dimensional embedding of Fig. 12.3 is thus not yet large enough to fully avoid self-intersections.
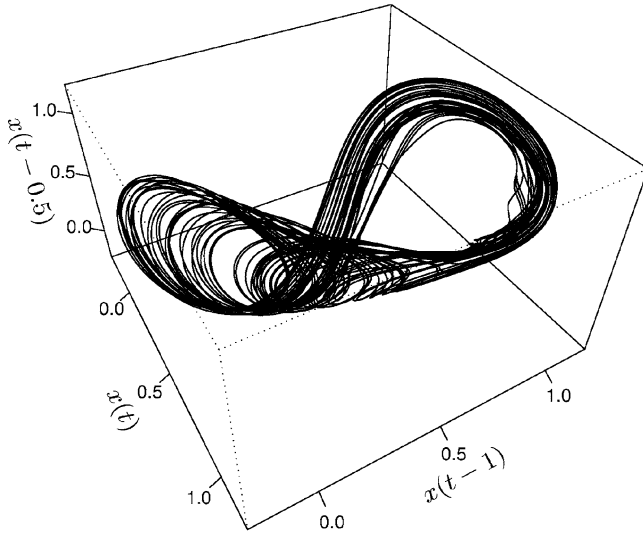
Fig. 12.3 Projection of the saddle of the logistic delay-differential equation ($F = -x(t)$ $-6.16x(t - \tau)[1 - x(t - \tau)]$ in (12.2) with $\tau = 1$) on the three-dimensional space of $x(t), x(t -1/2), x(t - 1)$. The embedding dimension is $m = 250$ [761] (copyright 2007, the American Physical Society)
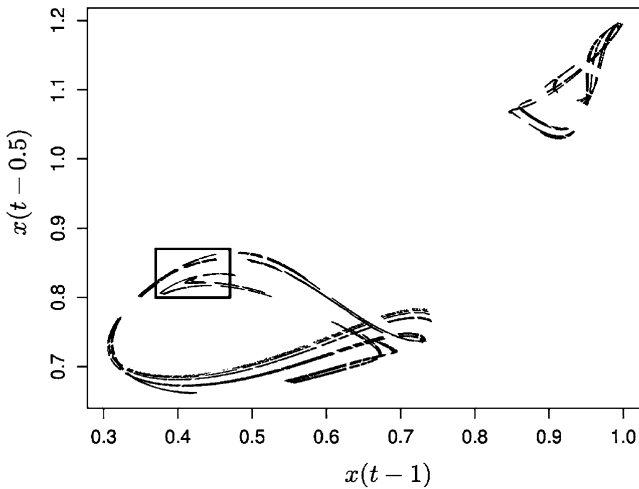
Fig. 12.4 Poincaré section through the chaotic saddle of the logistic delay-differential equation obtained by applying the condition $x(t) = 1$ to the trajectory of Fig. 12.3. The double Cantor structure can be seen up to a few regions where self-intersection occurs. This indicates that a faithful reconstruction would require an embedding of dimension somewhat higher than 3 [761] (copyright 2007, the American Physical Society)

12.2 Detection of Unstable Periodic Orbits

A fundamental feature distinguishing a deterministic chaotic system from a stochastic one is the existence of an infinite number of unstable periodic orbits that constitute the skeleton of the chaotic invariant set (see Sect. 1.2.3.3). Determination of unstable periodic orbits from system equations [63, 156, 157, 685] and their detection from experimental time series have been an active area of research [12, 37, 469, 588, 599, 722]. At a fundamental level, unstable periodic orbits embedded in a chaotic invariant set determine its natural measure (Sect. 2.6.4), the basis for defining physically important quantities such as the box-counting dimension and Lyapunov exponents. At a practical level, successful detection of unstable periodic orbits indicates the deterministic origin of the underlying dynamical process.

12.2.1 Extracting Unstable Periodic Orbits from Transient Chaotic Time Series

An effective algorithm for detecting unstable periodic orbits from chaotic time series was due to Lathrop and Kostelich (LK) [469]. The method is based on identifying sets of recurrent points in the reconstructed phase space. To do this, one first reconstructs a phase-space trajectory $\mathbf{x}(t)$ from a measured scalar time series $\{u(t)\}$ using the delay-coordinate embedding method described in Sect. 12.1. To identify unstable periodic orbits, one follows the images of $\mathbf{x}(t)$ under the dynamics until a value $t_1 > t$ is found such that $|\mathbf{x}(t_1) - \mathbf{x}(t)| < \varepsilon$, where ε is a predetermined small number that defines the size of the recurrent neighborhood at $\mathbf{x}(t)$. In this case, $\mathbf{x}(t)$ is called a (T, ε) recurrent point, and $T = t_1 - t$ is the *recurrence time*. A recurrent point is not necessarily a component of a periodic orbit of period T. However, if a particular recurrence time T appears frequently in the reconstructed phase space, it is likely that the corresponding recurrent points are close to some periodic orbits of period T. The idea is then to construct a histogram of the recurrence times and identify peaks in the histogram. Points that occur frequently are taken to be, approximately, components of the periodic orbits. The LK-algorithm was used to detect unstable periodic orbits, for instance from measurements of a chaotic chemical reaction [469].

The LK algorithm was also adapted to detecting unstable periodic orbits from short, transiently chaotic series [189]. The reason that the LK algorithm is applicable to transient time series lies in the statistical nature of the method, since a histogram of the recurrence times can be obtained even with short time series. Provided that there is a large number of such time series so that good statistics of the recurrence times can be obtained, unstable periodic orbits embedded in the underlying chaotic saddle can be identified. It is not necessary to concatenate many short time series to form a single long one (as done in Sect. 12.1). Intuitively, since the time series are short, periodic orbits of short periods can be detected.

To demonstrate the LK algorithm, here we describe the numerical examples in [189] with the following chaotic Rössler system in a periodic window of period 3:

$$dx/dt = -y - z,$$
$$dy/dt = x + 0.2y,$$
$$dz/dt = 0.2 + (x - 5.3)z. \tag{12.3}$$

In [189], ten such time series were generated by integrating the Rössler system from different initial conditions, and the corresponding time series $x(t)$ for $0 \leq t \leq 4$ are recorded. The average lifetime of the chaotic transients is about 4. These time series are assumed to be the only available information about the system. For each time series, a seven-dimensional vector space is reconstructed using the delay time $\tau_d = 0.02$. To obtain recurrence times, it is necessary to determine ε, the size of the recurrent neighborhood. The value of ε cannot be too large so as to avoid false positives, but if ε is too small, genuine recurrences will be missed. It was found in numerical experiments that the number of recurrences $N(\varepsilon)$ increases with the length and the number of the individual transient trajectories, and with ε. It tends to saturate when ε is too large. The value of ε at which $N(\varepsilon)$ saturates is taken to be the appropriate size of the recurrent neighborhood. For the Rössler system, using $\varepsilon = 2\%$ of the root-mean-square (rms) value of the amplitude of the chaotic signal is proper [189]. Figure 12.5a shows the histogram of the recurrence times for the ten transient chaotic time series from the period-3 window. Figure 12.5b–d show, in the plane of $x(t)$ versus $x(t + \tau_d)$, three recurrent orbits. The orbit in Fig. 12.5b has the shortest recurrence time, so it is a "period-1" orbit. Figure 12.5c, d show a
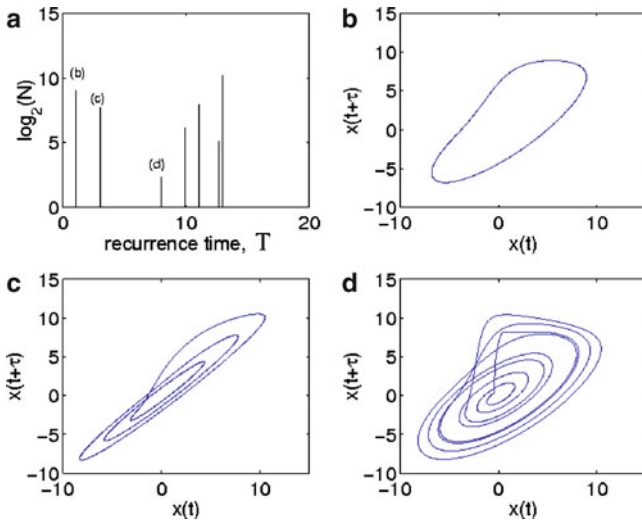
Fig. 12.5 For the Rössler system: (**a**) histogram $N(\varepsilon)$ of the recurrence time T for $\varepsilon = 0.02$, (**b**)–(**d**) period-1, period-3, and period-8 recurrent orbits extracted from the histogram in (**a**), respectively [189] (copyright 2000, the American Physical Society)
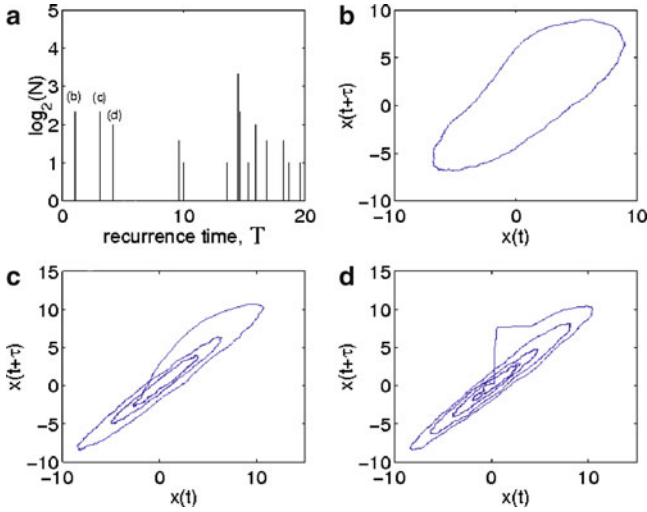
Fig. 12.6 For a noisy Rössler system: (**a**) histogram $N(\varepsilon)$ of the recurrence time T for $\varepsilon = 0.06$, (**b**)–(**d**) period-1, period-2, and period-4 recurrent orbits extracted from the histogram in (**a**), respectively. The rms value of the noise is about 0.5% of that of the chaotic signal [189] (copyright 2007, the American Physical Society)

period-3 and a period-8 orbit, respectively. The orbits are selected from the set of recurrent points generating the corresponding peaks in the histogram. In general, it was found [189] that the LK algorithm is capable of yielding many periodic orbits of low periods.

In an experimental setting, time series are contaminated by dynamical and/or observational noise. A question is whether periodic orbits can still be extracted from noisy transient chaotic time series. Figure 12.6 shows the number of recurrent points (a) and three periodic orbits (b)–(d) extracted from ten transient chaotic time series with additive weak noise in the form of a normal (Gaussian) distribution centered at zero and of variance 0.01. This noise level represents an rms value that is approximately 0.5% of that of the chaotic signal. It can be seen that at this low noise level, periodic orbits can still be reliably detected. It was found, however, that for the Rössler system at $\varepsilon = 2\%$ of the rms value of the chaotic signal with noise beyond 1%, no periodic orbits can be extracted from the histogram of recurrences. One way to assess the influence of noise is to compute, for different values of ε, how the number of recurrent points decreases as the noise amplitude (σ) is increased. Figure 12.7 shows the result of such computations for $\varepsilon = 2\%$ (a) and $\varepsilon = 6\%$ (b) of the rms value of the signal. It can be seen that the number of recurrent points goes to zero for $\sigma \approx \varepsilon/2$, which can be explained as follows. Under noise of amplitude σ, both the center and the boundary of the recurrent region are uncertain within σ. Thus, the effective phase-space volume in d dimensions in which two points can still be considered within distance ε (recurrent) is proportional to $(\varepsilon - \sigma)^d - \sigma^d$, which vanishes at $\sigma = \varepsilon/2$. Since ε should be small to guarantee recurrence, we see that the tolerable noise level is also small.
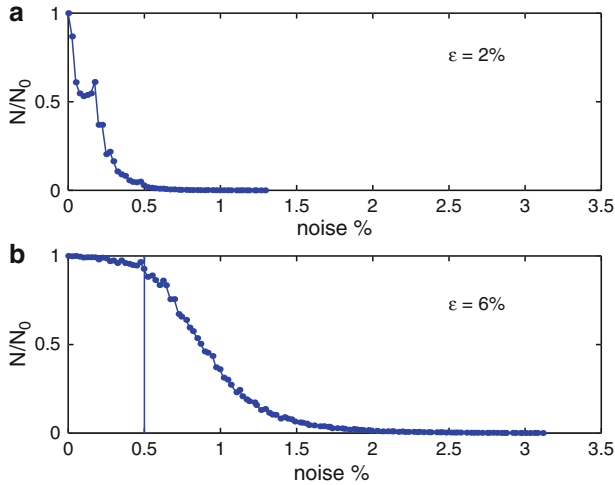
Fig. 12.7 For the noisy Rössler system, the relative number $N(\varepsilon, \sigma)/N_0(\varepsilon)$ of recurrent points versus the amplitude of noise for two values of the size of the recurrent neighborhood: (**a**) $\varepsilon = 2\%$ and (**b**) $\varepsilon = 6\%$ of the rms value of the chaotic signal, where $N_0(\varepsilon) \equiv N(\varepsilon, \sigma = 0)$. The vertical line in (**b**) denotes the noise level at which periodic orbits in Fig. 12.6 are extracted [189] (copyright 2000, the American Physical Society)

12.2.2 Detectability of Unstable Periodic Orbits from Transient Chaotic Time Series

Because trajectories about a chaotic saddle have a finite average lifetime $\tau \approx 1/\kappa$, it is difficult for a typical trajectory to contain periodic orbits of period larger than τ. The detectability of unstable periodic orbits from transient chaotic time series is thus a relevant issue. In particular, effort may be devoted to connecting short time series (as in Sect. 12.1) so that the resulting long time series will contain periodic orbits of larger period. Such a task may be difficult. If one fails to detect periodic orbits of high periods, the question is whether one should attempt to increase the number of measurements so that more time series are available. Alternatively, one may attempt to improve techniques to link these time series, a computationally demanding task. The main point is that the probability of detecting orbits of higher periods is typically exponentially small, as we shall point out here. This is an *intrinsic* dynamical property of the underlying chaotic set, and hence increasing the number of measurements or improving techniques of detection will not help to enhance the chance of detecting these orbits.

Let $\Phi(p)$ be the probability of detecting an orbit of period p. A scaling relation for $\Phi(p)$ can be derived [189, 190] by noting that $\Phi(p)$ is effectively the probability for a trajectory to stay in a small neighborhood of any periodic orbit of period p. For a trajectory to stay in a ν-neighborhood of all p points of the ith orbit of period p, the trajectory must come within $\delta = \nu e^{-\lambda_i^*(p)p}$ of any of the p points when it first

encounters the periodic orbit, where $\lambda_i^*(p) > 0$ is the Lyapunov exponent of this orbit. The probability of this event is $\phi_i(p) \sim \delta^{\alpha_i}$, where α_i is the crowding index $\alpha_i \equiv \alpha_{1i} + \alpha_{2i}$ (Sect. 2.6.4) of the natural measure about any one of the p points of this periodic orbit. The probability $\Phi(p)$ is the cumulative probability of all $\phi_i(p)$:

$$\Phi(p) = \sum_{i=1}^{N(p)} \phi_i(p) \sim \sum_{i=1}^{N(p)} v^{\alpha_i} \exp\left[-\lambda_i^*(p)\alpha_i p\right], \tag{12.4}$$

where $N(p)$ is the total number of periodic points of period p (see (1.26)). Since $\lambda_i^*(p)$ and α_i are the local positive Lyapunov exponent and pointwise dimension of periodic orbits of period p, for large p, we expect them to obey distributions centered at λ_1 and D_1, respectively, where λ_1 and D_1 are the positive Lyapunov exponent and the information dimension of the chaotic saddle. Thus, the main dependence of $\Phi(p)$ on p is

$$\Phi(p) \sim e^{-\lambda_1 D_1 p} N(p) \sim e^{(-\lambda_1 D_1 + K_0)p} \equiv e^{-\gamma p}, \tag{12.5}$$

where γ is an exponential scaling exponent and K_0 is the topological entropy. Using the Kantz–Grassberger formulas of two-dimensional maps (2.74) and (2.79) for chaotic saddles to express D_1 in terms of the Lyapunov exponents $\lambda_2 < 0 < \lambda_1$ and the escape rate κ, one obtains the scaling exponent as

$$\gamma = \lambda_1 - K_0 + \frac{\lambda_1^2}{|\lambda_2|} - \kappa\left(1 + \frac{\lambda_1}{|\lambda_2|}\right). \tag{12.6}$$

Equations (12.5) and (12.6) are applicable to chaotic saddles in two-dimensional invertible maps or in three-dimensional flows. Note that for chaotic attractors ($\kappa \to 0$), the scaling exponent becomes $\gamma \approx \lambda_1 - K_0 + \lambda_1^2/|\lambda_2|$.

To test (12.5) and (12.6) numerically, Dhamala et al. [189] used the Hénon map $(x, y) \to (1 - ax^2 + by, x)$, taking advantage of the fact that unstable periodic orbits embedded in the chaotic saddles of the map can be computed systematically [63]. For different values of a in the transiently chaotic regime, 10^6 initial conditions were chosen in the region $[-2, 2] \times [-2, 2]$ containing the chaotic saddle, which yield 10^6 transient time series. For a given period p, the fractions of times that these 10^6 time series get close to every periodic orbit of period p can be computed. These fractions are used to yield an estimated value for the probability $\Phi(p)$. The exponent γ can be read off from the plots $\ln\Phi(p)$ versus $\ln p$. To compute the theoretical scaling exponents in (12.6), it is necessary to compute the Lyapunov exponents, the topological entropy, and the escape rate of the chaotic saddles. The following techniques were used in the computation: (1) the PIM-triple procedure (Sect. 1.2.2.4) to obtain a long trajectory on the chaotic saddle from which the Lyapunov exponents can be computed; (2) the method by Chen et al. [125] (Sect. 3.1.1) to compute the topological entropy; and (3) the sprinkler method (Sect. 1.2.3) to compute κ. The numerical slopes appear to agree reasonably well with the theoretical ones, as shown in Table 12.1.

Table 12.1 Theoretical and numerical values of the scaling exponent γ for three different parameters of the Hénon map

a	1.6	1.8	2.0
λ_1	0.58	0.81	0.87
λ_2	-1.78	-2.01	-2.07
K_0	0.53	0.54	0.53
$1/\kappa$	11.2	4.7	5.4
γ (theoretical)	0.12	0.31	0.44
γ (numerical)	0.13 ± 0.04	0.32 ± 0.03	0.47 ± 0.04

12.3 Computation of Dimension

12.3.1 Basics

An often computed dimension in chaotic time-series analysis is the correlation dimension D_2. This is the generalized dimension D_q of order $q = 2$ in the definition (A.1), which is a lower bound of the box-counting and information dimension: $D_2 \leq D_1 \leq D_0$. Grassberger and Procaccia (GP) showed in their seminal contribution [287] that D_2 can be evaluated using the correlation integral $C(\varepsilon)$, which is the probability that a pair of points chosen randomly in the reconstructed phase space is separated by a distance less than ε. Let N be the number of points in the reconstructed vector time series $\mathbf{x}(t)$ with embedding dimension m. The correlation integral can be approximated by the following sum:

$$C_N(\varepsilon, m) = \frac{2}{N(N-1)} \sum_{j=1}^{N} \sum_{i=j+1}^{N} \Theta(\varepsilon - |\mathbf{x}_i - \mathbf{x}_j|), \tag{12.7}$$

where $\Theta(\cdot)$ is the Heaviside function and $|\mathbf{x}_i - \mathbf{x}_j|$ stands for the distance between points $\mathbf{x}_i$ and $\mathbf{x}_j$. Grassberger and Procaccia argued that the correlation dimension is given by [287]

$$D_2(m) = \frac{\log C_N(\varepsilon, m)}{\log \varepsilon} \tag{12.8}$$

for $\varepsilon \ll 1, N \gg 1$. In practice, for a time series of finite length, the sum in (12.7) also depends on the embedding dimension m. Due to such dependencies, the correlation dimension D_2 is usually estimated by examining the slope of the linear portion of the plot of $\log C_N(\varepsilon)$ versus $\log \varepsilon$ for a series of increasing values of m. For $m < D_2$, the dimension of the reconstructed phase space is not high enough to resolve the structure of the dynamical state, and hence the slope approximates the embedding dimension. As m increases, the resolution of the dynamical state in the reconstructed phase space is improved. Thus typically, the slope increases with m until it reaches a plateau, and the plateaued dimension value can be taken as an estimate of D_2 [193, 287]. For an infinite and noiseless time series, the value of m at which this plateau begins satisfies $m = \text{Ceil}(D_2)$, where $\text{Ceil}(D_2)$ is the smallest integer greater

than or equal to D_2 [193]. In a realistic situation, short data sets and observational noise can cause the plateau onset to occur at a value of m larger than Ceil(D_2). Even so, the slope at which the plateau is reached still provides a reasonably sharp upper bound for the true correlation dimension D_2. Dependencies of the length of the linear scaling region on fundamental parameters such as m, the time delay τ_d, and $m\tau_d$ were analyzed in [456, 457].

These points can be observed by utilizing the Hénon map for the standard parameter values $a = 1.4$ and $b = 0.3$, where there is a chaotic attractor. The theoretical value of the correlation dimension of the attractor is $D_2 \approx 1.2$ [456, 457]. To select the delay time τ_d, note that any discrete-time map can be regarded as arising from a Poincaré surface of section of a continuous-time flow. Thus, one iteration of the map corresponds to one period of oscillation of the continuous-time signal $x(t)$, which, for chaotic systems, is approximately the decay time of the autocorrelation of $x(t)$. As an empirical rule, the delay time can be chosen to be $\tau_d = 1$.

After the delay time τ_d is chosen, the correlation integral $C_N(\varepsilon, m)$ for a set of systematically increasing values of the embedding dimension m can be computed. Figure 12.8 shows, for $N = 2 \times 10^4$, the plots of $C_N(\varepsilon)$ versus ε on a logarithmic scale. The lines are approximately linear, and they are parallel for $m \geq 2$. Least-squares fits give $D_2 \approx 1.2$ for $m \geq 2$, indicating that the correlation dimension can be estimated reliably. The saturation of the slope occurs at $m = 2$, which is the smallest integer above the value of D_2. However, the embedding theorem (Sect. 12.1) requires a minimum embedding dimension of Ceil($2D_0$), which is 3 for the Hénon problem. This difference exists because the task here is to estimate the dimension only, while the embedding theorem guarantees a one-to-one correspondence between the reconstructed and the true phase spaces. A correlation-dimension estimate does not necessarily require such a one-to-one correspondence. For instance,
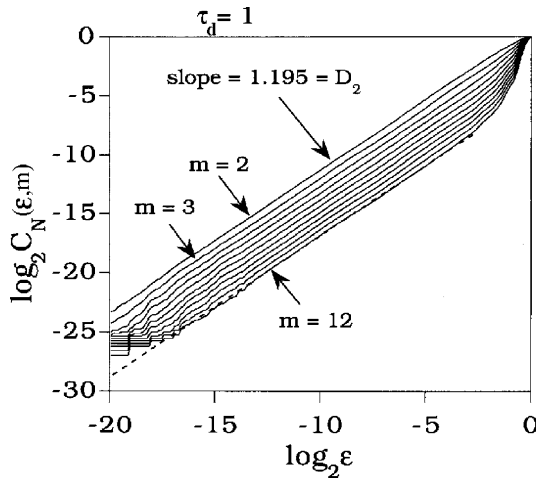
Fig. 12.8 For the standard Hénon & chaotic attractor, Plots of the correlation integral $C_N(\varepsilon, m)$ on a logarithmic scale for $m = 2, \ldots, 12$. Least-squares fits give $D_2 \approx 1.2$ for $m \geq 2$ [457] (with kind permission from Elsevier Science)

consider a two-dimensional surface in a three-dimensional space. The projection of this surface onto a two-dimensional plane is still a two-dimensional region. Thus, its dimension can be estimated correctly even in a two-dimensional subspace. One must be aware, however, of the fact that spuriously low dimension estimates can be obtained if the data are sparse, or if the set is sampled too finely, or if there are long-range correlations in the data set [284, 489, 562, 616].

12.3.2 Applicability to Transient Chaotic Time Series

The question is whether the GP paradigm ((12.7) and (12.8)) is applicable to transient time series from chaotic saddles. An argument was provided suggesting an affirmative answer to this question [190]. The starting point is the dimension spectrum (A.1) with $P_i \equiv \mu_i$ as the natural measure of the chaotic saddle contained in box i. Setting $q = 2$ gives, for $\varepsilon \ll 1$,

$$D_2 = \frac{\log \sum_{i=1}^{N(\varepsilon)} \mu_i^2}{\log \varepsilon} = \frac{\log \langle \mu_i \rangle}{\log \varepsilon}, \tag{12.9}$$

where $\langle \cdot \rangle$ denotes the phase-space average over the chaotic saddle. For an ergodic trajectory on the chaotic saddle, $\langle \mu_i \rangle$ is approximately the probability that the trajectory comes in the ε-neighborhood of a point $\mathbf{x}_i$ on the saddle in the ith box, which is given by the correlation sum in (12.7). From measurements, one does not have a long ergodic trajectory on the chaotic saddle. Instead, say l transient chaotic time series are available, each of length L. The probability p_i that the reconstructed trajectory comes to the neighborhood of $\mathbf{x}_i$ is

$$p_i \approx \frac{1}{l} \frac{1}{L(L-1)} \sum_{k=1}^{l} \sum_{j=1}^{L} \Theta(\varepsilon - |\mathbf{x}_j^k - \mathbf{x}_i|),$$

where $\mathbf{x}_j^k$ is the jth trajectory point reconstructed from the kth transient time series. Since l is in fact the number of initial conditions, the natural measure μ_i is (see (2.86))

$$\mu_i \approx \frac{p_i}{e^{-\kappa L}} \approx \frac{e^{\kappa L}}{lL(L-1)} \sum_{k=1}^{l} \sum_{j=1}^{L} \Theta(\varepsilon - |\mathbf{x}_j^k - \mathbf{x}_i|).$$

Averaging over all points $\mathbf{x}_i$ in the reconstructed phase space of dimension m gives

$$\langle \mu_i \rangle \approx e^{\kappa L} C_{l,L}(\varepsilon, m), \tag{12.10}$$

where

$$C_{l,L}(\varepsilon, m) \equiv \frac{1}{lL^2(L-1)} \sum_{k=1}^{l} \sum_{i=1}^{L} \sum_{j=1, j \neq i}^{L} \Theta(\varepsilon - |\mathbf{x}_j^k - \mathbf{x}_i^k|) \tag{12.11}$$

is the correlation integral associated with l observations of transient chaos, each of L points in the reconstructed phase space. For fixed L, the correlation dimension is then given by

$$D_2(m) = \frac{\log C_{l,L}(\varepsilon, m)}{\log \varepsilon} \tag{12.12}$$

for $\varepsilon \ll 1$, $l \gg 1$. Equation (12.12) indicates that if one computes the correlation integral as defined in (12.11), the GP formulation is applicable to transient chaotic time series as well.

To provide numerical support, transient chaotic time series from the Hénon map were used [190] for which the correlation dimension can be obtained both from the GP formulation (12.12) and from a straightforward implementation of the "box-counting" definition (12.9) by utilizing a long trajectory on the chaotic saddle generated by the PIM-triple method. For $a = 1.5$ and $b = 0.3$, there is a chaotic saddle of lifetime $\tau \approx 30$. The "box-counting" definition gives $D_2 \approx 1.2$. To apply the GP algorithm, $l = 5,000$ transient chaotic time series were used [190]. To guarantee that each time series reflects, approximately, the natural measure of the chaotic saddle, both the initial and final phases were disregarded, and only 20 points from the middle of the time series were kept. For a given embedding dimension m, the number of trajectory points corresponding to each time series is then $L = 20$. Each time series was normalized to the unit interval and the correlation sum $C_{l,L}(\varepsilon, m)$ was computed for 100 values of ε for $-30 < \log_2 \varepsilon < 0$ using embedding dimensions ranging from $m = 1$ to $m = 8$, as shown in Fig. 12.9a. For $m > 3$, the local slopes of the plots converge to a plateau value, as shown in Fig. 12.9b, which yields $D_2 \approx 1.12$. This agrees reasonably well with the value of D_2 obtained from the
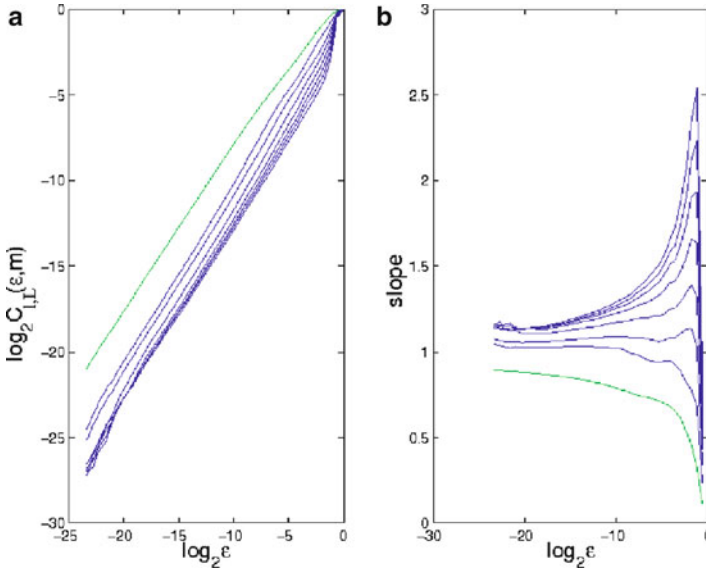
Fig. 12.9 For the Hénon map, (**a**) $\log_2 C_{l,L}(\varepsilon, m)$ versus $\log_2 \varepsilon$, and (**b**) $\log_2 C_{l,L}(\varepsilon, m)/\log_2 \varepsilon$ versus $\log_2 \varepsilon$ for $a = 1.5$, $b = 0.3$, $l = 5,000$, $L = 20$ for $m = 1$ (*green*) and $m = 2, \ldots, 8$ (*blue*). The curves with relatively higher slopes correspond to higher embedding dimensions [189] (copyright 2000, the American Physical Society)

"box-counting" definition. Note that due to the availability of only short time series, the embedding dimension needs to be larger than the value of D_2 itself to yield the correct plateau value for D_2, in contrast to the case of long time series from chaotic attractors, where $m \approx D_2$ usually suffices.

12.4 Computing Lyapunov Exponents from Transient Chaotic Time Series

The Lyapunov exponents characterize how a set of orthonormal, infinitesimal distances evolve under the dynamics. For an N-dimensional dynamical system, there are N Lyapunov exponents, denoted by λ_i for $i = 1, \ldots, N$, which define the Lyapunov spectrum. For a chaotic system, values of λ_i do not depend on the choice of the initial condition, insofar as it is chosen randomly.

   If the system equations are known, the Lyapunov spectrum can be computed using the standard procedure by Benettin et al. [55]. For chaotic time series, there exist several methods for computing the Lyapunov spectrum [100, 219, 220, 671, 832]. While the details of these methods differ, they share the same basic principle. Here we describe the one developed by Eckmann et al. [219]. The algorithm consists of three steps: (1) reconstructing the dynamics using delay-coordinate embedding and searching for neighbors of each point in the embedding space, (2) computing the tangent maps at each point by least-squares fits, and (3) deducing the Lyapunov exponents from the tangent maps.

12.4.1 Searching for Neighbors in the Embedding Space

Given an m-dimensional reconstructed vector time series ($m = ql$), in order to determine the tangent map at $\mathbf{x}_i \equiv (x_i, \ldots, x_{i+m-1})$, it is necessary to search for neighbors, i.e., search for $\mathbf{x}_j$ such that

$$\|\mathbf{x}_j - \mathbf{x}_i\| \leq r, \tag{12.13}$$

where, r is a small number, and $\|\cdot\|$ is defined as

$$\|\mathbf{x}_j - \mathbf{x}_i\| = \max_{0 \leq \alpha \leq m-1} |x_{j+\alpha} - x_{i+\alpha}|. \tag{12.14}$$

Such a definition of the distance is computationally convenient. If $m = 1$, the time series can be sorted to yield

$$x_{\Pi(1)} \leq x_{\Pi(2)} \leq \cdots \leq x_{\Pi(N)}, \tag{12.15}$$

where Π is the permutation that is stored, together with its inverse Π^{-1}. The neighbors of x_i can then be obtained by examining $k = \Pi^{-1}(i)$ and scanning the sorted

time series $x_{\Pi(s)}$ for $s = k \pm 1, k \pm 2, \ldots$ until $|x_{\Pi(s)} - x_i| > r$. For $m > 1$, values of s are first selected for which

$$|x_{\Pi(s)} - x_i| \leq r, \tag{12.16}$$

as for the case $m = 1$. The following conditions are further imposed:

$$|x_{\Pi(s)+\alpha} - x_{i+\alpha}| \leq r, \quad \alpha = 1, 2, \ldots, m-1, \tag{12.17}$$

resulting in a complete set of neighbors of $\mathbf{x}_i$ within distance r.

12.4.2 Computing the Tangent Maps

The task is to determine the $m \times m$ matrix T_i describing how the dynamics evolves a small vector about $\mathbf{x}_i$ to a small vector about $\mathbf{x}_{i+1}$:

$$T_i(\mathbf{x}_j - \mathbf{x}_i) \approx \mathbf{x}_{j+1} - \mathbf{x}_{i+1}. \tag{12.18}$$

A problem is that T_i may not span $\mathbf{R}^m$, because m is usually much larger than the actual phase-space dimension of the system to guarantee a proper embedding. Eckmann et al. proposed a strategy that allows T_i to be a $d_M \times d_M$ matrix, where the matrix dimension d_M is less than or equal to m. In such a case, T_i corresponds to the time evolution from $\mathbf{x}_i$ to $\mathbf{x}_{i+I}$, where $I \geq 1$ is the integer satisfying

$$m = (d_M - 1)I + 1. \tag{12.19}$$

A new set of embedding vectors of dimension d_M can then be constructed:

$$\mathbf{y}_i = (x_i, x_{i+I}, \ldots, x_{i+(d_M-1)I} \equiv x_{i+m-1}). \tag{12.20}$$

The new vector $\mathbf{y}_i$ is obtained by taking every Ith element in the time series, and hence T_i is defined in the new embedding space as follows:

$$T_i(\mathbf{y}_j - \mathbf{y}_i) \approx \mathbf{y}_{j+I} - \mathbf{y}_{i+I}, \tag{12.21}$$

or

$$T_i \begin{pmatrix} x_j - x_i \\ x_{j+I} - x_{i+I} \\ \cdots \\ x_{j+(d_M-2)I} - x_{i+(d_M-2)I} \\ x_{j+(d_M-1)I} - x_{i+(d_M-1)I} \end{pmatrix} = \begin{pmatrix} x_{j+I} - x_{i+I} \\ x_{j+2I} - x_{i+2I} \\ \cdots \\ x_{j+(d_M-1)I} - x_{i+(d_M-1)I} \\ x_{j+d_MI} - x_{i+d_MI} \end{pmatrix}. \tag{12.22}$$

That is, T_i can be expressed as

$$
T_i = \begin{pmatrix}
0 & 1 & 0 & \ldots & 0 \\
0 & 0 & 1 & \ldots & 0 \\
\ldots & \ldots & \ldots & \ldots & \ldots \\
0 & 0 & 0 & \ldots & 0 \\
a_1 & a_2 & a_3 & \ldots & a_{d_M}
\end{pmatrix}.
\tag{12.23}
$$

The task of finding T_i then reduces to that of finding the set of d_M matrix elements a_i ($i = 1, 2, \ldots, d_M$), which can be accomplished using least-squares fits. Let $S_i^E(r)$ be the set of indices j of neighbors $\mathbf{x}_j$ of $\mathbf{x}_i$ within distance r. The procedure is to minimize the quantity

$$
\sum_{j \in S_i^E(r)} \left[\sum_{k=0}^{d_M-1} a_{k+1}(x_{j+kI} - x_{i+kI}) - (x_{j+d_MI} - x_{i+d_MI}) \right]^2.
\tag{12.24}
$$

If $S_i^E(r)$ is large, the computation required is intensive. If $S_i^E(r)$ is too small, the least-squares fit may fail. Generally, it is necessary to choose r sufficiently large that $S_i^E(r)$ contains at least d_M elements. But r also needs to be small so that the linear-dynamics approximation about every $\mathbf{x}_i$ is valid. Eckmann et al. suggested the following empirical rule for choosing r: Count the number of neighbors of $\mathbf{x}_i$ corresponding to increasing values of r from a preselected sequence of possible values, and stop when the number of neighbors exceeds $\min(2d_M, d_M + 4)$ for the first time. Increase r further if T_i is singular.

12.4.3 Computing the Exponents

To compute the Lyapunov exponents from the tangent maps is relatively straightforward. Eckmann and Ruelle [220] suggested the following procedure. Starting from an identity matrix $Q_{(0)} \equiv 1$, one carries out the following matrix decomposition (QR-decomposition):

$$
\begin{aligned}
T_1 Q_{(0)} &= Q_{(1)} R_{(1)}, \\
T_{1+I} Q_{(1)} &= Q_{(2)} R_{(2)}, \\
&\cdots \\
T_{1+jI} Q_{(j)} &= Q_{(j+1)} R_{(j+1)}, \\
&\cdots
\end{aligned}
\tag{12.25}
$$

where the $Q_{(j)}$ are orthogonal matrices and the $R_{(j)}$ are upper triangular matrices with positive diagonal elements. The above decomposition is robust; an algorithm for it can be found in [615]. The Lyapunov exponents are then given by

$$\lambda_k = \frac{1}{I\tau_{\mathrm{d}}K} \sum_{j=0}^{K-1} \ln R_{(j)kk}, \tag{12.26}$$

where $R_{(j)kk}$ is the kth diagonal element of the matrix $R_{(j)}$, and K is the number of available matrices.

12.4.4 A Numerical Example

Here we give an example of computing the Lyapunov exponents from an ensemble of transient chaotic time series using the procedure outlined above. Again, consider the Hénon map in a parameter region where the map generates transient chaos. In [190], chaotic transients were generated from the Hénon map for the parameter pairs $(a,b) = (1.46, 0.3)$ and $(a,b) = (1.50, 0.3)$, and 21,000 points near each chaotic saddle were accumulated using 300 random initial conditions in $[-2,2] \times [-2,2]$ for the case $a = 1.46$ and 700 random initial conditions for $a = 1.50$. (The average lifetime of the chaotic saddle is about 70 iterates for $a = 1.46$ and 30 iterates for $a = 1.50$.) A two-dimensional embedding ($m = 2, d_M = 2, I = 1$) with the time delay of $\tau_{\mathrm{d}} = 1$ was used from each collection of time series. Local linear maps were computed using least-squares fits for each neighborhood.

For the case $a = 1.46$, each transient time series consists of about 70 iterates. Thus, the Lyapunov exponents computed are actually finite-time approximations, where a suitable product of the 70 or so linear maps associated with points on the individual transient time series was considered. Similarly, for $a = 1.50$, it was necessary to consider products of 30 or so linear maps. Figure 12.10a, b show the distributions of λ_1 and λ_2, respectively. It can be seen that for $a = 1.46$, $\lambda_1 = 0.44 \pm 0.05$ and $\lambda_2 = -1.72 \pm 0.06$. Similarly, for $a = 1.50$ (Fig. 12.10c, d), the exponents are $\lambda_1 = 0.54 \pm 0.06$ and $\lambda_2 = -1.77 \pm 0.08$. The estimated values of the exponents agree reasonably well with the true ones [190].

12.4.5 Remarks

The algorithm can in principle compute all the positive Lyapunov exponents reliably [219], although the correct identification of the negative exponents remains a challenging issue [677, 678]. There are three practical points. First, d_M cannot be too large; otherwise, spurious exponents may arise. Generally, d_M should be larger than the number of positive exponents. Second, the choice of r is critical, as discussed above. In the presence of noise, it may be useful to replace the ball $\{\mathbf{x}_j : \|\mathbf{x}_j - \mathbf{x}_i\| \le r\}$ by a shell $\{\mathbf{x}_j : r_{\min} < \|\mathbf{x}_j - \mathbf{x}_i\| \le r\}$ when searching for neighbors. Third, increasing the number of points in the time series at a fixed recording time is not helpful. In order to improve the computation, the total recording time should be increased.
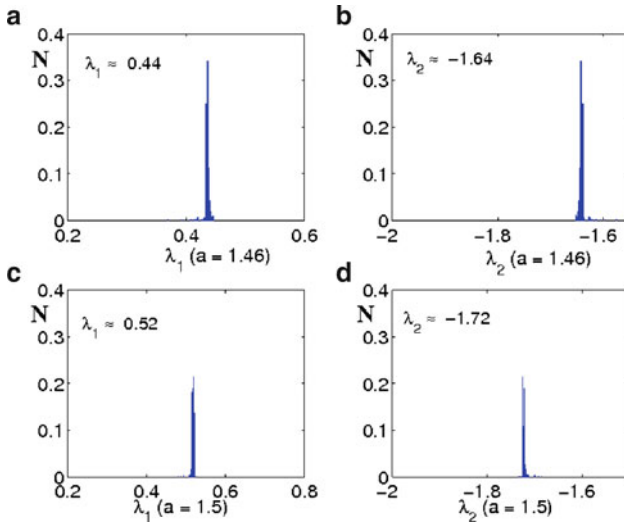
Fig. 12.10 (**a**)–(**d**) Distributions of Lyapunov exponents on the chaotic saddle of the Hénon map at the two parameter values of $a = 1.46$ and $a = 1.50$ ($b = 0.3$), respectively [189] (copyright 2000, the American Physical Society)

In brief summary, when computing the Lyapunov exponents from time series, the following rules should be followed:

1. Use long recording time, but not too small a delay time step τ_d.
2. Use large embedding dimension m.
3. Use a matrix dimension d_M somewhat larger than the expected number of *positive* Lyapunov exponents.
4. Choose r such that the number of neighbors is greater than the smaller of $2d_M$ and $d_M + 4$.
5. Otherwise, keep r as small as possible.
6. Take a product of as many matrices as possible to determine the Lyapunov exponents.

Final Remarks

There are two final remarks that the authors wish to convey to the readers of this book. First, for researchers in nonlinear dynamics and chaos, the message is that transient chaos can often be more relevant and fundamental than chaotic attractors. Second, for researchers from other disciplines or students who are beginning to study nonlinear dynamics and chaos, the suggestion is to be aware of the ubiquity of transient chaos and to develop ways of thinking based on transient chaos as early as possible. Indeed, as we have explored in this book, besides being fundamental to nonlinear systems, transient chaos arises and finds applications in a wide variety of disciplines.

At the time of writing, the authors recognize the rapid spreading of transient-chaos-related concepts in spatiotemporal systems, particularly in shear-flow turbulence. Further interesting results are expected, which may reinforce the view that chaos, in its transient form, is indeed related to fluid-mechanical turbulence. The authors speculate that the theory of transient chaos will find immediate applications in two further areas of significant recent interest: environmental science and nanoscience. In the former, understanding the spreading of beneficial or toxic materials in flows is becoming an essential component in environmental protection. The advection of inertial particles, a topic treated only briefly in this book, will play a fundamental role in addressing many issues of current concern, such as cloud dynamics. In the latter, manifestations of transient chaos in open quantum systems, for example transport in devices based on graphene, which has been mentioned but not treated in this book, will be increasingly appreciated. Having said that, the authors wish to emphasize that these speculations are completely their own personal opinions.

Appendix A
Multifractal Spectra

A.1 Definition of Spectra

The generalized dimensions [45] D_q follow from the scaling form

$$\sum_i P_i(\varepsilon)^q \sim \varepsilon^{(q-1)D_q}, \tag{A.1}$$

valid for $\varepsilon \ll 1$, where $P_i(\varepsilon)$ denotes the box probability defined in (1.13). The dimension of index $q = 0$ is the box-counting dimension, and the limit $q \to 1$ defines the information dimension D_1. The generalized entropies [45] K_q are defined for large m via the relation

$$\sum_{\{S_j\}} P(\{S_j\})^q \sim e^{(1-q)K_q m}, \tag{A.2}$$

where the summation is over all possible symbol sequences of length m, and $P(\{S_j\})$ are the path probabilities defined in Sect. 1.2.3.3. For $q = 0$, the left-hand side of (A.2) represents the number Ω_m of symbol sequences of length m. From (1.25) we see that $K_{q=0}$ is the topological entropy. The limit $q \to 1$ defines the metric entropy. In general hyperbolic cases, the spectra K_q and D_q are related. In general, it is insightful to explore the Legendre transforms of $(q-1)D_q$ and $(q-1)K_q$ with respect to q, the multifractal spectrum $f(\alpha)$, and the dynamical multifractal spectrum $g(\Lambda)$ [45]. These spectra are infact related to one another.

A.2 Multifractal Spectra for Repellers of One-Dimensional Maps

The key ingrediet in the so-called thermodynamical formalism [45] that generates all the spectra is the unique connection between symbol sequences and *microstates of spin chains*. In fact, one can interpret symbol 0 (1) of single humped maps (Fig. 2.1) as a spin pointing downward (upward) and the whole string as a state of a spin chain of length n. In order to define the interaction between spins, one can consider

the logarithm of a small dimensionless length scale. In one-dimensional maps, the cylinder size (Sect. 2.1.1) is chosen to be proportional to the internal energy E per spin in a given microstate:

$$E(\{S_j\}) = -\frac{1}{n}\log\varepsilon_i^{(n)}, \tag{A.3}$$

where $\{S_j\}$ is the symbol sequence of length n that belongs to the cylinder of size $\varepsilon_i^{(n)}$. This rule fixes the additive constant in the energy scale. The thermodynamic limit $n \to \infty$ corresponds to an infinitely refined coverage of the repeller. Equation (A.3) reflects that the energies associated with the cylinders remain finite as the partition is refined. In dynamical terms, any value of nE corresponds to a local stretching exponent (Λ_1 of Sect. 1.2.3.3), and the E-values thus to the *local Lyapunov exponent*.

The length distribution of the cylinders can be characterized by taking a certain real power β of the length scales and summing them at level n. The advantage of the statistical-physics analogy just mentioned is that due to (A.3), $\varepsilon_i^{(n)\beta}$ is effectively the Boltzmann factor $\exp(-\beta En)$ at the inverse temperature $1/\beta$. The corresponding sum over all configurations is the partition function, and since the free energy is extensive, an exponential scaling is expected for large n:

$$\sum_i \varepsilon_i^{(n)\beta} \sim e^{-\beta F(\beta)n}, \tag{A.4}$$

where $F(\beta)$ is the free energy per spin and is simply called the free energy in the dynamical context.[1] The function $\beta F(\beta)$ is monotonically increasing with a negative second derivative (as in thermodynamics; see also Fig. A.1). The free energy and
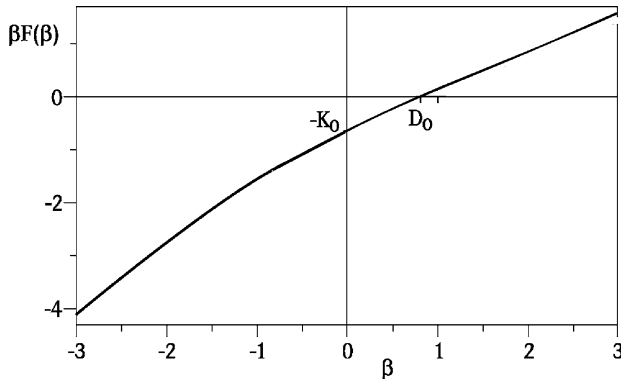
Fig. A.1 Free energy for the logistic map $f(x) = rx(1-x)$ at $r = 4.03$ in the range $|\beta| < 3$. The escape rate is $F(1)$ and the Lyapunov exponent is the slope of $\beta F(\beta)$ at $\beta = 1$

---

[1] In the mathematical literature, $-\beta F(\beta)$ is called the topological pressure [45, 83].

the Legendre transform of $\beta F(\beta)$, i.e., the entropy $S(E) = \beta(E - F(\beta))$, provide a description of the length distribution and, in view of (A.3), of the local Lyapunov exponents. Recalling that the total length of the cylinders at level n is proportional to the number $N(n)$ of surviving particles in the restraining region $\Gamma = I$, we obtain

$$F(1) = \kappa. \tag{A.5}$$

When calculating the generalized dimensions, we can use an extension of (1.20) in the form [45]

$$\sum_i \frac{\mu_i^{(n)q}}{\varepsilon_i^{(n)(q-1)D_q}} \sim 1, \tag{A.6}$$

where $\mu_i^{(n)}$ is the cylinder measure. Using (2.11) for hyperbolic systems, the left-hand side contains a term that includes the lengths $\varepsilon_i^{(n)}$ only, which can thus be expressed by the free energy. This leads to the following implicit relation:

$$\beta F(\beta) \,|_{\beta=q-(q-1)D_q} = \kappa q. \tag{A.7}$$

Since the cylinder measures are simultaneously the path probabilities, (2.12), the generalized entropies can also be expressed by the free energy based on (A.2), (A.4), and (2.11):

$$K_q = \frac{q(F(q) - \kappa)}{q - 1}. \tag{A.8}$$

Taking the limit $q \to 1$ in (A.8) leads to $K_1 = F'(1)$. Thus (2.15) implies that the Lyapunov exponent λ_1 is the derivative of $\beta F(\beta)$ evaluated at $\beta = 1$.

The free energy can also be obtained by using an eigenvalue formalism. Consider the recurrence scheme

$$\psi_{n+1}^{(\beta)}(x') = R(\beta) \sum_{x \in f^{-1}(x')} \frac{\psi_n^{(\beta)}(x)}{|f'(x)|^\beta}, \tag{A.9}$$

which is the extension of (2.2) for real exponents β and can be called the generalized Frobenius–Perron equation. Similar to the case of $\beta = 1$, the iteration of any smooth positive function $\psi_0^{(\beta)}$ on I leads to a finite limiting $\psi^{(\beta)}$ with a special and unique choice of $R(\beta)$ only. It can be shown [763] that this value is

$$R(\beta) = e^{\beta F(\beta)}. \tag{A.10}$$

The free energy is related to the leading eigenvalue of the generalized Frobenius–Perron operator defined by (A.9).

The relation (A.7) implies that the recurrence scheme

$$\phi_{n+1}^{(q)}(x') = \mathrm{e}^{\kappa q} \sum_{x \in f^{-1}(x')} \frac{\phi_n^{(q)}(x)}{\mid f'(x) \mid^{q-(q-1)D_q}} \tag{A.11}$$

provides an eigenvalue formalism for the order-q dimension. For $q = 0$, we recover the dimension equation (2.20). As a special case, the information dimension D_1 follows from the scheme

$$\hat{\rho}_{n+1}(x') = \frac{\mathrm{e}^{\kappa}}{\kappa}(1 - D_1) \sum_{x \in f^{-1}(x')} \frac{\hat{\rho}_n(x) \ln \mid f'(x) \mid}{\mid f'(x) \mid}, \tag{A.12}$$

which is obtained by taking the limit $q \to 1$ in (A.11).

The set of local Lyapunov exponents E defined by (A.3) can be considered random variables for large n. Since the natural measure of cylinder i is $\mu_i^{(n)} \sim \mathrm{e}^{\kappa n} \varepsilon_i^{(n)}$ (see (2.11)), the partition function can be written as

$$\sum_i \varepsilon_i^{(n)\beta} = \sum_i \varepsilon_i^{(n)\beta-1} \mathrm{e}^{-\kappa n} \mu_i^{(n)} = \langle \mathrm{e}^{-E(\beta-1)n} \rangle \mathrm{e}^{-\kappa n}. \tag{A.13}$$

The average is with respect to the natural measure. The cumulant expansion of a random variable u implies [624]

$$\ln \langle \mathrm{e}^{ku} \rangle = \sum_{l=1}^{\infty} \frac{k^l}{l!} C_l(u), \tag{A.14}$$

where k is a real parameter and $C_l(u)$ stands for the lth cumulant of variable u. In our case, $u = nE$, $k = 1 - \beta$, and the cumulants of nE can be shown [288] in dynamical systems to be linear in n: $C_l(nE) = nQ_l$ (with $Q_1 = \lambda_1$). Thus, from (A.4), (A.13) and (A.14), we obtain

$$\beta F(\beta) = \kappa + \lambda_1(\beta - 1) - \sum_{l=2}^{\infty} \frac{(1 - \beta)^l}{l!} Q_l. \tag{A.15}$$

The cumulants Q_l of the local Lyapunov exponent can thus be obtained from the lth derivative of $\beta F(\beta)$ at $\beta = 1$.

Applying this to the general expressions (A.7) and (A.8), we obtain

$$\kappa = (1 - D_q)\lambda_1 + \sum_{l=2}^{\infty} \frac{(1 - q)^{l-1}(1 - D_q)^l}{l!} Q_l,$$

$$K_q = \lambda_1 - \kappa + \sum_{l=2}^{\infty} \frac{(1 - q)^{l-1}}{l!} Q_l.$$

For $q = 0$, (2.21) and (2.22) are recovered. This shows that the relation between the escape rate and the generalized dimensions and entropies always contains the set of all cumulants Q_l. The only exception is the case $q = 1$, when (2.16) and (2.15) are recovered.

We note that the relations between the multifractal spectra $f(\alpha)$ and $g(\Lambda)$ and the entropy $S(E)$ of the local Lyapunov exponent E are explicit [83, 763, 766]:

$$f(\alpha) = \left.\frac{S(E)}{E}\right|_{E=\kappa/(1-\alpha)}, \quad g(\Lambda) = S(E)|_{E=\Lambda+\kappa}. \tag{A.16}$$

A.3 Multifractal Spectra of Saddles of Two-Dimensional Maps

For an invertible two-dimensional map, the free energy can be defined based on the length scales $\varepsilon_{1i}^{(n)}$ generated along the unstable direction (Sect. 2.6.1):

$$\sum_i \varepsilon_{1i}^{(n)\beta} \sim e^{-\beta F(\beta)n}, \tag{A.17}$$

where $F(1) = \kappa$. The partial generalized dimensions along the unstable direction can be calculated via (A.6) with $\mu_i^{(n)}$ as the natural measure inside the *stable* strips of length $\varepsilon_{1i}^{(n)}$ according to

$$\sum_i \frac{\mu_i^{(n)q}}{\varepsilon_{1i}^{(n)(q-1)D_q^{(1)}}} \sim 1. \tag{A.18}$$

The similarity of these relations to (A.4) and (A.6) implies that for the unstable direction, analogous relations can be obtained as for one-dimensional maps.

An eigenvalue formalism analogous to (A.9) can also be found [763]. The iterative scheme is

$$\psi_{n+1}^{(\beta)}(\mathbf{x}') = R(\beta) \frac{\psi_n^{(\beta)}(\mathbf{x})}{|J(\mathbf{x})\Pi(\mathbf{x})^{\beta-1}|_{\mathbf{x}\in\mathbf{f}^{-1}(\mathbf{x}')}}, \tag{A.19}$$

where $\Pi(\mathbf{x})$ is the local one-step stretching factor along the unstable manifold, and $R(\beta)$ is given by (A.10). The quantity $\Pi(\mathbf{x})$ yields the ratio of the length Δ_1 of the image of a small interval along the unstable direction to its original length Δ_0. (In the notation of Sect. 1.2.3.3, in box i, $\Pi_i = \exp(\Lambda_{1i}(1))$.) The value of $R(\beta)$ is set for any smooth $\psi_0^{(\beta)}(\mathbf{x})$ on a restraining region by the existence of a nontrivial limiting $\psi^{(\beta)}(\mathbf{x})$ for $n \to \infty$ whose integral remains finite over Γ. The leading eigenvalue $1/R(\beta)$ and the eigenvalue spectrum of the generalized Frobenius–Perron operator defined by (A.9) and (A.19), respectively, can also be obtained via a linear approximant of the operator [419], in a way similar to that in the search for almost invariant sets (Sect. 10.5.1). For $\beta \neq 1$, the eigenfunctions, however, do not appear to have any physical meaning.

Dynamical invariants associated with the stable direction, however, cannot be calculated from the free energy alone. To this end, a suitably defined partition function is needed which contains the length scales $\varepsilon_{2j}^{(n)}$ along the stable manifold [766].

A.4 Zeta Functions

The periodic-orbit property (2.85) stipulates that the length scales of a multifractal set can be expressed via the Lyapunov exponents of the unstable periodic orbits. In particular, we can write

$$\sum_i e^{-\lambda_{1i}^* n\beta} \sim e^{-\beta F(\beta)n}. \tag{A.20}$$

The sum contains *all* n-cycle points that are allowed to exist in the system. In general, certain cycles are repetitions of shorter ones. All have been included, includes the so-called *primitive* cycles that cannot be decomposed into more elementary ones.

The zeta-function approach allows one to concentrate on primitive cycles only. Consider the free energy, for example. Equation (A.20) can be rewritten as

$$\sum_i z^n e^{-\lambda_{1i}^* n\beta} \sim 1, \tag{A.21}$$

under the condition that the smallest z value that makes the sum balanced (the sum neither decays nor diverges) be just $z(\beta) = \exp[\beta F(\beta)]$. Examine now the expression

$$\Omega(z) = \sum_n \sum_i z^n e^{-\lambda_{1i}^* n\beta}, \tag{A.22}$$

which, according to (A.21), diverges at $z = z(\beta)$. A basic property of periodic orbits is useful, namely, that the eigenvalue is the same for all possible cyclic elements of the orbit. Furthermore, each period n can be written as r repetitions of a primitive cycle of length n_p: $n = rn_p$. (For primitive cycles, $r = 1$.) As a result, we have, for all points i belonging to an n-cycle, $\lambda_{1i}^* n = r\lambda_{1p}^* n_p$, where λ_{1p}^* is the Lyapunov exponent of a primitive cycle. The term on the right-hand side of (A.22) can be rearranged as a sum over all primitive cycles and a sum over repetitions

$$\Omega(z) = \sum_p n_p \sum_{r=1}^\infty \left(z^{n_p} e^{-\lambda_{1p}^* n_p\beta} \right)^r = \sum_p \frac{n_p z^{n_p} e^{-\lambda_{1p}^* n_p\beta}}{1 - z^{n_p} e^{-\lambda_{1p}^* n_p\beta}}, \tag{A.23}$$

which can be written as z times the derivative of the logarithm of the zeta function

$$\zeta_\beta(z) = \prod_p (1 - z^{n_p} e^{-\lambda_{1p}^* n_p\beta}). \tag{A.24}$$

Since a divergent term in $\Omega(z)$ corresponds to a zero of $\zeta(z)$, the free energy follows from the *smallest positive root* of the zeta function.

The advantage of this approach is that the zeta function is obtained as a *partial summation* over arbitrarily long trajectories. It is thus not surprising that accurate results can be obtained by keeping only a few short primitive cycles in the product of (A.24). An efficient computational tool, the *periodic orbit expansion* [149], is based on the fact that longer orbits can be approximately pieced together from a few short *fundamental* primitive cycles. A detailed description of the cycle expansion and its applications can be found in the e- book [151].

Appendix B
Open Random Baker Maps

B.1 Single Scale Baker Map

One of the simplest two-dimensional maps for transient chaos is the open area-preserving baker map, in which the two half-squares are stretched by the same factor a and are compressed by $1/a$, which is equivalent to setting $a = b$ and $c = d = 1/a$ in (2.54) and (2.55), as shown in Fig. 2.14. To generate a random map, the parameter a is allowed to take on different values at each iterate: $a_n = \bar{a} + \delta a_n > 2$ [544].

The escape rate of the dynamical process can be obtained as follows. After the first step, trajectories remaining inside the unit square from a uniform initial distribution fall into two columns, each having unit height and the width $1/a_1$. After n steps, there are 2^n identical columns, each of width $\Pi_{i=1}^{n}(1/a_i)$. A finite-time escape rate $\kappa^{(n)}$ can be defined for a given realization of the parameter fluctuation by identifying the quantity $\exp[-\kappa^{(n)}n]$ as the area of these columns, which is the same as the number of nonescaping trajectories up to time n. Thus, we have

$$-\kappa^{(n)}n = \ln \Pi_{i=1}^{n}(2/a_i) = -\sum_{i=1}^{n} \ln(a_i/2). \tag{B.1}$$

By dividing by $-n$, the right-hand side contains the arithmetic mean of the expressions $\ln(a_i/2)$, which for large n, converges to the average of the expression taken over all realizations of the parameter fluctuation. The quantities $\kappa^{(n)}$ thus converge to a *well-defined* number, which is the escape rate κ_r of the random map

$$\kappa^{(n)} \to \kappa_r = \langle \ln(a_i/2) \rangle = \langle \ln a_i \rangle - \ln 2, \tag{B.2}$$

where the bracket denotes averaging over all allowed parameter values.

The Lyapunov exponent can be calculated similarly. In particular, any short line segment is stretched, after n steps, by the factor $\Pi_{i=1}^{n}a_i$. The stretching exponent defined in (1.18) is thus $\Lambda_1(n) = \sum_{i=1}^{n} \ln a_i$, from which the finite-time Lyapunov exponent $\lambda_1^{(n)} = \Lambda_1(n)/n$ is

$$\lambda_1^{(n)} = \frac{1}{n} \sum_{i=1}^{n} \ln a_i. \tag{B.3}$$

The average Lyapunov exponent of the snapshot chaotic saddle is thus given by

$$\lambda_{1,r} = \langle \ln a_i \rangle. \tag{B.4}$$

To calculate the box-counting dimension, we cover the set of nonescaping points along the x-axis by intervals of widths $\varepsilon = \Pi_{i=1}^{n}(1/a_i)$. Since there are 2^n columns, we can define an order-n approximant $D_0^{(2,n)}$ to the partial box-counting dimension along the stable direction as

$$D_0^{(2,n)} = \frac{\ln 2^n}{\ln \Pi_{i=1}^{n}(a_i)} = \frac{\ln 2}{(1/n)\sum_{i=1}^{n} \ln a_i}, \tag{B.5}$$

where the denominator contains the arithmetic mean of $\ln a_i$. For large n (fine resolution), a limit exists, which is the partial fractal dimension. We obtain

$$D_{0,r}^{(2)} = \frac{\ln 2}{\langle \ln a_i \rangle}. \tag{B.6}$$

This expression illustrates that by gradually improving the resolution, all relevant length scales can be covered. This also implies that the ensemble of nonescaping trajectories traces out a fractal object after sufficiently long times, but this object changes constantly in time due to the nature of the random map. The box-counting dimension, however, converges to a constant. Since the random map is area-preserving, the two partial dimensions are equal: $D_{0r}^{(1)} = D_{0r}^{(2)}$. In addition, since the distribution is identical in each column, the dimensions are in fact the information dimensions.

Corrections to the results from the deterministic map can also be worked out. For small fluctuations we can write

$$\ln(\bar{a} + \delta a_i) = \ln \bar{a} + \ln(1 + \delta a_i/\bar{a}) \approx \ln \bar{a} + \delta a_i/\bar{a} - (\delta a_i/\bar{a})^2/2.$$

By taking the average, we see that the variance σ^2 of the parameter fluctuations appears: $\langle \ln(\bar{a} + \delta a_i) \rangle = \ln \bar{a} - (\sigma/\bar{a})^2/2$. Substituting this into (B.2) and (B.4), we can obtain the relation between the dynamical invariants of the weakly random map and those of the underlying deterministic map of parameter $\bar{a}$:

$$\kappa_r(\sigma) = \kappa - (\sigma/\bar{a})^2/2, \quad \lambda_{1r}(\sigma) = \lambda_1 - (\sigma/\bar{a})^2/2.$$

It can be seen that these dynamical invariants tend to be smaller for random maps. The box-counting dimension becomes

$$D_{0r}^{(1)}(\sigma) = D_0^{(1)}\left(1 + \frac{1}{2}\frac{\sigma^2}{\ln \bar{a}\, \bar{a}^2}\right),$$

which is actually enhanced by randomness. All these features indicate that a snapshot chaotic saddle is less unstable than its deterministic counterpart.

B.2 General Baker Map

We briefly show how to obtain the dynamical invariants of the random version of the general baker map defined by (2.54) and (2.55) with parameters a_n, b_n, c_n and d_n different at each iterate. Starting from a uniform distribution, after one iteration, trajectories are in two columns, one of height a_1 and width c_1, and the other of height b_1 and width d_1. The portion of particles remaining inside is $(1/a_1 + 1/b_1)$. In the next step, the parameters relevant to escape are a_2 and b_2, and a fraction $(1/a_1 + 1/b_1)(1/a_2 + 1/b_2)$ of the number of original trajectories survive. The "finite-time escape rate" is

$$\kappa^{(n)} = -\frac{1}{n}\sum_{i=1}^{n} \ln\left(\frac{1}{a_i} + \frac{1}{b_i}\right),$$

which gives

$$\kappa_{\mathrm{r}} = -\left\langle \ln\left(\frac{1}{a_i} + \frac{1}{b_i}\right)\right\rangle.$$

To compute the positive Lyapunov exponent, observe that after two steps, the stretching exponents for the four columns are $\ln(a_1 a_2)$, $\ln(a_1 b_2)$, $\ln(b_1 a_2)$, and $\ln(b_1 b_2)$, respectively. The probabilities $P_i^{(2)}$ for falling in these regions are $1/(a_1 a_2)\exp(+\kappa^{(2)}2)$, $1/(a_1 b_2)\exp(+\kappa^{(2)}2)$, etc. The order-2 finite-time Lyapunov exponent is thus

$$\lambda_1^{(2)}2 = \left(\frac{\ln(a_1 a_2)}{a_1 a_2} + \frac{\ln(a_1 b_2)}{a_1 b_2} + \frac{\ln(b_1 a_2)}{b_1 a_2} + \frac{\ln(b_1 b_2)}{b_1 b_2}\right) e^{+\kappa^{(2)}2}.$$

The order-n expression can be obtained by regrouping terms, yielding

$$\lambda_1^{(n)}n = \sum_{i=1}^{n} \ln a_i \frac{1/a_i}{1/a_i + 1/b_i} + \sum_{i=1}^{n} \ln b_i \frac{1/b_i}{1/a_i + 1/b_i}.$$

The average Lyapunov exponent of the snapshot chaotic saddle is given by

$$\lambda_{1r} = \left\langle \ln a_i \frac{1/a_i}{1/a_i + 1/b_i}\right\rangle + \left\langle \ln b_i \frac{1/b_i}{1/a_i + 1/b_i}\right\rangle.$$

To calculate the partial information dimension $D_1^{(1)}$ along the unstable manifold, we first note that the lengths $\varepsilon_{1i}^{(2)}$ along the manifold, generated by the inverted map after two steps, are $(1/a_1)(1/a_2)$ and $(1/a_1)(1/b_2)$, etc. Their logarithms are

exactly the negatives of the stretching exponents. The probabilities $P_i^{(2)}$ for finding these scales are the same as in the case of calculating the Lyapunov exponent. An order-n approximation to the dimension can then be defined based on the general relation (1.22):

$$D_1^{(1,n)} = \frac{\sum_i P_i^{(n)} \ln P_i^{(n)}}{\sum_i P_i^{(n)} \ln \varepsilon_i^{(n)}}. \tag{B.7}$$

It can be seen that the denominator is $-\lambda^{(n)}n$. The numerator is related to the denominator, since $P^{(n)} = \varepsilon^{(n)} \exp(\kappa^{(n)}n)$. We thus have

$$D_1^{(1,n)} = \frac{-\lambda_1^{(n)}n + \kappa^{(n)}n}{-\lambda_1^{(n)}n}, \tag{B.8}$$

which yields (4.51). The other partial information dimension can be determined in a similar way. It is given by the analogue of formula (2.78).

To find the partial box-counting dimension along the stable direction, we observe that after two steps, the widths become $(c_1 c_2)$, $(c_1 d_2)$, $(d_1 c_2)$, and $(d_1 d_2)$ for the four columns. The dimension D_0 of such a four-scale Cantor set can be obtained from (1.20) through $(c_1^{D_0} + d_1^{D_0})(c_2^{D_0} + d_2^{D_0}) = 1$, or $\sum_i \ln(c_i^{D_0} + d_i^{D_0}) = 0$. The partial box-counting dimension $D_{0r}^{(2)}$ of the random map is thus determined by the following implicit relation:

$$\langle \ln(c_i^{D_{0r}^{(2)}} + d_i^{D_{0r}^{(2)}}) \rangle = 0.$$

The other partial dimension follows from a similar equation in which c and d are replaced by $1/a$ and $1/b$, respectively.

Appendix C
Semiclassical Approximation

C.1 Semiclassical S-Matrix in Action-Angle Representation

For chaotic scattering, there can be infinitely many classical trajectories between the initial state before the scattering and the final state after the scattering. It is thus necessary to sum the contributions to the S-matrix elements from all the classically allowed trajectories.

In the action-angle coordinates the expression of the S-matrix elements in the action-angle representation is [76]

$$S_{II'} \equiv \langle I'|S|I \rangle = \left(\frac{1}{2\pi} \right)^{1/2} \sum_s \left| \frac{\partial I'}{\partial \theta} \right|_{(s)}^{-1/2} \exp \left[\frac{\mathrm{i}\bar{\Phi}^{(s)}(I',I)}{\hbar} - \mathrm{i}\nu_s \frac{\pi}{2} \right], \qquad \text{(C.1)}$$

where the summation is over all classically allowed trajectories s, I, θ and I', θ' are the classical action variables in the initial and the final states, respectively, $\bar{\Phi}^{(s)}(I',I)$ is the classical action integral along the path s, and ν_s is the Maslov index (discussed in detail in Sect. C.2). The preexponential factor in (C.1) can be regarded as the square root of the contribution of trajectory s to the total classical transition probability, denoted by $p_{I \to I'}^{(s)}$:

$$p_{II'}^{(s)} \equiv \frac{1}{2\pi} \left| \frac{\partial I'}{\partial \theta} \right|_{(s)}^{-1}. \qquad \text{(C.2)}$$

Equations (C.1) and (C.2) constitute the foundation in the study of quantum manifestations of chaotic scattering [75–78, 204, 205, 442], which relate the quantum-scattering matrix elements to classical quantities in the semiclassical regime $0 < \hbar \ll 1$. The semiclassical sum in (C.1) is valid under the condition that the difference in the actions between close orbits is larger than the Planck constant $\hbar$. For chaotic scattering, there are infinitely many trajectories lying closely in the phase space that contribute to the sum. For long trajectories, the coalescence of the corresponding actions can be a serious problem. However, the probability of having a long tra-

jectory decreases significantly with its length, exponentially for hyperbolic chaotic scattering and algebraically for nonhyperbolic chaotic scattering (cf. Chap. 6). For average quantities such as the correlation function between the S-matrix elements, the contributions from the long trajectories are negligible. The semiclassical sum in (C.1) is thus expected to be valid for chaotic scattering in general.

C.2 Stationary Phase Approximation and the Maslov Index

The stationary phase approximation is key to the semiclassical formulation of quantum mechanics, which enables the wave function in different representations to be expressed in terms of classical trajectories. An important outcome of this approximation is the $\pi/2$ phase shift in the wave function when the underlying classical trajectory encounters a turning point. The Maslov index in (C.1) is in fact the number of turning points along a classical path. For pedagogical purpose here we include a brief introduction to the stationary phase approximation and how it necessitates the inclusion of the Maslov index in semiclassical quantum mechanics using the simple system of particle motion in a one-dimensional potential well. The treatment here follows that in [60, 740].

The Schrödinger equation for a particle in a one-dimensional potential well is

$$-\frac{\hbar^2}{2}\frac{\mathrm{d}^2\Psi}{\mathrm{d}x^2} + V(x)\Psi = E\Psi, \tag{C.3}$$

where the particle is assumed to have unit mass, $\Psi(x)$ is the wave function in the coordinate representation, and the potential function $V(x)$ has a local minimum at $x = 0$ and it increases with both positive and negative x. In the semiclassical approximation, the wave function is written as [60]

$$\Psi(x) = A(x)\exp[\mathrm{i}\phi(x)], \tag{C.4}$$

where the amplitude function $A(x)$ is assumed to vary slowly as compared with the phase $\phi(x)$. Substituting this ansatz into the Schrödinger equation and neglecting the second derivative of $A(x)$, one obtains the following wave function in the semiclassical approximation:

$$\Psi(x) = \frac{\Psi_0}{\sqrt{|p(x)|}}\exp\left[\frac{i}{\hbar}\int_{x_0}^{x}p(x)\mathrm{d}x\right], \tag{C.5}$$

where Ψ_0 is an integration constant and $p(x) = \pm\sqrt{2[E - V(x)]}$ is the local momentum of the particle. Apparently, this approximation breaks down at the classical turning point where $p(x) = 0$. One way to overcome this difficulty is to make use of the momentum-space representation [212, 503]. This is based on the intuition

that if an approximation is poor in the coordinate space, it should be good in the momentum space, and vice versa. The momentum-space wave function $\bar{\Psi}(p)$ is the Fourier transform of the coordinate-space wave function,

$$\bar{\Psi}(p) = \frac{1}{\sqrt{2\pi\hbar}} \int \mathrm{d}x \Psi(x) \exp\left(-\frac{i}{\hbar}xp\right) \tag{C.6}$$

$$= \frac{\Psi_0}{\sqrt{2\pi\hbar}} \int \frac{\mathrm{d}x}{\sqrt{|p(x)|}} \exp\left[\frac{i}{\hbar}\left(\int_{x_0}^x p(x)\mathrm{d}x - xp\right)\right].$$

Note that in (C.6), $p(x)$ is the local momentum and p is the argument of $\bar{\Psi}(p)$. The integral in (C.6) is of the type

$$I_\Phi = \int \mathrm{d}x A(x) \exp\left[i\Phi(x)\right] \tag{C.7}$$

with the phase function

$$\Phi(x) = \frac{1}{\hbar}\left[\int_{x_0}^x p(x)\mathrm{d}x - xp\right].$$

In the semiclassical limit $\hbar \to 0$, the phase $\Phi(x)$ oscillates rapidly, so almost all contributions to the integral cancel each other except for points in the neighborhood of x_s at which the phase is stationary, i.e., $\Phi'(x_s) = 0$. Expanding $\Phi(x)$ up to $(x - x_s)^2$, substituting it in (C.7), and making use of the Fresnel integral

$$\int_{-\infty}^{\infty} e^{i\alpha x^2}\mathrm{d}x = \left(\frac{\pi}{|\alpha|}\right)^{1/2} \exp\left[i\frac{\pi}{4}\mathrm{sgn}(\alpha)\right],$$

one obtains

$$I_\Phi \approx \left[\frac{2\pi}{|\Phi''(x_s)|}\right]^{1/2} A(x_s)\exp\left\{i\Phi(x_s) + i\frac{\pi}{4}\mathrm{sgn}[\Phi''(x_s)]\right\}. \tag{C.8}$$

The first two derivatives of $\Phi(x)$ are $\Phi'(x) = [p(x) - p]/\hbar$ and $\Phi''(x) = p'(x)/\hbar$. The stationary point is thus determined by $p(x_s) = p$. Using (C.8) yields

$$\bar{\Psi}(p) \approx \frac{\Psi_0}{\sqrt{|p(x_s)p'(x_s)|}} \exp\left\{\frac{i}{\hbar}\left[\int_{x_0}^{x_s} p(x)\mathrm{d}x - px_s\right] + \frac{i\pi}{4}\mathrm{sgn}[p'(x_s)]\right\}, \tag{C.9}$$

where $p(x_s)p'(x_s) = (1/2)\mathrm{d}p^2/\mathrm{d}x|_{x=x_s} = -V'(x_s)$. Thus, in the vicinity of a generic turning point where $V'(x_s) \neq 0$, the semiclassical momentum-space wave function is well defined.

To understand the meaning of the Maslov index, consider a closed orbit in the classical phase space (x, p), as shown in Fig. C.1. There are two turning points at which the local momentum changes sign. To obtain the semiclassical wave function
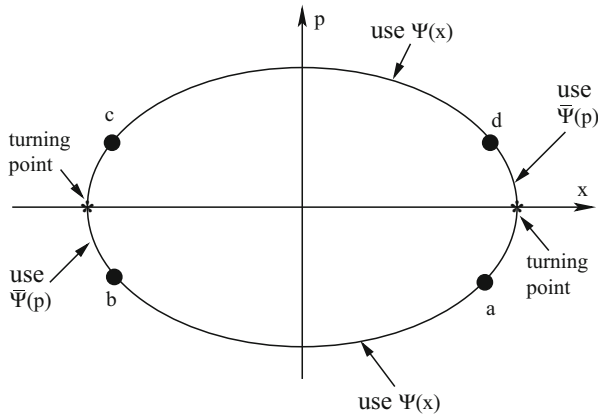
Fig. C.1 For motion in a one-dimensional potential well, a closed orbit in the classical phase space. There are two turning points at which the local momentum changes sign. Dividing the orbit into four segments, one uses either the momentum-space or the coordinate-space wave function, depending on whether the segment contains a turning point or not

for the entire orbit, one can divide the orbit into four segments, with the dividing points a, ..., d, and use the coordinate-space wave function for the two segments that do not contain any turning point (the segments between "a" and "b" and between "c" and "d") and the momentum-space wave function for the two segments each containing one turning point (the segments between "b" and "c" and between "d" and "a"). For example, for the segment between "a" and "b," the coordinate-space wave function is

$$\Psi(x) = \frac{\Psi_0}{|p(x)|^{1/2}} \exp\left[\frac{i}{\hbar} \int_{x_0}^{x} p(x)\mathrm{d}x\right]. \tag{C.10}$$

At point "b," it is necessary to transform into the momentum space. This can be done by replacing x_s and $p'(x_s)$ in (C.9) by $x(p)$ and $1/x'(p)$, respectively. Since $x'(p) < 0$ at point b, one has

$$\bar{\Psi}(p) = \Psi_0 \left|\frac{x'(p)}{p}\right|^{1/2} \exp\left\{\frac{i}{\hbar}\left[\int_{x_0}^{x(p)} p(x)\mathrm{d}x - px(p)\right] - \frac{i\pi}{4}\right\}. \tag{C.11}$$

At point "c" one transforms the wave function back to the position space. This can be accomplished by the Fourier transform of $\bar{\Psi}(p)$, which gives

$$\Psi(x) = \frac{1}{(2\pi\hbar)^{1/2}} \int \mathrm{d}p\,\bar{\Psi}(p) \exp\left(\frac{i}{\hbar}xp\right) \tag{C.12}$$

$$= \frac{\Psi_0}{(2\pi\hbar)^{1/2}} \int \mathrm{d}p \left|\frac{x'(p)}{p}\right|^{1/2} \exp\left\{\frac{i}{\hbar}\left[\int_{x_0}^{x(p)} p(x)\mathrm{d}x - px(p) + px\right] - \frac{i\pi}{4}\right\}.$$

A straightforward application of the stationary phase approximation gives

$$\Psi(x) = \frac{\Psi_0}{|p(x)|^{1/2}} \exp\left[\frac{i}{\hbar} \int_{x_0}^{x} p(x)\mathrm{d}x - \frac{i\pi}{2}\right].\qquad(\text{C.13})$$

Comparing (C.10) and (C.13), one sees that a phase loss of $\pi/2$ has occurred while passing through the turning point between points "b" and "c." Thus, after completing the closed orbit, the phase shift in the wave function is

$$\Delta\Phi = \frac{1}{\hbar}\oint p(x)\mathrm{d}x - \nu\frac{\pi}{2} = \frac{1}{\hbar}\oint x(p)\mathrm{d}p - \nu\frac{\pi}{2},\qquad(\text{C.14})$$

where ν is the number of turning points along the closed orbit, the Maslov index [60, 503].

In the semiclassical expression of the S-matrix elements in (C.1), it is thus necessary to include the phase accumulation $\nu\pi/2$, considering that a chaotic scattering trajectory can typically have many turning points in the phase space.

Appendix D
Scattering Cross Sections

D.1   Scattering Cross Sections in Classical Chaotic Scattering

In a typical scattering experiment, particles are not followed individually. Rather, a uniform beam of particles approaching the scattering region is examined and the fraction of the particle ensemble scattered into a given direction is determined. This process can be characterized by the differential cross section, generally defined as the number of particles scattered into a given direction per unit time divided by the incident intensity [268]. For chaotic scattering, the differential cross section is proportional to the probability that a particle is scattered into the given direction.

In we have seen in Chap. 6 that for chaotic scattering, a typical scattering function (deflection function or delay-time function) contains both smooth and discontinuous parts. In particular, the impact parameter line splits into an infinite number of intervals in which the scattering function is smooth, and the boundaries among the smooth intervals are points of discontinuity. The cross section can be obtained by fixing a deflection angle θ and a small increment $d\theta$ about θ and examining the values of the impact parameter that result in scattering with deflection angles falling in the interval $[\theta - d\theta/2, \theta + d\theta/2]$. If there is a one-to-one correspondence between the deflection angle and the impact parameter, as in regular scattering in classical mechanics [268], the differential cross section $\sigma(\theta)$ for scattering in direction θ in a two-dimensional problem is

$$c = \left| \frac{d\theta}{db}(b) \right|^{-1}. \tag{D.1}$$

For chaotic scattering there are typically infinitely many contributions to the same θ from the different intervals of continuity. As pointed out by Jung and Pott [368], it is necessary to determine all values b_s of the impact parameter that lead to the particular scattering angle θ. For each b_s the quantity c in (D.1) is measured and all the contributions are summed to yield the cross section for chaotic scattering:

$$\sigma(\theta) = \sum_s c_s = \sum_s \left| \frac{d\theta}{db}(b_s) \right|^{-1}. \tag{D.2}$$

The cross section is usually a complicated expression of the derivatives of the deflection function taken at b_s. In fact, the cross section is the total length of short impact parameter intervals db_s that lead to scattering into the angle interval $[\theta - d\theta/2, \theta + d\theta/2]$.

In each interval of continuity, the deflection function can have an infinite number of extrema. At such angles, the cross section is singular, implying that $\sigma(\theta)$ has much more contributions in certain regions than in others. Let θ_c denote an extremum value of the deflection function at b_c. The neighborhood of a nondegenerate extremum is quadratic. Locally, we can write

$$\theta(b) = \theta_c + a(b - b_c)^2. \tag{D.3}$$

In this neighborhood two impact parameter values, $b_{1,2} = b_c \pm [(\theta - \theta_c)/a]^{1/2}$, belong to a given angle θ. Their contributions to the cross section are $c_{1,2} = [4a(\theta - \theta_c)]^{-1/2}$. The cross section thus contains singularities of the type

$$\sigma(\theta) \sim (\theta - \theta_c)^{-1/2}. \tag{D.4}$$

These so-called *rainbow* singularities dominate the entire cross section function $\sigma(\theta)$, as illustrated by Fig. D.1 for a representative chaotic scattering system.

Trajectories starting in short intervals of continuity stay for a long time near the chaotic saddle, and leave the scattering region along the saddle's unstable manifold. This manifold is a fractal characterized by a partial box-counting dimension $D_0^{(2)} < 1$. As a result, the distribution of the rainbows in any short interval of continuity reflects the fractal pattern of the saddle in the phase space [368]. The conclusion is then that the box-counting dimension of the rainbow singularities coincides with
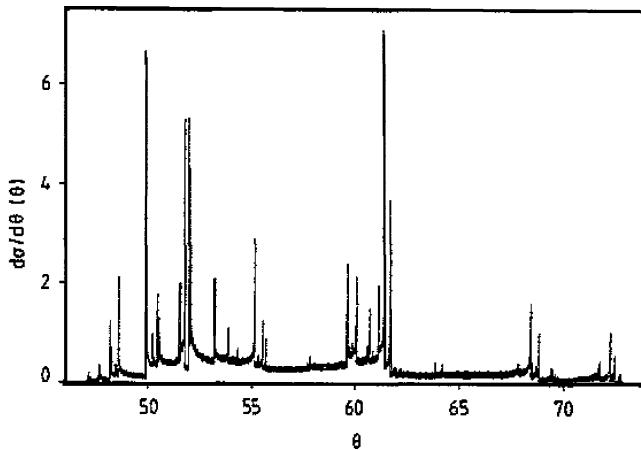
Fig. D.1 Differential cross section of a three-hill system in the scattering angle interval $[46°, 74°]$ for a fixed value of the energy. The rainbow singularities form a fractal set of dimension d_s [369] (with kind permission from the Institute of Physics)

the partial box-counting dimension $D_0^{(2)} = D_0^{(1)} \equiv d_s$ of the chaotic saddle. The technical difficulty that there are a large number of weak rainbow singularities, which can hardly be distinguished from the smooth background, can be overcome by applying rapidly converging methods for the determination of the dimension [369]. Rainbow singularities are present in nonhyperbolic chaotic scattering as well. As the scattering progresses from the regular to the chaotic regime, rainbow singularities are shown to be created in a series of cascades, related to the bifurcation cascades undergone in the chaotic saddle [680]. There are systems that exhibit chaotic scattering but still possess a smooth cross section without any singularities [164]. Such situations cannot occur in high-dimensional systems if the chaotic saddle is formed by normally hyperbolic invariant manifolds (Sect. 8.5.2) [366]. As pointed out in [367], knowledge about the rainbow singularities in the cross section allows one to reconstruct the development stage of the chaotic set defined in Sect. 6.4.2.

D.2   Semiclassical Scattering Cross Sections

In a scattering experiment, the incoming momentum (energy) is specified as precisely as possible, but the impact parameter is unspecified. The differential cross section is usually measured as a function of the angle and energy. The maximal amount of information that can be obtained from a scattering experiment on micro scales is provided by this cross section. When comparing classical and quantum-mechanical cross sections of the same process, the distinct feature in the quantum case is the *interference oscillations*. At the semiclassical level these oscillations contain relevant information about the classical chaotic saddle.

In a semiclassical approximation, the scattering amplitude follows from Miller's theory (C.1) as

$$f(\theta, E) = \sum_s c_s^{1/2} \exp\left[\frac{i\bar{\Phi}^{(s)}}{\hbar} - i\nu_s \frac{\pi}{2}\right]. \tag{D.5}$$

The summation is over all classical scattering trajectories s at energy E and with deflection angle θ. The quantity c_s is the contribution of trajectory s with impact parameter b_s to the classical cross section, as given by (D.1) evaluated at $b = b_s$, and $\bar{\Phi}^{(s)}$ and ν_s represent the classical action and the Maslov index associated with trajectory s, respectively (see Appendix C). Assuming that the angle θ is *away* from any classical rainbow singularities, we can express the differential cross section by the scattering amplitude as [301]

$$\sigma(\theta, E) = |f(\theta, E)|^2. \tag{D.6}$$

The interference effects in the cross section in the limit of small $\hbar$ can then be examined. Since, away from rainbow singularities, the classical contribution c_s is a slowly varying function, we can evaluate c_s at some reference values θ_0, E_0.

Away from caustics, ν_s is approximately constant. The only source of fast variation is then the phase $\bar{\Phi}^{(s)}/\hbar$, because $\hbar$ is small. For fixed energy, the action can be expanded about θ_0:

$$\bar{\Phi}^{(s)}(\theta) = \bar{\Phi}^{(s)}(\theta_0) + (\theta - \theta_0)L_s, \tag{D.7}$$

where $L_s = \partial\bar{\Phi}^{(s)}/\partial\theta|_{\theta_0}$ is the outgoing angular momentum associated with trajectory s. The cross section is then obtained from (D.6) and (D.5) as

$$\sigma(\theta, E) = \sum_s c_s + \sum_{r<s} 2(c_r c_s)^{1/2} \cos[\phi_{rs} - \theta(L_r - L_s)/\hbar], \tag{D.8}$$

where the ϕ_{rs} are constant. The first term is the classical contribution (D.2), and the double sum represents the interference oscillations. The values of the outgoing angular momentum differences form a fractal set of dimension $D_0^{(1)}$. The Fourier transform

$$g(L) = \int \sigma(\theta)\cos\left(\frac{\theta L}{\hbar}\right) d\left(\frac{\theta}{\hbar}\right) \tag{D.9}$$

for a fixed E_0 over a suitable range of θ about θ_0 away from classical rainbow positions thus contains singular contributions, as shown in Fig. D.2

The angular-momentum differences L belonging to singular values of the semiclassical cross section's Fourier transform form a set of box-counting dimension $D_0^{(1)} = D_0^{(2)} \equiv d_s$ [369]. It is remarkable that even in an angle range where the classical cross section is smooth, the interference oscillations reflect the fractal structure of the classical chaotic saddle.
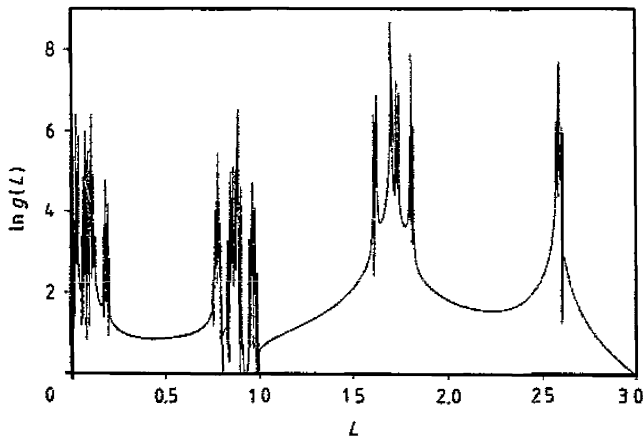
Fig. D.2 For a three-hill chaotic scattering system, logarithm of the Fourier transform $g(L)$ of the differential cross section as a function of the angular-momentum difference L. Integration is taken in the angle interval $(5.4, 5.402)$ with $\hbar = 2 \cdot 10^{-7}$ at a fixed energy. The singularities form a fractal set of dimension d_s [369] (with kind permission from the Institute of Physics)

References

1. R. Abraham and S. Smale. Nongenericity of Ω-stability. *Global Analysis, Proc. of Symposia in Pure Math. (AMS)*, 14:5–8, 1970.
2. R. L. Adler, A. G. Konheim, and M. H. McAndrew. Topological entropy. *Trans. Am. Math. Soc.*, 114:309, 1965.
3. V. S. Afraimovich and L. A. Bunimovich. Which hole is leaking the most: a topological approach to study open systems. *Nonlinearity*, 23:643–656, 2010.
4. J. Aguirre, F. d'Ovidio, and M. A. F. Sanjuán. Controlling chaotic transients: Yorke's game of survival. *Phys. Rev. E*, 69:016203, 2004.
5. J. Aguirre and M. A. F. Sanjuan. Limit of small exits in open Hamiltonian systems. *Phys. Rev. E*, 67:056201, 2003.
6. J. Aguirre, J. C. Vallejo, and M. A. F. Sanjuán. Wada basins and chaotic invariant sets in the Hénon-Heiles system. *Phys. Rev. E*, 64:066208, 2001.
7. J. Aguirre, R. L. Viana, and M. A. F. Sanjuán. Fractal structures in nonlinear dynamics. *Rev. Mod. Phys.*, 81:333–386, 2009.
8. J. Aguirregabiria and J. Etxebarria. Fractal basin boundaries of a delay-differential equation. *Phys. Lett. A*, 122:241–244, 1987.
9. G. Ahlers and R. Walden. Turbulence near onset of convection. *Phys. Rev. Lett.*, 44:445–448, 1980.
10. R. Akis, J. P. Bird, D. K. Ferry, and D. Vasileska. Nonuniform energy level broadening in open quantum dots: the influence of the closed dot eigenstates on transport. *Physica E*, 7:745–749, 2000.
11. J. C. Alexander, J. A. Yorke, Z. You, and I. Kan. Riddled basins. *Int. J. Bifur. Chaos Appl. Sci. Eng.*, 2:795–813, 1992.
12. S. Allie and A. Mees. Finding periodic points from short time series. *Phys. Rev. E*, 56:346–350, 1997.
13. H. Alt, H.-D. Gräf, H. L. Harney, R. Hofferbert, H. Rehfeld, A. Richter, and P. Schardt. Decay of classical chaotic systems: the case of the Bunimovich stadium. *Phys. Rev. E*, 53:2217–2222, 1996.
14. E. G. Altmann and H. Kantz. Hypotesis of strong chaos and anomalous diffusion in coupled symplectic maps. *EuroPhys. Lett.*, 78:10008, 2007.
15. E. G. Altmann. Emission from dielectric cavities in terms of invariant sets of the chaotic ray dynamics. *Phys. Rev. E*, 79:013830, 2009.
16. E. G. Altmann, E. C. da Silva, and I. L. Caldas. Recurrence time statistics for finite size intervals. *Chaos*, 14:975–981, 2004.
17. E. G. Altmann, A. E. Motter, and H. Kantz. Stickiness in Hamiltonian systems: from sharply divided to hierarchical phase space. *Phys. Rev. E*, 73:026207, 2006.
18. E. G. Altmann and T. Tél. Poincaré recurrences from the perspective of transient chaos. *Phys. Rev. Lett*, 100:174101, 2008.
19. E. G. Altmann and T. Tél. Poincaré recurrences and transient chaos in leaked systems. *Phys. Rev. E*, 79:016204, 2009.

20. E. G. Altmann and A. Endler. Noise-enhanced trapping in chaotic scattering. *Phys. Rev. Lett*, 105:244102, 2010.

21. M. Antoni and S. Ruffo. Clustering and relaxation in Hamiltonian long-range dynamics. *Phys. Rev. E*, 52:2361–2374, 1995.

22. F. T. Arecchi and F. Lisi. Hopping mechanism generating 1/F noise in non-linear systems Arecchi and Lisi Respond. *Phys. Rev. Lett.*, 50:1330–1330, 1983.

23. F. T. Arecchi, R. Meucci, G. Puccioni, and J. Tredicce. Experimental-evidence of sub-Harmonic bifurcations, multistability, and turbulence in a Q-switched gas-laser. *Phys. Rev. Lett.*, 49:1217–1220, 1982.

24. F. T. Arecchi, R. Badii, and A. Politi. Low-frequency phenomenon in dynamical systems with many attractors. *Phys. Rev. A*, 29:1006–1009, 1984.

25. H. Aref. Integrable, chaotic, and turbulent vortex motion in two-dimensional flows. *Annu. Rev. Fluid. Mech.*, 15:345–389, 1983.

26. H. Aref. Stirring by chaotic advection. *J. Fluid Mech.*, 143:1–21, 1984.

27. H. Aref and M.S. El Naschie. *Chaos Applied to Fluid Mixing*. Pergamon, New York, first edition, 1995.

28. J. Aristegui, P. Tett, A. Hernández-Guerra, G. Basterretxea, M. F. Montero, K. Wild, P. Sangrá, S. Hernández-Leon, M. Canton, J. A. Garca-Braun, M. Pacheco, and E. D. Barton. The influence of island-generated eddies on chlorophyll distribution: a study of mesoscale variation around Gran Canaria. *Deep Sea Res.*, 44:71–96, 1997.

29. L. Arnold. *Random Dynamical Systems*. Springer, Berlin, first edition, 1998.

30. P. Ashwin and E. Stone. Influence of noise near blowout bifurcation. *Phys. Rev. E*, 56:1635–1641, 1996.

31. E. Aurell, G. Boffetta, A. Crisanti, G. Paladin, and A. Vulpiani. Growth of noninfinitesimal perturbations in turbulence. *Phys. Rev. Lett.*, 77:1262–1265, 1996.

32. T. R. Auton, J. C. R. Hunt, and M. Prud'homme. The force exerted on a body in inviscid unsteady non-uniform rotational flow. *J. Fluid Mech.*, 197:241–257, 1998.

33. M. Avila, A. P. Willis, and B. Hof. On the transient nature of localized pipe flow turbulence. *J. Fluid. Mech.*, 646:127–136, 2010.

34. T. Baba. Photonic crystals and microdisk cavities based on GaInAsP-InP system. *IEEE Select. Top. Quantum Electron.*, 3:808–830, 1997.

35. A. Babiano, G. Boffetta, A. Provenzale, and A. Vulpiani. Chaotic advection in point vortex models and two-dimensional turbulence. *Phys. Fluids A*, 6:2465–2474, 1994.

36. A. Babiano, J. H. E. Cartwright, O. Piro, and A. Provenzale. Dynamics of a small neutrally buoyant sphere in a fluid and targeting in Hamiltonian systems. *Phys. Rev. Lett.*, 84:5764–5767, 2000.

37. R. Badii, E. Brun, M. Finardi, L. Flepp, R. Holzner, J. Pariso, C. Reyl, and J. Simonet. Progress in the analysis of experimental chaos through periodic orbits. *Rev. Mod. Phys.*, 66:1389–1415, 1994.

38. M. S. Baptista, S. Kraut, and C. Grebogi. Poincaré recurrence and measure of hyperbolic and nonhyperbolic chaotic attractors. *Phys. Rev. Lett.*, 95:094101, 2005.

39. H. U. Baranger. Quantum transport and chaos in semiconductor microstructures. *Physica D*, 83:30–45, 1995.

40. H. U. Baranger, R. A. Jalabert, and A. Douglas Stone. Quantum-chaotic scattering effects in semiconductor microstructures. *Chaos*, 3:665–682, 1993.

41. E. Barreto and P. So. Mechanisms for the development of unstable dimension variability and the breakdown of shadowing in coupled chaotic systems. *Phys. Rev. Lett.*, 85:2490–2493, 2000.

42. A. M. Barr, K. Na, L. E. Reichl, and C. Jung. Chaotic scattering in a molecular system. *Phys. Rev. E*, 79:026215, 2009.

43. W. Bauer and G.F. Bertsch. Decay of ordered and chaotic systems. *Phys. Rev. Lett*, 65:2213–2216, 1990.

44. P. D. Beale. Noise-induced escape from attractors in one-dimensional maps. *Phys. Rev. A*, 40:3998–4003, 1989.

45. C. Beck and F. Schlögl. *Thermodynamics of Chaotic Systems: An Introduction*. Cambridge University Press, Cambridge, UK, first edition, 1993.

46. C. W. J. Beenakker. Random matrix theory of quantum transport. *Rev. Mod. Phys.*, 69:731–808, 1997.

47. C. W. J. Beenakker and H. van Houten. Billiard model of a ballistic multiprobe conductor. *Phys. Rev. Lett.*, 63:1857–1860, 1989.

48. D. Beigie, A. Leonard, and S. Wiggins. Invariant manifold templates for chaotic advection. *Chaos Sol. Fract.*, 4:749–868, 1994.

49. A. Ben-Mizrachi, I. Procaccia, and P. Grassberger. Characterization of experimental (noisy) strange attractors. *Phys. Rev. A*, 29:975–977, 1984.

50. I. J. Benczik, T. Toroczkai, and T. Tél. Advection of finite-size particles in open flows. *Phys. Rev. E*, 67:036303, 2003.

51. I. J. Benczik, S. Z. Benczik, B. Schmittmann, and R. K. P. Zia. Lack of consensus in social systems. *Europhys. Lett.*, 82:48006, 2008.

52. I. J. Benczik, S. Z. Benczik, B. Schmittmann, and R. K. P. Zia. Opinion dynamics on an adaptive random network. *Phys. Rev. E*, 79:046104, 2009.

53. I. J. Benczik, Z. Toroczkai, and T. Tél. Selective sensitivity of open chaotic flows on inertial tracer advection: catching particles with a stick. *Phys. Rev. Lett.*, 89:164501, 2002.

54. J. Bene. Multifractal properties of a class of non-natural measures as an Eigenvalue problem. *Phys. Rev. A*, 39:2090–2096, 1989.

55. G. Benettin, L. Galgani, A. Giorgilli, and J. M. Strelcyn. Lyapunov characteristic exponents for smooth dynamical systems and for Hamiltonian systems: a method for computing all of them. Part 1: Theory. *Meccanica*, 15:9–20, 1980.

56. M. Berblinger and C. Schlier. The Double-Morse well and topological chaos. *Chem. Phys. Lett.*, 145:299–304, 1988.

57. S. Beri, R. Mannella, D. G. Luchinsky, A. N. Silchenko, and P. V. E. McClintock. Solution of the boundary value problem for optimal escape in continuous stochastic systems and maps. *Phys. Rev. E*, 72:036131, 2005.

58. M. V. Berry. Reflection on a Christmas-tree baule. *Phys. Edu.*, 7:1–6, 1972.

59. M. V. Berry. Regularity and chaos in classical mechanics, illustrated by three deformations of a circular "billiard". *Eur. J. Phys.*, 2:91–102, 1981.

60. M. V. Berry and K. E. Mount. Semiclassical approximations in wave mechanics. *Reps. Prog. Phys.*, 35:315–397, 1972.

61. J. J. B. Biemond, A. P. S. de Moura, G. Károlyi, C. Grebogi, and H. Nijmeijer. Onset of chaotic advection in open flows. *Phys. Rev. E*, 78:016317, 2008.

62. F. A. Bignone. Cells-genes interaction simulation on a coupled map lattice. *J. Theor. Biol.*, 161:231–249, 1993.

63. O. Biham and W. Wenzel. Characterization of unstable periodic orbits in chaotic attractors and repellers. *Phys. Rev. Lett.*, 63:819–822, 1989.

64. L. Billings, E. M. Bollt, and I. B. Schwartz. Phase-space transport of stochastic chaos in population dynamics of virus spread. *Phys. Rev. Lett.*, 88:234101, 2002.

65. L. Billings and I. B. Schwartz. Exciting chaos with noise: unexpected dynamics in epidemic outbreaks. *J. Math. Biol.*, 44:31–48, 2002.

66. L. Billings, I. B. Schwartz, D. S. Morgan, E. M. Bollt, R. Meucci, and E. Allaria. Stochastic bifurcation in a driven laser system: Experiment and theory. *Phys. Rev. E*, 70:026220, 2004.

67. J. P. Bird, R. Akis, and D. K. Ferry. Magnetoprobing of the discrete level spectrum of open quantum dots. *Phys. Rev. B*, 60:13676–13681, 1999.

68. J. P. Bird, R. Akis, D. K. Ferry, A. P. S. de Moura, Y.-C. Lai, and K. M. Indlekofer. Interference and interactions in open quantum dots. *Rep. Prog. Phys.*, 66:583–632, 2003.

69. J. P. Bird, R. Akis, D. K. Ferry, D. Vasileska, J. Cooper, Y. Aoyagi, and T. Sugano. Lead-orientation-dependent wave function scarring in open quantum dots. *Phys. Rev. Lett.*, 82:4691–4694, 1999.

70. J. A. Blackburn, N. Gronbech-Jensen, and H. J. T. Smith. Stochastic noise and chaotic transients. *Phys. Rev. Lett.*, 74:908–911, 1995.

71. R. E. Blahut. *Principles and Practice of Information Theory*. Addison-Wesley, Reading, MA, first edition, 1988.

72. S. Bleher, C. Grebogi, and E. Ott. Fractal boundaries for exit in Hamiltonian dynamics. *Phys. Rev. A*, 38:930–938, 108.

73. S. Bleher, E. Ott, and C. Grebogi. Routes to chaotic scattering. *Phys. Rev. Lett.*, 63:919–922, 1989.

74. S. Bleher, C. Grebogi, and E. Ott. Bifurcation to chaotic scattering. *Physica D*, 46:87–121, 1990.

75. R. Blümel. Quantum chaotic scattering. In B.-L. Hao, D.-H. Feng, and J.-M. Yuan, editors, *Directions in Chaos*. World Scientific, Singapore, 1991.

76. R. Blümel and U. Smilansky. Classical irregular scattering and its quantum-mechanical implications. *Phys. Rev. Lett.*, 60:477–480, 1988.

77. R. Blümel and U. Smilansky. A simple model for chaotic scattering II. Quantum mechanical theory. *Physica D*, 36:111–136, 1989.

78. R. Blümel and U. Smilansky. Random-matrix description of chaotic scattering: semiclassical approach. *Phys. Rev. Lett.*, 64:241–244, 1990.

79. S. Boccaletti, C. Grebogi, Y.-C. Lai, H. Mancini, and D. Maza. Control of chaos: theory and applications. *Phys. Rep.*, 329:103–197, 2000.

80. S. Boccaletti, J. Kurths, G. Osipov, D. L. Valladares, and C.-S. Zhou. The synchronization of chaotic systems. *Phys. Rep.*, 366:1–101, 2002.

81. T. Bódai, G. Károlyi, and T. Tél. Fractal snapshot components in chaos induced by strong noise. *Phys. Rev. E*, 83:in print, 2011.

82. G. Boffetta, G. Lacorata, G. Redaelli, and A. Vulpiani. Detecting barriers to transport: a review of different techniques. *Physica D*, 159:58–70, 2001.

83. T. Bohr and D. Rand. The entropy function for characteristic exponents. *Phys. D*, 25:387–398, 1987.

84. T. Bohr, P. Cvitanović, and M. H. Jensen. Fractal "aggregates" in the complex plane. *Europhys. Lett.*, 6:445–450, 1988.

85. T. Bohr, M. H. Jensen, G. Paladin, and A. Vulpiani. *Dynamical Systems Approach to Turbulence*. Cambridge University Press, Cambridge, 1998.

86. T. Bohr, A. W. Pedersen, and M. H. Jensen. Transition to turbulence in a discrete Ginzburg-Landau model. *Phys. Rev. A*, 42:3626–3629, 1990.

87. E. M. Bollt. The path towards a longer life: on invariant sets and the escape time landscape. *Int. J. Bif. Chaos*, 15:1615–1624, 2005.

88. E. M. Bollt and M. Dolnik. Encoding information in chemical chaos by controlling symbolic dynamics. *Phys. Rev. E*, 55:6404–6413, 1997.

89. E. M. Bollt and Y.-C. Lai. Dynamics of coding in communicating with chaos. *Phys. Rev. E*, 58:1724–1736, 1998.

90. E. M. Bollt, Y.-C. Lai, and C. Grebogi. Coding channel capacity and noise resistance in communicating with chaos. *Phys. Rev. Lett.*, 79:3787–3790, 1997.

91. R. Bonaccini and A. Politi. Chaotic-like behaviour in chains of stable nonlinear oscillators. *Physica D*, 103:362–368, 1997.

92. C. Bonatto, J. A. C. Gallas, and Y. Ueda. Chaotic phase similarities and recurrences in a damped-driven Duffing oscillator. *Phys. Rev. E*, 77:026217, 2008.

93. C. Bonatto, J. C. Garreau, and J. A. C. Gallas. Self-similarities in the frequency-amplitude space of a loss-modulated CO_2 laser. *Phys. Rev. Lett.*, 95:143905, 2005.

94. F. A. Borotto, A. C. L. Chian, and E. L. Rempel. Alfvén interior crisis. *Int. J. Bif. Chaos*, 14:2375–2380, 2004.

95. D. Borrero-Echeverry, R. Tagg, and M. F. Schatz. Transient turbulence in Taylor-Couette flow. *Phys. Rev. E*, 81:025301(R), 2010.

96. F. Bottausci, I. Mezic, C.D. Meinhart, and C. Cardonne. Mixing in the shear superposition micromixer: three-dimensional analysis. *Phil. Trans. Roy. Soc.*, 362:1001–1018, 2004.

97. P. T. Boyd and S. L. W. McMillan. Chaotic scattering in the gravitational three-body problem. *Chaos*, 4:507–524, 1993.

98. R. Braun and F. Feudel. Supertransient chaos in the two-dimensional complex Ginzburg-Landau equation. *Phys. Rev. E*, 53:6562–6565, 1996.

99. U. Brosa. Turbulence without strange attractor. *J. Stat. Phys.*, 55:1303–1312, 1989.

100. R. Brown, P. Bryant, and H. D. I. Abarbanel. Computing the Lyapunov spectrum of a dynamical system from an observed time series. *Phys. Rev. A*, 43:2787–2806, 1991.

101. H. Buljan and V. Paar. Many-hole interactions and the average lifetimes of chaotic transients that precede controlled periodic motion. *Phys. Rev. E*, 63:066205, 2001.

102. H. Buljan and V. Paar. Naturally invariant measure of chaotic attractors and the conditionally invariant measure of embedded chaotic repellers. *Phys. Rev. E*, 65:036218, 2002.

103. H. Buljan and V. Paar. Parry measure and the topological entropy of chaotic repellers embedded within chaotic attractors. *Physica D*, 172:111–123, 2002.

104. A. R. Bulsara, W. C. Schieve, and E. W. Jacobs. Homoclinic chaos in systems perturbed by weak Langevin noise. *Phys. Rev. A*, 41:668–681, 1990.

105. L.A. Bunimovich and C.P. Dettmann. Peeping at chaos: nondestructive monitoring of chaotic systems by measuring long-time escape rates. *Europhys. Lett.*, 80:40001, 2007.

106. K. Buszko and K. Stefanski. Measuring transient chaos in nonlinear one- and two-dimensional maps. *Chaos Sol. Fract.*, 27:630–646, 2006.

107. M. Büttiker. Four-terminal phase-coherent conductance. *Phys. Rev. Lett.*, 57:1761–1764, 1986.

108. M. Büttiker. Absence of backscattering in the quantum Hall effect in multiprobe conductors. *Phys. Rev. B*, 38:9375–9389, 1988.

109. T. Buzug and G. Pfister. Optimal delay time and embedding dimension for delay-time coordinates by analysis of the glocal static and local dynamic behavior of strange attractors. *Phys. Rev. A*, 45:7073–7084, 1992.

110. T. L. Carroll, L. M. Pecora, and F. J. Rachford. Chaotic transients and multiple attractors in spin-wave experiments. *Phys. Rev. Lett.*, 59:2891–2894, 1987.

111. T. L. Carroll, L. M. Pecora, and F. J. Rachford. Lyapunov exponents near a crisis in a spin-wave experiment. *Phys. Rev. A*, 40:4149–4152, 1989.

112. T. L. Carroll, L. M. Pecora, and F. J. Rachford. Chaos and chaotic transients in an Yttrium iron-garnet sphere. *Phys. Rev. A*, 40:377–386, 1989.

113. T. L. Carroll, F. J. Rachford, and L. M. Pecora. Occurrence of chaotic transients during transitions between Quasiperiodic states in Yttrium iron-garnet. *Phys. Rev. B*, 38:2938–2940, 1988.

114. M.L. Cartwright and J.E. Littlewood. On Non-linear differential equations of the second order: I. *J. Lond. Math. Soc.*, 20:180–189, 1945.

115. J. H. E. Cartwright et al. Dynamics of finite-size particles in chaotic fluid flows. In M. Thiel et al., editor, *Nonlinear Dynamics and Chaos: Advances and Perspectives*, pages 51–87. Springer, Berlin, Heidelberg, 2010.

116. G. Casati, G. Maspero, and D. L. Shepelyansky. Quantum fractal eigenstates. *Physica D*, 131:311–316, 1999.

117. G. Casati, G. Maspero, and D. L. Shepelyansky. Quantum Poincaré recurrences. *Phys. Rev. Lett.*, 82:524–527, 1999.

118. F. Cecconi, R. Livi, and A. Politi. Fuzzy transition region in a one-dimensional coupled-stable-map lattice. *Phys. Rev. E*, 57:2703–2712, 1998.

119. R. K. Chang and A. J. Campillo. *Optical Processes in Microcavities*. World Scientific, Singapore, first edition, 1996.

120. H. Chaté and P. Manneville. Transition to turbulence via spatiotemporal intermittency. *Phys. Rev. Lett.*, 58:112–115, 1987.

121. H. Chaté and P. Manneville. Spatio-temporal intermittency in coupled map lattices. *Physica D*, 32:409–422, 1988.

122. M. D. Chekroun, E. Simonnet, and M. Ghil. Stochastic climate dynamics: random attractors and time-dependent invariant measures. *Physica D*, 2010.

123. G. Chen. *Controlling Chaos and Bifurcations in Engineering Systems*. CRC Press, Boca Raton, FL, first edition, 1999.

124. Q. Chen, M. Ding, and E. Ott. Chaotic scattering in several dimensions. *Phys. Lett. A*, 145:93–100, 1990.

125. Q. Chen, E. Ott, and L. P. Hurd. Calculating topological entropies of chaotic dynamical systems. *Phys. Lett. A*, 156:48–52, 1991.

126. A. C. L. Chian, E. L. Rempel, E. E. Macau, R. R. Rosa, and F. Christiansen. High-dimensional interior crisis in the Kuramoto-Shivashinsky equation. *Phys. Rev. E*, 65:035203, 2002.

127. A. C. L. Chian, F. A. Borotto, and E. L. Rempel. Alfvén boundary crisis. *Int. J. Bif. Chaos*, 12:1653–1658, 2002.

128. A. C. L. Chian, F. A. Borotto, E. L. Rempel, and C. Rogers. Attractor merging crisis in chaotic business cycles. *Chaos Sol. Fract.*, 24:869–875, 2005.

129. A. C. L. Chian, E. L. Rempel, and C. Rogers. Complex economic dynamics: chaotic saddle, crisis and intermittency. *Chaos Sol. Fract.*, 29:1194–1218, 2006.

130. A. C. L. Chian, W. M. Santana, E. L. Rempel, F. A. Borotto, T. Hada, and Y. Kamide. Chaos in driven Alfvén systems: unstable periodic orbits and chaotic saddles. *Nolin. Proc. Geophys.*, 14:17–19, 2007.

131. A. C.-L. Chian, R. A. Miranda, E. L. Rempel, Y. Saiki, and M. Yamada. Amplitude-phase synchronization at the onset of permanent spatiotemporal chaos. *Phys. Rev. Lett.*, 104:254102, 2010.

132. H.-D. Chiang, I. Dobson, R. J. Thomas, J. S. Thorp, and L. Fekih-Ahmed. On voltage collapse in electric power systems. *IEEE Trans. Power Syst.*, 5:601–607, 1990.

133. S. Muralidharan, K. R. Sreenivas and R. Govindarajan. Dynamical systems model of entrainment due to coherent structures. *Phys. Rev. E*, 72:046308, 2005.

134. B. V. Chirikov and F. M. Izraelev. Degeneration of turbulence in simple systems. *Phys. D*, 2:30–37, 1981.

135. B. V. Chirikov and F. M. Izraelev. Some numerical experiments with a nonlinear mapping: stochastic component. *Colloques. Int. du CNRS* (Toulouse, Sept. 1973), 229:409–428, 1976.

136. B. V. Chirikov and D. L. Shepelyansky. Correlation properties of dynamical chaos in Hamiltonian systems. *Physica D*, 13:395–400, 1984.

137. F. Christiansen and P. Grassberger. Escape and sensitive dependence on initial conditions in a symplectic repeller. *Phys. Lett. A*, 181:47–53, 1993.

138. R. C. Churchill, G. Pecelli, and D. L. Rod. Isolated unstable periodic orbits. *J. Diff. Equat.*, 17:329–348, 1975.

139. C. C. Conley. Invariant sets in a monkey saddle. In W. A. Harris Jr. and Y. Sibuya, editors, *Proc. United States-Japan Seminar on Differential and Functional Equations*, pages 443–447. Benjamin, New York, 1967.

140. L. Cortelezzi and I. Mezić (eds.). *Analysis and Control of Mixing with an Application to Micro and Macro Flow Processes*. Springer, New York, 2009.

141. J. Coste. Iterations of transformations on the unit interval – approach to a periodic attractor. *J. Stat. Phys.*, 23:521–536, 1980.

142. C. Coulliette, F. Lekien, J. D. Paduan, G. Haller, and J.E. Marsden. Optimal pollution mitigation in Monterey Bay based on coastal radar data and nonlinear dynamics. *Environ. Sci. Technol.*, 41:6562–6572, 2007.

143. A. Crisanti, M. Falconi, A. Vulpiani, and G. Paladin. Lagrangian chaos: transport, mixing and diffusion in fluids. *Riv. Nuovo Cimento*, 14:1–80, 1991.

144. G. Cristadoro and R. Ketzmerick. Universality of algebraic decays in Hamiltonian systems. *Phys. Rev. Lett.*, 100:184101, 2008.

145. V. Croquette and C. Poitou. Cascade of period doubling and large-scale stochasticity from compass movements. *J. de Physique Lett.*, 292:1353–1356, 1981.

146. J. R. Crutchfield and K. Kaneko. Are attractors relevant to turbulence? *Phys. Rev. Lett.*, 60:2715–2718, 1988.

147. G. Csernák and G. Stépán. Life expentancy of transient microchaotic behaviour. *J. Nonlin. Sci.*, 15:63–91, 2005.

148. Y. Cuche, R. Livi, and A. Politi. Phase transitions in 2D linearly stable coupled map lattices. *Physica D*, 103:369–380, 1997.

149. P. Cvitanović. Invariant measurements of strange sets in terms of cycles. *Phys. Rev. Lett.*, 61:2729–2732, 1988.

150. P. Cvitanović, N. Sondergaard, G. Palla, G. Vattay, and C. P. Dettmann. Spectrum of stochastic evolution operators: Local matrix representation approach. *Phys. Rev. E*, 60:3936–3941, 1999.

151. P. Cvitanović, R. Artuso, P. Dahlquist, R. Mainieri, G. Tanner, and G. Vattay. Chaos: Classical and Quantum, e-book: http://ChaosBook.org/chapters/ChaosBook.pdf, 2010.

152. P. Cvitanović and B. Eckhardt. Periodic-orbit quantization of chaotic systems. *Phys. Rev. Lett.*, 63:823–826, 1989.

153. P. Cvitanović and J. F. Gibson. Geometry of turbulence in wall-bounded shear flows: periodic orbits. *Phys. Scr.*, T142, 014007, 2010.

154. D. Dangoisse, P. Glorieux, and D. Hennequin. Laser chaotic attractors in crisis. *Phys. Rev. Lett.*, 57:2657–2660, 1986.

155. S. Datta. *Electronic Transport in Mesoscopic Systems*. Cambridge University Press, Cambridge, first edition, 1995.

156. R. L. Davidchack and Y.-C. Lai. Efficient algorithm for detecting unstable periodic orbits in chaotic systems. *Phys. Rev. E*, 60:6172–6175, 1999.

157. R. L. Davidchack, Y.-C. Lai, A. Klebanoff, and E. M. Bollt. Towards complete detection of unstable periodic orbits in chaotic systems. *Phys. Lett. A*, 287:99–104, 2001.

158. R. L. Davidchack and Y.-C. Lai. Characterization of transition to chaos with multiple positive Lyapunov exponents by unstable periodic orbits. *Phys. Lett. A*, 270:308–313, 2000.

159. S. Dawson, C. Grebogi, T. D. Sauer, and J. A. Yorke. Obstructions to shadowing when a Lyapunov exponent fluctuates about zero. *Phys. Rev. Lett.*, 73:1927–1930, 1994.

160. A. de Lozar and B. Hof. An experimental study of the decay of turbulent puffs in pipe flow. *Phil. Trans. R. Soc. A*, 367:589–599, 2009.

161. A. P. S. de Moura. Strange nonchaotic repellers. *Phys. Rev. E*, 76:036218, 2007.

162. A. P. S. de Moura and C. Grebogi. Output functions and fractal dimensions in dynamical systems. *Phys. Rev. Lett.*, 86:2778–2781, 2001.

163. A. P. S. de Moura and C. Grebogi. Rainbow transition in chaotic scattering. *Phys. Rev. E*, 65:035206R, 2002.

164. A. P. S. de Moura and C. Grebogi. Countable and uncountable boundaries in chaotic scattering. *Phys. Rev. E*, 66:046214, 2002.

165. A. P. S. de Moura and C. Grebogi. Chemical and biological activity in three-dimensional flows. *Phys. Rev. E*, 70:026218, 2004.

166. A. P. S. de Moura, Y.-C. Lai, J. P. Bird, R. Akis, and D. K. Ferry. Tunneling and nonhyperbolicity in quantum dots. *Phys. Rev. Lett.*, 88:236804, 2002.

167. A. P. S. de Moura and P. S. Letelier. Mixmaster chaos. *Phys. Lett. A*, 285:127–131, 1999.

168. A. P. S. de Moura and P. S. Letelier. Chaos and fractals in geodesic motion around a nonrotating black hole with halos. *Phys. Rev. E*, 61:6506–6516, 2000.

169. A. P. S. de Moura and P. S. Letelier. Scattering map for two black holes. *Phys. Rev. E*, 62:4784–4791, 2000.

170. A. S. de Paula, M. A. Savi, and F. H. I. Pereira-Pinto. Chaos and transient chaos in an experimental nonlinear pendulum. *J. Sound and Vibration*, 294:585–595, 2006.

171. S. L. T. de Souza, I. L. Caldas, R. L. Viana, A. M. Batista, and T. Kapitaniak. Noise-induced basin hopping in a gearbox model. *Chaos Sol. Fract.*, 26:1523–1531, 2005.

172. L. Delfini, S. Denisov, S. Lepri, R. Livi, P. K. Mohanty, and A. Politi. Energy diffusion in hard-point systems. *Eur. Phys. J. Special Topics*, 146:21–35, 2007.

173. M. Dellnitz, G. Froyland, C. Honerkamp, and K. Pradberg. On the approximation of transport phenomena – a dynamical systems approach. *GAMM-Mitt.*, 32:47–60, 2009.

174. M. Dellnitz and O. Junge. Almost invariant sets in Chua's circuit. *Int. J. Bif. Chaos*, 7:2475–2485, 1997.

175. C. Dembowski, B. Dietz, T. Friedrich, H.-D. Gräf, A. Heine, C. Mejia-Monasterio, M. Miski-Ogen, A. Richter, and T. H. Seligman. First experimental evidence for quantum echoes in scattering systems. *Phys. Rev. Lett.*, 93:134102, 2004.

176. H. Deng, Q. Deng, and D. G. Deppe. Native-oxide laterally confined whispering-gallery mode laser with vertical emission. *Appl. Phys. Lett.*, 69:3120–3122, 1996.

177. B. Dennis, R. A. Desharnais, J. M. Cushing, S. M. Henson, and R. F. Constantino. Can noise induce chaos? *Oikos*, 102:329–339, 2003.

178. A. Destexhe. Self-sustained asynchronous irregular states and up-down states in thalamic, cortical and thalamocortical networks of nonlinear integrate-and-fire neurons. *J. Comput. Neurosci.*, 27:493–506, 2009.

179. C. P. Dettmann. Recent advances in open billiards with some open problems. In Z. Elhadj and J. C. Sprott, editors, Frontiers in the study of chaotic dynamical systems with open problems, Singapore, 2010. World Scientific.

180. C. P. Dettmann and O. Georgiou. Survival probability for the stadium billiard. *Phys. D*, 238:2395–2403, 2009.

181. C. P. Dettmann and O. Georgiou. Transmission and reflection in the stadium billiard: time reversal symmetry breaking. arXiv:1006.131, 2010.

182. C. P. Dettmann and T. B. Howard. Asymptotic expansions for the escape rate of stochastically perturbed unimodal maps. *Phys. D*, 238:2404–2408, 2009.

183. C. P. Dettmann, G. V. Morozov, M. Sieber, and H. Waalkens. Unidirectional emission from circular dielectric microresonators with a point scatterer. *Phys. Rev. A*, 80:063813, 2009.

184. R. Devaney and Z. Nitecki. Shift automorphisms in the Hénon mapping. *Commun. Math. Phys.*, 67:137–146, 1979.

185. M. Dhamala and Y.-C. Lai. Controlling transient chaos in deterministic flows with applications to electrical power systems and ecology. *Phys. Rev. E*, 59:1646–1655, 1999.

186. M. Dhamala and Y.-C. Lai. Unstable periodic orbits and the natural measure of nonhyperbolic chaotic saddles. *Phys. Rev. E*, 60:6176–6179, 1999.

187. M. Dhamala and Y.-C. Lai. The natural measure of nonattracting chaotic sets and its representation by unstable periodic orbits. *Int. J. Bif. Chaos*, 12:2991–3006, 2002.

188. M. Dhamala, Y.-C. Lai, and R. D. Holt. How often are chaotic transients in spatially extended ecological systems? *Phys. Lett.*, 280:297–302, 2001.

189. M. Dhamala, Y.-C. Lai, and E. J. Kostelich. Detecting unstable periodic orbits from transient chaotic time series. *Phys. Rev. E*, 61:6485–6489, 2000.

190. M. Dhamala, Y.-C. Lai, and E. J. Kostelich. Analysis of transient chaotic time series. *Phys. Rev. E*, 64:056207, 2001.

191. M. Ding. Topological entropy and bifurcation of chaotic scattering. *Phys. Rev. A*, 46:6247–6251, 1992.

192. M. Ding, T. Bountis, and E. Ott. Algebraic escape in higher dimensional Hamiltonian systems. *Phys. Letts. A*, 151:395–400, 1990.

193. M. Ding, C. Grebogi, E. Ott, T. D. Sauer, and J. A. Yorke. Plateau onset for correlation dimension: when does it occur? *Phys. Rev. Lett.*, 70:3872–3875, 1993.

194. M. Ding, C. Grebogi, E. Ott, and J. A. Yorke. Transition to chaotic scattering. *Phys. Rev. A*, 42:7025–7040, 1990.

195. M. Ding, E. Ott, and C. Grebogi. Crisis control – preventing chaos-induced capsizing of a ship. *Phys. Rev. E*, 50:4228–4230, 1994.

196. W. Ditto, S. Rauseo, R. Cawley, C. Grebogi, G. Hsu, E. Kostelich, E. Ott, H. Savage, R. Segnan, M. Spano, and J. Yorke. Experimental observation of crisis-induced intermittency and its critical exponent. *Phys. Rev. Lett.*, 63:923–926, 1989.

197. Y. Do and Y.-C. Lai. Superpersistent chaotic transients in physical space: advective dynamics of inertial particles in open chaotic flows under noise. *Phys. Rev. Lett.*, 91:224101, 2003.

198. Y. Do and Y.-C. Lai. Extraordinarily superpersistent chaotic transients. *Europhys. Lett.*, 67:914–920, 2004.

199. Y. Do and Y.-C. Lai. Scaling laws for noise-induced superpersistent chaotic transients. *Phys. Rev. E*, 71:046208, 2005.

200. I. Dobson and H.-D. Chiang. Towards a theory of voltage collapse in electric power systems. *Sys. Contr. Lett.*, 13:253–262, 1989.

201. J. R. Dorfmann. *An Introduction to Chaos in Nonequilibrium Statistical Mechanics*. Cambridge University Press, Cambridge, first edition, 1999.

202. E. Doron and U. Smilansky. Chaotic spectroscopy. *Phys. Rev. Lett*, 68:1255–1258, 1992.

203. E. Doron and U. Smilansky. Chaotic spectroscopy. *Chaos*, 2:117–124, 1992.

204. E. Doron, U. Smilansky, and A. Frenkel. Experimental demonstration of chaotic scattering of microwaves. *Phys. Rev. Lett.*, 65:3072–3075, 1990.

205. E. Doron, U. Smilansky, and A. Frenkel. Chaotic scattering and transmission fluctuations. *Physica D*, 50:367–390, 1991.

206. M. V. Dyke. *An Album of Fluid Motion*. The Parabolic Press, Stanford, 1982.

207. M. I. Dykman, I. B. Schwartz, and M. Shapiro. Scaling in activated escape of underdamped systems. *Phys. Rev. E*, 72:021102, 2005.

208. F. J. Dyson. Statistical theory of energy levels of complex systems (I). *J. Math. Phys.*, 3:140, 1962.

209. A. Eberspächer, J. Main, and G. Wunner. Fractal Weyl law for three-dimensional chaotic hard-sphere scattering systems. *Phys. Rev. E*, 82:046201, 2010.

210. B. Eckhardt. Fractal properties of scattering singularities. *J. Phys. A: Math. Gen.*, 20:5971–5979, 1987.

211. B. Eckhardt. Irregular scattering. *Physica D*, 33:89–98, 1988.

212. B. Eckhardt. Quantum mechanics of classically non-integrable systems. *Phys. Rep.*, 163:205–297, 1988.

213. B. Eckhardt. Turbulence transition in pipe flow: some open questions. *Nonlinearity*, 21:T1–T11, 2008.

214. B. Eckhardt and H. Aref. Integrable and chaotic motions of 4 vortices. 11. Collision dynamics of vortex pairs. *Philos. T. Roy. Soc. A*, 326:655–696, 1988.

215. B. Eckhardt, H. Faisst, A. Schmiegel, and T. M. Schneider. Dynamical systems and the transition to turbulence in linearly stable shear flows. *Philo. Trans. Roy. Soc. A*, 366:1297–1315, 2008.

216. B. Eckhardt and T. M. Schneider. How does flow in a pipe become turbulent? *Eur. Phys. J*, 64:457–462, 2008.

217. B. Eckhardt, T. M. Schneider, B. Hof, and J. Westerweel. Turbulence in pipe flows. *Annu. Rev. Fluid. Mech.*, 39:447–468, 2007.

218. J.-P. Eckman, L. Thomas, and P. Wittwer. Intermittency in the presence of noise. *J. Phys. A: Math. Gen.*, 14:3153–3168, 1981.

219. J.-P. Eckmann, S. O. Kamphorst, D. Ruelle, and S. Ciliberto. Lyapunov exponents from time series. *Phys. Rev. A*, 34:4971–4979, 1986.

220. J.-P. Eckmann and D. Ruelle. Ergodic theory of chaos and strange attractors. *Rev. Mod. Phys.*, 57:617–656, 1985.

221. S. P. Ellner and P. Turchin. When can noise induce chaos and why does it matter: a critique. *Oikos*, 111:620–631, 2005.

222. R. Engbert and F. R. Drepper. Chance and chaos in population biology - Models of recurrent epidemics and food chain dynamics. *Chaos Sol. Fract.*, 4:1147–1169, 1994.

223. I. R. Epstein. The consequence of imperfect mixing in chemical and biological systems. *Nature*, 374:321–327, 1995.

224. T. Ericson. Fluctuations of nuclear cross sections in the continuum region. *Phys. Rev. Lett.*, 5:430–431, 1960.

225. L. Ermann and D.L. Shepelyansky. Ulam method and fractal Weyl law for Perron-Frobenius operators. arXiv:0912.508302, 2010.

226. L. Ermann, G. G. Carlo, and M. Saraceno. Localization of resonance eigenfunctions on quantum repellers. *Phys. Rev. Lett.*, 103:054102, 2009.

227. T. Erneaux. *Applied Delay Differential Equation*. Springer, Berlin, first edition, 2009.

228. S. V. Ershov and A. B. Potapov. On the nature of nonchaotic turbulence. *Phys. Lett. A*, 167:60–64, 1992.

229. H. Faisst and B. Eckhardt. Traveling waves in pipe flow. *Phys. Rev. Lett.*, 91:224502, 2003a.

230. H. Faisst and B. Eckhardt. Lifetimes of noisy repellors. *Phys. Rev. E*, 68:026215, 2003b.

231. H. Faisst and B. Eckhardt. Sensitive dependence on initial conditions in transition to turbulence in pipe flow. *J. Fluid. Mech.*, 504:343–352, 2004.

232. K. Falconer. *The Geometry of Fractal Sets*. Cambridge University Press, Cambridge, 1985.

233. G. Falkovich, A. Fouxon, and M. G. Stepanov. Acceleration of rain initiation by cloud turbulence. *Nature*, 419:151–154, 2002.

234. J. D. Farmer. Sensitive dependence on parameters in nonlinear dynamics. *Phys. Rev. Lett.*, 55:661–664, 1985.

235. M. J. Feigenbaum. Quantitative universality for a class of nonlinear transformations. *J. Stat. Phys.*, 19:25–52, 1978.

236. M. J. Feigenbaum. The universal metric properties of nonlinear transformations. *J. Stat. Phys.*, 21:669–706, 1979.

237. W. Feller. *An Introduction to Probability Theory and Its Applications*. Wiley, New York, first edition, 1966.

238. D. K. Ferry and S. M. Goodnick. *Transport in Nanostructures*. Cambridge University Press, Cambridge, UK, first edition, 1997.

239. U. Feudel and C. Grebogi. Multistability and the control of complexity. *Chaos*, 7:301–310, 1997.

240. U. Feudel, C. Grebogi, B. R. Hunt, and J. A. Yorke. Map with more than 100 coexisting low-periodic atractors. *Phys. Rev. E*, 54:71–81, 1996.

241. U. Feudel, S. Kuznetsov, and A. Pikovsky. *Strange Nonchaotic Attractors*. World Scientific, Singapore, 2006.

242. S. Fishman, D. R. Grempel, and R. E. Prange. Temporal crossover from classical to quantal behavior near dynamical critical points. *Phys. Rev. A*, 36:289–305, 1987.

243. M. Franaszek. Influence of noise on the mean lifetime of chaotic transients. *Phys. Rev. A*, 44:4065–4067, 1991.

244. M. Franaszek and L. Fronzoni. Influence of noise on crisis-induced intermittency. *Phys. Rev. E*, 49:3888–3893, 1994.

245. W. J. Freeman. Neural networks and chaos. *J. Theor. Biol.*, 171:13–18, 1994.

246. M. I. Freidlin and A.D. Wentzell. *Random Perturbations of Dynamical Systems*. Springer, New York, 1984.

247. J. F. Freire, C. Bonatto, C. C. DaCamara, and J. A. C. Gallas. Multistability, phase diagrams and intransitivity in the Lorenz-84 low-order atmospheric circulation model. *Chaos*, 18:033121, 2008.

248. G. Froyland and K. Pradberg. Almost invariant sets and invariant manifold – connecting probabilistic and geometric descriptions of coherent structures in flows. *Phys. D*, 238:1507–1523, 2009.

249. G. Froyland, S. Lloyd, and N. Santitissadeekorn. Coherent sets for nonautonomous dynamical systems. *Phys. D*, 239:1527–1541, 2010.

250. G. Froyland, K. Pradberg, M.H. England, and A.M. Treguier. Detection of coherent oceanic structures via transfer operators. *Phys. Rev. Lett.*, 98:224503, 2007.

251. G. Froyland, N. Santitissadeekorn, and A. Monahan. Transport in time-dependent dynamical systems: Finite-time coherent sets. *Chaos*, 20:043116, 2010.

252. H. Fujisaka, K. Egami, and T. Yamada. Glassy dynamics in a spatially distributed dynamical system. *Phys. Lett.*, 174:103–110, 1993.

253. J. A. C. Gallas. Structure of the parameter space of the Hénon map. *Phys. Rev. Lett.*, 70:2714–2717, 1993.

254. J. A. C. Gallas. Dissecting shrimps: results for some one-dimensional physical models. *Physica A*, 202:196–223, 1994.

255. J. A. C. Gallas, C. Grebogi, and J. Yorke. Vertices in parameter space – double crises which destroy chaotic attractors. *Phys. Rev. Lett.*, 71:1359–1362, 1993.

256. C. W. Gardiner. *Handbook of Stochastic Methods*. Springer, New York, first edition, 1997.

257. P. Gaspard. *Chaos, Scattering and Statistical Mechanics*. Cambridge University Press, Cambridge, UK, first edition, 1998.

258. P. Gaspard and G. Nicolis. Transport properties, Lyapunov exponents, and entropy per unit time. *Phys. Rev. Lett*, 65:1693–1696, 1990.

259. P. Gaspard and S. Rice. Semiclassical quantization of the scattering from a classically chaotic repellor. *J. Chem. Phys.*, 90:2242–2254, 1989.

260. P. Gaspard and S. A. Rice. Scattering from a classically chaotic repellor. *J. Chem. Phys.*, 90:2225–2241, 1989.

261. M. Ghil, M. D. Chekroun, and E. Simonnet. Climate dynamics and fluid mechanics: natural variability and related uncertainties. *Physica D*, 327:2111–2126, 2008.

262. G. Giacomelli, S. Lepri, and A. Politi. Statistical properties of bidimensional patterns generated from delayed and extended maps. *Phys. Rev. E*, 51:3939–3944, 1995.

263. J. F. Gibson, J. Halcrow, and P. Cvitanović. Visualizing the geometry of state space in plane Couette flow. *J. Fluid. Mech*, 611:107, 2008.

264. F. Ginelli, R. Livi, and A. Politi. Emergence of chaotic behaviour in linearly stable systems. *J. Phys. A*, 35:499–516, 2002.

265. C. Gmachl, F. Capasso, E. E. Narimanov, J. U. Nöckel, A. D. Stone, J. Faist, and D. L. Sivco. High-power directional emission from microlasers with chaotic resonators. *Science*, 280:1556–1564, 1998.

266. A. L. Goldberger. Nonlinear dynamics, fractals and chaos – applications to cardiac electrophysiology. *Ann. Biomed. Eng.*, 18:195–198, 1990.

267. N. Goldenfeld, N. Guttenberg, and G. Gioia. Extreme fluctuations and the finite lifetime of the turbulent state. *Phys. Rev. E*, 81:035304(R), 2010.

268. H. Goldstein. *Classical Mechanics*. Addison-Wesley, Reading, MA, second edition, 1993.

269. J. P. Gollub. Order and disorder in fluid motion. *Proc. Natl. Acad. Sci. USA*, 92:6705–6711, 1995.

270. R. Gomulkiewicz and R. D. Holt. When does evolution by natural-selection prevent extinction. *Evolution*, 49:201–207, 1995.

271. C. L. Goodridge, L. M. Pecora, T. L. Carroll, and F. J. Rachford. Detecting functional relationships between simultaneous time series. *Phys. Rev. E*, 64:026221, 2001.

272. B. Goodwine and G. Stépán. Controlling unstable rolling phenomena. *J. Vib. Control*, 6:137–158, 2000.

273. M. Gorman, P. Widmann, and K. Robbins. Chaotic flow regimes in a convection loop. *Phys. Rev. Lett.*, 52:2241–2244, 1984.

274. M. Gorman, P. Widmann, and K. Robbins. Nonlinear dynamics of a convection loop – a quantitative comparison of experiment with theory. *Physica D*, 19:255–267, 1986.

275. L. Gottdiener and R. Carmona. Energy-transfer in high-energy atom-oscillator collisions. *J. Chem. Phys.*, 70:4207–4211, 1979.

276. E. Gouillart, O. Dauchot, J.-L. Thiffeault, and S. Roux. Open-flow mixing: experimental evidence for strange eigenmodes. *Phys. Fluids*, 21:023603, 2009.

277. A. Goussev and K. Richter. Loschmidt-echo decay from local boundary perturbations. *Phys. Rev. E*, 75:015201(R), 2007.

278. R. Govindarajan. Universal behavior of entrainment due to coherent structures in turbulent shear flows. *Phys. Rev. Lett.*, 88:134503, 2002.

279. R. Graham. Macroscopic potentials, bifurcations and noise in dissipative systems. In F. Moss and P. V. E. McClintock, editors, *Noise in Nonlinear Dynamical Systems, Vol. 1*, pages 225–278. Cambridge University Press, Cambridge, 1989

280. R. Graham and A. Hamm. Non-equilibrium potentials for dynamical systems weakly perturbed by noise. In G. Györgyi, I. Kondor, L. Sasvári, and T. Tél, editors, *From Phase Transitions to Chaos*, pages 449–469. World Scientific, Singapore, 1992

281. R. Graham, A. Hamm, and T. Tél. Nonequilibrium potentials for dynamical systems with fractal attractors and repellers. *Phys. Rev. Lett.*, 66:3089–3092, 1991.

282. R. Graham and T. Tél. Existence of a potential for dissipative dynamical systems. *Phys. Rev. Lett.*, 52:9–12, 1984.

283. P. Grassberger. Information flow and maximum entropy measures for 1-D maps. *Physica D*, 14:365–373, 1985.

284. P. Grassberger. Do climatic attractors exist? *Nature*, 323:609–612, 1986.

285. P. Grassberger. Noise-induced escape from attractors. *J. Phys. A*, 22:3283–3290, 1989.

286. P. Grassberger and H. Kantz. Universal scaling of long-time tails in Hamiltonian systems. *Phys. Lett. A*, 113:167–171, 1985.

287. P. Grassberger and I. Procaccia. Measuring the strangeness of strange attractors. *Physica D*, 9:189–208, 1983.

288. P. Grassberger and I. Procaccia. Dimensions and entropies of strange attractors from a fluctuating dynamics approach. *Physica D*, 13:34–54, 1984.

289. C. Grebogi, S. W. McDonald, E. Ott, and J. A. Yorke. Final state sensitivity: an obstruction to predictability. *Phys. Lett. A*, 99:415–418, 1983.

290. C. Grebogi, E. Ott, F. Romeiras, and J. Yorke. Critical exponents for crisis-induced intermittency. *Phys. Rev. A*, 36:5365–5380, 1987.

291. C. Grebogi, E. Ott, and J. Yorke. Critical exponent of chaotic transients in nonlinear dynamical systems. *Phys. Rev. Lett.*, 57:1284–1287, 1986.

292. C. Grebogi, E. Ott, and J. A. Yorke. Chaotic attractors in crisis. *Phys. Rev. Lett*, 48:1507–1510, 1982.

293. C. Grebogi, E. Ott, and J. A. Yorke. Crises, sudden changes in chaotic attractors and chaotic transients. *Physica D*, 7:181–200, 1983.

294. C. Grebogi, E. Ott, and J. A. Yorke. Fractal basin boundaries, long-lived chaotic transients, and unstable-unstable pair bifurcation. *Phys. Rev. Lett.*, 50:935–938, 1983.

295. C. Grebogi, E. Ott, and J. A. Yorke. Super persistent chaotic transients. *Ergod. Th. Dym. Syst.*, 5:341–372, 1985.

296. C. Grebogi, E. Ott, and J. A. Yorke. Basin boundary metamorphosis: changes in accessible boundary orbits. *Physica D*, 24:243–262, 1987.

297. C. Grebogi, E. Ott, and J. A. Yorke. Unstable periodic orbits and the dimensions of multifractal chaotic attractors. *Phys. Rev. A*, 37:1711–1724, 1988.

298. M. A. Green, C. W. Rowley, and G. Haller. Detection of Lagrangian coherent structures in 3D turbulence. *J. Fluid Mech.*, 572:111–120, 2007.

299. S. Grossmann. The onset of shear flow turbulence. *Rev. Mod. Phys.*, 72:603–618, 2000.

300. J. Guckenheimer and P. J. Holmes. *Nonlinear Oscillations, Dynamical Systems, and Bifurcations of Vector Fields*. Springer, New York, 1983.

301. M. C. Gutzwiller. *Chaos in Classical and Quantum Mechanics*. Springer, New York, first edition, 1990.

302. G. Györgyi and P. Ruján. Strange attractors in disordered systems. *J. Phys. C*, 17:4207–4212, 1984.

303. J. Halcrow, J. F. Gibson, and P. Cvitanović. Heteroclinic connections in plane Couette flow. *J. Fluid. Mech*, 621:365, 2009.

304. G. Haller. Distinguished material surfaces and coherent structures in three-dimensional fluid flows. *Physica D*, 149:248–277, 2001.

305. G. Haller. Lagrangian structures and the rate of strain in a partition of two-dimensional turbulence. *Phys. Fluids*, 13:3365–3385, 2001.

306. G. Haller. Exact theory of unsteady separation for two-dimensional flows. *J. Fluid Mech.*, 512:257–311, 2004.

307. G. Haller and A. C. Poje. Finite time transport in aperiodic flows. *Physica D*, 119:352–380, 1998.

308. G. Haller and T. Sapsis. Where do inertial particles go in fluid flows? *Physica D*, 237:573–583, 2008.

309. G. Haller and T. Sapsis. Localized instability and attraction along invariant manifolds. *SIAM J. Appl. Dyn. Syst.*, 9:611–633, 2010.

310. G. Haller and G. Yuan. Lagrangian coherent structures and mixing in two-dimensional turbulence. *Physica D*, 147:352–370, 2000.

311. A. Hamm and R. Graham. Noise-induced attractor explosions near tangent bifurcations. *J. Stat. Phys.*, 66:689–725, 1992.

312. A. Hamm, T. Tél, and R. Graham. Noise-induced attractor explosions near tangent bifurcations. *Phys. Lett. A*, 185:313–320, 1994.

313. G. Handke. Fractal dimensions in the phase space of two-electron atoms. *Phys. Rev. A*, 50:R3561–R3564, 1994.

314. P. Hänggi, P. Talkner, and M. Borkovec. Reaction-rate theory: fifty years after Kramers. *Rev. Mod. Phys.*, 62:251–342, 1990.

315. J. D. Hanson, J. Cary, and J. D. Meiss. Algebraic decay in self-similar Markov chains. *J. Stat. Phys.*, 39:327–345, 1985.

316. A. Hastings and K. Higgins. Persistence of transients in spatially structured ecological models. *Science*, 263:1133–1136, 1994.

317. A. Hastings, C. L. Hom, S. Ellner, P. Turchin, and H. C. J. Godfray. Chaos in ecology – is mother nature a strange attractor. *Ann. Rev. Ecol. Systemat.*, 24:1–33, 1993.

318. S. Hayes, C. Grebogi, and E. Ott. Communicating with chaos. *Phys. Rev. Lett.*, 70:3031–3034, 1993.

319. S. Hayes, C. Grebogi, E. Ott, and A. Mark. Experimental control of chaos for communication. *Phys. Rev. Lett.*, 73:1781–1784, 1994.

320. K. He and A. C.-L. Chian. Critical dynamic events at the crisis of transition to spatiotemporal chaos. *Phys. Rev. E*, 69:026207, 2004.

321. Y. He, Y.-M. Jiang, Y. Shen, and D.-R. He. Crisis induced by an escape from a fat strange set. *Phys. Rev. E*, 70:056213, 2004.

322. J. F. Heagy, T. L. Carroll, and L. M. Pecora. Experimental and numerical evidence for riddled basins in coupled chaotic systems. *Phys. Rev. Lett.*, 73:3528–3531, 1994.

323. J. F. Heagy and J. M. Yuan. Dynamics of an impulsively driven Morse oscillator. *Phys. Rev. A*, 41:571–581, 1990.

324. R. Hegger, H. Kantz, and R. Schreiber. *TISEAN*. http://www.mpipks-dresden.mpg.de/ tisean/TISEAN3.01/ index.html, Dresden, e-book edition, 2007.

325. M. Hénon. A two-dimensional mapping with a strange attractor. *Commun. Math. Phys.*, 50:69–77, 1976.

326. M. Hénon. Chaotic scattering modeled by an inclined billiard. *Physica D*, 33:132–156, 1988.

327. W. K. Hensinger, H. Häffer, A. Browaeys, N. R. Heckenberg, K. Helmerson, C. McKenzie, G. J. Milburn, W. D. Phillips, S. L. Rolston, H. Rubinsztein-Dunlop, and B. Upcroft. Dynamical tunnelling of ultracold atoms. *Nature*, 412:52–55, 2001.

328. D. Hensley. The Hausdorff dimensions of some continued-fraction cantor sets. *J. Number Theor.*, 33:182–198, 1989.

329. D. Hensley. Continued-fraction Cantor sets, Hausdorff dimension, and functional-analysis. *J. Number Theor.*, 40:336–358, 1992.

330. D. Hensley. A polynomial time algorithm for the Hausdorff dimension of continued fraction Cantor sets. *J. Number Theor.*, 58:9–45, 1996.

331. D. Hensley. *Continued Fractions*. World Scientific, Singapore, first edition, 2006.

332. H. Herzel, W. Ebeling, and T. Schulmeister. Nonuniform chaotic dynamics and effects of noise in biochemical systems. *Z. Naturforsch.*, 42a:136–142, 1987.

333. R. Hilborn. Quantitative measurement of the parameter dependence of the onset of a crisis in a driven nonlinear oscillator. *Phys. Rev. A*, 31:378–382, 1985.

334. B. Hof, A. de Lozar, D.J. Kuik, and J. Westerweel. Repeller or attractor? Selecting the dynamical model for the onset of turbulence in pipe flow. *Phys. Rev. Lett.*, 101:214501, 2009.

335. B. Hof, C. W. H. Dorne, J. Westerweel, F. T. M. Nieuwstadt, and H. Faisst. Experimental observation of nonlinear traveling wave in turbulent pipe flow. *Science*, 305:1594–1598, 2004.

336. B. Hof, J. Westerweel, T. M. Schneider, and B. Eckhardt. Finite lifetime of turbulence in shear flows. *Nature*, 443:59–62, 2006.

337. P. Holmes. Non-linear oscillator with a strange attractor. *Philos. T. Roy. Soc. A*, 292:419–448, 1979.

338. P. Holmes and D. Whitley. On the attracting set for Duffing equation.2. A geometrical model for moderate force and damping. *Physica D*, 7:111–123, 1983.

339. R. D. Holt and M. A. McPeek. Chaotic population dynamics favors the evolution of dispersal. *Am. Nat.*, 148:709–718, 1996.

340. S. M. Houghton, E. Knobloch, S. M. Tobias, and M. R. E. Proctor. Transient spatio-temporal chaos in the complex Ginzburg-Landau equation on long domains. *Phys. Lett. A*, 374:2030–2034, 2010.

341. G.-H. Hsu, E. Ott, and C. Grebogi. Strange saddles and the dimensions of their invariant manifolds. *Phys. Lett. A*, 127:199–204, 1988.

342. L. Huang, Y.-C. Lai, D. K. Ferry, R. Akis, S. M. Goodnick, and R. Akis. Transmission and scarring in graphene quantum dots. *J. Phys. Cond. Mat.*, 21:344203, 2009.

343. L. Huang, Y.-C. Lai, D. K. Ferry, S. M. Goodnick, and R. Akis. Relativistic quantum scars. *Phys. Rev. Lett.*, 103:054101, 2009.

344. G. Huber, P. Alstrom, and T. Bohr. Nucleation and transients at the onset of vortex turbulence. *Phys. Rev. Lett.*, 69:2380–2383, 1992.

345. L. Hufnagel, R. Ketzmerick, and M. Weiss. Conductance fluctuations of generic billiards: fractal or isolated? *Europhys. Lett.*, 54:703–708, 2001.

346. B. R. Hunt, E. Ott, and E. Rosa. Sporadically fractal basin boundaries of chaotic systems. *Phys. Rev. Lett.*, 82:3597–3600, 1999.

347. B. R. Hunt, E. Ott, and J. A. Yorke. Fractal dimensions of chaotic saddles of dynamical systems. *Phys. Rev. E*, 54:4819–4823, 1996.

348. J. Hyman, B. Nicolaenko, and S. Zaleski. Order and complexity in the Kuramoto-Shivashinsky model of weakly turbulent interfaces. *Physica D*, 23:265–292, 1986.

349. M. Iansiti, Q. Hu, R. M. Westervelt, and M. Tinkham. Noise and chaos in a fractal basin boundary regime of a Josephson junction. *Phys. Rev. Lett.*, 55:746–749, 1985.

350. V. In, S.E. Mahan, W.I. Ditto, and M.L. Spano. Experimental maintenance of chaos. *Phys. Rev. Lett.*, 74:4420–4423, 1995.

351. V. In, M.L. Spano, and M. Ding. Maintaining chaos in high dimensions. *Phys. Rev. Lett.*, 80:700–703, 1998.

352. J. Jacobs, E. Ott, T. Antonsen, and J. Yorke. Modeling fractal entrainment sets of tracers advected by chaotic temporally irregular fluid flows using random maps. *Physica D*, 110:1–17, 1997.

353. J. Jacobs, E. Ott, and C. Grebogi. Computing the measure of nonattracting chaotic sets. *Physica D*, 110:1–11, 1997.

354. J. Jacobs, E. Ott, and B.R. Hunt. Calculating topological entropy for transient chaos with an application to communicating with chaos. *Phys. Rev. E*, 57:6577–6588, 1998.

355. R. A. Jalabert, H. U. Baranger, and A. D. Stone. Conductance fluctuations in the ballistic regime: a probe of quantum chaos. *Phys. Rev. Lett.*, 65:2442–2445, 1990.

356. I. M. Jánosi, L. Flepp, and T. Tél. Exploring transient chaos in an NMR-laser experiment. *Phys. Rev. Lett.*, 73:529–532, 1994.

357. I. M. Jánosi and T. Tél. Time-series analysis of transient chaos. *Phys. Rev. E*, 49:2756–2763, 1994.

358. O. Jenkinson and M. Pollicott. Computing the dimension of dynamically defined sets: E-2 and bounded continued fractions. *Ergod. Theor. Dyn. Syst.*, 21:1429–1445, 2001.

359. Y.-M. Jiang, Y.-Q. Lu, X.-G. Chao, and D.-R. He. A crisis of a stochastic web. *Eur. Phys. J. D*, 29:285–292, 2004.

360. C. Jung. Poincaré map for scattering states. *J. Phys. A-Math. Gen.*, 19:1345–1353, 1986.

361. C. Jung and A. Emmanouilidou. Construction of natural partition of incomplete horseshoes. *Chaos*, 15:023101, 2005.

362. C. Jung, C. Lipp, and T. H. Seligman. The inverse scattering problem for chaotic Hamiltonian systems. *Ann. Phys.*, 275:151–189, 1999.

363. C. Jung, C. Mejia-Monasterio, O. Merlo, and T. H. Seligman. Self-pulsing effect in chaotic scattering. *New J. Phys.*, 6:48, 2004.

364. C. Jung, C. Mejia-Monasterio, and T. H. Seligman. Scattering one step from chaos. *Phys. Lett. A*, 198:306–314, 1995.

365. C. Jung, C. Mejia-Monasterio, and T. H. Seligman. Quantum and classical echoes in scattering systems described by simple Smale horseshoes. *Europhys. Lett.*, 55:616–622, 2001.

366. C. Jung, O. Merlo, T. H. Seligman, and W. P. K. Zapfe. The chaotic set and the cross section for chaotic scattering in three degrees of freedom. *New J. Phys.*, 12:103021, 2010.

367. C. Jung, G. Orellana-Riuadeneyra, and G. A. Luna-Acosta. Reconstruction of the chaotic set from classical cross section data. *J. Phys. A-Math. Gen.*, 38:567–585, 2005.

368. C. Jung and S. Pott. Classical cross-section for chaotic potential scattering. *J. Phys. A-Math. Gen.*, 22:2925–2938, 1989.

369. C. Jung and T. Tél. Dimension and escape rate of chaotic scattering from classical and semiclassical cross section data. *J. Phys. A-Math. Gen.*, 24:2793–2805, 1991.

370. C. Jung, T. Tél, and E. Ziemniak. Application of scattering chaos to particle transport in a hydrodynamical flow. *Chaos*, 3:555–568, 1993.

371. C. Jung and E. Ziemniak. Hamiltonian scattering chaos in a hydrodynamical system. *J. Phys. A Math. Gen.*, 25:3929–3943, 1992.

372. M. Kac. *Probability and Related Topics in Physical Sciences*. Interscience, New York, 1959.

373. L. P. Kadanoff and C. Tang. Escape from strange repellers. *Proc. Natl. Acad. Sci. USA*, 81:1276–1279, 1984.

374. E. T. Kai, V. Rossi, J. Sudre, H. Weimerskirch, C. López E. Hernández-Garcia, F. Marsac, and V. Garcon. Top marine predators track Lagrangian coherent structures. *Proc. Nat. Aca. Sci. USA*, 106:8245–8250, 2009.

375. K. Kaneko. Spatiotemporal intermittency in coupled map lattices. *Prog. Theor. Phys.*, 74:1033–1044, 1985.

376. K. Kaneko. Pattern dynamics in spatiotemporal chaos. *Physica D*, 34:1–41, 1989.

377. K. Kaneko. Supertransients, spatiotemporal intermittency amd stability of fully developed spatiotemporal chaos. *Phys. Lett. A*, 149:105–112, 1990.

378. K. Kaneko. *Theory and Applications of Coupled Map Lattices*. Wiley, Chichester, 1993.

379. K. Kaneko and I. Tsuda. *Complex Systems: Chaos and Beyond, a Constructive Approach with Applications in Life Sciences*. Springer, Berlin, 2000.

380. H. Kantz and P. Grassberger. Repellers, semi-attractors, and long-lived chaotic transients. *Physica D*, 17:75–86, 1985.

381. H. Kantz and P. Grassberger. Chaos in low-dimensional Hamiltonian maps. *Phys. Lett. A*, 123:437–443, 1987.

382. H. Kantz and T. Schreiber. *Nonlinear Time Series Analysis*. Cambridge University Press, Cambridge, UK, first edition, 1997.

383. T. Kapitaniak and J. Brindley. Preserving transient chaos. *Phys. Lett. A*, 241:41–45, 1998.

384. T. Kapitaniak, Y.-C. Lai, and C. Grebogi. Metamorphosis of chaotic saddle. *Phys. Lett. A*, 259:445–450, 1999.

385. A. Kaplan, N. Friedman, M. Andersen, and N. Davidson. Observation of islands of stability in soft wall atom-optics billiards. *Phys. Rev. Lett.*, 87:274101, 2001.

386. J. L. Kaplan and J. A. Yorke. Preturbulence: A regime observed in a fluid flow model of Lorenz. Comm. Math. Phys., 67:93–108, 1979.

387. R. Kapral, R. Livi, G. L. Oppo, and A. Politi. Dynamics of complex interfaces. *Phys. Rev. E*, 49:2009–2022, 1994.

388. C. F. F. Karney. Long-time correlations in the stochastic regime. *Physica D*, 8:360–380, 1983.

389. G. Karniakidis, A. Beskok, and N. Aluru. *Microflows and Nanoflows*. Springer, Berlin, first edition, 2005.

390. G. Károlyi. Fractal scaling of microbial colonies affects growth. *Phys. Rev. E*, 71:031915, 2005.

391. G. Károlyi, Á. Péntek, I. Scheuring, T. Tél, and Z. Toroczkai. Chaotic flow: the physics of species coexistence. *Proc. Nat. Aca. Sci. USA*, 97:13661–13665, 2000.

392. G. Károlyi, Á. Péntek, Z. Toroczkai, T. Tél, and C. Grebogi. Chemical or biological activity in open chaotic flows. *Phys. Rev. E*, 59:5468–5481, 1999.

393. G. Károlyi, I. Scheuring, and T. Czárán. Metabolic network dynamics in a open chaotic flows. *Chaos*, 12:460–469, 2002.

394. G. Károlyi and T. Tél. Chaotic tracer scattering and fractal basin boundaries in a blinking vortex-sink system. *Phys. Rep.*, 290:125–147, 1997.

395. G. Károlyi and T. Tél. Chemical transients in closed chaotic flows: the role of effective dimensions. *Phys. Rev. Lett.*, 95:264501, 2005.

396. G. Károlyi and T. Tél. Effective dimension and chemical reactions in fluid flows. *Phys. Rev. E*, 76:046315, 2007.

397. G. Károlyi, T. Tél, A. P. S. de Moura, and C. Grebogi. Reactive processes in random flows. *Phys. Rev. Lett.*, 92:174101, 2004.

398. Z. Kaufmann and H. Lustfeld. Comparision of averages of flows and maps. *Phys. Rev. E*, 64:055206(R), 2001.

399. Z. Kaufmann, H. Lustfeld, A. Németh, and P. Szépfalusy. Diffusion in normal and critical transient chaos. *Phys. Rev. Lett.*, 78:4031–4034, 1997.

400. Z. Kaufmann, A. Németh, and P. Szépfalusy. Critical states of transient chaos. *Phys. Rev. E*, 61:2543–2550, 2000.

401. R. L. Kautz. Activation energy for thermally induced escape from a basin of attraction. *Phys. Lett. A*, 125:315–319, 1987.

402. R. L. Kautz. Global stability of phase lock near a chaotic crisis in the RF-biased Josephson junction. *J. Appl. Phys.*, 62:198–211, 1987.

403. J.P. Keating, M. Novaes, S.D. Prado, and M. Sieber. Semiclassical structure of chaotic resonance eigenfunctions. *Phys. Rev. Lett.*, 97:150406, 2006.

404. J. D. Keeler and J. D. Farmer. Robust space-time intermittency and $1/f$ noise. *Physica D*, 23:413–435, 1986.

405. G. Kember and A. C. Fowler. A correlation-function for choosing time delays in phase portrait reconstructions. *Phys. Lett. A*, 179:72–80, 1993.

406. J. A. Kennedy and J. A. Yorke. Basins of Wada. *Physica D*, 51:213–225, 1991.

407. J. A. Kennedy and J. A. Yorke. The topology of stirred fluids. *Topology Appl.*, 80:201–238, 1997.

408. A. Y. Khinchin. *Continued Fractions.* Dover, New York, 1997.

409. L. Kim and J. Moehliss. Characterizing the edge of chaos for a shear flow model. *Phys. Rev. E*, 78:036315, 2008.

410. I. Z. Kiss, J. H. Merkin, and Z. Neufeld. Combustion initiation and extinction in a 2D chaotic flow. *Physica D*, 183:175–189, 2003.

411. R. Klages. *Microscopic Chaos, Fractal and Transport in Nonequilibrium Statistical Mechanics.* World Scientific, Singapore, first edition, 2007.

412. N. E. Kochin, I. A. Kibel, and N. V. Rose. *Theoretical Hydrodynamics.* Interscience, New York, 1964.

413. T.-Y. Koh and B. Legras. Hyperbolic lines and the stratospheric polar vortex. *Chaos*, 12:382–394, 2002.

414. M. Kopp and H. Schomerus. Fractal Weyl laws for quantum decay in dynamical systems with a mixed phase space. *Phys. Rev. E*, 81:026208, 2010.

415. H. J. Korsch and A. Wagner. Fractal mirror images and chaotic scattering. *Comp. Phys.*, 5:497–503, 1991.

416. E. J. Kostelich, I. Kan, C. Grebogi, E. Ott, and J. A. Yorke. Unstable dimension variability: a source of nonhyperbolicity in chaotic systems. *Physica D*, 109:81–90, 1997.

417. T. Kovács and B. Érdi. Transient chaos in the Sitnikov problem. *Cel. Mech. Dyn. Astron.*, 105:289–304, 2009.

418. Z. Kovács, K. G. Szabó, and T. Tél. Controlling chaos on fractal basin boundaries. In J. M. T. Thompson and S. R. Bishop, editors, *Nonlinearity and Chaos in Engineering Dynamics*, pages 155–162. Wiley, Chichester, England, 1994.

419. Z. Kovács and T. Tél. Scaling in multifractals: discretization of an eigenvalue problem. *Phys. Rev. E*, 40:4641–4647, 1989.

420. Z. Kovács and L. Wiesenfeld. Chaotic scattering in reactive collisions – a classical analysis. *Phys. Rev. E*, 51:5476–5494, 1995.

421. Z. Kovács and L. Wiesenfeld. Topological aspects of chaotic scattering in higher dimensions. *Phys. Rev. E*, 63:056207, 2001.

422. Z. Kowalik, M. Franaszek, and P. Pieranski. Self-reanimating chaos in the bouncing-ball system. *Phys. Rev. A*, 37:4016–4022, 1988.

423. S. Kraut and U. Feudel. Multistability, noise, and attractor hopping: the crucial role of chaotic saddles. *Phys. Rev. E*, 66:015207(R), 2002.

424. S. Kraut and C. Grebogi. Escaping from nonhyperbolic chaotic attractors. *Phys. Rev. Lett.*, 92:234101, 2004.

425. S. Kraut and U. Feudel. Enhancement of noise-induced escape through the existence of a chaotic saddle. *Phys. Rev. E*, 67:015204(R), 2003.

426. S. Kraut and U. Feudel. Noise-induced escape through a chaotic saddle: lowering of the activation energy. *Physica D*, 181:222–234, 2003.

427. U. Kuhl, H.-J. Stöckmann, and R. Weaver. Classical wave experiments on chaotic scattering. *J. Phys. A*, 38:10433–10463, 2005.

428. A. Kumar, S. Schrader, A. Aertsen, and S. Rotter. The high-conductance state of cortical networks. *Neural Comput.*, 20:1–43, 2008.

429. P. K. Kundu. *Fluid Mechanics*. Academic Press, San Diego, first edition, 1990.

430. L. Kuznetsov and G.M. Zaslavsky. Regular and chaotic advection in the flow field of a three-vortex problem. *Phys. Rev. E*, 58:7330–7349, 1998.

431. L. Kuznetsov and G.M. Zaslavsky. Passive particle transport in three-vortex flow. *Phys. Rev. E*, 61:3777–3792, 2000.

432. I. Kyprianidis, M. Petrani, J. Kalomiros, and A. Anagnostopoulos. Crisis-induced intermittency in a 3rd-order electrical circuit. *Phys. Rev. E*, 52:2268–2273, 1995.

433. Y.-C. Lai. Persistence of supertransients of spatiotemporal chaotic dynamics in noisy environment. *Phys. Lett. A*, 200:418–422, 1995.

434. Y.-C. Lai. Driving trajectories to a desirable attractor by using small control. *Phys. Lett. A*, 221:375–383, 1996.

435. Y.-C. Lai. Characterization of the natural measure by unstable periodic orbits in nonhyperbolic chaotic systems. *Phys. Rev. E*, 56:6531–6539, 1997.

436. Y.-C. Lai. Abrupt bifurcation to chaotic scattering with discontinuous change in fractal dimension. *Phys. Rev. E*, 60:R6283–R6286, 1999.

437. Y.-C. Lai. Transient fractal behavior in snapshot attractors of driven chaotic systems. *Phys. Rev. E*, 60:1558–1562, 1999.

438. Y.-C. Lai. Catastrophe of riddling. *Phys. Rev. E*, 62:R4505–R4508, 2000.

439. Y.-C. Lai. Encoding digital information using transient chaos. *Int. J. Bif. Chaos*, 10:787–795, 2000.

440. Y.-C. Lai. Superpersistent chaotic transients. In M. Thiel et al., editor, *Nonlinear Dynamics and Chaos: Advances and Perspectives*. Springer, Berlin, Heidelberg, 2010.

441. Y.-C. Lai and V. Andrade. Catastropic bifurcation from riddled to fractal basins. *Phys. Rev. E*, 64:056228, 2001.

442. Y.-C. Lai, R. Blümel, E. Ott, and C. Grebogi. Quantum manifestations of chaotic scattering. *Phys. Rev. Lett.*, 68:3491–3494, 1992.

443. Y.-C. Lai, E. M. Bollt, and C. Grebogi. Communicating with chaos using two-dimensional symbolic dynamics. *Phys. Lett. A*, 255:75–81, 1999.

444. Y.-C. Lai, A. P. S. de Moura, and C. Grebogi. Topology of high-dimensional chaotic scattering. *Phys. Rev. E*, 62:6421–6428, 2000.

445. Y.-C. Lai, M. Ding, C. Grebogi, and R. Blümel. Algebraic decay and fluctuations of the decay exponent in Hamiltonian systems. *Phys. Rev. A*, 45:4661–4669, 1992.

446. Y.-C. Lai, U. Feudel, and C. Grebogi. Scaling behaviors in the transition to chaos in quasiperiodically driven dynamical systems. *Phys. Rev. E*, 54:6070–6073, 1996.

447. Y.-C. Lai and C. Grebogi. Converting transient chaos into sustained chaos by feedback control. *Phys. Rev. E*, 49:1094–1098, 1994.

448. Y.-C. Lai and C. Grebogi. Intermingled basins and two-state on-off intermittency. *Phys. Rev. E*, 52:R3313–R3316, 1995.

449. Y.-C. Lai and C. Grebogi. Modeling of coupled chaotic oscillators. *Phys. Rev. Lett.*, 82:4803–4806, 1999.

450. Y.-C. Lai, C. Grebogi, R. Blümel, and M. Ding. Algebraic decay and phase-space metamorphoses in microwave ionization of hydrogen Rydberg atoms. *Phys. Rev. A*, 45:8284–8287, 1992.

451. Y.-C. Lai, C. Grebogi, R. Blümel, and I. Kan. Crisis in chaotic scattering. *Phys. Rev. Lett.*, 71:2212–2215, 1993.

452. Y.-C. Lai, C. Grebogi, and J. Kurths. Modeling of deterministic chaotic systems. *Phys. Rev. E*, 59:2907–2910, 1999.

453. Y.-C. Lai, C. Grebogi, and T. Tél. Stabilizing chaotic scattering trajectories using control. *Phys. Rev. E*, 48:709–717, 1993.

454. Y.-C. Lai, C. Grebogi, J. A. Yorke, and I. Kan. How often are chaotic saddles nonhyperbolic? *Nonlinearity*, 6:779–797, 1993.

455. Y.-C. Lai, C. Grebogi, J. A. Yorke, and S. Venkataramani. Riddling bifurcation in chaotic dynamical systems. *Phys. Rev. Lett.*, 77:55–58, 1996.

456. Y.-C. Lai and D. Lerner. Effective scaling regime for computing the correlation dimension in chaotic time series analysis. *Physica D*, 115:1–18, 1998.

457. Y.-C. Lai, D. Lerner, and R. Hayden. An upper bound for the proper delay time in chaotic time series analysis. *Phys. Lett. A*, 218:30–34, 1996.

458. Y.-C. Lai, Z. Liu, L. Billings, and I. B. Schwartz. Noise-induced unstable dimension variability and transition to chaos in random dynamical systems. *Phys. Rev. E*, 67:026210, 2003.

459. Y.-C. Lai, Y. Nagai, and C. Grebogi. Characterization of the natural measure by unstable periodic orbits in chaotic attractors. *Phys. Rev. Lett.*, 79:649–652, 1997.

460. Y.-C. Lai, E. Ott, and C. Grebogi. Temporal crossover from classical to quantum behavior: a Markov-chain approach. *Phys. Lett. A*, 173:148–152, 1993.

461. Y.-C. Lai, T. Tél, and C. Grebogi. Controlling transient chaos in dynamical systems. In M. Yamaguti, editor, *Towards the Harnessing of Chaos*, pages 153–167. Elsevier, Amsterdam, 1994.

462. Y.-C. Lai and R. L. Winslow. Extreme sensitive dependence on parameters and initial conditions in spatiotemporal chaotic dynamical systems. *Physica D*, 74:353–371, 1994.

463. Y.-C. Lai and R. L. Winslow. Fractal basin boundaries in coupled map lattices. *Phys. Rev. E*, 50:3470–3473, 1994.

464. Y.-C. Lai and R. L. Winslow. Riddled parameter space in spatiotemporal chaotic dynamical systems. *Phys. Rev. Lett.*, 72:1640–1643, 1994.

465. Y.-C. Lai and R. L. Winslow. Geometric properties of the chaotic saddle responsible for supertransients in spatiotemporal chaotic dynamical systems. *Phys. Rev. Lett.*, 74:5208–5211, 1995.

466. Y.-C. Lai, K. Zyczkowski, and C. Grebogi. Universal behavior in the parametric evolution of chaotic saddles. *Phys. Rev. E*, 59:5261–5265, 1999.

467. H. Lamb. *Hydrodynamics*. Cambridge University Press, Cambridge, 1932.

468. R. Landauer. Electrical resistance of disordered one-dimensional lattices. *Philos. Mag.*, 21:863–867, 1970.

469. D. P. Lathrop and E. J. Kostelich. Characterization of an experimental strange attractor by periodic orbits. *Phys. Rev. A*, 40:4028–4031, 1989.

470. Y.-T. Lau, J. M. Finn, and E. Ott. Fractal dimension in nonhyperbolic chaotic scattering. *Phys. Rev. Lett.*, 66:978–981, 1991.

471. F. Ledrappier and L.-S. Young. Dimension formula for random transformations. *Commun. Math. Phys.*, 117:529–548, 1988.

472. K. Lee, C. Jung, and L. E. Reichl. Scattering echoes in a waveguide with a ripple cavity. *Phys. Rev. B*, 73:195315, 2006.

473. K.-C. Lee. Long-time tails in a chaotic system. *Phys. Rev. Lett.*, 60:1991–1994, 1988.

474. S.-Y. Lee, S. Rim, J.-W. Ryu, T.-Y. Kwon, M. Choi, and C.-M. Kim. Quasiscarred resonances in a spiral-shaped microcavity. *Phys. Rev. Lett*, 93:164102, 2004.

475. O. Legrande and D. Sornette. Coarse-grained properties of the chaotic trajectories in the stadium. *Physica D*, 44:229–247, 1990.

476. O. Legrande and D. Sornette. Fractal set of recurrent orbits in billiards. *Europhys. Lett.*, 11:583–588, 1990.

477. F. Lekien, C. Coulliette, A. J. Mariano, E. H. Ryan, L. K. Shay, G. Haller, and J. Marsden. Pollution release tied to invariant manifolds: a case study for the coast of Florida. *Physica D*, 210:1–20, 2005.

478. V. Lepiller, A. Prigent, F. Dumochel, and I. Mutabazi. Transition to turbulence in a tall annulus submitted to a radial temperature gradient. *Rhys. Fluids*, 19:054101, 2007.

479. R. Leven, B. Pompe, C. Wilke, and B. Koch. Experiments on periodic and chaotic motions of a parametrically forced pendulum. *Physica D*, 16:371–384, 1985.

480. R. Leven and M. Selent. Construction and quantitative characterization of a chaotic saddle from a pendulum experiment. *Chaos. Soliton. Fract.*, 4:2217–2222, 1994.

481. A. F. J. Levi, R. E. Slusher, S. L. McCall, S. J. Pearton, and W. S. Hobson. Room-temperature lasing action in $In_{0.51}Ga_{0.49}P/In_{0.2}Ga_{0.8}As$ microcylinear laser diodes. *Appl. Phys. Lett.*, 62:2021–2023, 1993.

482. N. Levinson. A second order differential equation with singular coefficients. *Ann. Math.*, 50:127–153, 1949.

483. T. Li and J. A. Yorke. Period 3 implies chaos. *Am. Math. Mon.*, 82:985–992, 1975.

484. W. Liebert, K. Pawelzik, and H. G. Schuster. Optimal embeddings of chaotic attractors from topological considerations. *Europhys. Lett.*, 14:521–526, 1991.

485. W. Liebert and H. G. Schuster. Proper choice of the time-delay for the analysis of chaotic time-series. *Phys. Lett. A*, 142:107–111, 1989.

486. Z. Liu and Y.-C. Lai. Chaotic scattering in deformed optical microlasing cavities. *Phys. Rev. E*, 65:046204, 2002.

487. R. Livi, G. Martinez-Mekler, and S. Ruffo. Periodic orbits and long transients in coupled map lattices. *Physica D*, 45:452–460, 1990.

488. E. N. Lorenz. Deterministic nonperiodic flow. *J. Atmos. Sci.*, 20:130–141, 1963.

489. E. N. Lorenz. Dimension of weather and climate attractors. *Nature*, 353:241–244, 1991.

490. E. N. Lorenz. Compound windows of the Hénon map. *Physica D*, 237:1689–1704, 2008.

491. H.-W. Lorenz and H. E. Nusse. Chaotic attractors, chaotic saddles, and fractal basin boundaries: Goodwin's nonlinear accelerator model reconsidered. *Chaos Sol. Fract.*, 13:957–965, 2002.

492. J. Losson, M.C. Mackey, and A. Longtin. Solution multistability in first-order non-linear differential delay equations. *Chaos*, 3:167–176, 1993.

493. W. Lu, M. Rose, K. Pance, and S. Sridhar. Quantum resonances and decay of a chaotic fractal repeller observed using microwaves. *Phys. Rev. Lett.*, 82:5233–5236, 1999.

494. W. Lu, S. Sridhar, and M. Zworski. Fractal Weyl laws for chaotic open systems. *Phys. Rev. Lett.*, 91:154101, 2003.

495. Z.-M. Lu, J. F. Heagy, M. Calliéres, and J. M. Yuan. Quantum dissociation boundary of a kicked Morse oscillator. *Phys. Rev. A*, 43:1118–1121, 1991.

496. Z.-M. Lu, M. Valliéres, J. M. Yuan, and J. F. Heagy. Controlling chaotic scattering: impulsively driven Morse potential. *Phys. Rev. A*, 45:5512–5523, 1992.

497. H. Lustfeld and P. Szépfalusy. Correlation functions on the border lines of transient chaos. *Phys. Rev. E*, 53:5882–5889, 1996.

498. R. S. MacKay, J. D. Meiss, and I. C. Percival. Stochasticity and transport in Hamiltonian systems. *Phys. Rev. Lett.*, 52:697–700, 1984.

499. A. M. Mancho, D. Small, and S. Wiggins. A tutorial on dynamical systems concepts applied to Lagrangian transport in oceanic flows defined as finite time data sets: theoretical and computational issues. *Phys. Rep.*, 437:55–124, 2006.

500. P. Manneville. On the statistics of turbulent transients in dissipative dynamical-systems. *Phys. Lett. A*, 90:327–328, 1982.

501. C. M. Marcus, S. R. Patel, A. G. Huibers, S. M. Cronenwett, M. Switkes, I. H. Chan, R. M. Clarke, J. A. Folk, and S. F. Godijn. Quantum chaos in open versus closed quantum dots: signatures of interacting particles. *Chaos Solitons & Fractals*, 8:1261–1279, 1997.

502. A. P. Martin. Phytoplankton patchiness: the role of lateral stirring and mixing. *Progr. Oceanogr.*, 57:125–174, 2003.

503. V. P. Maslov and M. V. Fedoriuk. *Semiclassical Approximation in Quantum Mechanics*. D. Reidel, Dordrecht, 1981.

504. M. Mathur, G. Haller, T. Peacock, J. E. Ruppert-Felsot, and H. L. Swinney. Uncovering the Lagrangian skeleton of turbulence. *Phys. Rev. Lett.*, 98:144502, 2007.

505. R. D. Mattuck. *A guide to Feynman diagrams in the many-body problem*. Courieer Dover, Dover, 1992.

506. M. R. Maxey and J. J. Riley. Equation of motion for a small rigid sphere in a nonuniform flow. *Phys. Fluids*, 26:883–889, 1983.

507. R. M. May. Simple mathematical models with very complicated dynamics. *Nature*, 261:459–467, 1976.

508. R. M. May. Necessity and chance – deterministic chaos in ecology and evolution. *Bull. Am. Math. Soc.*, 32:291–308, 1995.

509. S. L. McCall, A. F. J. Levi, R. E. Slusher, S. J. Pearton, and R. A. Logan. Whispering-gallery mode microdisk lasers. *Appl. Phys. Lett.*, 60:289–291, 1991.

510. K. McCann and P. Yodzis. Nonlinear dynamics and population disappearances. *Am. Nat.*, 144:873–879, 1994.

511. S. W. McDonald, C. Grebogi, E. Ott, and J. A. Yorke. Fractal basin boundaries. *Physica D*, 17:125–153, 1985.

512. J. McLaughlin. Stochastic behavior in slightly dissipative systems. *Phys. Rev. A*, 20:2114–2119, 1979.

513. J. D. Meiss, J. R. Cary, C. Grebogi, J. D. Crawford, A. N. Kaufman, and H. D. I. Abarbanel. Correlations of periodic, area-preserving maps. *Physica D*, 6:375–384, 1983.

514. J. D. Meiss and E. Ott. Markov-tree model of intrinsic transport in Hamiltonian systems. *Phys. Rev. Lett.*, 55:2741–2744, 1985.

515. J. D. Meiss and E. Ott. Markov tree model of transport in area-preserving maps. *Physica D*, 20:387–402, 1986.

516. M. Meixner, S. Bose, and E. Schöll. Analysis of complex and chaotic patterns near a codimension-2 Turing-Hopf point in a reaction-diffusion model. *Physica D*, 109:128–138, 1997.

517. M. Meixner, A. De Wit, S. Bose, and E. Schöll. Generic spatiotemporal dynamics near codimension-2 Turing-Hopf bifurcations. *Phys. Rev. E*, 55:6690–6697, 1997.

518. M. Meixner, S. M. Zoldi, S. Bose, and E. Schöll. Karhunen-Loeve local characterization of spatiotemporal chaos in a reaction-diffusion system. *Phys. Rev. E*, 61:1382–1385, 2000.

519. A. Mekis, J. U. Nöckel, G. Chen, A. D. Stone, and R. K. Chang. Ray chaos and Q spoiling in lasing droplets. *Phys. Rev. Lett.*, 75:2682–2685, 1995.

520. F. Mellibovsky, A. Meseguer, T. M. Schneider, and B. Eckhardt. Transition in localized pipe flow turbulence. *Phys. Rev. Lett.*, 103:054502, 2009.

521. G. Metcalfe and J. M. Ottino. Autocatalytic processes in mixing flows. *Phys. Rev. Lett.*, 72:2875–2878, 1994.

522. E. E. Michaelides. *Particles, Bubbles and Drops: Their Motion, Heat and Mass Transfer*. World Scientific, Singapore, first edition, 2007.

523. A. P. Micolich, R. P. Taylor, A. G. Davies, J. P. Bird, R. Newbury, T. M. Fromhold, A. Ehlert, H. Linke, L. D. Macks, W. R. Tribe, E. H. Linfield, D. A. Ritchie, J. Cooper, Y. Aoyagi, and P. B. Wilkinson. Evolution of fractal patterns during a classical-quantum transition. *Phys. Rev. Lett.*, 87:036802, 2001.

524. P. D. Miller, C. K. R. T. Jones, A. M. Rogerson, and L. J. Pratt. Quantifying transport in numerically generated velocity fields. *Physica D*, 110:105–122, 1997.

525. W. H. Miller. The classical S-matrix in molecular collisions. *Adv. Chem. Phys.*, 30:77–136, 1975.

526. R. A. Miranda, E. L. Rempel, A. C. L. Chian, and F. A. Borotto. Intermittent chaos in nonlinear wave-wave interactions in space plasmas. *J. Atm. Sol-Terr. Phys.*, 67:1852–1858, 2005.

527. K. A. Mitchell. The topology of nested homoclinic and heteroclinic tangles. *Physica D*, 238:737, 2009.

528. F. C. Moon and G.-X. Li. Fractal basin boundaries and homoclinic orbits for periodic motion in a two-well potential. *Phys. Rev. Lett.*, 55:1439–1442, 1985.

529. P. Moresco and S. P. Dawson. The PIM-simplex method: an extension of the PIM-triple method to saddles with an arbitrary number of expanding directions. *Physica D*, 126:38–48, 1999.

530. D. Morgan, E.M. Bollt, and I. B. Schwartz. Constructing constrained invariant sets in multiscale continuum systems. *Phys. Rev. E*, 68:056210, 2003.

531. H. Morita and K. Kaneko. Collective oscillation in a Hamiltonian system. *Phys. Rev. Lett.*, 96:050602, 2006.

532. F. Mortessagne, O. Legrande, and D. Sornette. Transient chaos in room acoustics. *Chaos*, 3:529–542, 1993.

533. J. Moser. *Stable and random motions in dynamical systems*. Princeton University Press, Princeton, NJ, 1973.

534. A. E. Motter and Y.-C. Lai. Dissipative chaotic scattering. *Phys. Rev. E*, 65:015205, 2002.

535. A. E. Motter and P. S. Letelier. Hausdorff dimension of repellors in low sensitive systems. *Phys. Lett. A*, 277:18–24, 2000.

536. A. E. Motter and P. S. Letelier. Mixmaster chaos. *Phys. Lett. A*, 285:127–131, 2001.

537. A. E. Motter, Y.-C. Lai, and C. Grebogi. Reactive dynamics of inertial particles in nonhyperbolic chaotic flows. *Phys. Rev. E*, 68:056307, 2003.

538. J. Nagler. Crash test for the Copenhagen problem. *Phys. Rev. E*, 69:066218, 2004.

539. J. Nagler, M. Krieger, M. Linke, J. Schönke, and J. Wiersig. Leaking billiards. *Phys. Rev. E*, 75:046204, 2007.

540. J. Nagel, D. Speer, T. Gaber, A. Sterck, R. Eichhorn, P. Reimann, K. Ilin, M. Siegel, D. Koelle, and R. Kleiner. Observation of negative absolute resistance in a Josephson junction. *Phys. Rev. Lett.*, 100:217001, 2008.

541. A. Németh and P. Szépfalusy. Properties of border states of transient chaos. *Phys. Rev. E*, 52:1544–1549, 1995.

542. Z. Neufeld, P. Haynes, and G. Picard. The effect of forcing on the spatial structure and spectra of chaotically advected passive scalars. *Phys. Fluids*, 12:2506–2513, 2000.

543. Z. Neufeld, P. H. Haynes, V. Garcon, and J. Sudre. Ocean fertilization experiments may initiate a large scale Phytoplankton bloom. *Geophys. Res. Lett.*, 29:10.1029/2001GL013677, 2002.

544. Z. Neufeld and T. Tél. Advection in chaotically time-dependent open flows. *Phys. Rev. E*, 57:2832–2842, 1998.

545. Z. Neufeld and E. Hernández-Garcia. *Chemical and Biological Processes in Fluid Fows: A Dynamical Systems Approach*. Imperial College Press, Cambridge, first edition, 2009.

546. S. E. Newhouse. The abundance of wild hyperbolic sests and non-smooth stable sets for diffeomorphisms. *Publ. Math. IHES*, 51:101–151, 1979.

547. S. E. Newhouse. Lectures on dynamical systems. In J. Guckenheimer, J. Moser, and S. E. Newhouse, editors, *Dynamical Systems, C.I.M.E. Lectures*, Birkhauser, Boston, 1980.

548. S. E. Newhouse and T. Pignataro. On the estimation of topological-entropy. *J. Stat. Phys.*, 72:1331–1351, 1993.

549. P. Newton. *The N-vortex Problem*. Springer, New York, 2001.

550. T. Nishikawa, Z. Toroczkai, and C. Grebogi. Advective coalescence in chaotic flows. *Phys. Rev. Lett.*, 87:038301, 2001.

551. T. Nishikawa, Z. Toroczkai, C. Grebogi, and T. Tél. Finite-size effects on active chaotic advection. *Phys. Rev. E*, 65:026216, 2002.

552. J. U. Nöckel and A. D. Stone. Ray and wave chaos in asymmetric resonant optical cavities. *Nature*, 385:45–47, 1997.

553. J. U. Nöckel, A. D. Stone, and R. K. Chang. Q spoiling and directionality in deformed ring cavities. *Opt. Lett.*, 19:1693–1695, 1994.

554. J. U. Nöckel, A. D. Stone, G. Chen, H. L. Grossman, and R. K. Chang. Directional emission from asymmetric resonant cavities. *Opt. Lett.*, 21:1609–1611, 1996.

555. D. W. Noid, S. Gray, and S. A. Rice. Fractal behavior in classical collisional energy transfer. *J. Chem. Phys.*, 84:2649–2652, 1986.

556. S. Nonnenmacher and M. Zworski. Fractal Weyl laws in discrete models of chaotic scattering. *J. Phys. A*, 38:10683–10702, 2005.

557. H. Nusse and J. A. Yorke. A procedure for finding numerical trajectories on chaotic saddles. *Physica D*, 36:137–156, 1989.

558. H. E. Nusse, E. Ott, and J. A. Yorke. Saddle-node bifurcations on fractal basin boundaries. *Phys. Rev. Lett.*, 75:2482–2485, 1995.

559. H. E. Nusse and J. A. Yorke. Basins of attraction. *Science*, 271:1376–1380, 1996.

560. H. E. Nusse and J. A. Yorke. Wada basin boundaries and basin cells. *Physica D*, 90:242–261, 1996.

561. H. E. Nusse and J. A. Yorke. Fractal basin boundaries generated by basin cells and the geometry of mixing chaotic flows. *Phys. Rev. Lett.*, 84:626–629, 2000.

562. A.R. Osborne and A. Provenzale. Finite correlation dimension for stochastic systems with power-law spectra. *Physica D*, 35:357–381, 1989.

563. H. M. Osinga. Locus of boundary crisis: expect infinitely many gaps. *Phys. Rev. E*, 74:035201(R), 2006.

564. E. Ott. *Chaos in Dynamical Systems*. Cambridge University Press, Cambridge, UK, second edition, 2002.

565. E. Ott, J. C. Alexander, I. Kan, J. C. Sommerer, and J. A. Yorke. The transition to chaotic attractors with riddled basins. *Physica D*, 76:384–410, 1994.

566. E. Ott, C. Grebogi, and J. A. Yorke. Controlling chaos. *Phys. Rev. Lett.*, 64:1196–1199, 1990.

567. E. Ott, J. C. Sommerer, J. C. Alexander, I. Kan, and J. A. Yorke. Scaling behavior of chaotic systems with riddled basins. *Phys. Rev. Lett.*, 71:4134–4137, 1993.

568. E. Ott and T. Tél (eds.). Focus issue on chaotic scattering. *Chaos*, 3:417–706, 1993.

569. J. M. Ottino. *The Kinematics of Mixing: Stretching, Chaos and Transport*. Cambridge University Press, Cambridge, UK, first edition, 1989.

570. J. F. Owen, P. W. Barber, P. B. Dorain, and R. K. Chang. Enhancement of fluorescence induced by microstructure resonances of dielectric fiber. *Phys. Rev. Lett.*, 47:1075–1078, 1981.

571. V. Paar and H. Buljan. Bursts in the chaotic trajectory lifetimes preceding controlled periodic motion. *Phys. Rev. E*, 62:4869–4872, 2000.

572. V. Paar and N. Pavin. Bursts in average lifetime of transients for chaotic logistic map with a hole. *Phys. Rev. E*, 55:4112–4115, 1997.

573. V. Paar and N. Pavin. Discontinuous pattern of cumulative separation between orbits of chaotic transient. *Physics Lett. A*, 235:139–144, 1997.

574. V. Paar and N. Pavin. Overlapping of two truncated crisis scenarios: generator of peaks in mean lifetimes of chaotic transients. *Phys. Rev. E*, 68:036222, 2003.

575. N. H. Packard, J. P. Crutchfield, J. D. Farmer, and R. S. Shaw. Geometry from a time series. *Phys. Rev. Lett.*, 45:712–716, 1980.

576. K. Pance, W. Lu, and S. Sridhar. Quantum fingerprints of classical Ruelle-Pollicott resonances. *Phys. Rev. Lett.*, 85:2737–2740, 2000.

577. F. Papoff, D. Dangoisse, E. Poite-Hanoteau, and P. Glorieux. Chaotic transients in a CO_2-laser with modulated parameters – critical slowing-down and crisis-induced intermittency. *Opt. Commun.*, 67:358–362, 1988.

578. B.-S. Park, C. Grebogi, and Y.-C. Lai. Abrupt dimension changes at basin boundary metamorphoses. *Int. J. Bifur. Chaos Appl. Sci. Eng.*, 2:533–541, 1992.

579. M. Pattantyús-Ábrahám, T. Tél, T. Krámer, and J. Józsa. Mixing properties of a shallow basin due to wind-induced chaotic flow. *Adv. Water Res.*, 30:525–534, 2008.

580. T. Peacock and J. Dabiri (eds.). Lagrangian coherent structures in fluid flows. *Chaos, Focus Issue*, 23:017501–019902, 2010.

581. L. M. Pecora and T. L. Carroll. Synchronization in chaotic systems. *Phys. Rev. Lett.*, 64:821–824, 1990.

582. L. M. Pecora and T. L. Carroll. Discontinuous and nondifferentiable functions and dimension increase induced by filtering chaotic data. *Chaos*, 6:432–439, 1996.

583. L. M. Pecora and T. L. Carroll. Master stability functions for synchronized coupled systems. *Phys. Rev. Lett.*, 80:2109–2112, 1998.

584. L. M. Pecora, T. L. Carroll, and J. F. Heagy. Statistics for mathematical properties of maps between time series embeddings. *Phys. Rev. E*, 52:3420–3439, 1995.

585. L. M. Pecora, T. L. Carroll, and J. F. Heagy. Statistics for continuity and differentiability: an application to attractor reconstruction from time series. *Fields Inst. Commun.*, 11:49–62, 1997.

586. L. M. Pecora, L. Moniz, and J. Nichols. A unified approach to attractor reconstruction. *Chaos*, 17:013110, 2007.

587. J. M. Pedrosa, G. G. Carlo, D. A. Wisniacki, and L. Ermann. Distribution of resonances in the quantum open baker map. *Phys. Rev. E*, 79:016215, 2009.

588. X. Pei and F. Moss. Characterization of low-dimensional dynamics in the crayfish caudal photoreceptor. *Nature*, 379:618–621, 1996.

589. J. Peixinho and T. Mullin. Decay of turbulence in pipe flow. *Phys. Rev. Lett.*, 96:094501, 2006.

590. Á. Péntek, T. Tél, and Z. Toroczkai. Chaotic advection in the velocity field of leapfrogging vortex pairs. *J. Phys. A*, 28:2191–2216, 1995.

591. Á. Péntek, T. Tél, and Z. Toroczkai. Fractal tracer patterns in open hydrodynamical flows: the case of leapfrogging vortex pairs. *Fractals*, 3:33–53, 1995.

592. Á. Péntek, Z. Toroczkai, T. Tél, C. Grebogi, and J. A. Yorke. Fractal boundaries in open hydrodynamical flows: signatures of chaotic saddles. *Phys. Rev. E*, 51:4076–4088, 1995.

593. A. Peres. Stability of quantum motion in chaotic and regular systems. *Phys. Rev. A*, 30:1610–1615, 1984.

594. J. M. Petit and M. Hénon. Satellite encounters. *Icarus*, 66:536–555, 1986.

595. G. Pianigiani. Conditionally invariant-measures and exponential decay. *J. Math. Anal. Appl.*, 82:75–88, 1981.

596. G. Pianigiani and J. A. Yorke. Expanding maps on sets which are almost invariant – decay and chaos. *Trans. Am. Math. Soc.*, 252:351–366, 1979.

597. R. T. Pierrehumbert and H. Young. Global chaotic mixing on isentropic surfaces. *J. Atm. Sci.*, 50:2462–2480, 1993.

598. R. T. Pierrehumbert. Tracer microstructure in the large-eddy dominated regime. *Chaos Sol. Fract.*, 4:1091–1110, 1994.

599. D. Pierson and F. Moss. Detecting periodic unstable points in noisy chaotic and limit-cycle attractors with applications to biology. *Phys. Rev. Lett.*, 75:2124–2127, 1995.

600. A. Pikovsky and O. Popovich. Persistent patterns in deterministic mixing flows. *Europhys. Lett.*, 61:625–631, 2003.

601. A. Pikovsky, O. Popovich, and B. Eckhardt. Abnormal mixing of passive scalar in chaotic flows. *Phys. Rev. E*, 75:036308, 2007.

602. A. Pikovsky, M. Rosenblum, and J. Kurths. *Synchronization – A Universal Concept in Nonlinear Sciences*. Cambridge University Press, Cambridge, UK, first edition, 2001.

603. A. Pikovsky. Escape exponent for transient chaos and chaotic scattering in non-hyperbolic Hamiltonian systems. *J. Phys. A*, 25:L477–L481, 1992.

604. S. L. Pimm. *The Balance of Nature?: Ecological Issues in the Conservation of Species and Communities*. University of Chicago Press, Chicago, first edition, 1991.

605. C. M. Place and D. K. Arrowsmith. Control of transient chaos in tent maps near crisis. I. Fixed point targeting. *Phys. Rev. E*, 61:1357–1368, 2000a.

606. C. M. Place and D. K. Arrowsmith. Control of transient chaos in tent maps near crisis. II. Periodic orbit targeting. *Phys. Rev. E*, 61:1369–1381, 2000b.

607. A. Pluchino, V. Latora, and A. Rapisarda. Metastable states, anomalous distributions and correlations in the HMF model. *Physica D*, 193:315–328, 2004.

608. H. Poincaré. *Les Méthodes Nouvelles de la Mécanique*. Gauthier-villars, Paris, 1892.

609. A. Politi, R. Livi, G. L. Oppo, and R. Kapral. Unpredictable behaviour in stable systems. *EuroPhys. Lett.*, 22:571–576, 1993.

610. A. Politi and A. Torcini. Linear and non-linear mechanism of information propagation. *EuroPhys. Lett.*, 28:545–550, 1994.

611. A. Politi and A. Torcini. Stable chaos. In M. Thiel et al., editor, *Nonlinear Dynamics and Chaos: Advances and Perspectives*. Springer, Berlin, Heidelberg, 2010

612. Y. Pomeau and P. Manneville. Intermittent transition to turbulence in dissipative dynamical systems. *Commun. Math. Phys.*, 74:189–197, 1980.

613. L. Poon, J. Campos, E. Ott, and C. Grebogi. Wada basin boundaries in chaotic scattering. *Int. J. Bifur. Chaos Appl. Sci. Eng.*, 6:151–165, 1996.

614. J. S. E. Portela, I. L. Caldas, R. L. Viana, and M. A. F. Sanjuán. Fractal and Wada exit basin boundaries in tokamaks. *Int. J. Bif. Chaos*, 17:4067, 2007.

615. W. H. Press, B. P. Flannery, S. A. Teukolsky, and W. T. Vetterling. *Numerical Recipies*. Cambridge University Press, Cambridge, UK, first edition, 1986.

616. I. Procaccia. Complex or just complicated? *Nature*, 333:498–499, 1988.

617. K. Pyragas. Continuous control of chaos by self-controlling feedback. *Phys. Lett. A*, 170:421–428, 1992.

618. S.-X. Qian, J. B. Snow, H.-M. Tzeng, and R. K. Chang. Lasing droplets – highlighting the liquid-air interface by laser emission. *Science*, 231:486–488, 1986.

619. Z.-L. Qu and G. Hu. Spatiotemporal periodic states, periodic windows, and intermittency in coupled-map lattices. *Phys. Rev. E*, 49:1099–1108, 1994.

620. J. A. Ramilowski, S. D. Prado, F. Borondo, and D. Farrelly. Fractal Weyl law behavior in an open Hamiltonian system. *Phys. Rev. E*, 80:055201(R), 2009.

621. D. A. Rand and H. B. Wilson. Chaotic stochasticity: a ubiquitous source of unpredictablity in epidemics. *Proc. Roy. Soc.*, B 246:179–184, 1991.

622. C. C. Rankin and W. H. Miller. Classical S-matrix for linear reactive collisions of H+Cl$_2$. *J. Chem. Phys.*, 55:3150, 1971.

623. S. Ree and L. E. Reichl. Fractal analysis of chaotic classical scattering in a cut-circle billiard with two openings. *Phys. Rev. E*, 65:055205, 2002.

624. L.E. Reichl. *A Modern Course in Statistical Physics*. Wiley, New York, second edition, 1998.

625. P. Reimann. Noisy maps near crises. *Z. Naturforsch.*, 49a:1248–1250, 1994.

626. P. Reimann. Noisy one-dimensional maps near a crisis I: weak Gaussian white and colored noise. *J. Stat. Phys.*, 82:1467–1501, 1996.

627. P. Reimann. Noisy one-dimensional maps near a crisis II: general uncorrelated weak noise. *J. Stat. Phys.*, 85:403–425, 1996.

628. P. Reimann, R. Müller, and P. Talkner. Decay of metastable states with discrete dynamics. *Phys. Rev. E*, 49:3670–3682, 1994.

629. P. Reimann and P. Talkner. Invariant densities for noisy maps. *Phys. Rev. A*, 44:6348–6393, 1991.

630. P. Reimann and P. Talkner. Escape rates for noisy maps. *Phys. Rev. E*, 51:4105–4113, 1995.

631. E. L. Rempel and A. C. Chian. High-dimensional chaotic saddles in the Kuramoto-Shivashinsky equation. *Phys. Lett. A*, 319:104–109, 2003.

632. E. L. Rempel and A. C. Chian. Intermittency induced by attractor-merging crisis in the Kuramoto-Shivashinsky equation. *Phys. Rev. E*, 71:016203, 2005.

633. E. L. Rempel and A. C. Chian. Origin of transient and intermittent dynamics in spatiotemporal chaotic systems. *Phys. Rev. Lett.*, 98:014101, 2007.

634. E. L. Rempel, A. C. Chian, E. E. Macau, and R. R. Rosa. Analysis of chaotic saddles in high-dimensional dynamical systems: The Kuramoto-Shivashinsky equation. *Chaos*, 14:545–556, 2004.

635. E. L. Rempel, A. C. Chian, and R. A. Miranda. Chaotic saddles at the onset of intermittent spatiotemporal chaos. *Phys. Rev. E*, 76:056217, 2007.

636. E. L. Rempel and A. C. Chian. Alfvén chaotic saddles. *Int. J. Bif. Chaos*, 14:4009–4017, 2004.

637. E. L. Rempel, A. C. Chian, E. E. N. Macau, and R. R. Rosa. Analysis of chaotic saddles on low-dimensional dynamical systems: the derivative nonlinear Schrödinger equation. *Physica D*, 199:407–424, 2004.

638. E. L. Rempel, R. A. Miranda, and A. C. Chian. Spatiotemporal intermittency and chaotic saddles in the regularized long-wave equation. *Phys. Fluids*, 21:074105, 2009.

639. E. L. Rempel, G. Lesur, and M. R. E. Proctor. Supertransient magnetohydrodynamic turbulence in Keplerian shear flows. *Phys. Rev. Lett.*, 105:044501, 2010.

640. H. Risken. *The Fokker-Planck Equation*. Springer, Berlin, first edition, 1989.

641. C. Robert, K. T. Alligood, E. Ott, and J. A. Yorke. Outer tangency bifurcations of chaotic sets. *Phys. Rev. Lett.*, 80:4867–4870, 1998.

642. C. Robert, K. T. Alligood, E. Ott, and J. A. Yorke. Explosions of chaotic sets. *Phys. D*, 144:44–61, 2000.

643. D. L. Rod. Pathology of invariant sets in the monkey saddle. *J. Diff. Equat.*, 14:129–170, 1973.

644. C. S. Rodrigues, A.P.S. de Moura, and C. Grebogi. Random fluctuation leads to forbidden escape of particles. *Phys. Rev. E*, 82:026211, 2010a.

645. C. S. Rodrigues, C. Grebogi, and A.P.S. de Moura. Escape from attracting sets in randomly perturbed systems. *Phys. Rev. E*, 82:046217, 2010b.

646. R. Rollins and E. Hunt. Intermittent transient chaos at interior crises in the diode resonator. *Phys. Rev. A*, 29:3327–3334, 1984.

647. V. Rom-Kedar, A. Leonard, and S. Wiggins. An analytical study of transport, mixing and chaos in an unsteady vortical flow. *J. Fluid Mech.*, 214:347–394, 1990.

648. F. Romeiras, C. Grebogi, and E. Ott. Multifractal properties of snapshot attractors of random maps. *Phys. Rev. A*, 41:784–799, 1990.

649. P. Romeiras, C. Grebogi, and E. Ott. Critical exponents for power spectra scaling at merging of chaotic bands. *Phys. Rev. A*, 38:463–468, 1988.

650. E. Rosa, S. Hayes, and C. Grebogi. Noise filtering in communicating with chaos. *Phys. Rev. Lett.*, 78:1247–1250, 1997.

651. E. Rosa and E. Ott. Mixed basin boundary structures of chaotic systems. *Phys. Rev. E*, 59:343–352, 1999.

652. E. Rosa, E. Ott, and M. H. Hess. Transition to phase synchronization of chaos. *Phys. Rev. Lett.*, 80:1642–1645, 1998.

653. M. G. Rosenblum, A. S. Pikovsky, and J. Kurths. Phase synchronization of chaotic oscillators. *Phys. Rev. Lett.*, 76:1804–1807, 1996.

654. M. T. Rosenstein, J. J. Collins, and C. J. De Luca. Reconstruction expansion as a geometry-based framework for choosing proper delay times. *Physica D*, 73:82–98, 1994.

655. V. Rossi, C. López, E. Hernández-Garcia, J. Sudre, V. Garcon, and Y. Morel. Surface mixing and biological activity in the four Eastern boundary upwelling systems. *Nonlin. Proc. Geophys.*, 16:557–568, 2009.

656. M. L. Roukes and O. L. Alerhand. Mesoscopic junctions, random scattering, and strange repellers. *Phys. Rev. Lett.*, 65:1651–1654, 1990.

657. B. Rückerl and C. Jung. Scaling properties of a scattering system with an incomplete horseshoe. *J. Phys. A-Math. Gen.*, 27:55–77, 1994.

658. P. Ruján. Calculation of free-energy of Ising systems by a recursion method. *Physica A*, 91:549–562, 1978.

659. P. Rupp, R. Richter, and I. Rehberg. Critical exponents of directed percolation in spatiotemporal intermittency. *Phys. Rev. E*, 67:036209, 2003.

660. J.-W. Ryu, S.-Y. Lee, C.-M. Kim, and Y.-J. Park. Survival probability time distribution in dielectric cavities. *Phys. Rev. E*, 73:036207, 2006.

661. J. Sabuco, S. Zambrano, and M. A. F. Sanjuán. Partial control of chaotic transients using escape times. *New J. Phys.*, 12:113038, 2010.

662. P. G. Saffman. *Vortex Dynamics*. Cambridge University Press, Cambridge, UK, 1992.

663. D. Samanta, A. de Lozar, and B. Hof. Experimental investigation of laminar turbulent intermittency in pipe flow. *arXiv:1008.2294v1*, 2010.

664. M. Sandulescu, E. Hernández-Garcia, C. E. López, and U. Feudel. Kinematic studies of transport accross an island wake, with aplication to the Canary islands. *Tellus A*, 58:605–605, 2006.

665. M. Sandulescu, C. E. López, E. Hernández-Garcia, and U. Feudel. Plankton blooms in vortices: the role of biological and hydrodynamics timescales. *Nonlin. Process. Geophys.*, 14:1–12, 2007.

666. M. Sandulescu, C. E. López, E. Hernández-Garcia, and U. Feudel. Biological activity in the wake of an island close to costal upwelling. *Ecol. Complex.*, 5:228–237, 2008.

667. M. A. F. Sanjuán and C. Grebogi. *Recent Progress in Controlling Chaos*. World Scientific, Singapore, first edition, 2010.

668. M. A. F. Sanjuán, T. Horita, and K. Aihara. Opening a closed Hamiltonian map. *Chaos*, 13:17–24, 2003a.

669. M. A. F. Sanjuán, J. A. Kennedy, E. Ott, and J. A. Yorke. Indecomposable continua and the characterization of strange sets in nonlinear dynamics. *Phys. Rev. Lett.*, 78:1892, 1997.

670. M. A. F. Sanjuán, J. A. Kennedy, C. Grebogi, and J. A. Yorke. Indecomposable continua in dynamical systems with noise: fluid flow past an array of cylinders. *Chaos*, 7:125–138, 1997.

671. M. Sano and Y. Sawada. Measurement of the Lyapunov spectrum from a chaotic time series. *Phys. Rev. Lett.*, 55:1082–1085, 1985.

672. T. Sapsis and G. Haller. Instabilities in the dynamics of neutrally bouyant particles. *Phys. Fluids*, 20:017102, 2008.

673. T. Sapsis and G. Haller. Inertial particle dynamics in a hurricane. *J. Atmos. Sci.*, 66:2481–2492, 2009.

674. T. Sapsis and G. Haller. Clustering criterion for inertial particles in two-dimensional time-periodic and three-dimensional steady flows. *Chaos*, 20:017515, 2010.

675. J. Sartorelli, W. Goncalves, and R. Pinto. Crisis and intermittency in a Leaky-Faucet experiment. *Phys. Rev. E*, 49:3963–3975, 1994.

676. T. D. Sauer, C. Grebogi, and J. A. Yorke. How long do numerical chaotic solutions remain valid? *Phys. Rev. Lett.*, 79:59–62, 1997.

677. T. D. Sauer, J. A. Tempkin, and J. A. Yorke. Spurious Lyapunov exponents in attractor reconstruction. *Phys. Rev. Lett.*, 81:4341–4344, 1998.

678. T. D. Sauer and J. A. Yorke. Reconstructing the Jacobian from data with observational noise. *Phys. Rev. Lett.*, 83:1331–1334, 1999.

679. T. D. Sauer, J. A. Yorke, and M. Casdagli. Embedology. *J. Stat. Phys.*, 65:579–616, 1991.

680. A. B. Schelin, A. P. S. de Moura, and C. Grebogi. Transition to chaotic scattering: signatures in the differential cross section. *Phys. Rev. E*, 78:046204, 2008.

681. A. B. Schelin, Gy. Károlyi, A. P. S. de Moura, N. A. Booth, and C. Grebogi. Chaotic advection in blood flow. *Phys. Rev. E*, 80:016213, 2009.

682. I. Scheuring, T. Czárán, P. Szabó, G. Károlyi, and Z. Toroczkai. Spatial models of prebiotic evolution: soup before pizza? *Orig. Life Evol. Biosph.*, 33:319–355, 2003.

683. I. Scheuring and G. Domokos. Only noise can induce chaos in discrete populations. *Oikos*, 116:361–366, 2007.

684. S. J. Schiff, K. Jerger, D. H. Duong, T. Chang, M. L. Spano, and W. L. Ditto. Controlling chaos in the brain. *Nature*, 370:615–620, 1994.

685. P. Schmelcher and F. K. Diakonos. Detecting unstable periodic orbits of chaotic dynamical systems. *Phys. Rev. Lett.*, 78:4733–4736, 1997.

686. A. Schmiegel and B. Eckhardt. Fractal stability border in plane Couette flow. *Phys. Rev. Lett.*, 79:5250–5253, 1997.

687. J. Schneider, V. Fernández, and E. Hernández-Garcia. Leaking method approach to surface transport in the Mediterranean sea from a numerical ocean model. *J. Mar. Syst.*, 57:111–126, 2000.

688. J. Schneider, T. Tél, and Z. Neufeld. Dynamics of leaking Hamiltonian systems. *Phys. Rev. E*, 66:066218, 2002.

689. J. Schneider, J. Schmalzl, and T. Tél. Lagrangian avenues of transport in the Earth's mantle. *Chaos*, 17:033115, 2007.

690. T. M. Schneider, B. Eckhardt, and J. Vollmer. Statistical analysis of coherent structures in transitional pipe flows. *Phys. Rev. E*, 75:066313, 2007.

691. T. M. Schneider, B. Eckhardt, and J. A. Yorke. Turbulence transition and the edge of chaos in pipe flow. *Phys. Rev. Lett.*, 99:034502, 2007.

692. T. M. Schneider, J. F. Gibson, M. Lagha, F. De Lillo, and B. Eckhardt. Laminar-turbulent boundary in plane Couette flow. *Phys. Rev. E*, 78:037301, 2007.

693. W. Schoepe. Fluctuations and stability of superfluid turbulence at mK temperatures. *Phys. Rev. Lett.*, 92:095301, 2004.

694. E. Schöll and H. G. Schuster (eds.). *Handbook of Chaos Control*. Wiley-VCH, Weinheim, second edition, 2007.

695. H. Schomerus, J. Wiersig, and J. Main. Lifetime statistics in chaotic dielectric microresonators. *Phys. Rev. A*, 79:053806, 2009.

696. I. B. Schwartz, L. Billings, and E.M. Bollt. Dynamical epidemic suppression using stochastic prediction and control. *Phys. Rev. E*, 70:046220, 2004.

697. I. B. Schwartz and I. Triandaf. Sustaining chaos by using basin boundary saddles. *Phys. Rev. Lett.*, 77:4740–4743, 1996.

698. I. B. Schwartz, I. Triandaf, R. Meucci, and T. W. Carr. Open-loop sustained chaos and control: A manifold approach. *Phys. Rev. E*, 66:026213, 2002.

699. H. G. L. Schwefel, N. B. Rex, H. E. Tureci, R. K. Chang, A. D. Stone, T. Ben-Messaoud, and J. Zyss. Dramatic shape sensitivity of directional emission patterns from similarly deformed cylindrical polymer lasers. *J. Opt. Soc. Am.*, B 21:923–934, 2004.

700. S. Scott, B. Peng, A. Tomlin, and K. Showalter. Transient Chaos in a Closed Chemical-System. *J. Chem. Phys.*, 94:1134–1140, 1991.

701. P. Seba. Quantum irregular scattering in the presence of a classical stability island. *Phys. Rev. E*, 47:3870–3878, 1993.

702. J. M. Seoane, J. Aguirre, M. A. F. Sanjuán, and Y.-C. Lai. Basin topology in dissipative chaotic scattering. *Chaos*, 16:023101, 2006.

703. J. M. Seoane, L. Huang, M. A. F. Sanjuán, and Y.-C. Lai. Effect of noise on chaotic scattering. *Phys. Rev. E*, 79:047202, 2009.

704. J. M. Seoane, M. A. F. Sanjuán, and Y.-C. Lai. Fractal dimension in dissipative chaotic scattering. *Phys. Rev. E*, 76:016208, 2007.

705. J. M. Seoane and M. A. F. Sanjuán. Exponential decay and scaling laws in noisy chaotic scattering. *Phys. Lett. A*, 372:110–116, 2008.

706. J. M. Seoane, S. Zambrano, I. P. Marino, and M. A. F. Sanjuán. Basin boundary metamorphoses and phase control. *Europhys. Lett.*, 90:30002, 2010.

707. S. C. Shadden, F. Lekien, and J. E. Marsden. Definition and properties of Lagrangian coherent structures from finite-time Lyapunov exponents in two-dimensional aperiodic flows. *Physica D*, 212:271–304, 2005.

708. C. E. Shannon and W. Weaver. *The Mathematical Theory of Communication*. The University of Illinois Press, IL, first edition, 1964.

709. K. Shariff and A. Leonard. Vortex rings. *Ann. Rev. Fluids Mech.*, 24:235–279, 1992.

710. K. Shariff, A. Leonard, and J. H. Ferziger. Dynamical systems analysis of fluid transport in time-periodic vortex ring flows. *Phys. Fluids*, 18:047106, 2006.

711. J.-L. Shen, H.-W Yin, J.-H. Dai, and H.-J. Zhang. Dynamical behavior, transient chaos, and riddled basins of two charged particles in a Paul trap. *Phys. Rev. A*, 55:2159–2164, 2009.

712. D. L. Shepelyansky. Fractal Weyl law for quantum fractal eigenstates. *Phys. Rev. E*, 77:015202(R), 2008.

713. H. Shibata, H. Fujisaka, and H. Mori. Scaling structures for dynamics of intermittent switching just after the 3-band crisis. *Physica A*, 189:554–574, 1992.

714. T. Shimizu and N. Morioka. Transient behavior in periodic regions of the Lorenz model. *Phys. Lett. A*, 69:148–150, 1978.

715. B. Shraiman. Order, disorder, and phase turbulence. *Phys. Rev. Lett.*, 57:325–328, 1986.

716. L. Shulenburger, Y.-C. Lai, T. Yalcinkaya, and R. D. Holt. Controlling transient chaos to prevent species extinction. *Phys. Lett. A*, 260:156–161, 1999.

717. A. N. Silchenko, S. Beri, D. G. Luchinsky, and P. V. E. McClintock. Fluctuational transitions through a fractal basin boundary. *Phys. Rev. Lett.*, 91:174104, 2003.

718. A. N. Silchenko, S. Beri, D. G. Luchinsky, and P. V. E. McClintock. Fluctuational transitions across different kinds of fractal basin boundaries. *Phys. Rev. E*, 71:046203, 2005.

719. C. Siopis, H. E. Kandrup, G. Contopoulos, and R. Dvorak. Universal properties of escape in dynamical systems. *Cel. Mech. Dyn. Astr.*, 65:57–68, 1997.

720. J. D. Skufca, J. A. Yorke, and B. Eckhardt. Edge of chaos in a parallel shear flow. *Phys. Rev. Lett.*, 96:174101, 2006.

721. S. Smale. Differentiable dynamics systems. *Bull. Am. Math. Soc.*, 73:747–817, 1967.

722. P. So, E. Ott, S. J. Schiff, D. T. Kaplan, T. D. Sauer, and C. Grebogi. Detecting unstable periodic orbits in chaotic experimental data. *Phys. Rev. Lett.*, 76:4705–4708, 1996.

723. J. C. Sommerer. A universal scaling for noise-induced metastability. *Phys. Lett. A*, 176:85–88, 1993.

724. J. C. Sommerer, W. L. Ditto, C. Grebogi, E. Ott, and M. L. Spano. Experimental confirmation of the scaling theory for noise-induced crises. *Phys. Rev. Lett.*, 66:1947–1950, 1991.

725. J. C. Sommerer, H. Ku, and H. Gilreath. Experimental evidence for chaotic scattering in a fluid wake. *Phys. Rev. Lett.*, 77:5055–5058, 1996.

726. J. C. Sommerer and E. Ott. Particles floating on a moving fluid: a dynamically comprehensive physical fractal. *Science*, 259:335–339, 1993.

727. J. C. Sommerer and E. Ott. Blowout bifurcations – the occurrence of riddled basins and on-off intermittency. *Phys. Lett. A*, 188:39–47, 1994.

728. J. C. Sommerer, E. Ott, and C. Grebogi. Scaling law for characteristic times of noise-induced crises. *Phys. Rev. A*, 43:1754–1769, 1991.

729. S. M. Soskin, R. Mannella, M. Arrayás, and A. N. Silchenko. Strong enhancement of noise-induced escape by nonadiabatic periodic driving due transient chaos. *Phys. Rev. E*, 63:051111, 2001.

730. D. Speer, R. Eichhorn, and P. Reimann. Brownian motion: anomalous response due to noisy chaos. *Eur. Phys. Lett*, 79:10005, 2007.

731. D. Speer, R. Eichhorn, and P. Reimann. Transient chaos induced anomalous transport properties of an underdamped Brownian particle. *Phys. Rev. E*, 76:051110, 2007.

732. M. A. Spina, I. Garcia-Mata, and M. Saraceno. Weyl law for fat fractals. *J. Phys. A*, 43:392003, 2010.

733. T. M. Squires and S. R. Quake. Microfluidics: fluid physics at the nanoliter scale. *Rev. Mod. Phys.*, 77:977–1026, 2005.

734. D. Stahlke and R. Wackerbauer. Transient spatiotemporal chaos is extensive in the reaction-diffusion networks. *Phys. Rev. E*, 80:056211, 2009.

735. D. A. Steck, W. H. Oskay, and M. G. Raizen. Observation of chaos-assisted tunneling between islands of stability. *Science*, 293:274–278, 2001.

736. A. F. Steklain and P. S. Letelier. Newtonian and pseudo-Newtonian Hill problem. *Phys. Lett. A*, 352:398–4003, 2006.

737. G. Stépán. *Retarded Dynamical Systems: Stability and Characteristic Functions*. Wiley, New York, first edition, 1989.

738. G. Stépán. Chaotic motion of wheels. *Vehicle Syst. Dyn.*, 20:341–351, 1991.

739. G. Stépán. Delay, nonlinear oscillations and shimmying wheels. In F.C. Moon, editor, *IUTAM Symposium on New Applications of Nonlinear and Chaotic Dynamics in Mechanics*, pages 373–387. Kluwer, Amsterdam, 1999.

740. H.-J. Stöckmann. *Quantum Chaos – An Introduction*. Cambridge University Press, Cambridge, first edition, 1999.

741. M. C. Strain and H. S. Greenside. Size-dependent transition to high-dimensional chaotic dynamics in a two-dimensional excitable medium. *Phys. Rev. Lett.*, 80:2306–2309, 1998.

742. A.V. Straube and A. Pikovsky. Mixing-induced global models in open active flows. *Phys. Rev. Lett.*, 99:184503, 2007.

743. A. Surana, O. Grunberg, and G. Haller. Exact theory of three-dimensional flow separation. Part I. Steady separation. *J. Fluid Mech.*, 564:57–103, 2006.

744. D. Sweet, H. E. Nusse, and J. A. Yorke. Stagger-and-step method: detecting and computing chaotic saddles in higher dimensions. *Phys. Rev. Lett.*, 86:2261–2264, 2001.

745. D. Sweet and E. Ott. Fractal basin boundaries in higher-dimensional chaotic scattering. *Phys. Lett. A*, 266:134–139, 2000.

746. D. Sweet and E. Ott. Fractal dimension of higher-dimensional chaotic repellors. *Physica D*, 139:1–27, 2000.

747. D. Sweet, E. Ott, and J. A. Yorke. Complex topology in chaotic scattering: a laboratory experiment. *Nature*, 399:315–317, 1999.

748. D. Sweet, B. W. Zeff, E. Ott, and D. P. Lathrop. Three-dimensional optical billiard chaotic scattering. *Physica D*, 154:207–218, 2001.

749. K. G. Szabó, Y.-C. Lai, T. Tél, and C. Grebogi. Critical exponent for gap filling at crisis. *Phys. Rev. Lett.*, 77:3102–3105, 1996.

750. K. G. Szabó, Y.-C. Lai, T. Tél, and C. Grebogi. Topological scaling and gap filling at crises. *Phys. Rev. E*, 61:5019–5032, 2000.

751. K. G. Szabó and T. Tél. Thermodynamics of attractor enlargement. *Phys. Rev. E*, 50:1070–1082, 1994.

752. K. G. Szabó and T. Tél. Transient chaos as the backbone of dynamics on strange attractors beyond crisis. *Phys. Lett. A*, 196:173–180, 1994.

753. P. Szépfalusy and T. Tél. New approach to the problem of chaotic repellers. *Phys. Rev. A*, 34:2520–2523, 1986.

754. D. Takács, G. Orosz, and G. Stépán. Delay effects in shimmy dynamics of wheels with string-like tyres. *Eur. J. Mech. A Solids*, 28:516–525, 2009.

755. D. Takács, G. Stépán, and S.J. Hogan. Isolated large amplitude periodic motions of towed rigid wheels. *Nonlin. Dyn.*, 52:27–34, 2008.

756. F. Takens. Detecting strange attractors in fluid turbulence. In D. Rand and L. S. Young, editors, *Dynamical Systems and Turbulence*, Vol. 898 of *Lecture Notes in Mathematics*, pages 366–381. Springer, Berlin, 1981.

757. S. Takesue and K. Kaneko. Fractal basin structure. *Prog. Theor. Phys.*, 71:35–49, 1984.

758. P. Tallapragada and S. D. Ross. Particle segregation by Stokes number for small neutrally buoyant spheres in a fluid. *Phys. Rev. E*, 78:036308, 2008.

759. W. Tang, G. Haller, J.-J. Baik, and Y.H. Ryu. Locating and atmospheric contamination source using slow manifolds. *Phys. Fluids*, 21:043302, 2009.

760. W. Tang, M. Mathur, G. Haller, D. C. Hahn, and F. H. Ruggiero. Lagrangian coherent structures near a subtropical jet stream. *J. Atm. Sci.*, 2010.

761. S. R. Taylor and S.A. Campbell. Approximating chaotic saddles in delay differential equations. *Phys. Rev. E*, 75:046215, 2007.

762. T. Tél. Invariant curves, attractors, and phase-diagram of a piecewise linear map with chaos. *J. Stat. Phys.*, 33:195–221, 1983.

763. T. Tél. Dynamic spectrum and thermodynamic functions of strange sets from an eigenvalue problem. *Phys. Rev. A*, 36:2507–2510, 1987.

764. T. Tél. Escape rate from strange sets as an Eigenvalue. *Phys. Rev. A*, 36:1502–1505, 1987.

765. T. Tél. On the organization of transient chaos: application to irregular scattering. *J. Phys. A-Math. Gen.*, 22:L691–L697, 1989.

766. T. Tél. Transient chaos. In B.-L. Hao, editor, *Directions in Chaos (3): Experimental Study and Characterization of Chaos*, pages 149–211. World Scientific, Singapore, 1990.

767. T. Tél. Controlling transient chaos. *J. Phys. A-Math. Gen*, 24:L1359–L1368, 1991.

768. T. Tél. Thermodynamics of chaotic scattering at abrupt bifurcation. *Phys. Rev. A*, 44:1034–1043, 1991.

769. T. Tél. Crossover between the control of permanent and transient chaos. *Int. J. Bif. Chaos*, 3:757–764, 1993.

770. T. Tél. Transient chaos: a type of metastable state. In B.-L. Hao, editor, *STATPHYS 19: The Proceedings of the 19th IUPAP Conference on Statistical Physics*, pages 346–362. World Scientific, Singapore, 1996.

771. T. Tél, A. P. S. de Moura, C. Grebogi, and G. Károlyi. Chemical and biological activity in open flows: a dynamical system approach. *Phys. Rep.*, 413:91–196, 2005.

772. T. Tél, C. Grebogi, and E. Ott. Conditions for the abrupt bifurcation to chaotic scattering. *Chaos*, 3:495–503, 1993.

773. T. Tél and M. Gruiz. *Chaotic Dynamics: An Introduction Based on Classical Mechanics*. Cambridge University Press, Cambridge, 2006.

774. T. Tél, G. Károlyi, A. Péntek, I. Scheuring Z. Toroczkai, C. Grebogi, and J. Kadtke. Chaotic advection, diffusion, and reactions in open flows. *Chaos*, 10:89–98, 2000.

775. T. Tél and Y.-C. Lai. Chaotic transients in spatially extended systems. *Phys. Rep.*, 460:245–275, 2008.

776. T. Tél and Y.-C. Lai. Quasipotential approach to critical scaling in noise-induced chaos. *Phys. Rev. E*, 81:056208, 2010.

777. T. Tél, Y.-C. Lai, and M. Gruiz. Noise-induced chaos: a consequence of long deterministic transients. *Int. J. Chaos Bif.*, 18:509–520, 2008.

778. T. Tél, J. Vollmann, and W. Breymann. Transient chaos: the origin of transport in driven systems. *Europhys. Lett.*, 35:659–664, 1996.

779. J. Theiler. Spurious dimension from correlation algorithms applied to limited time series data. *Phys. Rev. A*, 34:2427–2432, 1986.

780. J. M. T. Thompson. Chaotic phenomena triggering the escape from a potential well. *Proc. R. Soc. Lond. A*, 421:195–225, 1989.

781. J. M. T. Thompson. Global unpredictability in nonlinear dynamics – capture, dispersal and the indeterminate bifurcations. *Physica D*, 58:260–272, 1992.

782. J. M. T. Thompson and H.B. Stewart. *Nonlinear Dynamics and Chaos*. Wiley, New York, second edition, 2002.

783. S. Tomsovic. Tunneling and chaos. *Phys. Scripta*, T90:162–165, 2001.

784. A. Torcini, P. Grassberger, and A. Politi. Error propagation in extended systems. *J. Phys. A*, 27:4533–4541, 1995.

785. Z. Toroczkai. Geometric method for stabilizing unstable periodic-orbits. *Phys. Lett. A*, 190:71–78, 1994.

786. Z. Toroczkai, G. Károlyi, Á. Péntek, T. Tél, and C. Grebogi. Advection of active particles in open chaotic flows. *Phys. Rev. Lett.*, 80:500–503, 1998.

787. Z. Toroczkai, G. Károlyi, Á. Péntek, T. Tél, C. Grebogi, and J. A. Yorke. Wada dye boundaries in open hydrodynamical flows. *Physica A*, 239:235–243, 1997.

788. I. Triandaf, E.M. Bollt, and I. B. Schwartz. Approximating stable and unstable manifolds in experiments. *Phys. Rev. E*, 67:037201, 2003.

789. I. Triandaf and I. B. Schwartz. Quality factor control in a lasing microcavity model. *Phys. Rev. E*, 61:3601–3609, 2000.

790. G. Troll and U. Smilansky. A simple model for chaotic scattering. *Physica D*, 35:34–64, 1989.

791. P. Turchin and S. P. Ellner. Living on the edge of chaos: population dynamics of fennoscandian voles. *Ecology*, 81:3099–3116, 2000.

792. L. F. L. Turci, E. E. N. Macau, and T. Yoneyama. Chaotic transient and the improvement of system flexibility. *Phys. Lett. A*, 365:328–334, 2007.

793. I. Tuval, J. Schneider, O. Piro, and T. Tél. Opening up fractal structures of three-dimensional flows via leaking. *EuroPhys. Lett.*, 65:633–639, 2004.

794. E. Tyrkiel. On the role of chaotic saddles in generating chaotic dynamics in nonlinear driven oscillators. *Int. J. Bif. Chaos*, 15:1215–1238, 2005.

795. D. Umberger, C. Grebogi, E. Ott, and B. Afeyan. Spatiotemporal dynamics in a dispersively coupled chain of nonlinear oscillators. *Phys. Rev. A*, 39:4835–4842, 1989.

796. T. Usuki, M. Saito, M. Takatsu, R. A. Kiehl, and N. Yokoyama. Numerical analysis of ballistic-electron transport in magnetic fields by using a quantum point contact and a quantum wire. *Phys. Rev. B*, 52:8244–8255, 1995.

797. D. B. Vasconcelos, R. L. Viana, S. R. Lopes, and S. E. de S. Pinto. Conversion of local transient chaos into global laminar states in coupled map lattices with long-range interactions. *Physica A*, 367:158–172, 2006.

798. R. D. Vilela, A. P. S. de Moura, and C. Grebogi. Finite-size effects on open chaotic advection. *Phys. Rev. E*, 73:026302, 2006.

799. R. D. Vilela and A. E. Motter. Can aerosols be trapped in open flows? *Phys. Rev. Lett.*, 99:264101, 2007.

800. D. Viswanath and P. Cvitanović. Stable manifolds and the transition to turbulence in pipe flow. *J. Fluid. Mech*, 627:215, 2009.

801. F. Vivaldi, A. Casati, and I. Guarneri. Origin of long-time tails in strongly chaotic systems. *Phys. Rev. Lett.*, 51:727–730, 1983.

802. J. Vollmer. Chaos, spatial extension, transport, and non-equilibrium thermodynamics. *Phys. Rep.*, 372:131–267, 2002.

803. J. Vollmer, T. M. Schneider, and B. Eckhardt. Basin boundary, edge of chaos, and edge state in a two-dimensional model. *New J. Phys.*, 11:013040, 2009.

804. J. Vollmer, T. Tél, and W. Breymann. Dyanmical-system models of transport: chaos characteristics, the macroscopic limit, and irreversibility. *Physica D*, 187:108–127, 2004.

805. G. A. Voth, G. Haller, and J. P. Gollub. Experimental measurements of stretching fields in fluid mixing. *Phys. Rev. Lett.*, 88:254501, 2002.

806. H. Waalkens, A. Burbancks, and S. Wiggins. A computational procedure to detect a new type of high-dimensional chaotic saddle and its application to the 3D Hill's problem. *J. Phys. A*, 37:L257–L265, 2004.

807. H. Waalkens, A. Burbanks, and S. Wiggins. Escape from planetary neighbourhoods. *Mon. Not. R. Astron. Soc*, 361:763–775, 2004.

808. H. Waalkens, A. Burbanks, and S. Wiggins. Phase space conduits for reaction in multidimensional systems: HCN isomerization in three dimensions. *J. Chem. Phys.*, 121:6207–6225, 2004.

809. H. Waalkens, A. Burbanks, and S. Wiggins. Efficient procedure to compute the microcanonical volume of initial conditions that lead to escape trajectories from a multidimensional potential well. *Phys. Rev. Lett.*, 95:084301, 2005.

810. H. Waalkens, R. Schubert, and S. Wiggins. Wigner's dynamical transition state theory in phase space: classical and quantum. *Nonlinearity*, 21:R1–R118, 2008.

811. H. Waalkens and S. Wiggins. Direct construction of a dividing surface of minimal flux for multi-degree-of-freedom systems that cannot be crossed. *J. Phys. A-Math. Gen.*, 37:L435–L445, 2004.

812. A. Wacker, S. Bose, and E. Schöll. Transient spatio-temporal chaos in a reation-diffusion model. *Europhys. Lett.*, 31:257–262, 1995.

813. R. Wackerbauer. Master stability analysis in transient spatiotemporal chaos. *Phys. Rev. E*, 76:056207, 2007.

814. R. Wackerbauer and S. Kobayashi. Noise can delay and advance the collapse of spatiotemporal chaos. *Phys. Rev. E*, 75:066209, 2007.

815. R. Wackerbauer and K. Showalter. Collapse of spatiotemporal chaos. *Phys. Rev. Lett.*, 91:174103, 2003.

816. F. Waleffe. Three-dimensional coherent states in plane shear flows. *Phys. Rev. Lett.*, 81:4140–4143, 1998.

817. J. Walker. The distorted images seen in Christmas-tree ornaments and other reflecting balls. *Sci. Am.*, 259:84–87, The Amateur Scientist, December, 1988.

818. H. O. Wang and E. H. Abed. Control of nonlinear phenomena at the inception of voltage collapse. In *Proceedings of the 1993 American Control Conference*, pages 2071–2075, San Francisco, 1993.

819. H. O. Wang, E. H. Abed, and A. M. A. Hamdan. Bifurcations, chaos and crises in voltage collapse of a model power system. *IEEE Trans. Circ. Syst. I: Fund. Theor. Appl.*, 41:294–302, 1994.

820. J. Wang, P. G. Sorensen, and F. Hynne. Transient period doublings, torus oscillations, and chaos in a closed chemical-system. *J. Phys. Chem.-US*, 98:725–727, 1994.

821. J. Wang, P. G. Sorensen, and F. Hynne. Transient complex oscillations in the closed Belousov-Zhabotinsky reaction: Experimental and computational studies. *Z. Phys. Chemie*, 192:63–76, 1995.

822. Y. Wang, J. Singer, and H. Bau. Controlling chaos in a thermal-convection loop. *J. Fluid Mech.*, 237:479–498, 1992.

823. P. Widmann, M. Gorman, and K. Robbins. Nonlinear dynamics of a convection loop. 2. Chaos in laminar and turbulent flows. *Physica D*, 36:157–166, 1989.

824. M. Widom, D. Bensimon, L. Kadanoff, and S. Shenker. Strange objects in the complex-plane. *J. Stat. Phys.*, 32:443–454, 1983.

825. J. Wiersig and J. Main. Fractal Weyl law for chaotic microcavities: Fresnel's laws imply multifractal scattering. *Phys. Rev. E*, 77:036205, 2008.

826. S. Wiggins. *Chaotic Transport in Dynamical Systems*. Springer, Berlin, first edition, 1992.

827. S. Wiggins. The dynamical systems approach to Lagrangian transport in ocean flows. *Annu. Rev. Fluid Mech.*, 37:295–338, 2005.

828. S. Wiggins, G. Haller, and I. Mezić. *Normally Hyperbolic Invariant Manifolds in Dynamical Systems*. Springer, New York, 1994.

829. S. Wiggins, L. Wiesenfeld, C. Jaffé, and T. Uzer. Impenetrable barriers in phase-space. *Phys. Rev. Lett.*, 86:5478–5481, 2001.

830. J. W. Wilder. Effect of initial condition sensitivity and chaotic transients on predicting future outbreaks of gypsy moths. *Ecological Modelling*, 136:49–66, 2001.

831. F. H. Willeboordse. Supertransients and suppressed chaos in the diffusively coupled logistic lattice. *Chaos*, 89:89–98, 1994.

832. A. Wolf, J. B. Swift, H. L. Swinney, and J. A. Vastano. Determining Lyapunov exponents from a time series. *Physica D*, 16:285–317, 1985.

833. S. Wolfram. *Cellular Automata and Complexity*. Addison-Wesley, Reading, MA, first edition, 1994.

834. M. Woltering and M. Markus. Riddled-like basins of transient chaos. *Phys. Rev. Lett.*, 84:630–633, 2000.

835. Z.-B. Wu. Generalization of the JTZ model to open plane wakes. *Chaos*, 20:013122, 2010.

836. Y. Xiao, Y. Wang, and Y.-C. Lai. Dependence of intermittency scaling on threshold in chaotic systems. *Phys. Rev. E*, 80:057202, 2009.

837. B. Xu, Y.-C. Lai, L. Zhu, and Y. Do. Experimental characterization of transition to chaos in the presence of noise. *Phys. Rev. Lett.*, 90:164101, 2003.

838. T. Yalcinkaya and Y.-C. Lai. Chaotic scattering. *Comp. Phys.*, 9:511–518, 1995.

839. Y. Y. Yamaguchi, J. Barré, F. Bouchet, T. Dauxois, and S. Ruffo. Stability criteria of the Vlasov equation and quasi-stationary sates of the HMF model. *Physica A*, 337:36–66, 2004.

840. W. Yang, M. Ding, A. J. Mandell, and E. Ott. Preserving chaos: control strategies to preserve complex dynamics with potential relevance to biological disorders. *Phys. Rev. E*, 51:102–110, 1995.

841. H. W. Yin, J. D. Dai, and H. J. Zhang. Average lifetime and geometric properties for superlong transients in a hybrid optical bistable system. *Phys. Rev. E*, 54:371–375, 1996.

842. S. Yonker and R. Wackerbauer. Nonlocal coupling can prevent the collapse of spatiotemporal chaos. *Phys. Rev. E*, 73:026218, 2006.

843. J. A. Yorke and E. D. Yorke. Metastable chaos: the transition to sustained chaotic behavior in the Lorenz model. *J. Stat. Phys.*, 21:263–277, 1979.

844. L. Yu, E. Ott, and Q. Chen. Fractal distribution of floaters on a fluid surface and the transition to chaos for random maps. *Physica D*, 53:102–124, 1991.

845. J. C. Zahnow and U. Feudel. Moving finite-size particles in a flow: a physical example of pitchfork bifurcations of tori. *Phys. Rev. E*, 77:026215, 2008.

846. J. C. Zahnow, R. D. Vilela, U. Feudel, and T. Tél. Aggregation and fragmentation dynamics of inertial particles in chaotic flows. *Phys. Rev. E*, 77:055301, 2008.

847. J. C. Zahnow, R. D. Vilela, U. Feudel, and T. Tél. Coagulation and fragmentation dynamics of inertial particles. *Phys. Rev. E*, 80:026311, 2009.

848. S. Zambrano and M. A. F. Sanjuán. Exploring partial control of chaotic systems. *Phys. Rev. E*, 79:026217, 2009.

849. S. Zambrano, M. A. F. Sanjuán, and J.A. Yorke. Partial control of chaotic systems. *Phys. Rev. E*, 77:055201(R), 2008.

850. J. Zamora-Munt, C. Masoller, and J. García-Ojalvo. Transient low-frequency fluctuations in semiconductor lasers with optical feedback. *Phys. Rev. A*, 81:033820, 2010.

851. G. Zaslavsky. Chaotic dynamics and the origin of statistical laws. *Phys. Today*, 52:39–45, 1999.

852. G. Zaslavsky. Chaos, fractional kinetics, and anomalous transport. *Phys. Rep.*, 371:461–580, 2002.

853. G. Zaslavsky and M. K. Tippett. Connection between recurrence-time statistics and anomalous transport. *Phys. Rev. Lett.*, 67:3251–3254, 1991.

854. E. Ziemniak, C. Jung, and T. Tél. Tracer dynamics in open hydrodynamical flows as chaotic scattering. *Physica D*, 76:123–146, 1994.

855. R. Zillmer, N. Brunel, and D. Hansel. Very long transients, irregular firing, and chaotic dynamics in networks of randomly connected inhibitory integrate-and-fire neurons. *Phys. Rev. E*, 79:031909, 2009.

856. R. Zillmer, R. Livi, A. Politi, and A. Torcini. Desynchronization in diluted neural networks. *Phys. Rev. E*, 74:036203, 2006.

857. H. Zou, S. Guan, and C.-H. Lai. Dynamical formation of stable irregular transients in discontinuous map systems. *Phys. Rev. E*, 80:046214, 2009.

858. A. Zumdieck, M. Timme, T. Geisel, and F. Wolf. Long chaotic transients in complex networks. *Phys. Rev. Lett.*, 93:244103, 2004.

Index